From the Max Planck Institute of Biochemistry,

Department: Molecular Medicine

Director: Prof. Dr. Reinhard Fässler

Dissertation

zum Erwerb des Doctor of Philosophy (Ph.D.) an der

Medizinischen Fakultät der

Ludwig-Maximilians-Universität München

The role of parvins in the cardiovascular system

submitted by

Sarah Scholze

from

Dresden, Germany

Munich, 2021

_____

First supervisor:	Prof. Dr. Dr. med Oliver Söhnlein
Second supervisor:	Dr. Ralph Böttcher
Dean:	Prof. Dr. med. dent. Reinhard Hickel
Date of oral defense:	19.01.2021

TABLE OF CONTENT

LIST OF ABBREVIATIONS

ANP	Atrial natriuretic peptide
ATP	Adenosine triphosphate
α-pv	α-parvin
α-SMA	α-smooth muscle actin
β-PIX	PAK-interacting exchange factor-beta
β-pv	β-parvin
Cas9	CRISPR-associated protein 9
Cdc42	Cell division cycle 42
CH	Calponin homology domain
CdGAP	Cdc42 GTPase-activating protein
CRISPR	Clustered regularly interspaced short palindromic repeats
DAG	Diacylglycerol
ddH_2O	double-distilled water
DLC-1	Deleted in liver cancer 1
ECC	Excitation-contraction coupling
ECM	Extracellular matrix
EGFR	Epidermal growth factor receptor
ERK	Extracellular signal-regulated kinase
FA	Focal adhesion
FAK	Focal adhesion kinase
FAT	Focal adhesion targeting domain
FBS	Fetal bovine serum
FN	Fibronectin
GAP	GTPase-activating protein
GDI	Guanine nucleotide dissociation inhibitor
GEF	Guanine nucleotide exchange factor
HEK293	Human embryonic kidney cells
HEPES	2-[4-(2-hydroxyethyl)-piperazin-1-yl]ethanesulfonic acid
Hic-5	Hydrogen peroxide inducible clone-5
IF	Immunofluorescence
ILK	Integrin-linked kinase
i.p.	intraperitoneal
IP	Immunoprecipitation
IPP	ILK-PINCH-parvin complex
IP_3	Inositol 1,4,5-triphosphate
LC-MS/MS	Liquid chromatography-tandem mass spectrometry
LCP-1	Lymphocyte cytosolic protein 1
LIMK	LIM (Lin11, Isl1, Mec3) kinase
MAPK	Mitogen-activated protein kinases
MCM	MerCreMer
MLC	Myosin light chain
MLCK	Myosin light chain kinase
MLCP	Myosin light chain phosphatase
MOVAS	Mouse vascular smooth muscle cells
Mprip	Myosin phosphatase RhoA-interacting protein

MYPT1	Myosin phosphatase target subunit 1
NPxY motif	Asn-Pro-X-Tyr motif
NMVCs	Neonatal mouse ventricular cardiomyocytes
NRVCs	Neonatal rat ventricular cardiomyocytes
o/n	overnight
PAK1	p21-activated kinase
PBS	Phosphate buffered saline
PCR	Polymerase chain reaction
PD	Pulldown
PDGRF	Platelet-derived growth factor receptor
PECAM-1	Platelet endothelial cell adhesion molecule 1
PH	Pleckstrin homology
PINCH	Particularly interesting Cys-His-rich protein
PIP2 (PtdIns-4,5-P_2)	Phosphatidylinositol-4,5-bisphosphate
PIP3	Phosphatidylinositol-3,4,5-trisphosphate
PKC	Protein kinase C
PLC	Phospholipase C
Rac	Ras-related C3 botulinum toxin substrate 1
RhoA	Ras homologous gene A
ROCK	Rho-associated kinase
RSU-1	Ras suppressor protein 1
RT	room temperature
s.d.	Standard deviation
SDS-PAGE	Sodium dodecyl sulfate polyacrylamide gel electrophoresis
SMMHC	Smooth muscle myosin heavy chain
START	Steroidogenic acute regulatory (StAR)-related lipid transfer
TESK1	Testicular protein kinase 1
TGF-β	Transforming growth factor β
TpnT	Troponin-T
VEGFR2	Vascular endothelial growth factor receptor 2
vSMC	Vascular smooth muscle cells
WASP	Wiskott-Aldrich Syndrome Protein
WH2	WASP-homology 2 domain

LIST OF FIGURES

LIST OF TABLES

SUMMARY

Cell adhesion is a fundamental feature of multicellular organisms that allows cells to attach to each other or to the extracellular matrix (ECM) to form functional tissues and organs. One important class of cell adhesion molecules are integrins, α/β heterodimeric transmembrane receptors that lack intrinsic enzymatic activity and actin binding sites. As a result, these receptors rely on the recruitment of adaptor and signaling molecules to their cytoplasmic tails to connect to the actin cytoskeleton and to transmit signals bidirectional across the membrane. Thus, the recruited cytoplasmic tail interactors are important for the ability of the integrin receptors to regulate various cellular functions, including cell spreading, migration, proliferation, differentiation and survival. Among the recruited adaptor molecules that link the integrins to the actin cytoskeleton, are members of the parvin family.

Parvins are a family of three (α-, β- and γ-parvin) actin-binding focal adhesion (FA) proteins that consist of two in tandem calponin homology (CH) domains. Each member of the protein family forms a complex together with integrin-linked (pseudo-)kinase (ILK) and particularly interesting new cysteine-histidine protein (PINCH) termed ILK-PINCH-parvin (IPP) complex which is critically involved in integrin-dependent signaling. As such, the IPP complex is a key regulator in vascular development and *in vivo* deletion of ILK, PINCH or α-parvin results in embryonic lethality as consequence of multiple cardiovascular defects (e.g. hemorrhages, edema, aneurysm). Yet, a detailed analysis of the cardiac defects upon α-parvin deletion *in vitro* and *in vivo* in neonatal and adult mice is lacking. Cells depleted in one of the IPP complex members exhibit adhesion, spreading and migration defects due to defective integrin signaling. Among other defects, these cells are hypercontractile, accompanied by increased RhoA/ROCK/MLC2 signaling. However, it is unknown how the IPP complex, in particular α-parvin, regulates RhoA activity. The first aim of my thesis was therefore to investigate the molecular function of α-parvin in isolated neonatal mouse ventricular cardiomyocytes (NMVCs) and vascular smooth muscle cells (vSMCs) *in vitro*, the contractile cells in the heart and blood vessels, respectively. While α-parvin is ubiquitously expressed, except in hematopoietic cells, the expression of its family member β-parvin is enriched in the heart and skeletal muscle. However, whether β-parvin can compensate the loss of α-parvin in neonatal and adult cardiomyocytes is not known. Another aim of my thesis was therefore, to investigate the functional divergence and potential compensatory behavior between the two parvin isoforms *in vitro* and *in vivo*.

To achieve these goals, I first analyzed the subcellular localization of α- and β-parvin in isolated neonatal and adult cardiomyocytes and in vSMCs. In cardiomyocytes, α- and β-parvin localized to costameres and Z-discs; costameres being the main attachment sites which resemble 'focal adhesion'-like matrix attachment sites. Furthermore, the localization of both parvin isoforms to focal adhesions in vSMCs could

be confirmed. Second, I generated and investigated the loss of α-parvin in isolated α-parvin knockout NMVCs and in CRISPR α-parvin knockout MOVAS, a vSM cell line. Deletion of α-parvin in NMVCs resulted in a severe spreading defect on stiff and compliant substrates which was not further enhanced by simultaneous deletion of β-parvin. NMVCs lost the ability to undergo hypertrophic growth and to spontaneously contract upon α-parvin deletion. Additionally, I also investigated the function of α-parvin in adult mice *in vivo*. Surprisingly, Cre deleted mice died very rapidly (within 3-5 days) after tamoxifen induction. However, due to the lethality of control animals, further investigations are necessary to confirm this phenotype. α-parvin deletion in MOVAS cells resulted in early adhesion, spreading and migratory defects which were linked to elevated levels of active GTP-RhoA and phospho-Myosin light chain 2 (pMLC2) indicating an hypercontractile phenotype. Furthermore, conditional deletion of α-parvin specifically from smooth muscle cells in adult mice induced severe intestinal defects with an enlarged stomach, ileum and cecum within 9 weeks.

To identify novel α- or β-parvin-specific interactors, I determined the parvin interactome in cardiomyocytes and smooth muscle cells using two complementary approaches, GFP immunoprecipitation and proximity-dependent biotin identification assays, with subsequent mass spectrometry analysis. A potentially interesting interactor, Myosin phosphatase RhoA interacting protein (Mprip) was further investigated. Although the loss of α-parvin in MOVAS did not lead to altered Mprip expression levels or its mislocalization, Mprip function was impaired in the absence of α-parvin.

In summary, this study shows that α-parvin is an essential component of the integrin-mediated signaling network in contractile cells of the cardiovascular system *in vitro* and *in vivo* in mice, to regulate cell morphology, adhesion, spreading and migration. On a molecular level, the loss of α-parvin can be linked to a misregulation of RhoA activity and two possible pathways connecting α-parvin with RhoA have been identified. Further investigations will be necessary to fully characterize these pathways.

In addition to my main thesis project, I was involved in two other studies. Cytosolic integrin interactors regulate integrin signaling but also integrin activation on the cell surface. While most studies focus on integrin activators, talin and kindlin, integrin inactivators that prevent unwanted integrin activation are less studied. Hui-yuan Tseng, a PhD student under the supervision of Prof. Dr. Reinhard Fässler, took the task to identify conformation-specific αMβ2 integrin interactors using an unbiased proteomics approach (paper I). He incorporated recombinant integrin domains into bicelles and identified lymphocyte cytosolic protein 1 (LCP1) as interactor of associated, inactive αMβ2 integrin. I was involved in the subsequent cell biological analysis in which we were able to show that the knockdown of LCP1 in macrophage cells and in

differentiated neutrophils results in increased αMβ2 integrin surface levels and enhanced cell adhesion in non-activated macrophages.

In the second paper together with the department of Prof. PhD Petra Schwille and Prof. Wolfgang Baumeister, we analyzed the structural architecture of sarcomeres during cardiomyocyte contraction. Although the overall mechanism of muscle contraction is widely known (sliding filament theory), it remained elusive how the sarcomeres produce contractile forces on the structural level. We therefore used *in situ* cryo-electron tomography to analyze sarcomere contraction in frozen-hydrated neonatal rat ventricular cardiomyocytes (paper II). The quantitative analysis revealed that myosin filaments organize in a hexagonal lattice with actin filaments located at trigonal positions already at the neonatal state. Furthermore, we resolved the *de novo* structure of F-actin in complex with tropomyosin at 20.7 Å resolution and analyzed the polarity of thin filaments within the sarcomere.

1 INTRODUCTION

1.1 The integrin family of adhesion receptors

In all tissues, cells are surrounded by a three-dimensional (3D) non-cellular crosslinked network of macromolecules, proteoglycans and fibrous proteins, that form the extracellular matrix (ECM). The ECM fulfills both structural and signaling roles, by providing physical support to the cells and through the initiation of important biochemical and biomechanical cues crucial for tissue morphogenesis, differentiation and homeostasis. [1] Cell adhesion is a fundamental feature of a cell to attach to each other into functional tissues and organs or to attach a cell to the ECM, thereby allowing the transfer of cellular and extracellular environment information. The formation of adhesion structures and their dynamic regulation are indispensable for cell migration, proliferation, differentiation, survival and tissue organization, as well as for wound healing and tumorigenesis. As a result, they play a central role in embryogenesis, remodeling and homeostasis of tissues and organs. [2-4] Cell-cell or cell-ECM attachment is mediated by transmembrane receptors, of which the integrins constitute a major group. [5] Integrins are non-covalently associated heterodimeric transmembrane receptors composed of α and β subunits that mediate the bidirectional communication. [6, 7] Each subunit consists of a large amino-terminal (N-terminal) extracellular domain (ectodomain), a single membrane-spanning domain and a short carboxy-terminal (C-terminal) cytoplasmic tail (except β4 integrin) (**Fig. 1A**). [8] Vertebrates express 18 α- and 8 β-subunits, which assemble in 24 heterodimeric integrin receptors with distinct ligand-binding specificities and signaling properties (**Fig. 1B**). [9] Furthermore, numerous splice variant isoforms of individual α and β subunits exist which can be differentially expressed or modified throughout the development of an organism. [7]

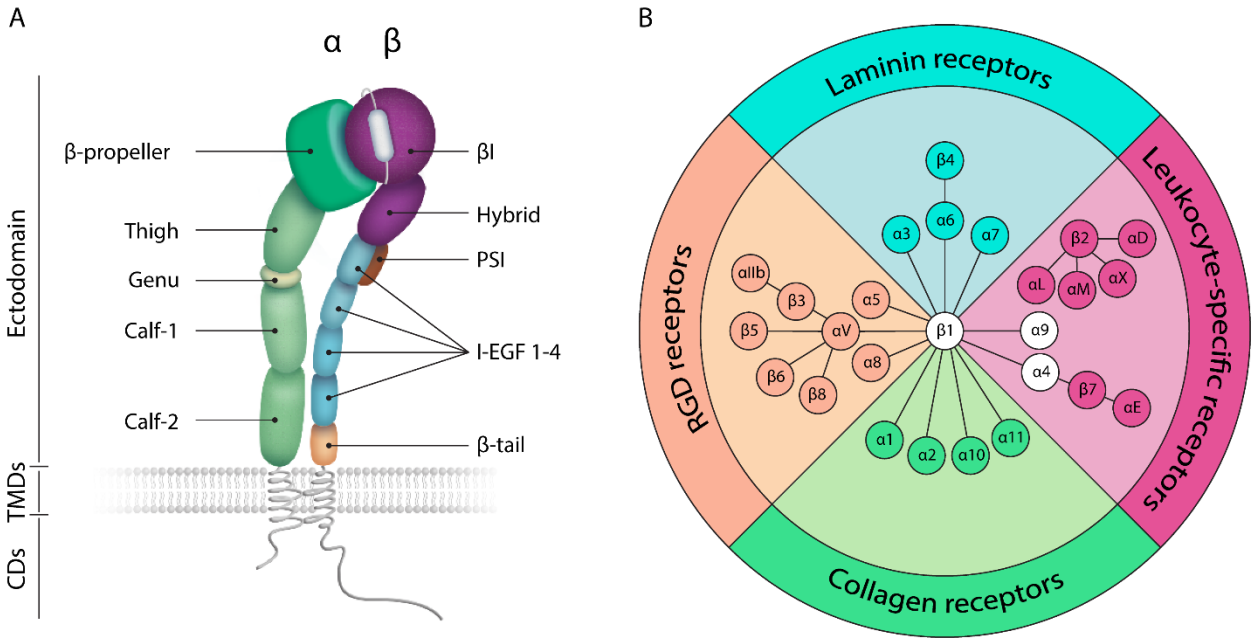

Fig. 1. Integrin architecture and diversity of integrin subunits. (A) Domain organization of the α and β polypeptide chains. CDs, cytoplasmic domains; TMDs, transmembrane domains; PSI, plexin-semaphorin-integrin. Adapted from Luo et al. [10] (B) Classification of integrin heterodimers based upon their classical binding profile. Adapted from LaFoya et al. [11]

The main function of integrins is to establish a link between the ECM and the actin cytoskeleton, thereby providing mechanical support to the cell. [12] The extracellular domain of integrins binds to ECM proteins (ligands) such as collagens and fibronectin or counter receptors on adjacent cells while the cytoplasmic tail interacts with adaptor proteins to create the linkage between the integrin receptor and the cytoskeleton. Apart from the mechanical support, integrins also transmit signals bidirectional between the ECM and the cytoplasm to control a wide range of cellular events such as cell adhesion, migration, proliferation, differentiation and apoptosis. [5, 13-17]

Integrin function can be regulated at different levels, such as cell type-specific expression of integrin heterodimers and the regulation of their cell surface levels. Most notably however, integrin function is controlled through the regulation of the ligand-binding affinity, involving huge conformational changes within the receptor. [10]

1.1.1 Integrin activation and ligand binding

Integrins are expressed in an inactive state on the cell surface, with a low affinity towards their ligands and being unable to transmit signals. [18] It is commonly accepted in the field that integrins adapt distinct conformations with different ligand-binding affinities: a bent-closed low affinity, an extended-closed intermediate affinity and an extended-open high affinity state. [10] 'Integrin activation' is defined as the shift from the low affinity bent-closed conformation to the high affinity extended-open conformation through the mechanism of either 'inside-out' or 'outside-in' activation (**Fig. 2**). [19]

According to the conventional model, integrin activation occurs through the mechanism of 'inside-out' activation (**Fig. 2A**). [19] Integrins in the bent-closed confirmation have the transmembrane domains of the α and β subunits closely associated and their cytoplasmic tails clasped. Activation of integrins by agonists lead to the binding of integrin activation proteins, talin and kindlins, to the cytoplasmic β integrin tail and changes the tilt angle of the β integrin transmembrane domain, resulting in the separation of the α/β transmembrane and cytoplasmic domains. This separation causes the extension and opening of the ectodomain, allowing ligand binding. [19, 20]

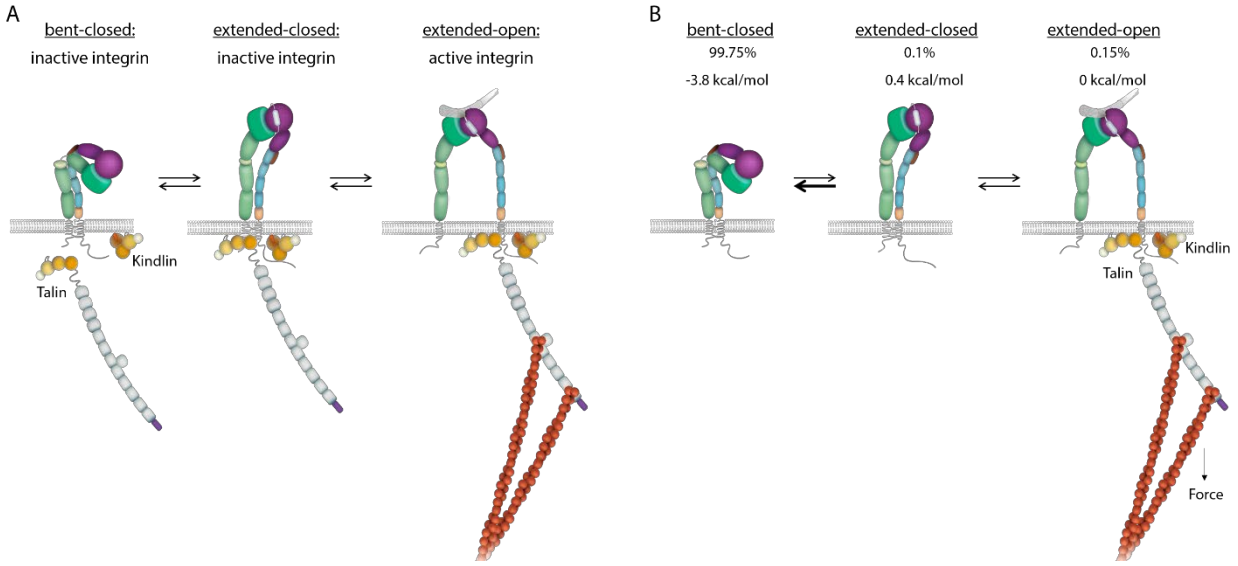

Fig. 2. Models of integrin activation. (A) Conventional model of integrin 'inside-out' activation. Talin recruitment to the β integrin cytoplasmic tail disrupts the association of α and β integrin transmembrane domains, leading to a reorientation of the transmembrane tilt, extension of the ectodomain and opening of the integrin ligand-binding pocket. (B) New model of integrin 'outside-in' activation. According to thermodynamic measurements, integrins favor and adapt the stable bent-closed conformation (indicated by the bold arrow bar). However, due to the existing thermodynamic equilibrium, integrins can fluctuate to the extended-closed and -open conformations. Adapted from Sun et al. [19]

In a recent model it was proposed that integrin activation happens through the mechanism of 'outside-in' activation which is induced by an ECM ligand or counter receptor expressed on another cell (**Fig. 2B**). [19] According to Springer and colleagues who measured the free energy required to obtain the distinct conformations and ligand-binding affinities of α5β1 and α4β1 integrins, the thermodynamic equilibrium plays an important role. [18, 21, 22] The bent-closed conformation has the lowest free energy and is therefore the energetic favored integrin conformation, with 99.75% of surface integrins staying in the bent-closed state. [21, 23] However, due to the thermodynamic equilibrium, integrins also adapt the extended-closed and -open conformations. Once integrins are in the extended-open state binding of talin and kindlins to the β integrin cytoplasmic tail stabilizes integrins in the extended-open conformation through engaging with the force-generating actin cytoskeleton and the transduction of small mechanical forces. [23] This shifts the thermodynamic equilibrium of the distinct integrin conformations in favor of the extended-open state. [19]

Integrin activation must be tightly controlled by integrin activators but also integrin inactivating proteins. Indeed, spontaneous integrin activation in resting cells was shown to have pathological consequences such as thrombosis or tumor metastasis. Furthermore, during cell migration a tight control of the active and inactive state of integrins is important. [24] On the basis of the existing data, integrin activation can be prevented or reduced by at least three mechanisms: (i) preferential binding of adaptor molecules to the clasped integrin, thereby holding the integrin in its inactive state, (ii) competitional binding of adaptor proteins with talin and kindlin or (iii) altering the integrin trafficking, thereby reducing the integrin surface levels. [25] Among the identified integrin inactivators, filamin competes with talin for β integrin tail binding whereas SHANK-associated RH domain-interacting protein (SHARPIN) was shown to bind to the α integrin tails, stabilizing integrins in their bent-closed conformation. [26-28] Additionally, we have previously shown that LCP1, a member of the plastin family of actin-bundling proteins, is part of a ternary complex with αMβ2 integrin and maintains it in its low affinity conformation (paper I). [29]

After their activation, integrins bind to ligands and establish a link between the ECM and the cell. However, the adhesion force of one integrin alone is too weak for a cell to firmly attach to the matrix. Therefore, the lateral association of integrins synergistically combines numerous weak links to the ECM, a process termed 'integrin clustering'. Upon clustering, integrins recruit hundreds of adaptor and signaling molecules to their cytoplasmic tails to assemble a dynamic macromolecular network of proteins that is collectively known as the 'integrin adhesome'. [30] The three-dimensional structure of the integrin adhesome was analyzed by super-resolution fluorescence microscopy and a three-layered structure was described. [31] Vertically, the cytoplasmic tails of integrins, the focal adhesion kinase (FAK) and paxillin belong to the membrane-apposed

integrin signaling layer which is followed by an intermediate force-transduction layer containing talin and vinculin. Zyxin and α-actinin belong to the uppermost actin-regulatory layer. [31] As the short cytoplasmic integrin tails lack intrinsic catalytic activity and actin binding domains, they depend on their cytosolic interactors to transmit signals from the outside across the plasma membrane. [32]

1.1.2 Integrin outside-in signaling and connection to the actin cytoskeleton

Integrin outside-in signaling initiates downstream signaling events that can be grouped into three temporal stages (**Fig. 3**): (i) immediate (<10 min), (ii) short-term (10-60 min) and (iii) long-term effects (>60 min). [33] Rapid phosphorylation of substrates and the upregulation of lipid kinase activity that results in increased phosphatidylinositol-4,5-bisphosphate (PtdIns-4,5-P_2, PIP2) and PtdIns-3,4,5-P_3 (PIP3) concentrations are immediate intracellular effects of integrin activation. [33] Most noticeable are phosphorylation events by FAK and Src kinases. Autophosphorylation of FAK at Tyr397 occurs in response to integrin-ECM adhesion and allows the interaction with Src family kinases via their SH2 domain, thereby stabilizing the active conformation of Src. Phosphorylation of Src Tyr416 and subsequent tyrosine phosphorylations on FAK fully activate the two kinases. [34] The activated FAK/Src complex phosphorylates early focal adhesion proteins including paxillin and p130Cas, thereby generating versatile signaling platforms. [33]

Within a few minutes, the enhanced tyrosine phosphorylation and the increased concentration of lipid second messengers lead to the activation of several signaling pathways including the rat sarcoma (Ras)/rapidly accelerated fibrosarcoma (Raf)/extracellular signal-regulated kinase (ERK)/mitogen-activated protein kinase (MAPK) cascade, or c-Jun N-terminal kinase (JNK) and Akt signaling. Furthermore, the activation of Ras homolog (Rho) family GTPases and other actin regulatory proteins that are involved in actin cytoskeletal reorganization also belong to the short-term effects. [33]

One key role of the integrin outside-in signaling is the establishment and regulation of the connection between the cytoplasmic domain of integrins and the cellular actin cytoskeleton. As integrins lack actin binding sites, this link is mediated by their binding partners, which belong to one of the four classes: (1) integrin interactors that directly bind the actin cytoskeleton and function as structural adapters (e.g. talin, filamin, α-actinin,); (2) integrin-bound proteins that function as scaffolds for actin-binding proteins, thereby being indirectly involved in the association with the actin cytoskeleton (e.g. paxillin, ILK, and FAK); (3) non-integrin-associated actin-binding proteins like parvin or vinculin and (4) adaptor and signaling molecules that regulate integrin signal transduction but do not interact with integrins or the actin cytoskeleton themselves. [35]

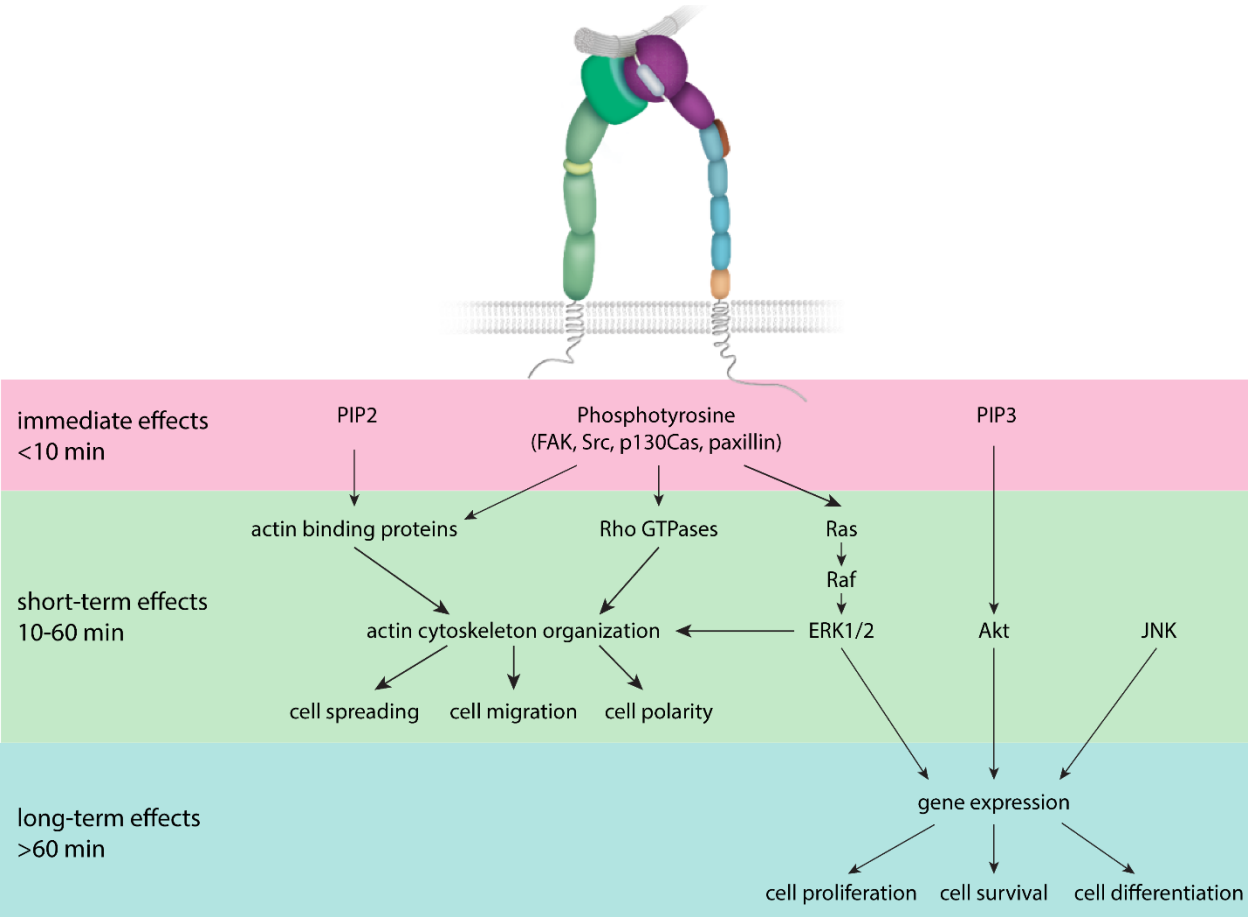

Fig. 3. Integrin outside-in signaling. Integrin activation stimulates downstream signaling events that can be divided into three temporal stages: immediate, short-term and long-term effects. Adapted from Legate et al. [33]

Upon ECM binding and integrin clustering, talin is recruited to the β integrin tail to establish the initial link to the actin cytoskeleton. [36] Talin binds and activates the PIP2-producing enzyme type Iγ phosphatidylinositol 4-phosphate 5-kinase (PIPKIγ) in an integrin and growth factor signaling-dependent fashion, leading to an enhanced PIP2-mediated talin activation at the plasma membrane. [37, 38] The importance of talin binding was shown in an *in vivo* study reporting that mice lacking *talin-1* die during gastrulation due to defects in cytoskeletal organization and cell migration. Furthermore, talin depletion from mouse skeletal muscle impaired muscle development *in vivo*. [39-41] After talin binding to the β integrin cytoplasmic domain, vinculin is quickly recruited to the talin rod domain upon mechanical stretching or PIP2-induced exposure of cryptic binding sites, to reinforce the linkage to the actin cytoskeleton. [42] In the absence of PIP2, vinculin can also be recruited to the integrin adhesion sites by directly binding paxillin. [43] Upon actin binding, vinculin recruits the Arp2/3 complex and induces actin polymerization. [44] Furthermore, α-actinin is recruited to FAs in a force-dependent manner by either vinculin, talin or direct β integrin interaction and serves as actin crosslinker. [45] Moreover, several other

proteins interact with α-actinin such as zyxin, vinculin, and ERK1/2, showing that α-actinin also exhibits an important role as scaffold within integrin-dependent adhesion sites. [46] The interaction of α-actinin to the actin filaments is highly regulated; while PIP2 binding increases the interaction, FAK-mediated phosphorylation of α-actinin reduces its actin binding affinity. [46] Another focal adhesion protein that binds to the β integrin cytoplasmic domain is the scaffolding protein integrin-linked (pseudo-)kinase (ILK). [47] Together with PINCH and parvin, which both harbor a Wiskott-Aldrich syndrome protein (WASP)-homology 2 (WH2) domain, it constitutes the ILK-PINCH-parvin (IPP) complex and establishes a link to the actin cytoskeleton. [16] ILK as well as parvins directly interact with paxillin and the integrin-actin cytoskeletal connection can also be mediate via this linkage. [48-50]

Following the upregulation of several integrin-dependent signaling pathways eventually leads to alterations in the genetic program that controls cell proliferation, differentiation and survival (long-term consequences). [33]

In addition, integrin-mediated signaling is also regulated by the cross-talk of integrins with several growth factor receptors (e.g. EGFR, VEGFR2, PDGFR), which intersects at multiple levels and results in the differential regulation of downstream effectors. [51-55] An excellent example of the interactive growth factor and integrin signaling is the Ras/ERK/MAPK pathway downstream of the FAK/Src complex. The phosphorylation of ERK2 leads to myosin light chain kinase (MLCK)-dependent changes in FA dynamics, as well as cyclin D1 and PI-3-kinase activity-dependent regulation of cell proliferation, cell cycle progression, and cell survival. [56, 57] In addition, p21-activated kinase 1 (PAK1) is activated by the FAK/Src complex, leading to the phosphorylation of MEK1 on Ser298. [58]

Overall, the connection between integrins and the actin cytoskeleton is established and regulated on multiple levels and the individual actin-binding components within integrin-mediated adhesions are highly interconnected. Furthermore, integrin activation initiates the formation of numerous phosphoprotein complexes that regulate the actin cytoskeleton, in particular through the activation of Rho GTPases (see 1.1.4).

1.1.3 Integrin-dependent adhesion structures

Integrin-dependent adhesion structures localize in distinct areas of the cells, differing between cell types and can be classified by their morphology, molecular composition and dynamics. [3, 4] Cells grown in a 3D environment develop a variety of 3D adhesion structures which represent an *in vivo* composite of focal (α-actinin, phosphorylated paxillin-rich) and fibrillar (α5β1 integrin-rich) adhesion components. [4, 59] However, the full diversity of *in vivo* adhesion structures and their functions still remain to be characterized.

The central focus of various studies are *in vitro* adhesion structures in cells grown on rigid 2D surfaces. Here, a number of integrin-dependent adhesion structures have been defined: nascent adhesions, focal complexes, focal and fibrillar adhesions, as well as podosomes, reticular adhesions and costameres. Comparable adhesive structures were also observed *in vivo* such as apical plaques and focal adhesions in endothelial cells in guinea pig aorta or paxillin-positive dense plaques in chicken gizzard smooth muscle tissues. [60, 61]

Nascent adhesions are the first integrin-based adhesion structures observable, emerging within the lamellipodium (**Fig. 4**). [62] They contain only few integrins and are dot-shaped, very small (~100 nm in diameter) and highly transient structures that either disassemble very fast ('turning over') or mature into focal complexes. The maturation into focal complexes is characterized by further integrin clustering and recruitment of adaptor proteins to the cytoplasmic tail. Focal complexes are adhesions in the early state of maturation, still exhibiting a punctate structure. They are larger than nascent adhesions (>100 nm in diameter), grow at the lamellipodium-lamellum interface and are induced by Rac1. [62-64] If further stabilized, they will mature and form focal adhesions (FAs), a transition that is dependent on myosin IIA motor activity. Focal adhesions are sites of tight integrin-mediated cell-ECM adhesion. Structurally, they are flat elongated structures within the cell periphery at the termini of actin stress fibers. Stress fibers consist of contractile bundles of actin and myosin filaments that contain a large number of additional accessory proteins such as the actin filament crosslinker α-actinin. [3, 65] One distinct marker for mature FAs is the LIM-domain protein zyxin, which localizes to FAs but not nascent adhesions or focal complexes. [66] Fibrillar adhesions arise from further maturing focal adhesions and are elongated structures that form mainly along fibronectin fibrils localized more centrally within a cell. In contrast to FAs, fibrillar adhesions are not associated with stress fibers and contain only α5β1 integrin. The maturation process is characterized by the recruitment of tensin and the actomyosin-dependent centripetal translocation of fibronectin receptors (e.g. α5β1 integrin). [67]

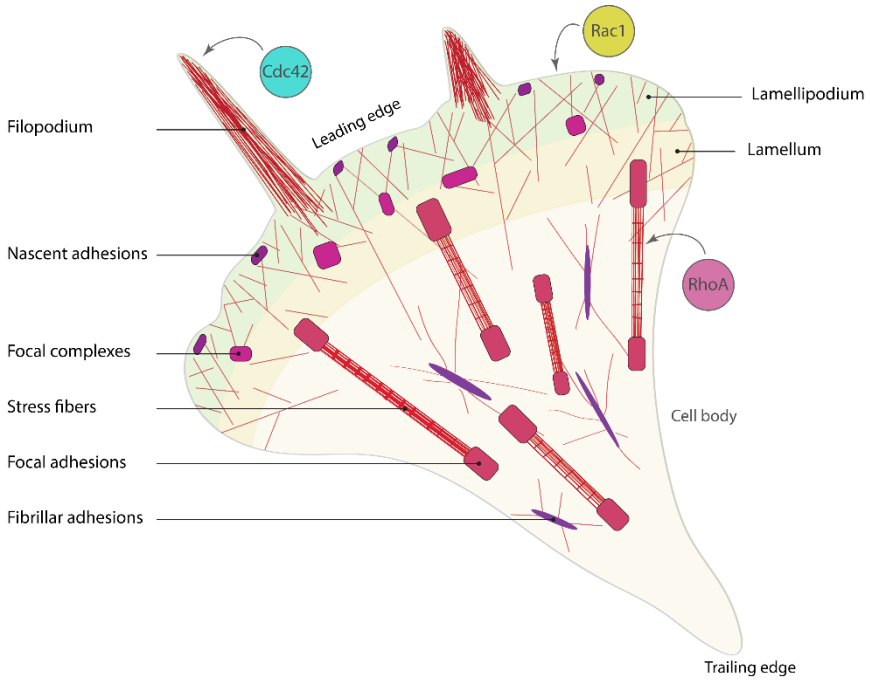

Fig. 4. Cell adhesion structures commonly found on 2D substrates and actin-based motility structures. Adapted from Ladoux and Nicolas. [68]

Podosomes, which are mainly found in fast migratory and invasive cell lines such as osteoclasts, macrophages and dendritic cells, represent structurally and functionally different adhesion structure. [69] They are small (0.5-1 µm in diameter), ring-like adhesions with a core containing F-actin and actin-associated proteins which is surrounded by a ring structure of plaque proteins such as vinculin and talin. Functionally, podosomes are able to participate in ECM degradation, which clearly distinguishes them from other adhesion structures (except invadopodia). [69]

Reticular adhesions are the most recently described class of cell-matrix attachment structures. They are formed by αVβ5 integrin during interphase, persist through mitosis and thereby provide cells the ECM anchor for an efficient cell division. Interestingly, these adhesion structures have an unique adhesome lacking many consensus adhesome components such as talin and vinculin, but are highly enriched in PIP2-binding proteins. [70]

Cardiomyocytes, the contractile units of the heart, exhibit yet another cell-matrix integrin-dependent adhesion structure, known as costameres (**Fig. 14B**). Many adhesion proteins found in focal adhesions, including talin, vinculin and the IPP complex are also components of costameres. [71] Costameres are subsarcolemmal, Z-line associated adhesion plaques found in striated muscle which provide a mechanical linkage between the cytoskeleton and the ECM. Similar structures were found above the M-lines of the contractile apparatus. [72] Costameres are mainly composed of two complexes, the dystrophin-

glycoprotein complex and integrins. Furthermore, desmin is an important subunit of the intermediate filaments, being among other proteins responsible for the organization of costameres. Intermediate filaments surround the Z-discs and link the contractile unit of muscle cells to the sarcolemma, nucleus and other cytoplasmic organelles, thereby providing structural solidity and integrity to the cell. [73] All three components are required for efficient signal transduction and mechanical sensing, hence, deletion of or mutations in costamere proteins are linked to many types of muscle dystrophy. [74]

Despite their differences in size and appearance, all cell-matrix adhesion structures described are mediated by integrins and fulfill two functions: (i) they physically link the extracellular matrix to the intracellular actin cytoskeleton and (ii) they function as sites of localized cell signaling. [75]

1.1.4 Actin dynamics and Rho GTPase signaling

Cell migration is important for development and homeostasis of multicellular organisms and highly depends on dynamic assembly and disassembly of actin filaments. These filaments organize into defined subcellular structures, such as lamellipodia and filopodia, and the formation of these different actin structures depends on the function of a class of small Rho GTPases Ras homologous gene A (RhoA), Ras-related C3 botulinum toxin substrate 1 (Rac1) and cell division cycle 42 (Cdc42) (**Fig. 4**).

The Rho family of GTPases, a subfamily of the rat sarcoma (Ras) protein family, is a family of small (~21 kDa) signaling G proteins found in all eukaryotes that are key regulators of the intracellular actin dynamics. [76] They regulate cytoskeleton organization and various cellular functions such as adhesion, migration, proliferation, and apoptosis. The cycling of G proteins between the active GTP-bound and the inactive GDP-bound state (**Fig. 5**), is spatiotemporally controlled by three classes of regulatory proteins: guanine nucleotide exchange factors (GEFs), GTPase-activating proteins (GAPs) and guanine nucleotide dissociation inhibitors (GDIs). [77] GDIs retain the Rho GTPases in an inactive state in the cytoplasm by forming a high-affinity complex with the geranylgeranyl membrane-targeting moiety present at the C-terminus of the Rho GTPases. After dissociation from the GDI, Rho GTPases relocate to the plasma membrane and insert into the lipid bilayer through their isoprenylated C-terminus. [78] At the plasma membrane, the Rho GTPases interact with membrane-associated GEFs that exchange GDP for GTP, thus, activating the GTPase. In contrast, GAPs inactivate the Rho GTPases by promoting the GTP hydrolysis to GDP. [76]

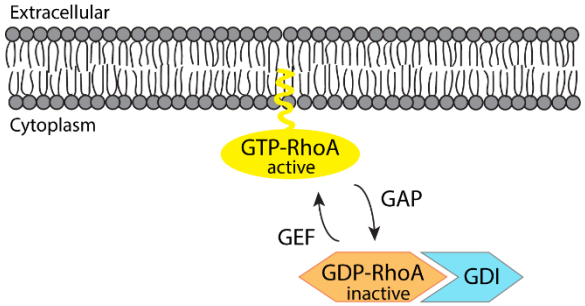

Fig. 5. The RhoA GTPase activation cycle. GDIs bind and retain inactive GDP-bound RhoA in the cytoplasm. After being released from the GDIs RhoA GTPases translocate to the plasma membrane where their activation status is regulated by GEFs and GAPs. Adapted from Huveneers and Danen. [76]

The expression of constitutively activated mutants of RhoA and Rac1 in fibroblasts was shown to induce the assembly of contractile actomyosin filaments (stress fibers) and actin-rich surface protrusions called lamellipodia, respectively. [79, 80] Cdc42 was shown to induce the formation of filopodia, actin-rich, finger-like membrane extensions (**Fig. 4**). [81, 82] Although Rac1 and Cdc42 lead to the formation of morphologically distinct plasma membrane protrusions, they both initiate actin polymerization through the actin-nucleating activity of the Arp2/3 complex that they indirectly activate through members of the Wiskott-Aldrich syndrome protein (WASP) family. [83] For lamellipodia formation, for example, the WASP family verprolin homologous protein (WAVE) complex, which accumulates at the lamellipodia tip, activates the Arp2/3 complex at the interface between the plasma membrane and the growing actin network. [84, 85] The small Rho GTPase Rac1 directly targets and activates the heteropentameric WAVE complex, thereby stimulating lamellipodia formation. [86, 87] In addition to activating the WAVE complex, Rac1 and Rac2, as well as Cdc42, activate the formin mDia2, thereby inducing actin polymerization. [88, 89] Another signaling pathway involved in lamellipodia or filopodia formation involves serine/threonine kinases of the p21-activated kinase (PAK) protein family. PAK proteins are regulated by Rac and Cdc42 and are direct activators of LIM (Lin11, Isl1, Mec3) kinase (LIMK). LIMK phosphorylates and thereby inhibits the depolymerizing activity of cofilin, which effects the lamellipodia and filopodia turnover. [87]

While the diaphanous-related formin (DRF) protein family member mDia2 is a target of Rac and Cdc42, RhoA targets mDia1. Direct binding of GTP-RhoA to mDia1 leads to the relief of an autoinhibitory interaction and the exposure of an formin homology 2 (FH2) domain on mDia1 that directly interacts with the barbed end of actin filaments. Binding of mDia1 to actin, which is enhanced through the binding of profilin to the FH1 domain of mDia1, prevents the binding of other capping proteins to the actin filament. [90]

During the initial phase of integrin-mediated cell adhesion and spreading, GTP-RhoA levels are inhibited while Rac1 and Cdc42 are activated. This occurs through the activation of FAK through

autophosphorylation, resulting in the presentation of a binding site for the Src-homology 2 (SH2) domain of Src. [91] As mentioned above, the activated FAK-Src complex phosphorylates various adaptor proteins including p130Cas and paxillin. Phosphorylation of p130Cas results in the recruitment of an unconventional two-part GEF for Rac1 composed of the dedicator of cytokinesis (Dock180) and engulfment and cell motility protein 1 (ELMO1), while phosphorylated paxillin recruits the Cdc42 and Rac1-specific GEF PAK-interacting exchange factor-beta (β-PIX). [92, 93] The FAK-Src complex also inhibits RhoA activity through the regulation of p190RhoGAP. [94-96] As spreading ends, Rac1 and Cdc42 activity decreases and RhoA activity is gradually increased, driving stress fiber formation and focal adhesion maturation. This well-established antagonism between Rac and RhoA results in the suppression of one another's activity. One other example of this antagonism is the phosphorylation of FilGAP by the Rho-associated kinase ROCK, which stimulates its GAP activity towards Rac, leading to the suppression of lamellipodia formation. [97]

The actin-driven processes described are involved in cell-cell or cell-ECM attachment and cell spreading but also regulate cell migration. A cell requires the tight spatiotemporal coordination of assembly and disassembly of cell-ECM adhesions with membrane protrusion and contraction to move directional along gradients of ECM components. This is achieved by the tightly regulated activation and inactivation of Rho GTPases and their downstream effectors in space and time. [76] For example, Rho activity is associated with FA assembly, cell body contraction and cell tail retraction in migrating cells. At the retracting end, non-muscle myosin II localizes to stress fibers, promoting the movement of the cell body through contraction and thereby facilitating the detachment of the cell rear during migration. [98]

1.1.5 RhoA/ROCK/MLC2 signaling in contractile cells

In vascular smooth muscle cells, RhoA and the serine/threonine protein kinase ROCK are major regulators of cell contraction. [99] The Rho-associated kinases (ROCKs) have been identified as one of the first downstream targets of RhoA. [100, 101] In mammals, two highly homologous ROCK isoforms consist, ROCK1 and ROCK2. While ROCK2 is mainly expressed in the central nervous system (e.g. neurons, cerebral cortex) and the heart, ROCK1 is mainly found in non-neural tissue such as the lung, kidney and skeletal muscle. [102-104] The domain structure of ROCK is composed of an N-terminal kinase domain, an α-helical coiled-coil domain containing a Rho binding site and a cysteine-rich domain located within the pleckstrin homology (PH) motif at the C-terminus. [103] Activated GTP-bound RhoA binds to the α-helical coiled-coil domain of ROCK thereby removing the autoinhibition of this kinase. This allows ROCK to phosphorylate and activate its downstream targets, most notable myosin light chain 2 (MLC2). [105, 106] It was reported that ROCK can influence the phosphorylation state of MLC2 in two calcium-independent ways: either by directly

phosphorylating MLC2 at Ser19 or indirectly through the phosphorylation of the regulatory subunit of myosin light chain phosphatase (MYPT1) at the two inhibitory phosphorylation sites Thr696 and Thr853 (**Fig. 6**). [107-109] Myosin light chain phosphatase (MLCP) is a heterotrimer composed of a catalytic subunit of type 1 phosphatase δ isoform (PP1δ) and two regulatory subunits: myosin phosphatase target subunit 1 (MYPT1), consisting of seven ankyrin repeats followed by a PP1c-binding motif and a smaller regulatory subunit (M20). [110] Both the direct and indirect pathway result in increased levels of cytoplasmic phosphorylated MLC (pMLC) which in turn leads to increased cell contractility. MLC2 Ser19 is also phosphorylated by the MLC kinase (MLCK) in a calcium/calmodulin-dependent manner. [111] In addition to controlling MLC phosphorylation, ROCK also activates LIMK1 and 2 by phosphorylating Thr508 and Thr505, respectively. Activated LIMK phosphorylates cofilin at Ser3, thereby inhibiting the cofilin-mediated disassembly of actin filaments resulting in increased stress fiber stability (**Fig. 6**). [83, 112-114]

The RhoA/ROCK pathway is involved in many pathologies including atherosclerosis, coronary vasospasm, cerebral ischemia, hypertension, myocardial hypertrophy, pulmonary hypertension and vascular remodeling. [115-122] Not surprising, many inhibitors of the RhoA/ROCK signaling pathway have been tested in clinics or are presently in clinical trials for beneficial effects on these cardiovascular diseases, however, only fasudil and its derivative ripasudil (trade name Glanatec), as well as netarsudil (trade name Rhopressa) have been licenced for clinical use. [123-129]

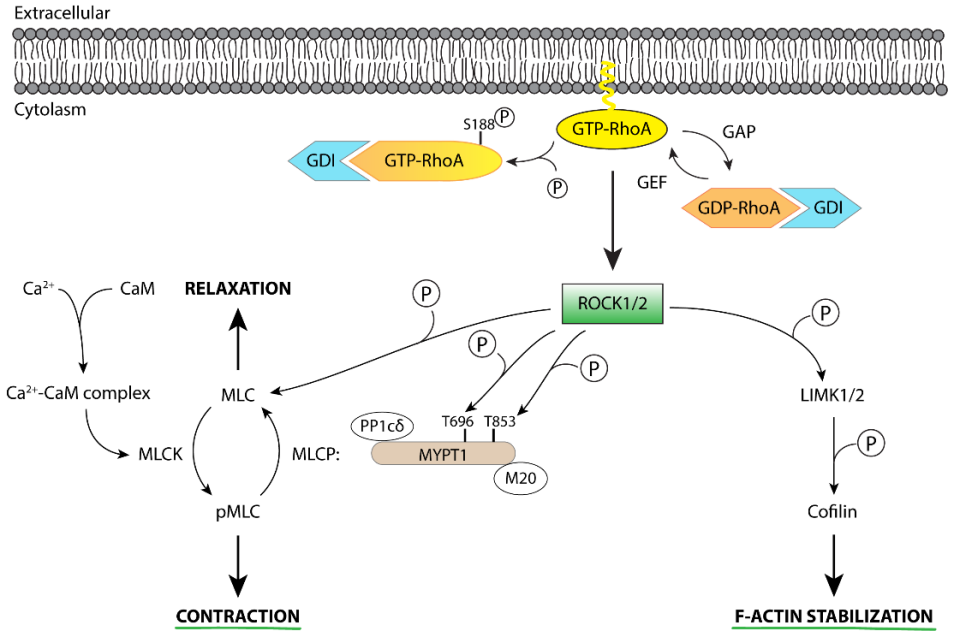

Fig. 6. Model for the RhoA/ROCK signaling pathway. Extracellular signals activate RhoA through specific RhoA GEFs which in turn stimulates the activity of ROCK1/2. The phosphorylation of downstream effectors by ROCK such as MLC, MLCP, or LIMK1/2 induces actomyosin contractility and F-actin stabilization. Adapted from Huveneers and Danen, and Mulherkar and Tolias. [76, 129]

The myosin superfamily consists of more than 20 distinct classes based on phylogenetic analysis and the human genome encodes more than 40 myosin genes. [130, 131] Myosins from distinct classes have a unique structure and serve different functions. The myosin II subfamily, also termed 'conventional' myosins is the largest myosin class and includes skeletal, cardiac and smooth muscle myosins, as well as non-muscle myosin II (NMII). [132] In mammals, three different non-muscle myosins, NMIIA, NMIIB and NMIIC, are encoded by different genes (*MYH9*, *MYH10* and *MYH14*). Although non-muscle myosins are also expressed in muscle tissue, their participation in force generation is controversial and muscle-specific myosin II isoforms provide the molecular motors for cell contraction. [133-135] All conventional myosin molecules exhibit the same hexameric domain structure consisting of two globular head domains, two heavy chains (~ 230 kDa), as well as two regulatory (~20 kDa) and two essential light chains (~17 kDa). [136] While the regulatory light chains, which regulate the ATPase activity, can be phosphorylated by ROCK or MLCK at Ser19 to activate the actomyosin crossbridge cycle, the short non-helical C-terminal tails regulate myosin filament assembly. [134] Contraction in striated muscle (cardiac and skeletal muscle) is generated by the ATP-dependent interaction of bipolar myosin II heads that pull two actin filaments of opposing polarity towards each other, thereby shortening the sarcomere (**Fig. 7A**). In contrast, smooth muscle contraction is initiated by monomeric myosin which assembles into thick filaments in a non-helical, side-polar configuration (**Fig. 7B**). Like most other myosins (except myosin VI), myosin II moves towards the barbed (+) end of actin. [137]

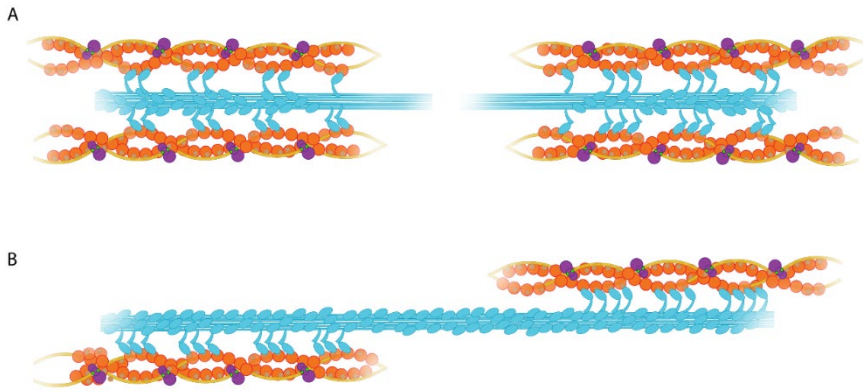

Fig. 7. Comparison of the (A) bipolar arrangement of myosin in cardiac and skeletal muscle and (B) the side-polar arrangement of myosin in smooth muscle. Adapted from Dasbiswas et al. [138]

1.1.6 Integrins in the cardiovascular system

Integrins are indispensable for normal mammalian development and the establishment and function of the cardiovascular (CV) system. Hence, all cell types of the CV system, including blood cells, smooth muscle cells, cardiomyocytes and non-muscle cardiac cells express integrins.

1.1.6.1 Integrins in the myocardium

The precise spatial and temporal expression of integrins is critical for a proper organ function. In mouse myocytes, α1, α3, α5, α6, α7, α9 and α10 subunits are expressed and developmentally regulated. These individual α subunits associate nearly exclusively with splice variants of the β1 integrin subunit, with the β1D integrin isoform being the major β1 subunit expressed in the postnatal heart. [139, 140] While the laminin binding α7β1 heterodimer is the predominant integrin in adult cardiomyocytes, mouse CMs during embryonic development express the α5β1 fibronectin and the α6β1 laminin receptor. [141, 142]

The connection of the ECM and the actin cytoskeleton via β1 integrin in CMs is pivotal for the organization and maintenance of these cells in the heart. Cardiomyocyte-specific β1 integrin depletion results in myocardial fibrosis and development of dilated cardiomyopathy within 6 months of age in mice. [143] Especially the *in vivo* relevance of the β1D isoform in CMs has been studied intensively. A unique amino acid sequence at the cytoplasmic domain that is absent in β1A integrin, allows the high affinity binding of talin which strengthens the ECM connection to sarcomeric proteins, thus, stabilizing costameres. [15, 142, 144, 145]

Integrins exhibit a wide variety of functions in cardiomyocytes. These range from adhesion, formation of ECM-cytoskeletal junctions and signaling, to the point of modulation of ion channel function, modification of hypertrophic growth responses, mechanotransduction and protection of CMs from ischemic stress. [145] In striated and cardiac muscle, the FA equivalent is the costamere, subsarcolemmal protein assemblies that transmit force from the Z-discs and M-lines of the sarcomere (**Fig. 14**) to the extracellular matrix.

1.1.6.2 Integrins in the vasculature

Vessel formation in both vasculogenesis, the *in-situ* formation of a new network of endothelial tubes from mesoderm-derived cells and angiogenesis, the generation of new vessels from preexisting vasculature by either vessel sprouting or intussusceptive vessel growth, is a dynamic and complex biological process that depends on the ability of cells to interact with adhesive substrates and regulatory factors. [146] Especially the role of integrins as crucial components of vascular development and major mediators of cell adhesion and migration has been extensively investigated. [147, 148]

Integrins participate in many aspects of vasculogenesis, such as angioblast repositioning, protrusive activity, lumen formation and vascular fusion. In addition, integrins are also important for endothelial cell behavior during angiogenesis. Angiogenesis is highly regulated and involves the coordinated activation of several signaling pathways (e.g. Notch, VEGF, TGF-β) that can cross talk with integrin-mediated signaling pathways. [149] Notch signaling regulates cell fates during embryogenesis. During vessel maturation, vSMCs recognize the Notch ligand Jagged1 on endothelial cells, which leads to the expression of αvβ3 integrin and results in the adhesion of vSMCs to the von Willebrand factor. Hence, αvβ3 integrin acts downstream of Notch activation, allowing vSMC attachment to the endothelial basement membrane. [150] Furthermore, synergistic cross-activation of αvβ3 integrin and the tyrosine kinase receptor vascular endothelial growth factor receptor 2 (VEGFR2) is required for a full angiogenic response to vascular endothelial growth factor (VEGF). [54, 151] Moreover, Rap1b was shown to promote VEGF-mediated angiogenesis through the activation of VEGFR2 in ECs via αvβ3 integrin. [152] Transforming growth factor β (TGF-β) controls numerous cellular responses such as cell migration, differentiation, proliferation and apoptosis. [153] However, TGF-β is always produced as an inactive (latent) cytokine that needs to be activated before it can bind to its receptor and activate signaling cascades that lead to the modulation of gene transcription. Out of the 24 integrin receptors, four integrins (αvβ3, αvβ5, αvβ6 and αvβ8) have been shown to activate TGF-β in fibroblasts and epithelial cells. [153]

Altogether sixteen distinct integrin heterodimers are reportedly involved in vascular biology, including eight out of ten β1 family members and two members of the β3 integrin family. [154, 155] In the absence of β1 integrin, vSMCs show a highly rounded morphology with disorganized α-smooth muscle actin (α-SMA)-positive fibers leading to poorly covered blood vessels and the development of vascular aneurysm. [156] The round cell morphology of β1 depleted vSMCs is not due to altered levels of MLC phosphorylation as it has been observed in vSMCs lacking the expression of IPP complex components. [157] Although β1 integrin mediates cell adhesion, cell migration and controls fibrillogenesis through the formation of functional complexes with various α subunits, the knockout of β1 does not lead to alterations in vSMC survival or proliferation. Here, αvβ3 and αvβ5 are sufficient to transduce pro-mitotic and anti-apoptotic signals. [156, 158]

Microscopically, smooth muscle cells do not have striations and no highly ordered sarcomeric organization typical for striated muscle. [159] However, as in striated muscle, Z-disc homologues, called dense bodies, are enriched in α-actinin and bind the actin filament barbed ends. Furthermore, similar to Z-discs in sarcomeres, these dense bodies are also connected by desmin-rich intermediate filaments. [159] Dense

plaques, which are structurally akin to dense bodies and focal adhesions in non-muscle cells, are found at the plasma membrane where they mediate the adhesion and force transduction of SMCs to the ECM. [160]

1.2 The Parvins

As described above, the short cytoplasmic domain of integrins has no actin binding capacity and intrinsic catalytic activity, thus, integrin signaling depends on the recruitment of intracellular adaptor and signaling proteins. One key component of the integrin adhesome and integrin outside-in signaling is a ternary protein complex consisting of integrin-linked (pseudo)kinase (ILK), particularly interesting new cysteine-histidine-rich protein (PINCH) and parvin (IPP complex).

The parvins are a family of three cytoplasmic adaptor proteins- α-, β- and γ-parvin that localize to focal adhesions, thereby connecting integrin receptors with the actin cytoskeleton. [48, 161-163] The murine α-parvin gene (*PARVA*) lies on chromosome 7, while the murine *PARVB* and *PARVG* can be found on chromosome 15, adjacent to each other. α-parvin, originally termed actopaxin, together with its closely related paralogue β-parvin (74% identity, 85% similarity), originally called affixin, and the more distant γ-parvin (42% identity, 67% similarity), identified in human and mice, forms a separate family of small α-actinin related proteins belonging to the α-actinin superfamily. [164, 165] In contrast to vertebrates, lower organisms like *C. elegans* and *D. melanogaster* only express one parvin-like protein, sharing 48% identity and 66% similarity to mouse α-parvin. [165] Like other members of the α-actinin superfamily, all three parvin isoforms contain a pair of unconventional calponin homology domains (CH1 and CH2) separated by a linker of about 60 amino acids in their C-terminal region (**Fig. 8**). [16, 161, 164-166] It was initially thought that α- and β-parvin interact with F-actin via their CH domains. However, the parvin CH domains do not share high homology to typical F-actin binding CH domains and it was recently discovered that both protein isoforms contain a N-terminal WASP (Wiskott-Aldrich syndrome protein)-homology 2 (WH2) domain that mediates actin binding. [16, 167] The WH2 domain is a small (20-50 amino acids) actin-binding motif that sequesters G-actin and promotes the nucleation, elongation and bundling of F-actin via distinct mechanisms. [16, 168] The N-terminal polypeptide stretch of α- and β-parvin harbors two putative nuclear localization signals (NLS) and three potential Src homology 3 (SH3)-binding sites. [165] γ-parvin on the other hand, which is predominantly expressed in hematopoietic and lymphoid tissues, lacks the NLS and SH3-binding sites as well as the WH2 motif. [16, 165, 169, 170] In humans and mice, α-parvin is expressed in all tissues except in hematopoietic cells, while human β-parvin shows highest expression levels in skeletal muscle and weaker in heart. [163, 164, 170] Mouse β-parvin is predominantly expressed in heart and moderate levels can be found in lung, spleen and skeletal muscle. [164] In contrast to the

uniform expression of α-parvin, β-parvin expression increases during mouse embryonic development and γ-parvin is transcribed throughout embryonic development, but downregulated at embryonic day 11 (E11). [164, 165]

Although α- and β-parvin share a high sequence homology, the loss of α-parvin expression *in vivo* causes embryonic lethality between E11.5 and E14.5, whereas mice deficient in *β-parvin* are viable and fertile. [171] However, the loss of β-parvin expression in mouse heart is to a large part functionally compensated through the induction of α-parvin expression. [172] Similarly, siRNA-mediated knockdown (KD) of α-parvin in human cells dramatically increased the β-parvin level, hence, the authors hypothesized that α-parvin might suppress β-parvin expression in cells expressing both members. [173] Nonetheless, the two parvin isoforms do not have completely redundant functions as they also exhibit specific interactors. [174] Parvins are not catalytically active but function as adaptor molecules for a number of proteins, most notably ILK, which will be discussed as part of the IPP complex in a separate chapter (**Fig. 8**). [174] Another pan-parvin binding partner is paxillin which is contributing to the correct recruitment of parvins to focal adhesions. [50, 169, 175, 176] Interestingly, up to date only α-parvin has been shown to bind to the paxillin-related protein hydrogen peroxide inducible clone-5 (Hic-5). [48, 175] Furthermore, both parvin isoforms interact with the Rac1/Cdc42 GEF β-PIX while α-PIX has been identified as a specific β-parvin interactor to activate Rac1. [177-179] Moreover, only β-parvin directly interacts with α-actinin, a scaffold protein playing a critical role in actin polymerization at focal adhesions. [180, 181] In contrast, α-parvin specifically interacts with the serine/threonine kinase testicular protein kinase 1 (TESK1) in a phosphorylation-dependent manner, inhibiting the kinase activity and phosphorylation of cofilin. [182] Upon cell adhesion, the MAPK extracellular signal-regulated protein kinase (ERK) is activated, recruited to focal adhesions by paxillin and phosphorylates α-parvin. [183] Phosphorylated α-parvin releases TESK1 which phosphorylates cofilin, leading to F-actin polymerization at lamellipodia and subsequent cell spreading and motility. [182] Furthermore, the correct spatiotemporal regulation of the Cdc42 GTPase-activating protein (CdGAP) function, a GAP for Rac1 and Cdc42, was shown to be dependent on its interaction with α-parvin. [184] In summary, this shows that although α- and β-parvin can bind to the same interactors, they additionally interact with isoform-specific binding partners and exhibit distinct functions to regulate integrin-dependent signaling.

During early cell attachment, integrins bind to ECM proteins and nascent adhesions are established. The recruitment of adaptor and signaling proteins such as talin, paxillin, ILK, PINCH, parvin, vinculin and FAK allows the maturation of nascent adhesions to FAs. [174] As previously mentioned, parvins have been identified as ILK and paxillin binding partners and these protein-protein interactions are critically important

for their subcellular localization. Both α- and β-parvin were observed in lamellipodia in spreading cells as well as in FAs. [163, 165] Furthermore, α-parvin was found to localize in focal adhesions and tensin-containing fibrillar adhesions as well as in nuclei in well-spread transfected fibroblasts. The nuclear targeting of α-parvin is in agreement with the two putative NLS, which can be found in the N-terminus of the protein. [165] In isolated neonatal ventricular rat cardiomyocytes (NRVCs) α-parvin showed a costamere localization. [5] β-parvin was found to co-localize with α-actinin at the junction of FAs and at fine but not well-developed thick stress fibers. [180] Furthermore, in human skeletal muscle cells β-parvin was reported to co-localize with ILK at the striated structures, to which Z-discs anchor. [163]

The N-terminal domain of α-parvin but not β-parvin contains phosphorylation sites for prolin-directed serine/threonine kinases including ERK and Cdc2 that play a role in mitotic events, lamellipodia formation and cell migration. [183, 185, 186] Other differences between the two isoforms were observed in the regulation of Rac1. While α-parvin knockdown in Hela cells stimulated Rac1 activation and enhanced lamellipodia formation, siRNA-mediated KD of β-parvin did not have the same effect. [173] Furthermore, overexpression of β-parvin in Hela cells significantly increased caspase-3 activity, a key regulator of apoptosis, whereas overexpression of α-parvin did not. [173] The pro-apoptotic function of α-parvin is mediated through the activation of Akt, primarily through facilitating the membrane translocation of this serine/threonine-specific protein kinase. [187]

Together these findings show that despite possessing identical domain architecture, sharing a high sequence homology and some interactors, α- and β-parvin also bind distinct interacting partners and play different roles in integrin-mediated cell regulation. It is therefore of great interest to understand the functional divergence between the two parvin isoforms in more detail.

1.2.1 The ILK-PINCH-parvin (IPP) complex

Proteins of the parvin family do not exhibit intrinsic catalytic activity and their function is mediated by the recruitment of different interacting proteins. One of the most important binding partners of parvins is ILK, a pseudokinase that functions as scaffolding molecule and directly interacts with PINCH. Simultaneous interaction of ILK with PINCH and parvin results in the formation of a stable ternary complex, called the IPP complex. [188] The IPP complex is formed in the cytosol before its localization to the integrin adhesions, at which the complex provides the physical link between the integrin receptor and the actin cytoskeleton. [189, 190] The protein stabilities of ILK, PINCH and parvin depend on each other and deletion of one IPP complex component leads to proteasome-mediated degradation of the remaining members. [190-192] In mammalian cells, multiple IPP complexes can assemble depending on the PINCH or parvin members

incorporated into a give IPP complex. The binding of PINCH1 and PINCH2 to ILK is mutually exclusive and the three parvin protein family members, whose binding is also mutually exclusive, further expand the repertoire of different IPP complexes. [173, 193]

ILK is a widely expressed multidomain adhesion protein involved in the regulation of FA assembly, cytoskeleton organization and signaling. [16, 189] Although initially identified as a serine/threonine kinase, structural and functional studies show that ILK lacks enzymatic activity and is now widely recognized as a pseudokinase containing an unusual pseudo-active site that is incapable of catalyzing phosphorylation. [16, 47, 194-197] This pseudokinase is a scaffolding protein comprising five N-terminal ankyrin (ANK) repeats, a short pleckstrin-homology (PH) domain and a C-terminal serine/threonine kinase-like domain. [198] ILK binds to the cytoplasmic tail of β integrins (either directly or via kindlin) and with high affinity to particularly interesting new cysteine-histidine-rich (PINCH) protein, a FA protein containing five LIM domains. [47, 199] In mammals, two PINCH proteins, PINCH1 and PINCH2, which share a high sequence and structural similarity, have been described. [200] ILK binds to the second Zinc (Zn) finger of the LIM1 domain via its N-terminal ankyrin repeat domain (**Fig. 8**). [189] This interaction is obligatory for targeting the IPP complex to integrin membrane sites. In addition to PINCH, ILK interacts with the parvins (α-, β- and γ-parvin, **Fig. 8**) through its C-terminal domain and the CH2 domain of parvin. [162, 163]

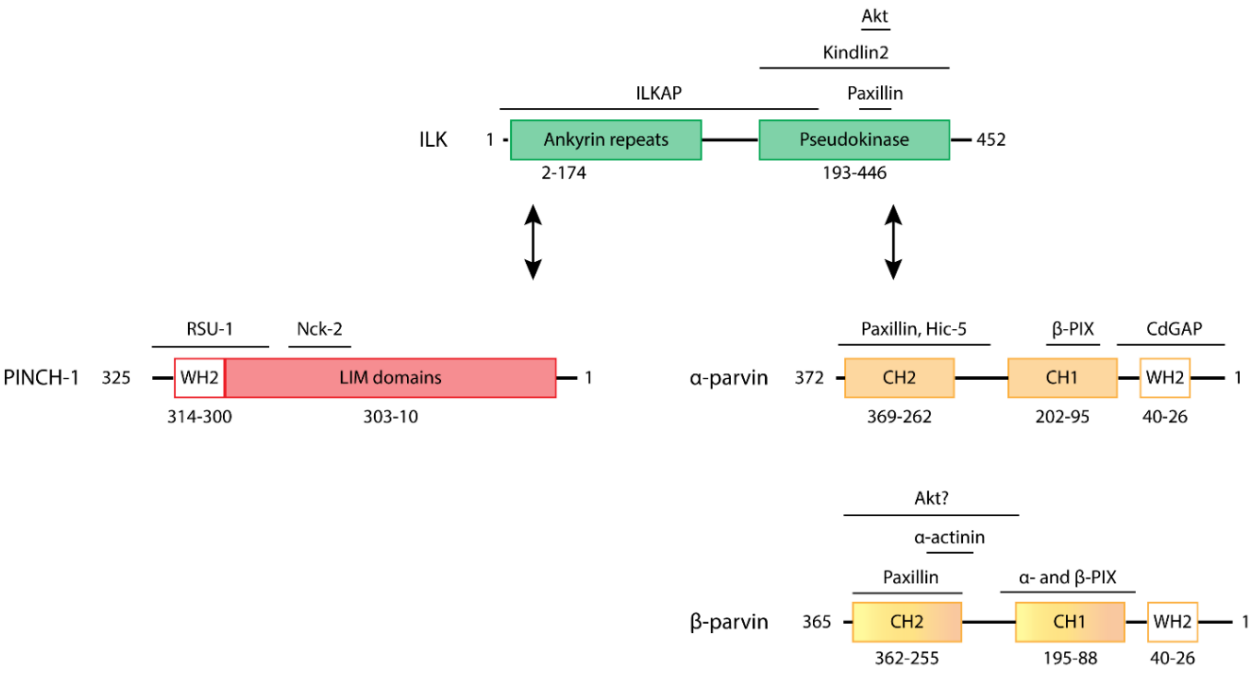

Fig. 8. Schematic organization of the ILK-PINCH-parvin complex based on structural data. ILK binds to PINCH LIM1 via its ankyrin domain and α-parvin CH2 via its pseudo-kinase domain. The WH2 domains indicated in PINCH and parvin were just recently discovered. Interacting proteins with known binding sites are displayed. Adapted from Vaynberg et al. [16]

In the past years several knockout (KO) studies have been performed in *C. elegans*, *D. melanogaster* and mice to understand the function of the IPP complex *in vivo* and the specific roles of each individual component. [170, 171, 195, 196, 201-206] In *C. elegans* deletion of PAT-4 (ILK), UNC-95 (PINCH) or PAT-6 (parvin) results in paralyzed, arrested embryos where the dense bodies, M-lines and myofilaments fail to organize into mature structures. [196, 201, 202] Similar observations were made in *D. melanogaster*, where the deletion of ILK and PINCH resulted in abnormal muscle attachments. In contrast to integrin mutants, where the primary defect in muscle attachment is due to the detachment of the plasma membrane from the ECM, the defects in ILK and PINCH mutants results from the detachment of actin filaments from the muscle ends. [195, 203] In mice, the genetic ablation of *ILK*, *PINCH1* and *α-parvin* results in lethality at different stages during embryonic development. [171, 204, 205] Mice deficient in *PINCH2*, *β-* or *γ-parvin* however, are without an obvious phenotype, probably due to compensation by PINCH1 or α-parvin. [170, 171, 206] Both, ILK and PINCH knockout embryos die at the peri-implantation state at embryonic day (E) 5.5-6.5 and E6.5, respectively, whereas α-parvin deficient embryos survive till E10.5 to E14.5. While the loss of *ILK* and *PINCH* leads to abnormal epiblast polarity, impaired cavitation, detachment of the endoderm from the basement membrane and abnormal actin reorganization, loss of α-parvin primarily results in severe cardiovascular malformations. [171, 204, 205] Additionally, mice lacking *α-parvin* developed severe kidney agenesis/dysgenesis due to an impaired invasion of the ureteric bud into the metanephric mesenchyme. [207] Although β-parvin can stabilize ILK and PINCH protein levels, it cannot fully compensate for the loss of α-parvin function in vascular smooth muscle cells (vSMCs). These cells displayed a strong hypercontractile phenotype with elevated RhoA and pMLC2 levels. [171] Comparable results were obtained from ILK-deficient vSMCs. [157] SiRNA-mediated knockdown of PINCH-1 in vSMCs disrupted the cytoskeleton and caused apoptosis. [208] Since vSMCs are one of the analyzed contractile cell types of the cardiovascular system in the present thesis, the role of the IPP complex within these cells will be discussed in more detail in a separate chapter (1.2.1.2).

In summary, all these studies confirmed a pivotal role for the IPP complex and its individual components as adaptor between integrins and the intracellular actin cytoskeleton.

1.2.1.1 Role of the IPP complex and its members in cardiomyocytes

In cardiac muscle the IPP complex localizes at costameres and sarcomeric Z-discs. [5, 209, 210] Ablation of *ILK* in the mouse myocardium results in the disruption of the focal adhesion complex and disaggregation of adjacent cardiomyocytes, leading to cardiomyopathy, increased interstitial fibrosis and heart failure. [194, 209-211] Furthermore, cardiac-specific expression of ILK induces physiological CM hypertrophy in

transgenic mice while the loss of *ILK* in heart also causes initial pathological hypertrophy. [5, 194, 212] While mice with the cardiac-specific ablation of either *PINCH1* or *PINCH2* have no phenotype, probably because of compensation between these two isoforms, the generation of cardiac-specific *PINCH1/2* double knockout mice revealed an essential role of these proteins in myocardial growth, maturation, remodeling and function. [211, 213] *PINCH1/2* double KO mice died of cardiomyopathy and heart failure within four weeks after birth, showing changes in the myocardial architecture as a result of abnormal cardiomyocyte attachment, cell growth and death. [211] Heart-specific *parvin* KO mice have not been generated, however, Montanez and colleagues observed heart abnormalities in α-parvin knockout embryos and hypothesized that α-parvin is important to maintain the structure and the stability of the sarcomeres. [171] Additionally, current investigations of the involvement of β-parvin in cardiac hypertrophy, revealed a potential function as volume-load mechanosensor (Thievessen et al., submitted). Nevertheless, a detailed analysis of α-parvin function during neonatal development and in adult CMs is still missing.

1.2.1.2 Role of the IPP complex and its members in vascular smooth muscle cells

Conventional *α-parvin* KO mice develop severe cardiovascular defects, ranging from aberrant vascular beds with dilated blood vessels to whole-body edema and vessel rupture, and die during the embryonic development between E10.5 and E14.5. The reason for these defects can be found on the cellular level. Mural cells developed a hypercontractile phenotype after α-parvin depletion, indicative by elevated active RhoA and pMLC levels, which resulted in an impaired coverage of blood vessels with pericytes (around capillaries and venules) and vSMCs. [171] At the same time, ILK deficiency in murine vSMCs showed defective vascular remodeling due to increased contractility which also resulted in embryonic lethality (E18.5). [157] Shen et al. showed that ILK plays a crucial role in vSMC homeostasis and structural organization of arteries. [160] Using conditional *ILK* knockout mice expressing a Cre recombinase under the transcriptional control of the *SM22α* promotor they found that the loss of ILK in vSMC causes perinatal lethality. Further investigation showed that the tunica media in arteries was disrupted resulting in defects in arterial morphogenesis and structure (e.g. aneurismal dilation of the aorta). However, in contrast to previous reports, Shen et al. found less active RhoA in ILK deficient vSMCs. [160] PINCH1 was also shown to exhibit important roles in vSMCs. PINCH1 KD resulted in actin depolymerization, cell rounding and apoptosis while mechanical stretch-induced stabilization of PINCH1 prevented vSMC apoptosis. [208]

1.2.2 Potential novel parvin interactors

1.2.2.1 Myosin phosphatase RhoA interacting protein (Mprip)

Originally identified as RhoA binding partner in a yeast two-hybrid screen, myosin phosphatase interacting protein (Mprip; also known as p116^{Rip}) interacts with the regulatory myosin-binding subunit of MLCP and is essential for Rho-regulated cell contractility. [214, 215] Mprip is ubiquitously expressed, but most studies analyzed its function in vascular smooth muscle cells. It contains several potential NLSs and protein and phospholipid interaction motifs, including two PH domains flanking two proline-rich regions that are putative binding sites for SH3 domain-containing proteins, and a C-terminal coiled-coil domain (**Fig. 9**). [215]

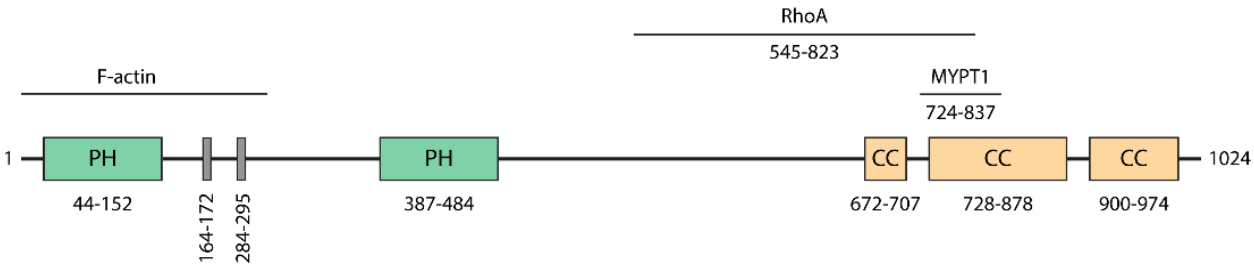

Fig. 9. Schematic representation of Mprip, with the PH and coiled-coiled domains. Minimal regions for actin (number of aa for binding is unknown), RhoA (278 aa) and MYPT1 binding (113 aa) are indicated. PH, pleckstrin homology; CC, coiled-coil. Adapted from Surks et al., Koga et al. and Lee et al. [216-218]

Mprip can be found in the cytoplasm and the nucleus but also localizes to F-actin (e.g. stress fibers or filopodia) via its N-terminal region. [219] The C-terminal coiled-coil domain of the protein (residues 724-837) directly interacts with the C-terminal leucine-zipper domain (residues 991-1030) of the regulatory myosin-targeting subunit of MLCP (MYPT1). [216-218, 220] Whether Mprip directly interacts with RhoA is debated. [216, 217, 219] Mulder et al. suggest that Mprip may act as a scaffolding protein linking the MLCP complex to the actin cytoskeleton, without directly binding RhoA. [219, 220] Others performed direct binding assays with recombinantly expressed His-RhoA and GST-Mprip to confirm a direct interaction between the two proteins, independent of the RhoA activity state. [216] In addition, Surks and colleagues claimed to see a 47% reduction in stress fiber-associated RhoA after Mprip silencing in A7r5 vSMCs. They hypothesized that Mprip not only fulfills the function of targeting MLCP to the actin cytoskeleton but also colocalizes RhoA and MLCP to further facilitate the MLCP activity. [221]

Furthermore, Mprip was identified as a target of the cGMP-dependent protein kinase G type Iα (PKGIα), the main PKG isoform in smooth muscle, that directly binds to MYPT1. [222] PKGIα coimmunoprecipitates with Mprip and can bind to MYPT1 and Mprip simultaneously. [216] The activation of PKGIα leads to an

increased Mprip phosphorylation resulting in a stronger Mprip-MYPT1 association and increased MLCP activity in gastrointestinal smooth muscle cells. [223]

Overexpression of Mprip disrupts the actin cytoskeleton and inhibits actomyosin contractility (loss of stress fibers) by facilitating the myosin-MLCP interaction and stimulating the MLCP holoenzyme activity without affecting the catalytic subunit. [217, 219] Expectedly, RNA interference (RNAi)-mediated silencing of Mprip prevents the localization of MBS to F-actin stress fibers resulting in increased MLC phosphorylation and phenotypical changes in vSMCs. These changes are a result of the MLCP uncoupling from stress fibers and not a change in cellular MLCP, MLCK or RhoA activity. [221, 224]

1.2.2.2 Deleted in liver cancer 1 (DLC-1)

DLC-1, also known as ARHGAP7 or p122RhoGAP, was initially identified as a phospholipase Cδ1 (PLCδ1) binding protein. [225] It is widely expressed with the highest expression levels in heart, liver and lung and was originally reported to be a potential tumor suppressor that is often deleted or downregulated in various cancers (e.g. liver, breast, lung, brain, stomach). [226-228]

The C-terminus of DLC-1 consists of a Rho GAP domain and a steroidogenic acute regulatory (StAR)-related lipid transfer (START) domain that binds to PLCδ1 (**Fig. 10**). The N-terminus contains a sterile alpha motif (SAM) domain followed by a focal adhesion targeting (FAT) sequence that binds to the Src Homology 2 (SH2) domains of tensins. [227, 229]

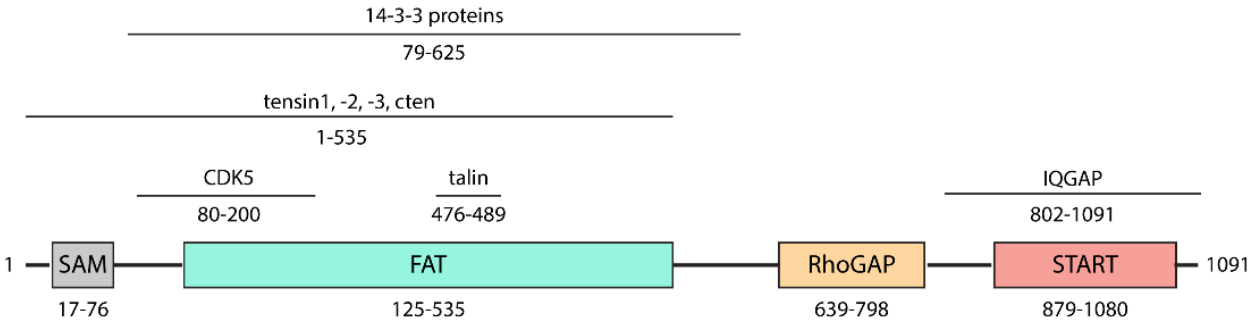

Fig. 10. Schematic representation of DLC-1 with the N-terminal SAM domain, RhoGAP domain and the C-terminal START domain including known interacting partners. SAM, sterile alpha motif; FAT, focal adhesion targeting; START, steroidogenic acute regulatory-related lipid transfer. Adapted from Liao et al., Zacharchenko et al., Scholz et al. and Tanaka et al. [229-232]

DLC-1 exhibits various regulatory activities including the regulation of cell shape by influencing actin cytoskeleton organization and FA formation, and the induction of apoptosis. [233, 234] As mentioned above, it was first isolated as a PLCδ1 binding protein that potentiates PLCδ1 activity to hydrolyze the intracellular second messenger PIP2. The hydrolysis of PIP2 leads to the generation of diacylglycerol (DAG),

which is a physiological activator of protein kinase C (PKC) and inositol 1,4,5-triphosphate (IP_3) that leads to the release of Ca^{2+} from internal stores. [225] The Rho GAP and the PLCδ1-enhancing activity of DLC-1 might act synergistically to regulate cytoskeletal and morphological changes in cells. *DLC-1* knockout mice die before E10.5 due to defects in the heart, placenta neural tube, and brain. [235, 236]

DLC-1 is a RhoA-specific GAP that functions as a regulator of cell proliferation and migration. [237] Its tumor suppressor function requires its GAP activity and is tensin-dependent. [229, 238, 239] Tensins are a protein family of four focal adhesion proteins, tensin1, tensin2, tensin3 and C-terminal tensin-like (cten) containing a SH2 domain and a phosphotyrosine-binding (PTB) domain which allows binding to the NPxY motif in the cytoplasmic tail of β integrins. [238] Additionally, tensin1-3 contain two actin-binding domains (ABD). [240] It has been previously suggested that the DLC-1 Rho GAP activity is controlled by an intramolecular interaction with its SAM domain that functions as a negative intramolecular regulator. [241, 242] The binding of tensin3 ABD and DLC-1s SAM domain competes for the intramolecular autoinhibitory interaction, enhancing the GAP activity of DLC-1 and decreasing the cellular GTP-RhoA level. [242] This model got further defined when DLC-1 was identified as a target of the cytoplasmic serine/ threonine cyclin-dependent kinase 5 (CDK5). CDK5 phosphorylates four serines (S120, S205, S422 and S509) in DLC-1 which reduce the binding between the SAM and Rho GAP domain. The release from the autoinhibitory state renders DLC-1 active, including its ability to bind to tensin and talin, its localization to FAs and its Rho GAP activity. [243] In addition to CDK5, mitogen-activated protein kinase kinase (MEK)/ERK phosphorylation of DLC-1 on T301 and S308 seem to be critical for the activation of its Rho GAP activity. [244] An opposing effect was seen for a tyrosine kinase Src-dependent phosphorylation of Y451 and Y701 on DLC-1, which decreases the DLC-1-tensin interaction and downregulates the Rho GAP activity. This effect got further enhanced by ERK1/2 phosphorylation of DLC-1 on S129. [245] However, contradictory results were found in human kidney epithelial cells (HEK293T) where the binding of TNS1-3, but not cten, enhanced the RhoA activity in a DLC-1 dependent fashion. [246]

1.3 The cardiovascular system

The distribution of gases and fluids into organs and cells in vertebrates requires a sophisticated transportation system and cannot simply rely on diffusion. This transportation task is performed by the cardiovascular system, consisting of the heart and blood vessels, including the blood itself, that allows the blood to circulate and transport essential nutrients, hormones and oxygen to the body cells and simultaneously remove metabolite waste products and carbon dioxide from the cells. [247] The system thereby nourishes the cells, protects the body from pathogens and regulates the body temperature, blood pressure and pH to maintain homeostasis.

The heart is the first functional organ to be formed in the developing embryo. [248, 249] It is a hollow muscular organ, lying between the lungs in the left chest area and beating more than two billion times in an average human life. [250] At the anatomic level, the heart is composed of four cavities (left and right atrium and ventricle, respectively), four valves (mitral, tricuspid, aortic and pulmonary valve), large arteries and veins, that all act in concert to achieve proper pump function (**Fig. 11A**). [251] Oxygen-rich blood flows from the left side of the heart to the body (systemic circulation), while the right heart side pumps blood through the pulmonary valve and artery to be oxygenated in the lungs (pulmonary circulation). During contraction the four heart valves function as inlet and outlet check-points for the ventricles that allow an unidirectional blood flow by preventing the passive opening and closing of valves due to pressure gradients. [252] The heart´s own blood supply is ensured by the left (LCA) and the right coronary artery (RCA). [252]

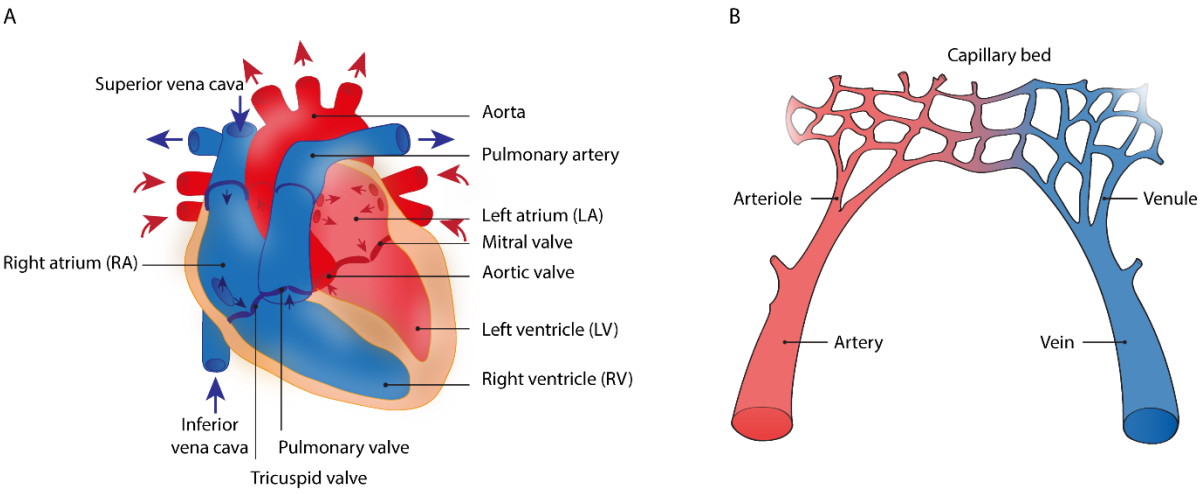

Fig. 11. (A) Anatomy of the heart and (B) vasculature. Adapted from the Texas Heart Institute [253]; Adams and Alitalo [254]

The blood vessels are a highly branched, tree-like tubular network which is organized in a hierarchical structure (**Fig. 11B**). Large vessels are called arteries or veins, which either carry oxygen-rich blood under

high pressure to all tissues or return deoxygenated blood under low pressure back to the heart. According to their function, arteries can be classified into elastic (e.g. aorta, pulmonary arteries) and muscular arteries (e.g. radial, femoral and splenic artery). Latter ones distribute the blood to the specific organs and eventually give rise to the arterioles, small (<100 µm in diameter) high resistance vessels of the body which feed the capillary bed. They exhibit a crucial role in regulating the amount of blood flowing to the tissues by dilating or constricting. [255] The capillary bed is a dense interweaving network of capillaries which supply all tissues and organs with gases, fluids and signaling molecules. Post-capillary venules then allow the deoxygenated blood to return from the capillary bed to veins and subsequently get oxygenated in the lungs. [256, 257]

1.3.1 The wall of the heart and blood vessels

Atria and ventricles are histologically similar and consist of an external layer, the epicardium, which is separated from the endocardium, the inner lining of the cavities and valves, by the myocardium (**Fig. 12A**). [258, 259] Epi- and endocardium are also morphologically similar, consisting of loose connective tissue and elastic fibers. Both, the epicardial and endocardial layer, are additionally flanked by a single layer of squamous epithelial or endothelial cells, respectively. [260] The epicardium assists in the production of pericardial fluid, a liquid running between the fibrous and serous pericardium, lubricating and protecting the heart during contraction. [261] The myocardium, the thick middle layer, contains the contractile elements of the heart and is made of multiple layers of cardiac muscle fibers. Although histological similar, the myocardial thickness is directly related to the pressure present in each chamber; thus, the atria exhibit thin walls whereas the ventricle walls are thicker. Furthermore, as blood is pumped into the high-pressure systemic circuit via the left ventricle (LV), the LV wall is approximately threefold thicker than the wall of the right ventricle (RV), which is part of the low-pressure pulmonary circulation. [259]

Arteries and arterioles, as part of the systemic circulation, are recipients of blood with high pressure, therefore requiring thicker vessel walls in comparison to veins and venules, which usually have larger lumens with thinner and less well-organized walls. [262] Hence, in cross sections, arteries appear round, whereas veins exhibit an elliptical shape (**Fig. 12B**, **C**). However, all types of blood vessels, except capillaries, share the same general features and vary only slightly in the composition of the wall layers (tunica intima, tunica media and tunica externa) and the fraction of different cells within those layers. [263]

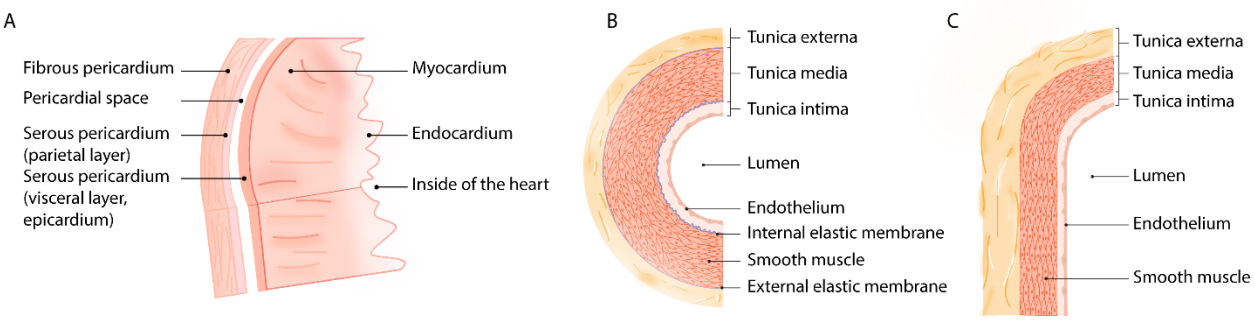

Fig. 12. Schematic representation of the heart and blood vessel wall. (A) Structure of the heart wall. Adapted from Miller et al. [256] (B) Arteries and (C) veins share the same general features but the wall of arteries are much thicker. Adapted from [264].

Endothelial cells form the inner tunica intima layer, thereby separating blood and organs. Their function and gene expression are constantly influenced by signals coming from both the vessel inside (luminal) and outside (abluminal). [265] These include alterations in the blood composition, its mechanical forces, or the composition of the ECM components of the vessel wall. [252, 265] The middle layer of vessel walls, also referred to as tunica media, consists of circumferentially oriented smooth muscle cells, that alternate with rings of the internal elastic lamellae in large elastic arteries. Collagen bundles are located between these lamellae which lack a pattern at physiological pressure but provide enhanced strength and flexibility with increasing pressure by becoming circumferentially aligned. [266] In contrast to large arteries, arterioles have less smooth muscle layers, and capillaries are covered by a discontinuous coat of pericytes instead of SMCs. [267] Furthermore, in comparison to arteries of similar size, veins have a thinner media and are more compliant but both vessel types have an outer tunica externa (adventitia) comprised of fibroblasts, progenitor cells and the ECM. The tunica externa is comparable to the epicardium of the heart and holds the vessels in place. [267, 268]

1.3.2 Cell types of the heart and blood vessels

The adult human heart consists of mainly four different cell types which maintain the structural, mechanical, electrical and functional integrity of the heart- cardiac fibroblasts, cardiomyocytes, smooth muscle cells and endothelial cells. [269] The proportional distribution with respect to number and volume, however, remains controversial. Cardiac fibroblasts are mesenchymal cells which constitute about half of all heart cells, being dispersed throughout the ECM and exerting contractile force on myocytes. [270] They are interconnected by long filopodia and provide mechanical support to the heart as they produce and maintain the extracellular matrix, primarily collagens type I and III. [250, 271] However, increased pathological stress and changes in mechanical stretch alter the physical mechanics of fibroblasts, which

impair fibroblast function, increase fibrosis and modify the ECM metabolism. Furthermore, changes in gene expression and the secretion of growth factors (e.g. TGF-β) and cytokines such as TGF-α or interleukin 6 (IL-6) stimulate the differentiation of fibroblasts to myofibroblasts, which actively participate in the inflammatory response. [271] Morphologically, myofibroblasts contain bundles of actin microfilaments with associated contractile proteins (e.g. non-muscle myosin), that terminate on the myofibroblast cell surface in the fibronexus, a specialized adhesion complex where the intracellular actin is linked to the extracellular fibronectin filaments via integrins. [272] Cardiomyocytes, the contractile cells of the heart, form the myocardium and contribute about 20-30% to the total cell number in the heart but, given their size, account for over 70% of the total cardiac mass. [250, 273-275] In contrast, smooth muscle cells, which provide support to the coronary arteries and vasculatures, and endothelial cells that form the interior lining of the heart (endocardium), blood vessels and cardiac valves, are less abundant in the heart. [250]

The walls of blood vessels consists of cell types that affect the smooth muscle tone to control resistance, arterial diameter and tissue blood flow. [276] Endothelial cells (ECs) line the entire vasculature and have been a subject of numerous studies. They can be identified by several well-characterized markers such as vascular endothelial (VE)-cadherin, platelet endothelial cell adhesion molecule 1 (PECAM-1, CD31), vascular endothelial growth factor receptors (VEGFRs) and isolectin B4. [267] During embryonic development, most mesodermal-derived ECs coalesce into initial blood tubes through the process of vasculogenesis, the *de novo* formation of blood vessels, and give rise to further vessels by sprouting and intussusceptive microvascular growth involving EC proliferation, migration and invasion during angiogenesis. [277, 278] Approximately 24 hours after blood circulation is initiated, mural cells (vSMCs or pericytes) are recruited to the endothelial tubes in a PDGF-B-dependent manner, promoting EC quiescence and long-term vessel stabilization. [147, 267] As endothelial cells differentiate, they establish a concentration gradient of platelet-derived growth factor-B (PDGF-B) that is sensed by the surrounding vSMCs via specific tyrosine kinase receptors (PDGFR-β) and promotes vSMC migration and proliferation, leading to vSMC recruitment to the vessel wall. [279] Although the importance of the cross talk between EC and vSMCs is well established, a variety of other signaling pathways, such as transforming growth factor β (TGF-β), Notch, epidermal growth factor (EGF) and angiopoietin-1 (Ang-1)/Tie2 signaling also contribute to mural cell differentiation, recruitment and stabilization. [254, 280-290] The Angiopoietin-1/Tie2 pathway, for example, may not contribute to mural cell recruitment but was shown to be crucial to maintain the physical EC-SMC interaction, as well as for the regulation of vascular integrity through EC-ECM adhesion and matrix composition. [291] Furthermore, integrins, especially α5β1, have been implicated in the signaling of the Ang/Tie system, either by the constitutive interaction with Tie2 and the concomitant modulation of Tie2

activity or the direct interaction with Ang-2. Latter interaction was shown to induce FAK phosphorylation, resulting in the activation of Rac1, EC migration and sprouting angiogenesis. [291-294] ECs do not only play a key role in angiogenesis but also in various other processes including inflammation, blood flow regulation and dynamic modulation of ECM components. [295] Given these multiple functions, ECs are essential to maintain vascular homeostasis and an altered angiogenic balance or EC dysfunction is commonly involved in pathological disorders, such as systemic and pulmonary hypertension, atherosclerosis, stroke, inflammatory syndromes and cancer. [295]

The tunica externa (adventitia) additionally plays crucial roles during homeostasis and disease of the vasculature. [296] The collagen-rich (type I and III collagens) adventitial layer is located outside the external elastic lamella and provides vessel wall rigidity to prevent wall rupture at high pressure. [267] This is an important site for innate immune responses and surveillance as inflammatory cells traffic into and out of the vessel walls. [296] It furthermore plays a role in regulating the lumen of blood vessels, either by short-term regulation of smooth muscle contraction or the long-term control of vessel wall remodeling. [297, 298] The adventitia consists of a complex cellular community, including resident mast cells, macrophages, T and B cells, dendritic cells and fibroblasts embedded in a collagen-rich ECM. [296]

SMCs, the contractile cells of the tunica media, regulate vascular tone through dynamic cycles of cell contraction and relaxation. Since vSMCs are one of the two cell types analyzed in the present thesis, their morphology, regulation and function will be discussed in detail in a separate chapter (1.3.2.2).

1.3.2.1 The structural unit of the myocardium- the cardiomyocytes

Cardiomyocytes ensure that the heart effectively pumps the blood to all organs and tissues within an organism. These cells are required to contract in unison, a phenomenon achieved by the spatial regulation of ion channels that control the influx and efflux of calcium (Ca^{2+}) ions. For controlling the Ca^{2+} release, the electrical activity of the sarcolemma plays an important role and hence controls the cells contractility (1.3.2.1.3). [248]

During late development and early postnatal life, cardiomyocytes undergo physiological hypertrophic growth, realign cytoskeletal components and acquire a mature, adult cytoarchitecture to meet the increased hemodynamic load. Cardiac hypertrophy is an acute compensatory or adaptive mechanism by which the organism tries to preserve cardiac function in response to pressure or volume overload. Clinically, two forms of hypertrophy can be described: physiological and pathological hypertrophy. [299] While physiological hypertrophy is defined as an increase in cardiac mass with preserved myocardial architecture and function in response to normal postnatal maturation or exercise, pathological hypertrophy is

associated with increased CM death and fibrosis, as well as reduced cardiac function caused by mechanical stress (e.g. hypertension). [299, 300] Cardiac hypertrophy is usually characterized by three different aspects: (i) an increase in the assembly of sarcomeres and expanded cell spreading area due to an increase in global mRNA and protein synthesis, (ii) the re-activation of fetal genes such as atrial natriuretic peptide (ANP) and (iii) an increase in CM survival. In the early stage, hypertrophic growth exhibits a protective role as it allows the heart to generate the necessary contractile forces. However, continued hypertrophic growth often results in heart failure as cardiomyocytes fail to generate the contractile force required for an effective cardiac output. In addition to hypertrophic growth, pathological conditions often cause CMs to induce apoptotic and necrotic responses leading to the reduction in the cell number. [248]

1.3.2.1.1 From early fetal to adult cardiomyocytes- cardiomyocyte maturation

The mammalian heart development is a highly dynamic process during which the cardiomyocytes undergo changes that allow them to sustain billions of contraction-relaxation cycles. These include changes in cell structure, metabolism, function and gene expression and can be combined under the term 'cardiomyocyte maturation'. [301] Four distinct developmental CM stages can be described *in vivo*: early and late fetal, neonatal and adult CMs.

Cardiac looping transforms the initial straight embryonic heart tube into a helical wound loop. [302] During this process cardiomyocytes are divided into early fetal and late fetal CMs, which are either found during the early or late cardiac looping stages, respectively. [303] In mammals, the cells during the first two weeks after birth are referred to neonatal CMs, while adult CMs represent the fully developed, mature stage. [303, 304] When comparing the four different developmental stages, they show severe morphological differences. While early and late fetal CMs are single nucleated cells with a round morphology and a spreading area of about 1000-1300 μm^2, neonatal CMs switch to a more elongated, fibroblast-like morphology, with some cells being binucleated. [303] During embryogenesis, the heart grows primarily by hyperplasia and cardiomyocyte proliferation is regulated by several pathways, most notably the Neuregulin-1 (NRG-1)/ErbB/ERK signaling cascade. Furthermore, while Bone Morphogenetic Protein (BMP) signaling and the Insulin-like growth factor (IGF)/phosphatidylinositol 3-kinase (PI3K) pathways are required for hyperplastic growth after midgestation, the Hippo pathway is involved in CM proliferation and organ size control throughout the development and after birth. [305] In the days after birth, mouse CMs undergo one to two rounds of cell division without cytokinesis that results in binucleation in some cells. [306] Furthermore, at the same time as neonatal CMs switch from hyperplastic to hypertrophic growth, contractile proteins switch from fetal to adult isoforms. [248, 307] Mature adult CMs are elongated and

rod-shaped (**Fig. 13B**), with a spreading area of about 10000-14000 µm^2. About 30% of adult CMs are binucleated. [303] It was long thought that adult CMs represent a terminally differentiated, specialized and structured cell type, however, this dogma was challenged by the characterization of CMs, which re-enter the cell cycle during cardiac regeneration. [308] The identification of cardiac progenitor cells and the investigations of the transcriptional regulation of cardiac regeneration revealed new insights into the self-renewal ability of adult CMs. [307-309]

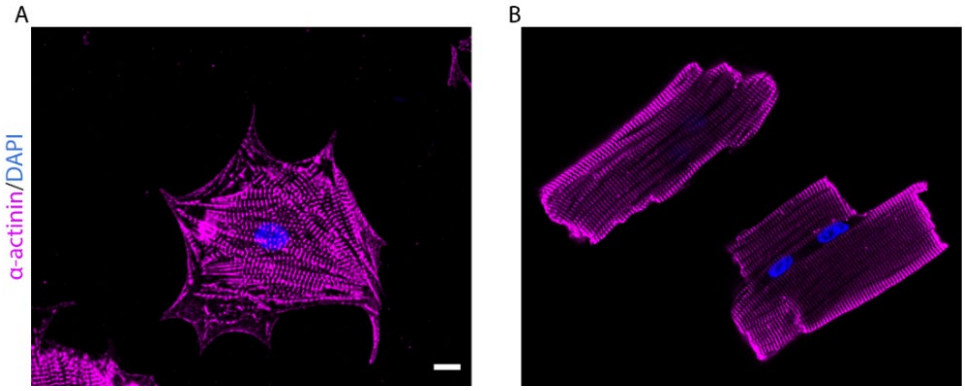

Fig. 13. Cell morphology of (A) neonatal versus (B) adult cardiomyocytes. Neonatal mouse CMs were plated on fibronectin and fixed 3 days after isolation. Adult mouse CMs were plated on laminin for 1.5 h before fixation. Both, neonatal and adult CMs were stained using an antibody against the Z-disc marker α-actinin. DAPI was used to stain the nuclei. Note, the rod-shaped cell morphology of adult CMs in comparison to the star-like morphology of neonatal cardiomyocytes. Scale, 10 µm.

Cardiomyocyte maturation is not only characterized by morphological but also by structural cell changes (**Fig. 13**). [310, 311] Myofibrils massively increase with CM maturation as new sarcomeres are continuously added in alignment with pre-existing myofibrils. In addition, the ultrastructural organization of the sarcomeres develops with the CM maturation. In early fetal CMs, Z-discs only start to form, while late fetal CMs have completely developed Z-discs as well as I- and A-bands, and H zones. The typical muscular striated patterning is visible from the late fetal stage onwards, although M-lines only develop during the neonatal period. [310, 311] It is not surprising, that contemporaneous with the changes in CM structure and morphology the expression of contractile proteins changes in temporal relation to the alterations of functional properties (sarcomeric isoform switching). The most well-known switch in rodents is the myosin heavy chain (MHC) switch. During embryonic development β-MHC (*MYH7*) is predominantly expressed and starts to decrease rapidly around birth. α-MHC (*MYH6*) is also already present during the embryonic development but the ratio of α-MHC to β-MHC increases in neonatal CMs until α-MHC becomes the only isoform in adult CMs. [312] Other proteins that experience isoform switching include the regulatory light chain of myosin, which switches from *MYL7* in early fetal CMs to *MYL2* in adult ventricular CMs and the

troponin I isoform that switches from slow skeletal troponin I (*TNNT1*) in fetal and neonatal CMs to cardiac troponin I (*TNNT2*) in adult CMs. [312-315] Other hallmarks of the cardiomyocyte maturation process, which will not be further discussed in this thesis, are the electrophysiology, the calcium handling and the metabolism. [301, 303]

1.3.2.1.2 The sarcomere and its function

To provide an effective pump action and to guarantee an adequate blood perfusion of all organs and tissues within an organism, the hearts' contractile cells, the cardiomyocytes, need to contract in unison. [248] Cardiomyocytes are specialized muscle cells that are composed of bundles of myofibrils (1-2 µm diameter) that contain myofilaments. Two proteins, actin and myosin, assemble in two types of myofilaments, thin actin filaments (6-7 nm diameter) and thick myosin filaments (15-16 nm diameter). [316] These myofilaments are organized into repeating microanatomical subunits, called sarcomeres, along the length of the myofibril (**Fig. 14A**). The sarcomere is responsible for generating the force during CM contraction, thus, it comprises the fundamental structural and functional unit of these cells. [317] It is bordered on both ends by a roughly 100 nm thick protein-rich structure, the Z-disc. Due to the highly organized assembly of actin and myosin filaments within the sarcomere, their overlapping and non-overlapping patterns produce distinct bands. These bands can be observed under a microscope and are called the A-band (anisotropic) and I-band (isotropic). [316] The A-band is located in the center of the sarcomere in the area where thick and thin filaments overlap. However, a less dense region where the thin filaments are absent, the H zone, can be found within the A-band. The I-band, on the other hand, is the region on either side of a Z-disc that contains only thin filaments and titin. Titin, a gigantic elastic protein, builds up the connecting filament within the sarcomeres. It connects the Z-disc with the middle of the myosin filament at the M-line, the region in the middle of a sarcomere, thereby anchoring the thick filament during contraction and relaxation. [316, 317] In contrast, the actin filaments are crosslinked and anchored to the Z-disc by α-actinin. Upon muscle contraction, the thick myosin filament slides on the thin actin filaments (sliding filament theory, 1.3.2.1.3), resulting in the shortening of the I-band and the movement of the Z-discs towards each other. On the ultrastructural level the force required to pump blood through the circulatory system is generated by the shortening of individual sarcomeres. This force transmission can occur either longitudinal, from one sarcomere to the next one within one myofibril until it reaches the intercalated disc, or lateral. Lateral force transmission occurs from the Z-disc of one myofibril to the next one until it reaches the sarcolemma via the costameres. [318] Costameres are complex protein structures that flank the M-lines and Z-discs and overlie the I-bands of the immediately subjacent sarcomeres

(**Fig. 14B, C**). [319] They thereby serve as a direct link and anchor point for the Z-disc with the sarcolemmal membrane and the ECM, providing stability to the sarcomeres. [145] In addition, they are able to transmit the contractile forces generated by the myofilaments directly to the ECM (inside-out signaling) and act as a mechanical sensor that transduces changes in mechanical force to cellular signaling cascades (outside-in signaling). Two major protein complexes have been described at the costameres: the dystrophin-glycoprotein and the integrin complex. Latter one is related to integrin-containing adhesion structures found in most non-muscle cell types (1.1.1). [318]

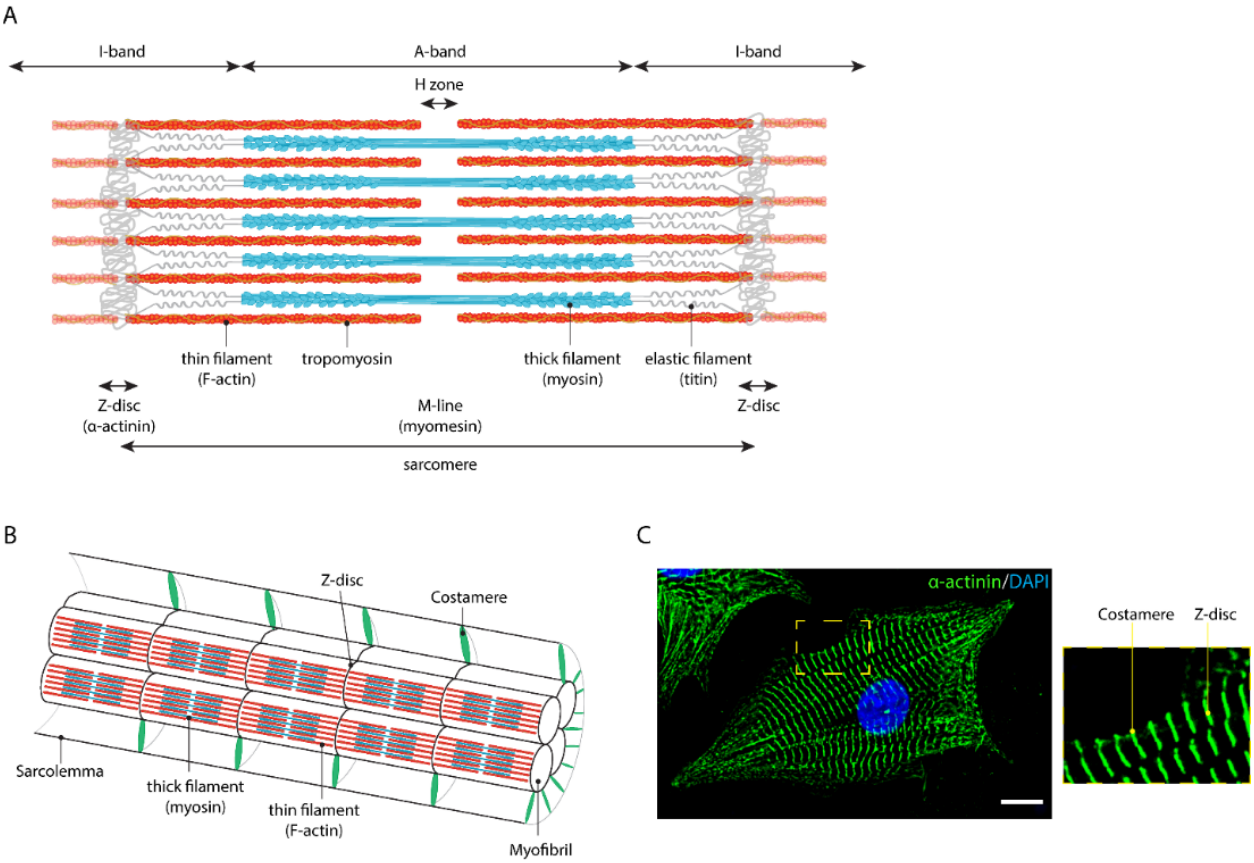

Fig. 14. Sarcomere structure and cellular localization of costameres in cardiomyocytes. (A) Drawing of a cardiac sarcomere illustrating the three major filament types: actin-based thin filaments, myosin-based thick filaments and elastic titin. Z-disc and M-line marker proteins are α-actinin and myomesin, respectively. Adapted from Burbaum et al. (paper II). [320] (B) Schema illustrating costameres that physically couple myofibrils to the sarcolemma at the Z-discs. Adapted from Ervasti. [321] (C) Isolated neonatal ventricular rat cardiomyocyte plated on fibronectin showing α-actinin-positive Z-discs and costamere localization. DAPI was used to stain nuclei. Scale, 10 µm.

1.3.2.1.3 Cardiomyocyte contraction- the sliding filament theory

Given their role in heart function, cardiomyocytes are required to work together as a syncytium. They are connected with each other at the intercalated discs and spread the action potentials through gap junctions to support the synchronized contraction of the myocardium. In cardiac and skeletal muscle tissue, contraction occurs through a mechanism known as excitation-contraction coupling (ECC). Cardiac ECC is the process by which the electrical activation of cardiomyocytes through an action potential from the neurons leads to a mechanical response that facilitates muscle movement. [322] In CMs, the ECC is dependent on calcium-induced calcium release, which involves the influx of calcium ions (Ca^{2+}) into the cells through ryanodine receptors, triggering further release of ions into the cytoplasm from stores in the sarcoplasmic reticulum (SR). [323] The actual mechanical contraction response can be described via the sliding filament theory (**Fig. 15A**): [322, 324, 325]

1) The pacemaker cells in the sinoatrial node induce an action potential, which is conducted to the cardiomyocytes through gap junctions.
2) The action potential travels through the sarcomeres and activates calcium channels in the T-tubules, leading to a calcium influx into the cytoplasm.
3) Ca^{2+} in the cytoplasm binds to the cardiac troponin-C, causing conformational changes within the troponin complex that allow the tropomyosin to expose the myosin binding sites on actin. (**Fig. 15B**) Subsequently, this movement permits the myosin heads to bind to actin and form a cross-bridge.
4) Myosin then uses energy stored as adenosine triphosphate (ATP). The ATPase activity in the myosin head hydrolyzes the ATP and tilts the head towards the M-line upon the release of an inorganic phosphate molecule (P_i) and energy (power stroke). The sarcomere shortens as the actin is pulled toward the M-line. Upon the binding of a new ATP molecule, the myosin is released from the actin filament and the myosin head returns to its starting position.
5) For cardiac relaxation, the intracellular Ca^{2+} concentration must decline under a certain threshold, allowing the Ca^{2+} to dissociate from the troponin-C and terminate the myofilament crossbridge cycle.

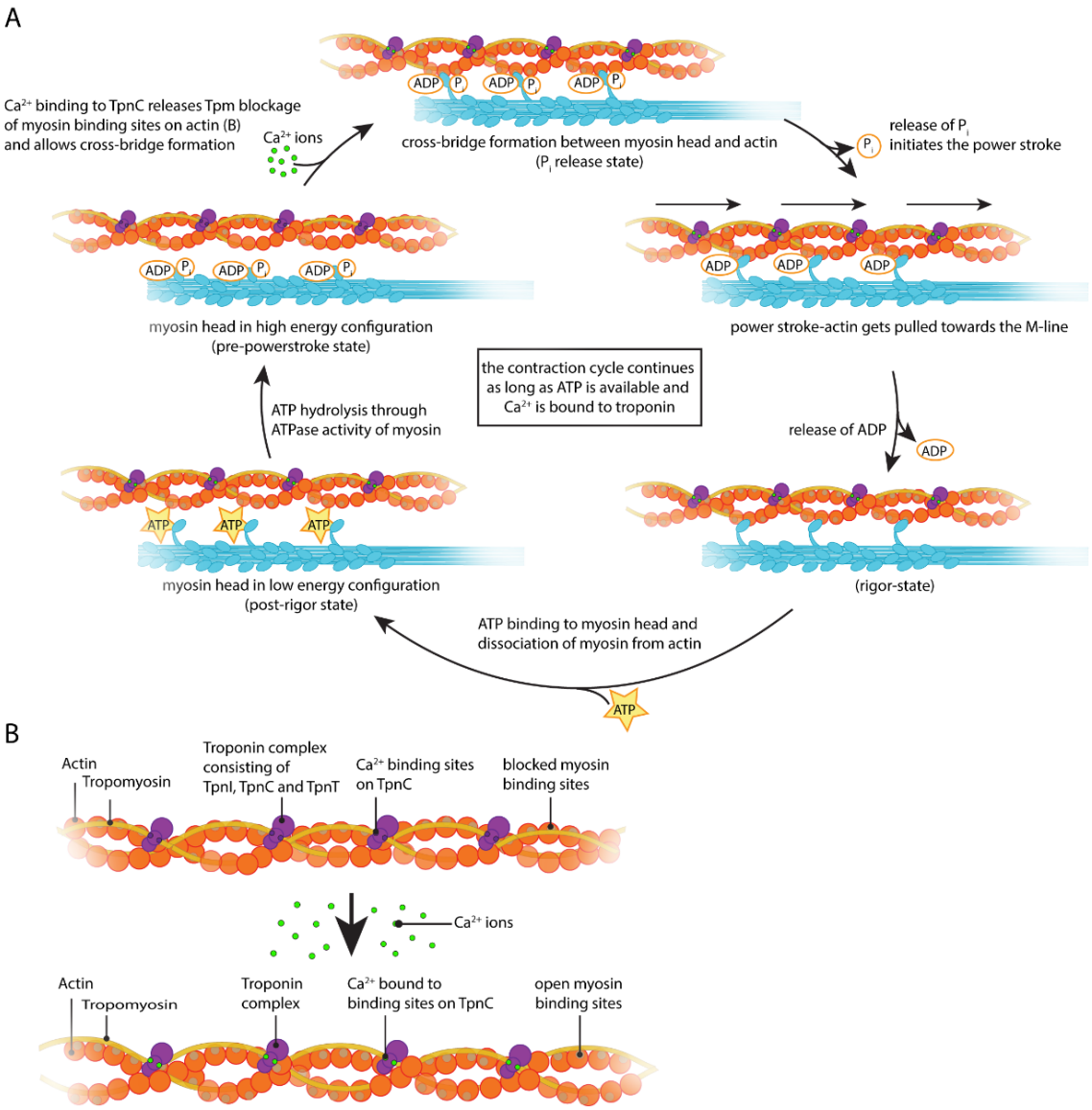

Fig. 15. Sliding filament theory of muscle contraction. (A) The interaction between myosin and actin as basis for muscle contraction. (B) The role of regulatory proteins and calcium ions in muscle contraction. Adapted from Campell and Reece. [326]

The central feature of muscle contraction is the interaction of myosin with the actin filaments. Crystal structures of myosin in different states and the actomyosin complex have provided important insights into the structural changes driven by the binding of myosin to actin filaments during muscle contraction. [327-330] There is a general agreement in the field that the sequential releases of P_i and ADP, catalyzed by actin, drives the motor activity of myosin by inducing conformational changes in the myosin motor that allow movement and force generation. [329] Four structural states of myosin have been identified: the rigor, post-rigor, pre-powerstroke and the P_i release state (**Fig. 15A**). [329] The rigor state is the nucleotide free

state in which myosin is bound to F-actin and the actomyosin interface is mainly stabilized by hydrophobic interactions. [328] Upon ATP binding, myosin rapidly dissociates from the actin filament (post-rigor state) and subsequent ATP hydrolysis primes myosin for force production by inducing the pre-powerstroke (PPS) state. In this state, ADP and P_i are still trapped within the motor and actin binding is required to induce structural rearrangements that are necessary to open up an alternative escape route for phosphate (P_i release state). The release of P_i will subsequently induce the power stroke. [327, 329, 330]

1.3.2.2 The contractile cells of blood vessels- smooth muscle cells

Smooth muscle cells are the major cell type found in the tunica media of blood vessels but are also present in the walls of almost all other organs such as stomach, bladder, intestine, uterus and the eye. These cells fulfill a variety of functions in the body such as the transport of the food bolus through the intestine, the sealing of body orifices (e.g. pylorus, uterus) and the shrinking of the pupils in eyes. [331] In mature blood vessels, vSMCs critically regulate vessel contraction and relaxation, thereby maintaining vascular tone and allowing the blood perfusion of downstream tissues. Furthermore, they respond to environmental stress and are involved in the repair of the blood vessel wall after vascular injury. [332-334] Consequently, abnormalities in vSMC anatomy or physiology contribute to various vessel pathologies leading to cardiovascular disease (CVD), the number one cause of morbidity and mortality worldwide. [335] The most common form of CVD is a disorder called atherosclerosis, a progressive inflammatory disease characterized by the accumulation of lipids and ECM (plaque) inside large arteries which can lead to stroke, heart attack and thrombosis. [335] SMCs elicit central roles in all developmental stages of this disease, especially in the formation of the fibrous cap and the plaque stability in advanced atherosclerosis. [335-337]

Microscopically, smooth muscle cells appear homogeneous in contrast to cardiac or skeletal muscle, in which a regular sarcomeric pattern of contractile proteins can be observed. SMCs are spindle-shaped or rhomboidal cells, 30-200 µm in length with a single central nucleus, and are surrounded by a basal lamina. Long thick myosin filaments are intermingled with thin actin filaments, which are either anchored by cytoplasmic dense bodies, an analogous to the sarcomeric Z-disc, or attached to dense plaques on the plasma membrane. [338, 339] The dense bodies also anchor the desmin-positive intermediate filaments, which run from one end of the cell to the other, thereby preventing excess stretching. [339] α-actinin is a well-known component of both dense bodies and plaques, whereas vinculin and talin are only present in latter ones. [340] The thick filaments are thought to have a non-helical, side-polar arrangement of crossbridges (**Fig. 7B**), in contrast to the bipolar kind found in cardiac and skeletal muscle (**Fig. 7A**). [341, 342]

After their recruitment to an EC tube during angiogenesis, SMCs assemble into a functional monolayer and differentiate, adapting a quiescent state with low cell migration, proliferation and ECM synthesis. [343] However, in contrast to mature terminally differentiated cardiomyocytes and skeletal muscle cells, adult SMCs have been shown to modulate their phenotype (phenotypic switching) in response to injury or disease, resulting in differential gene expression of SMC marker, upregulated proliferation potential and migration properties. Thus, depending on environmental and intracellular cues, SMCs can adapt virtually every phenotype between a fully differentiated contractile state and an undifferentiated, highly migratory and proliferative synthetic state. [333, 344] A variety of useful markers allow to label and distinguish the different SMC pools (**Fig. 16**). Quiescent vSMC express high levels of proteins required for their contractile functions, such as smooth muscle myosin heavy chain (SM-MHC) isoforms and α-smooth muscle actin (α-SMA), the central components of the contractile apparatus. [343] A late stage differentiation marker is the contractile filament smoothelin B, which is exclusively expressed in mature vSMC and often rapidly downregulated in proliferating SMC cultures. [345] Other well-characterized markers of mature vSMC include the actin crosslinking protein SM22α, also known as transgelin, and the calcium binding protein calponin. [343, 344] However, α-SMA and other SMC differentiation marker were also found to be expressed in a variety of non-SMC cell types, for example in endothelial cells during vascular remodeling, myofibroblasts during wound repair and in cardiomyocytes during normal development or as marker for myocardial hypertrophy in adult hearts. [343, 346-348] This bedevils the correct identification of primary vSMCs, where a contamination with other cell types may happen. [343]

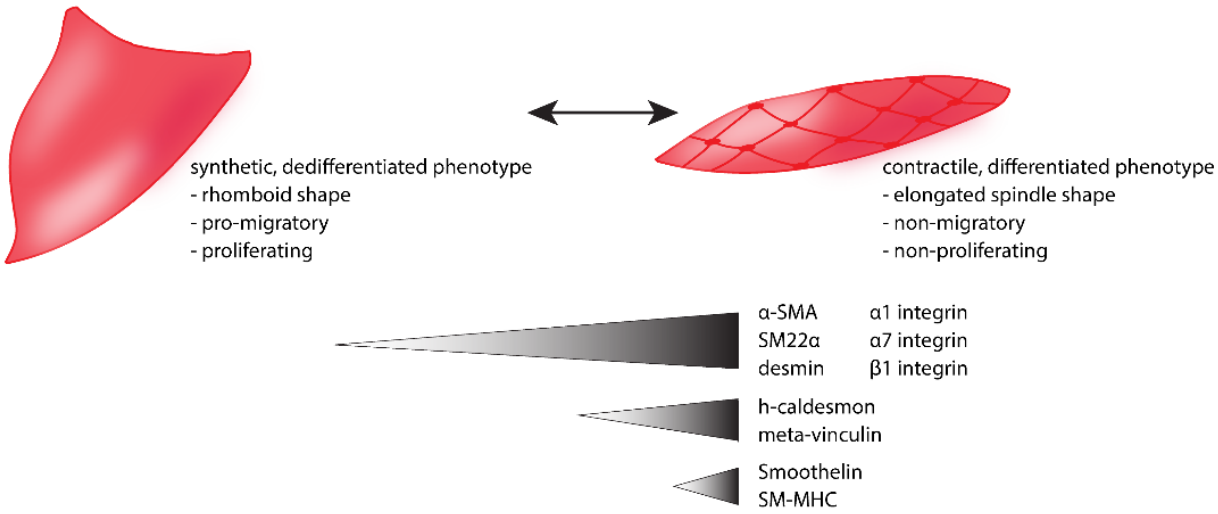

Fig. 16. Phenotypic switching by vascular smooth muscle cells and schematic representation of expression levels of genes associates with the contractile phenotype. Mature SMC are able to switch between a contractile and synthetic phenotype. Adapted from Milewicz et al. [349]

Phenotypic switching occurs as e.g. the endothelial monolayer or the vSMC-ECM interaction is disrupted, in case of injury, wound healing or vascular remodeling as well as when cells are exposed to growth factors (e.g. PDGF-BB) which initiate intracellular signaling cascades that lead to a rapid downregulation of contractile proteins and the acquisition of a dedifferentiated phenotype. [350] Although markers for the contractile state of vSMCs are well defined, only the upregulation of myosin heavy chain embryonic (SMemb) and tropomyosin 4 (TM4) have been linked to the proliferative phenotype. [351]

1.3.2.2.1 Regulation of smooth muscle cell contractility

SMCs contract in response to an increase in the intracellular calcium levels through neuronal or hormonal stimulation. This Ca^{2+}-increase can be either mediated through the opening of voltage-dependent L-type calcium channels in the plasma membrane or through the release from internal calcium stores by IP_3 receptors. [352] The elevated level of cytoplasmic Ca^{2+} results in force generation. The thin filaments in SMCs contain actin and tropomyosin, but also caldesmon and calponin as regulatory proteins instead of troponin, which results in a different regulation of the contractile system compared to that in cardiac cells. While in cardiomyocytes Ca^{2+} binding to troponin-C exposes myosin binding sites on the actin filaments, Ca^{2+} binding to calmodulin activates MLCK. As a result, the regulation of contractility in CMs is linked to the thin actin filaments, whereas in SMCs it is linked to the myosin filaments. [353] Furthermore, cardiac muscle contracts fast in a process known as excitation-contraction coupling, as described above, whereas smooth muscle cells do not undergo the same type of ECC leading to slower cell contraction. [354]

Following the increase of the cytoplasmic Ca^{2+} concentration through the production of IP_3, Ca^{2+} binds to calmodulin, resulting in the activation of MLCK and the subsequent phosphorylation of the regulatory light chain of myosin II (pMLC) (**Fig. 17B**). [355] In addition, the Ca^{2+}/calmodulin complex inhibits calponin and caldesmon, two proteins that are holding tropomyosin in place and prevent actin-myosin interaction, and facilitates to turn on the actin-myosin ATPase cycle. Upon tropomyosin movement, myosin heads attach to the actin binding sites, pull on the thin filaments which then slide past the thick filaments, causing the entire muscle fiber to contract by pulling the ends towards the center (corkscrew motion) (**Fig. 17A**). [36] The phosphorylation of MLC can be reversed by the myosin light chain phosphatase. [355] During recent years, a parallel signaling pathway was described that partially inhibits this phosphatase in a Ca^{2+}-independent manner. This regulation involves the monomeric guanosine triphosphate (GTP)-binding protein RhoA. [355-357] Receptors coupled to trimeric G-proteins activate this small GTPase, which in turn activates ROCK. [358] ROCK directly phosphorylates MYPT1, the myosin binding subunit of MLCP, and prevents the dephosphorylation of MLC. [355, 359, 360]

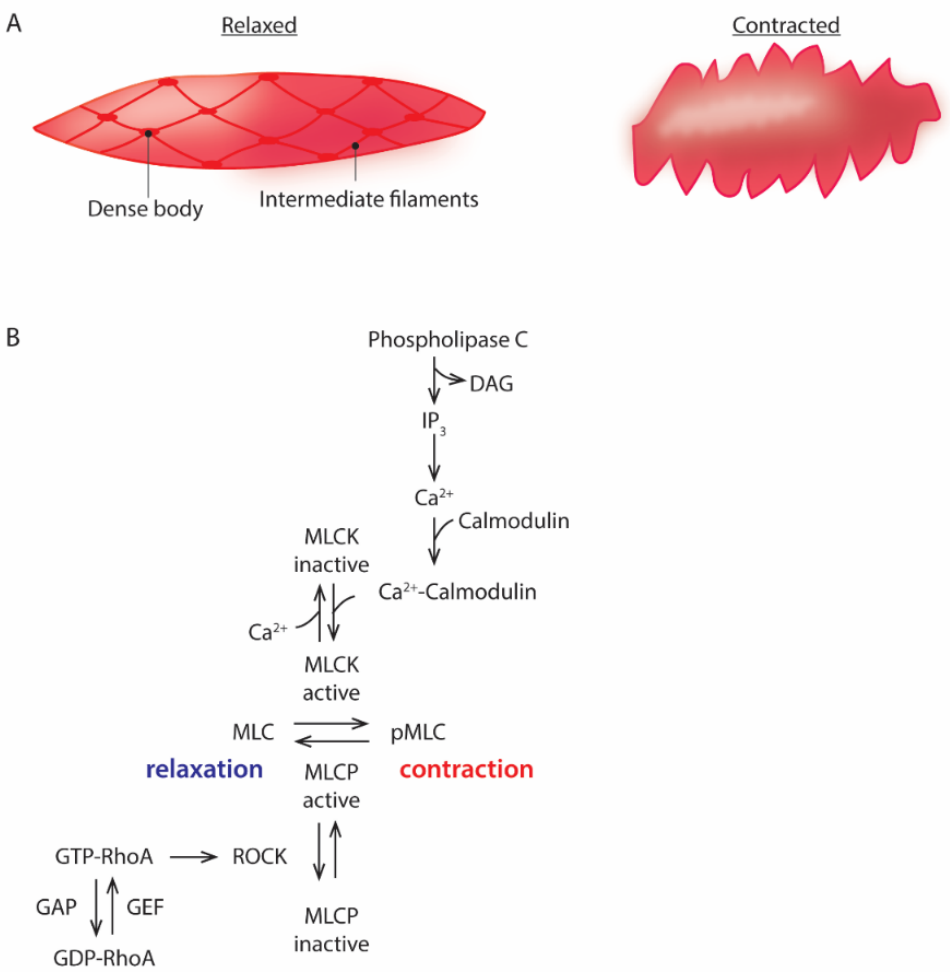

Fig. 17. Activation of smooth muscle cell contraction. (A) Due to the attachment of thin filaments at the plasma membrane through dense plaques, spindle-shaped SMCs develop pleats as they contract. (B) Biochemical pathway controlling phosphorylation of the regulatory myosin light chain of myosin II. Receptor stimulation results in the production of inositol 1,4,5-triphosphate (IP_3) by phospholipase C. Through binding to specific receptors induces IP_3 the efflux of Ca^{2+} ions from internal stores. Ca^{2+} binds calmodulin and together activate MLCK. Active MLCK phosphorylates MLC, a process reversed by MLCP. Activation of RhoA by GTP loading stimulates ROCK, which phosphorylates and inactivates MLCP. Adapted from Pollard et al. [339]

To maintain blood pressure, stabilize vessels and also regulate intestinal peristaltic, normal RhoA/ROCK signaling is crucial, while dysfunctional Rho signaling has been observed in a variety of pathologies including hypertension, asthma, pulmonary fibrosis and gut motility disorders. [361-364]

1.4 Cell-cell communication within the heart and blood vessels

The adult heart is a complex system of cellular and acellular tissue, harboring a pool of distinct cell types which physically interact with each other and communicate through a variety of soluble paracrine, autocrine and endocrine factors. Following an injury, dramatic alterations in the distinct cardiac cell populations were observed that affect the cell-cell and cell-ECM interactions and cardiac function. [270, 365, 366]

In the myocardium, cardiomyocytes are surrounded by the endomysium, a collagen-rich connective tissue that also harbors cardiac fibroblasts. [367] Both cell types express several voltage-gated potassium (K^+) channels which have been connected to the Angiotensin II (Ang II) pathway. Ang II upregulation leads to an enhanced secretion of cytokines and growth factors by cardiomyocytes, including TGF-β and endothelin-1, a potent vasoconstrictor stimulating cardiac hypertrophy. [368] Furthermore, fibroblasts also express specific Ang II receptors and Ang II binding promotes their proliferation and ECM synthesis. [270] PDGF is another signaling molecule secreted by CMs that was found to induce cardiac fibrosis, observed as increased fibroblast proliferation, migration and ECM deposition, with the subsequent development of a lethal dilated cardiomyopathy *in vivo*. [369] Additionally, CMs secret other growth factors and cytokines, such as VEGF and tumor necrosis factor-α (TNF-α), respectively. [370, 371] Although found in lower abundance, endothelial cells are also in direct contact to cardiomyocytes and CM-EC interactions allow for nitric oxide (NO) involvement in cardiomyocyte contraction. NO is activated by the nitric oxide synthase (NOS), a family of three isoforms, neuronal NOS (nNOS), inducible NOS (iNOS) and endothelial NOS (eNOS), which are all expressed in the heart. [372] Interestingly, eNOS-generated NO inhibits L-type Ca^{2+} channels whereas nNOS-generated NO stimulates sarcoplasmic reticulum (SR) Ca^{2+} release, leading to opposed effects on myocardial contractility. [373]

Heart function requires not only the chemical communication between cells but also the mechanical and electrical coupling between CMs. This is achieved by specialized adhesive structures called the intercalated disc. Three complexes form the intercalated disc: adherens junctions and desmosomes, that physically link the actin and intermediate filament cytoskeleton of neighboring CMs, respectively, and gap junctions that electrically couple cardiomyocytes. [374] Unlike gap junctions, which allow the exchange of ions and small molecules between adjacent cells, adhesion complex communication is another form of intracellular signaling and involves cascades that are triggered by cell-cell or cell-ECM engagement. Cardiomyocytes primarily attach to the ECM and detect mechanical forces via integrins (see 1.1.6.1).

To maintain normal cardiac function, cells of the myocardium have to communicate among each other but also to the vascular network. In blood vessels, ECs and SMCs utilize various signaling tactics to exchange

information, which can be mechanistically divided into two signaling strategies- diffusible or juxtracrine (contact-dependent) signaling. [279] The secretion of diffusible factors and the establishment of concentration gradients are important strategies employed during blood vessel formation. These include the already mentioned secretion of the polypeptide PDGF-B or the growth factors Ang-1 and TGF-β during development. [279] Furthermore, ECs and vSMCs are in close proximity in mature blood vessels, enabling highly efficient signaling via secreted factors. Endothelial-derived factors such as NO, prostacyclin and hyperpolarizing factor (EDHF) diffuse to SMCs causing vascular relaxation, while contracting agents like endothelin-1 and angiotensin II, released from ECs, are perceived by SMCs, increasing cell contraction and vascular tone. [276, 339, 375] As observed in cardiomyocytes, also ECs and fibroblasts form homo- and heterocellular gap junctions, known as myoendothelial junctions (MEJ), allowing a direct and rapid intercellular communication to control and coordinate vascular function. [376] Connexins (Cx) are transmembrane proteins that make up these gap junctions, which directly connect the cytoplasm of adjacent cells, allowing the exchange of ions and metabolites. Gap junctions are made up of six connexin subunits, called connexon or hemichannel, on both sides of the plasma membrane assembling into functional channels. [377, 378] Vascular gap junctions are made up of one or more of the four connexin proteins- Cx37, Cx40, Cx43 and Cx45, however, only Cx37, Cx40 and Cx43 are present in MEJ. [376]

The evolutionarily conserved Notch signaling pathway is important to control cell fates during embryonic development, vascular repair of injury and vascular pathology in mammals. [350] Membrane-bound Notch receptors (Notch1-4) are activated by transmembrane ligands of the Jagged (Jag) or Delta-like (Dll) family (Jag-1, and -2 as well as Dll-1, -3, and -4) on adjacent cells. [379] The Notch pathway plays a major role in arteriovenous identity, tip cell specification, angiogenic sprouting and SMC differentiation. [350, 380] Perturbations in the expression of Notch pathway components in vSMCs and ECs result in a variety of vascular defects such as dilated or collapsed aorta, hemorrhaging, defective arterial branching and disorganized elastic lamina. [350] Moreover, vSMC recognition of the Notch ligand Jag-1 on endothelial cells induces vessel maturation by regulating integrin-mediated cell adhesion and can be inhibited by the von Willebrand factor. [150, 381] Furthermore, Notch signaling also regulates the development of the aortic valve, ventricles and outflow tract. [382]

In summary, cells of the cardiovascular system need to adhere to each other and the ECM, and communicate with each other to maintain body homeostasis. Integrins and their cytosolic adaptor proteins at cell-cell and cell-ECM adhesion sites are integral components of the signal transduction machinery in the cardiovascular system to transmit signals bidirectional across the membrane.

2 AIMS OF THE THESIS

The cardiovascular system is a central organ system that is required for the distribution of blood containing important nutrients and oxygen to all tissues and organs. The development of the heart and blood vessels as well as the maintenance of body homeostasis is critically influenced by biological processes on the cellular level. The interactions of cells with each other and the ECM influence hereby for example cell adhesion, spreading, migration and proliferation. Integrins, as the main receptors for cell adhesion are well known for their pivotal function during these processes. However, these heterodimeric receptors lack actin binding capacity and intrinsic catalytic activity, thus, they depend on adaptor proteins to fulfill this function. Previous studies have shown that β1 integrin as well as members of the IPP complex play a vital role in maintaining the sarcomeric stability in CMs and in the proper recruitment of vSMCs to maturing blood vessels. Constitutive deletion of α-parvin results in embryonic lethality due to the missing establishment of two outflow tracts during heart development and the formation of edema and aneurismal dilations of the aorta. However, the embryonic lethality prevented the investigation of α-parvin function during late development or in adult mice.

Aim 1

The primary aim of this thesis was to investigate the role of α-parvin in contractile cells of the cardiovascular system after embryonic development. I thereby focused on the *in vitro* generation of α-parvin knockout NMVCs and MOVAS, through AdenoCre transduction or CRISPR-mediated deletion, respectively, and the characterization of these cells in respect to integrin-mediated functions. We furthermore analyzed whether the loss of α-parvin is functionally compensated through the upregulation of β-parvin. Additionally, the *in vivo* function of cardiac or SMC-specific α-parvin was investigated using adult *αMHC-MerCreMer* or *SMMHC-CreER^{T2}* transgenic mice, respectively.

Aim 2

To further increase our understanding of α-parvin regulation in the cardiovascular system, the identification and characterization of novel α-parvin interacting partners in CMs and vSMCs was another aim of this thesis. I used GFP immunoprecipitation and proximity-dependent biotin labeling identification assays to search for new α- or β-parvin isoform specific or pan-parvin interactors with a special focus on regulators of the RhoA/ROCK/MLC2 signaling pathway, which was shown to be misregulated in cells lacking IPP complex members.

3 MATERIALS AND METHODS

3.1 Animals

Mice used in this study were housed under specific pathogen free (SPF) and 12 h:12 h light:dark conditions in an animal facility of the Max Planck Institute (MPI) of Biochemistry in Martinsried. They had continuous access to water and standard rodent food. At an age of three weeks, mice were gender-matched, marked with an ear tag and genotyped using PCR (see 3.4.7.1). For breeding, mice of an age of ≥ 6 weeks were used. All adult animals used for experiments were euthanized by CO_2 or cervical dislocation. Alternatively, neonatal mice (three days after birth (P3)) were decapitated. All experiments were carried out in accordance with the German Animal Protection Law.

3.1.1 Breeding scheme

Constitutive deletion of α-parvin results in embryonic lethality between E10.5 and E14.5, preventing the analysis of α-parvin function in neonatal and adult animals. [171] Therefore, we used the Cre-*loxP* system to control gene disruption in a time and tissue-specific manner. The Cre protein is a tyrosine site-specific DNA recombinase that recognizes specifically two directly repeated DNA fragment sequences, known as *loxP* (locus of X-over P1) sites and mediates site-specific deletion of the *loxP* flanked (floxed (fl)) DNA. [383] A mouse strain carrying *loxP* sites flanking exon2 of the *PARVA* gene (*α-pv(fl/fl)*) was originally generated by Altstätter et al. [384] These mice were intercrossed with constitutive *β-parvin* knockout mice and backcrossed to C57/Bl6 background (F10) to obtain *α-pv(fl/fl) β-pv(-/-)* mice. The constitutive *β-parvin* KO mice were originally generated by Thievessen through the replacement of a part of exon2, intron2 and a part of exon 3 by an internal ribosome entry site (IRES)-regulated lacZ-reporter-gene and a phosphoglycerate-kinase (PGK)-driven neo-resistance cassette. [385]

To delete α-parvin in CMs, *MerCreMer* transgenic mice were bred into a background of *α-pv(fl/fl)* and *α-pv(fl/fl) β-pv(-/-)* mice. *MerCreMer* transgenic mice express the Cre recombinase under the control of the mouse cardiac-specific *alpha-myosin heavy chain* (αMHC; *MYH6*) promotor. [386] The estrogen receptor was mutated at glycine 525 to arginine, rendering the receptor insensitive to its natural ligand, 17β-estradiol. This mutant estrogen receptor (Mer) is instead sensitive to the estrogen antagonist tamoxifen (TAM) and permits a tamoxifen-inducible activity within targeted mammalian cells. [387]

SMMHC-CreER^{T2} mice were kindly provided by the Offermanns lab from the MPI for Heart and Lung Research. [388] To delete α-parvin in SMCs, *SMMHC-CreER^{T2}* transgenic mice were bred into a background of *α-pv(fl/fl)* and *α-pv(fl/fl) β-pv(-/-)* mice. In *SMMHC-CreER^{T2}* mice, Cre recombinase is expressed under control of the mouse *smooth muscle myosin, heavy polypeptide 11* (*MYH11*) promotor. In this mouse strain,

the Cre recombinase is fused to a mutated, TAM-inducible human estrogen receptor. [389] Due to the original insertion of the BAC transgene on the Y chromosome, only male animals are carrier of the Cre recombinase and only male animals were used for the experiments. [388]

3.1.2 Tamoxifen-induced knockout of α-parvin

Tamoxifen (Sigma-Aldrich, #T5648) was dissolved in warm corn oil at a stock concentration of 100 mg/mL. Shortly before use, TAM was further diluted to 10 mg/mL and used at the indicated doses and frequencies. Gene inactivation in adult *MerCreMer (MCM)* mice (12-15 weeks) was triggered by intraperitoneal injection (i.p.) of 30 or 40 mg/kg tamoxifen per day for three consecutive days. As controls *α-pv(fl/fl) MCM* mice treated with vehicle (corn oil) and *MerCreMer* mice treated with TAM were used.

Gene inactivation in adult *SMMHC-CreER^{T2}* male mice (16-20 weeks) was triggered by i.p. administration of 50 mg/kg tamoxifen per day for five consecutive days. Gender and age-matched *α-pv(fl/fl) SMMHC-CreER^{T2}* mice treated with vehicle (corn oil) and *α-pv(+/+) SMMHC-CreER^{T2}* mice were used as controls.

3.2 Common material

We purchased basic chemical compounds from the following companies: Merck (Darmstadt, Germany), Sigma-Aldrich (St. Louis, Missouri, USA), Thermo Fisher Scientific (Waltham, Massachusetts, USA) or Carl Roth GmbH (Karlsruhe, Germany). To prepare the solutions and buffer stocks we used double-distilled water (ddH_2O), purified with the Milli-Q®-System (MilliporeSigma, Burlington, Massachusetts, USA). Stock solutions of running buffer, transfer buffer and TBS were diluted with normal distilled water (dH_2O).

3.3 Antibodies

3.3.1 Primary antibodies

Table 1. List of primary antibodies used in this thesis.

Antigen	Species	Application	Dilution	Source
α-actinin	mouse	IF	1:200	Sigma (#A7811)
α-parvin	rabbit	WB/ IF	1:1000/ 1:200	Cell Signaling (#8190)
β1 integrin	rat	IF	1:400	Merck (#MAB1997)
β-parvin	rabbit	IF	1:200	home made
cTnT	mouse	IF	1:200	Thermo Fisher Scientific (#MA5-12960)
GAPDH	mouse	WB	1:1000	Calbiochem (#CB1001)
ILK	mouse	WB	1:5000	BD Bioscience (#611803)
Mprip	rabbit	WB/ IF	1:2000/ 1:200	Merck (#HPA022901)
Myomesin B4	mouse	IF	1:200	DSHB by Perriard, J.-C.
NFK3 kinase	rabbit	WB	1:1000	Abcam (#ab211442)
Paxillin	mouse	IF	1:600	BD Bioscience (#610051)
PINCH1	rabbit	IF	1:200	Epitomics (#2823-1)
pan-PINCH	mouse	WB	1:500	BD Bioscience (#612710)
pMLC (Ser19)	mouse	WB/ IF	1:1000/ 1:200	Cell Signaling (#3675)
pMLC (Thr18/ Ser19)	rabbit	WB/ IF	1:1000/ 1:200	Cell Signaling (#3674)
RhoA	mouse	WB	1:500	Cytoskeleton (#ARH05)
Rsu-1	rabbit	WB	1:1000	gift from Xing-An Wang
Talin-1	mouse	WB	1:1000	Sigma (#T3287)
Tubulin	rat	WB	1:1000	Merck (#MAB1864)

3.3.2 Secondary antibodies

Table 2. List of secondary antibodies used in this work.

Antigen	Species	Application	Dilution	Source
mouse IgG-HRP	donkey	WB	1:10000	Jackson ImmunoResearch (#715035151)
rabbit IgG-HRP	donkey	WB	1:10000	Jackson ImmunoResearch (#711035152)
rat IgG-HRP	donkey	WB	1:10000	Jackson ImmunoResearch (#712035150)
Streptavidin-HRP		WB	1:10000	Vector Laboratories (#SA-5004)
mouse lgG Alexa Fluor™ 647	donkey	IF	1:600	Thermo Fisher Scientific (#A31571)
rabbit lgG Alexa Fluor™ 488	goat	IF	1:600	Thermo Fisher Scientific (#A11008)
Alexa Fluor™ 488 Phalloidin		IF	1:600	Thermo Fisher Scientific (#A12379)
Cy3™ rabbit lgG	donkey	IF	1:600	Jackson ImmunoResearch (#711165152)
Cy3™ α-SMA	mouse	IF	1:800	Sigma (#C6198)

3.4 Molecular biological methods

3.4.1 Plasmids

Only original plasmids are depicted in Table 3. Plasmids that I cloned myself are not included.

Table 3. List of plasmids received from others and used in my thesis.

Plasmid	Received from
pEGFP(C1) α-parvin	Dr. Ralph Böttcher
pEGFP(N1) α-parvin	Dr. Ralph Böttcher
pEGFP(C1) β-parvin	Dr. Ralph Böttcher
pRetroQ AcGFP (C1)	Dr. Ralph Böttcher
pRetroQ AcGFP (N1)	Dr. Ralph Böttcher
pRetroQ (C1) myc-BioID2	Dr. Ralph Böttcher
pRetroQ (C1) TurboID	Dr. Guan Wang
rrl-cPPT-CMV-eGFP-WPRE	Dr. Markus Moser
pSpCas9(BB)-2A-GFP (px458)	Dr. Peter Krenn
pSpCas9(BB)-2A-Puro (px459)	Dr. Peter Krenn

3.4.2 Primer and Oligonucleotides

Table 4. List of primers used for genotyping, cloning, sequencing, RT-qPCR and CRISPR/Cas9-mediated knockout.

Genotyping primer	5' → 3'
APloxPf	CTG AGT GAC ATG GAG TTT GAG
APloxPr	GGA CTT GTG GAC TAG TTA GAC
APE2f	GAA GGA ATG AAC GCC ATC AAC
PGKf	GAT TAG ATA AAT GCC TGC TC
1EmBPi2F	GTG AAC TTC ACT GGA CTC TT
2BPE3r	TCC TTG AAC TTG GGG TCT TCT
Slz3_SMMHC-CreERT2 P5	TGA CCC CAT CTC TTC ACT CC
Slz4_SMMHC-CreERT2 P6	AAC TCC ACG ACC ACC TCA TC
Slz5_SMMHC-CreERT2 P7	AGT CCC TCA CAT CCT CAG GTT
79_28887_WT_rev	CCA ACT CTT GTG AGA GGA GCA
80_28886_Common	TCT ATT GCA CAC AGC AAT CCA
81_28888_Mut_rv	CCA GCA TTG TGA GAA CAA GG

Cloning primer	5' → 3'
RTB597_BioID_rv	GGA ATT TAC GTA GCG GCC GCT CTA TGC GTA ATC CGG TAC ATC GT
RTB598_BioID_fw_C	CAG ATC CGC TAG CCA CCA TGG AAC AAA AAC TC
RTB599_BioID_rev_C	GAG CTC GAG ATC TGA GTC CGG AGC TTC TTC TCA GGC TGA ACT CG
Slz6_LV_mBio_fw	ATA GAA GAC ACC GAC AAC CGT CAG ATC CGC TAG CCA CC
Slz7_LV_eGFP_fw	ATA GAA GAC ACC GAC GCT ACC GGT CGC CAC CAT GG
Slz8_LV_apv_rv	ATC CAG AGG TTG ATT GTC GAC GGT ACC GTC GAC TGC ATC A
Slz9_LV_bpv_rv	ATC CAG AGG TTG ATT GTC GAG CGG TAC CGT CGA CTG CTC A
Slz10_LV_mBio_rv	ATC CAG AGG TTG ATT GTC GAC CCC TAC CCG GTA GAA TTA TGA
Slz11_LV_eGFP_rv	ATC CAG AGG TTG ATT GTC GAT CAT AAT TCT ACC GGG TAG GGG AGG C
Slz82_pACEBac-IPP_rv	CGC CAT TAA CCT GAT GTT C
SLZ83_pACEBac-IPP_fw	GGG CCC CTG GAA CAG AAC
Slz84_pACEBac-IPP_bpv_fw	AGA ACA TCA GGT TAA TGG CGT CAC TCC ACA TCC TTG TAC TTG GTG
Slz85_pACEBac-IPP_bpv_rv	AAG TTC TGT TCC AGG GGC CCA TGT CCT CCG CGC CAC CA
Slz100_LP1 PreScission	GGG CCC CTG GAA CAG AAC TTC CAG
Slz101_LP2 ccdB	CGC CAT TAA CCT GAT GTT CTG GGG
Slz102_pCoofy1_Mprip_fw	AAG TTC TGT TCC AGG GGC CCA TGT CGG CGG CCA AGG
Slz103_pCoofy1_Mprip_rv	CCC CAG AAC ATC AGG TTA ATG GCG TCA GTT ATC CCA TGA GAC CTG CTC AAT TAC
Slz174_RetroQ_pvTagless_f	AGC AGA GCT GGT TTA GTG AAC CCA GAT CTC GAG CTC AAG CTT CG
Slz175_RetroQ_pvTagless_r	CGA AGC TTG AGC TCG AGA TCT GGG TTC ACT AAA CCA GCT CTG CT

Sequencing primer	5’ → 3’
RTB602_αPv_500 fw	CCC TGA AGC TTC CTC CCA GG
RTB603_αPv_600 rv	GGA AAC ATG GTC TGG GAG TCG
RTB600_βPv_500 fw	CGT TGG AAT GTG GAC TCT ATC C
RTB601_βPv_600 rv	CCA CCT GCA CGG TGA CAT GC
Slz12_Lenti fw	AAA TGG GCG GTA GGC GTG TAC G
Slz13_Lenti rev	AAG CCA TAC GGG AAG CAA TAG C
Slz208_TurboID_fw	AGA CAA GGT GCG AGT CAA ATG G
Slz104_Mprip_fw	ACG GGA ACC AGG ACT AGA AAG C
Slz105_Mprip_rv	AGA TCC GAG GCT TCT TTC TGG
Slz108_Mprip_int2_fw	TTC TGA TTC TGG TGA CCC TGG
Slz109_pCoofy1-Mprip_fw	GCG TAG AGG ATC GAG ATC TCG
Slz110_Mprip_int3_fw	GAA AGT AGA GCC ACC TAC C
Slz111_Mprip-pCoofy1_fw	AAG TGC CTG GAG AAT GCA CAC C

RT-qPCR primer	5’ → 3’
rtqPCR apv_p2_fw	GGT CCC CAA ATC ACC CAC TC
rtqPCR apv_p2_rv	GGA ACT CGG ATA CTT CTT TGG CT
rtqPCR bpv_p1_fw	GCA CTC GCT TAT GTC CTC C
rtqPCR bpv_p1_rv	CTG TAA GTC AGT CAC CTC CCT G
rtqPCR_ILK_fw	GCT CAG CAG ACA TGT GGA GT
rtqPCR_ILK_rev	TTC CAG TGC CAC CTT CAT CC
rtqPCR_Lims1_fw	CCG GAA TGA CCA ACA GCA AC
rtqPCR_Lims1_rv	TCA CGA TCT TCT CAG CAG GC

CRISPR/Cas9 primer	5’ → 3’
Slz92_apv_1.5 fw	TAA TAC GAC TCA CTA TAG CGT TCT TGG GGA AAC TCG
Slz93_apv_1.5 rev	TTC TAG CTC TAA AAC TCC GAG TTT CCC CAA GAA C
Slz115_apv1.5seq_fw	GAA TAA TTC CGC TTC CGT TTG GA
Slz116_apv1.5seq_rev	CCC GAG AAA ACT TTC CAG CAG AAA C
Slz164_bpv_1.1_fw	TAA TAC GAC TCA CTA TAG CGA GTC TTT CTT GGG CAA GT
Slz165_bpv_1.1_rev	TTC TAG CTC TAA AAC ACT TGC CCA AGA AAG ACT CGC
Slz166_bpv_1.1_PCR_fw	ACC TCG GGG TCA GTA GGC
Slz167_bpv_1.1_PCR_rv	CAA ATG TCT TAC GGA CAG GGA C
Slz168_bpv_1.1_Seq_rv	ACA GGA GGG CTC ATT GGC G
Slz169_bpv_5.1_fw	TAA TAC GAC TCA CTA TAG AGG TGA CGC AGT CCG AGA T
Slz170_bpv_5.1_rev	TTC TAG CTC TAA AAC ATC TCG GAC TGC GTC ACC TC
Slz171_bpv_5.1_PCR_fw	ATG GTC TCT CAA GTC AGC TTC C
Slz172_bpv_5.1_PCR_rv	CAA GAG GAT GCA TTG GTT CTT A
Slz173_bpv_5.1_Seq_fw	GCT AAG AGG CTG GAT TCC TAG TG
Slz199_bpv1.1_px459_fw	CAC CGC GAG TCT TTC TTG GGC AAG T

Slz200_bpv1.1_px459_rv	AAA CAC TTG CCC AAG AAA GAC TCG C
Slz201_bpv5.1_px459_fw	CAC CGG AGG TGA CGC AGT CCG AGA T
Slz202_bpv5.1_px459_rv	AAA CAT CTC GGA CTG CGT CAC CTC C
Slz154_Mprip_8.1_fw	TAA TAC GAC TCA CTA TAG ACG GGC CAT CCC TAG AAA G
Slz155_Mprip_8.1_rv	TTC TAG CTC TAA AAC CTT TCT AGG GAT GGC CCG TC
Slz156_Mprip_8.1_PCR_fw	GAC TTG AGA CGA AGT CCA CCT T
Slz157_Mprip_8.1_PCR_rv	CAA GAG GCT AAC TGG AAA GGA A
Slz158_Mprip_8.1_Seq_fw	CCC AGG TAA TTG AGA AAT TTG AGG

3.4.3 DNA cloning

3.4.3.1 Digestion of DNA with restriction enzymes

All restriction enzymes were purchased from New England Biolabs (NEB, Ipswich, USA) together with their optimized reaction buffers. Digestion was performed according to manufacturer's recommendation. Table 5 depicts the general reaction conditions used:

Table 5. DNA digestion protocol.

Component	analytical digestion	preparative digestion
DNA	1 µg	2-10 µg
10x NEBuffer	2 µL	5 µL
Restriction enzyme	0.3 µL	1-2 µL
ddH_2O	ad 20 µL	ad 50 µL

Digestions were performed at 37 °C. An analytical digestion was carried out for 1-2 h while a preparative digestion was done overnight (o/n).

3.4.3.2 Agarose gel electrophoresis

After digestion (3.4.3.1) DNA fragments were separated by agarose gel electrophoresis in 1x Tris-acetate-EDTA (TAE) buffer (for 50x: 2 M Tris; 63 mM EDTA; 60 mM acetic acid ad 1 L ddH_2O). Depending on the size of the desired fragments, different agarose concentrations (1-3% w/v) were used. UltraPure™ agarose (Invitrogen™, #16500-500) was dissolved in 1x TAE buffer and mixed with ethidium bromide (EtBr, Roth, #2218.2), which intercalates in the DNA and can be visualized with ultraviolet (UV) light. DNA samples were mixed with 6x loading buffer to visualize the migrating front and sizes were compared to the 1 Kb Plus DNA ladder (Invitrogen, #10787026). Electrophoresis was carried out at 100-120 V at RT.

3.4.3.3 Extraction of DNA from agarose gels

Bands of the correct size were isolated and purified using the QIAquick® Gel Extraction Kit (QIAGEN, #28704) according to the supplied protocol. Purified DNA was eluted in 30 µL ddH_2O or elution buffer (EB).

3.4.3.4 Dephosphorylation of plasmid DNA

DNA digestion using restriction enzymes generates a 3'-hydroxyl group and a 5'-phosphate group. To prevent self-ligation of digested plasmids, the 5'-phosphate group was removed using antarctic alkaline phosphatase (NEB, #MO289). Table 6 depicts the set up for the dephosphorylation reaction that was carried out at 37 °C for 30 min. Subsequently, dephosphorylation was stopped by heat-inactivation at 80 °C for 2 min.

Table 6. General pipetting scheme for DNA dephosphorylation.

Component	Used
DNA	1 pmol
10x Antarctic phosphatase reaction buffer	2 µL
Antarctic phosphatase	5 U
ddH_2O	ad 20 µL

3.4.3.5 Ligation of DNA fragments

Vector and insert were ligated for 20 min at RT using the Fast-Link™ DNA ligation kit (Lucigen, # LK0750H, Table 7). The insert-to-vector ratio was always 3:1 and the required insert mass (m_{insert}) was calculated based on the number of nucleotides in both, the insert (N_{insert}) and vector (N_{vector}), by

$$\mathrm{m_{insert}\ [ng]} = 3 \times \frac{\mathrm{N_{insert}\ [bp]}}{\mathrm{N_{vector}\ [bp]}} \mathrm{m_{vector}\ [ng]}$$

Table 7. General pipetting scheme for DNA ligation.

Component	Used
molar ratio insert:vector DNA	3:1
10 mM ATP	1.5 µL
10x Fast-Link ligation buffer	1.5 µL
Fast-Link DNA ligase	1 µL
ddH_2O	ad 15 µL

Following ligation, the Fast-Link™ DNA ligase was heat-inactivated at 70 °C for 15 min. 2-5 µL ligation product were used for transformation (3.4.5.2).

3.4.3.6 Gibson assembly

Known today as the Gibson assembly is an exonuclease-based approach to seamlessly assemble multiple overlapping DNA fragments without the need of previous digestion with restriction enzymes under isothermal conditions. [390] The assembly was performed as previously published using the Gibson

Assembly master mix provided by the Core Facility of the MPI of Biochemistry. [391] Prior assembly, we designed and amplified (3.4.7.2) specific DNA inserts with 15-20 bp overlapping ends.

Table 8. Gibson Assembly reaction set-up.

Component	Used
vector DNA	100 ng
insert DNA	3-fold molar excess
2x Gibson Assembly Master Mix	10 µL
ddH_2O	ad 20 µL

For the assembly of two to three DNA fragments, samples were incubated at 50 °C for 30 min. Following incubation, samples were used for transformation (3.4.5.2) and stored at -20 °C.

3.4.4 CRISPR/Cas9 genome editing

Clustered regularly interspaced short palindromic repeats (CRISPR)/CRISPR-associated protein 9 (Cas9) is a powerful method for site-specific genomic targeting of a gene of interest in any organism. [392] There are two components needed in the system: the DNA cutting nuclease Cas9 and a single guide RNA molecule (sgRNA). Bound together, these two components form a complex that can identify and cut specific sections of DNA. Hereby locates and binds the Cas9 enzyme the complex first to a common sequence in the genome, called the protospacer adjacent motif (PAM). Once the PAM is bound, the sgRNA, which is designed to particularly bind a specific sequence in the DNA, unwinds the part of the double helix and Cas9 cuts the DNA leading to a double-strand break precisely three base pairs 5' upstream of the PAM sequence. The double-strand break causes the cell to activate its own DNA repair mechanisms, non-homologous end joining (NHEJ) and homology-directed repair (HDR). Without a suitable repair template, double-strand breaks can produce frame shifts and stop codons, thereby disrupting the gene of interest (knockout). [392]

3.4.4.1 Identification of target sites

The specificity of the Cas9 nuclease is determined by the sgRNA. The sgRNA consists of a 20-nt guide CRISPR (crRNA) sequence that is specific to the DNA target and a trans-activating crRNA (tracrRNA) sequence that interacts with the Cas9 protein. [392]

CRISPR target sites were mapped to the *PARVA* coding sequence within exon1 and identified using the 'ChopChop' design tool (https://chopchop.cbu.uib.no/) hosted by the Valen lab. [393] This tool additionally provides information about possible 'off-target' sites in the mouse genome. Two DNA target sites immediately preceding a 5'-NGG PAM (5'-CGTTCTTGGGGAAACTCGGAGGG-3' and 5'-AGAAGGATGACTCGTTCTTGGGG-3') were identified which fulfilled the criteria.

For the generation of α/β-parvin double KO MOVAS (serial targeting), the CRISPR target sites were mapped to the *PARVB* coding sequence within exon 1 and 5 using the 'ChopChop' design tool. Two DNA target sites immediately preceding a 5'-NGG PAM (5'- CGAGTCTTTCTTGGGCAAGTTGG-3' and 5'-GAGGTGACGCAGTCCGAGATCGG-3', respectively) were identified. Only one off-target sequence with three mismatches was reported for both these target sites.

3.4.4.2 Approaches for sgRNA construction

For the construction and delivery of the sgRNA, two different approaches, *in vitro* transcription and cloning of sgRNA expressing vectors, were tested.

The GeneArt™ Precision gRNA Synthese-kit (Thermo Fisher Scientific, #A29377) was used for generating sgRNA, targeting *PARVA* or *PARVB*, by *in vitro* transcription. Briefly, two short single-stranded oligonucleotides that code for the target sequence, are assembled with a T7 promotor in a polymerase chain reaction (PCR, 3.4.7.2) using the Phusion® High-Fidelity DNA polymerase (NEB, #M0530). The assembled product was subsequently used as template in an *in vitro* transcription reaction followed by a purification step using the Monarch® RNA Cleanup Kit (NEB, #T2040) according to the manufacturer's instructions. The resulting sgRNA was used for lipid-mediated cell transfection (3.4.4.3).

For generating an sgRNA expression plasmid to target *PARVB*, a pair of partially complementary oligonucleotides, encoding the 20-nt guide sequence, was cloned into the pSpCas9(BB)-2A-GFP (px458) or pSpCas9(BB)-2A-Puro (px459) vector. These vectors carry both the Cas9 enzyme and the remains of the sgRNA as a scaffold immediately following the oligo cloning site.

3.4.4.3 Approaches for sgRNA delivery

Following the sgRNA assembly by *in vitro* transcription and purification, TrueCut™ Cas9 protein v2 (Thermo Fisher Scientific, #A36496) was directly transfected with the sgRNA. Before transfection, the Cas9 nuclease/sgRNA ribonucleoprotein complex (RNP) was generated to allow rapid targeting of cells. Transfection was performed using the Lipofectamine CRISPRMAX according to manufacturer's protocol and cells were incubated for 24 h at 37 °C and 5% CO_2.

When using the px458 or px459 vector, transfection was performed using Lipofectamine™ 2000 (Thermo Fisher Scientific, #11668027) by following the manufacturer's instructions. Cells were incubated for 24 h at 37 °C and 5% CO_2.

3.4.4.4 Clonal isolation of MOVAS cells after CRISPR transfection

The isolation of clonal cell lines with α- or α/β-parvin knockout was desired. Therefore, single cells were isolated after transfection by flow cytometry-based cell sorting in 96 multi-well plates. Cells were incubated at 37 °C and 5% CO_2 until colonies were big enough to be expanded to 24 multi-well plates for subsequent clone analysis. Treatment of cells with puromycin, an antibiotic which terminates protein synthesis, to pre-select px459 transfected MOVAS cells resulted in complete cell death. Therefore, single cells of px459 transfected MOVAS were also isolated using flow cytometry.

3.4.4.5 Identification of knockout cells

Wild-type MOVAS cells transfected with Cas9 nuclease/sgRNA RNPs targeting *PARVA* were initially identified by western blot (WB) analysis (3.6.9) followed by immunofluorescent (IF) microscopic analysis (3.5.4), mass spectrometry (MS) (3.8) and sequencing (3.4.5.4). α-parvin KO #3 MOVAS that were subjected for further β-parvin deletion were analyzed by sequencing (3.4.5.4).

3.4.5 Bacteria culture

3.4.5.1 Strain, growth conditions, media

The One Shot® OmniMAX 2 T1R strain of Escherichia coli (*E. coli*) was used for all cloning steps. *E. coli* were cultured in Luria broth (LB) medium (10 g NaCl; 10 g Tryptone-peptone; 5 g yeast extract ad 1 L ddH_2O) which was autoclaved at 120 °C for 20 min and stored at RT. Before use, it was supplemented with the appropriate antibiotic (100 µg/mL Ampicillin; 50 µg/mL Kanamycin).

Medium for LB-Agar plates (10.5 g agar-agar in 500 mL LB medium) was autoclaved at 120 °C for 20 min. The solution was cooled down to ~50 °C before adding antibiotics and pouring the solution into 100 mm Petri dishes. After the medium solidified, plates were stored at 4 °C.

3.4.5.2 Transformation of chemically competent bacteria

50 µL competent bacteria were thawed on ice and incubated with the assembled DNA from a ligation (3.4.3.5) or a Gibson assembly (3.4.3.6) for 20 min on ice. Bacteria were transferred to a 42 °C warm water bath for 90 sec (heat shock) to allow temporary pore formation in the cell membrane enabling the transfer of plasmid DNA into the cell. Subsequently, samples were cooled down on ice (3 min), and incubated shaking with 600 µL of antibiotic-free LB medium (3.4.5.1) for 30 min at 37 °C (Thermomixer, Eppendorf). Next, bacteria were pelleted for 30 sec at 13,000 rpm (microcentrifuge, Eppendorf), resuspended in 100 µL LB medium, streaked on antibiotic-containing LB-agar plates (3.4.5.1) and incubated at 37 °C o/n. Colonies appeared within 12-16 h.

3.4.5.3 Plasmid DNA preparation from bacterial cultures

To amplify the DNA, single colonies were picked after transformation (3.4.5.2) and inoculated in 5 mL LB medium containing the appropriate antibiotic (3.4.5.1). Bacterial cultures were grown at 37 °C o/n. The bacteria were pelleted and the DNA was isolated using the QIAPrep® Spin Miniprep kit (QIAGEN, #27106). 1 mL of non-pelleted bacteria was stored at 4 °C for subsequent big scale DNA amplification after sequence verification. The final concentration and purity of plasmid DNA was determined by spectrophotometric measurement at 260 nm (NanoDrop, ND-1000, peQlab Biotechnologie GmbH). Average yield of a high copy plasmid purified from 2 mL of bacteria culture was 5-10 µg. Miniprep plasmid DNA was used for sequencing (3.4.5.4) and stored at -20 °C.

After verifying the correct DNA sequence, previously non-pelleted bacteria were used to inoculate 250 mL antibiotic-containing LB medium and grown shaking overnight at 37 °C. Subsequently, bacteria were pelleted and DNA extraction was conducted using either the QIAGEN® Plasmid Maxi Kit (QIAGEN, #12162) or the NucleoBond® Extra Midi kit (Machery-Nagel, #740410) following the supplied protocols. Plasmid DNA was eluted in 200-300 µL buffer EB or ddH_2O, followed by an isopropanol precipitation and stored at -20 °C. The concentration and purity of plasmid DNA was determined by spectrophotometric measurement at 260 nm. Average yield of a high copy plasmid was 200-400 µg.

3.4.5.4 Sequencing

After cloning, transformation and purification of plasmid DNA, samples were sequenced to confirm that correct changes, but no unwanted mutations, were introduced. 50-100 ng/µL sample were sent for sequencing to Eurofins Genomics (Ebersberg, Germany).

MOVAS cells subjected to CRISPR/Cas9-mediated knockout of *PARVA* or *PARVB* were sequenced to confirm genomic indel mutations. Therefore, specific sequencing primer (3.4.2) were designed to amplify the region of interest from a PCR product, amplified from genomic DNA. Sample were sent for sequencing to Eurofins Genomics (Ebersberg, Germany).

3.4.6 Isolation of genomic DNA from tissue

For mice genotyping, genomic DNA was extracted from clipped tails. Tail tips were incubated with lysis buffer containing proteinase K at 55 °C o/n (**Table 9**). Next day, proteinase K digestion was stopped by adding ddH_2O in a 1:1 ratio and incubating tissue samples at 95 °C for 15 min. Following a centrifugation step, 15 min at 14,000 rpm, 2 µL sample were used for PCR (3.4.7.1).

Table 9. Lysis buffer components for genotyping.

Component	Used
10x complete reaction buffer for mi-Taq (metabion)	5 µL
10x incomplete reaction buffer for mi-Taq (metabion)	5 µL
proteinase K	2 µL
ddH_2O	90 µL

3.4.7 Polymerase chain reaction (PCR)

The polymerase chain reaction is an *in vitro* molecular biological method to amplify DNA fragments of interest using two specific primers (forward and reverse). Genomic, plasmid or complementary DNA serves as template and is replicated during cycling steps consisting of template denaturation, primer annealing and elongation of the newly synthesized strand.

3.4.7.1 Mice genotyping

Genomic DNA isolated from mouse tail tips (3.4.6) was amplified using specific primers designed to recognize alterations introduced into *PARVA* or *PARVB* or the presence of the *Cre* transgene (483.4.2). **Table 10** to **Table 15** depict PCR reactions and programs used.

Table 10. α- and β-parvin genotyping set-up.

Components for *α-parvin*	Used
10x complete reaction buffer	2 µL
10 mM dNTPs	0.4 µL
APloxPf	0.2 µL
APloxPr	0.2 µL
APE2f	0.2 µL
DMSO	0.6 µL
mi-Taq DNA polymerase	0.3 µL
ddH_2O	14.4 µL

Components for *β-parvin*	Used
10x complete reaction buffer	2 µL
10 mM dNTPs	0.4 µL
PGKf	0.2 µL
1EmBPi2F	0.2 µL
2BPE3r	0.2 µL
mi-Taq DNA polymerase	0.3 µL
ddH_2O	15 µL

Table 11. PCR protocol for α- and β-parvin.

step	Temperature	Time	Description
1	95 °C	3 min	Initial denaturation
2	95 °C	30 sec	Denaturation
3	53 °C	30 sec	Primer annealing
4	72 °C	30 sec	Elongation
5	72 °C	5 min	Final elongation
6	4 °C	∞	Storage

Steps 2-4 were repeated 34x.

Table 12. α-MHC-MerCreMer genotyping set-up.

Reaction A-components	Used
10x complete reaction buffer	2 µL
10 mM dNTPs	0.4 µL
79_28887_WT_rev	0.2 µL
80_28886_Common	0.2 µL
DMSO	0.6 µL
mi-Taq DNA polymerase	0.3 µL
ddH_2O	14.3 µL

Reaction B-components	Used
10x complete reaction buffer	2 µL
10 mM dNTPs	0.4 µL
80_28886_Common	0.2 µL
81_28888_Mut_rv	0.2 µL
DMSO	0.6 µL
mi-Taq DNA polymerase	0.3 µL
ddH_2O	14.3 µL

Table 13. PCR protocol for α-MHC-MerCreMer (reaction A and B).

step	Temperature	Time
1	94 °C	2 min
2	94 °C	20 sec
3	65 °C	15 sec
4	68 °C	10 sec
5	94 °C	15 sec
6	60 °C	15 sec
7	72 °C	10 sec
8	72 °C	2 min
10	10 °C	∞

Steps 2-4 were repeated 10x with dT= 0.5 °C.
Steps 5-7 were repeated 28x.

Table 14. SMMHC-CreER^{T2} genotyping set-up.

Components	Used
10x complete reaction buffer for mi-Taq	2.5 µL
10 mM dNTPs	1 µL
Slz3_SMMHC-CreERT2 P5	1.5 µL
Slz4_SMMHC-CreERT2 P6	0.8 µL
Slz5_SMMHC-CreERT2 P7	1.5 µL
mi-Taq DNA polymerase	0.1 µL
ddH_2O	17 µL

Table 15. PCR protocol for SMMHC-CreER^{T2}.

step	Temperature	Time
1	95 °C	5 min
2	95 °C	45 sec
3	58 °C	45 sec
4	72 °C	2 min
5	72 °C	10 min
6	4 °C	∞

Steps 2-4 were repeated 30x.

After the reaction was finished, PCR products were analyzed by agarose gel electrophoresis (3.4.3.2). Table 16 lists product sizes and represented genotypes.

Table 16. Genotyping PCR products for α- and β-parvin, α-MHC-MerCreMer and SMMHC-CreER^{T2}.

α-parvin			
wild type (+/+)	1100 bp	180 bp	
heterozygote (fl/+)	1100 bp	180 bp	240 bp
mutant (fl/fl)			240 bp

β-parvin		
wild type (+/+)	600 bp	
heterozygote (+/-)	600 bp	350 bp
mutant (-/-)		350 bp

α-MHC-MerCreMer	reaction A	reaction B
negative (wild type, +/+)	300 bp	
heterozygote (+/-)	300 bp	300 bp
positive (mutant, -/-)		300 bp

SMMHC-CreER^{T2}		
negative (-)	220 bp	
positive (+)	220 bp	280 bp

3.4.7.2 Preparative PCR

For subcloning a PCR product into a vector (e.g. via the Gibson Assembly, see 3.4.3.6), higher amounts of DNA fragments were required and Table 17 depicts the prepared reaction mix.

Table 17. Reaction mix used for preparative PCR.

Component	Used
10x PfuII buffer	5 µL
10 µM dNTPs	1 µL
10 pmol/µL forward primer	1 µL
10 pmol/µL reverse primer	1 µL
DNA	50-100 ng
ddH_2O	ad 50 µL

3.5 Cell culture material and techniques

3.5.1 Primary cardiomyocytes

3.5.1.1 Isolation and culture of primary neonatal mouse and rat cardiomyocytes

3.5.1.1.1 Neonatal mouse ventricular cardiomyocytes (NMVC)

Dissected hearts from decapitated three-day old neonatal (P3) control, *α-pv(fl/fl)* and *α-pv(fl/fl)* β-*pv(-/-)* mice were transferred into a PBS containing dish. The great vessels, atria and connective tissue were removed before the remaining blood was pumped out of the ventricles. Subsequently, ventricles were cut into small pieces and the digestion was performed at 37 °C for 1 h using the Neonatal Heart Dissociation kit (Miltenyi Biotec, #130-098-373). Briefly, enzyme mix 1 was preheated at 37 °C for 5 min before being added to ice-cold enzyme mix 2. The chopped ventricular tissue was subsequently transferred into the reaction tube containing enzyme mix 1+2. During digestion the cell suspension was gently disrupted every 10 min by pipetting. Tissue remainders were separated by passing the cell suspension through a 70 µm cell strainer. To enrich the suspension for cardiomyocytes, the pellet after centrifugation at 300 g for 15 min, was resuspended in 10 mL cardiomyocyte medium and pre-plated onto a non-coated cell culture dish for 90 min. Thereafter and following another centrifugation step (300 g for 15 min), NMVCs were re-suspended in the requested amount of CM medium (1 mL medium per heart, Table 18) and seeded on a plastic surface pre-coated with 10 µg/mL fibronectin (FN) and cultured at 37 °C in 5% CO_2 in a maximum saturated humidity. The growth medium was changed 24 h after isolation and every other day onwards. Primary NMVCs were cultured for up to seven days before fixation and immunofluorescence staining (3.5.3).

Table 18. Cardiomyocyte medium composition.

Component	Concentration	Company
DMEM/F12 1:1		Life technologies #31330-038
Fetal Bovine Serum (FBS)*	5%	Thermo Fisher Scientific #10270-106
Horse Serum (HS)*	5%	Thermo Fisher Scientific #16050122
Penicillin/ Streptomycin (Pen/Strep)	5%	ThermoFisher Scientific #15140122
L-glutamine	2 mM	ThermoFisher Scientific #25030-081
Ascorbic acid	0.1 mM	Sigma #A4034
Bovine serum albumin (BSA)	0.2%	Sigma # A7409
Cytarabine (ara-C)	20 µM	Sigma #C1768
Sodium pyruvate	3 mM	Sigma #S8636
Insulin-transferrin-selenite (ITS)	1:200	Invitrogen #51300044

*FBS and HS were heat-inactivated at 56 °C for 30 min before use.

3.5.1.1.2 Neonatal rat ventricular cardiomyocytes (NRVC)

Dissected hearts from decapitated three-day old neonatal Wistar rat strain pups were transferred into a dish containing PBS and primary NRVCs were isolated following the protocol described under 3.5.1.1.1. NRVCs were cultured on either 10 µg/mL FN or 50 µg/mL collagen I (Matrix BioScience, #50301) pre-coated dishes under the same conditions as NMVCs using the same medium.

3.5.1.2 Isolation and culture of primary cardiomyocytes from adult mice

The isolation of primary adult mouse ventricular cardiomyocytes was carried out according to the protocol from Ackers-Jonson et al. [394] Briefly, the mouse was killed by CO_2 and transferred to the surgery area directly after noticing lack of toe-pinch reflex. The chest was wiped with 70% Ethanol (EtOH), opened and 7 mL EDTA buffer were steadily injected into the base of the right ventricle while the descending aorta was cut. Subsequently, the heart was removed and transferred into a dish containing EDTA buffer. A series of injections (EDTA, Perfusion and Collagenase buffer, Table 19) was applied to the LV and the heart was placed in dishes containing the same buffers. After complete digestion, atria were removed and ventricles were teased apart in a separate dish to avoid contamination. Trituration using a 1 mL pipette helped to further digest the tissue. The digestion was stopped by adding stop buffer and remaining tissue pieces were separated from the cell suspension via transfer through a 100 µm pore-size cell strainer (Corning®, #431752). To remove cell debris and non-myocytes from the cell suspension, cells were allowed to settle by gravity in four rounds re-introducing a calcium-containing medium. If cells were used for IF labeling or WB analysis, the final myocyte pellet was resuspended in plating medium and cells were seeded at the desired density on plates pre-coated with 5 µg/mL laminin (Thermo Fisher Scientific, #23017015) in PBS (≥1 h at 37 °C). After one hour at 37 °C, plating medium was aspirated and culture medium was added. The culture medium was changed every two days onwards.

Table 19. Compositions of buffers needed for the isolation of adult CMs.

EDTA buffer

Compound	Final conc. [mmol/L]
NaCl	130
KCl	5
$NaH_2PO_4*H_2O$	0.5
HEPES	10
Glucose*H_2O	10
BDM	10
Taurine	10
EDTA*2 H_2O	5

*BDM, 2,3-Butanedione monoxime

Perfusion buffer

Compound	Final conc. [mmol/L]
NaCl	130
KCl	5
$NaH_2PO_4*H_2O$	0.5
HEPES	10
Glucose*H_2O	10
BDM	10
Taurine	10
$MgCl_2$	1

Collagenase buffer

Enzyme	Final conc. [mg/mL]
Collagenase 2	0.5
Collagenase 4	0.5
Protease XIV	0.05

Stop buffer

Solution/compound	Final conc.
Perfusion buffer	
FBS	5%

Plating medium

Compound	Final conc.
M199	
FBS	5%
BDM	10 mmol/L
Penicillin/Streptomycin	1x

Culture medium

Compound	Final conc.
M199	
BSA	0.1%
ITS	1x
BDM	10 mmol/L
CD lipid	1x
Penicillin/Streptomycin	1x

*ITS, insulin-transferrin-selenium

Calcium reintroduction buffers

Solution	Used for buffer 1	Used for buffer 2	Used for buffer 3
Perfusion buffer	15 mL	10 mL	5 mL
Culture media	5 mL	10 mL	15 mL

3.5.2 Vascular smooth muscle cells (MOVAS cell line)

3.5.2.1 Culture, freezing and thawing of MOVAS cell line

SV40 large T-immortalized mouse vascular smooth muscle cells from aorta (MOVAS) were previously described, obtained from ATCC® (#CRL-2797™) and used to analyze α-parvin function *in vitro*. [395] Cells were maintained in MOVAS complete medium (Table 20) in a humidified atmosphere at 37 °C and 5% CO_2. In order to subculture the cells, cells were washed once with PBS and treated with Trypsin-EDTA solution (Table 20) until the cell layer was dispersed. Subsequently, cells were taken up in MOVAS complete medium, centrifugated, resuspended in fresh medium and an appropriate aliquot was distributed to a new culture dish (passaging).

As the number of passages can have a negative effect on the cell properties, multiple aliquots were frozen at the beginning of the thesis and of every modified cell line as soon as possible. Cells that reached an optimal density for freezing (~80%) were trypsinized as described above and resuspended in ice-cold MOVAS complete medium supplemented with 5% dimethylsulfoxide (DMSO, Serva, #20385.0). The cell suspension was frozen on dry-ice and stored at -80 °C. For long-time storage, cells were transferred to liquid nitrogen.

To revitalize cells, a cryogenic vial was placed in a 37 °C water bath to quickly thaw cells and minimize the exposure to toxic DMSO. When freezing medium was thawed, cells were added to pre-warmed MOVAS complete medium, centrifugated and resuspended in fresh MOVAS complete medium. Cells were seeded in a dish of appropriate size.

Table 20. Composition of Trypsin-EDTA solution and MOVAS complete medium.

Trypsin-EDTA solution

Component	Used	Company
10x Trypsin-EDTA	5 mL	Thermo Fisher Scientific #15400054
1x PBS	25 mL	Sigma-Aldrich #P4417

MOVAS complete medium

Component	Final conc.	Company
DMEM		Thermo Fisher Scientific #31966021
FBS	10%	
Penicillin/ Streptomycin	5%	
Geneticin™ selective antibiotic (G-418)	0.2 mg/mL	ThermoFisher Scientific #10131027

3.5.3 Viral transduction and transient transfection of cells

Transient transfections for generating CRISPR/Cas9 knockout cell lines were carried out with Lipofectamine 2000 or CRISPRMAX (Invitrogen) according to the manufacturer's protocol. Transduction with lentiviral vectors was used to generate stable MOVAS KO rescue cell lines. All cell lines were tested by PCR for mycoplasma contamination on a regular basis and only mycoplasma-free cell lines were used for experiments.

Isolated NRVCs or NMVCs and adult mouse CMs were transduced using lentiviral or adenoviral vectors, respectively.

3.5.4 Immunofluorescence (IF) microscopy

Cells intended for IF analysis were grown on either plastic IBIDI dishes (primary NMVCs and NRVCs) or glass coverslips (MOVAS) coated with the suitable ECM substrate (FN, collagen I or laminin). At indicated time points cells were washed in PBS and fixed for 10 min in ice-cold 4% paraformaldehyde (PFA)/PBS. After washing with PBS, permeabilization with 0.1% Triton X-100/PBS was performed for 10 min before blocking with 3% BSA/PBS at 4 °C for >1 h. Primary antibodies (3.3.1) were applied and incubated at 4 °C o/n. Next day, dishes were washed with PBS (3x 5 min), before secondary antibodies (3.3.2) were added and incubated at RT for 1 h in the dark. Subsequently, dishes were washed with PBS, followed by DAPI staining (1:6000 in PBS) at RT for 15 min in the dark. After additional washing steps with PBS (3x 5 min), dishes were stored at 4 °C.

Confocal image acquisition was performed on a ZEISS (Oberkochen, Germany) LSM780 confocal laser scanning microscope equipped with a ZEISS Plan-Apo 40x/1.4 oil immersion objective. To determine morphological parameters of NMVCs the confocal imaging was performed at the Imaging Facility of the MPI of Biochemistry (Martinsried) on a Leica (Wetzlar, Germany) Thunder inverted widefield microscope equipped with a Leica HC PL FLUOTAR 10x/0.32 and L 20x/0.40 CORR objective. Image analysis was conducted using ImageJ version 1.52p.

3.5.5 'Plate and Wash' adhesion assay

The adhesion assay was performed in 96 multi-well flat bottom plates. Control wells were coated with 3% BSA/PBS while test wells were coated with 10 µg/mL fibronectin/PBS at RT for 2 h. After plate washing using PBS, wells were blocked with 1% BSA/PBS at RT for 1 h. After washing the wells with PBS, 50,000 cells (MOVAS or fibroblasts) per well were seeded in MOVAS complete medium in triplicates and incubated at 37 °C and 5% CO_2 for 10 min or 30 min. The medium was decanted and non-adherent or loosely attached cells were removed by stringently washing the wells (3x PBS) using a multichannel pipette. Following the

last washing step, plates were dried by gently hitting on a paper tissue and 50 µL Fix and Stain solution (20% methanol, 0.1% crystal violet in ddH_2O water) were added per well. After overnight incubation at 4 °C on a shaker, plates were washed with ddH_2O to remove unspecific staining and dried. For permeabilization 0.1% Triton X-100 in ddH_2O water was added to the wells for 6 h. Absorbance was measured at 595 nm wavelength.

3.5.6 Cell spreading assay

Culture dishes were pre-coated with 10 µg/mL fibronectin in PBS (37 °C, 1 h) and cells were seeded at the right densities in MOVAS and NMVCs complete medium, respectively. After indicated time points, cells were fixed using 4% PFA and immunofluorescent labeled as described under 3.5.3. Morphological cell parameters were assessed manually using ImageJ version 1.52p.

3.5.7 Time-lapse phase contrast video microscopy of 2D random cell migration

Polystyrene 12-well plates were coated with 10 µg/mL fibronectin in PBS (pH 7.4) at 37 °C for 1 h followed by blocking with 1% BSA/PBS at 37 °C for 1 h. Cells were sparsely seeded onto the FN-coated wells in 1% FBS-containing MOVAS medium for 2 h at 37 °C and 5% CO_2. Subsequently, cell migration was recorded with a Nikon Eclipse Ti-E inverted live cell microscope equipped with a Plan Fluor 10x-numerical aperture 0.3 objective, a motorized stage, an environment chamber (Visitron Systems GmbH) and a cooled electron multiplying charge-coupled device (EMCCD) camera (Teledyne Princeton Instruments) at 37 °C and 5% CO_2 for 4 h with 5 min time intervals. Image acquisition and microscope control were carried out with the VisiView® software Version 4.2.0.6 (Visitron Systems GmbH). The acquired images were analyzed using the manual tracking MTrack plugin in ImageJ version 1.52p. [396] For each cell line, 20 cells were tracked.

3.5.8 Wound closure assay

24-well plates were coated with 10 µg/mL FN in PBS at 37 °C for 2 h. After washing, plate surface was allowed to completely dry. Silicone culture-inserts 2 well from IBIDI® (#80209) were attached to each well and cells were plated within the insert wells. After incubation at 37 °C and 5% CO_2 for 3 h, medium was changed to 1% FBS-containing MOVAS medium. Monolayer formation was checked after overnight incubation and following washing with PBS, fresh 1% FBS-containing MOVAS medium including 0.01 mg/mL mitomycin was added for 2 h to inhibit cell proliferation. After incubation, the culture-inserts were gently removed with sterile tweezers and cell debris and non-attached cells were removed by washing. Cell imaging was performed at 37 °C and 5% CO_2 for 24 h at 15 min intervals using a Nikon Eclipse Ti-E inverted live cell microscope equipped with a Plan Fluor 10x/0.3 objective, a motorized stage, an

environment chamber (Visitron Systems GmbH) and a cooled electron multiplying charge-coupled device (EMCCD) camera (Teledyne Princeton Instruments). The resulting image stacks were analyzed with ImageJ version 1.52p, using an internally programmed script. For each cell line, three fully independent experiments were conducted. For single cell tracking during collective cell migration, the MTrack plugin in ImageJ version 1.52p was used. [396]

3.6 Biochemical methods

3.6.1 Preparation of total protein lysates from adherent cells

For preparing protein lysates, cells were grown in normal conditions until the desired density (~80-90%) was reached. Before cell lysis, cells were washed once with ice-cold PBS to remove all medium. Subsequently, cells were lysed in a specific cell lysis buffer including a cOmplete protease inhibitor cocktail (Roche, #04693159001). Depending on the cell type and the following experiments either purchased mammalian protein extraction reagent (M-PER™, Thermo Fisher Scientific #78501) or prepared radioimmunoprecipitation assay (RIPA) buffer containing 20 mM Tris, pH 8.0; 150 mM NaCl; 1% Triton X-100; 0.5% sodium deoxycholate and 0.1% sodium dodecyl sulfate (SDS) were used. Cells were immediately collected and the suspension was transferred to a tube. After incubation for 10 min on ice, cell lysates were centrifuged at 14000 rpm for 10 min at 4 °C. Utilizing the BCA protein assay kit (3.6.4), the protein concentration of the cleared lysate was determined and normalized, and lysates were either directly processed (3.6.6; 3.6.7) or the appropriate amount of 2x SDS sample buffer (1 M Tris, pH6.8; 20% SDS; 0.5 M EDTA; 87% glycerol; 0.005% bromophenol blue) containing 5% 2-mercaptoethanol was added. For denaturation, lysates were incubated at 95 °C for 5 min and either directly subjected to SDS-PAGE (3.6.8) or stored at -20 °C.

3.6.2 Preparation of total protein lysates from mouse heart

Liquid nitrogen-frozen mouse heart tissue samples were homogenized using a mortar and pestle. 0.1 g of powdered sample were resuspended in 1 mL ice-cold home-made RIPA buffer (50 mM Tris, pH7.4; 150 mM NaCl; 1% Nonidet P40; 0.5% sodium deoxycholate; 0.1% SDS; 1 mM EDTA; 1 mM EGTA), containing protease and phosphatase inhibitors (Cocktail 2 and 3, Sigma, #P5726 and #P0044), and homogenized using a 27 G needle. Subsequently, samples were incubated on ice for 10 min and centrifuged (20,000 g, 10 min, 4 °C) to pellet cell debris. The protein concentration of the cleared cell lysate was determined using the BCA protein assay kit (3.6.4). After protein concentrations were adjusted, the appropriate amount of

2x SDS sample buffer was added and samples were denaturated at 95 °C for 5 min and either directly subjected to SDS-PAGE (3.6.8) or stored at -20 °C.

3.6.3 Cell fractionation

Subcellular fractionation is the process of separating cellular components while preserving their individual functions. In the scope of the present thesis, cellular fractionation was performed to determine α-parvin localization within the cell and to enrich the protein for subsequent mass spectrometry-based proteomics. One day before cell fractionation, cells were seeded at an appropriate density and allowed to adhere and spread overnight at 37 °C and 5% CO_2. On the experimental day, cells were washed twice with ice-cold 1x PBS containing protease and phosphatase inhibitor as well as 1 mM DTT. Subsequently, plates were placed on ice, subcellular buffer (250 mM sucrose; 10 mM HEPES, pH7.4; 5 mM KCl; 1.5 mM $MgCl_2$; 1 mM EDTA) was added and cells were immediately scrapped off and transferred to an Eppendorf tube. Cell lysis occurred by passing the lysate through a 26G needle. Following an incubation on ice for 15 min, cell lysates were cleared by centrifugation (5 min, 700 g, 4 °C) and the supernatant was transferred to a new tube.

The cell pellet was washed once with buffer F1 (20 mM Tris, pH7.4; 0.1 mM EDTA; 2 mM $MgCl_2$) and three to five times with buffer F1 including 0.7% Chaps. After washing, the pellet was resuspended in buffer A (20 mM HEPES, pH 7.4; 0.4 mM NaCl; 2.5% Glycerol; 1 mM EDTA; 0.5 mM NaF), sonicated (2x 10 sec, 28%, pulse) and denatured after addition of 2x SDS-LD at 95 °C for 5 min (nuclear fraction).

The supernatant was further cleared in an Optima™ MAX-XP ultracentrifuge (Beckman Coulter, USA) at 40,000 g for 60 min at 4 °C, and carefully transferred to a new tube. 4x SDS-LD was added and samples were denatured at 95 °C for 5 min (cytosolic fraction).

The denatured samples were stored at -20 °C until analyzed by western blotting (3.6.8).

3.6.4 Determination of protein concentration

Protein concentration was assessed using a colorimetric assay based on the reduction of Cu^{2+} to Cu^{1+} by protein under alkaline conditions (biuret reaction) and the presence of BCA (Pierce™ BCA protein assay kit). Bicinchoninic acid (BCA) selectively chelates Cu^{+1} ions [2:1] and thereby forms water soluble, purple-colored complexes with a strong absorbance at 562 nm. The Pierce™ BCA protein assay kit was used according the enclosed manufacturer protocol.

3.6.5 Proximity-dependent biotinylation of proteins for MS analysis (BioID2 and TurboID)

The identification of protein-protein interactions is of fundamental importance to understand complex biological processes. Various biochemical and genetic techniques, including affinity-captured complex purifications and yeast two-hybrid screens, have been used to search for new molecular associations. Furthermore, a relatively new approach for proximity-dependent labeling of proteins was published, which is based on a biotin ligase, originally from *E. coli* (BioID) and later from *A. aeolicus* (BioID2), fused to a target protein. [397] Biotinylation occurs within the near vicinity of the target protein and biotinylated proteins can be captured by affinity using Streptavidin and identified using mass spectrometry. [397, 398] Nowadays, two engineered promiscuous mutants of the biotin ligase, called TurboID and miniTurbo, which catalyze the biotinylation reaction much faster compared to BioID and BioID2, are also components of the protein-protein interaction identification tool box. [399]

For each BioID2 and TurboID-fused construct (BioID2-α-pv, BioID2-β-pv, TurboID-α-pv, TurboID-β-pv) as well as for the BioID2- and TurboID-only controls, three biological replicates were performed and analyzed via mass spectrometry (MS). Specifically, for performing BioID2 experiments, cells were either stably expressing the BioID2 fusion proteins (wt MOVAS) or transduced with lentiviral expression vectors 36 h after isolation (NRVCs, 3.5.1.1.2). 24 h before cell lysis, cells were washed and incubated with either MOVAS or CM complete medium containing 50 µM biotin. After an additional incubation in complete medium without biotin for 30 min at 37 °C and 5% CO_2, cell lysis was performed following the protocol described under 3.6.6.

For conducting proximity-dependent biotinylation using TurboID in CMs, NRVCs were isolated from P3 Wistar rats (3.5.1.1.2) and transduced with the retroviral expression vectors 36 h after isolation. 72 h after isolation, NRVCs were washed with 1x PBS and cultured in CM complete medium containing 50 µM biotin for 20 min at 37 °C and 5% CO_2. Subsequently, cells were washed twice and incubated for 30 min in fresh CM complete medium. After additional washing steps, cells were lysed and pulldown assays were performed (3.6.6). For performing proximity-dependent biotinylation using TurboID in α-pv KO #3 MOVAS the same protocol as described for CMs was followed. The only difference lies in the use of a cell line, stably expressing the TurboID-fusion proteins.

3.6.6 Immunoprecipitation and Streptavidin pulldown

For immunoprecipitation of GFP-tagged proteins, cells were lysed in M-PER™ (Thermo Scientific, #78501) or RIPA buffer (3.6.1) and immunoprecipitated using the µMACS GFP Isolation Kit (Miltenyi Biotec, #130-091-125) following the manufacturer's instruction. Elutes were separated in SDS-PAGE for Western blotting (3.6.9) or for in-gel digestion and subsequent mass spectrometry analysis (3.8.1.1).

For Streptavidin pulldown experiments following the biotinylation of proteins with subsequent mass spectrometric analysis, cells were either lysed in M-PER™ (Thermo Scientific, #78501) buffer (MOVAS) or RIPA buffer (3.6.1, NRVCs) containing protease and phosphatase inhibitors and pulled down using either high performance Streptavidin Sepharose® (Merck, #GE17-5113-01; BioID2) or magnetic Dynabeads™ MyOne™ Streptavidin C1 beads (Thermo Fisher Scientific, #65002; TurboID) overnight at 4 °C. The following day, beads were washed three times in Wash buffer I (1 M NaCl; 1% Triton X-100 in PBS), twice in Wash buffer II (50 mM Tris-HCl, pH7.6; 50 mM NaCl in ddH_2O) and twice in PBS. Samples were eluted from the beads (BioID2) through the addition of 2x SDS-LD, denatured at 95 °C and separated by SDS-PAGE (3.6.8). On-bead digestion (TurboID) was performed before subsequent mass spectrometry analysis (3.8.1.2).

3.6.7 RhoA pulldown activation assay

Measurement of GTP-bound RhoA was determined using the RhoA pulldown activation assay biochem kit (Cytoskeleton, Inc., #BK036). Briefly, one day before the pulldown experiment, plates were coated with 5 µg/mL fibronectin in PBS for 1 h at 37 °C. Subsequently, cells were plated at a density of $3\text{-}4 \cdot 10^6$ cells/mL. The following day, cells were washed with PBS and serum deprived for 4 h. Meanwhile, new plates were coated with 10 µg/mL FN in PBS for 2 h at RT and blocked with 1% BSA/PBS for 1 h at 37 °C. In parallel to the blocking, cells were trypsinized and resuspended in serum-free MOVAS medium containing 1x Trypsin-Inhibitor. After washing, cells were kept in suspension in serum-free MOVAS medium for 1 h at 37 °C and the tubes were occasionally flipped. Following the blocking and washing of the plates, the same number of cells were seeded in serum-free MOVAS medium for the indicated time points at 37 °C. After incubation, medium was aspirated and cells were washed with ice-cold Hanks balanced salt solution (HBS; 20 mM HEPES; 150 mM NaCl) containing 0.5% MgCl. To remove HBS remnants, plates were tilted for an additional minute. Cells were lysed in 500 µL ice-cold lysis buffer (included in the kit), harvested and clarified by centrifugation at 15,000 g for 5 min at 4 °C. 80 µL lysate were used for WB quantification of total RhoA, while the remaining lysate was snap frozen in liquid nitrogen. Equal lysate volumes were added to rhotekin-RBD beads and incubated for 1 h on a rotator. The rhotekin-RBD beads were pelleted by centrifugation at 5,000 g and 4 °C for 1 min. Supernatant was removed and beads were washed three times with 500 µL lysis

buffer. 30 µL 2x Laemmli sample buffer were used to resuspend the beads. The samples were boiled for 5 min at 95 °C and used for analysis by Western blotting (active RhoA; 3.6.9).

3.6.8 One-dimensional SDS polyacrylamide gelelectrophoresis (SDS-PAGE)

Following protein denaturation in the presence of SDS and 2-Mercaptoethanol, two reagents that reduce disulfide bonds, individual proteins were separated electrophoretically according to their molecular weight using a Mini-PROTEAN® 3 system (Bio-Rad). Homemade 10% acrylamide gels (**Table 21**) and 1x SDS-PAGE running buffer (10x stock: 2 M Glycine; 250 mM Tris; 30 mM SDS filled up to 1 L with ddH_2O) were used for SDS-PAGE. Electrophoresis was performed at 80-120 V at RT. As a size reference, the Kaleidoscope™ Precision Plus Protein Standard (Bio-Rad, #1610375) was run with the samples.

Table 21. Components of the SDS-PAGE gel.

Separation gel (10%, 2 gels)

Component	Used
ddH_2O	7.9 mL
1.5 M Tris-HCl, pH 8.8	5.0 mL
30% acrylamide	6.7 mL
10% SDS	200 µL
10% APS	200 µL
TEMED	8 µL

Stacking gel (4%, 2 gels)

Component	Used
ddH_2O	2.7 mL
1.0 M Tris-HCl, pH 6.8	500 µL
30% acrylamide	670 µL
10% SDS	40 µL
10% APS	40 µL
TEMED	4 µL

*APS, ammonium persulfate; TEMED, N, N, N', N'-tetramethylethylenediamine

3.6.9 Western blot analysis

After protein separation by SDS-PAGE (3.6.8) the separating gel was shortly equilibrated in 1x WB transfer buffer (10x stock: 2 M Glycine; 250 mM Tris ad 1 L with ddH_2O) containing 20% Methanol. After activating the Immobilon®-P polyvinylidene difluoride (PVDF) membrane (Millipore, #IPVH00010) with isopropanol, a transfer sandwich was assembled and proteins were electrically transferred for 1.5-2 h with 100 V at 4 °C. Then, membranes were washed in 1x TBS-T (10x stock: 200 mM Tris, 1.4 M NaCl ad 1 L with ddH_2O; 1x TBS including 0.1% Tween-20), blocked for 1 h at RT in 3% BSA/TBS-T and incubated with primary antibody (3.3.1) diluted in 3% BSA/TBS-T o/n at 4 °C. Next day, membranes were washed with 1x TBS-T (3x 5 min) and incubated with secondary antibody (3.3.2) at RT for 1 h. After the final washing (3x 5 min), bound antibodies were visualized with Immobilon® Western Chemiluminescent HRP Substrate (Millipore, #WBKLS0500) following the protocol provided by the manufacturer.

For the sequential detection of several different proteins on one membrane, membranes were incubated at 55 °C for 20 min in 0.5% 2-mercaptoethanol containing stripping buffer (12.7 mL 1 M Tris-HCl, pH 6.8;

20 mL 20% SDS ad 200 mL with ddH_2O), washed with TBS-T (3x 10 min) and blocked 3% BSA/TBS-T before applying the next primary antibody.

3.7 Analysis of mRNA expression

3.7.1 RNA extraction

Total RNA, a mix of ribosomal, messenger and different kinds of small plus non-coding RNAs, was extracted from primary CMs or MOVAS using the Qiagen RNeasy Mini Kit (QIAGEN, #74104) following the provided protocol with small modifications. Briefly, cells were washed with PBS and incubated in RLT buffer containing 2-mercaptoethanol for 1 min before being scraped off and transferred to a tube. After the addition of 70% EtOH, samples were mixed, transferred to QiaShredder columns (QIAGEN, #79654) and centrifugated at 10,000 g for 1.5 min at RT. The flow-through was transferred to a spin cartridge harboring an RNA binding membrane and washed according to the manufacturer's instructions. Following washing, the column membrane was dried by centrifugation (1 min at full speed) and RNA was eluted in 30 µL RNase-free water. The concentration and purity of isolated RNA was assessed spectrophotometrically at 260 nm using the NanoDrop system. Samples with poor RNA quality (260/230 ratio below 1.5) were excluded from direct further processing and cDNA synthesis (3.7.2). Instead, RNA was reprecipitated using 3 M sodium acetate (NaOAc), pH 5.5 and isopropanol. After an incubation at RT for 20 min and centrifugation at 13,000 rpm for 10 min at 4 °C, RNA was washed twice with ice-cold 70% EtOH. Finally, the RNA pellet was air-dried for 15 min and resuspended in 15 µL RNase-free water. The concentration and quality of RNA was reassessed spectrophotometrically at 260 nm.

3.7.2 Reverse transcription of total RNA (cDNA synthesis)

A complementary DNA (cDNA) to a given RNA template is produced by the activity of an RNA depending DNA polymerase, e.g. reverse transcriptase (RT). Synthesis of cDNA was performed with iScript™ reverse transcriptase (Bio-Rad, #1708840) according to the protocol provided by the manufacturer.

Table 22. Composition of cDNA reaction mix and used PCR protocol.

Component	Volume/reaction
5x iScript™ Reaction Mix	4 µL
iScript™ Reverse Transcriptase	1 µL
Nucleae-free water	variable
RNA template (250 ng)	variable

PCR protocol

Step	Temperature	Time	Description
1	25 °C	5 min	Priming
2	46 °C	20 min	Reverse transcription
3	95 °C	1 min	RT inactivation
4	4 °C	∞	

3.7.3 Real-time quantitative PCR (qPCR)

To quantitatively analyze the mRNA expression real-time PCR was performed using iQ™ SYBR® Green Supermix (Bio-Rad, #1708880). The cDNA obtained in a first-strand synthesis (3.7.2) was amplified with primers specific for the gene of interest (3.4.2). As reference, a reaction with primers for *GAPDH* was conducted for each sample.

Table 23. qPCR reaction mix.

Component	Volume/reaction
cDNA	0.5 µL
2x iQ™ SYBR® Green Supermix	10 µL
10 µM Primer forward	0.2 µL
10 µM Primer reverse	0.2 µL
ddH_2O	4.6 µL

Triplicate repeats were prepared for each primer set and samples were transferred to a special 96 multi-well plate (LightCycler480 Multiwell Plate 96, white, #04729692001). The amplification progress was monitored in LightCycler480 with the cycling instructions depicted in Table 24.

Table 24. Protocol for quantitative real-time PCR.

Step	Temperature	Time
1	95 °C	3 min
2	95 °C	15 sec
3	60 °C	30 sec
Melting curve	55 °C to 95 °C	1 °C in 30 sec

Step 2-3 were repeated 40x.

For the interpretation of qPCR results ΔCt values (correction to the control) and the relative expression levels ($2^{-\Delta Ct}$) were calculated using Excel2010. Additionally, the mean of normalized expression followed by the calculation of standard deviation of each gene was taken and plotted using Prism 8 (GraphPad Software, USA).

3.8 Mass spectrometry driven functional proteomics

3.8.1 Sample preparation

3.8.1.1 In-gel digestion of proteins immunoprecipitated after GFP-IP or Streptavidin pulled down proteins after proximity-dependent biotinylation using BioID2

Samples obtained from the GFP-IPs or the streptavidin pulldowns after proximity-dependent biotinylation using BioID2 were eluted from the beads using 2x SDS-LD and were seperated by SDS-PAGE (3.6.8). The gel was stained with InstantBlue® Coomassie Protein stain (Abcam, #ab119211) according to manufacturer's instructions. Each sample/lane was cut and washed in destaining solution (50:50 of 50 mM ammonium bicarbonate (ABC) buffer:100% ethanol) before dehydrating in 100% ethanol. The dried gel pieces were rehydrated in enzyme solution (12.5 ng/µl in 50 mM ABC buffer) and incubated overnight at 37°C. The next day, peptides were extracted using extraction buffer (30% acetonitrile; 3% trifluoroacetic acid). The gel pieces were dehydrated in 100% acetonitrile solution and the recovered supernatant was combined with the supernatant after addition of extraction buffer. To remove the acetonitrile, the combined supernatant was dried using a SpeedVac vacuum concentrator and resuspended in 2 M Tris-HCl buffer. Before desalting and concentrating the samples using StageTips (3.8.1.4), 25 mM Tris-HCl buffer containing 10 mM TCEP and 40 mM chloroacetamide was added to the samples.

3.8.1.2 On-bead digestion of Streptavidin pulled down proteins after proximity-dependent biotinylation using TurboID

Magnetic Dynabeads™ MyOne™ Streptavidin C1 beads (Thermo Fisher Scientific, #65002) were washed twice using 1x PBS. The magnetic rack was used to remove all PBS remnants, followed by the addition of 1 volume sodium deoxycholate (SDC) buffer (100 mM Tris, pH 8.5; 1% SDC; 10 mM TCEP; 40 mM chloroacetamide (CAA)). To allow reduction and alkylation of proteins, samples were incubated for 20 min at 37 °C. Subsequently, equal volume of LC-MS water was added, followed by the addition of trypsin to perform overnight digestion at 37 °C.

3.8.1.3 Desalting of peptides using SCX StageTips

After overnight on-bead digestion (3.8.1.2), the magnetic rack was used to collect the supernatant which was acidified by addition of 1% trifluoroacetic acid (TFA) solution. After centrifugation, the extracted peptides were then desalted and concentrated using a strong cation exchanger (SCX) stop and go extraction (Stage) Tips prior to LC-MS/MS analysis. [400] Therefore, samples were loaded on to the StageTips and washed in 1% TFA solution followed by 0.2% TFA solution. Peptides were eluted from the StageTips in

5% ammonia and 80% acetonitrile. Following centrifugation (10 min, 400 g), eluted peptides were centrifugated at 30 °C for 30 min using a SpeedVac vacuum concentrator, resuspended in LC-MS water and stored at -20 °C until loading in the mass spectrometer.

3.8.1.4 Desalting of peptides using SDB-XC StageTips

After overnight in-gel digestion (3.8.1.1), the extracted peptides were desalted and concentrated using a styrene divinyl benzene extraction disc (SDB-XC) StageTips prior to LC-MS/MS analysis. Therefore, samples were loaded on to the StageTips and washed in 0.1% formic acid. Peptides were eluted from the StageTips in 0.1% formic acid and 80% acetonitrile in ddH_2O. Following centrifugation (10 min, 400 g), eluted peptides were centrifugated at 30 °C for 30 min using a SpeedVac vacuum concentrator, resuspended in LC-MS water and stored at -20 °C until loading in the mass spectrometer.

3.8.1.5 Sample loading onto C_{18} columns and peptide separation

To separate the peptides, samples were loaded onto a reverse phase column with an inner diameter of 75 µm that was packed in-house with ReproSil-Pur C18-AQ 1.9 µm beads (Dr Maisch GmbH) using the autosampler of the EASY-nLC™ 1200 system (Thermo Fisher Scientific). Sample loading was performed in buffer A (0.1% formic acid) at 250 nL/min. For performing whole proteome analysis 30 cm long columns were used at 60 °C, while 15 cm columns at 50 °C were used for interaction proteomics.

For performing whole proteome analysis, peptides were separated using a 120 min gradient from 2 to 30%, 10 min from 30 to 60%, 5 min from 60 to 95% and 10 min maintained at 95% of buffer B (80% acetonitrile, 0.1% formic acid) at 250 nL/min.

For performing interaction proteomic analysis, peptides were separated using a 60 min gradient from 2 to 30%, 15 min from 30 to 60%, 5 min from 60 to 95% and 10 min maintained at 95% of buffer B (80% acetonitrile, 0.1% formic acid) at 250 nL/min.

3.8.2 Data acquisition on the Q Exactive™ HF and timsTOF™ mass spectrometer

Eluting peptides from the GFP-IP and BioID2 experiments were analyzed on a Thermo Scientific™ Q Exactive™ HF hybrid quadrupole-Orbitrap mass spectrometer in a data-dependent acquisition mode. According to Schrott et al. “survey scans were acquired in the Orbitrap at a resolution of 60,000 at *m/z* =200 ranging from 300 to 1750 *m/z* and up to 15 of the most abundant precursors were selected for fragmentation in the linear ion trap. Here, higher energy collisional dissociation (HCD) with a normalized collision energy of a value of 28 was used and the MS2 spectra were logged at a resolution of 15,000

(at *m/z* = 200). AGC target for MS scans was set to 3E6, within a maximum injection time of 100, while for MS2 scans it was set to 1E5, within a maximum injection time of 25 ms". [401, 402]

Eluting peptides from TurboID experiments were analyzed by trapped ion mobility spectrometry coupled with quadrupole time-of-flight mass spectrometry (timsTOF™ Pro; Bruker Daltonics) using otofControl 6.0. The mass spectrometer was operated in data-dependent parallel accumulation serial fragmentation (PASEF) mode with one survey TIMS-MS and ten PASEF MS/MS scans per acquisition cycle. [403] Analysis was performed according to the protocol of Meier et al. in a mass scan range from 100-1700 m/z and "an ion mobility range from 1/K0 = 1.6 Vs/cm^2 to 0.6 Vs/cm^2 using equal ion accumulation and ramp time in the dual TIMS analyzer of 100 ms each at a spectra rate of 9.52 Hz. Suitable precursor ions for MS/MS analysis were isolated in a window of 2 Th for *m/z* < 700 and 3Th for *m/z* > 700 by rapidly switching the quadrupole position in sync with the elution of precursors from the TIMS device. The collision energy was lowered stepwise as a function of increasing ion mobility, starting from 52 eV for 0-19% of the TIMS ramp time, 47 eV from 19-38%, 42eV from 38-57% 37 eV from 57-76% and 32 eV until the end. The *m/z* and ion mobility information were used to exclude singly charged precursor ions with a polygon filter mask and 'dynamic exclusion' was further used to avoid re-sequencing of precursors that reached a 'target value' of 20,000 a.u. The ion mobility dimension was calibrated linearly using three ions from the Agilent ESI LC/MS tuning mix (*m/z*, 1/K0: 622.0289, 0.9848 Vs/cm^2; 922.0097, 1.1895 Vs/cm^2; 1221.9906, 1.3820 Vs/cm^2)." [404]

3.8.3 Data analysis

For all immunoprecipitation or pulldown experiments, the raw files were processed using the MaxQuant computational platform. [405] Subsequently, utilizing the Andromeda search engine, the peak lists generated by the MaxQuant platform were searched against the Mouse Uniprot proteome sequence database. [406] The peptide precursors were searched according to the protocol published by Schorr et al. "with an initial precursor mass deviation of up to 4.5 ppm for the main search and an allowed fragment mass deviation of 20 ppm. [407] MaxQuant by default enables individual peptide mass tolerance which was used in the search. Cysteine carbamidomethlylation was used as a fixed modification and oxidation of methionine and N terminal protein acetylation were set as variable modification for the database search. The match between the run feature was enabled, and proteins were quantified across samples using the label-free quantification algorithm in MaxQuant as label-free quantification (LFQ) intensities." [408] Notably, LFQ intensities depend on the peptide amounts and also on their ionization efficiencies; thus, they

do not reflect true copy numbers and cannot be used for the comparison of different protein abundances within one sample." [402]

Statistical analysis was performed using Perseus bioinformatics version 1.6.2.3. Proteins that were identified in the decoy reverse database or only by site modification as well as potential contaminants were excluded from data analysis. Data were further filtered to include identified proteins that were expressed in all three biological replicates of at least one group (control, α- or β-parvin) and missing value imputation was performed on the basis of normal distribution (down shift=1.8, width=0.3). "PCA analysis of the three groups was based on the decomposition of single values and the orthogonal transformation of the original protein space into a set of linearly uncorrelated principal components which account for different types of variability in the datasets. LFQ intensities were z-scored and hierarchical clustering was utilized using Euclidean as a distance measure for column and row clustering. Volcano plots were used to visualize the mean log2 ratios of biological triplicates and the corresponding *p* values." [250]

3.9 Recombinant protein expression and purification

In the course of the present study, various protocols and optimization steps were undertaken to improve the yield of purified Twin-Strep-Mprip. However, herein only the successful protocol for the recombinant production and purification, resulting in Twin-Strep-Mprip used for pulldown assays, is described.

3.9.1 Recombinant protein production in High Five insect cells

Recombinant Mprip production was performed in High Five insect cells using the *E.coli* transposition-based recombinant Bac-to-Bac (EMBacY) expression system. [409, 410]

Chemical competent *E.coli* OmniMAX cells were transformed with the pCoofy51 vector containing the expression cassette for Mprip. The transformation was carried out as described under 3.4.5.2. Following transformation, bacteria were plated on super optimal broth (SOB) agar plates (20 g/L tryptone; 5 g/L yeast extract; 0.5 g/L NaCl; 0.186 g/L KCl; 15 g agar-agar) containing 100 µg/mL Ampicillin. Colonies were picked and plasmids purified using the NucleoSpin Tissue kit (Macherey-Nagel, #740952).

To prepare the Bacmid, chemical competent *E.coli* DH10Bac EmBacY cells were transformed, following the same transformation protocol (3.4.5.2) but with an extended 24 h long incubation phase at 37 °C. Subsequently, bacteria were plated on a LB agar plate containing 50 µg/mL kanamycin, 7 µg/mL gentamycin, 100 µg/mL Bluo-Gal (halogenated indolyl-β-galactoside), 10 µg/mL tetracycline and 1 mM Isopropyl β-D-1-thiogalactopyranoside (IPTG) for blue-white screening. Colonies that remained white after 48 h incubation at 37 °C contained the desired Bacmids and were selected for Bacmid preparation. Two positive colonies were used to inoculate 200 mL LB medium and cells were incubated overnight at

37 °C and 250 rpm. Cells were harvested by centrifugation (4000 rpm, 20 min, 4 °C) and the Bacmid DNA was isolated and purified using the Nucleobond Bac100 kit (Macherey Nagel, Germany, #740579) according to manufacturer's protocol.

For baculovirus production, Sf9 insect cells were transfected with Bacmid DNA and incubated for five days at 26 °C and 120 rpm. Successful transfection was indicated by increased cell diameter and reduced cell count and viability, monitored on a Vi-CELL® instrument (Beckman Coulter, Germany). Furthermore, the presence of YFP helps to directly observe virus performance by using a fluorescence spectrometer. [410] Cultures producing baculovirus were harvested by centrifugation (200 rpm, 10 min) and the cleared supernatant was sterile filtered (0.22 µm filter) and directly used for recombinant protein production in High Five insect cells. Therefore, 10 mL viral supernatant were added to 1 L culture volume and incubated for 3 days at 26 °C and 120 rpm. 72 h post-transfection, cells were harvested (800 rpm, 20 min, 4 °C), washed once with 1x PBS and frozen in -80 °C. Until protein purification was performed, cell pellets were stored at -80 °C.

3.9.2 Recombinant protein purification

3.9.2.1 Cell disruption and preparation of cell lysate for purification

For cell disruption and subsequent protein purification, the Strep-Tactin®XT purification kit (IBA GmbH, #2-5998-000) was used and the enclosed protocol was followed.

Briefly, the High Five insect cell pellet was quickly thawed and resuspended in buffer W (100 mM Tris-HCl, pH 8.0; 150 mM NaCl; 1 mM EDTA) supplemented with 1 mM PMSF. Cells were disrupted by sonication at 4 °C using 1s pulses for 10 min at 60% amplitude. After addition of Benzonase and BioLock Biotin blocking solution (IBA, #2-0205-050) cells were incubated for 15 min on ice to allow cleavage of cellular DNA and masking of biotin from the insect cell medium. Cell debris were removed by centrifugation (15,000 rpm, 15 min, 4 °C) and the supernatant was cleared by passing through a 0.45 µm membrane filter.

3.9.2.2 Strep-Tactin®XT purification of Twin-Strep-Mprip

Prior sample application, the Strep-Tactin®XT 4Flow® gravity flow column was washed with 2 column volumes (CV) with ddH_2O, followed by equilibration with 3 CV of buffer W (100 mM Tris-HCl, pH 8.0; 150 mM NaCl; 1 mM EDTA). The cleared cell lysate was loaded onto the column at 4 °C using gravity. Subsequently, the column was washed five times with 1 CV buffer W, followed by protein elution using first 0.6 CV (E1), then 1.6 CV (E2) and finally 0.8 CV (E3) buffer BXT (100 mM Tris-HCl, pH 8.0; 150 mM NaCl; 1 mM EDTA; 50 mM biotin). The protein concentration and purity within the three elution fractions (E1-E3) was determined by spectrophotometric measurement at 260 nm (NanoDrop, ND-1000, peQlab

Biotechnologie GmbH). The pulled sample (E1-E3) was dialyzed overnight at 4 °C in buffer W to remove the biotin and concentrated using Microcon- 10 kDa centrifugal filter units (Merck, #MRCPRT010). The concentrated Twin-Strep-Mprip was snap frozen in liquid nitrogen and stored at -80 °C.

3.10 Statistical analysis

Statistical analysis was carried out in Prism8 (GraphPad Software). All datasets were analyzed with the D'Agostino-Pearson omnibus K2 normality test. Datasets that followed a normal distribution were analyzed with either Students' *t* test to compare two conditions or with the one-way ANOVA Turkey test to compare multiple conditions. The Kruskal-Wallis test with Dunn's comparison (multiple comparison) was used for the evaluation of statistical significance of datasets that did not follow a normal distribution. In case of the morphological analysis in NMVCs and MOVAS, outlier identification and data cleaning due to apparent discrepancies was carried out prior normality testing. All results are depicted as mean ± s.d. as indicated in figure legends and all experiments that were statistically analyzed were performed at least three times. Experiments lacking statistical analysis were conducted once or twice. Statistical and bioinformatics analysis of mass spectrometry data was performed using Perseus bioinformatics (version 1.6.2.3) [411]

4 RESULTS

4.1 *In vitro* subcellular localization of α- and β-parvin in contractile cells of the cardiovascular system

α- and β-parvin are two calponin-homology domain containing focal adhesion proteins that share a high sequence and structural homology. In addition, these two parvin isoforms show an overlapping tissue expression pattern (e.g. lung, spleen, kidney). However, while α-parvin is nearly ubiquitously expressed in vertebrates (except in hematopoietic cells), β-parvin is preferentially found in heart and skeletal muscle. [385] Furthermore, the two parvins display a diverse pattern of temporal regulation, with α-parvin being present at high levels throughout mouse development whereas β-parvin is progressively upregulated. [164, 385] In addition to the tissue and temporal expression, the subcellular localization of especially α-parvin has been investigated in various cell types (fibroblasts, keratinocytes, epithelial cells). [50, 165] In contrast, the subcellular localization of α- and β-parvin in contractile cells of the cardiovascular system, cardiomyocytes and smooth muscle cells, has not been analyzed in detail. Especially the direct comparison of the two parvin isoforms in the same cell type is missing. As cardiomyocytes, the contractile units of the heart, express both α- and β-parvin, they are a perfect cell type to investigate the subcellular localization and function of the two parvin isoforms abreast and potential compensatory mechanisms.

4.1.1 Subcellular localization of α- and β-parvin in neonatal ventricular cardiomyocytes

The subcellular localization of α- and β-parvin in contractile cells of the cardiovascular system has not been described in detail yet. To achieve this and to investigate potential differences in the subcellular localization of the two parvin isoforms, we examined the localization of endogenous and eGFP-tagged α- and β-parvin in isolated neonatal cardiomyocytes by immunofluorescence.

As introduced, cardiomyocytes transmit signals bidirectional between the ECM and the cytoplasm via focal adhesion-like structures called costameres. However, it was shown that isolated neonatal and adult cardiomyocytes remodel their adhesive structures to adapt to the two-dimensional cell culture. [412, 413] During this adaptation, costameres of neonatal CMs are reorganized as the cells attach and spread, leading to adhesion sites that are structurally akin to typical focal adhesions found in non-muscle cells such as fibroblasts. [414] In unison, from adult CMs that are kept in culture (>1 week) and stimulated to contract, vinculin-positive FAs and intercellular junctions emerge. [413] Therefore, costameres and focal adhesion structures are present in cultured CMs to retain the mechanical communication between the contractile machinery of the cell and the ECM. [319]

Neonatal ventricular cardiomyocytes (NMVCs) were isolated from 3-day-old mice and plated on fibronectin-coated culture dishes. Cells were fixed three days after isolation, stained against α-parvin and co-stained with anti-α-actinin, anti-paxillin or anti-β1 integrin antibodies.

α-parvin displayed a clear focal adhesion (white arrowhead) and costamere (orange arrowhead) localization (**Fig. 18**). Given that many, if not all, of the costamere proteins can also be found in focal adhesions, distinct markers for the two adhesive structures are missing. [319] The presence of paxillin and β1 integrin in both adhesion structures additionally reflects the similar composition of these two cell-ECM contact sites. In addition, α-parvin co-localized with the Z-disc marker α-actinin (**Fig. 18**).

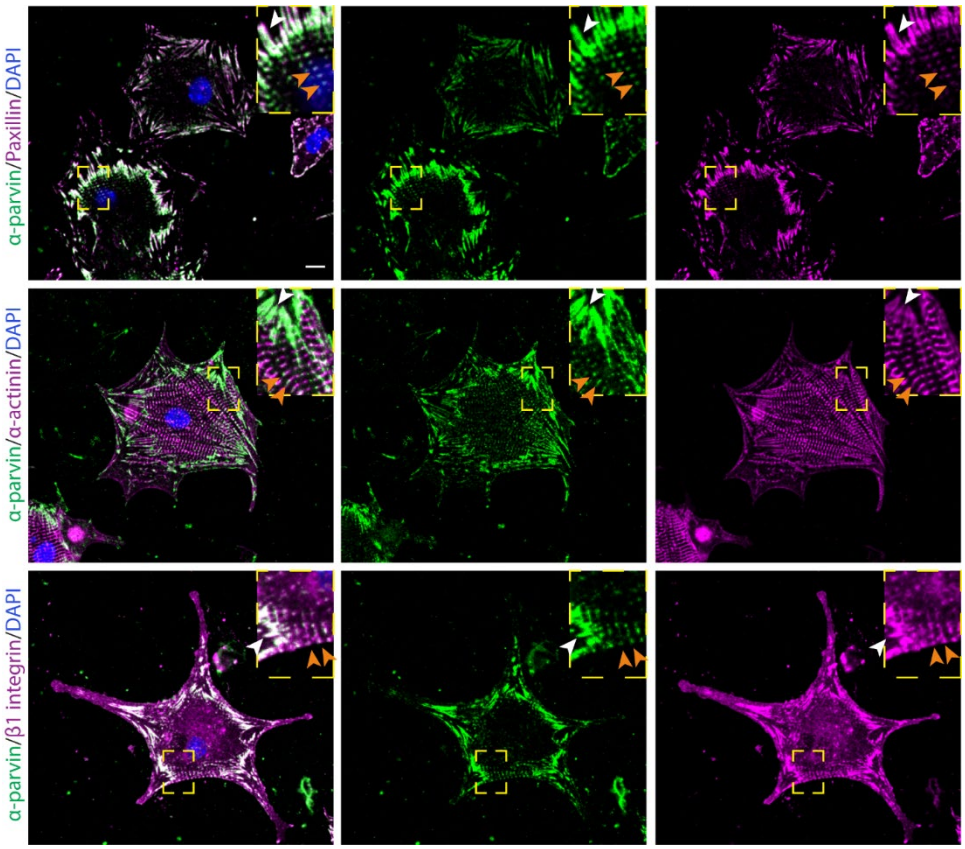

Fig. 18. Subcellular localization of endogenous α-parvin in isolated mouse ventricular cardiomyocytes. Isolated NMVCs were kept in culture for three days before fixation and co-stained with anti-α-parvin, anti-α-actinin, anti-β1 integrin and anti-paxillin antibodies. DAPI was used to stain nuclei. Note, α-parvin localized to focal adhesions (white arrow head), costameres and Z-discs (orange arrow head). Scale, 10 µm.

Isolation of neonatal ventricular CMs from rats yields higher cell numbers and more viable CMs which can be cultured *ex vivo* for a longer period of time. For this reason, some of the biochemical assays and immunostainings were conducted in isolated NRVCs instead of NMVCs, including the localization of α- and β-parvin and the other two IPP complex member, ILK and PINCH.

NRVCs were isolated from 3-day-old rats and plated on FN-coated culture dishes. Cells were fixed three days after isolation and immunofluorescently labeled with either anti-α- or anti-β-parvin antibodies. To confirm focal adhesion and Z-disc localization observed for α-parvin in NMVCs, we co-stained against paxillin or Troponin-T (TpnT), respectively. TpnT is a member of the troponin complex and a marker for the thin actin filaments, hence, the Z-disc localization is confirmed by the absence of TpnT. Both parvin isoforms co-localized with paxillin in FAs (**Fig. 19A**, **B** white arrow heads). Furthermore, a clear localization of endogenous β-parvin to TpnT-negative Z-discs was observed (**Fig. 19B**, orange arrow heads). A similar localization was detected for α-parvin although the Z-disc staining was less obvious in most cells.

IPP complex formation was shown to occur prior the localization of this complex to focal adhesions. [50] Therefore, as expected, ILK and PINCH showed the same localization pattern as α- and β-parvin and localized to FAs (white arrow head) and phalloidin-negative Z-discs (**Fig. 19C**).

In summary, these findings show that both endogenous α- and β-parvin localize to the same adhesive structures, costameres and focal adhesions, as well as to sarcomeric Z-discs in mouse and rat neonatal cardiomyocytes. Furthermore, as reported in literature, both α- and β-parvin assemble with ILK and PINCH into trimeric IPP complexes, demonstrated by the same localization pattern of all three proteins.

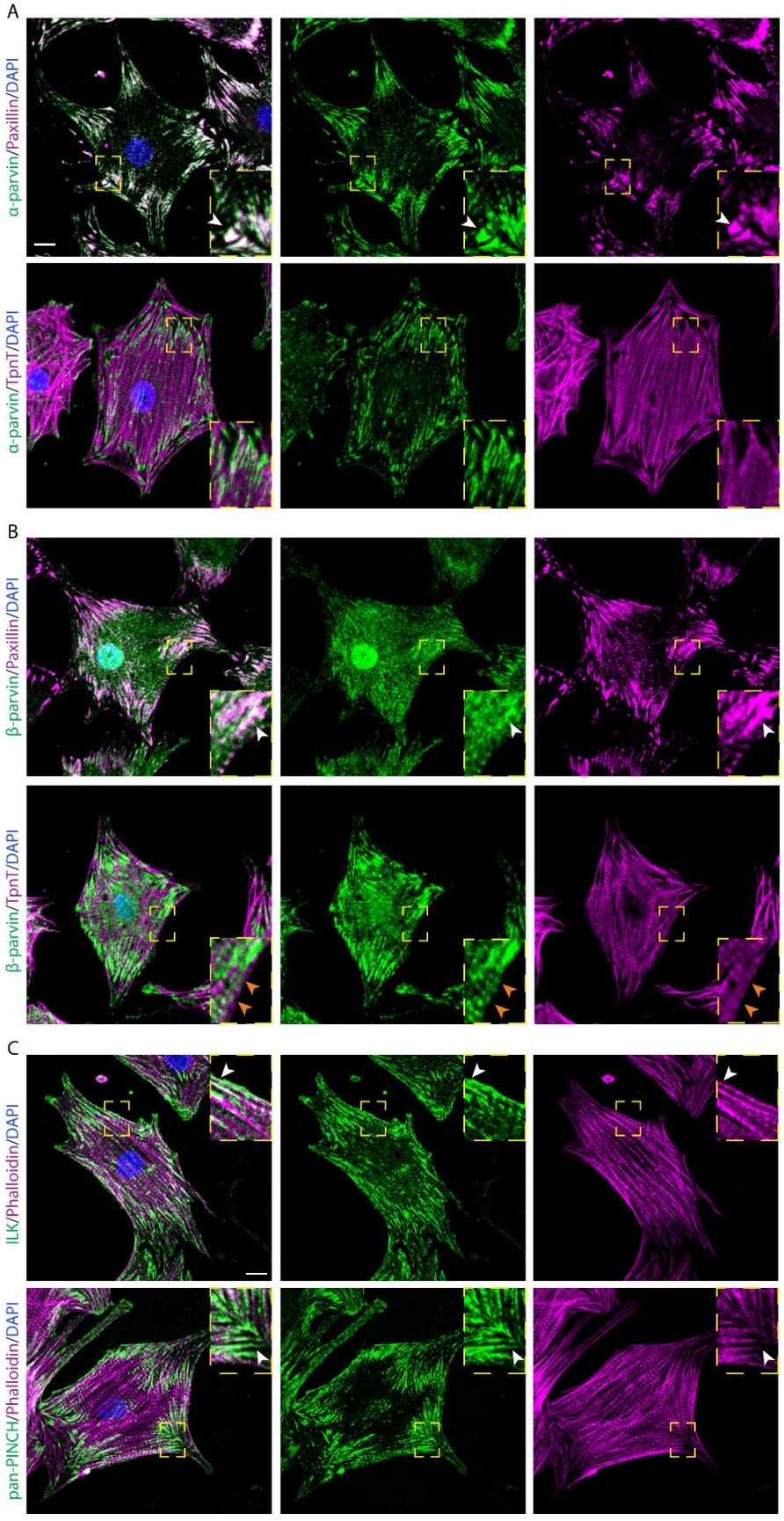
A
α-parvin/Paxillin/DAPI
α-parvin/TpnT/DAPI
B
β-parvin/Paxillin/DAPI
β-parvin/TpnT/DAPI
C
ILK/Phalloidin/DAPI
pan-PINCH/Phalloidin/DAPI

Fig. 19. Subcellular localization of endogenous IPP complex in isolated NRVCs. NRVCs were fixed and co-stained with either anti- (A) α- or (B) β-parvin and anti-paxillin or anti-TpnT antibodies three days after isolation. Both parvin isoforms localized to paxillin-positive FAs and TpnT-negative Z-discs. DAPI was used to stain nuclei. (C) ILK and PINCH localized to FAs, costameres and Z-discs in isolated NRVCs. DAPI was used to stain nuclei. Note, white arrow heads point to FAs while orange arrow heads mark Z-discs. Scale, 10 µm.

To complement the immunostainings of endogenous proteins and to rule out potential cross-reactivity of the parvin antibodies we analyzed CMs for the localization of eGFP-tagged α- und β-parvins. Therefore, NRVCs were isolated, plated on FN-coated culture dishes and transduced with a lentivirus carrying either an eGFP-α- or eGFP-β-parvin construct. As negative control, NRVCs were transduced with an empty eGFP vector. Cells were fixed three days after transduction, corresponding to five days after isolation, and immunofluorescently labeled. Both eGFP-α- and eGFP-β-parvin displayed a clear focal adhesion (white arrow head) and Z-disc (orange arrow head) localization, where they co-localize with paxillin and α-actinin, respectively (**Fig. 20A**, **B**). Furthermore, a nuclear signal for eGFP-α- and eGFP-β-parvin was observed. The nuclear localization could be either specific, given that α- and β-parvin harbor two putative nuclear localization signals at their N-terminal polypeptide stretch, or unspecific, given that transduction of NRVCs with the empty eGFP vector also resulted in a nuclear signal. In addition, eGFP-α-parvin localized to striations observed between α-actinin-positive Z-discs, corresponding to M-lines while eGFP-β-parvin did not. Interestingly, M-line localization of endogenous α-parvin, ILK or PINCH was neither observed in mouse nor in rat ventricular CMs and co-staining with myomesin did not confirm M-line localization of α-parvin (**Fig. 20C**, red arrow heads). These findings lead to the conclusion that the observed M-line localization of α-parvin might be an eGFP-induced artefact or an antibody sensitivity problem. However, both endogenous and GFP-tagged PAT-6, the sole homolog of α-parvin in *C. elegans*, was reported to be one of the M-line components of the muscle attachment structures in *C. elegans*. [201, 415] Furthermore, while late fetal cardiomyocytes show completely developed Z-discs, I- and A-bands and H zones, the M-lines were shown to develop during the neonatal period. [310] Therefore, another possibility could be the two days' time difference between the observed localization of endogenous and eGFP-tagged α-parvin and that the recruitment of α-parvin to the M-line might be time-dependent.

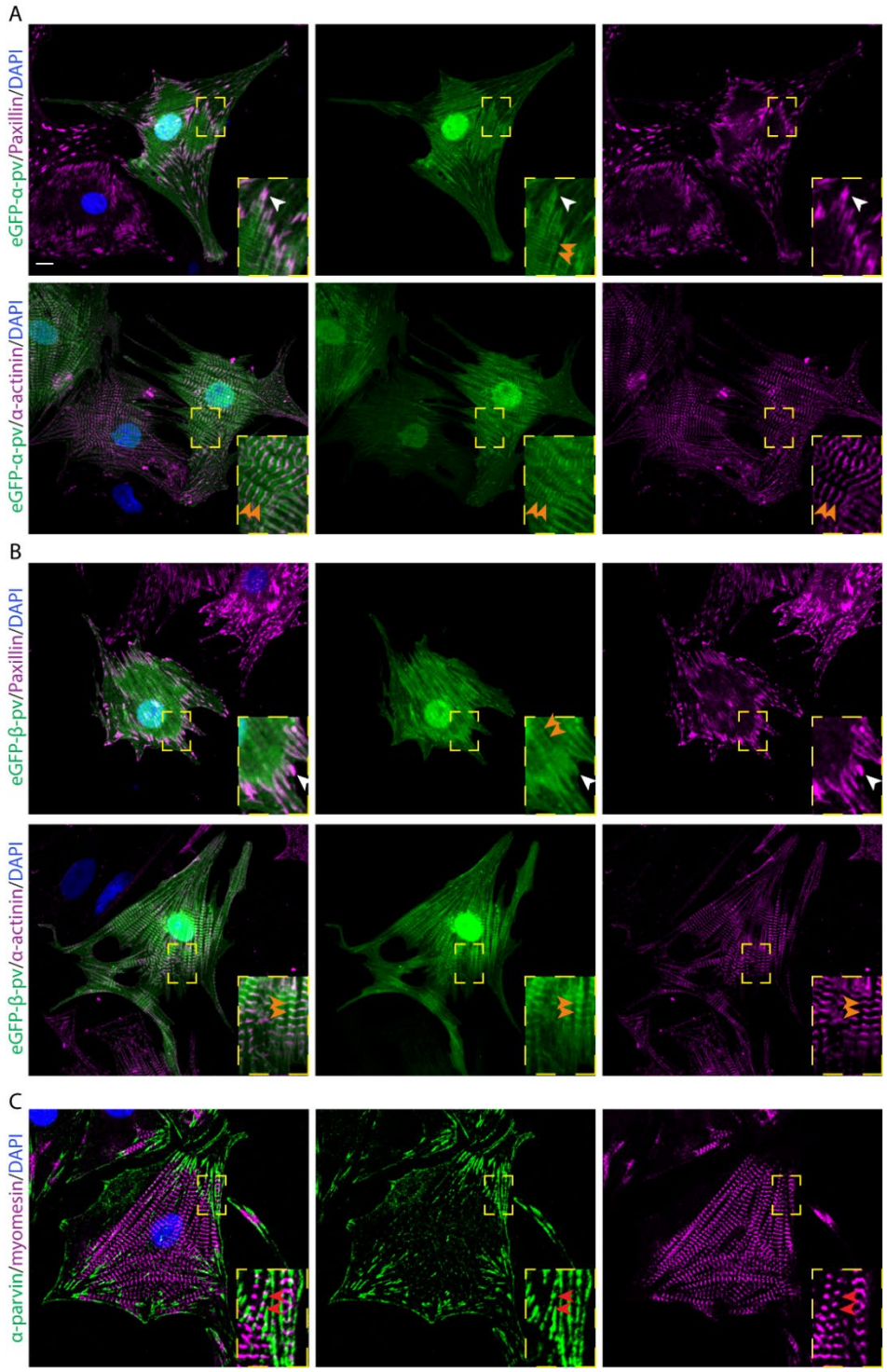

Fig. 20. Subcellular localization of eGFP-α- and β-parvin in isolated neonatal rat CMs. NRVCs were transduced with eGFP-tagged (A) α- or (B) β-parvin, fixed five days after isolation and co-stained with either anti-paxillin or anti-α-actinin antibodies. DAPI was used to stain nuclei. Both eGFP-tagged parvin isoforms localized to focal adhesions (white arrow head), costameres and Z-discs (orange arrow head). Note, eGFP-tagged α-parvin also localized to striations lying between α-actinin-positive Z-discs, which mark the M-lines while eGFP-tagged β-parvin did not. (C) Co-staining of endogenous α-parvin and myomesin (M-line marker) did not reveal localization of α-parvin to M-lines in NRVCs fixed three days after isolation (red arrow head). DAPI was used to stain nuclei. Scale, 10 µm.

Together these data show that endogenous as well as eGFP-tagged α- and β-parvin localize to the same subcellular structures - focal adhesions, costameres and Z-discs. The specific localization of eGFP-α-parvin to the M-line needs to be further investigated, for example by co-staining myomesin, a M-line marker. Furthermore, the localization of endogenous α-parvin, ILK and PINCH during CM maturation and the potential time-dependent recruitment to the M-line needs to be analyzed.

4.1.2 Subcellular localization of α- and β-parvin in adult ventricular cardiomyocytes

In NRVCs and NMVCs α-and β-parvin share a similar subcellular localization, with the only difference of eGFP-tagged α-parvin additionally localizing to the M-lines. To analyze whether the two parvin isoforms also share the same localization pattern in adult heart, adult ventricular mouse CMs were isolated and plated on laminin-coated culture dishes. Cells were fixed 1.5 hours after plating and co-stained with anti-α-actinin or anti-myomesin and either anti-α- or anti-β-parvin antibodies.

α- and β-parvin displayed a clear localization to costameres and Z-discs (**Fig. 21A**), while they did not localize to the M-line (**Fig. 21B**).

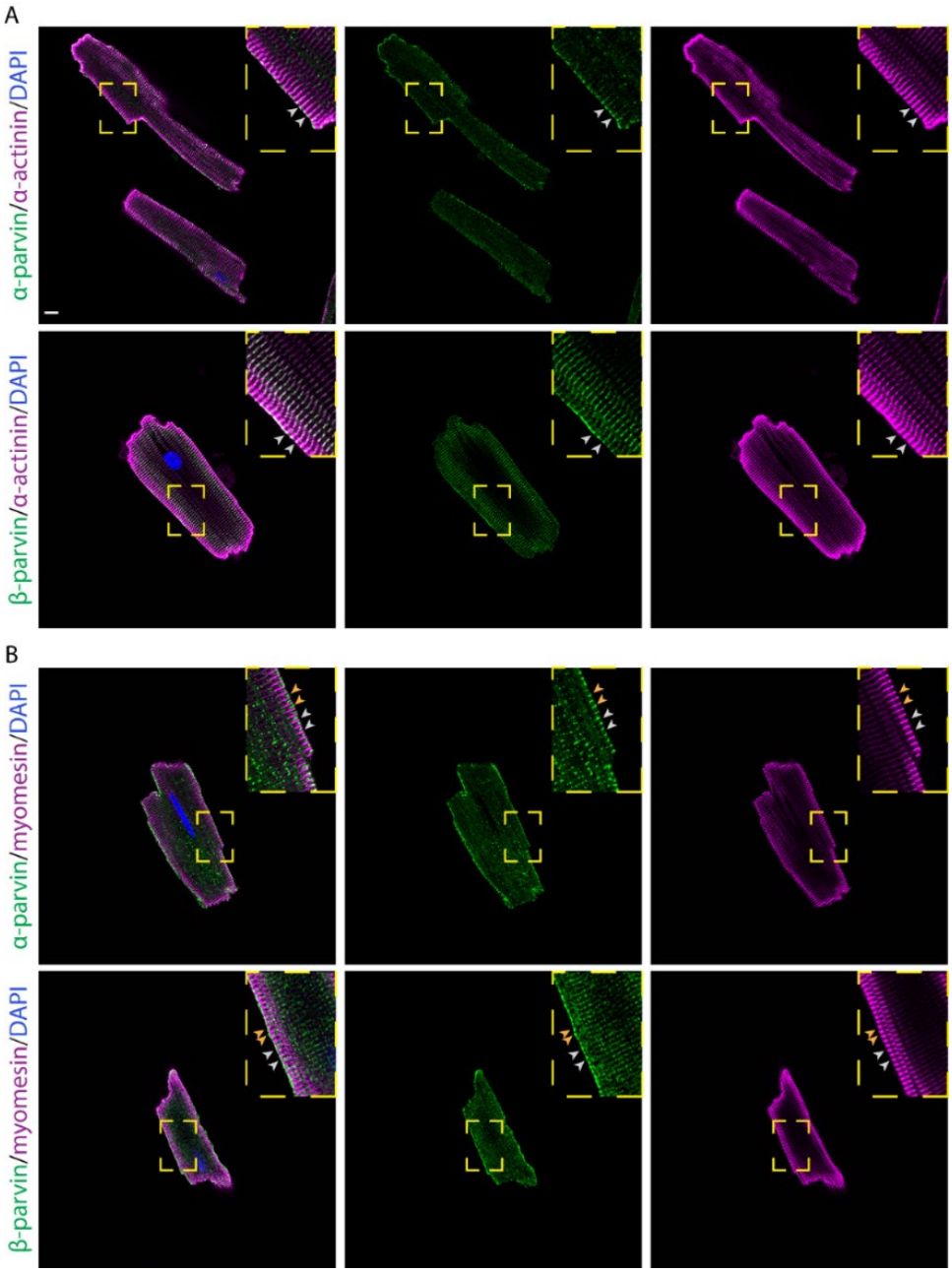

Fig. 21. Subcellular localization of α- and β-parvin in isolated adult mouse cardiomyocytes. (A) Representative fluorescence images of adult mouse ventricular myocytes on laminin co-stained with anti-α- or anti-β-parvin and anti-α-actinin antibodies. DAPI was used to stain nuclei. Note, α- and β-parvin localized to Z-discs and costameres (arrow head). Scale bar, 10 µm. (B) Representative fluorescence images of adult mouse ventricular CMs on laminin co-stained with anti-α- or anti-β-parvin (orange arrow head) and anti-myomesin (white arrow head) antibodies. DAPI was used to stain nuclei. Note, α- and β-parvin did not localize to M-lines. Scale bar, 10 µm.

Similar to α- and β-parvin, ILK and PINCH, as well as β1 integrin colocalized with α-actinin at costameres and Z-discs (**Fig. 22**, white arrowhead).

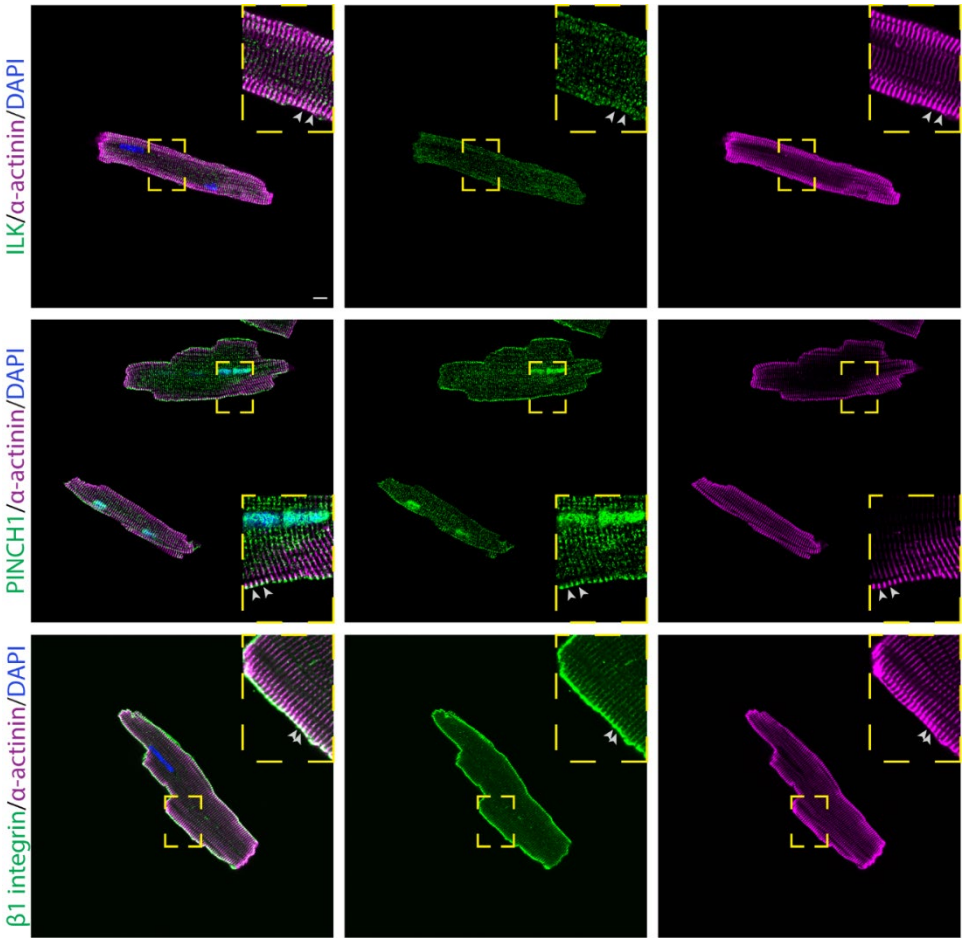

Fig. 22. Subcellular localization of IPP complex members and β1 integrin in isolated adult mouse cardiomyocytes on laminin. Co-immunostaining of anti-ILK, anti-PINCH1 and anti-β1 integrin with anti-α-actinin, revealed localization of all three proteins to costameres and Z-discs (arrow head). DAPI was used to stain nuclei. Scale bar, 10 µm.

Overall, α- and β-parvin share the same subcellular localization pattern in both isolated neonatal and adult ventricular cardiomyocytes. Both isoforms localize together with the other two IPP complex member, ILK and PINCH, to focal adhesions, costameres and Z-discs. Whether α-parvin additionally, and in contrast to β-parvin, localizes to the sarcomeric M-line during postnatal development needs to be further explored.

4.1.3 Subcellular localization of α-parvin in MOVAS, a vascular smooth muscle cell line

In addition to the subcellular localization of α- and β-parvin in cardiomyocytes, I investigated the localization of α-parvin in MOVAS, an immortalized mouse vascular smooth muscle cell line (MOVAS). Smooth muscle cells are the contractile cells of blood vessels which express α-parvin as the main parvin isoform. Although β-parvin is highly expressed in heart and skeletal muscle, endogenous β-parvin level in SMCs are low but are induced by the loss of α-parvin. [163]

In the beginning of my thesis, I analyzed the MOVAS cells in respect to the expression of smooth muscle cell specific markers, such as α-smooth muscle actin (α-SMA), and compared the localization of endogenous α-parvin in MOVAS and primary vascular SMCs (vSMCs). For this, primary vSMCs were isolated from the aorta of adult mice and plated on collagen I-coated culture dishes. Cells were fixed 16 days after plating and co-stained with anti-α-SMA and anti-α-parvin antibodies. MOVAS cells were plated on FN-coated culture dishes and either stained with anti-α-SMA antibody or co-stained with anti-α-parvin, anti-paxillin and anti-phalloidin antibodies.

Immunostaining of endogenous α-parvin in primary vSMCs revealed a clear focal adhesion localization, especially at the termini of α-SMA-positive stress fibers (**Fig. 23A**). Consistently, ILK showed the same FA localization (**Fig. 23A**). Immunostaining and western blot analysis for the expression of smooth muscle-specific α-actin in MOVAS confirmed the phenotypic identity of these cells (**Fig. 23B**, **C**). Furthermore, α-parvin co-localized with paxillin in FAs found at the cell border (**Fig. 23D**, white arrow head) or centrally of the cell in fibrillar adhesions (**Fig. 23D**, yellow arrow). As expected, endogenous ILK also localized to focal adhesions (**Fig. 23E**).

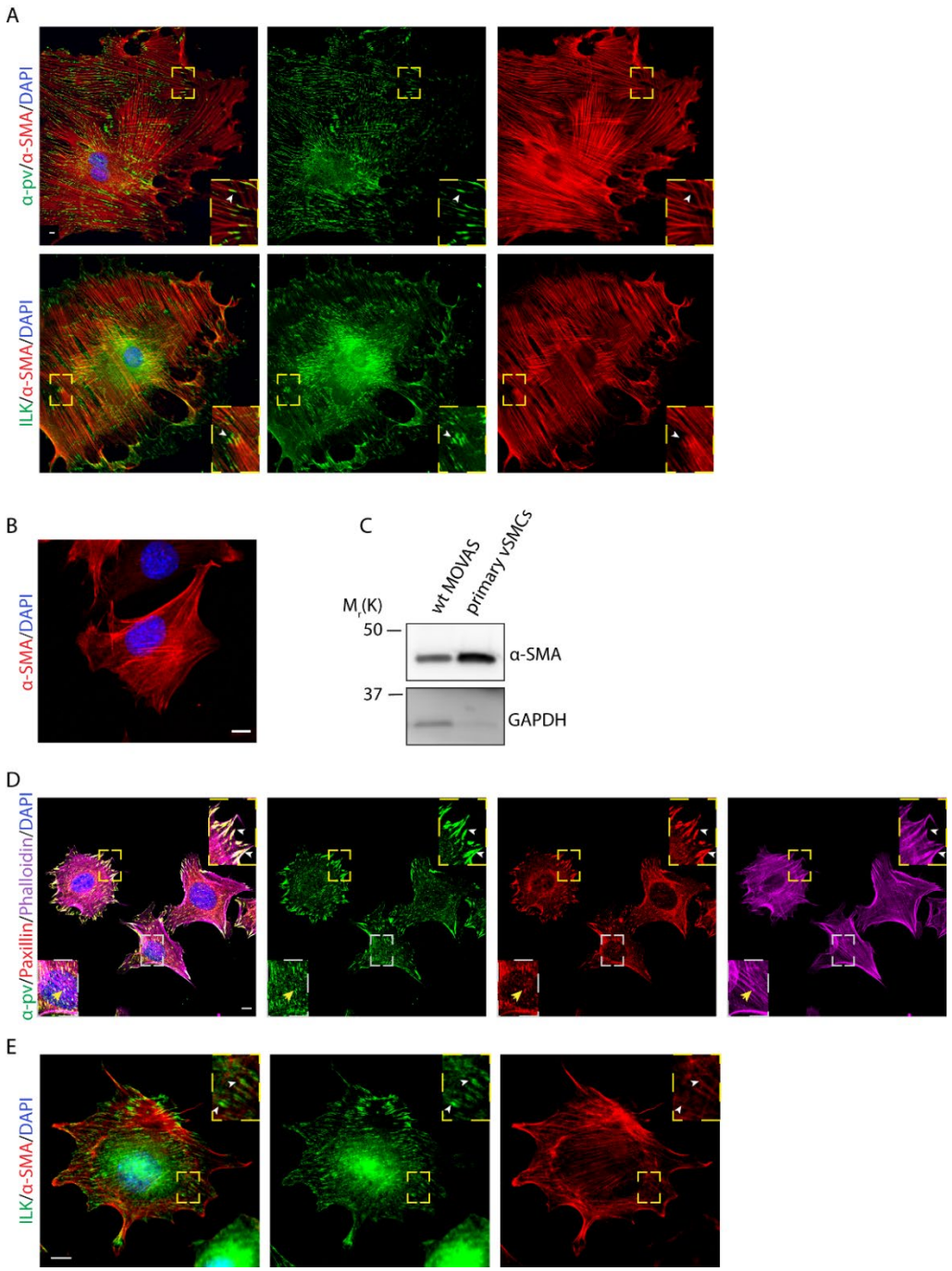

Fig. 23. α-parvin localization in primary vSMCs and MOVAS. (A) Representative fluorescence image of primary vSMCs stained with anti-α-parvin, anti-ILK and anti-α-SMA seeded on type I collagen. Cells were fixed and stained 16 days after isolation. DAPI was used to stain nuclei. Scale bar, 10 µm. (B) Representative fluorescence image of MOVAS stained with anti-α-SMA, seeded on fibronectin. DAPI was used to stain nuclei. Scale bar, 10 µm. (C) Western Blot analysis of α-SMA expression in MOVAS and primary vSMCs. GAPDH was used as a loading control. (D) Immunofluorescence analysis of α-parvin (green), paxillin (red) and phalloidin (purple) in wt MOVAS seeded on FN. Note, α-parvin localization to FAs at the cell border (white arrowhead) and centrally in fibrillar adhesions (yellow arrow). Scale bar, 10 µm. (E) Representative fluorescence image of MOVAS stained with anti-α-SMA and anti-ILK antibodies, seeded on fibronectin. DAPI was used to stain nuclei. Note, ILK localized to FAs (white arrowhead). Scale bar, 10 µm.

4.2 Generation of α-parvin knockout cells

Montanez et al. analyzed the *in vivo* role of α-parvin in mice during embryonic development. The disruption of *PARVA* leads to the evolvement of severe cardiovascular defects, resulting in embryonic lethality at around E10.5, preventing the functional analysis of α-parvin during neonatal development and adulthood. [171] To investigate the effect of α-parvin deletion in contractile cells of the cardiovascular system we focused on primary NMVCs and MOVAS.

4.2.1 *In vitro* knockout of α-parvin in isolated NMVCs using AdenoCre

Embryos lacking α-parvin expression showed heart abnormalities and cardiomyocytes with a round cell morphology. [171] However, a further detailed analysis of α-parvin loss in mouse CMs is still missing.

To explore the effect of α-parvin ablation in neonatal CMs, NMVCs were isolated from a mouse strain carrying *loxP*-flanked *PARVA* (*α-pv(fl/fl)*). [384] To analyze potential compensatory mechanisms between α- and β-parvin, NMVCs were additionally isolated from *PARVB* knockout mice carrying *loxP*-flanked *PARVA* (*α-pv(fl/fl) β-pv(-/-)*). The floxed alleles were deleted from NMVCs twenty-four hours after their isolation by transduction with an adenovirus expressing Cre recombinase (AdCre). As a control, an adenovirus carrying an empty GFP construct (AdGFP) was used. The successful knockout of α-parvin was analyzed by western blotting and RT-qPCR (**Fig. 24A**, **C**).

Western blot analysis revealed significantly reduced α-parvin protein expression levels in NMVCs after AdCre transduction compared to the AdGFP-infected NMVCs (**Fig. 24A**, **B**). As expected, the protein expression levels of ILK and PINCH were also reduced after the *in vitro* knockout of α-parvin. Furthermore, protein levels of ILK and PINCH were further reduced in α-pv(fl/fl) β-pv(-/-) NMVCs compared to α-pv(fl/fl) NMVCs after adenoviral transduction as both α- and β-parvin-containing IPP complexes were ablated in these cells. α-parvin KO NMVCs seemed to die faster in cell culture despite no effect of caspase-3 mediated apoptosis (**Fig. 24D**).

In summary, these data show that we can successfully generate α-parvin and α/β-parvin double KO NMVCs.

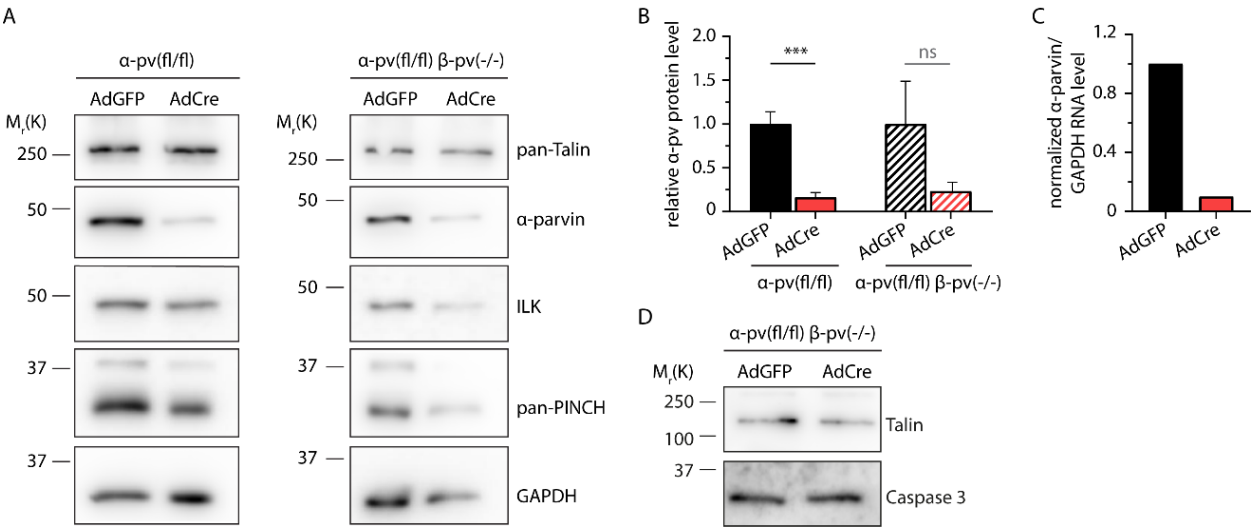

Fig. 24. *In vitro* knockout of α-parvin in isolated NMVCs after adenoviral Cre expression. (A) Western blot analysis depicts reduced expression levels of α-parvin, ILK and PINCH three days after transduction. GAPDH served as loading control. (B) Densitometric quantification of WB analysis. Data are expressed as mean ± s.d., n=3. ***P<0.001 as analyzed using an unpaired Student's *t*-test. ns, not significant. (C) Normalized *α-parvin* mRNA level three days after transduction. n=1 (D) Western blot analysis of caspase-3 protein levels in control and α/β-parvin KO NMVCs three days after isolation. Talin served as loading control.

4.2.2 CRISPR-mediated knockout of α-parvin in MOVAS

Immortalized cell lines are a powerful tool for numerous research applications such as drug screening, antibody production and studying gene function. Especially for the investigation of basic biological processes and the manipulation of cell function, the use of a cell line instead of primary cells can be an advantage. Although I was able to isolate primary mouse SMCs from aorta and the Cre-mediated *in vitro* deletion of α-parvin with concomitant reduction of PINCH levels was successful (**Fig. 25**), the number of cells isolated was not enough for biochemical and cell-based assays. Therefore, we decided to use an immortalized vascular smooth muscle cell line (MOVAS) to analyze α- and β-parvin function with help of the CRISPR/Cas9 system.

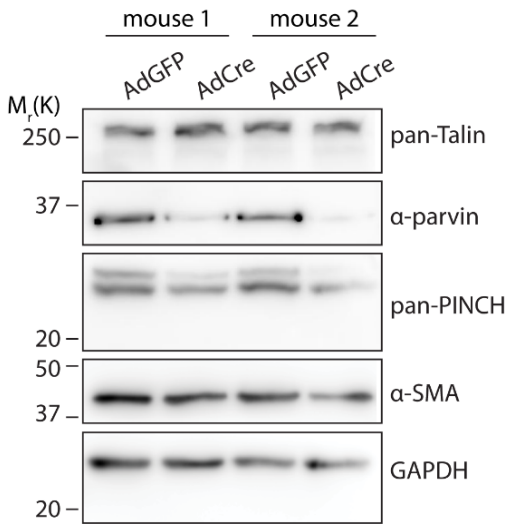

Fig. 25. *In vitro* knockout of α-parvin in isolated vSMCs from two mice after adenoviral Cre expression. Western blot analysis depicts reduced expression levels of α-parvin and PINCH four days after viral transduction. GAPDH and α-SMA served as loading control.

The CRISPR/Cas9 technology is nowadays one of the most widely used techniques to edit endogenous genomic DNA in eukaryotic cells by taking advantage of the cells own DNA repair mechanisms. This technology has rapidly evolved and improved protocols have been established over the last years.

To generate α-parvin knockout MOVAS cells, we first tested different delivery approaches and transfection reagents (e.g. CRISPRMAX, Lipofectamine 2000, Viromer CRISPR). At the beginning of my thesis, I used Cas9 nuclease bearing CRISPR DNA vectors for gene editing that allowed the selection of successfully transfected cells by either FACS or puromycin prior cell sorting into 96 multi-well plates. [392] However, while all MOVAS cells pre-treated with puromycin died, either due to a low transfection efficiency or a single-nucleotide polymorphism (SNP) that was reported in the puromycin gene of this particular vector, transfecting cells with the GFP-containing CRISPR vector only resulted in monoallelic knockout cells (data not shown). One of the most challenging applications of the CRISPR/Cas9 system is, however, the introduction of biallelic DNA changes. [416] As a result, we changed the CRISPR strategy and transfected cells directly with the Cas9 ribonucleoprotein (RNP) complex. Direct delivery of the active Cas9 nuclease together with the sgRNA accelerates the targeting time and enhances the cutting efficiency with lower off-target effects. [417, 418]

For the design of sgRNAs, CRISPR target sites were mapped to the *PARVA* coding sequence within exon 1. Selected sites were predicted by the 'ChopChop' design tool (https://chopchop.cbu.uib.no/) hosted by the Valen lab to possess a minimal number of off-target sites in the mouse genome. [393] Two sites were identified which fulfilled the criteria. The sgRNA target site is depicted in **Fig. 26A**. Following the preparation

of Cas9 nuclease/gRNA RNP complexes MOVAS were transfected with the Cas9/gRNA-lipid complexes and cultured for 24 hours. Positive clones were isolated by sorting single cells into 96 multi-well plates.

Loss of α-parvin protein expression was shown by western blotting and immunofluorescence (IF) analysis. While wt MOVAS robustly expressed α-parvin, knockout MOVAS displayed no α-parvin expression (**Fig. 26B**). Three clones (#3, #25 and #32) were selected for further investigation. IF analysis confirmed the absence of α-parvin in focal adhesions and the cytoplasm (**Fig. 26C**). Furthermore, whole proteome mass spectrometry (MS) was used to confirm the absence of α-parvin peptides in all three clones.

It has been previously reported that the loss of α-parvin expression results in an upregulation of β-parvin or vice versa to stabilize the IPP complex. [171, 385] To check for β-parvin expression in control and α-parvin KO clones, I used RT-qPCR to quantify *β-parvin* mRNA expression levels as an antibody that reliably recognizes endogenous denatured β-parvin was not available. Among the three clones tested clone #3 exhibited the lowest *β-parvin* expression (**Fig. 26D**). As expected, *β-parvin* mRNA expression levels were upregulated with increased passage number over time (**Fig. 26E**). To avoid an interference of β-parvin when analyzing α-parvin KO MOVAS, only cells with a low passage number (P6-P10) were used for the subsequent analysis.

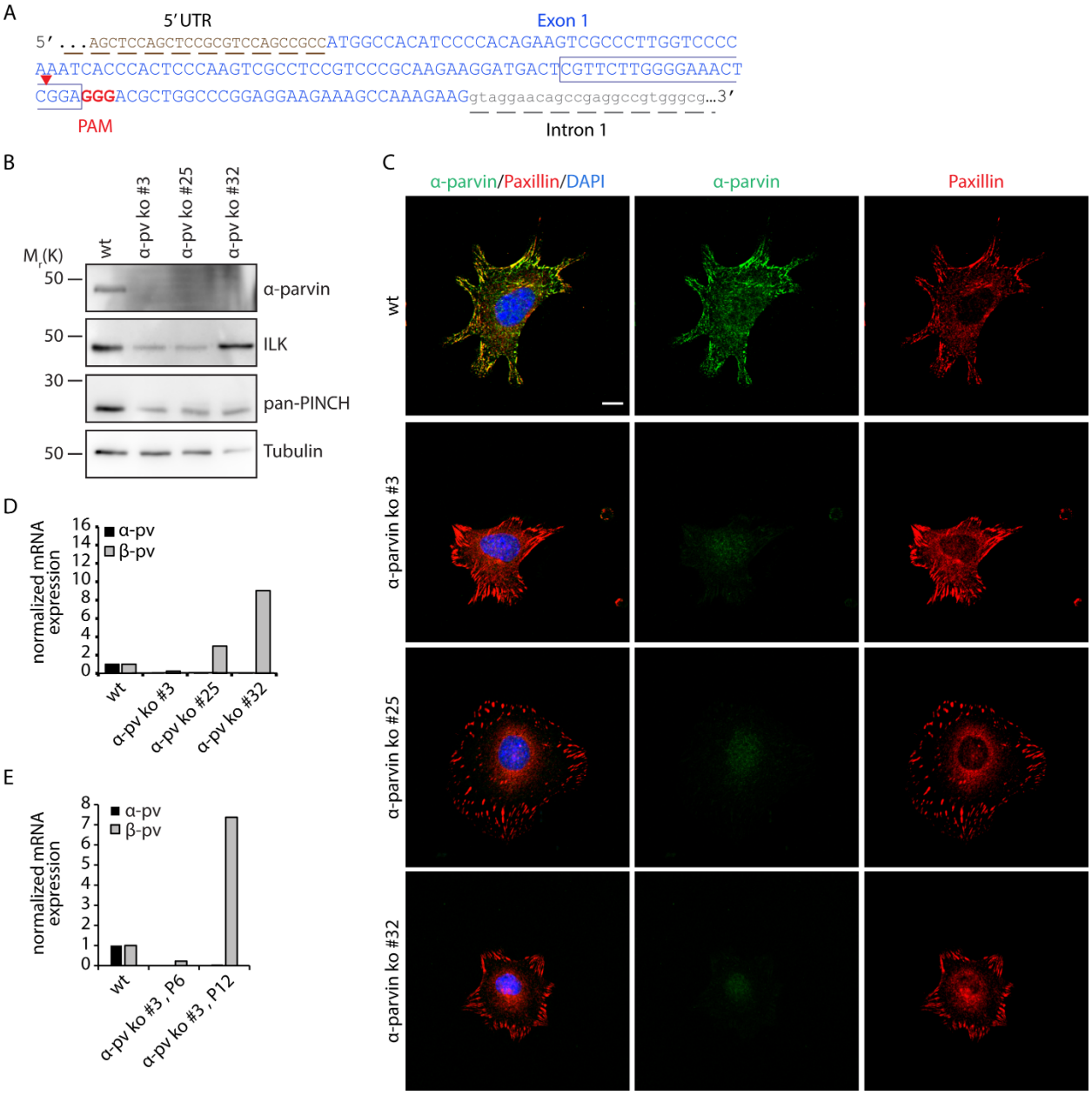

Fig. 26. Generation of CRISPR/Cas9-mediated knockout of α-parvin in MOVAS. (A) Sequence of sgRNA (boxed) targeting exon 1 in mouse *PARVA*. The proto-spacer adjacent motif (PAM) is denoted as red nucleotides. Exon sequence is represented in blue. The red arrowhead indicates site of Cas9 DNA cutting. (B) Western blot analysis of α-parvin, ILK and PINCH expression in the three α-parvin KO clones. Note, loss of α-parvin expression resulted in downregulation of ILK and PINCH protein level. Tubulin served as loading control. (C) Representative IF images confirmed loss of α-parvin protein. Scale bar, 10 µm. (D) RT-qPCR analysis of *PARVA* and *PARVB* expression in α-parvin KO MOVAS. The expression level was normalized to GAPDH. n=2 (E) Upregulation of *PARVB* mRNA expression in α-parvin KO MOVAS over time (here represented by passage number). n=2

In summary, α-parvin KO clone #3 (from now on called α-parvin KO #3) MOVAS showed no detectable α-parvin protein expression in WB analysis or IF and no detectable peptides in MS. In addition, this clone

exhibited the lowest *β-parvin* mRNA expression levels. Therefore, most of the following experiments were conducted using this particular α-parvin KO clone.

Similar to α-parvin depleted CMs, we observed reduced levels of IPP complex member in α-parvin KO MOVAS (**Fig. 27A**). To confirm that the observed reduction of PINCH and ILK expression levels was a direct result of α-parvin deletion and not a clonal artefact, α-parvin KO #3 MOVAS were transduced with a lentiviral eGFP-α-parvin construct controlled by a *CMV* promoter. MOVAS cells stably expressing eGFP-α-parvin were selected by FACS and analyzed by western blotting. **Fig. 27A** shows that the re-expression of eGFP-tagged α- or β-parvin partially rescued ILK and PINCH expression levels irrespective of the eGFP-tag localization (N-terminal vs. C-terminal). To analyze whether the eGFP-tag influences the ability of α-parvin to rescue ILK and PINCH protein level, a lentivirus carrying a tagless α-parvin construct was generated and α-parvin KO #3 MOVAS were transduced. The re-expression of tagless α-parvin fully rescued ILK levels, while the PINCH expression levels were not rescued to wt level (**Fig. 27B**). Interestingly, the monoallelic deletion of α-parvin already resulted in reduced PINCH level whereas ILK level remained unaltered (**Fig. 27B**) suggesting that PINCH protein levels might be less stable in the absence of α-parvin.

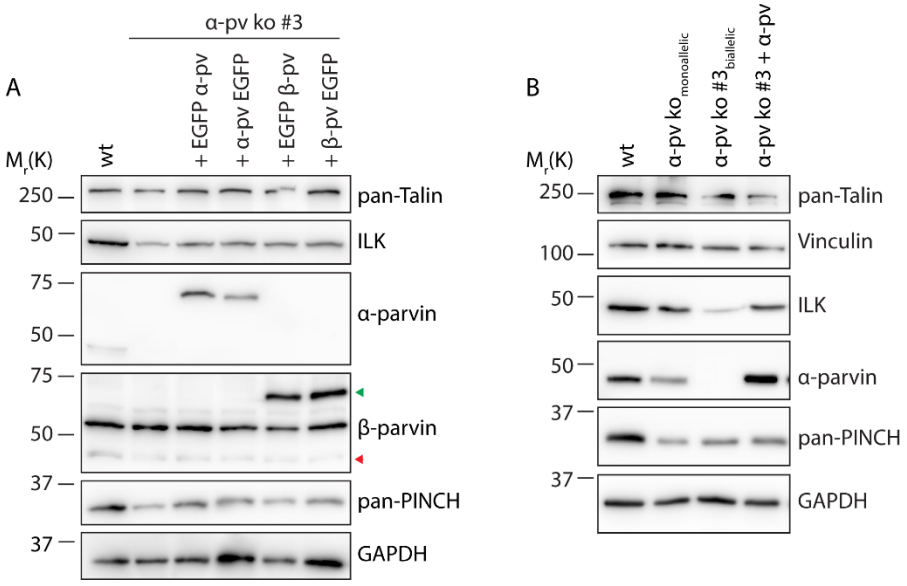

Fig. 27. Depletion of α-parvin results in reduced ILK and PINCH levels. (A) Western Blot analysis of wt and α-parvin KO #3 MOVAS revealed strongly reduced ILK and PINCH expression after α-parvin depletion. Re-expression of eGFP-tagged α- or β-parvin (green arrow head) partially rescued ILK and PINCH protein level. Endogenous β-parvin protein level are marked by a red arrow head. GAPDH served as loading control. (B) Re-expression of tagless α-parvin in α-parvin KO #3 MOVAS rescued ILK levels shown by WB analysis. Note, monoallelic α-parvin depletion also led to reduced PINCH protein level whereas ILK levels remained unaltered. GAPDH served as loading control.

4.3 Characterization of α-parvin deficient cardiomyocytes and MOVAS

Next, we analyzed the role of α-parvin in integrin-mediated processes such as adhesion, spreading and migration in the established α-parvin deficient cells.

4.3.1 Analysis of integrin-mediated processes in α-parvin deficient, mononucleated NMVCs

4.3.1.1 α-parvin deletion impairs cell spreading and induces sarcomere-containing protrusions in NMVCs

To investigate if the loss of α-parvin has an effect on the phenotype of NMVCs, cell morphological parameters were measured and the spreading kinetics were analyzed. Therefore, I isolated NMVCs from *α-pv(fl/fl)* and *α-pv(fl/fl) β-pv(-/-)* mice, plated them on fibronectin and deleted the floxed alleles by adenoviral expression of Cre recombinase (AdCre) 24 hours after isolation as described in 4.2.1.. To exclude side-effects of the viral infection to the cells, one half of the isolated NMVCs were infected with an adenovirus carrying an empty GFP (AdGFP) as control. Cells were fixed three and five days after adenoviral infection and immunostained with an anti-α-actinin antibody to measure the cell morphological parameters.

AdGFP-infected NMVCs isolated from *α-pv(fl/fl)* and *α-pv(fl/fl) β-pv(-/-)* mice displayed a star-like cell morphology with well-organized α-actinin striations (Fig. 28A). No difference in spreading area between isolated NMVCs expressing or lacking β-parvin expression was observed three or five days after adenoviral infection (Fig. 28B). The cell size increased from three to five days in culture, indicative of hypertrophic growth of AdGFP-infected NMVCs on FN-coated cell dishes. In contrast, AdCre-infected NMVCs were smaller and failed to increase their cell size over time (Fig. 28B). Surprisingly, we did not observe differences in the spreading area of NMVCs lacking only α-parvin or both parvin isoforms (α- and β-pv) after adenoviral infection. Unfortunately, isolated NMVCs seeded on collagen I-coated culture dishes, to circumvent FN-induced hypertrophic growth, did either not attach or died shortly after attachment, preventing further analysis. We additionally analyzed the morphology of control, α-parvin and α/β-parvin KO NMVCs according to the following parameter: major and minor axis, perimeter, circularity and aspect ratio. Whereas the cell perimeter gives complemental information about cell protrusive activity, circularity is a measure of the roundness of cells, where values approaching 0 indicate an increasingly elongated cell shape. AdGFP-infected NMVCs, isolated from *α-pv(fl/fl)* mice, grew in both length (major axis) and width (minor axis) and exhibited a larger cell perimeter (Fig. 28C-E). The same observation was made for AdGFP-infected NMVCs isolated from *α-pv(fl/fl) β-pv(-/-)* mice, although the increase was not statistically significant. Although not statistically significant AdGFP-infected NMVCs displayed a reduced circularity, indicative of a more elongated cell shape five days after transduction which additionally confirmed the hypertrophic

growth of these cells (Fig. 28F). In contrast, AdCre-infected NMVCs from *α-pv(fl/fl)* mice did not increase in cell length, width or perimeter and NMVCs lacking α- and β-parvin expression showed a significant decrease of the cell perimeter and increase in circularity (Fig. 28C-F). No difference in cell length, width, perimeter or circularity between isolated NMVCs expressing or lacking β-parvin expression was observed three or five days after adenoviral infection. The reduction in cell length, width, perimeter and circularity in AdCre-infected NMVCs in comparison to AdGFP-infected cells reflect the results of the spreading area analysis. The cellular aspect ratio did neither change in AdGFP- or AdCre-infected NMVCs isolated from *α-pv(fl/fl)* or *α-pv(fl/fl) β-pv(-/-)* mice (Fig. 28G).

Overall, these data show that α-parvin plays an important role in cardiomyocyte spreading and hypertrophic growth. While AdGFP-infected NMVCs were able to induce hypertrophic growth, AdCre-infected NMVCs from either *α-pv(fl/fl)* and *α-pv(fl/fl) β-pv(-/-)* mice were not. However, unexpectedly, β-parvin did not functionally compensate for the loss of α-parvin in isolated NMVCs plated on fibronectin.

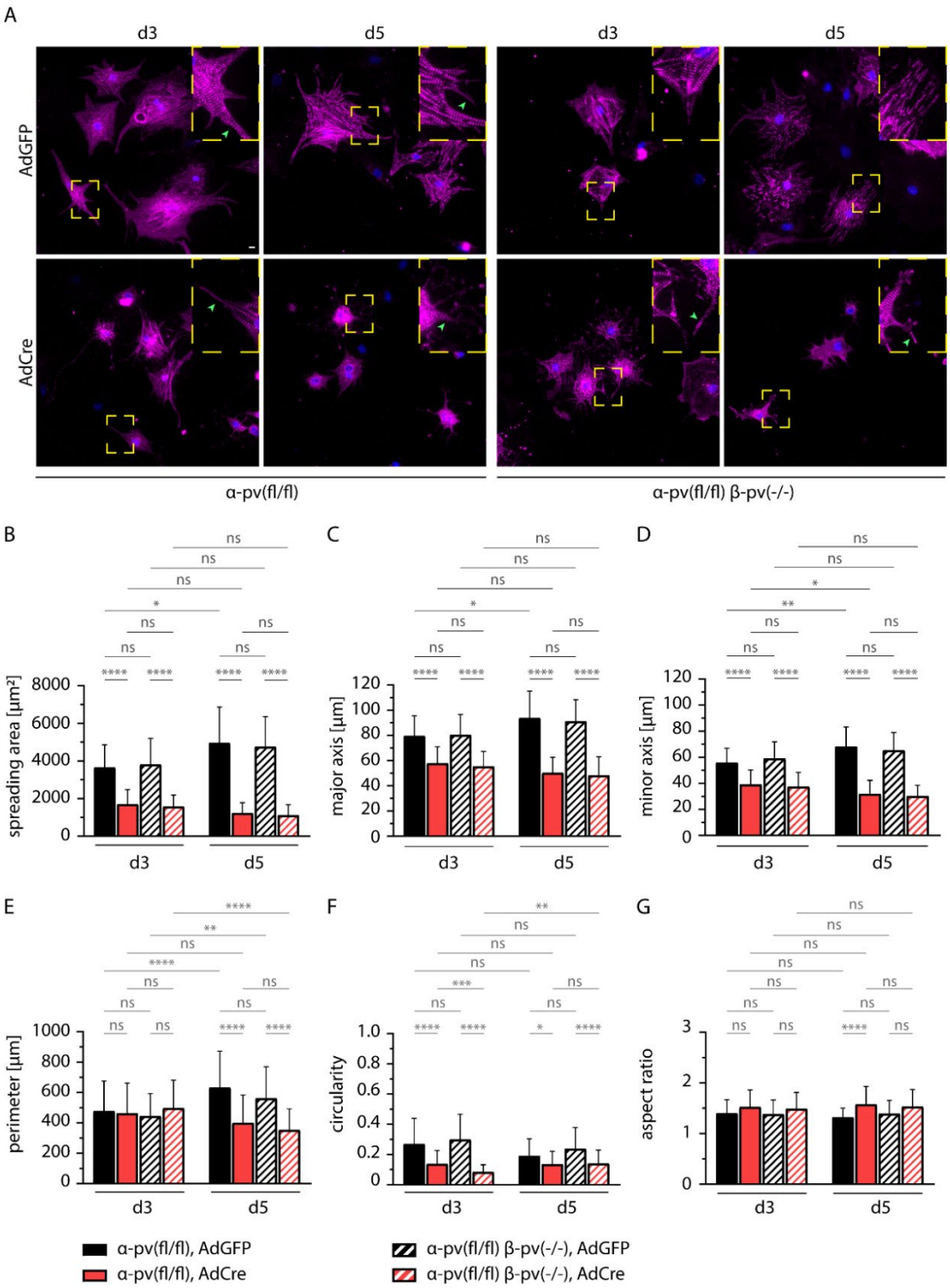

Fig. 28. α-parvin expression is important for spreading and hypertrophic growth of NMVCs. (A) Representative images of NMVCs isolated from *α-pv(fl/fl)* and *α-pv(fl/fl) β-pv(-/-)* mice three and five days after adenoviral transduction and immunostaining using an anti-α-actinin antibody. DAPI was used to stain nuclei. Green arrow heads mark sarcomere-containing protrusions. Scale, 10 µm. (B-G) Quantification of spreading area (B), major (C) and minor (D) axis, cell perimeter (E), circularity (F) and aspect ratio (G) of NMVCs plated on FN. Data is presented as mean ± s.d. ****P<0.0001, **P<0.01, *P<0.1 as analyzed using a Kruskal-Wallis test. ns, not significant. 30-40 cells were measured per condition, n=3.

We also observed the formation of long, often branching α-actinin-positive protrusions (Fig. 28A, green arrow heads) in control and α-parvin KO NMVCs. These protrusions have been observed before during trabeculation in the zebrafish heart. [419] This process first depends on the extension of long protrusions, which sometimes, coming from different cardiomyocytes, extend towards each other to make contact. AdCre-infected NMVCs from both *α-pv(fl/fl)* and *α-pv(fl/fl) β-pv(-/-)* mice seem to develop longer, thinner and often more α-actinin-positive protrusions in comparison to control NMVCs.

Healthy heart tissue exhibits an elastic Young´s modulus ranging between 10-15 kPa. [420] To study the effect of matrix rigidity on NMVC morphological characteristics, isolated NMVCs from *α-pv(fl/fl)* and *α-pv(fl/fl) β-pv(-/-)* mice were plated on FN-coated PDMS substrates with Young´s modulus of 1.5, 15 or 28 kPa. Adenoviral infection was performed 24 hours after isolation and cells were fixed three days later and subjected to immunostaining with anti-α-actinin antibodies.

It was previously reported that NRVCs on collagen I-coated rigid substrates align their sarcomeres with defined striations, whereas most of the NRVCs on compliant substrates displayed disorganized sarcomeres. [421] We, however, observed organized sarcomeric structures even in NMVCs cultured on soft substrates (Fig. 29A). In comparison to NMVCs cultured on a plastic surface (Fig. 28), NMVCs on softer substrates (1.5-28 kPa) were smaller. Surprisingly, NMVCs plated on 15 kPa substrates did not show intermediate parameters among the three tested compliant substrates (1.5, 15 and 28 kPA) in terms of their cell morphologies (Fig. 29B). On the contrary, NMVCs plated on 15 kPa substrates exhibited the largest spreading area, cell length, width and perimeter whereas cells cultured on 1.5 or 28 kPa did not show significant differences in these parameters (Fig. 29B-E). These results fit to the reported data of NRVCs plated on different collagen I-coated substrate stiffnesses. The authors also observed a slight konvex behavior of the spreading area of NRVCs plated on softer substrate stiffnesses (1-50 kPa). [421] Among the analyzed cell morphological parameters, cell circularity and cellular aspect ratio were not altered, neither in AdGFP- nor in AdCre-infected NMVCs from *α-pv(fl/fl)* or *α-pv(fl/fl) β-pv(-/-)* mice (Fig. 29F, G). However, AdCre-infected NMVCs were smaller on all three substrate stiffnesses, displaying a decreased spreading area, cell length (major axis), width (minor axis) and perimeter in comparison to AdGFP-infected NMVCs (Fig. 29B-E).

Altogether these findings indicate that α-parvin is required for cardiomyocyte spreading in response to physiological mechanical stimuli such as substrate compliance. Furthermore, β-parvin does not seem to compensate for the functional loss of α-parvin.

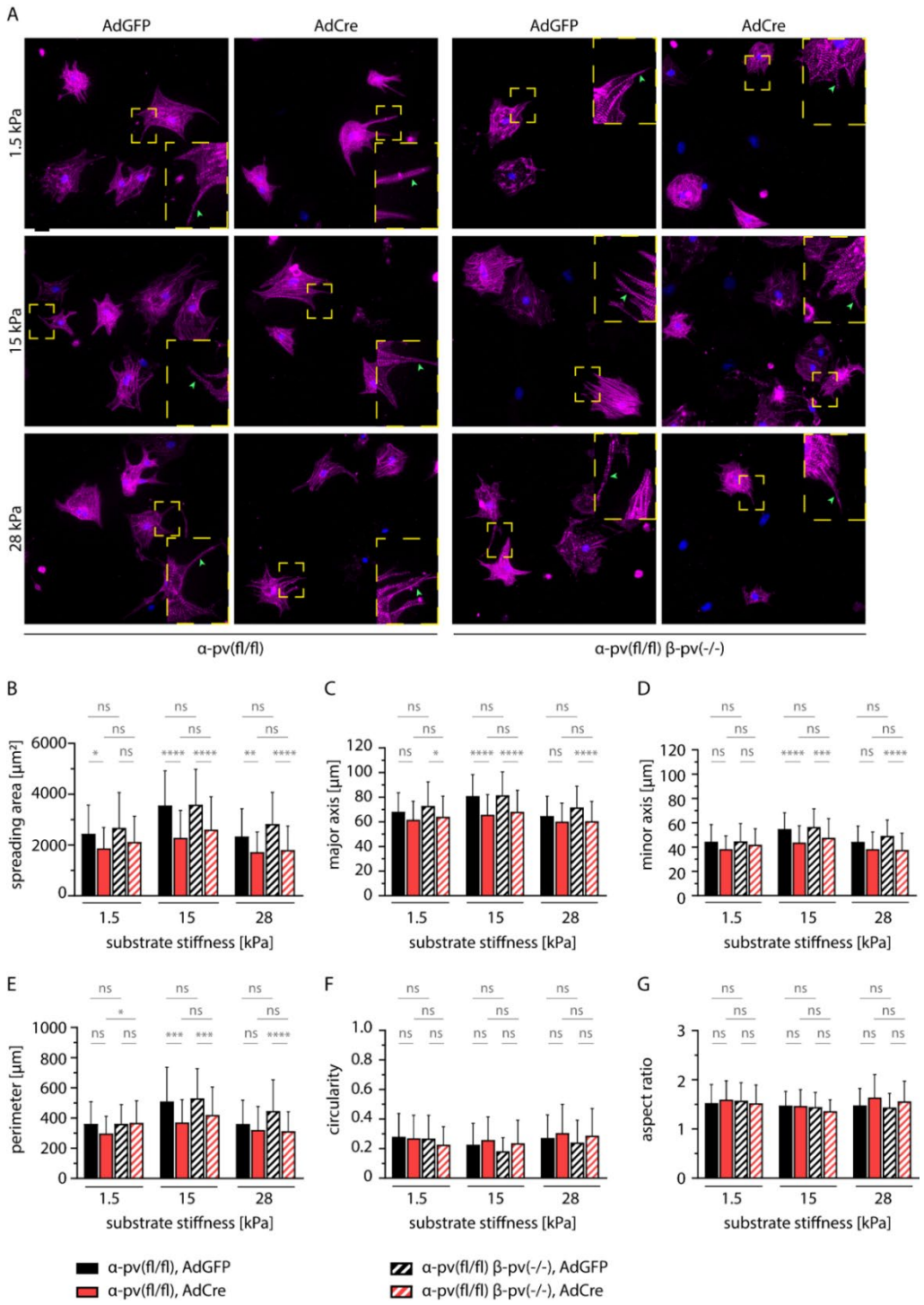

Fig. 29. Substrate stiffness influences NMVC spreading. (A) Representative images of NMVCs isolated from either *α-pv(fl/fl)* or *α-pv(fl/fl) β-pv(-/-)* mice three days after adenoviral transduction and immunostaining using an anti-α-actinin antibody. DAPI was used to stain nuclei. NMVCs were plated on FN-coated elastic surfaces with defined elastic modulus of 1.5, 15 and 28 kPa. Green arrow heads mark sarcomere-containing protrusions. Scale, 10 µm. (B-G) Quantification of spreading area (B), major (C) and minor (D) axis, cell perimeter (E), circularity (F) and aspect ratio (G) of NMVCs plated on FN-coated elastic surfaces. Data are presented as mean ± s.d. ****P<0.0001, ***P<0.001, **P<0.01, *P<0.1 as analyzed using a Kruskal-Wallis test. ns, not significant. 30-40 cells were measured per condition, n=3.

4.3.1.2 Loss of α-parvin effects the contractility of cardiomyocytes

Isolated NMVCs exhibit spontaneous contractions *in vitro* 24 hours after isolation. Depending on the cell density, two patterns of spontaneous contractions were observed: single cell contraction or small cell colonies exhibiting various non-synchronous contractions. Over time, the contractions of the colonies became more synchronous. The effect of α-parvin deletion on cell contraction was evaluated by videomicroscopy three and five days after adenoviral expression of Cre recombinase in isolated NMVCs. While 50% of the AdGFP-infected control cells were beating on day three, only 30% of parvin-depleted cells showed spontaneous contractions (**Fig. 30**). On day five, 65% of control cells, but only 20% of AdCre-infected NMVCs were beating. The loss of spontaneous contractions was further enhanced in α/β-parvin double KO NMVCs, indicating that β-parvin here functionally compensates for the loss of α-parvin.

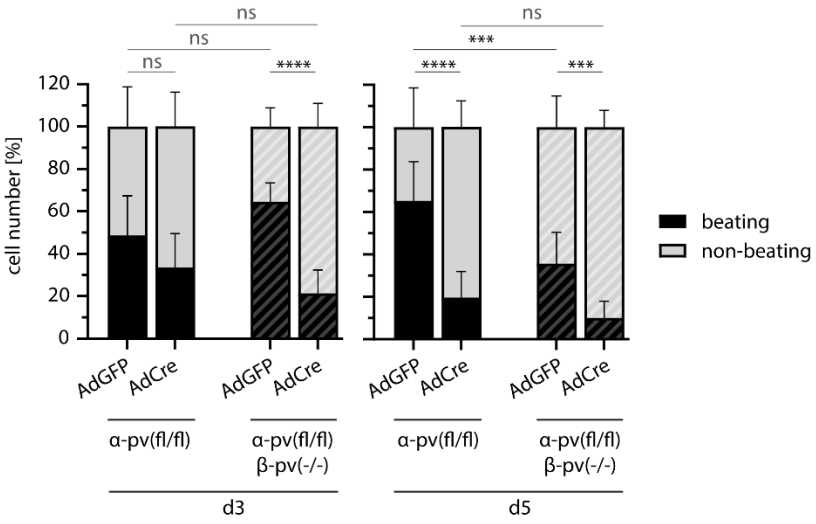

Fig. 30. α-parvin deletion effects spontaneous contractions of NMVCs. Quantification of NMVCs still showing spontaneous contractions three and five days after adenoviral transduction. Data are presented as mean ± s.d. ****P<0.0001, ***P<0.001 as analyzed using an ordinary one-way ANOVA test. ns, not significant. 30-40 cells were analyzed per condition, n=3.

4.3.2 Analysis of integrin-mediated processes in α-parvin knockout MOVAS

4.3.2.1 α-parvin depletion results in an early adhesion defect in MOVAS

Cell-cell and cell-ECM adhesion mechanisms determine the overall architecture of a tissue. Hence, they play a pivotal role in tissue cohesion and integrity. To investigate if α-parvin deletion affects the adhesion of MOVAS cells to the ECM protein fibronectin, an *in vitro* 'plate and wash' assay was conducted. For this, I cultured wild-type (wt) and α-parvin KO MOVAS on FN-coated 96 multi-well plates and allowed them to attach for 10 and 30 min at 37 °C. After washing, the fraction of remaining cells attached to the multi-well plate was quantified.

α-parvin deletion reduced the adhesion of all three α-parvin KO MOVAS clones after 10 min significantly compared to wt MOVAS (**Fig. 31A**). This was still the case 30 min after seeding, although the difference was not significant anymore. Re-expression of eGFP-tagged α-parvin in α-parvin KO #3 MOVAS cells resulted in an intermediate phenotype but did not rescue the adhesion defect up to wt level (**Fig. 31B**). This observation correlates with the observed partial rescue of the IPP complex in eGFP-α-parvin rescued MOVAS (**Fig. 27A**). Similar results were observed with α-parvin KO and α/β-parvin double KO fibroblasts (**Fig. 31C**). Deletion of both α- and β-parvin severely impaired the adhesion ability of fibroblasts to fibronectin compared to the sole loss of α-parvin. Re-expression of either eGFP-tagged α- or β-parvin partially rescued the observed adhesion phenotype.

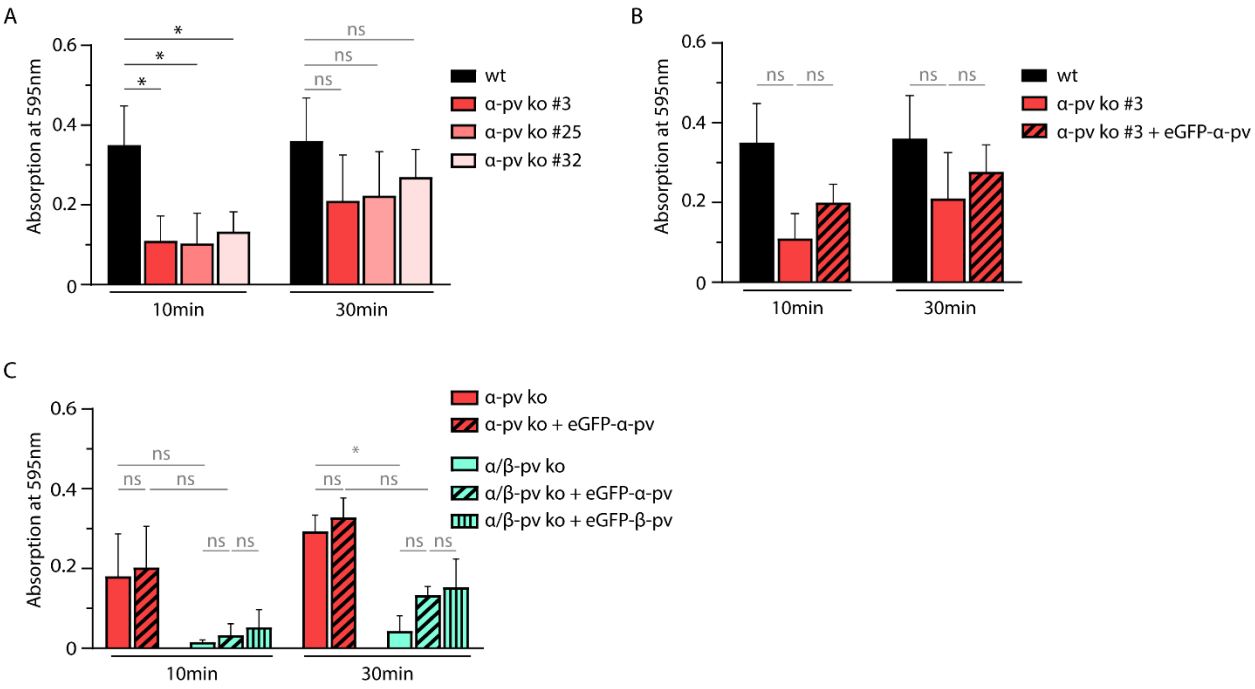

Fig. 31. MOVAS require α-parvin for strong cell adhesion to the ECM protein fibronectin during early spreading. (A) Colorimetric quantification of adhesion to FN of wt and α-parvin KO MOVAS clones 10 and 30 min after plating. Note, loss of α-parvin resulted in a significant reduction of early cell adhesion. (B) Re-expression of eGFP-tagged α-parvin resulted in an intermediate adhesion phenotype and could not significantly enhance adhesion ability to FN of α-parvin KO #3 MOVAS. (C) Colorimetric quantification of adhesion to FN of fibroblasts lacking α- or α- and β-parvin expression 10 and 30 min after plating. Note, re-expression of either eGFP-tagged α- or β-parvin partially rescued the adhesion defect. Data are expressed as mean ± s.d., n=3. **P*<0.1 as analyzed using an unpaired Student's *t*-test (A, B). A Kruskal-Wallis test was performed for data shown in C. ns, not significant.

Overall, these data show that α-parvin plays an important role in cell-ECM adhesion and deletion of α-parvin can be partially compensated by β-parvin.

4.3.2.2 α-parvin is important for cell spreading in MOVAS

Cell spreading over a substrate happens in distinct stages. Early cell attachment and deformation are characterized as passive events while later stages of cell spreading are more active, involving actin polymerization and myosin contraction. [422]

Montanez et al. showed that SMA-positive cells isolated from either embryos or yolk sac of *α-parvin* KO mice exhibit a strong spreading defect. [171] To analyze whether the knockout of α-parvin results in a similar spreading defect in MOVAS cells, wt and α-parvin KO #3 MOVAS were seeded on FN-coated culture dishes. Cells were fixed 10, 30, 60 and 360 min after plating and co-stained with anti-α-parvin and anti-paxillin antibodies (**Fig. 32**-**Fig. 35**). The cell spreading area was determined using ImageJ and the quantification results are visualized in **Fig. 35A**.

At 10 min of cell spreading wt MOVAS showed a round cell morphology with α-parvin and paxillin-positive nascent adhesions and FAs at the cell periphery. In contrast, α-parvin KO MOVAS were smaller, exhibiting a round cell morphology with only paxillin-positive nascent adhesions at the cell periphery (**Fig. 32**).

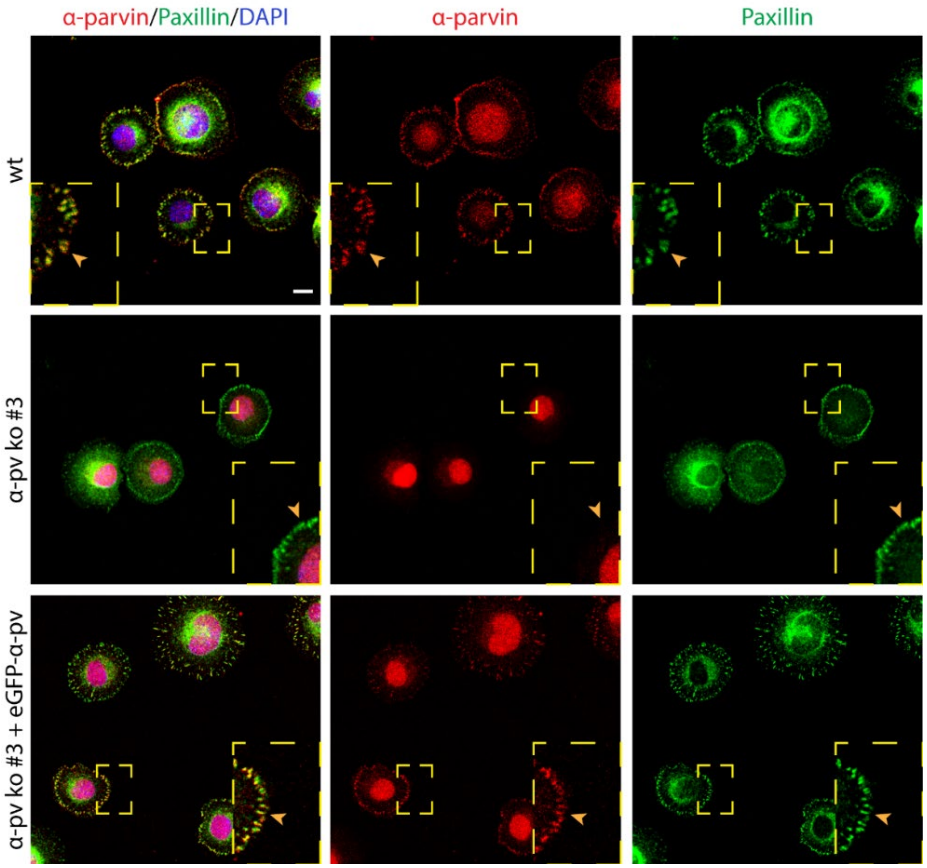

Fig. 32. Spreading of α-parvin deficient MOVAS. Double-fluorescent labeling for α-parvin and paxillin of wt and α-parvin KO #3 MOVAS cultured on fibronectin for 10 min. Orange arrow heads mark cell-ECM contact sites at the cell periphery. Nuclei were visualized with DAPI. Scale, 10 µm.

After 30 min, some wt MOVAS cells started to become polygonal, showing focal adhesions at the cell periphery. Unlike wt MOVAS, α-parvin KO #3 MOVAS were still smaller, exhibiting a round cell morphology with only few cells that established paxillin-positive FAs at the cell periphery (**Fig. 33**).

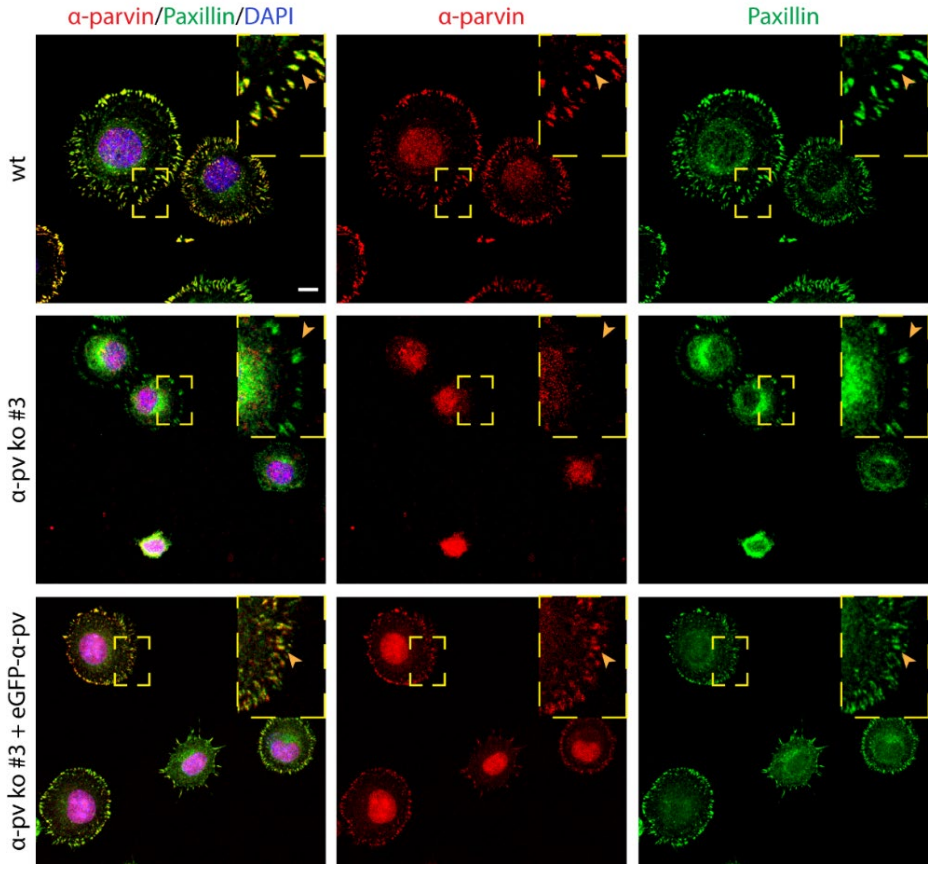

Fig. 33. Spreading of α-parvin deficient MOVAS. Double-fluorescent labeling for α-parvin and paxillin of wt and α-parvin KO #3 MOVAS cultured on fibronectin for 30 min. Orange arrow heads mark cell-ECM contact sites at the cell periphery. Nuclei were visualized with DAPI. Scale, 10 µm.

60 min after plating, wt MOVAS had developed a polygonal cell morphology with large FAs at the cell border (orange arrow head) and smaller fibrillar adhesions in the cell center (white arrow head). Some of the fully spread α-parvin deficient MOVAS could form larger FAs, which were nearly exclusively located at the cell periphery (**Fig. 34**). In addition, α-parvin KO #3 MOVAS started to change their cell phenotype, becoming more polygonal. 360 min after plating cells exhibited the same cell morphology observed at the 60 min time point. However, while wt MOVAS were still slightly growing in size, α-parvin KO #3 MOVAS did not further spread (**Fig. 35A**).

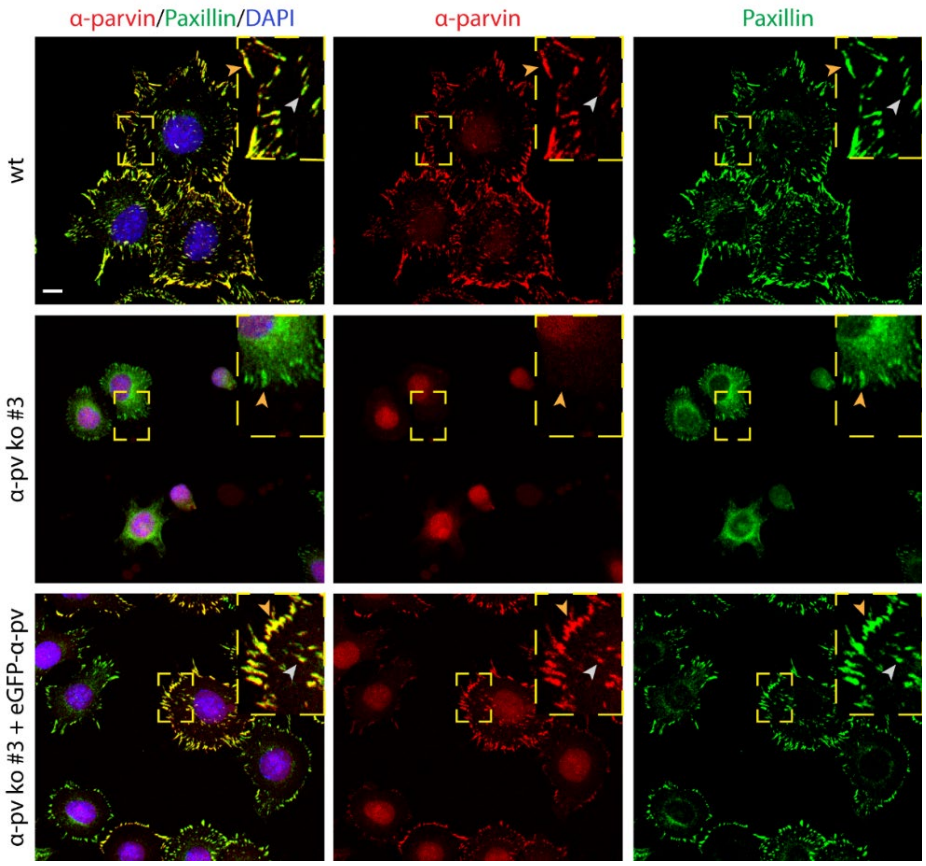

Fig. 34. Spreading of α-parvin deficient MOVAS. Double-fluorescent labeling for α-parvin and paxillin of wt and α-parvin KO #3 MOVAS cultured on fibronectin for 60 min. White arrow heads indicate FAs within the cell whereas orange arrow heads mark FAs localized at the cell periphery. Nuclei were visualized with DAPI. Scale, 10 µm.

Importantly, re-expression of eGFP-α-parvin rescued FA formation and partially cell spreading. Rescue cells were smaller compared to wt MOVAS at all time points analyzed (**Fig. 35B**). In contrast, α-parvin KO #3 MOVAS re-expressing eGFP-α-parvin were able to form stable FAs at the cell border (**Fig. 34**, orange arrowhead) and fibrillar adhesions in the cell center (white arrow head).

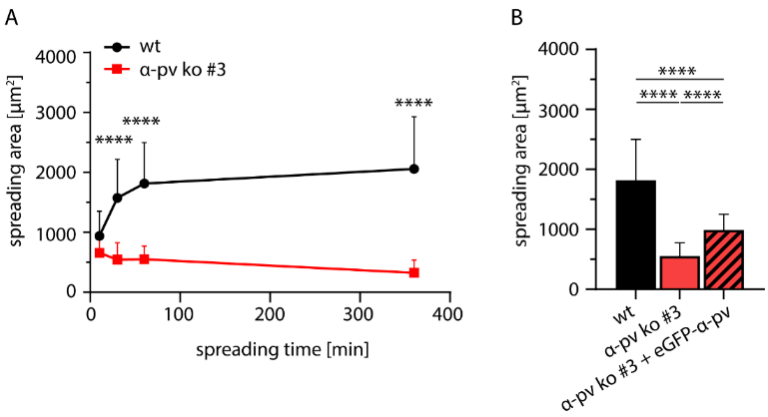

Fig. 35. Quantification of cell spreading behavior. (A) α-parvin KO #3 MOVAS exhibit a significant defective cell spreading behavior compared to wt MOVAS. (B) Re-expression of eGFP-tagged α-parvin partially rescue the spreading defect of cells seeded on FN for one hour. Data are expressed as mean ± s.d. ****P<0.0001 as analyzed using a Kruskal-Wallis test. 20-40 cells were measured in n=1 experiment.

Taken together, these data show that α-parvin is important for cell spreading and focal adhesion formation as well as for their maturation into fibrillar adhesions.

4.3.2.3 α-parvin is required for collective cell migration in MOVAS

Cell migration is crucial for numerous physiological and pathological processes such as embryonic development, angiogenesis, cell investment into the vessel wall, cancer metastasis, and wound healing. [423] Montanez and colleagues showed that α-parvin is indispensable for the persistent migration of mural cells, vSMCs and pericytes, into the vessel walls. [171] To test whether this holds true for vascular smooth muscle cells *in vitro*, α-parvin KO #3 MOVAS were subjected to *in vitro* wound healing assays that are frequently used to study collective cell migration. 24 multi-well plates were coated with FN prior the experiment. The culture-inserts 2 well from IBIDI were placed into the wells leaving a defined 500 µm ± 100 µm large gap. Cells were seeded into the wells and the confluent cell monolayers were treated with mitomycin C, a proliferation inhibitor. Time-lapsed microscopy allowed the visualization of migrating cells into the wound.

Fig. 36A shows that wt MOVAS closed the gap within 12-15 hours, while at that time point the gap in α-parvin KO #3 MOVAS remained to 40% open. After 24 h α-parvin KO #3 MOVAS still did not completely close the wound. While wt MOVAS closed the gap as monolayer (collective cell migration), MOVAS lacking α-parvin expression migrated as single cells (**Fig. 36B**). To analyze whether α-parvin KO #3 MOVAS are still able to establish cell-cell contacts mediated by cadherins, we fixed the cells at different time points of the wound closure assay (t = 0 h, 12 h, 24 h) and immunofluorescently labeled cadherins. However, due to the lack of a functional cadherin antibody, no conclusions could be drawn from the experiment. It is therefore

important to investigate whether cadherin expression might be altered in MOVAS cells lacking α-parvin expression which would be a possible explanation for the disturbed collective cell migration.

When assessing the cell velocity and directionality during wound closure, it was observed that α-parvin KO #3 MOVAS migrated slightly faster compared to wt MOVAS but less directional, leading to the observed wound closure defect (**Fig. 36C**).

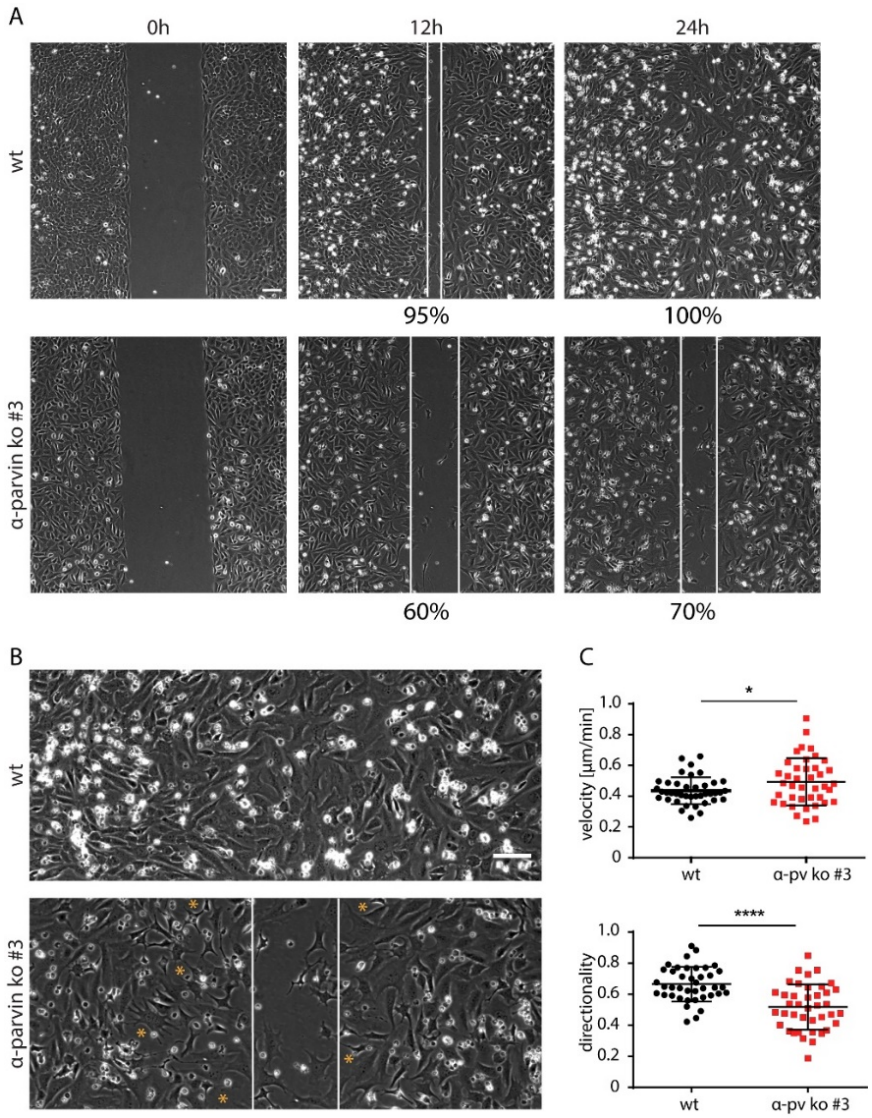

Fig. 36. α-parvin is required for directional cell migration. (A) Representative phase-contrast images of wt and α-parvin KO #3 MOVAS in a wound healing assay (t=0, 12 and 24 h after barrier removal). The white lines indicate the unclosed wound area. Scale, 10 µm. (B) Representative zoom-in phase-contrast images of wt and α-parvin KO #3 MOVAS at t=24 h. Note, α-parvin KO #3 MOVAS did not migrate collectively but as single cells (orange star indicate holes in the cell monolayer). Scale, 10 µm. (C) Quantification of velocity and directionality of single cells tracked during wound healing. Data are presented as mean ± s.d. from two independent experiments. 20 cells each were tracked. ****P<0.0001, *P<0.1 as analyzed using a Student's t-test.

Re-expression of eGFP-tagged α-parvin, irrespective of the eGFP-tag localization (N-terminal vs. C-terminal) did not rescue the observed phenotype (**Fig. 37A**). No wound closure was achieved after 24 h and eGFP-α-parvin expressing cells still migrated as single cells. Given its size (~32 kDa) the eGFP-tag probably interferes with the α-parvin structure and function, thereby interfering with IPP complex formation and the rescue of the migratory defects. Importantly, however, α-parvin KO #3 MOVAS expressing either tagless α- or β-parvin completely rescued the defect in collective cell migration (**Fig. 37B**).

These data indicate that α-parvin is important for collective cell migration of MOVAS cells and that β-parvin is able to compensate for the loss of α-parvin in this assay.

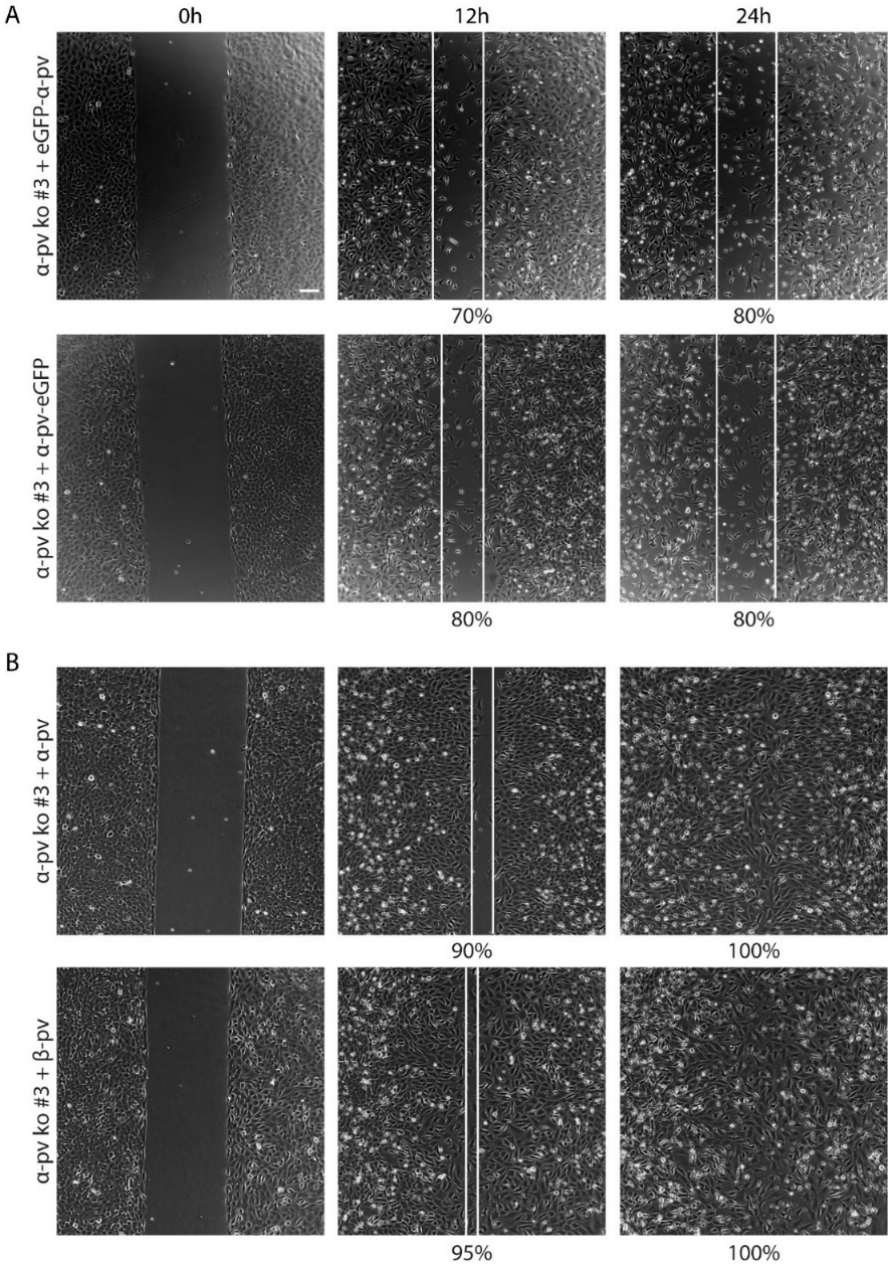

Fig. 37. Re-expressing tagless α- or β-parvin rescues the migration defects. (A) Representative phase-contrast images of α-parvin KO #3 MOVAS re-expressing eGFP-tagged α-parvin. Note, re-expressing eGFP-tagged α-parvin did not rescue the migration defects. (B) Representative phase-contrast images of α-parvin KO #3 MOVAS re-expressing either tagless α- or β-parvin. Note, both tagless parvin isoforms were capable of rescuing the migration defects. The white lines indicate the unclosed wound area. Scale, 10 µm.

4.3.2.4 α-parvin deletion leads to increased contractility in MOVAS

The RhoA/ROCK/MLC2 signaling pathway is involved in multiple cellular functions including cytoskeletal reorganization, cell migration, proliferation and angiogenesis. [424] Integrins regulate RhoA activity in different pathways and the IPP complex plays an important role to downregulate RhoA-dependent contractility to facilitate cell spreading and migration. [157, 171, 425] For example, α-parvin deletion in isolated SMA-positive cells from yolk sac or E9.5 embryos results in a hypercontractile phenotype and also the vSMC-specific deletion of ILK resulted in an increased RhoA activity. [157, 171]

To assess whether α-parvin plays a role in the RhoA/ROCK/MLC2 signaling pathway in MOVAS, GTP-RhoA binding to the Rhotekin-Rho binding domain was used to determine the level of RhoA activation in control and α-parvin depleted cells. MOVAS lacking α-parvin showed elevated levels of active GTP-RhoA, while total RhoA expression levels remained unchanged (**Fig. 38A**). Immunofluorescent labeling of pMLC2 did not show obvious alterations in intensity between wt and α-parvin KO #3 MOVAS (**Fig. 38B**), probably due to the significant differences in cell size observed between wt and α-parvin KO #3 MOVAS. We therefore plated cells on FN-coated micropatterns to eliminate cell size and shape differences, thus, reducing variability, as cell attachment and spreading only occurs on the FN-coated shapes and not on the surrounding polyethylene glycol (PEG). However, while wt MOVAS cells readily attached to the patterns, α-parvin KO #3 MOVAS cells did either not adhere or were washed away during cell fixation, and adaptations of the fixation protocol did not increase the number of attached cells. This might indicate that α-parvin KO #3 MOVAS cells exhibited either a too strong adhesion defect or too strong contraction forces that did not allow prober attachment and FA formation on these micropatterns. We therefore utilized western blot analysis, which revealed higher pMLC2 levels in α-parvin KO #3 MOVAS compared to wt MOVAS (**Fig. 38C**).

These results support published data showing that α-parvin is involved in cell contractility regulation. [171]

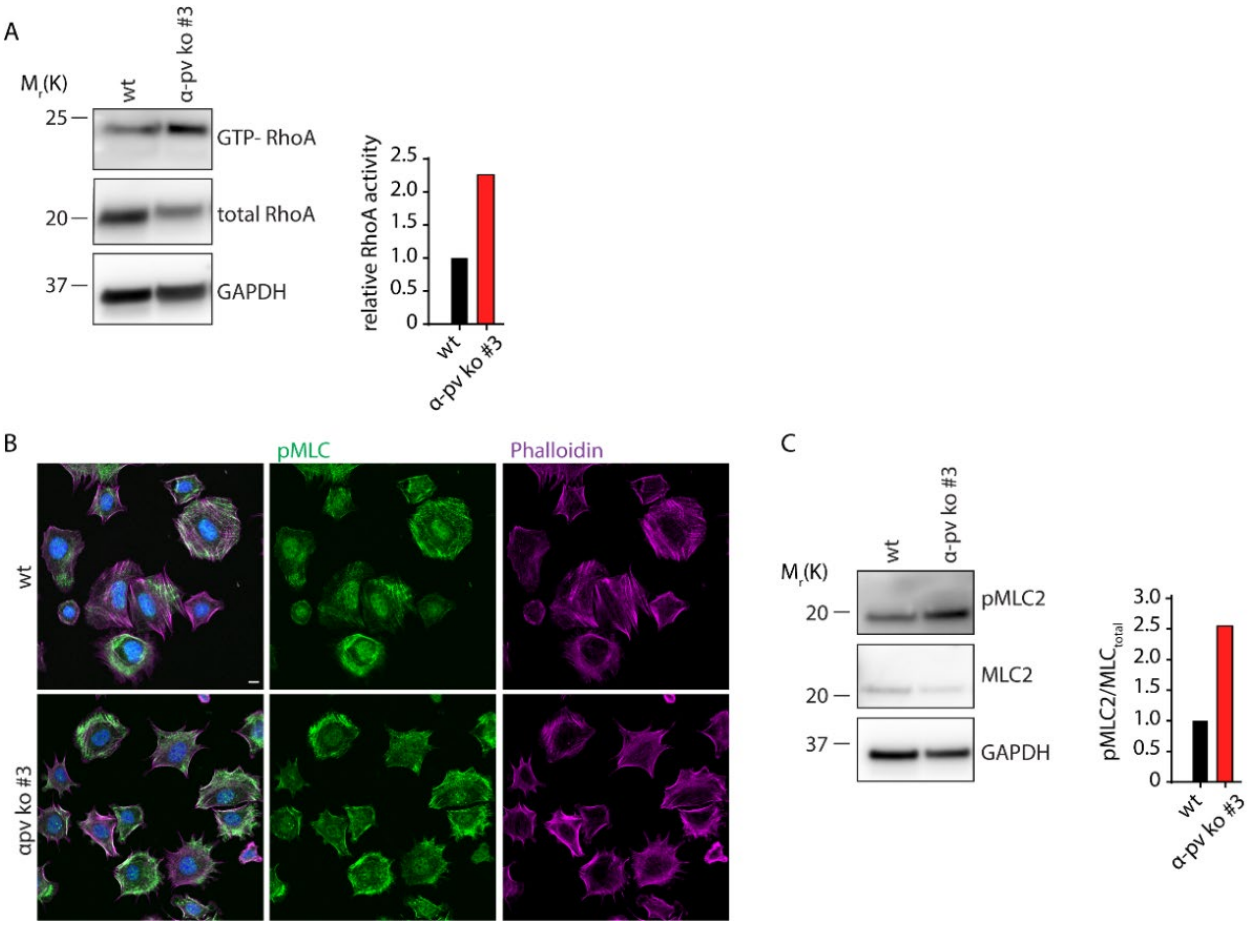

Fig. 38. Absence of α-parvin results in elevated RhoA activity after 45 min of spreading on fibronectin. (A) α-parvin KO #3 MOVAS showed increased RhoA activity. Data are presented as mean of n=2. (B) Immunofluorescent labeling of phospho-MLC2 and phalloidin in wt and α-parvin KO #3 MOVAS cultured on FN. (C) Increased RhoA activity resulted in concomitant increase of MLC2 phosphorylation. GAPDH served as loading control. Data are presented as mean of n=2.

4.4 Mass spectrometric analysis of the mouse cardiomyocyte whole proteome

To analyze if the abundance of α- and β-parvin, as well as of ILK, PINCH and β1 integrin changes during the process of cardiomyocyte maturation, we analyzed the whole proteome of freshly isolated and cultured NMVCs as well as samples from adult CMs by mass spectrometry.

For an overall assessment of proteomic similarities and differences among the three conditions, we employed principle component analysis (PCA). Samples of freshly isolated, five days cultured NMVCs and adult CMs clustered separately with the biological replicates tightly grouped together (**Fig. 39B**). 5430 proteins were initially identified, of which 4856 proteins remained after the exclusion of potential contaminants and the removal of proteins identified in the decoy reverse database or only by site modifications, normalization and missing-value imputation. These proteins were subsequently analyzed by hierarchical clustering revealing severe differences in intensities between neonatal and adult cardiomyocytes (**Fig. 39A**). The zoom-in of the heat map (**Fig. 39C**) as well as the LFQ intensity plots (**Fig. 39D**) show significant differences among the α- and β-parvin intensities within the three conditions with both proteins being less abundant in adult CMs. Interestingly, β-parvin expression seems to increase with cardiomyocyte maturation which is in line with reported findings showing a gradual upregulation of β-parvin expression during embryonic development. [164, 165] Unexpectedly, β-parvin abundance was not higher in adult CMs compared to neonatal ones which might be due to the different cell isolation techniques used as well as the inability to completely align the cell numbers across the different conditions. However, we cannot rule out that our findings reflect the true cellular situation, as to our knowledge, such a proteomic analysis was not performed before. Our data further supports this hypothesis by the identification of the correct myosin and troponin isoforms, according to the well-established isoform switching, in neonatal and adult CMs. [312, 313, 315] While we identified *MYH7* and the slow skeletal type of troponin (*TNNT1*) in freshly isolated neonatal CMs, MYH6 and cardiac troponin (*TNNT2*) was specifically found in adult CMs. Furthermore, while α- and β-parvin, as well as PINCH and β1 integrin intensities increased with CM maturation, ILK abundance did not change (**Fig. 39D**).

Overall, the whole proteome analysis revealed expectedly significant differences among the protein abundances between neonatal and fully differentiated adult cardiomyocytes (e.g. *MYH6*, *MYL2*, *TNNT2*). Additionally, hierarchical clustering showed differential protein expression in freshly isolated NMVCs compared to five-day old cultured NMVCs (e.g. *ITGB1, ITGB5*, *ITGA3*, *TNNT1*, *EFHD2*). Furthermore, it is important to remember that LFQ intensities, because they depend on the number of peptides as well as on their ionization efficiencies, can only be used to compare abundances of the same protein in different samples and not for the comparison of different proteins among each other. [405, 408, 426] Therefore, no

conclusion of the relative α- and β-parvin expression levels within neonatal or adult cardiomyocytes can be drawn from the experiment.

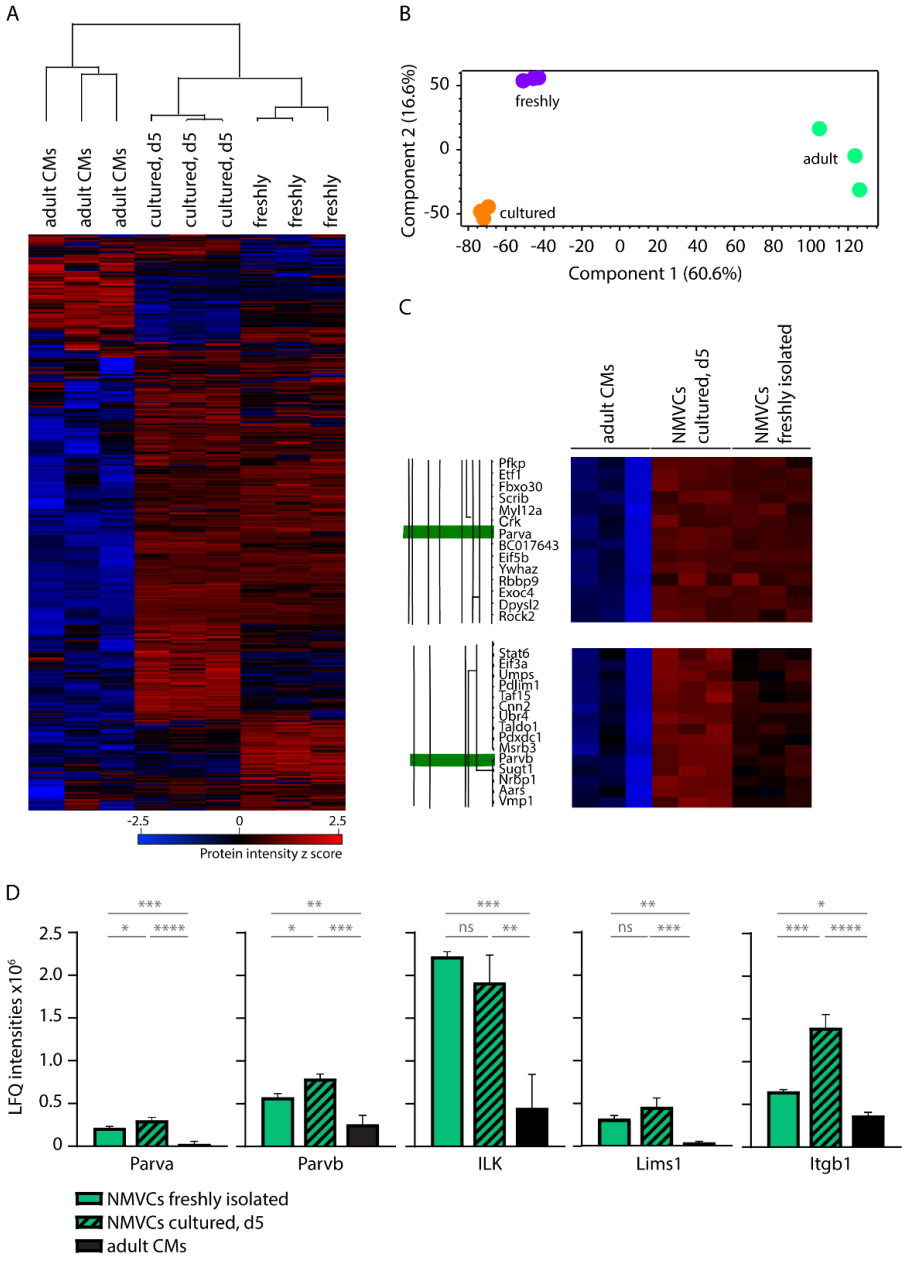

Fig. 39. Whole proteome analysis of isolated NMVCs and adult CMs. (A) Heat map of z-scored protein abundances (LFQ intensities) of the identified proteins (ANOVA, FDR < 0.5) after hierarchical clustering. (B) Principal component analysis of the different conditions (freshly isolated NMVCs, five days cultured NMVCs and adult CMs) based on their proteomic expression profiles. The first and second component segregate the fusion proteins and account for 60.6 and 16.6% of the variability, respectively. (C) Zoom-in view of the heat map showing *PARVA* and *PARVB* abundance. (D) LFQ intensities of *PARVA*, *PARVB*, *ILK*, *LIMS1* and *ITGB1* in freshly isolated, five days cultured NMVCs and adult CMs. Note, LFQ intensities only serve to compare abundances of the same protein in different samples. Data is presented as mean ± s.d. ****P<0.0001, ***P<0.001, **P<0.01, *P<0.1 as analyzed using an ordinary one-way ANOVA test. ns, not significant.

4.5 Proteomic mass spectrometry screening analysis of the α- vs. β-parvin interactome

To identify cell type-dependent parvin/IPP complex interactors in CMs and smooth muscle cells, as well as to identify pan-α- and β-parvin interactors and isoform-specific binding partners, we applied three different approaches (**Fig. 40A**): (1) a classical immunoprecipitation of GFP-fusion proteins, (2) the proximity-dependent biotin identification (BioID) method using a smaller and improved biotin ligase (BioID2) and (3) using an engineered mutant of biotin ligase called TurboID. We payed special attention on potential interactors that could establish a link between parvins/IPP complex and the RhoA/ROCK/MLC2 signaling pathway since it was misregulated in many cell types including MOVAS.

The identification of protein-protein interactions is very important for studying protein functions and subcellular proteomes as well as for understanding complex biological processes. Here, immunoprecipitation is one of the most widely used methods to isolate proteins and binding partners from cell or tissue lysates. In contrast, proximity-dependent labeling of proteins is a relatively new technique to identify potential interactors in the near vicinity of the target protein. [397] This method relies on a biotin ligase, originally from *E. coli* (BioID) and later from *A. aeolicus* (BioID2), fused to the target protein. Biotinylation occurs within the near vicinity of the target protein and biotinylated proteins can be captured by affinity using streptavidin and identified using mass spectrometry. [397, 398] In comparison to conventional screening methods, proximity-dependent biotinylation can be used to identify weak or transient interactions in a relatively natural setting. Furthermore, the temporal induction of the biotin labeling allows a spatiotemporal analysis of protein-protein interactions. [427] However, one disadvantage of using BioID2 is the relatively long biotin labeling time (> 16 h). Therefore an engineered promiscuous mutant of the biotin ligase, called TurboID, was published which catalyzes the biotinylation reaction much faster compared to BioID2 (10-30 min). [399] When utilizing proximity-dependent labeling of proteins, identified biotinylated proteins fall under one of the three categories: (i) direct interactions, (ii) indirect interactions or (iii) proteins that neither interact directly nor indirectly with the target protein (background labeling). [397]

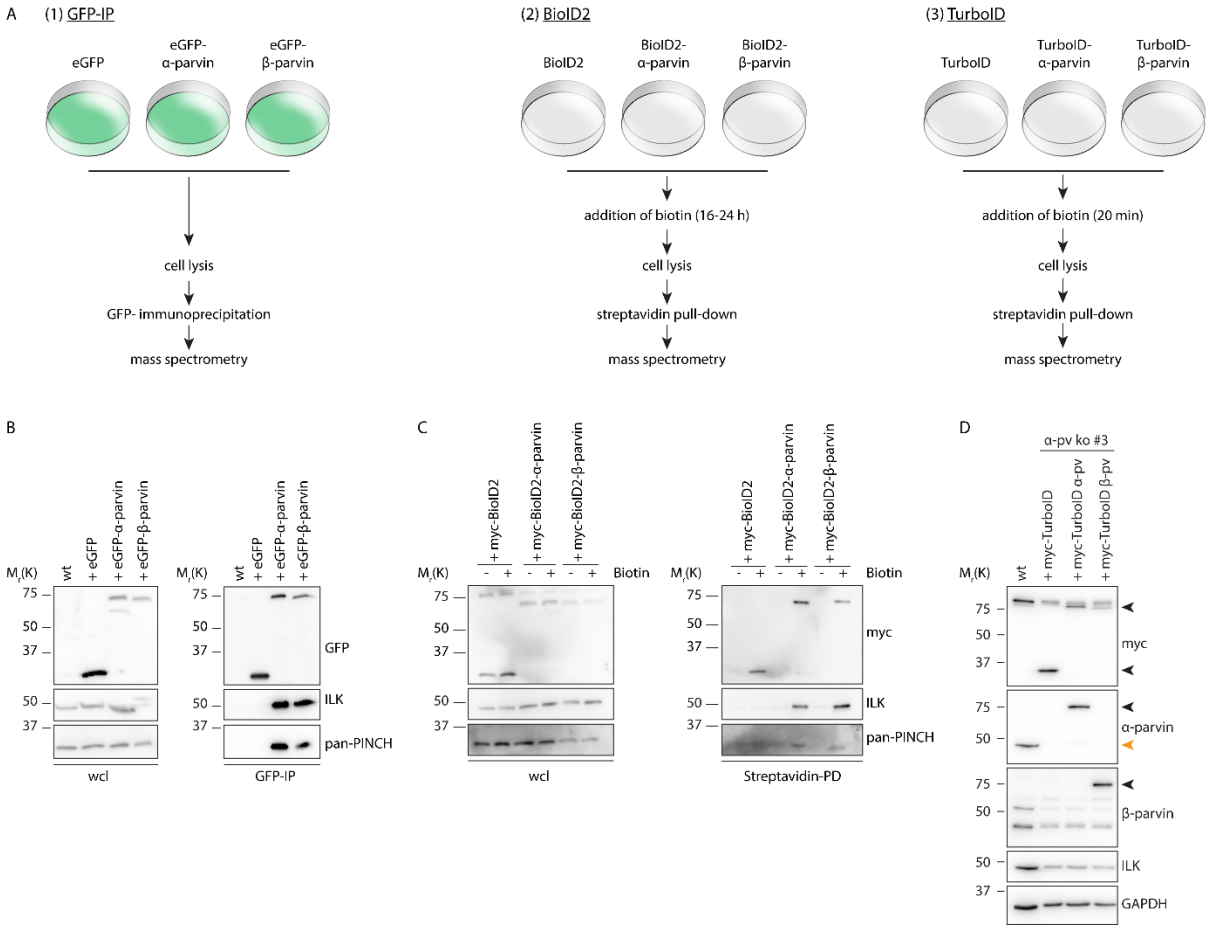

Fig. 40. Schematic representation and validation of the three approaches used to search for novel α- and/or β-parvin interactors. (A) Workflow of the GFP-IP, BioID2 and TurboID. (B-D) Western blot analysis of the expression levels of eGFP (B), BioID2 (C) and TurboID (D) fusion proteins. ILK and PINCH were identified as α- and β-parvin interactors in both GFP-IP (B) and streptavidin PD (C) verifying the functionality of the used approaches. (D) black arrow heads mark the overexpressed proteins whereas the orange arrow head marks the size of the endogenous α-parvin.

To analyze the α- and β-parvin interactome in MOVAS cells, stable cell lines were generated by viral infection, FACS sorted for equal expression and verified by western blotting (**Fig. 40B-D**). Despite the adjustment of the expression levels of eGFP-fusion proteins, the eGFP control was expressed about 10 times more (**Fig. 40B**). Adjusting the BioID2 and TurboID expression levels, however, was much easier (**Fig. 40C, D**). The identification of ILK and PINCH after GFP-IP or streptavidin-PD verified the functionality of the used approaches.

4.5.1 Identification of the α- and β-parvin interactome in isolated NRVCs using

4.5.1.1 Classical immunoprecipitation of GFP-fusion proteins

To characterize the α- and β-parvin interactome in NRVCs and MOVAS and to identify new parvin interactors, we immunoprecipitated eGFP-tagged α-parvin after transduction of isolated NRVCs (**Fig. 41**) or wt MOVAS (**Fig. 43**). As control, cells were transduced with an empty eGFP vector. To investigate whether β-parvin interacts with other potential RhoA regulators, cells were also transduced with eGFP-tagged β-parvin. After cell lysis GFP-tagged proteins were immunoprecipitated with magnetic beads coated with anti-GFP antibodies, washed and eluted under denaturing conditions. The co-immunoprecipitated proteins were resolved using SDS-PAGE and identified using mass spectrometry (MS).

We employed principal component analysis for an overall assessment of proteomic similarities and differences of the two eGFP fusion proteins and the control. The different eGFP constructs clearly clustered separately with the biological triplicates tightly grouped together (**Fig. 41B**). The segregation of the α- and β-parvin groups was mainly driven by the other IPP complex member, ILK and PINCH1 as well as RSU-1, a protein nowadays seen as fourth member of the IPP complex (**Fig. 41C**).

For a functional view of the proteomic differences between the three groups, we performed hierarchical clustering of the 125 proteins (18.5% of identified proteins) that were statistically different across the three groups (FDR < 0.5) (**Fig. 41A**). The heat map shows four obviously different clusters: one major cluster of immunoprecipitated proteins from NRVC lysates using eGFP-β-parvin as bait (orange), one minor cluster using the eGFP-α-parvin protein (magenta) and one intermediate cluster using the eGFP control (blue) as well as one cluster of proteins that show similar protein intensities in eGFP-α- or β-parvin transduced NRVCs (green).

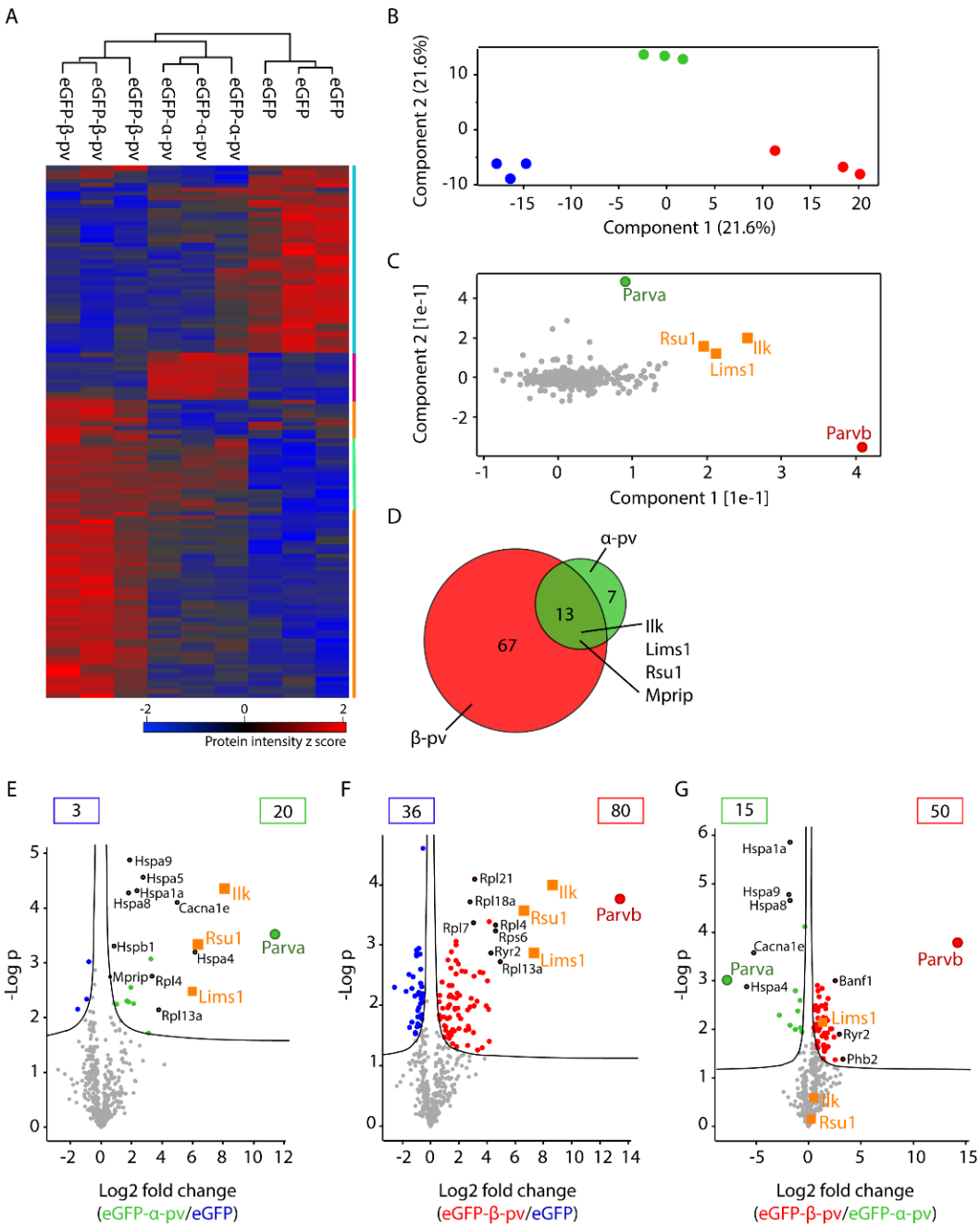

Fig. 41. GFP immunoprecipitation from isolated and transduced NRVCs. (A) Heat map of z-scored protein abundances of the immunoprecipitated proteins (ANOVA, FDR < 0.5) after hierarchical clustering. Four distinct clusters are color-coded (eGFP, blue; eGFP-α-pv only, magenta; eGFP-β-pv only, orange; eGFP-α- and β-pv, green). (B) PCA of the three overexpressed eGFP fusion proteins (eGFP-α-pv, green; eGFP-β-pv, red; eGFP control, blue) based on their proteomic expression profiles. The first and second component segregate the fusion proteins and account for 21.6% each of the variability. (C) Proteins driving the segregation between the eGFP fusion proteins. Note, the importance of the IPP complex member, ILK and PINCH1, as well as RSU-1 in driving the segregation. (D) Overlap of proteins identified as interactors of eGFP-tagged α- and β-parvin. Note, ILK, PINCH1 and RSU-1 were immunoprecipitated in both α- and β-parvin GFP-IPs. (E-G) Volcano plots of the *p*-values vs. the log2 protein abundance difference between the eGFP fusion proteins and eGFP control. Proteins outside the significance lines are colored in blue (control), green (α-pv) and red (β-pv) (FDR < 0.5). Comparison of eGFP-α-parvin (E) or eGFP-β-parvin (F) vs. control or between each other (G).

To further investigate the identified proteins, we used volcano plots to compare immunoprecipitated proteins of eGFP-tagged α- and β-parvin to the eGFP control or among each other (**Fig. 30Fig. 41E-G**). As expected, ILK, PINCH1 and RSU-1 were the immunoprecipitated proteins found with the highest significance when using eGFP-tagged α- or β-parvin compared to the eGFP control (**Fig. 41E**, **F**). Other identified interactors included heat-shock proteins of the Hsp70 protein family, ribosomal proteins and subunits of voltage-gated residual (R)-type or ligand-gated calcium channels (ryanodine receptor). Furthermore, out of the 20 proteins immunoprecipitated with eGFP-α-parvin, seven seemed to be α-parvin-specific interactors whereas the other 13 proteins overlapped with the 80 proteins identified in the β-parvin GFP-IP (**Fig. 41D**). As we especially searched for RhoA regulators, one identified protein, myosin phosphatase Rho-interacting protein (Mprip), caught our interest as a potential pan-parvin interactor (**Fig. 41D**). Mprip targets the myosin phosphatase to the myosin filaments, thereby enhancing its dephosphorylation activity resulting in muscle relaxation. [221] Furthermore, the protein was shown to be able to either directly bind to RhoA or to regulate its nucleotide-binding state. [216, 217] It is therefore an interesting protein that could establish a link between parvins/IPP complex and the RhoA signaling pathway and will be further discussed in a separate chapter (4.5.5).

Finally, we had a closer look at α- and β-parvin-specific interactors. Most of these were not strongly enriched with either α- or β-parvin and, unfortunately, we only identified heat-shock and ribosomal proteins, as well as a mitochondria chaperone and calcium channel subunits which are unlikely parvin-specific interactors (**Fig. 41G**).

Taken together, these results show that the GFP immunoprecipitation approach to identify novel parvin interactors in isolated rat cardiomyocytes works as the known IPP complex members were identified. However, most of the identified potential interactors were mainly histones and ribosomal proteins and were therefore not of interest for us. Only Mprip could establish a potential link to the RhoA/ROCK/MLC2 signaling cascade and was, thus, further analyzed.

4.5.1.2 Proximity-dependent biotin identification using TurboID

In addition to the classical GFP immunoprecipitation, we also performed proximity-dependent biotin identification using TurboID to characterize the α- and β-parvin interactome in both NRVCs and MOVAS. To test whether the labeling time has an effect on the α- and β-parvin interactome, isolated NRVCs and α-parvin KO #3 MOVAS were transduced with TurboID-α- or β-parvin. As control, cells were transduced with a plasmid carrying an empty TurboID-tag. After treating the cells with biotin for 20 min, cells were lysed and biotinylated proteins were enriched with streptavidin beads. Following on-bead digestion to peptides, peptides were identified by mass spectrometry.

PCA showed that the different TurboID constructs clearly clustered separately with the biological triplicates grouped together (**Fig. 42B**). As observed in the GFP-IP samples, the segregation of the α- and β-parvin groups was mainly driven by ILK, PINCH1 and RSU-1 (**Fig. 42C**). The hierarchical clustering of the 2207 proteins (59.0% of identified proteins) with statistical differences across the groups (FDR < 0.5) revealed a lot of background labeling (~2/3 of clustered proteins) coming from the TurboID control (**Fig. 42A**). This shows the importance of an empty vector control to exclude false positives from the eluted proteins. The high number of identified proteins in the control lysates might be a result of the extended labeling time that we decided to use for our analysis (20 min instead of 10 min).

As expected, ILK, PINCH1 and RSU-1 were among the proteins with the highest significance identified in both TurboID-α- and β-parvin transduced NRVCs (**Fig. 42E**, **F**). Among the significant hits were also other known adhesion proteins such as talin-2, kindlin-2, tensins and deleted in liver cancer 1 (DLC-1). Comparing the α-and β-parvin interactome, 423 proteins were overlapping, among which known interacting partners, such as paxillin and α- as well as β-PIX were identified (**Fig. 42D**). The direct comparison of statistical different proteins identified in TurboID-α- or β-parvin transduced NRVCs, however, revealed no proteins known to be involved in RhoA regulation (**Fig. 42G**).

Overall, the TurboID approach is a suitable complementary technique to the traditional IP for the identification of the α- and β-parvin interactome and DLC-1 could be a pan-parvin interactor, establishing a link to RhoA signaling.

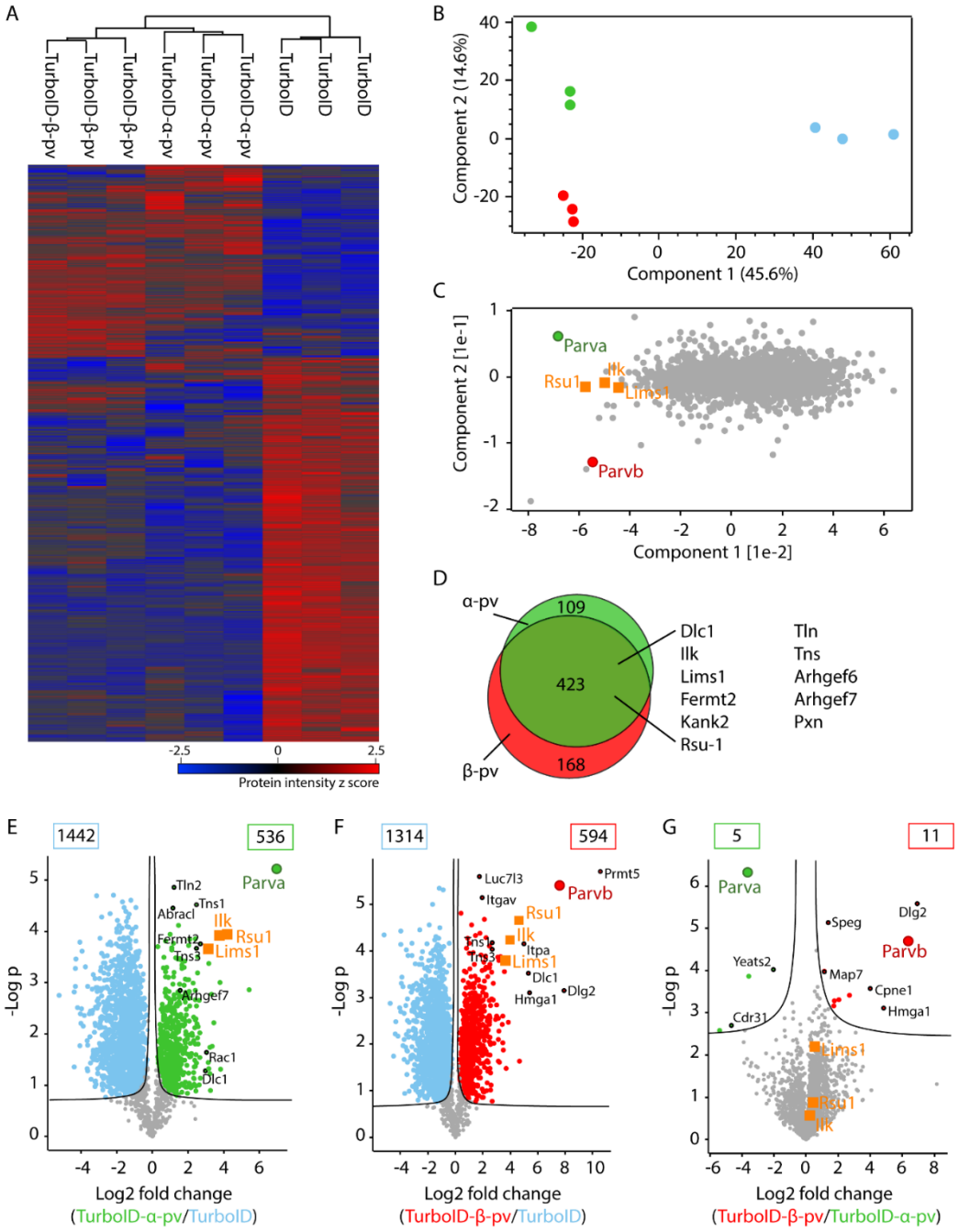

Fig. 42. Streptavidin pulldown of biotinylated proteins from isolated NRVCs using TurboID. (A) Heat map of z-scored LFQ intensities of the pulled down proteins (ANOVA, FDR < 0.5) after hierarchical clustering. (B) PCA of the three overexpressed TurboID fusion proteins (TurboID-α-pv, green; TurboID-β-pv, red; TurboID control, blue) based on their proteomic expression profiles. The first and second component segregate the fusion proteins and account for 45.6 and 14.6% each of the variability, respectively. (C) Proteins driving the segregation between the TurboID fusion proteins. Note, the importance of the IPP complex member, ILK and PINCH1, as well as RSU-1 in driving the segregation. (D) Overlap of proteins identified as interactors of α- and β-parvin. Note, ILK, PINCH1 and RSU-1 were identified as common α- and β-parvin interactors, as well as some other known FA components such as paxillin, talin and kindlin. (E-G) Volcano plots of the *p*-values vs. the log2 protein abundance difference between the TurboID fusion proteins and TurboID control. Proteins outside the significance lines are colored in blue, green and red (FDR < 0.5). Comparison of TurboID-α-parvin (E) or TurboID-β-parvin (F) vs. control or between each other (G).

4.5.2 Identification of the α- and β-parvin interactome in MOVAS using

4.5.2.1 GFP immunoprecipitation

We not only aimed to characterize the α- and β-parvin interactome and identify new parvin interactors in NRVCs but also in MOVAS cells, a cell line representing the contractile cells of blood vessels. Therefore, we used the same methods as applied for NRVCs (GFP-IP, BioID2 and TurboID) with the same experimental settings, allowing us to identify cell type-specific and cell type-independent parvin interactors.

We employed principal component analysis for the overall assessment of proteomic similarities and differences of the two eGFP fusion proteins and the control. The different eGFP constructs clearly clustered separately with the biological triplicates grouped together (**Fig. 43B**). The segregation of the α- and β-parvin groups was driven by a lot of proteins, among which ILK, PINCH1 and RSU-1 can be found (**Fig. 43C**).

2043 proteins were in total immunoprecipitated from wt MOVAS cells transduced with either eGFP-tagged α- or β-parvin or the eGFP control vectors. 33.1% of these proteins were statistically different across the three groups (FDR < 0.5) and hierarchically clustered (**Fig. 43A**). In comparison to the heat map of statistically different proteins identified from NRVCs, the heat map of immunoprecipitated proteins from MOVAS cells showed a major cluster of proteins that are overlapping in the α- and β-parvin interactome.

As expected, ILK, PINCH1 and RSU-1 were identified as significant interactors of both α- and β-parvin (**Fig. 43E**, **F**). Other known adhesion proteins, such as kindlin-2 and IQGAP1 were also identified in both cell lines (**Fig. 43D**). Mprip, which has been identified in NRVCs as potential pan-parvin interactor (**Fig. 41D**), was also found in MOVAS cells and could therefore be a cell type-independent pan-parvin interactor. Other identified proteins are involved in e.g. DNA replication (*TOP1*, *TOP2b*) or repair (*XRCC1*), histone modification (*HDAC1*), ribosomal processing (*NOLC1*) or splicing (*SRSF1*, *SRSF7*) (**Fig. 43E**-**G**). Unfortunately, α-parvin was not identified as the protein with the highest abundance in eGFP-α-parvin transduced cells (**Fig. 43E**) and ILK, PINCH1 and RSU-1 were not among the proteins showing the highest significance (**Fig. 43E**, **F**), which weakens the confidence in the findings of this experiment.

In summary, immunoprecipitation against eGFP-tagged α- or β-parvin in MOVAS cells worked to identify potential interactors, among which known binding partners, such as ILK, PINCH-1 and RSU-1 were found. Interestingly, the total number of identified proteins in MOVAS cells was three times higher compared to the number of proteins immunoprecipitated from NRVCs. Furthermore, while in NRVCs about 10 times more β-parvin-specific interactors were found (**Fig. 41D**), the number of α- and β-parvin-specific interactors in transduced wt MOVAS is nearly equal (**Fig. 43D**). As Mprip was identified in both NRVCs and MOVAS as potential pan-parvin interactor, further analysis of this protein was conducted (4.5.5).

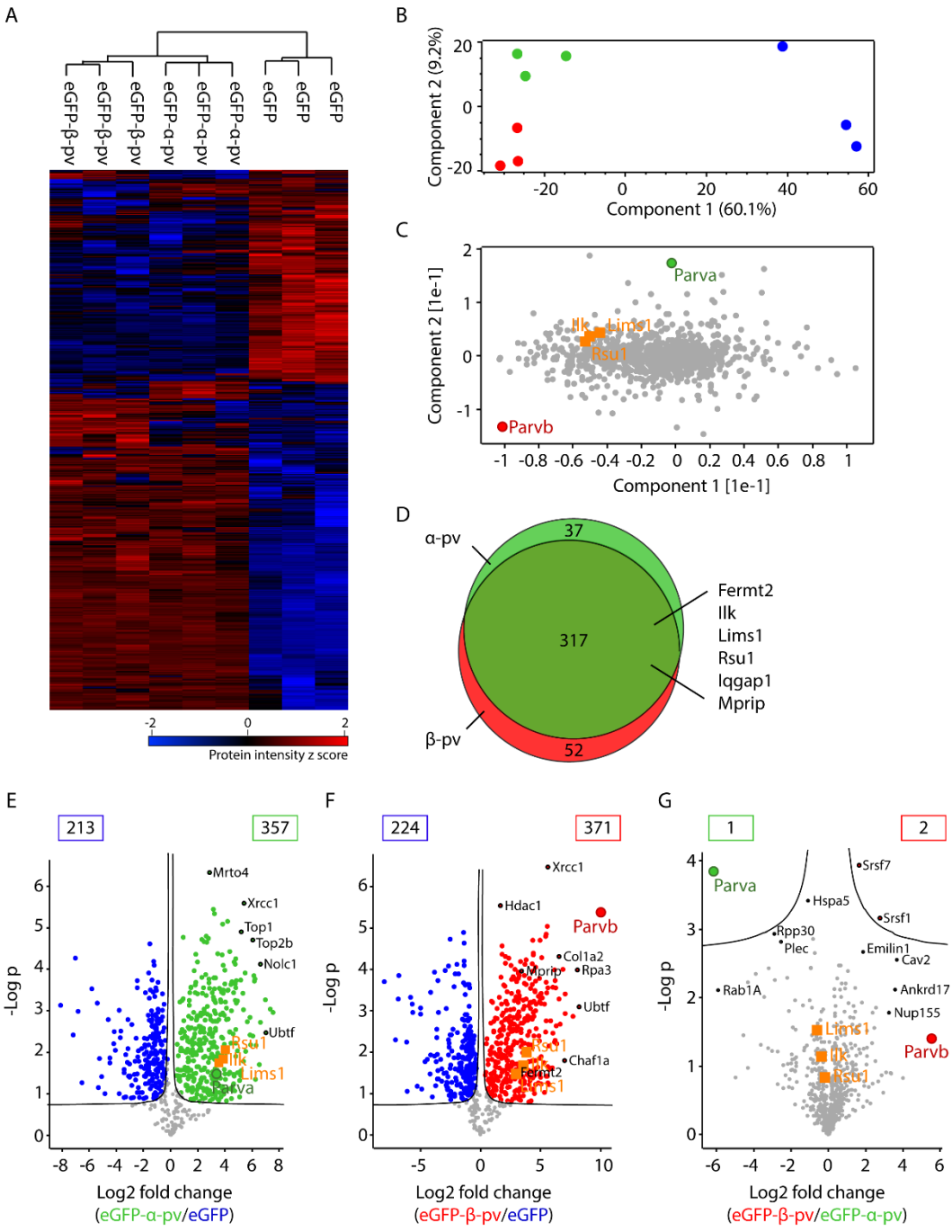

Fig. 43. GFP immunoprecipitation from wild-type MOVAS cells. (A) Heat map of z-scored protein abundances of the immunoprecipitated proteins (ANOVA, FDR < 0.5) after hierarchical clustering. (B) Principal component analysis of the three overexpressed eGFP fusion proteins (eGFP-α-pv, green; eGFP-β-pv, red; eGFP control, blue) based on their proteomic expression profiles. The first and second component segregate the fusion proteins and account for 60.1 and 9.2% of the variability, respectively. (C) Proteins driving the segregation between the eGFP fusion proteins. (D) Overlap of proteins identified as interactors of eGFP-tagged α- and β-parvin. Note, ILK, PINCH1 and RSU-1 were identified as α- and β-parvin interactors. (E-G) Volcano plots of the *p*-values vs. the log2 protein abundance difference between the eGFP fusion proteins and eGFP control. Proteins outside the significance lines are colored in blue, green and red (FDR < 0.5). Comparison of eGFP-α-parvin (E) or eGFP-β-parvin (F) vs. control or between each other (G).

4.5.2.2 Proximity-dependent biotin identification (BioID2)

Wild-type MOVAS cells were transduced with BioID2-tagged α- or β-parvin constructs and biotinylation was allowed for 18 h. As control, cells were transduced with an empty BioID2 vector and biotinylated proteins were identified by mass spectrometry.

PCA showed that the different BioID2 constructs clearly clustered separately with the biological triplicates tightly grouped together (**Fig. 44B**). ILK, PINCH1 and RSU-1 are among the major drivers responsible for the segregation of the α- and β-parvin groups (**Fig. 44C**). Furthermore, hierarchical clustering of the 1422 proteins (69.6% of identified proteins) showing statistical differences among the three groups (FDR < 0.5) revealed four obvious clusters (**Fig. 44A**): one of background labeled proteins identified in BioID2 transduced control cells (blue), two very small clusters of proteins pulled down from BioID2-tagged α- (magenta) or β-parvin transduced MOVAS (orange) and one bigger cluster of identified proteins that overlap in the parvin transduced cells (green).

All IPP complex components, including α- and β-parvin as well as RSU-1, were identified as biotinylated proteins with the highest significance (**Fig. 44E**, **F**). Out of the 465 and 508 identified significant proteins in α- and β-parvin BioID2, respectively, 429 proteins including known adhesion proteins such as tensins, paxillin, kank2 and kindlin-2, overlapped (**Fig. 44D**). Unfortunately, no proteins that show an obvious link to the RhoA/MLC2 signaling pathway were identified. Instead, nuclear proteins, histones and mitochondrial proteins were among the potential interactors (**Fig. 44E-G**).

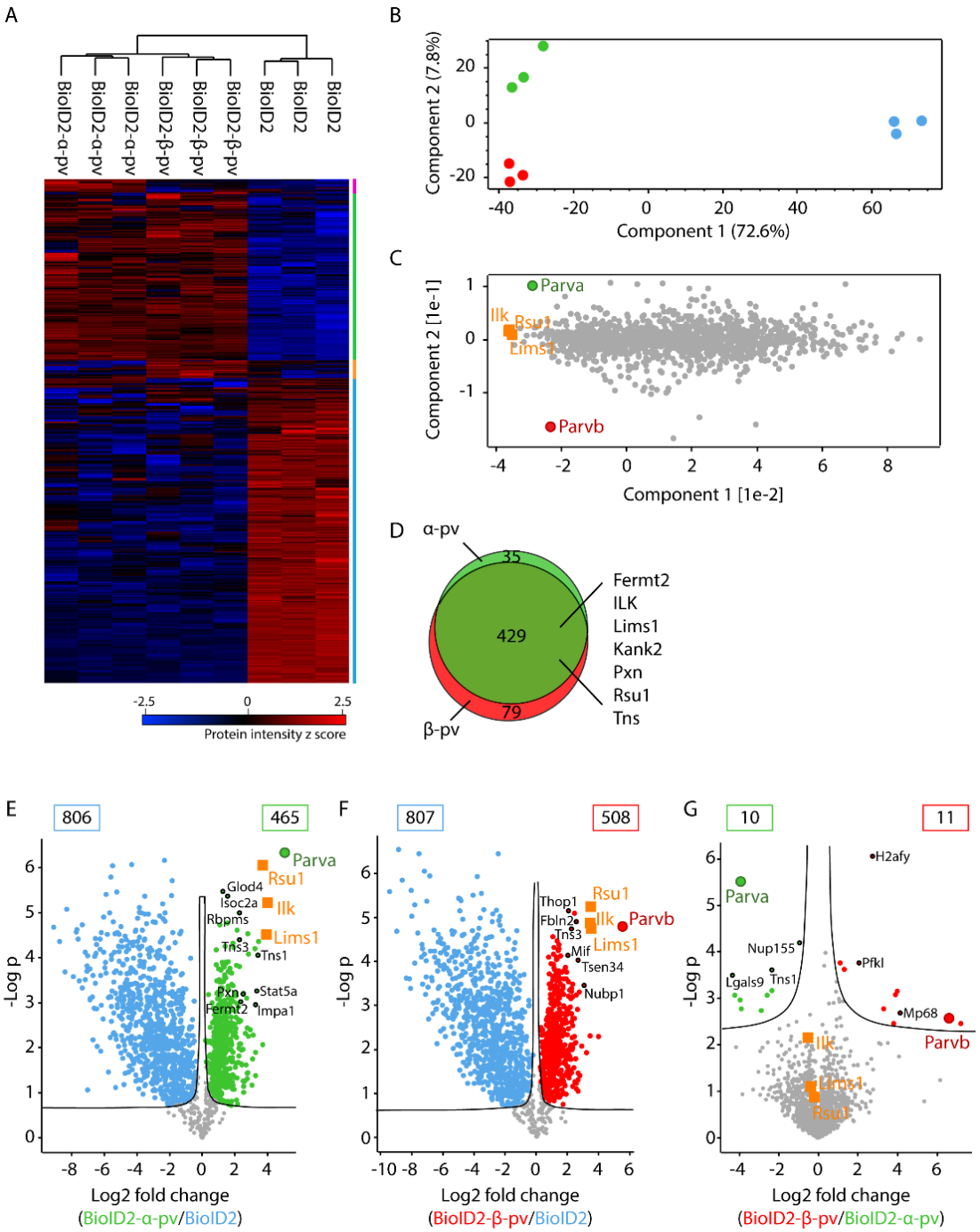

Fig. 44. Streptavidin pulldown of biotinylated proteins from wild-type MOVAS cells. (A) Heat map of z-scored LFQ intensities of the pulled down proteins (ANOVA, FDR < 0.5) after hierarchical clustering. Four distinct clusters are color-coded. (B) PCA of the three overexpressed BioID2 fusion proteins (BioID2-α-pv, green; BioID2-β-pv, red; BioID2 control, blue) based on their proteomic expression profiles. The first and second component segregate the fusion proteins and account for 72.6 and 7.8% of the variability, respectively. (C) Proteins driving the segregation between the BioID2 fusion proteins. (D) Overlap of proteins identified as interactors of α- and β-parvin. Note, the IPP complex members were among the identified α- and β-parvin interactors, as well as e.g. kindlin-2, paxillin and kank2. (E-G) Volcano plots of the *p*-values vs. the log2 protein abundance difference between the BioID2 fusion proteins and BioID2 control. Proteins outside the significance lines are colored in blue, green and red (FDR < 0.5). Comparison of BioID2-α-parvin (E) or BioID2-β-parvin (F) vs. control or between each other (G).

4.5.2.3 Proximity-dependent biotin identification using TurboID

Giving the results obtained from TurboID-α- and β-parvin transfected NRVCs (4.5.1.2), we conducted the same experiment in MOVAS cells. Both previous experiments, GFP-IP and BioID2, were performed at the beginning of my thesis, where no α-parvin depleted cells were available and wt MOVAS were transduced. However, as I executed the TurboID experiment at the end of my thesis, I transduced α-parvin KO #3 MOVAS instead.

The different TurboID-parvin constructs clustered clearly separately from the TurboID control vector. However, the separation between the parvin constructs is not as clear, complicating the identification of specific α- or β-parvin interactors (**Fig. 45B**). This is in line with the large number of proteins that overlap between the α- and β-parvin interactome (**Fig. 45D**). Nonetheless, ILK, PINCH1 and RSU-1 are driving the segregation of the α- and β-parvin groups (**Fig. 45C**) and were found to be among the proteins with the highest significance (**Fig. 45E**, **F**). Hierarchical clustering was performed on 1539 proteins (49.1% of identified proteins) showing statistical differences among the three groups (FDR < 0.5). The heat map revealed two distinct clusters, one of which is generated by biotinylated proteins found in TurboID transduced MOVAS cells (~2/3 of clustered proteins, background labeling) (**Fig. 45A**). Interestingly, other proteins found with high significance are tensins, paxillin, kindlin-2, β-PIX, kank2, zyxin and talin, known focal and fibrillar adhesion molecules (**Fig. 45E**, **F**). Furthermore, DLC-1 was identified in α-parvin KO #3 MOVAS cells transduced with TurboID-tagged α- and β-parvin, a protein that we already identified in NRVCs (**Fig. 42D**) and that might be a cell type-independent pan-parvin interactor. Direct comparison of statistical different interactors in TurboID-α- and β-parvin transduced cells resulted in the identification of proteins involved in proteasomal degradation, splicing and transcriptional regulation (**Fig. 45G**). However, AKAP13, found as specific β-parvin interactor, encodes the A-kinase anchoring protein (AKAP) 13, belonging to a protein family that bind the regulatory subunit of protein kinase A (PKA) and function as PKA-anchoring proteins. [428] Furthermore, the protein not only coordinates PKA signaling but also functions as selective GEF for RhoA. Publications demonstrate that AKAP13 can nucleate a Gα12-mediated RhoA signaling pathway as well as be activated by α6β4 integrin to induce its GEF activity. [428, 429]

Overall, the identification of known parvin interactors and adhesion proteins strengthens the confidence in the TurboID approach as a suitable method to identify novel parvin binding partners. Indeed, some of the detected proteins with statistical differences among the groups are involved in RhoA regulation such as DLC-1 and AKAP13 which could be subjects for further investigations. Furthermore, ARHGAP22 was identified as a key mediator that suppresses Rac1 downstream of RhoA. [430]

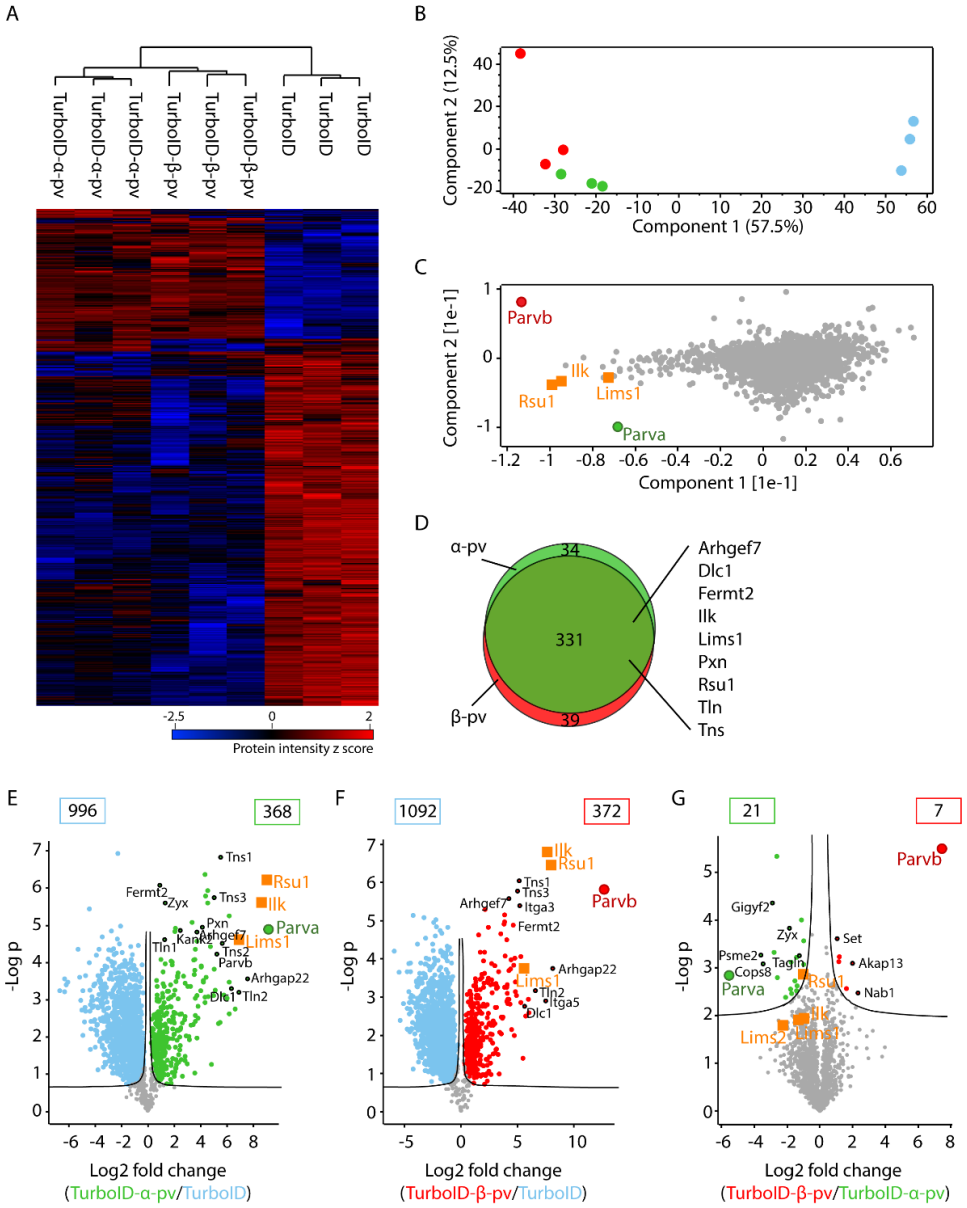

Fig. 45. Streptavidin pulldown of biotinylated proteins from α-parvin KO #3 MOVAS using TurboID. (A) Heat map of z-scored abundances of the pulled down proteins (ANOVA, FDR < 0.5) after hierarchical clustering. (B) PCA of the three overexpressed TurboID fusion proteins (TurboID-α-pv, green; TurboID-β-pv, red; TurboID control, blue) based on their proteomic expression profiles. The first and second component segregate the fusion proteins and account for 57.5 and 12.5% of the variability, respectively. (C) Proteins driving the segregation between the TurboID fusion proteins. Note, the importance of the IPP complex member, ILK and PINCH1, as well as RSU-1 in driving the segregation. (D) Overlap of proteins identified as interactors of α- and β-parvin. Note, ILK, PINCH1 and RSU-1 were identified as common α- and β-parvin interactors, as well as some other known FA components such as paxillin, talin and kindlin-2. (E-G) Volcano plots of the *p*-values vs. the log2 protein abundance difference between the TurboID fusion proteins and TurboID control. Proteins outside the significance lines are colored in blue, green and red (FDR < 0.5). Comparison of TurboID-α-parvin (E) or TurboID-β-parvin (F) vs. control or between each other (G).

4.5.3 Large numbers of nuclear proteins identified by mass spectrometry in contractile cells of the cardiovascular system

We observed a large number of nuclear and ribosomal proteins as potential parvin interactors in all our proteomic approaches. **Fig. 46A** and **B** represent identified nuclear proteins (green) when using the GFP-IP approach, both in NRVCs and MOVAS. Since we primarily focused on novel parvin interactors that connect the IPP complex to the RhoA/MLC2 signaling pathway, nuclear proteins were neglected. However, biochemical fractionation of cells revealed that both endogenous and eGFP-tagged α-parvin, as well as ILK and PINCH, can be found in the nuclear and cytosolic fraction (**Fig. 46D**). Fluorescence imaging of eGFP-α- and β-parvin expressing MOVAS after leptomycin treatment, which inhibits nuclear export of proteins, showed an accumulation of both eGFP-α- and β-parvin in the nucleus (**Fig. 46C**). These data suggest that the IPP complex could have a nuclear function in CMs and MOVAS and indicate that the nuclear proteins identified as potential parvin interactors could be true binding partners.

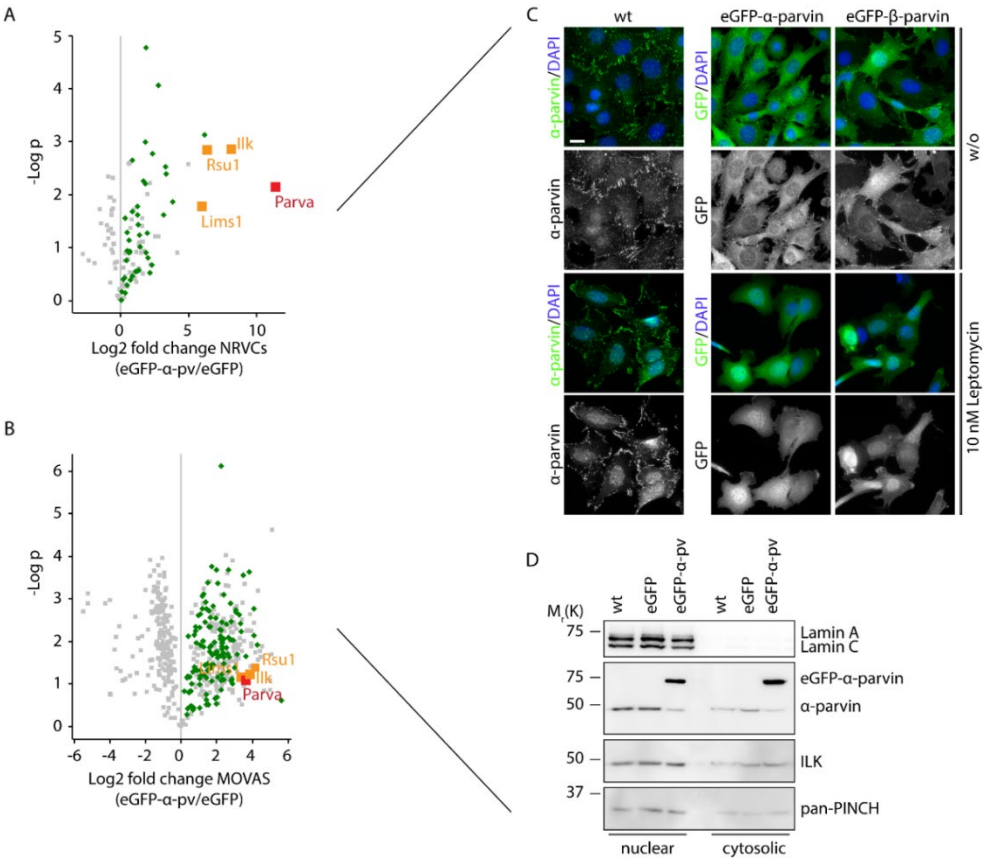

Fig. 46. Interactome analysis of immunoprecipitated α-parvin in (A) MOVAS and (B) NRVCs revealed a large number of nuclear proteins (green) as potential interactors. (C) Representative fluorescence images of wt MOVAS treated with 10 nM leptomycin. Note, blocking the nuclear export results in an accumulation of eGFP-α-parvin in the nucleus. Scale, 10 µm. (D) Cell fractionation of wt MOVAS and MOVAS stably expressing eGFP or eGFP-α-parvin results in the localization of IPP complex members in both, nuclear and cytosolic fractions.

4.5.4 Comparison of the used methods to identify the α- and β-parvin interactome in isolated NRVCs and MOVAS with focus on RhoA/MLC2 signaling

Many proteins, including parvins, perform their biological function as part of multi-protein complexes which form large networks of molecular interactions, called the interactome. This interactome is very diverse and used by the cell to adapt rapidly its signaling in response to environmental changes. Factors that influence the interactome include the expression stoichiometry and co-localization of proteins within the same cellular compartment, post-translational modifications, cell type-specific interactors and the presence of chaperones which might be necessary for the complex assembly. [431] It is therefore not surprising that the use of different approaches to identify protein-protein interactions might result in the identification of different proteins, depending on the experimental settings and methods used. However, a potential binding partner identified with distinct methods would be considered a high confidence interactor. That is why we used three different approaches, GFP immunoprecipitation and two proximity-dependent labeling techniques, to identify the α-parvin interactome in both isolated NRVCs and MOVAS with the focus of binding partners known for their function in RhoA signaling. To see whether β-parvin might bind different RhoA regulators, we also analyzed the β-parvin interactome in these two cell types.

Our analysis identified 674 and 3739 proteins in eGFP and TurboID transduced NRVCs, respectively, and 2043, 2043 and 3134 proteins in eGFP, BioID2 and TurboID transduced MOVAS, respectively. In total, 543 proteins were significantly enriched in the α-parvin interactome in NRVCs (**Fig. 47A**), identified across the two methods, whereas 1017 proteins were identified in MOVAS (**Fig. 47D**). The β-parvin interactome constitutes 638 and 1054 proteins in NRVCs (**Fig. 47B**) and MOVAS (**Fig. 47E**), respectively.

In isolated NRVCs nine potential α-parvin interactors were identified in both GFP-IP and TurboID, of which all nine were also found in the β-parvin interactome (**Fig. 47C**). We identified ILK, LIMS1 and RSU1 among the nine interactors, as well as HSPB1, a member of the small heat-shock protein (HSP20) family, that was reported to be involved in controlling F-actin dynamics in a PKA-dependent manner. [432] Furthermore, proteins of the 40S (*RPS6*) and 60S (*RPL4*, *RPL13A*) ribosomal subunits, as well as prohibitin (*PHB*), a mitochondrial chaperone which protects cardiomyocytes from oxidative stress-induced damage and sequesters mDia1, thereby dampening its anti-myogenic activity during myoblast differentiation, were identified as pan-parvin interactors. [433, 434]

In MOVAS, 11 potential α-parvin interactors were identified at the intersection of GFP-IP, BioID2 and TurboID (**Fig. 47D**), of which nine were also part of the β-parvin interactome (**Fig. 47F**). In addition to the IPP complex components (ILK, PINCH1, RSU1), we also identified kindlin-2 (*FERMT2*) as pan-parvin interactor (**Fig. 47F**) which is not surprising, as kindlin-2-mediated integrin activation and focal adhesion targeting was

reported to require ILK/IPP complex binding. [435] Furthermore, as in NRVCs, we also identified prohibitin in MOVAS as pan-parvin interactor. Interestingly, kank2 was identified as β-parvin-specific and cell type-independent interactor. However, no known parvin interactors, such as paxillin, TESK1, α- and β-PIX or CdGAP were identified across the three methods, and no novel binding partners that are known RhoA regulators were found.

Fig. 47. Comparison of the identified proteins in GFP-IP, BioID2 and TurboID. Comparison of the (A, D) α-parvin and (B, E) β-parvin interactome in (A, B) NRVCs and (D, E) MOVAS cells. Intersecting proteins known for their localization to integrin-dependent adhesion sites are depicted. (C, F) Representation of pan-parvin or α- and β-parvin-specific interactors found at the intersection of A and B or D and E, respectively. Note, as expected ILK, PINCH1 and RSU1 were identified in both cell types as pan-α- and β-parvin interactors.

Overall, using MS-based approaches is a common tool to identify protein-protein interactions and all three methods tested in the present thesis resulted in the identification of statistically different enriched parvin interactors. As expected, we identified ILK, PINCH and RSU-1 in both cell types as significant hits, showing that α- and β-parvin function most abundantly via the IPP complex. We furthermore identified potential new interactors, either pan-parvin or isoform-specific, that need to be investigated. However, the comparison of the used approaches did not yield the expected identification of novel parvin interactors

that are involved in RhoA regulation. We therefore compared the proteins that we identified in both cell types using either GFP-IP or TurboID with each other (**Fig. 48**).

Eight α-parvin interactors were identified in both NRVCs and MOVAS using traditional GFP-IP (**Fig. 48A**), all of which were also found as β-parvin interactors (except α-parvin itself) (**Fig. 48C**). Among the 26 β-parvin interactors (**Fig. 48B**), we identified IQGAP1 and kank2*,* two known focal adhesion proteins. Furthermore, an actin and MLCP-binding protein that is involved in RhoA regulation is Mprip, which we identified as potential pan-parvin interactor in both NRVCs and MOVAS (**Fig. 48C**).

Surprisingly, proximity-dependent biotinylation using TurboID revealed a lot of proteins known to locate to integrin-dependent adhesion sites, including talin (*TLN*), FAK (*PTK2*), Peak1 and integrin subunits (*ITGAV*, *ITGB1*), that we neither identified in conventional IP nor using BioID2, showing that the labeling time has an enormous effect on the identification of interacting proteins. Here, we also identified the known parvin interactors β-PIX (*ARHGEF7*), paxillin (*PXN*) and CdGAP (*ARHGAP31*). While β-PIX and paxillin are known pan-α- and β-parvin interactors, CdGAP was up to date reported to be an α-parvin-specific interactor, binding to the N-terminus of α-parvin. [184] However, the mapped binding region (1-95aa) in α-parvin exhibits ~57% homology to β-parvin, raising the possibility that β-parvin might also interact with CdGAP. From the 104 proteins identified in the α-parvin interactome (**Fig. 48D**), 93 were also found as β-parvin interactors (**Fig. 48F**). As expected, ILK, PINCH and RSU-1 were among the proteins found in both α- and β-parvin interactomes, strengthening our hypothesis that both parvins mainly function via the IPP complex. Furthermore, we identified FilGAP (*ARHGAP24)* and DLC-1 as potential pan-parvin interactors. While FilGAP is a filamin A-binding protein whose Rac GAP activity is stimulated by ROCK phosphorylation and that regulates integrin-mediated cell spreading *in vivo*, DLC-1 was shown to be a direct RhoA regulator. [97, 242, 436]

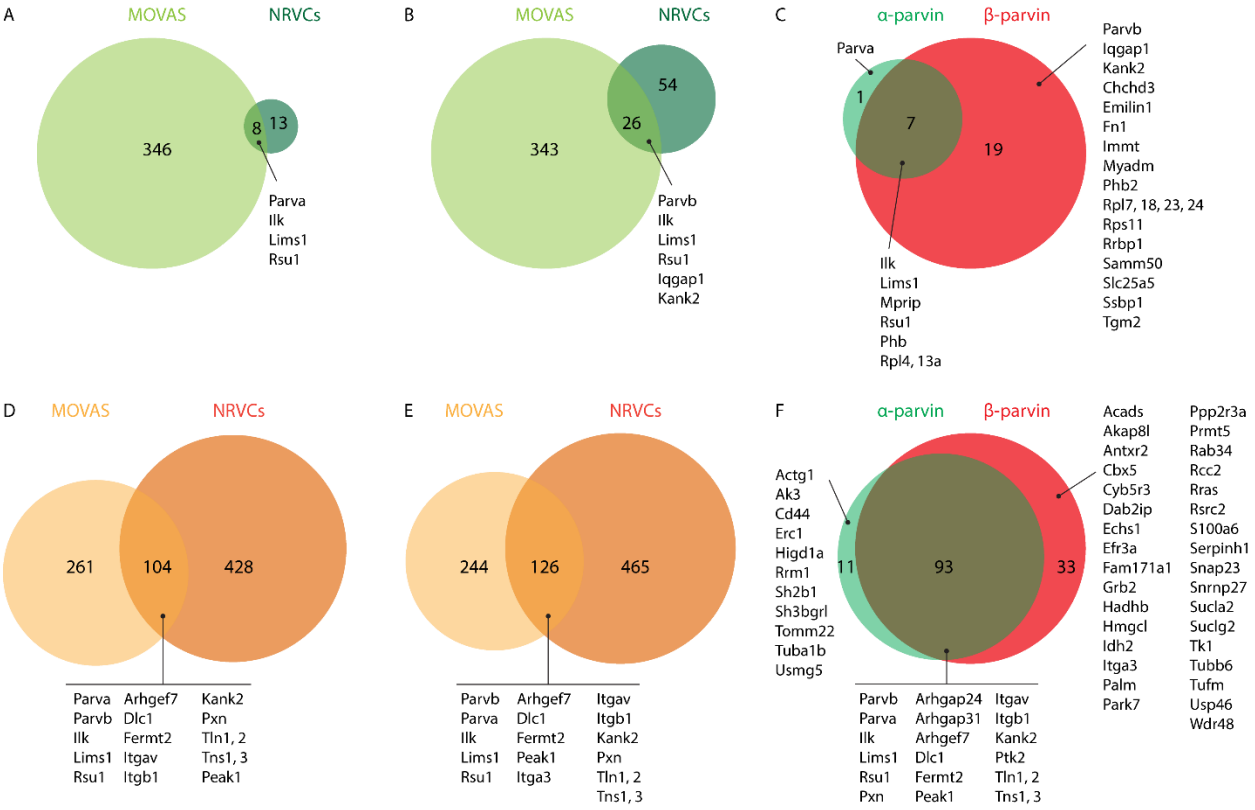

Fig. 48. Comparison of the identified proteins in NRVCs and MOVAS using GFP-IP or TurboID. Comparison of the (A, D) α-parvin and (B, E) β-parvin interactome in NRVCs and MOVAS using (A, B) GFP-IP or (D, E) TurboID. Intersecting proteins known for their localization to integrin-dependent adhesion sites are depicted. (C, F) Representation of pan-parvin or α- and β-parvin-specific interactors found at the intersection of A and B or D and E, respectively. (C, F) All identified interactors are depicted. Note, as expected ILK, PINCH1 and RSU1 were identified in both cell types as pan-α- and β-parvin interactors.

Taken together, our data clearly shows that both α- and β-parvin mainly function via the IPP complex and RSU-1, as these proteins were identified across all our proteomic approaches. Furthermore, we were able to identify not only potential pan-parvin but also parvin isoform-specific interactors that need to be investigated. Moreover, in respect to RhoA signaling, we identified two potential candidates, Mprip and DLC-1, that might function as molecular link between α-parvin/IPP complex and RhoA regulation. Due to time constraints, however, we only further investigated Mprip, but as DLC-1 functions via tensins, which were also identified in the near vicinity of α- and β-parvin, DLC-1 might also be of interest for further investigations.

4.5.5 Myosin phosphatase RhoA interacting protein as potential novel parvin interactor

The actin-binding protein myosin phosphatase RhoA interacting protein (Mprip) was among the proteins co-immunoprecipitated with the eGFP-tagged α-parvin both in isolated NRVCs and MOVAS (**Fig. 49A**). Mprip is a protein that targets myosin phosphatase to the actin cytoskeleton thereby facilitating the dephosphorylation of phosphorylated MLC2.

To verify Mprip as potential α-parvin interactor, HEK293 cells were co-transfected with plasmids carrying eGFP-tagged Mprip and BioID2-tagged α-parvin or eGFP only as control (**Fig. 49B**). BioID2-tagged α-parvin co-immunoprecipitated with the eGFP-tagged Mprip (red arrow head) but not eGFP alone. However, when we immunoprecipitated eGFP-tagged α-parvin we were able to co-IP ILK but not Flag-tagged Mprip (**Fig. 49B**).

In an alternative approach, purified recombinant Twin-Strep-tagged Mprip was immobilized to Strep-Tactin beads and cell lysate from wt MOVAS was used to analyze α-parvin-Mprip interaction. **Fig. 49C** shows α-parvin as well as ILK and PINCH binding to Twin-Strep-tagged Mprip further supporting an interaction of Mprip with the IPP complex. Interestingly, ILK and PINCH were also pulled down from α-parvin KO #3 MOVAS cell lysate using recombinant Twin-Strep-Mprip (**Fig. 49D**) indicating that Mprip might act via ILK or PINCH rather than α-parvin.

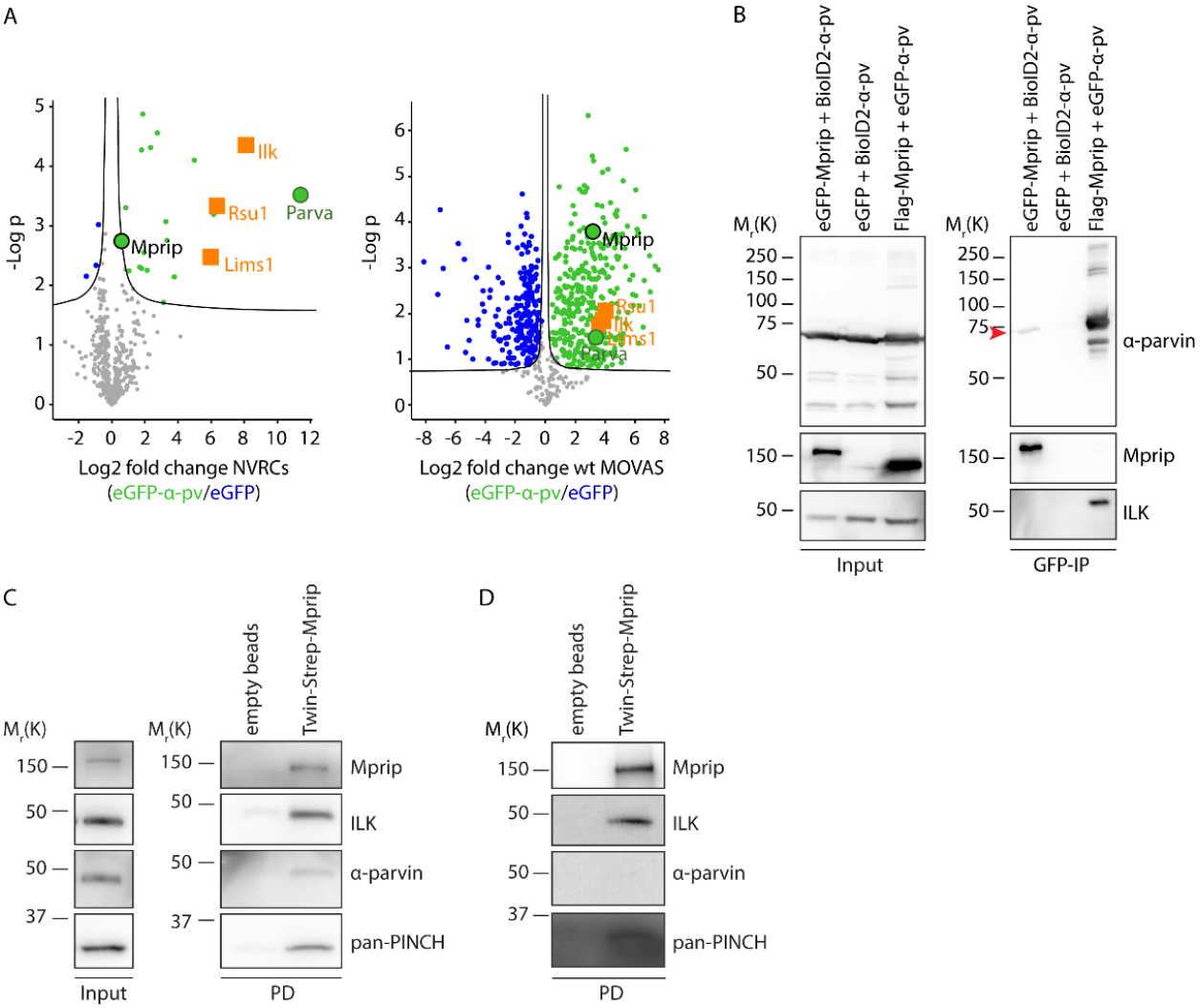

Fig. 49. Mprip as potential molecular linker between α-parvin and the RhoA signaling pathway. (A) Volcano plot showing *t*-test difference of protein intensities versus *t*-test *p*-value for proteins interacting with eGFP-α-parvin versus empty eGFP control in isolated NRVCS (left) and wt MOVAS (right). (B) WB analysis of α-parvin co-immunoprecipitation with eGFP-Mprip from HEK293 cells. Note, BioID2-α-parvin immunoprecipitated with eGFP-Mprip (red arrow head) but not eGFP empty control. (C, D) WB analysis of the IPP complex pulled down from wt MOVAS (C) and α-parvin KO #3 MOVAS (D) cell lysate using recombinant Twin-Strep-Mprip. Note, ILK and PINCH were pulled down even in the absence of α-parvin.

To investigate if Mprip links the IPP complex to the RhoA/MLC2 signaling pathway, Mprip localization and expression was investigated in wild-type and α-parvin KO #3 MOVAS. As described in literature, Mprip localized to α-SMA-positive stress fibers but not paxillin-positive focal adhesions (**Fig. 50A**). As α-parvin is a FA protein, we did not observe a co-localization of α-parvin and Mprip in MOVAS (**Fig. 50B**), although we cannot rule out that the cytosolic pools of proteins interact. In addition, neither Mprip localization to stress fibers (**Fig. 50B**) nor the expression levels (**Fig. 50C**) were altered upon the loss of α-parvin. However, we observed a significant co-localization of Mprip and phosphorylated MLC2 in α-parvin KO #3 MOVAS but not

in wt MOVAS (**Fig. 50D**, **E**), indicating that the loss of α-parvin might impair Mprip function. Mprip usually enhances MLCP activity by bringing MLCP and myosin filaments together, facilitating the dephosphorylation of MLC2 by PP1c, the catalytic subunit of MLCP. Although α-parvin depletion has no obvious influence on the Mprip localization to myosin filaments, it seems to affect Mprip function in a way that MLCP is unable to dephosphorylate myosin II.

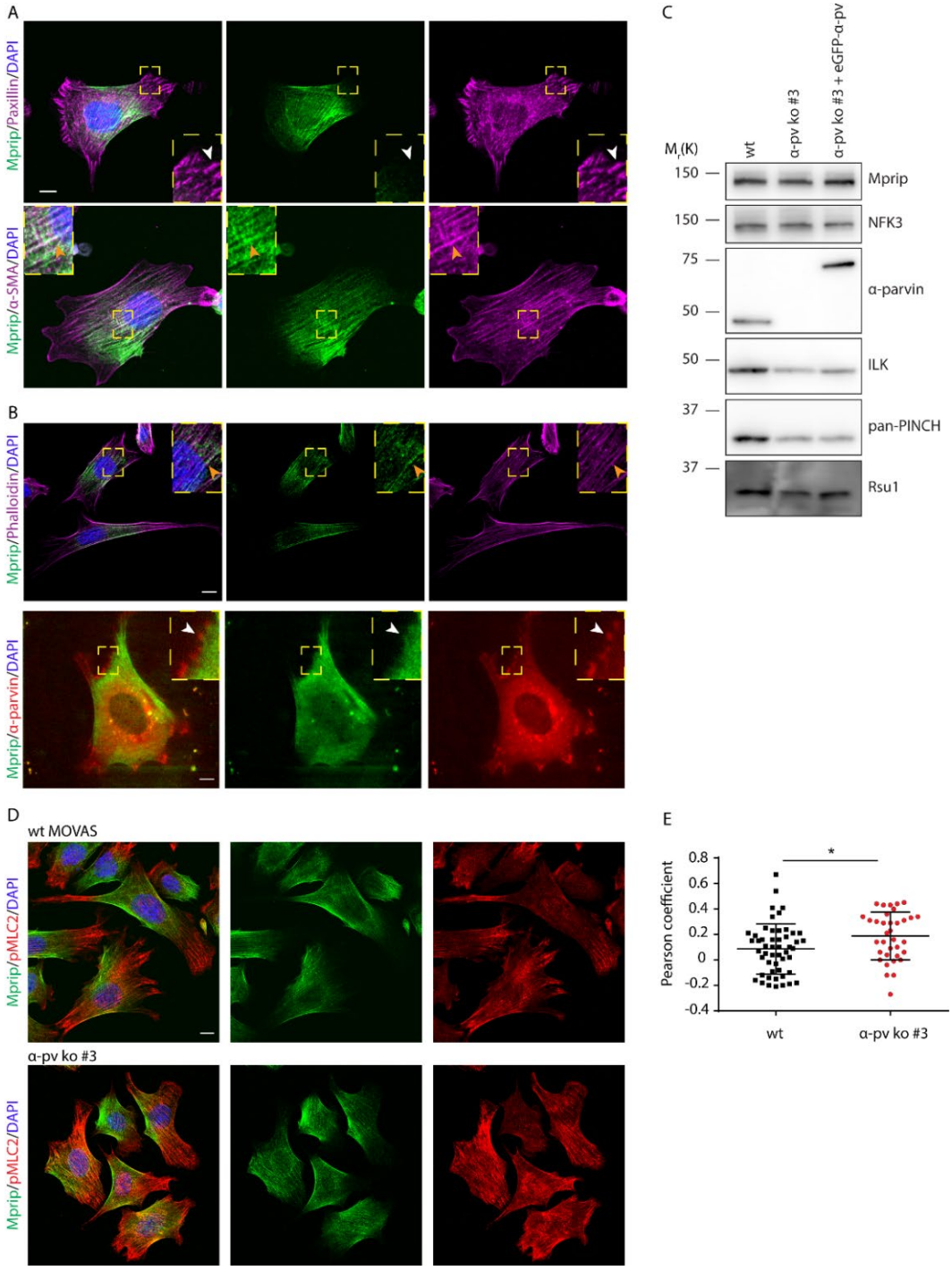

Fig. 50. α-parvin regulates Mprip function. (A) Representative immunofluorescent images showing that Mprip localized to α-SMA-positive stress fibers (orange arrow head) but not paxillin-positive FAs (white arrow head) in wt MOVAS cells plated on FN. DAPI was used to stain nuclei. Scale, 10 µm. (B) Mprip localization in fixed α-parvin KO #3 MOVAS and co-localization of eGFP-tagged Mprip and mCherry-tagged α-parvin in living wt MOVAS. Note, Mprip localization was not affected by the loss of α-parvin and Mprip did not co-localize with α-parvin. DAPI was used to stain nuclei. Scale, 10 µm. (C) WB analysis of wt, α-parvin KO #3 and α-parvin KO #3 re-expressing eGFP-α-parvin MOVAS. NFK3 was used as loading control. Note, knockout of α-parvin results in decreased ILK, PINCH and RSU1 level, but Mprip protein levels were unaltered. (D) Confocal imaging of Mprip and pMLC2 in wt and α-parvin KO #3 MOVAS. DAPI was used to stain nuclei. Note, increased co-localization of Mprip and pMLC2 in α-parvin KO #3 MOVAS compared to wt MOVAS. Scale, 10 µm. (E) Quantification of the co-localization of Mprip and pMLC2 in wt and α-parvin KO #3 MOVAS using the Pearson coefficient. *P<0.1 as analyzed using a Student's t-test.

Altogether these findings show that Mprip interacts with the IPP complex to potentially regulate the RhoA/MLC2 signaling pathway upon integrin activation. The data also indicate that α-parvin does not alter Mprip expression or localization to stress fibers, but might be involved in controlling Mprip function.

4.5.6 DLC-1 as potential novel pan-parvin interactor identified by proximity-dependent biotin identification using TurboID

The GTPase-activating protein DLC-1 was among the binding partners pulled down from cell lysates of both isolated NRVCs and α-parvin KO #3 MOVAS transduced with either TurboID-α- or β-parvin (**Fig. 51**) and might be a cell type-independent pan-parvin interactor. Interestingly, DLC-1 was reported to be recruited to focal adhesions in a tensin-dependent mechanism and tensins were also identified as parvin proximity partners in NRVCs (**Fig. 51A**, **B**) and MOVAS (**Fig. 51C**, **D**).

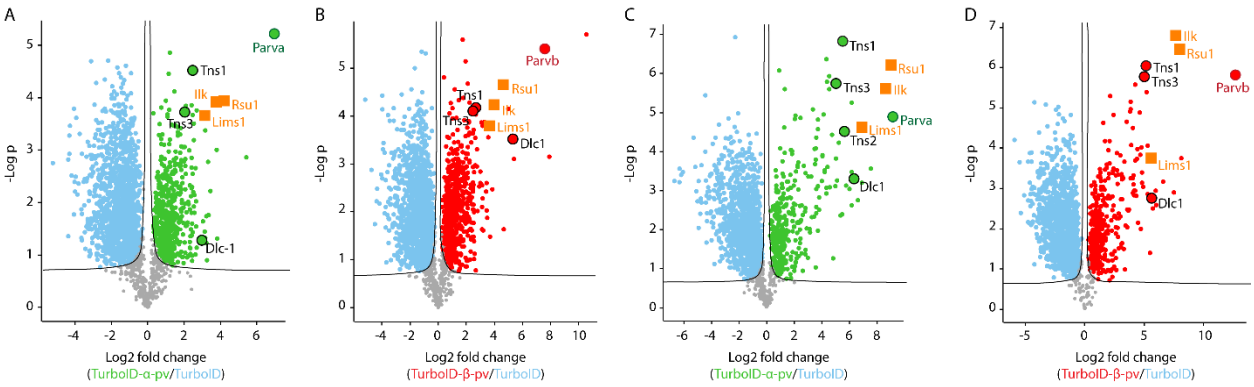

Fig. 51. DLC-1 might be a novel pan-parvin interactor. Volcano plot showing t-test difference of protein intensities versus t-test p-value for proteins interacting with (A, C) TurboID-α-parvin or (B, D) TurboID-β-parvin versus empty TurboID control in (A, B) isolated NRVCS and (C, D) α-parvin KO #3 MOVAS. Note, IPP complex members are depicted in orange. Dlc-1 was shown to function in a tensin-dependent manner, therefore Dlc-1 and tensins are marked.

DLC-1 consists of three characterized domains: a N-terminal SAM domain which is involved in regulating cell migration, a Rho GAP domain that is responsible for the negative regulation of RhoA and a C-terminal

lipid binding START domain which interacts with PLCδ1 to enhance the hydrolysis of PIP2, thereby regulating actin stress fiber formation. [225, 227, 242, 437, 438] It was demonstrated in literature that tensin 3 binds to DLC-1 which leads to the release of the autoinhibitory interaction between the SAM and Rho GAP domain results in RhoA inactivation with the concomitant loss of stress fibers and decrease in cell motility. [242] As protein that is provenly recruited to focal adhesions, the major localization sites of parvins/IPP complex, and direct RhoA regulator, DLC-1 might be accountable for the misregulation of RhoA signaling in cells depleted of α-parvin. The potential pan-parvin-DLC-1 interaction was not further investigated in the present study and will be a subject to future investigations.

4.6 *In vivo* analysis of cardiac and vascular α-parvin

4.6.1 Inducible cardiac-specific deletion of α-parvin

The deletion of α-parvin in mice was shown to result in embryonic lethality due to severe cardiovascular defects. [171] During embryonic development, α-parvin seems to be important for establishing the sarcomeric organization within CMs. However, it has not been investigated, whether α-parvin is also important for maintaining the sarcomeric organization in adult animals. Therefore, *α-pv(fl/fl)* mice were intercrossed with mice expressing a Cre recombinase under the control of the mouse *cardiac-specific alpha-myosin heavy chain (αMHC)* promotor. [386] Intraperitoneal injection of tamoxifen induced the deletion of α-parvin. Unexpectedly, mice died within three to five days after tamoxifen-induced Cre expression showing signs of cardiac failure (e.g. pale ears and foot, pumping problems) whereas vehicle-injected mice showed no such signs (**Fig. 52A**). The cardiac-specific ablation of *ILK* or *PINCH* in mice *in vivo* results in lethality within 4 to 6 weeks and we expected a similar phenotype for cardiac-specific α-parvin depletion. [194, 211, 213] On a cellular level, CMs from tamoxifen-treated animals exhibited a round cell morphology, while the isolation of adult CMs from vehicle-treated animals resulted in rod-shaped cells that spontaneously contracted (**Fig. 52B**). Unfortunately, up to date problems during cell lysis of the round CMs prevented western blotting to analyze α-parvin reduction upon tamoxifen administration to confirm that the observed phenotype is induced by α-parvin deletion. Therefore, the reason for the observed phenotype remains a subject for further analysis.

We additionally tried to deplete α-parvin from adult CMs *in vitro* by isolating CMs from *floxed* mice and AdCre-mediated removal of α-parvin. However, we did not notice a significant decrease of endogenous α-parvin three days after viral transduction (**Fig. 52C**) and as a result did not observe phenotypic changes in the isolated adult CMs (**Fig. 52D**, **E**), which might be due to the low turn-over of costamere proteins in fully differentiated cardiomyocytes.

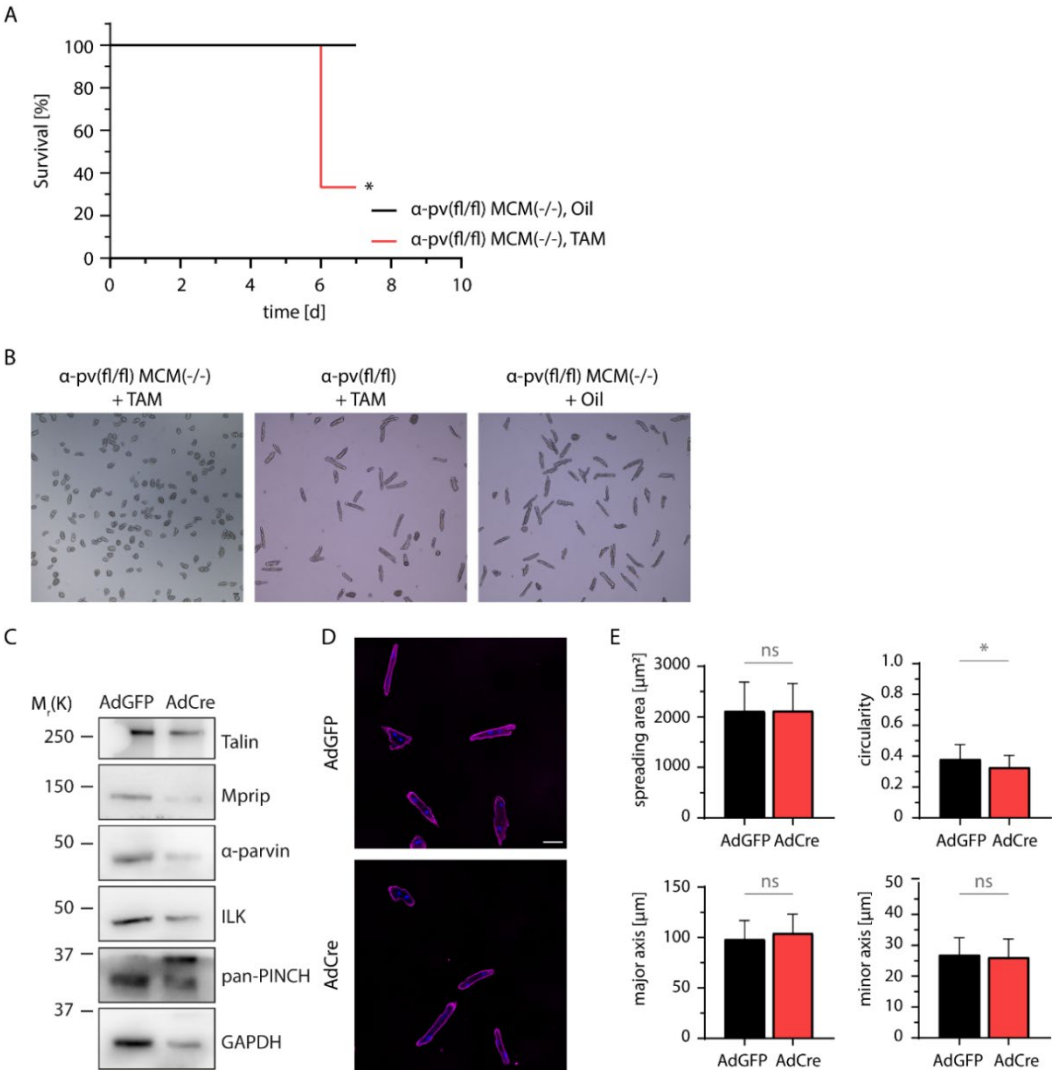

Fig. 52. Deletion of cardiac α-parvin results in rapid mouse death. (A) Kaplan-Meier survival curve for vehicle (Oil)-treated *α-pv(fl/fl) MCM(-/-)* control mice (black line) and TAM-treated *α-pv(fl/fl) MCM(-/-)* mice (red line). n=6 per group. Survival curves were compared using the log-rank Mantel-Cox test. **P*<0.1 (B) Representative live cell image of isolated adult CMs from either TAM-treated *α-pv(fl/fl)* or Oil-treated *α-pv(fl/fl) MCM(-/-)* control mice and TAM-treated *α-pv(fl/fl) MCM(-/-)* mice. Note, no rod-shaped CMs could be isolated from TAM-treated *α-pv(fl/fl) MCM(-/-)* mice. Scale, 10 µm. (C) WB analysis of α-parvin knockout efficiency in isolated adult CMs from *α-pv(fl/fl)* mice three days after *in vitro* transduction with adenoviral Cre. GAPDH was used as loading control. Note, reduction of α-parvin, ILK and Mprip observed in WB were due to differences in protein loading (GAPDH). (D) Representative IF images of isolated adult CMs from *α-pv(fl/fl)* mice three days after adenoviral transduction stained with TpnT. DAPI was used to stain nuclei. Scale, 50 µm. (E) Quantification of spreading area, major and minor axis as well as circularity of adult CMs from *α-pv(fl/fl)* mice three days after adenoviral transduction plated on laminin. Data is presented as mean ± s.d. **P*<0.1 as analyzed using an unpaired Student's *t*-test. 30 cells were measured per condition, n=1.

Overall, these data implicate that α-parvin is important for the proper function of adult cardiomyocytes. The rapid mouse death (within 3-5 days) upon tamoxifen treatment was unexpected and an increase in the number of analyzed mice will be necessary to rule out unspecific Cre-mediated defects and to properly assign the role of cardiac α-parvin in adult mice.

4.6.2 Inducible deletion of α-parvin results in smooth muscle defects in the GI tract

α-parvin plays a pivotal role in the development of a mature vasculature, the kidneys and gastrointestinal (GI) tract. [36, 171, 186] However, the function of α-parvin in SMC of an adult organism remains unclear. Therefore, male *α-pv(fl/fl) SMMHC-CreER^{T2}* mice which express the Cre recombinase under the control of the *smooth muscle myosin heavy chain (SMMHC)* promoter, were treated with tamoxifen to induced the deletion of SMC-α-parvin.

No phenotypic alterations were observed until day 55 to 60 after tamoxifen induction. However, following 55 days male *SMMHC-CreER^{T2}*-positive mice rapidly lost weight, developed a swelled abdomen and finally died 58-65 days after induction (**Fig. 53A**). No phenotypic changes were observed in *α-pv(+/+) SMMHC-CreER^{T2}* and *α-pv(fl/fl) SMMHC-CreER^{T2}* mice after TAM and Oil treatment, respectively, excluding a TAM-related or Cre-specific toxicity as a reason for lethality (**Fig. 53B**, **C**).

Dissection of the GI tract of *α-pv(fl/fl) SMMHC-CreER^{T2}* mice after tamoxifen treatment revealed an extreme dilation of the stomach, small intestine and cecum suggesting that the loss of α-parvin in intestinal SMC (iSMC) alters the peristalsis of the GI tract and mice starve to death (**Fig. 53A**). In contrast, dissection of the aorta of *α-pv(fl/fl) SMMHC-CreER^{T2}* mice after TAM treatment did not reveal an obvious phenotype. This result was not surprising as a discrepancy in the phenotype between *α-pv(fl/fl) SMMHC-CreER^{T2}* and *α-pv(fl/fl) PDGFRβ-Cre* mice after the deletion of α-parvin was already reported by Rohwedder in her thesis. While the aortas of *α-pv(fl/fl) PDGFRβ-Cre* mice, where α-parvin is deleted in vSMCs and pericytes, displayed abdominal aortic aneurysms, *α-pv(fl/fl) SMMHC-CreER^{T2}* did not display any abnormalities in the vasculature. [36] One possible explanation could be the severe intestinal phenotype which might not leave enough time for the mice to develop a vascular phenotype. To test whether α-parvin deletion results in a vascular phenotype in *SMMHC-CreER^{T2}* mice one could challenge them, for example through the injection of angiotensin or by transverse aortic constriction to increase the pressure within the cardiovascular system.

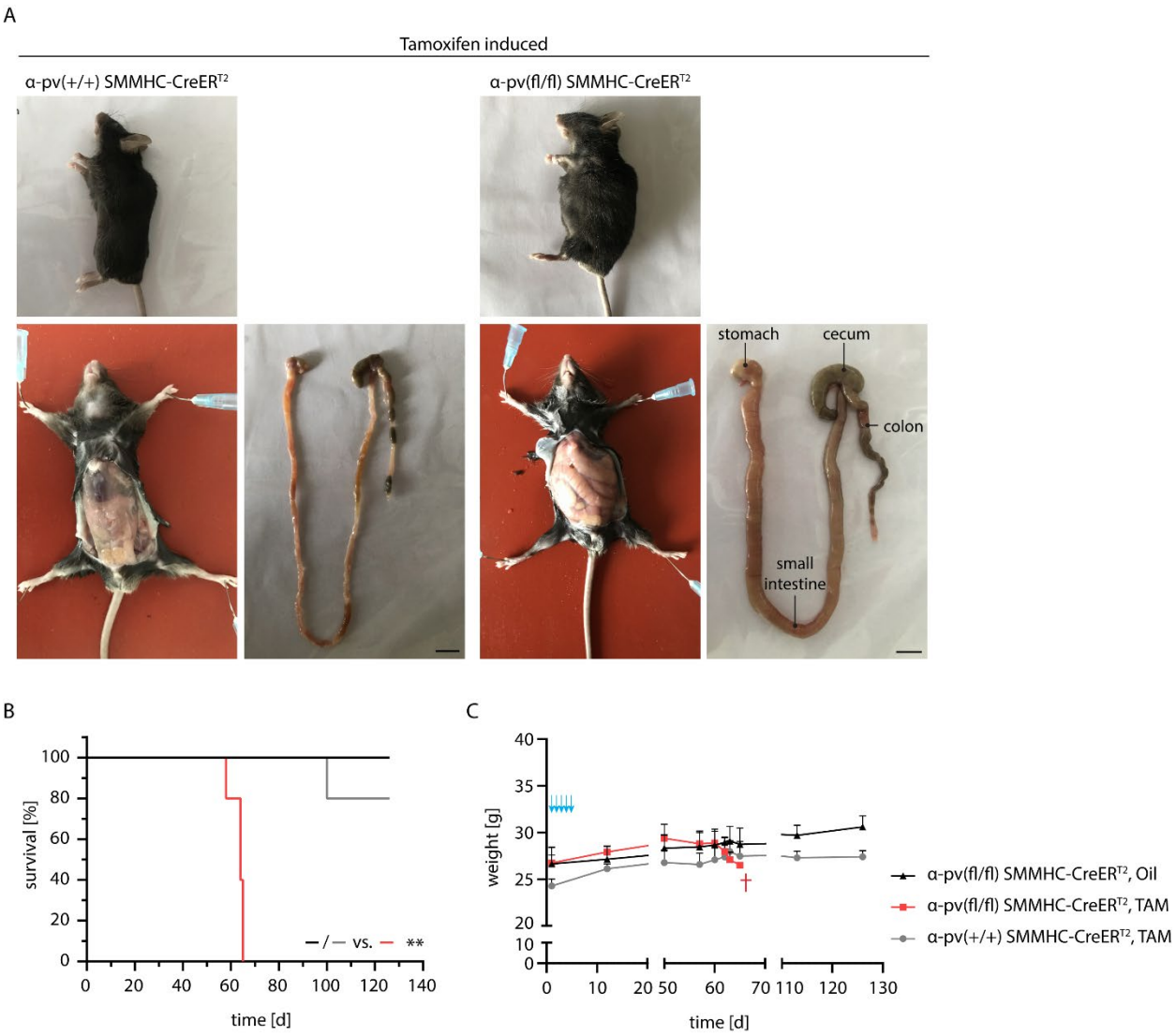

Fig. 53. *α-pv(fl/fl) SMMHC-CreERT2* mice succumb from intestinal defects after tamoxifen-induced α-parvin deletion. (A) Representative images of *α-pv(+/+) SMMHC-CreER^{T2}* and *α-pv(fl/fl) SMMHC-CreER^{T2}* mice and dissected GI tract at day 63 after tamoxifen treatment. Note, enlargement of stomach, small intestine and cecum. Scale, 1 cm. (B) Kaplan-Meier survival curve for TAM- or vehicle (Oil)-treated *α-pv(+/+)* (gray line) or *α-pv(fl/fl) SMMHC-CreER^{T2}* control mice (black line), respectively, and TAM-treated *α-pv(fl/fl) SMMHC-CreER^{T2}* mice (red line). n=5 per group. Survival curves were compared using the log-rank Mantel-Cox test. ***P*<0.01. (C) Body weight changes in *SMMHC-CreER^{T2}* mice treated with TAM or vehicle. n=5 per group. Blue arrows denote individual injections. Note, mice rapidly lose weight two to three days before they die.

Taken together, the data demonstrates that α-parvin is of pivotal importance for the function of intestinal SMCs in adult mice *in vivo* while the effect of α-parvin deletion in vSMCs *in vivo* needs to be further analyzed.

5 DISCUSSION

The IPP complex has an important role for integrin-mediated processes as it establishes a connection to the actin cytoskeleton and regulates intracellular signaling pathways. It is therefore not surprising that dysfunction of components of the IPP complex is connected to many diseases including heart failure, diabetes and cancer and that mice lacking the expression of ILK, PINCH1 or α-parvin, die during the embryonic development. [161, 171, 197, 204, 205, 300, 439, 440] Although parvins have been linked to cardiovascular defects the early embryonic lethality prevented the investigation of α-parvin function in the contractile cells of the CV system during late development or in adulthood. [157, 160, 194, 208-213]

In the present thesis I therefore analyzed the function of α-parvin in contractile cells of the cardiovascular system, namely cardiomyocytes and vascular smooth muscle cells, *in vitro* and *in vivo.* We focused on the role of α-parvin in integrin-mediated processes, in particular through its ability to regulate the actin cytoskeleton and payed special attention to what extend loss of α-parvin is functionally compensated by β-parvin. To increase our understanding of α-parvin regulated pathways, we furthermore set out to identify and characterize new α- and/or β-parvin interactors in both CMs and vSMCs with special focus on regulators of the RhoA signaling pathway.

5.1 Tissue- and cell type-specific expression of α- and β-parvin

Previous studies investigated the tissue-specific expression of the individual parvin isoforms and showed that α- and β-parvin are nearly ubiquitously expressed while γ-parvin expression is restricted to the hematopoietic system. [163-165, 170, 385] Although α- and β-parvin exhibit an partly complementary expression pattern suggesting that the two isoforms function in redundant fashion, the protein amount in various tissues, e.g. heart, lung, spleen, liver and kidney, differs and the two parvin isoforms also have their individual binding partners. [164] As reported in literature, we also observed that α-parvin is the predominant parvin isoform expressed in various cell types (fibroblasts, SMCs, NRVCs), in which β-parvin mRNA and protein expression was comparably weak. However, β-parvin was reported to be highly expressed in striated muscle, the peripheral nervous system and the bone marrow (e.g. megakaryocytes). [385] Additionally, we and others observed a gradual upregulation of β-parvin expression during embryonic development and postnatal cardiomyocyte maturation, while α-parvin is expressed at constant levels throughout early development (**Fig. 39**). [164, 165] These results are in line with findings of our collaboration partner who identified the ILK/PINCH/β-parvin complex as a volume load-specific mechanosensor at CM-ECM adhesion sites (Thievessen et al., submitted). At birth, pulmonary blood flow increases six fold and the gradual increase of β-parvin expression, concomitant to increase in volume load, promotes physiological CM hypertrophy by inducing CM elongation via PIX-mediated Rac1 activation (Thievessen et al., submitted). [441] The ILK/PINCH/α-parvin complex, however, seems to be unable to compensate for this functional property *in vivo.* Furthermore, Thievessen used western blot analysis to analyze the expression pattern of α- and β-parvin in adult organs. While α-parvin expression was weak compared to other tissues (e.g. lung, uterus), β-parvin was highly expressed in adult heart. [385] We also observed lower α-parvin protein expression in isolated adult versus neonatal CMs in immunofluorescence stainings. While the α-parvin antibody gave a strong IF signal in neonatal CMs (**Fig. 18**), it was harder to detect α-parvin in adult cardiomyocytes (**Fig. 21**). Although this could be due to the immunostaining protocol which might not be optimal for the thickness of these cells (>10µm), immunofluorescent labeling β-parvin, ILK and PINCH worked fine using the same protocol (**Fig. 22**). In addition, whole proteome analysis of isolated adult mouse CMs identified more unique peptides for β-parvin compared to α-parvin. Even though the LFQ intensities of the two proteins cannot directly be compared with each other, we and others think that β-parvin is the predominantly expressed parvin isoform in adult CMs, with α-parvin expression being downregulated under physiological but upregulated under pathological conditions (e.g. dilated cardiomyopathy). [385, 442] Nonetheless, Doll et al. identified both parvin isoforms, α- and β-parvin, among the top 75% of most abundant proteins in human adult heart, which is an effect of the various cell types contributing to the

cellular composition of the heart. [250] Unfortunately, they did not investigate the proteome of CMs, so no conclusion about the abundance of α- and β-parvin in adult human CMs can be drawn.

In addition to CMs, we also investigated the expression of α- and β-parvin in MOVAS cells. Although β-parvin is highly expressed in heart and skeletal muscle, endogenous β-parvin level in SMCs are low and due to the lack of a suitable antibody, we were unable to detect endogenous β-parvin in IF or WB analysis. However, using RT-qPCR we showed that β-parvin expression is expectedly upregulated upon the loss of α-parvin (Fig. 26). The expression of both parvin isoforms in tracheal smooth muscle cells was also shown in a recent publication, revealing differential interactions of paxillin with α- or β-parvin-containing IPP complexes depending on the phosphorylation status, thereby regulating the activation of Akt and, thus, the phenotype of airway SMCs. [443]

5.2 *In vitro* subcellular localization of α- and β-parvin

To assemble into functional tissues and organs, cells form various cell-cell or cell-ECM adhesion structures. An integral component of these adhesion sites are the heterodimeric integrin receptors with their adaptor molecules that facilitate integrin-dependent bidirectional signaling. α- and β-parvin IPP complexes are known to localize to these integrin-associated adhesion structures such as FAs, dense bodies and costameres. [48, 50, 197] Furthermore, both parvin isoforms have been observed in lamellipodia in spreading cells and especially α-parvin is also found at fibrillar adhesions and cadherin-containing epithelial cell-cell junctions. [165] We also observed colocalization of eGFP-tagged α- and β-parvin with E-cadherin in transduced ureteric bud cells at cell junctions in the course of the present study (data not shown). In addition to the cytoplasmic and adhesion localization, ILK and PINCH also localize to the nucleus and β-parvin has been detected in the nucleus in human laryngeal carcinoma. [193, 444-447] Additionally, ILK, in contrast to PINCH and α-parvin, localizes to centrosomes, organizing mitotic spindles and regulating centrosome clustering. [448, 449]

Given that the IPP complex members are able to localize to different cellular components and because, to our knowledge, nobody analyzed and compared α- and β-parvin localization in contractile cells of the cardiovascular system, we examined the subcellular localization of these two focal adhesion proteins. We payed special attention to potential differences in the localization of α- and β-parvin, as is observed for kindlin-1 and kindlin-2. Kindlins are another family of FA proteins and while both kindlin-1 and -2 can be found at integrin-mediated adhesion sites, only kindlin-2 localizes to cell-cell contacts in differentiated keratinocytes, showing that two protein isoforms can have distinct localization patterns within a cell.

Further studies showed that kindlins also exhibit cell type-dependent differences in subcellular localization, which could also be the case for α- and β-parvin. [450, 451]

5.2.1 Subcellular localization of α- and β-parvin in isolated cardiomyocytes

Both endogenous and eGFP-tagged α- and β-parvin localized to the same adhesive structures, focal adhesions and costameres, as well as to the sarcomeric Z-discs in NMVCs and NRVCs (**Fig. 18**-**Fig. 20**). As expected, also ILK and PINCH showed the same localization pattern within mouse and rat neonatal CMs. Furthermore, a nuclear signal was observed in eGFP-α- and β-parvin transduced NRVCs. We only noticed one difference between α- and β-parvin subcellular localization in transduced NRVCs: whereas eGFP-tagged α-parvin localized to M-lines, eGFP-tagged β-parvin did not. In isolated adult CMs, we found no differences in α- and β-parvin localization and both isoforms co-localized with α-actinin to Z-discs and costameres, while neither isoform co-localized with myomesin at the M-lines (**Fig. 21**). As expected, a similar expression pattern was observed for ILK, PINCH1 and β1 integrin (**Fig. 22**).

Taken together, these findings show that α- and β-parvin-containing IPP complexes localize to the same adhesive and sarcomeric structures in neonatal and adult cardiomyocytes. This is in line with reports demonstrating that ILK and PINCH1 colocalize with α-actinin and vinculin at sarcomeric Z-discs in neonatal rat and adult zebrafish heart. [209, 210] Furthermore, β-parvin was also shown to colocalize with ILK at sarcomeric Z-discs. [210] Another important observation is the fact that the two parvin isoforms were always found together with ILK and PINCH indicating that parvins do not seem to exhibit IPP complex-independent functions in cardiomyocytes. However, the nuclear signal observed in eGFP-α- and β-parvin transduced NRVCs could indicate an integrin-independent function of the IPP complex. The nuclear localization of α- and β-parvin was not unexpected given the reported NLS found at the N-terminal polypeptide stretch of the two proteins and the already reported localization of ILK and PINCH to the nucleus. The distribution of the IPP complex in both the nuclei and focal adhesions raises the possibility that these proteins are actively involved in linking nuclear processes to cell shape changes. Indeed, PINCH1 expression is upregulated in response to TGF-β1 stimulation and functions as a transcriptional regulator after translocating to the nucleus and binding to the Wilms tumor 1 (WT1) protein, which is essential for the regulation of podocyte-specific gene expression including podocalyxin in adult kidney. [445] Podocalyxin is a transmembrane protein that is linked to the cortical actin cytoskeleton via ezrin and Na^+/H^+-exchange regulatory cofactor 2 (NHERF2) and is important for maintaining the podocyte foot structures. [445] Such a nucleocytoplasmic shuttling of PINCH-1 was also observed in Schwann cells after chronic constriction injury. [452] Furthermore, ILK harbors a N-terminal sequence which exhibits no

homology to consensus NLS motifs but is essential for nuclear import. [444] Nuclear localization of this pseudo-kinase was reported in HeLa, COS-1, MCF-1 and Hec1A cells as well as in primary epidermal keratinocytes. [444, 446, 453] In latter cells, ILK nuclear localization is associated with increased DNA synthesis, whereas ILK was shown to interact and negatively affect the expression of the *Connector Enhancer of Kinase Suppressor of Ras 3* (*CNKSR3)* gene in epithelial cells. [444, 446] The shuttling of proteins between focal adhesions and the nucleus has been observed for a variety of integrin adhesome constituents including zyxin, paxillin and Hic-5, and is not restricted to the IPP complex members. [454] Zyxin, for example, was the first focal adhesion and LIM domain-containing protein reported to shuttle to the nucleus. Stimulation of CMs with atrial natriuretic peptide (ANP) resulted in elevated cyclic guanosine monophosphate (cGMP) levels and subsequent translocation of Akt kinase and zyxin to the nucleus, leading to the stimulation of anti-apoptotic signaling and increased CM survival. [455] Furthermore, zyxin was shown to translocate to the nucleus upon cyclic stretching of vSMCs, where it controls the expression of mechanosensitive genes (e.g. endothelin B receptor (ET_B-R), tenascin-C). [456] In contrast, nuclear localization of the two paxillin family members, paxillin and Hic-5, is amongst other functions, involved in cell motility control. Paxillin was shown to interact with the poly(A)-binding protein 1 (PABP1) and the complex undergoes nucleocytoplasmic shuttling, thereby facilitating the export of PABP1-bound mRNAs into the cytoplasm, an event necessary for the turnover of FAs at the leading edge of migrating cells. [457] Hic-5 influences cell migration by inducing the site-specific production of reactive oxygen species (e.g. H_2O_2). The recruitment of the TNF Receptor Associated Factor 4 (TRAF4) to Hic-5 leads to the accumulation of the NADPH oxidase, which directly interacts with TRAF4, to nascent lamellar focal complexes in motile endothelial cells, resulting in the localized production of H_2O_2 at these sites. H_2O_2 production subsequently inactivates the protein tyrosine phosphatase PTP-PEST, activates Rac1 and enhances cell motility in endothelial cells. [458] Whether paxillin or Hic-5, which both directly interact with α-parvin *in vitro*, are involved in nucleocytoplasmic shuttling of α-parvin is a subject for another study. However, the observed nuclear localization of α-parvin could explain the large number of nuclear proteins identified in our interactome screens (4.5.3). [48]

The only subcellular difference observed between α- and β-parvin was the M-line localization of eGFP-tagged α-parvin in transduced NRVCs (**Fig. 20**). This finding is in line with a report showing that α-parvin (*C. elegans* PAT-6) localizes to M-lines and is required for M-line assembly in *C. elegans* muscle. The body wall attachments are *in vivo* homologs of focal adhesions in non-muscle cells and costameres of vertebrate muscle cells. [201, 459-461] As PAT-6 (vertebrate α-parvin) is the solely expressed parvin isoform in *C. elegans*, no conclusion can be drawn for the localization of β-parvin. However, also PAT-4 (vertebrate

ILK) and UNC-97 (vertebrate PINCH) localized to the M-lines in *C. elegans*. [196, 201] Whether the eGFP-tagged α-parvin localization to M-lines is specific remains to be determined as we did not detect endogenous α-parvin at M-lines in isolated NRVCs. Nevertheless, a possible explanation for this discrepancy could be the time cells were kept in culture and the concomitant time for CMs to mature. The subcellular localization of endogenous α-parvin was conducted in NMVCs or NRVCs kept in culture for three days, and no localization to M-lines was observed. However, viral transduced NRVCs were kept in culture two days longer, allowing sarcomeres to mature and possibly recruit α-parvin to M-lines in a time-dependent fashion during postnatal development. This hypothesis could be true as eGFP- and Flag-tagged PINCH1 and PINCH2 were reported to primarily localize to Z-discs in primary NRVCs cultured for 3 days, however, sometimes faint signals were also observed at the M-lines. [200] Unfortunately, the authors of this study did not analyze the localization of PINCH proteins in NRVCs at a later time point but time-dependent recruitment of PINCH proteins to M-lines might be conceivable.

In adult mouse heart, α-parvin protein levels are reduced compared to neonatal CMs and no M-line localization was detected (**Fig. 21**), which could be an indication that this isoform is not required at M-lines anymore later in age. Further investigations are needed to analyze if this hypothesis is true and whether ILK and PINCH also localize to M-lines in isolated NRVCs in a time-dependent manner. In addition, it should be investigated if the localization to the M-line is parvin isoform-specific and if true, the underlying role of this divergence in the subcellular localization between α- and β-parvin needs to be analyzed.

5.2.2 Subcellular localization of α- and β-parvin in MOVAS

We also determined the localization of α-parvin in MOVAS, an immortalized vascular smooth muscle cell line (**Fig. 23**). As expected, endogenous and eGFP-tagged α-parvin was found in paxillin-positive focal adhesions at the cell periphery in primary vSMCs and wild-type MOVAS similar to ILK. This indicates that α-parvin exhibits IPP complex-dependent functions in vSMCs, as observed in CMs. Due to the low expression level, we did not detect endogenous β-parvin by immunostaining in wt MOVAS but eGFP-tagged β-parvin localized to FAs. The IPP complex is involved in the maturation of FAs to fibrillar adhesions by stabilizing the integrin-actin connection. [462] Indeed, we also identified endogenous α-parvin and eGFP-tagged β-parvin in fibrillar adhesions in the cell center of wt MOVAS cells.

5.3 MOVAS-a vascular smooth muscle cell line

Only a limited amount of primary vSMC can be isolated from mice and these cells grow slowly and undergo rapid dedifferentiation hindering their use for large-scale biochemical assays such as interaction proteomics and Rho GTPase assays. [395] Immortalized mouse vSMC lines have been used to study vSMC function *in vitro* and complement *in vivo* mouse models. Therefore, we decided to use a commercially available vSMC line, called MOVAS, which has already been successfully used and proven as a reliable *in vitro* smooth muscle cell system in studies investigating the regulation of plasma membrane Ca^{2+} ATPase-4, the circadian rhythm and the vascular calcification process associated with different diseases (e.g. diabetes, atherosclerosis). [395, 463, 464]

As vascular smooth muscle cells in adult animals are highly specialized cells with a unique physiology, being able to modulate their phenotype from a contractile to synthetic state, I used smooth muscle α-actin and smoothelin to verify the contractile smooth muscle character of MOVAS. Given the use of a cell line, the contamination of MOVAS with other α-SMA or smoothelin-expressing cells was neglected. However, the true phenotypic state of these cells is somewhere between the contractile and synthetic state as cells expressed contractile proteins while contemporaneously proliferating and migrating. Given this phenotypic state, MOVAS are a suitable cell line to investigate the loss of α-parvin in vascular smooth muscle cells. However, to increase the *in vivo* relevance, findings should be compared to or verified in primary cells.

5.4 *In vitro* technologies to generate α-parvin knockout cells

To analyze α-parvin function in CMs and MOVAS using cellular and biochemical assays, we generated α-parvin KO cells by either using *in vitro* Cre-mediated recombination or by utilizing the CRISPR/Cas9 system.

5.4.1 Viral Cre-*loxP* system induced knockout of α-parvin in NMVCs and adult cardiomyocytes

The CRISPR/Cas9 system has transformed the genome editing technology, providing an efficient method to introduce specific changes in the mammalian genome. [465, 466] While a number of studies show that cardiomyocytes can be edited in the postnatal murine heart using CRISPR/Cas9 *in vivo*, we were able to generate α-parvin knockout NMVCs via Cre-*loxP*-mediated recombination *in vitro*. [467-469] For this, NMVCs were isolated from *loxP*-flanked *α-parvin* mice (*α-pv(fl/fl)*), pre-plated to reduce contamination with other cell types (e.g. cardiac fibroblasts, endothelial cells), and transduced with a recombinant adenovirus expressing a functional Cre recombinase. To exclude adenovirus infection-induced cellular responses that are independent of α-parvin deletion, control cells were also infected with an adenovirus expressing GFP.

Western blot analysis showed an efficient downregulation of α-parvin expression levels three days after adenoviral transduction (Fig. 24). α-parvin deletion was also evident by reduced ILK and PINCH expression in AdCre-transduced cells. The expression of the IPP complex was further decreased in CMs lacking β-parvin in addition to α-parvin depletion, indicating that β-parvin compensates for the loss of α-parvin in NVMCs by stabilizing the IPP complex. Importantly, however, the observed spreading and cell morphological defects clearly indicate that the β-parvin-containing IPP complex cannot fully compensate all aspects of α-parvin.

We also tried to deplete α-parvin from adult cardiomyocytes *in vitro*, using the same adenovirus-mediated strategy used in NMVCs. However, endogenous α-parvin did not decrease significantly over a period of three days after viral transduction and as a result we did not observe phenotypic changes in the isolated adult CMs (Fig. 52). Since the successful infection was obvious by the IRES-GFP expression and by an adenovirus carrying an empty GFP construct as control, the low turn-over of costamere proteins in fully differentiated cardiomyocytes might be the reason why we failed to deplete endogenous α-parvin protein levels. Although the Cre-mediated *in vitro* deletion of α-parvin worked fine in NRVCs, the inability to keep adult viable CMs in culture for an extended time might be the limiting factor here.

5.4.2 CRISPR/Cas9-mediated knockout of α-parvin in MOVAS

We used the CRISPR/Cas9 technology to knockout α-parvin in the MOVAS vascular smooth muscle cell line. After testing different CRISPR/Cas9 targeting strategies, cells were directly transfected with Cas9 protein together with the targeting sgRNA using the Lipofectamine CRISPRMAX. Single cell clones were expanded and the α-parvin knockout was validated by sequencing, western blotting, RT-qPCR and mass spectrometry (Fig. 26).

We also generated α/β-parvin double knockout MOVAS to prevent compensatory mechanisms by β-parvin upregulation upon the loss of α-parvin and to distinguish between α- and β-parvin-specific cell functions. For this, α-parvin KO #3 MOVAS cells were either transfected with a CRISPR vector, co-expressing the sgRNAs targeting β-parvin and Cas9, or directly transfected with the gRNA/Cas9 ribonucleoprotein complexes. Positive α/β-parvin double knockout single cell clones were validated by sequencing and their biallelic mutations were shown to be mostly heterozygous. Instead of sequencing, an easier screening method using the *in vitro* cleavage assay kit from Takara Bio USA could be used in the future to differentiate between wt, mono- and biallelic mutations. [470] Despite very low *β-parvin* mRNA expression in wt MOVAS, we also generated β-parvin knockout MOVAS. However, due to time restrictions, I was only able to fully

analyze the α-parvin knockout MOVAS, while the analysis of α/β-parvin double KO und β-parvin KO MOVAS will be the focus of future studies.

5.4.3 *In vitro* depletion of α-parvin leads to an increase in β-parvin expression and a decrease in ILK and PINCH protein levels

After the successful generation of α-parvin and α/β-parvin double KO NMVCs and MOVAS cells, these cells were first analyzed for changes in IPP complex level. Deletion of α-parvin resulted in an upregulation of β-parvin expression in both cell types to stabilize ILK and PINCH levels. A similar observation was previously reported when Flag-tagged PINCH2 was overexpressed in PINCH-1 deficient HeLa cells, stabilizing ILK and α-parvin protein level. [192] However, while PINCH2 could restore the IPP complex assembly, the ILK/PINCH2/α-parvin complex failed to compensate for the functional defects (e.g. cell shape and survival) caused by the ablation of PINCH1. [192] Furthermore, keratinocytes express two isoforms of the FA protein kindlin that are also unable to functionally compensate for each other. [451] The same phenomenon was observed by us and others for the parvin protein family, as the upregulation of β-parvin is also not sufficient to functionally compensate for the loss of α-parvin even if ILK and PINCH expression is rescued. [36, 171] This is a clear indication for differences between the α- and β-parvin-containing IPP complexes, either through the distinct binding to known or unknown interactors to parvin family members, or through different physical properties such as complex stability or binding affinities. Interestingly, although we did not analyze it in detail, we observed different IPP complex stabilities when recombinantly expressing and purifying the complex. Here, the α-parvin-containing IPP complex tends to aggregate and precipitate, preventing its use in biophysical assays, whereas the β-parvin-containing IPP complex is more stable and now routinely used for biophysical analysis in our lab.

To confirm that the observed decrease in PINCH and ILK expression levels was a direct result of α-parvin ablation and not a clonal artefact, we generated stable rescue cell lines by transducing α-parvin KO MOVAS with either eGFP-tagged or tagless α- or β-parvin. While the expression of eGFP-α- or β-parvin, irrespectively of the eGFP-tag localization (N-terminal vs. C-terminal), resulted in a partial rescue, the re-expression of tagless α-parvin led to fully rescued ILK levels while PINCH levels were only partially upregulated (**Fig. 27**).

Overall, our data confirm that the stability of the individual IPP complex components depends on the assembly of the complex which is in line with reports showing that ILK or PINCH depletion leads to a decrease in the protein levels of the other complex members. [192, 204] Furthermore, our results demonstrate that the re-expression of the depleted IPP complex component rescues the protein level of

the others, thus, stabilizing the IPP complex, although caution should be taken when choosing a protein tag.

5.5 *In vitro* characterization of α-parvin deficient contractile cells

5.5.1 Loss of α-parvin in NMVCs impairs CM hypertrophy and induces protrusion formation

Cardiomyocytes communicate with the surrounding extracellular matrix through costameres and dysfunction in costamere adhesion can lead to cardiomyopathy and heart failure. Myocardial cell-matrix adhesion at costameres is mediated by β1 integrin receptors which recruit the IPP complex and other proteins to establish a link to the actin cytoskeleton. In this way, integrin-mediated signaling plays an important role in maintaining cardiac structure and function, and is involved in the hypertrophic response to mechanical stimuli during postnatal development. [471] To analyze whether α- and β-parvin as part of the IPP complex influence hypertrophic growth of isolated CMs, we measured cell morphological parameters of AdGFP- or AdCre-transduced NMVCs at two distinct time points (d3 and d5) (**Fig. 28**).

As expected, AdGFP-infected NMVCs from *α-pv(fl/fl)* mice increased in cell size, length, width and perimeter from three to five days in culture, while the cell circularity slightly decreased. Although not statistically significant, we observed the same tendencies in increasing cell size, length, width, perimeter and decreasing circularity in AdGFP-infected NMVCs from *α-pv(fl/fl) β-pv(-/-)* mice over time. These observations indicate that wt as well as β-parvin knockout NMVCs are able to undergo hypertrophic growth when plated on FN-coated culture dishes. In contrast, AdCre-infected NMVCs were generally smaller and failed to undergo hypertrophic growth over time. Surprisingly, when we compared the measured cell morphological parameters of α-parvin to α/β-parvin double KO NMVCs, we did not detect differences at day three, day five or over time. Overall, our data show that α-parvin plays an important role in cardiomyocyte spreading and hypertrophic growth, whereas the concomitant loss of β-parvin does not exacerbate the observed phenotype.

Postnatal hypertrophy is induced by the increasing demand of blood circulation in the developing organism which activates many stimuli for cell growth. The initiation of physiological hypertrophic growth (e.g. during postnatal development and during exercise) occurs via different ligands, such as insulin, growth hormones (e.g. VEGFs) and insulin-like growth factor (IGF) 1. IGF1 activates the phosphoinositide-3 kinase (PI3K)-Akt-phosphoinositide-dependent protein kinase 1 (PDK1)-glycogen synthase kinase 3β (GSK3β) pathway. [472, 473] Remodeling of the extracellular matrix is also part of the cellular response to hemodynamic overload and changes in the ECM are sensed by integrins. [474] Given the importance of the IPP complex in linking integrins to the actin cytoskeleton, we expected that the loss of α-parvin has an effect on hypertrophic

growth. Contrary to a previously reported hypothesis in which the decrease of costamere α-parvin was thought to induce NRVC hypertrophy, however, we observed no hypertrophic growth in α-parvin knockout NMVCs. [5] This is more in line with a publication showing that the overexpression of ILK in isolated human cardiomyocytes induced hypertrophic growth. [212] Further investigation of the underlying molecular mechanism is necessary to unravel the role of α-parvin in postnatal cardiomyocyte hypertrophy.

β-parvins role in inducing cardiomyocyte hypertrophy confirms the findings of an unpublished study investigating the role of β-parvin in NVRCs (Thievessen et al., submitted). While Thievessen and colleagues found that β-parvin depleted CMs are unable to induce physiological hypertrophic growth *in vitro* and *in vivo*, they also observed that the induction of pathological cardiac hypertrophy, induced by aortic constriction, was unaffected *in vivo*. This effect can be observed *in vitro* using different ECM components, fibronectin versus collagen I, to coat the culture dishes prior CM plating. Physiological hypertrophy is characterized by a normal cardiac structure and conserved or improved cardiac function, whereas pathological hypertrophy results in cardiac dysfunction, reactivation of the fetal gene program and interstitial fibrosis. [475] Various studies demonstrated that fibronectin actively participates in processes leading to CM hypertrophy, including the increase in global mRNA and protein synthesis, enhanced myofibrillogenesis and sarcomeric assembly. [476, 477] Furthermore, FN was shown to increase the expression of fetal genes including *ANP*, *BNP*, *β-myosin heavy chain* (*β-MHC*) and *α-skeletal actin*. Moreover, fibronectin elicited actin reorganization and the enhanced formation of FAs and costameres. [476, 477] Given these roles of FN in inducing cardiomyocyte hypertrophy, we hypothesize that plating NMVCs on FN-coated culture dishes induced pathological hypertrophy, whereas collagen I coating activates signaling cascades involved in physiological hypertrophy. Therefore, our findings are in line with the unpublished study, showing that β-parvin indeed plays a role in physiological but not pathological hypertrophy. We also tested plating NMVCs on collagen-coated culture dishes to circumvent FN-induced hypertrophy and to test our hypothesis, but encountered insufficient cell attachment.

The IPP complex components are crucial for cell survival in various cell types, including fibroblasts, HeLa cells and cardiomyocytes. [5, 187, 192, 211] Depletion of ILK and PINCH1, for example, were reported to result in decreased phosphorylation of Akt, an well-known signaling component of the survival pathway. [192] Furthermore, cardiac-specific ablation of PINCH1 and PINCH2 reduces Akt phosphorylation and concomitant increase of cell death, shown by increased caspase-3 activation. [211] Additionally, when correctly localized to costameres in isolated NRVCs, ILK and α-parvin show anti-apoptotic functions. [5] Although not quantified, we also noted increased cell death in α-parvin knockout NMVCs compared to control cells despite similar caspase-3 levels, a marker for apoptosis. However, in addition to apoptosis

other cell death mechanisms have also been identified in cardiomyocytes including autophagy and necroptosis. [478, 479] A more detailed analysis would be necessary to conclusively address the role of α-parvin in cell survival of isolated NMVCs.

Cardiomyocytes depleted in PINCH1 and PINCH2 were reported to exhibit disrupted FAs and disorganized cytoskeletal structures, whereas we still observed α-actinin-positive striated cytoskeletal organization in α-parvin and α/β-parvin-depleted NMVCs. [211] However, the loss of α-parvin induced the formation of long sarcomeric-positive protrusions, an effect even further pronounced in NMVCs lacking both parvin isoforms. Contrary to our findings, β-parvin siRNA-treated NRVCs displayed a disorganized sarcomeric structure with defects in protrusion formation in an unpublished study (Thievessen et al., submitted). It cannot be ruled out that the ECM component used for culture dish coating (FN vs. Col I) also plays an important role.

Taken together, our data demonstrates that α-parvin is required to induce cardiac hypertrophy and plays a role in cardiomyocyte survival. Furthermore, β-parvin stabilizes ILK and PINCH protein level but cannot compensate for the loss of α-parvin function in hypertrophic growth.

5.5.2 α-parvin is required for cardiomyocyte spreading in response to substrate compliance

Previous *in vitro* studies have shown that the elastic modulus of the substrate has an effect on cell proliferation, differentiation and tissue formation. [480] We therefore investigated the effect of surfaces with different elastic moduli (1.5, 15, 28 kPa) on the spreading behavior of control and α-parvin depleted NMVCs to resembles physiological substrate stiffness (heart: 10 to 20 kPa) more closely. [421]

NMVCs plated on 15 kPa substrates promoted cell spreading compared to 1.5 and 28 kPa, very similar to NMVCs seeded on plastic surfaces (**Fig. 29**). As expected, α-parvin depletion reduced the spreading area while the simultaneous depletion of β-parvin did not further increase the spreading defect. Furthermore, we did not observe an effect of the substrate stiffness on the overall development of sarcomeres and cell structure in control and α-parvin depleted NMVCs as judged by immunofluorescent stainings.

This is in contrast to a previous publication showing that cardiomyocytes grown on 10 kPa or softer substrates developed aligned sarcomeres, fewer stress fibers and generated greater mechanical forces than CMs on stiffer substrates. In addition, the authors reported that the effects of substrate stiffness on NRVC maturation is regulated through the RhoA/ROCK signaling pathway. [480] However, we did not conduct a time-dependent analysis of the maturation process which would help to see whether NMVCs mature differently on more compliant substrates upon α-parvin deletion.

5.5.3 α-parvin ablation effects cardiomyocyte contractility

Upon the α-parvin knockout, NMVCs lost their ability to spontaneously contract five days after Cre induction and this effect was further pronounced in NMVCs additionally lacking β-parvin expression, which show a significant loss of contractility three days after adenoviral infection (**Fig. 30**). The sole loss of β-parvin in NMVCs resulted in a significant loss of contractility at day five (AdGFP infection) which, however, was not as pronounced as after sole α-parvin deletion.

These findings suggest an additive role of α- and β-parvin in maintaining NMVC contractility and are in line with a study demonstrating an important role for zILK and β-parvin in maintaining cardiac contractility in zebrafish heart. [210] Although the authors did not investigate whether α-parvin expression is upregulated upon β-parvin knockdown, ILK expression levels were reported to be reduced suggesting that α-parvin is unable to stabilize the IPP complex in the absence of β-parvin in zebrafish heart. [210] It is therefore conceivable that the contractility regulation occurs via a functional IPP complex as the single knockout of either parvin isoform mildly reduces ILK and PINCH protein levels, whereas the knockout of both parvin isoforms dramatically affects ILK and PINCH stabilization, resulting in a more pronounced reduction of these proteins.

5.5.4 α-parvin is important for cell-matrix adhesion and focal complex maturation in MOVAS

The development of the vasculature is a complex multi-step process that requires the interaction of endothelial cells, pericytes and smooth muscle cells with one another, and is dependent on surrounding cells and the extracellular matrix. Upon plating the cells on ECM proteins, integrins become activated, recruit intracellular proteins and cluster to form nascent adhesions that mature into focal complexes and subsequently focal adhesions. [481]

In my study, wildtype MOVAS cells rapidly attached to the fibronectin-coated culture dish with concomitant formation of FAs, whereas the adhesion of α-parvin KO MOVAS to fibronectin and FA formation was delayed (**Fig. 31**). These data furthermore indicate that β-parvin might be involved in FA maturation. Moreover, the adhesion defect was not restricted to MOVAS cells but was also observed in α-parvin KO and α/β-parvin double KO fibroblasts.

This is in line with a recent study showing impaired adhesion of keratinocytes isolated from *α-parvin*$^{\Delta K}$ mice. [482] Furthermore, our experiments using α-parvin knockout and α/β-parvin double knockout fibroblasts clearly showed that the deletion of α- and β-parvin resulted in a stronger adhesion defect compared to the sole loss of α-parvin, indicating that the parvin family members can compensate for some of their functions, in particular the stabilization of the IPP complex. As shown in literature, the stability of each complex

member highly depends on the complex assembly. [197, 483] Re-expression of either eGFP-tagged α- or β-parvin alone only partially rescued the adhesion defects. This could either be due to the fact that the eGFP tag prevents full parvin activity and does not allow IPP complex stabilization or both parvin isoforms are required during the early adhesion process in fibroblasts. Indeed, re-expression of eGFP-tagged α- or β-parvin to endogenous levels only allowed a mild rescue of ILK and PINCH expression levels while only high overexpression of eGFP-tagged α-parvin (~10 times more) fully rescued ILK and PINCH levels. This is in line with other observations made during my thesis indicating that re-expression of tagless α- or β-parvin provides a better rescue compared to eGFP-tagged parvin proteins. However, we cannot conclude whether this is due to different binding partners or to a changed stability of the IPP complex.

Although the spatiotemporal recruitment of α-parvin into early adhesion structures has not been analyzed, a study in *C. elegans* showed that ILK is recruited to nascent adhesion complexes to establish a link to the underlying cytoskeleton. [196] Furthermore, another study investigated the formation of nascent adhesions in CHO cells and hypothesized that the recruitment of ILK to these adhesions happens as soon as they are formed. [484] This hypothesis is plausible as ILK was reported to directly bind to β1 integrin and ILK localization into integrin-containing adhesion structures was shown to be dependent on the integrin activator kindlin-2. [47, 339, 485] Based on these reports, showing the importance of ILK during cell-matrix adhesion, we hypothesize that α-parvin plays a comparable role in focal complex formation as both function as part of the IPP complex. Furthermore, our data clearly indicate that α-parvin plays an essential role in focal complex maturation, as the formation of centrally located FAs was impaired in α-parvin KO MOVAS. As both α-parvin and ILK have been previously identified as essential proteins in the FA maturation process, immunofluorescent labeling of wt and α-parvin KO MOVAS using anti-zyxin, anti-tensin and anti-phosphotyrosine antibodies would confirm the importance of α-parvin during FA maturation in MOVAS. [462, 486] Interestingly, we observed that the upregulation of β-parvin levels upon α-parvin deletion stabilized ILK protein levels and promoted focal adhesion maturation, indicating that β-parvin is here able to partially functionally compensate the loss of α-parvin.

In summary, our data show that α-parvin is essential for cell attachment and concomitant loss of β-parvin exacerbates the adhesion defect. Furthermore, α-parvin is important for the maturation of focal adhesions, a function that is compensated by β-parvin.

5.5.5 Hypercontractility associated spreading defects in α-parvin knockout MOVAS

Cell adhesion and spreading on ECM substrate are critical for cell movement, growth and the organization of tissues. [487] Integrin-dependent cell spreading is characterized by the protrusion of cell membranes and the underlying cytoskeleton (filopodia, lamellipodia) while cells are attached to ECM ligands. The small GTPase Cdc42 has been shown to mediate filopodia formation, while lamellipodia are regulated by Rac1. The third, equally well characterized member of the small GTPase family, RhoA, is important for the formation of stress fibers. [79] It has been previously shown by siRNA-mediated knockdowns of RhoA and the use of dominant negative RhoA mutants or RhoA inhibitors that RhoA-mediated contraction serves as a limiting factor in cell spreading and has to be transiently inhibited in a Src or FAK-dependent fashion during early cell spreading. [94, 96, 488]

In line with these reports we observed a severe spreading defect in α-parvin KO MOVAS (**Fig. 35**) concomitant with elevated RhoA activity levels and increased MLC2 phosphorylation (**Fig. 38**), suggesting that deletion of α-parvin causes integrin outside-in signaling defects leading to increased RhoA activity and impaired cell spreading.

Our results furthermore confirm earlier reports showing that ILK deletion results in increased contractility of vSMCs *in vitro* and *in vivo* as well as that α-parvin deletion enhances RhoA/MLC2 signaling in SMA-positive cells and primary vSMCs of *α-pv(fl/fl) PDGFRβ* Cre mice. [36, 157, 171] In contrast to these findings, Rohwedder reported in her doctoral thesis that the lack of α-parvin expression in immortalized smooth muscle cells isolated from the ureter did not lead to substantial changes in MLC2 phosphorylation. [36] This suggest a smooth muscle cell type specific regulation of the RhoA/MLC2 signaling pathway depending on the source of the smooth muscle cells.

Unexpectedly, α-parvin KO MOVAS did not show an obvious increase in or differential distribution of actin stress fibers, a process directly linked to RhoA/MLC2 signaling. [489] This finding was surprising as previous reports show that ILK deletion in vSMCs or epithelial cells resulted in locally concentrated thick cortical α-SMA positive actin fibers. [157, 490] Furthermore, downregulation of ILK increases stress fiber formation in bovine aortic endothelial cells. [491] Moreover, deletion of α-parvin revealed thick α-SMA-positive actin bundles traversing the cytoplasm in mural cells in E13.5 yolk sac. [171] However, the presence of stress fibers in the cytoskeleton is not indicative of the overall contractile potential of a cell. [492-494] Therefore, α-parvin KO MOVAS can still exhibit a hypercontractile phenotype while not showing an overall increase in stress fiber formation.

As described above, we observed reduced cell adhesion of α-parvin KO MOVAS to the ECM protein fibronectin which contributes to the delayed onset of cell spreading. However, this observation cannot be

the exclusive cause of the impaired cell spreading as ILK-depleted endothelial cells show an increase in cell adhesion but still exhibit a severe cell spreading defect. [491] We believe that the delayed onset and the altered RhoA signaling, that we observed and other studies reported for different cell types, combined are responsible for the observed spreading defect. However, the molecular mechanisms for the parvin-mediated contractility regulation are not clear yet, as the link between parvin and RhoA/MLC2 signaling is unknown. The use of suitable inhibitors of the RhoA/MLC2 pathway, such as Y-27632, ML-9 or CPI-17 to inhibit ROCK, MLCK or MLCP, respectively, would further narrow down the important α-parvin-dependent modulators. We utilized immunoprecipitation and proximity-dependent biotin ligation assays combined with mass spectrometric analysis to identify novel parvin interactors and two proteins that potentially fill this gap between α-parvin and RhoA signaling will be discussed later on (see 5.6.3 and 5.6.4.)

5.5.6 α-parvin controls cell migration in MOVAS

Random cell migration refers to the intrinsic property of cells to migrate with a directional persistence. [495] Our data show that, when allowed to move freely on a 2D surface coated with fibronectin, α-parvin KO MOVAS migrated faster but less directional compared to wt cells. Furthermore, single cell tracking of α-parvin-depleted MOVAS in an *in vitro* 'wound healing' assay confirmed the faster but less directional migration that led to a failure to completely close the wound within 24 h (**Fig. 36**). Additionally, we observed defects in collective cell migration upon α-parvin depletion in MOVAS which were rescued upon re-expression of tagless α- or β-parvin (**Fig. 37**).

Cells polarize in response to a pro-migratory stimulus by extending a lamellipodium at the leading edge, where integrins and Rac1 establish a positive feedback loop. In contrast, RhoA activity is necessary for the generation of contractile forces and retraction of the cell tail. [496] We showed that MOVAS lacking α-parvin expression fail to spread due to increased RhoA activity, resulting in elevated MLC2 phosphorylation. MLC2 phosphorylation was reported to initiate cell migration in SMCs. [497] We hypothesize that the impaired persistence in cell migration could be caused by the inability of α-parvin KO MOVAS to polarize, given the upregulated RhoA and pMLC2 levels. This would be in line with data showing that α-parvin knockout cells, isolated from mouse embryos, continuously formed instable lamellipodia-like protrusions that caused frequent changes in the direction of cell movement. [171] Furthermore, sustained Rac1 activity, which is important in lamellipodia formation and thus in directed cell migration, was shown to be suppressed through the elevated RhoA activity. Moreover, the authors of the study demonstrated that the use of ROCK inhibitor Y-27632, which concomitantly blocks the RhoA/ROCK/MLC2 signaling

cascade, reversed the effect of α-parvin loss on cell motility. [171] ROCK inhibitor treatment and Rac1 activity measurements will show the contribution of Rac1 and RhoA to the observed phenotype in MOVAS. During collective migration cells interact mechanically and biochemically through cell-cell adhesions in the monolayer. [498] We hypothesize that upon the loss of α-parvin, MOVAS cells lose the ability to form stable cell-cell contacts, resulting in a disturbed collective cell migration. N-cadherin is the major cell-cell adhesion molecule found in vSMCs and essential for vSMC migration. Inhibition of N-cadherin function reduces vSMCs migration and increases apoptosis. [499] Furthermore, a large amount of research demonstrates interactions between cadherins and integrins and different laboratories showed an involvement of ILK in regulating the 'cadherin switch' during epithelial-mesenchymal transition (EMT) in cancer cells. [500, 501] Moreover, α-parvin was shown to be required for maintaining cell-cell junctions in endothelial cells. [502] It is therefore possible that α-parvin or the IPP complex is involved in cell-cell adhesion regulation in MOVAS, for example through the regulation of N-cadherin expression or function. To confirm this hypothesis, cell-cell contact formation by looking at cadherins and cell polarity of α-parvin KO MOVAS needs to be analyzed. Interestingly, the defect in collective cell migration could be rescued by re-expressing either tagless α- or β-parvin, indicating that β-parvin here not only stabilizes the IPP complex but also functionally compensates for the loss of α-parvin.

5.5.7 Loss of α-parvin affects integrin-mediated processes in CMs and vSMCs *in vitro*

We analyzed several integrin-dependent processes in isolated NMVCs and MOVAS. Taken together, our data show that loss of α-parvin impairs cell attachment and focal complex formation and maturation (5.5.4), cell spreading (5.5.2, 5.5.5), random cell migration and wound closure (5.5.6), as well as cardiac hypertrophic growth (5.5.1) and cell contractility (5.5.3). α-parvin could hereby influence these integrin-dependent processes through modulating (i) integrin activation (inside-out signaling), (ii) integrin expression and surface levels or (iii) integrin outside-in signaling.

We did not investigate whether integrin activation is disturbed upon the loss of α-parvin but there are a few publications reporting a role of the IPP complex in integrin inside-out signaling. [503-507] It has been reported that the loss of ILK inhibits integrin activation (e.g. αIIbβ3, β1 integrins) *in vitro* and *in vivo* in platelets and endothelial cells as assessed by the binding of ligand-mimetic or conformation-specific antibodies and soluble ligands. [503-507] Furthermore, kindlin-2 binding to the β integrin cytoplasmic tail and the IPP complex was shown to be crucial for kindlin-2-mediated integrin β1 activation in fibroblasts. [435] However, in contrast to the overexpression of talin-F3 domain in talin knockdown cells, which rescued the impaired integrin activation phenotype, overexpression of ILK did not, indicating that ILK might not be

sufficient for integrin activation. [503] Furthermore, gene ablation of *ILK*, *PINCH* or *parvin* in different cell types results in defects characteristic for impaired integrin-dependent outside-in, but not inside-out signaling. [5, 171, 204, 211, 462, 502, 508, 509] In conclusion, we cannot exclude the possibility that impaired integrin inside-out signaling might play a role in the defective integrin-dependent processes that we observed in isolated NMVCs and MOVAS, although the evidence for the IPP complex as integrin activator is weak.

Although one publication claims that the loss of ILK affects αIIbβ3 surface levels in platelets, other reports do not support this finding and a role of the IPP complex in regulating integrin surface levels is not established. [169, 505, 507] Flow cytometric analysis of γ-parvin leukocyte mutants additionally showed that the surface expression levels of α4β1, α5β1, and αMβ2 integrins were not affected by their overexpression, which is in line with our FACS analysis revealing no major differences between the surface level of β1 and β3 integrin upon the deletion of α-parvin. [169] We therefore have no indications to believe that α-parvin regulates integrin expression or surface levels in isolated NMVCs or MOVAS.

Upon ligand binding, integrins become activated, recruit other intracellular adaptor and signaling proteins and subsequent clustering of ligand-bound integrins results in intracellular molecular rearrangements (e.g. FA formation, cell spreading). As we observed impaired FA maturation and actin cytoskeletal organization, as well as enhanced RhoA activity, we believe that α-parvin depletion mainly affects integrin outside-in signaling in isolated NMVCs and MOVAS. As the IPP complex directly connects integrins with the actin cytoskeleton via the WH2 domains of α-parvin and PINCH, disturbed actin cytoskeleton organization can be attributed to the missing link upon α-parvin depletion and concomitant reduced IPP complex stability. This is in line with reports showing that the cardiac-specific ablation of *ILK* or *PINCH* in mice result in ultrastructural abnormalities including disturbed intercalated disc structures, sarcomeric disarray and increased distances between sarcolemma and sarcomeres. [194, 211] Furthermore, ILK is important to maintain the link between the contractile actin filaments and the plasma membrane at the end of Drosophila muscles. [195] In contrast, PINCH or ILK knockout zebrafish hearts do not show ultrastructural abnormalities, indicating differences in the structural and functional role of the IPP complex in distinct organisms. [209, 210] These reports show that the IPP complex has an important role in establishing and maintaining the link between the ECM and the actin cytoskeleton in mice, and ultrastructural analysis of sarcomeres in α-parvin and α/β-parvin double knockout NMVCs would show whether parvins play the same role. However, we did not observe obvious alterations in sarcomeric organization by immunofluorescent imaging. For this reason, and because we and others observed increased RhoA signaling upon the deletion of IPP complex components, it is also conceivable that loss of α-parvin primarily alters GTPase signaling.

GEFs, such as α- or β-PIX, p115 RhoGEF and Leukemia-Associated Rho GEF (LARG), and GAPs, such as CdGAP, that activate or inactivate GTPases, respectively, are obvious modulators. The interaction of β-parvin with α-PIX is well established, resulting in the activation of Rac1 at the leading edge of migrating cells to induce membrane ruffling and lamellipodia formation. [179] Furthermore, α-parvin was shown to regulate cell spreading and migration by recruiting the Cdc42- and Rac-specific GAP CdGAP to FAs. [184] Moreover, paxillin, a FA protein to which both α- and β-parvin bind, recruits the DOCK180/ELMO/Crk complex to induce integrin-dependent Rac activation in epithelial cells. [510] As Rac1 and RhoA have antagonistic functions and the crosstalk between both are important for integrin-dependent processes such as cell adhesion, migration and spreading, we specifically searched for RhoA GEFs or GAPs in our proteomic approaches that could explain the observed cellular phenotype upon α-parvin depletion.

Furthermore, the IPP complex functions as a signaling platform through the direct interaction with regulators of various signaling pathways involved in cell spreading, proliferation, migration and survival as well as angiogenesis and epithelial-mesenchymal transition. [161] Other integrin outside-in signaling cascades could therefore also be affected upon α-parvin depletion, such as GSK3β or Akt signaling. Akt activation depends on the phosphorylation of Thr308 and Ser473 by PI3K-dependent kinase-1 (PDK-1) and PDK-2, respectively. Numerous studies show that the knockdown of ILK, PINCH and α-parvin correlates with reduced Akt phosphorylation in fibroblasts, HeLa and HEK-293 cells as well as in human umbilical vein endothelial cells (HUVEC) and macrophages. [187, 192, 511-513] This is in line with reports showing that inactivation of ILK, PINCH and β-parvin results in reduced Akt activation and subsequent heart failure in zebrafish heart. [209, 210] Moreover, α-parvin is required for the correct targeting of Akt to the plasma membrane in HeLa cells. [187] It therefore seems likely that α-parvin depletion also effects Akt signaling in isolated NMVCs and MOVAS cells.

Together our data show that α-parvin is a crucial regulator of integrin-mediated processes including cell adhesion, spreading and migration as well as an important contributor to cardiac physiology in regulating hypertrophic growth, cell contractility and cardiomyocyte survival. As we do not have any indications for disturbed integrin activation or altered integrin surface levels, we hypothesize that integrin outside-in signaling is the major cause for the observed phenotypical abnormalities in α-parvin depleted cells. However, the molecular link between α-parvin and RhoA signaling was missing and therefore we utilized MS-based α- and β-parvin interactomics to identify novel parvin interactors. β-parvin is upregulated upon the loss of α-parvin in CMs and MOVAS, but cannot fully compensate α-parvin function despite its ability to stabilize the IPP complex.

5.6 Mass spectrometry-based interactomics

A prerequisite to fully understand protein function is the identification of interacting partners. Although a number of parvin and IPP complex interactors are known, none of these establish a molecular link to the hypercontractile phenotype observed in various cell types upon the deletion of IPP complex components. Therefore, we aimed to identify novel pan-parvin or parvin isoform-specific interactors in neonatal CMs and vSMC that molecularly link the IPP complex to the RhoA/MLC2 signaling pathway.

We used two different approaches, GFP-immunoprecipitation and proximity-dependent biotinylation: While GFP-IP enriches proteins on the basis of their affinity to α- and β-parvin, proximity-dependent biotinylation is based on the identification of proteins in the near vicinity of the two parvin isoforms. Both techniques are complementary to each other, enabling us to obtain the full spectrum of parvin interactors and the idea was to further analyze proteins identified in both methods.

5.6.1 Comparison of the two techniques used: GFP-IP versus proximity-dependent biotinylation

Although GFP-IP versus proximity-dependent biotinylation are complementary to each other, proximity labeling processes, nowadays ranging from antibody-based approaches such as enzyme-mediated activation of radical sources (EMARS) over the ascorbate peroxidase-based approach (APEX) to the biotin-ligase-based approaches (e.g. BioID, TurboID), have some advantages over the traditional IP. [397, 398, 514, 515]

Proximity biotinylation allows the detection of weak and transient interactions that are often not identified by immunoprecipitation. [516] This allows the identification of spatiotemporal regulated interacting partners in the dynamic intracellular setting. For example, in a study of the dynamic human centrosome-cilium interface the authors compared the identified proteins using Flag-IP and BioID in parallel. They found that >40% of all interactors identified in the FLAG-IP were also detected by BioID, however, these shared interactors accounted only for 21% of the interactors identified by BioID. Thus, BioID identifies more functionally relevant interactors. [517] Furthermore, BioID and co-IP were previously used for the identification of interactions involved in the nonsense-mediated mRNA decay (NMD), a surveillance pathway that controls proper gene expression by eliminating mRNAs that are unable to terminate translation correctly, e.g. by the presence of a premature stop codon. [518] The Eukaryotic Translation Initiation Factor 4A2 (EIF4A2) was identified by BioID proximity labeling, but missed by conventional IP, probably due to the transient nature of this interaction. [519]

Another major advantage of proximity-dependent biotinylation over traditional IP is the potential decrease in the detection of false positives, thus, the enrichment of true interactors. [516] Using proximity-

dependent biotinylation allows the detection of interactors in living cells, whereas IP is performed with cell lysates, enabling the detection of potential interactors that in a living cell do not have a common interface. In addition, the strong covalent biotin-streptavidin interaction allows stringent washing, further reducing the detection of false positive protein-protein interactions that might occur post-lysis. [516] Indeed, a study analyzing the interactions of ribonucleoprotein complexes found evidence for the re-association of RNA-binding proteins after cell lysis, which did not reflect the *in vivo* situation. [520]

Taken together, proximity-dependent labeling strategies have a number of advantages over traditional IP to discover novel protein-protein interactors, thus, being an important complementary approach to our GFP-IP. We used two proximity-dependent biotin labeling approaches, BioID2 and TurboID. The main difference of these two strategies lies in the labeling kinetics: while BioID2 biotinylates proteins in its near vicinity (~10 nm) within 15 to 18 h, its directed-evolution variant TurboID allows efficient biotinylation within 10 to 20 min. [398, 399] Given the ability to faster biotinylate proximate proteins, TurboID permits to study temporal differences in parvin protein associations. Furthermore, using two distinct methods for the identification of the α- and β-parvin interactome, enabled us to compare identified proteins and matching binding partners would be considered as high confidence interactors.

We used the well-established interaction between parvins, ILK and PINCH, as well as RSU-1, to confirm the success of our mass spectrometric-based α- and β-parvin interactomics. We identified all three FA proteins as top hits in both cell types using GFP-IP and proximity-dependent biotinylation, demonstrating the important of this complex (**Fig. 47**). Moreover, α- and β-parvin seem to mainly function via the IPP complex in NRVCs and MOVAS. We also identified the integrin activator kindlin-2 at the intersection of all three MS-based approaches as pan-parvin interactor in MOVAS, while the FA protein kank2 might be a cell type-independent β-parvin-specific interactor. However, known parvin interactors such as paxillin and β-PIX, or RhoA regulators, were not found at the intersection of the three MS-based approaches, which might be due to differences in sample preparation. Furthermore, as mentioned above, we noticed that eGFP-tagged α- and β-parvin only partially rescue the ILK and PINCH protein levels in α-parvin KO MOVAS, indicating that the eGFP-tag might be influencing the IPP complex formation. It is therefore conceivable, that the eGFP-tag might also influence the binding of proteins to parvins/IPP complex, which would explain the absence of known parvin interactors from the GFP-IP. We therefore changed our strategy and compared the proteins identified by GFP-IP or TurboID in both cell types (**Fig. 48**).

Using GFP-IP we identified the FA protein kank2 and the F-actin binding protein and Rac and Cdc42 effector IQGAP1 as potential β-parvin-specific interactors in both isolated NRVCs and MOVAS. IQGAP1 plays a pivotal role in cell-cell adhesion, cell polarization and migration through connecting the Rho GTPases to the

actin cytoskeleton and microtubules, latter of which has been reported to be ILK-dependent. [521, 522] Furthermore, we identified the Rho GTPase activating protein ARHGAP24, also known as FilGAP, as pan-parvin interactor in both NRVCs and MOVAS using proximity-dependent biotinylation. FilGAP is a filamin A-binding Rac-specific GTPase that suppresses leading edge protrusion, stimulates cell retraction and regulates integrin-mediated cell spreading *in vivo*. Furthermore, the protein is a mediator of the Rac-RhoA antagonism, as FilGAP phosphorylation by ROCK stimulates its Rac GAP activity. [97, 436] However, to my knowledge FilGAP, as well as IQGAP1, have not been shown to exhibit a direct function on RhoA regulation, thus, in our setting these proteins could only influence RhoA activity indirectly through regulating Rac1 activity. Although an earlier study shows that Rac1 activation occurs normally in α-parvin KO SMA-positive cells isolated from embryos, its sustained activation is suppressed by the strong increase in RhoA activity. [171] We can therefore not exclude that FilGAP or IQGAP1 might indirectly be involved in α-parvin-dependent RhoA regulation.

In contrast to our GFP-IP, we identified a number of known focal adhesion proteins (e.g. kindlin-2, Peak1, FAK) and parvin interactors, including paxillin, β-PIX and CdGAP, in both cell types using proximity-dependent biotinylation (TurboID), strengthening our confidence in this technique. [177, 178, 184] Furthermore, these findings demonstrate the effect of different labeling times on the identification of potential interactors, given the dynamic nature of adhesion structures.

Although we identified a number of potential α- and/or β-parvin interactors that could be interesting to follow up on (e.g. kank2), we were focusing on the identification of interactors that are directly involved in RhoA regulation. We identified two interesting proteins, Mprip and DLC-1, which are reported RhoA regulators. [216, 221] Their potential role in linking parvin/IPP complex to the RhoA/MLC2 signaling pathway will be discussed in detail in another chapter (see 5.6.3 and 5.6.4).

5.6.2 Identification of nuclear interactors

In line with our observations of the nuclear localization of parvins in isolated NMVCs, we identified a large number of nuclear and ribosomal proteins in both IP and proximity labeling (**Fig. 46**). Most of the ribosomal proteins found were hereby either components of the small 40S (e.g. Rps3, Rps11, Rps14, Rps26, Rps27) or the large 60S ribosome subunit (e.g. Rpl9, Rpl10, Rpl23). Nuclear proteins identified ranged from nuclear pore complex proteins (e.g. Nup54 and Nup88) to histones (e.g. Hist1h1a, Hist1h1e), replication (e.g. Mcm7) and translation initiation factors (e.g. Eif2b5, Eif4a3, Eif6) to chromatin assembly proteins (e.g. Chaf1a). Furthermore, a number of heat-shock proteins were identified (e.g. Hspa1, Hspa4, Hspa8, Hspa14, Hspb8).

As both parvin isoforms harbor nuclear localization (NLS) and export signals (NES) this result is not too surprising, although a nuclear function of parvins has not been studied yet. [165, 174] Furthermore, a report suggests that the NLS is indeed functional due to nuclear targeting of GFP-α-parvin. [165] We could show nuclear localization of α-parvin in MOVAS by cell fractionation and the use of leptomycin, which inhibits the nuclear export, additionally confirmed nuclear association of α-parvin in our MOVAS cells. Although already discussed in a different chapter (see 5.2.1), it has been previously shown that mRNA, RNA-binding proteins and ribosomes rapidly and specifically localize to integrin adhesions sites. [523, 524] Paxillin, for example, directly interacts with PABP1, thereby facilitating the transport of mRNA from the nucleus to the leading lamella during cell migration. [457, 525] Furthermore, vinculin was shown to directly interact with the RNA-binding protein raver-1, which shuttles from the nucleus to costameres during muscle differentiation. [526] Moreover, FAK can also shuttle to the nucleus, where it impairs the transcription of p53-dependent genes and participates directly in the transcriptional regulation of VEGFR2. [527, 528] These and other publications revealing a role for ILK and PINCH in the nucleus enhance the possibility that also α- and β-parvin exhibit nuclear functions. [444-446, 452, 453] However, in the scope of the present study, potential nuclear interacting partners of both parvin isoforms were not further analyzed.

5.6.3 GFP immunoprecipitation revealed Mprip as potential parvin interactor

Previous publications and our own data show that α-parvin is an important regulator of the RhoA/MLC2 signaling pathway. [36, 171] However, the molecular link between the IPP complex component and the signaling cascade remains unknown. To characterize parvin interaction partners we utilized GFP-IP with subsequent proteomic analysis in isolated NVRCs and MOVAS cells and identified Mprip. Previous studies show that Mprip functions as a scaffolding protein that targets MLCP to the contractile apparatus to dephosphorylate MLC2. [220, 224] Some labs also reported a direct interaction with RhoA to regulate RhoA activity but this is controversially discussed. [216, 217, 221] Nevertheless, its proposed function sets Mprip as prime candidate for the missing link between α-parvin and the regulation of vSMC contractility.

Vascular smooth muscle cell contraction is tightly linked to the phosphorylation of the regulatory myosin light chain (MLC) of myosin II. [529] Ca^{2+}-dependent MLCK and MLCP regulate the phosphorylation state of MLC2 by opposing activities. While MLCK leads to the phosphorylation, MLCP dephosphorylates MLC2, leading to the relaxation of vSMCs. MLCP activity is highly regulated by various signaling cascades, one of which is the RhoA/ROCK pathway. Activation of RhoA by GTP loading results in the activation of its downstream effector ROCK which in turn phosphorylates MYPT1 of MLCP at the two inhibitory sites Thr696 and Thr850. [101, 107, 108, 530, 531]

Initial pulldown experiments confirmed the interaction between α-parvin and Mprip in HEK293 cells and recombinantly expressed Twin-Strep-Mprip pulled-down endogenous α-parvin, ILK and PINCH from MOVAS cell lysate (Fig. 49). Unfortunately, we were not able to express and purify the Twin-Strep-Mprip to an extend required for further biophysical measurements.

Subsequent experiments using the Twin-Strep-Mprip showed ILK and PINCH pulled down from α-parvin KO MOVAS cells. Although only performed once, this result indicates that Mprip might directly interact with ILK or PINCH rather than α-parvin. To test this hypothesis ILK knockout and PINCH knockout cells need to be tested for interaction with Mprip. Unexpectedly, despite their interaction *in vitro* α-parvin/IPP and Mprip did not show obvious co-localization within the cell. While Mprip localized to stress fibers, α-parvin/IPP was found in focal adhesions at the tips of stress fibers. However, α-parvin/IPP and Mprip might interact in the cytosol (both are known to have a cytosolic pool) which is difficult to stain. On the other hand, we cannot rule out that the interaction might be an *in vitro* artifact. To judge if α-parvin deletion impacts Mprip function, we analyze MOVAS for Mprip expression levels or localization to actin stress fibers but did not observe any alteration. Still, loss of α-parvin might impact Mprip function without altering its subcellular localization. As reported by Surks et al. Mprip localizes to stress fibers and thereby targets MLCP to regulate vSMC contractility. [216] Importantly, we observed a significant colocalization of phosphorylated MLC2 and Mprip in α-parvin KO MOVAS indicating that MLCP targeting by Mprip might be impaired (Fig. 50). A previous study reported that phosphorylation of Mprip by cGMP-dependent protein kinase (PKG) enhances the association between Mprip and MYPT1 of MLCP and thereby increases MLCP activity. [223] PKG is a serine/threonine-specific protein kinase that is implicated in the regulation of smooth muscle cell relaxation and it was shown that the function of MLCK and MLCP activities are both affected by NO/PKG/cGMP signaling. [111, 532, 533] It is therefore conceivable, that post-translational phosphorylation of Mprip might be altered upon α-parvin deletion. Further analysis, e.g. by determining the phosphorylation of serine and threonine residues by mass spectrometry, is necessary to prove this hypothesis. Furthermore, the use of an PKG inhibitor (e.g. Rp-cGMPS) or a non-hydrolysable cGMP analog (e.g. 8-pCPT-cGMP) could help to validate whether Mprip phosphorylation occurs in the α-parvin knockout setting.

In summary, our findings show an interaction of Mprip with the IPP complex and that Mprip function might be controlled in an α-parvin-dependent manner. Further analysis is necessary to unravel the molecular signaling between α-parvin/IPP complex and Mprip.

5.6.4 A potential parvin-DLC-1 interaction was identified by proximity-biotinylation using TurboID

In addition to Mprip, the search for novel parvin interactors that link the RhoA/MLC2 signaling pathway to α-parvin using TurboID-based proximity labeling in isolated NRVCs and MOVAS identified DLC-1 (**Fig. 51**). Although I did not have enough time left to investigate the functional impact of parvin-DLC-1 interaction for parvin-mediated signal transduction, DLC-1 might be a very interesting candidate for further studies.

DLC-1 is a focal adhesion protein that negatively regulates cell migration and spreading due to its ability to regulate RhoA and Cdc42 activity. [241, 242, 246, 437, 534-536] The protein is recruited to FAs via its FAT domain and through the interaction with various focal adhesion proteins, such as tensin, talin and FAK. [229, 238, 239, 242, 537, 538] Essential for DLC-1 binding to talin and FAK is an LD-like motif of DLC-1 which shows great homology to the LD motif of paxillin in the hinge region. [537] Interestingly, among the proteins that exhibit an affinity for LD motifs are the α- and β-parvin, which both directly interact with paxillin. [50, 175] Therefore, we hypothesize that parvins are able to recruit DLC-1 either through a direct interaction via the LD-like motif or through an indirect interaction via tensin. Tensin and talin bind to β1, β3, β5 and β7 integrin tails in a temporally regulated manner. [539, 540] However, whereas talin is recruited to all adhesion sites including nascent adhesions and focal complexes, tensin is usually detected at mature FAs and fibrillar adhesions. [66, 486] α-parvin KO MOVAS failed to form centrally located fibrillar adhesions and therefore should exhibit defects in tensin recruitment to adhesion structures. Publications show that tensin-DLC-1 interaction is important for DLC-1 recruitment to focal adhesions and for the regulation of DLC-1's Rho GAP activity. Immunofluorescent labeling of α-parvin KO MOVAS using anti-tensin and anti-DLC-1 antibodies would reveal whether maturation of FAs and concomitant DLC-1 recruitment is disturbed upon α-parvin deletion. Furthermore, a number of different studies showed how DLC-1's Rho GAP activity is fine-tuned through post-translational modifications that result in either enhanced or reduced RhoA signaling. [242-246, 541, 542] Therefore, α-parvin might influence DLC-1's Rho GAP activity by altering DLC-1 or tensin protein levels, disturbing the recruitment to FAs or influencing post-translational modifications.

Besides its ability to regulate RhoA activity, DLC-1 could additionally regulate smooth muscle contraction through PLCδ1 binding. PLC, although often activated through GPCR signaling, directly binds β1 integrin tails and modulates integrin-mediated cell adhesion. [543] Furthermore, published data show that the Pyk2/paxillin/Rac signaling, involved in cell spreading and migration, can be activated in a PLC-dependent fashion. [544] As PLCδ1 interactor, DLC-1 enhances the hydrolyzation of PIP2, leading to the increased release of DAG and IP_3, latter of which mobilizes Ca^{2+} from the endoplasmic-sarcoplasmic reticulum and

elicits rapid contraction of vascular smooth muscle cells. [545] IP_3-induced Ca^{2+} release leads to the activation of the Ca^{2+}/calmodulin-dependent MLCK and the subsequent phosphorylation of MLC2. Indeed, *in vivo* deletion of IP_3 receptors resulted in a dramatical reduction of MLC2 phosphorylation due to increased MYPT1 phosphorylation and concomitant inactivation. [546] Furthermore, vSMC-specific overexpression of DLC-1 was shown to result in enhanced PLCδ1 activity in isolated vSMCs and the *in vivo* analysis of mice revealed an important role for DLC-1 in the pathogenesis of coronary spasm. [545] Conversely, DLC-1 knockdown resulted in lower PLCδ1 activity leading to lower cellular Ca^{2+} concentrations in human coronary artery SMCs. [547] Based on our proteomic results and published studies we hypothesize that α-parvin-depletion impairs FA recruitment of DLC-1 protein levels or its PLCδ1 binding capability, hence, leading to a decrease in MLCK activity and increased MLC2 dephosphorylation. Whether PLCδ1-induced Ca^{2+} increase plays a role in the upregulation of RhoA in α-parvin KO MOVAS needs to be investigated.

5.7 *In vivo* analysis of α-parvin function

5.7.1 *In vivo* deletion of cardiac α-parvin

Constitutional deletion of α-parvin results in embryonic lethality at day E10.5-14.5 due to cardiovascular defects including aberrant heart development. [171] To investigate the function of α-parvin in post-developmental heart, we generated a new mouse line, *α-pv(fl/fl) α-MHC-MerCreMer*, that allows the tamoxifen-induced excision of *PARVA* in cardiomyocytes. [386]

A single dose injection of TAM into *α-pv(fl/fl) α-MHC-MerCreMer* mice did not induce obvious phenotypic changes and mice exhibited normal heart weight to tibia length ratio. However, after increasing the TAM administration from a single dose to three doses on consecutive days, mice showed severely decreased activity and appeared ill within five days after the last TAM injection, while vehicle-treated control mice exhibited a normal appearance (**Fig. 52**). Reduction of the TAM amount injected on the three consecutive days did not alter the fast onset of the lethal phenotype but reduced the number of *α-pv(fl/fl) α-MHC-MerCreMer* mice dying in the experiment.

The cardiac-specific deletion of *ILK* in adult mice was reported to result in death between 6 to 12 weeks of age after TAM administration and cardiac-specific *PINCH* double knockout mice died within one month. [194, 211] Although α-parvin does play an important role in maintaining sarcomeric stability, we were surprised that *α-pv(fl/fl) α-MHC-MerCreMer* mice showed a much faster onset of the lethal phenotype compared to mice dying after *ILK* or *PINCH* deletion. [171] Given the importance of the IPP complex and the stabilizing effect of the complex components among each other, it was rather expected that mice

lacking α-parvin expression would die in a similar time frame. However, personal communications revealed that α-parvin KO mice revealed the strongest kidney phenotype among the IPP components, so that differences in the phenotype intensity between the IPP complex components are conceivable. Furthermore, induced ablation of the *ATPase H(+)-transporting lysosomal-interacting protein 2 (Atp6ap2)* in adult animals, an important protein of the renin/angiotensin system, resulted in rapid lethality within five days after the last TAM injection, showing that such a quick onset of a lethal phenotype is feasible. [548] However, an important caveat of the *α-MHC-MerCreMer* mouse line are potential unspecific effects after tamoxifen-induced Cre activation which are independent of *loxP* sites. Various laboratories have tested different tamoxifen administration protocols, ranging from single to multiple TAM injections, to enhance the efficiency and to avoid Cre-mediated toxicity in control mice. [386, 549-552] However, Cre-induced DNA damage leads to gene dysregulation, cardiomyocyte apoptosis, cardiac fibrosis and subsequently results in dose-dependent cardiac dysfunction. [550-553] Therefore, the optimal conditions for maximizing recombination while minimizing cardiac defects upon activation of the Cre-*loxP* system where reported to be 30 µg/g TAM per day, injected on three consecutive days. This TAM dosage was shown to result in 10% Cre-induced mortality. [552] Lexow and colleagues even went down to the administration of a single injection of 40 µg/g TAM to effectively avoid cardiac defects. [550] Furthermore, an alternative selective estrogen receptor modulator, called raloxifene, was shown to circumvent TAM-induced cardiac dysfunction. [551] Despite using the reported TAM administration protocols, the unexpected fast onset of the observed lethal phenotype indicates that our *α-pv(fl/fl) α-MHC-MerCreMer* mice might suffer from TAM-induced Cre toxicity rather than from α-parvin depletion. Therefore, further investigation is needed to study the effect of α-parvin deletion in adult mice beyond the Cre-induced cardiac defects and subsequent experiments should include an analysis of Kaplan-Meier curves with the associated mortality of *α-pv(fl/fl) α-MHC-MerCreMer* mice and TAM-treated *α-MHC-MerCreMer* control mice. Echocardiographic, histological and cellular analysis would provide additional information about the role of cardiac α-parvin in adult mice.

To analyze the effect of α-parvin deletion *in vivo* in mice at the cellular level, I isolated adult cardiomyocytes from TAM or vehicle-treated animals. Healthy, rod-shaped CMs could be isolated in high numbers from vehicle-treated control mice. In contrast, cell suspensions from TAM-treated *α-pv(fl/fl) MerCreMer* hearts only contained high yields of contracted but no healthy-looking rod-shaped cardiomyocytes. In contrast, we did not observe cell morphological alterations in isolated adult CMs after *in vitro* knockout of α-parvin using adenoviral expression of Cre. This discrepancy could be a result of the Cre toxicity of *MerCreMer* heart cells but also of an insufficient *in vitro* α-parvin knockout given that adult CMs can only be kept in culture

for three days and α-parvin-specific deletion defects might not be effectively induced. This goes in hand with the times needed to develop cardiac defects after the knockout of the other IPP complex members, ILK and PINCH, or other integrin-associated proteins such as talin and vinculin. [194, 211, 554, 555] Costameres are very stable structures compared to adhesion structures in migrating cells, thus, the turnover of adhesion molecules could be very slow, resulting in a longer half-life time of α-parvin in costameres. [556, 557] Furthermore, from the analysis of neonatal CMs we know that α-parvin deletion leads to severe spreading and contractility defects five days after Cre infection. On this account it seems reasonable that no phenotype in isolated, fully differentiated, adult CMs, can be observed within the three days after adenoviral transduction.

One aim of my thesis was to investigate the function of α-parvin as well as the functional divergence between α- and β-parvin in cardiomyocytes in neonatal and adult animals. Therefore, we also generated an *α-pv(fl/fl) β-pv(-/-)* mouse strain expressing the fusion construct of Cre recombinase to the modified estrogen receptor under the control of the *α-MHC* promotor (*α-pv(fl/fl) β-pv(-/-) α-MHC-MerCreMer*). Unfortunately, these experiments were haltered by the poor breeding performance of *β-pv(-/-)* mice. Female mice were either not pregnant or the litter was lost by still-born pups or pups that stopped moving after a couple of days. According to a published report, infanticide does not play an important role in litter loss, so other factors must be involved. [558] The mating of *β-parvin* heterozygous mice in the *Bl/6* background (*β-pv(+/-)*) did usually not result in 25% *β-pv(-/-)* offsprings, according to Mendelian ratio, that reached the weaning age. This observation was surprising as no overt phenotype of constitutional *β-pv(-/-)* mice in a mixed background was reported and mice were viable and fertile, reaching a wildtype-comparable age. In addition, Thievessen did not find any alterations in the structure of the heart in *β-pv(-/-)* mice under homeostasis. [385] Considering the strong expression of β-parvin in the heart, this result was remarkable. However, it also underlines the importance of compensation between the α- and β-parvin isoform as the loss of β-parvin led to the upregulation of α-parvin, resulting in the stabilization of the IPP complex (Thievessen, submitted). For this reason, *α-pv(fl/fl) β-pv(-/-) MerCreMer* mice should be analyzed in comparison to *α-pv(fl/fl) MerCreMer* mice; either in a different genetic background or by setting up significantly more matings to increase the chances to obtain enough offspring for a detailed analysis.

5.7.2 *In vivo* deletion of α-parvin results in smooth muscle specific defects in the GI tract but not the aorta

Finally, we aimed to analyze the function of α-parvin in adult SMCs *in vivo* using a tamoxifen inducible *α-pv(fl/fl) SMMHC-CreER^{T2}* mouse strain. Homozygous mice died within 9 weeks after the last tamoxifen administration, illustrating the importance of α-parvin for SMC function *in vivo* (**Fig. 53**). While the dissection of the GI tract revealed a bloated stomach, ileum and cecum, other organs including the aorta seemed superficially fine. Following the assumption that intestinal SMCs (iSMCs) show a comparable behavior as we observed in MOVAS upon the knockout of α-parvin, this phenotype might be due to a hypercontractility of the cells in the smooth muscle layer of the GI tract. This hypercontractility could lead to an impairment of the muscular layer, resulting in the disturbance of the intestine peristalsis leading to a paralytic ileus. A disturbed peristalsis would also explain the fast weight loss mice exhibit shortly before they die. A related phenotype was observed in mice lacking the SMC-specific expression of the serum response factor (SRF), which resulted in the downregulation of key contractility signaling effectors such as smooth muscle-MLCK, α-SMA and SM-MHC. [559] In line with our assumption that hypercontractile α-parvin KO iSMCs could impair the intestine muscle layer, a previous doctoral study reported major defects in the SMC layer of the small intestine in *SMMHC-CreER^{T2}* mice after TAM treatment. [36] Although the *in vivo* analysis of α-parvin function in adult iSMCs was not subject of my thesis, I also observed defects in the SMC muscular layer by histological analysis. Interestingly, even though vascular defects upon the knockout of α-parvin were described for a PDGFR-β-CreER^{T2} mouse strain, no phenotype was observed in the aorta of induced *α-pv(fl/fl) SMMHC-CreER^{T2}* mice, probably due to the severity of the intestinal defect leading to death. [36] It is possible, that the development of vascular defects needs more time under physiological conditions than the given 9 weeks. To investigate if the deletion of α-parvin results in vascular defects, mice could be challenged (e.g. stimuli-induced hypertension, physiological exercise) to increase the strain and allow mouse analysis before the intestinal-induced death.

Another possible explanation for the absence of an obvious aortic phenotype could be the fact that the conditional deletion of α-parvin occurs solely in SMCs in *SMMHC-CreER^{T2}* mice, while the *PDGFR-β-CreER^{T2}* mouse strain depletes α-parvin in vascular pericytes and SMCs. [388, 560] Given these circumstances, a direct comparison between *SMMHC-CreER^{T2}* and *PDGFR-β-CreER^{T2}* mice might just not be appropriate.

Short summaries of publications

Paper I: LCP1 preferentially binds clasped αMβ2 integrin and attenuates leukocyte adhesion under flow

Integrins are α/β heterodimeric cell surface receptors that can adapt different affinity states towards their ligands. The switch from an unbound, low-affinity ('inactive' state) to the bound, high-affinity ('active' state) conformation is accompanied by the separation of the α and β integrin subunits. It is known that the separation of the two subunits can be reversed, however how the cell differentiates between active and inactive integrins and avoids unwanted integrin activation was unknown on the molecular level. Therefore, it was hypothesized that interacting proteins, besides the previously reported filamin-1, might exist that preferentially bind to the clasped conformation, keeping the integrin in an inactive state. In order to identify such conformational-specific interactors recombinant αM and β2 proteins (TMcyto domains only) were dimerized by Jun-Fos dimerization domains. αMβ2 TMcyto heterodimers were formed in a 1:1 ratio and incorporated into bicelles to maintain the native protein conformation and promote protein-lipid interactions. Subsequently, the αMβ2 TMcyto domains were used in pulldown experiments and the interactome was analyzed by liquid chromatography–tandem mass spectrometry (LC-MS/MS).

In a first experiment, single α5, αM and αIIb as well as β1, and β3 integrin TMcyto domains were incorporated into negatively charged bicelles to investigate whether this incorporation affects the affinity of proteins for the integrin cytoplasmic tails. We found qualitative differences between the interactomes of the diverse integrin subunits when performing pulldown experiments from bone marrow derived macrophage lysates. In addition, the results demonstrated the feasibility of a bicelles-incorporated integrin cytoplasmic tail screening approach.

Using the Jun-Fos-dimerized αMβ2 TMcyto domains as baits, we identified a number of conformation-specific integrin interactors, including L-plastin (LCP1). Subsequent experiments revealed that LCP1 functions as talin-1 competitor for its binding to the integrin cytoplasmic domain. Furthermore, we showed that LCP1 depletion positively influences integrin αMβ2 surface level and cell attachment to fibrinogen and ICAM in unstimulated cells. LCP1 functioned as an αMβ2 integrin inactivator under flow conditions, thereby negatively regulating the adhesion strength and resistance to shear forces. [29]

Paper II: Bridging length scales in sarcomere organization within native cardiomyocytes

Cardiomyocytes are striated self-beating muscle cells that contain sarcomeric structures as contractile apparatus. Although the overall structure of sarcomeres, containing thin (actin), thick (myosin) and elastic (titin) filaments, has been revealed decades ago, much remains to be discovered about how the molecular players interact together within the cellular environment. We used i*n situ* cryo-electron tomography (cryo-ET) to obtain molecular views of cardiac myofilaments in frozen-hydrated NRVCs.

We cultured isolated NRVCs on fibronectin-coated gold EM grids, cryo-fixed them and prepared lamellas using cryo-focused ion beam (cryo-FIB) milling. Using Transmission Electron Microscopy (TEM) images, we obtained a view of the CM interior, in which we identified long myofibrils, mitochondria and the sarcoplasmic reticulum. Myofibrils were subsequently imaged and quantitatively analyzed in 3D by cryo-ET. The quantitative analysis revealed that the 3D architecture of myofilaments is conserved within cardiac and skeletal muscle where thick myosin filaments organize in a hexagonal lattice with thin actin filaments located at trigonal positions. Furthermore, we used subtomogram averaging to produce a *de novo* structure of F-actin in complex with tropomyosin resolved at 20.7 Å. In addition, filament polarity was analyzed allowing the localization of Z-discs and M-lines within the myofilaments of NRVCs. These findings were corroborated by thin filaments found in the open myosin state at the molecular level. [320]

REFERENCES

1. Frantz, C., Stewart, K.M., and Weaver, V.M., *The extracellular matrix at a glance.* 2010. **123**(24): p. 4195-4200.
2. Berrier, A.L. and Yamada, K.M., *Cell-matrix adhesion.* J Cell Physiol, 2007. **213**(3): p. 565-73.
3. Geiger, B., Spatz, J.P., and Bershadsky, A.D., *Environmental sensing through focal adhesions.* Nat Rev Mol Cell Biol, 2009. **10**(1): p. 21-33.
4. Geiger, B. and Yamada, K.M., *Molecular architecture and function of matrix adhesions.* Cold Spring Harb Perspect Biol, 2011. **3**(5).
5. Chen, H., et al., *Role of the integrin-linked kinase/PINCH1/alpha-parvin complex in cardiac myocyte hypertrophy.* Lab Invest, 2005. **85**(11): p. 1342-56.
6. Valencik, M.L., et al., *A lethal perinatal cardiac phenotype resulting from altered integrin function in cardiomyocytes.* J Card Fail, 2002. **8**(4): p. 262-72.
7. Ross, R.S. and Borg, T.K., *Integrins and the myocardium.* Circ Res, 2001. **88**(11): p. 1112-9.
8. Shattil, S.J. and Ginsberg, M.H., *Perspectives series: cell adhesion in vascular biology. Integrin signaling in vascular biology.* J Clin Invest, 1997. **100**(1): p. 1-5.
9. Hynes, R.O., *Integrins: bidirectional, allosteric signaling machines.* Cell, 2002. **110**(6): p. 673-87.
10. Luo, B.H., Carman, C.V., and Springer, T.A., *Structural basis of integrin regulation and signaling.* Annu Rev Immunol, 2007. **25**: p. 619-47.
11. LaFoya, B., et al., *Beyond the Matrix: The Many Non-ECM Ligands for Integrins.* Int J Mol Sci, 2018. **19**(2).
12. Kechagia, J.Z., Ivaska, J., and Roca-Cusachs, P., *Integrins as biomechanical sensors of the microenvironment.* Nature Reviews Molecular Cell Biology, 2019. **20**(8): p. 457-473.
13. Yamada, K.M. and Miyamoto, S., *Integrin transmembrane signaling and cytoskeletal control.* Curr Opin Cell Biol, 1995. **7**(5): p. 681-9.
14. Schwartz, M.A., Schaller, M.D., and Ginsberg, M.H., *Integrins: emerging paradigms of signal transduction.* Annu Rev Cell Dev Biol, 1995. **11**: p. 549-99.
15. Belkin, A.M., et al., *Muscle beta1D integrin reinforces the cytoskeleton-matrix link: modulation of integrin adhesive function by alternative splicing.* J Cell Biol, 1997. **139**(6): p. 1583-95.
16. Vaynberg, J., et al., *Non-catalytic signaling by pseudokinase ILK for regulating cell adhesion.* Nat Commun, 2018. **9**(1): p. 4465.
17. Giancotti, F.G. and Ruoslahti, E., *Integrin signaling.* Science, 1999. **285**(5430): p. 1028-32.
18. Su, Y., et al., *Relating conformation to function in integrin alpha5beta1.* Proc Natl Acad Sci U S A, 2016. **113**(27): p. E3872-81.
19. Sun, Z., Costell, M., and Fässler, R., *Integrin activation by talin, kindlin and mechanical forces.* Nature Cell Biology, 2019. **21**(1): p. 25-31.
20. Kim, C., Ye, F., and Ginsberg, M.H., *Regulation of integrin activation.* Annu Rev Cell Dev Biol, 2011. **27**: p. 321-45.
21. Li, J., et al., *Conformational equilibria and intrinsic affinities define integrin activation.* Embo j, 2017. **36**(5): p. 629-645.
22. Li, J. and Springer, T.A., *Energy landscape differences among integrins establish the framework for understanding activation.* J Cell Biol, 2018. **217**(1): p. 397-412.
23. Li, J. and Springer, T.A., *Integrin extension enables ultrasensitive regulation by cytoskeletal force.* Proc Natl Acad Sci U S A, 2017. **114**(18): p. 4685-4690.
24. Xu, Y., et al., *Filamin A regulates focal adhesion disassembly and suppresses breast cancer cell migration and invasion.* J Exp Med, 2010. **207**(11): p. 2421-37.
25. Pouwels, J., et al., *Negative regulators of integrin activity.* 2012. **125**(14): p. 3271-3280.

26. Kiema, T., et al., *The molecular basis of filamin binding to integrins and competition with talin.* Mol Cell, 2006. **21**(3): p. 337-47.
27. Rantala, J.K., et al., *SHARPIN is an endogenous inhibitor of β1-integrin activation.* Nat Cell Biol, 2011. **13**(11): p. 1315-24.
28. Bouvard, D., et al., *Integrin inactivators: balancing cellular functions in vitro and in vivo.* Nat Rev Mol Cell Biol, 2013. **14**(7): p. 430-42.
29. Tseng, H.-Y., et al., *LCP1 preferentially binds clasped αMβ2 integrin and attenuates leukocyte adhesion under flow.* Journal of Cell Science, 2018. **131**(22): p. jcs218214.
30. Winograd-Katz, S.E., et al., *The integrin adhesome: from genes and proteins to human disease.* Nat Rev Mol Cell Biol, 2014. **15**(4): p. 273-88.
31. Kanchanawong, P., et al., *Nanoscale architecture of integrin-based cell adhesions.* Nature, 2010. **468**(7323): p. 580-4.
32. Baade, T.P., C.; Baldrich, A.; Hauck, C. R., *Clustering of integrin β cytoplasmic domains triggers nascent adhesion formation and reveals a protozoan origin of the integrin-talin interaction.* Scientific Reports, 2019. **9**(1): p. 5728.
33. Legate, K.R., Wickström, S.A., and Fässler, R., *Genetic and cell biological analysis of integrin outside-in signaling.* 2009. **23**(4): p. 397-418.
34. Thomas, J.W., et al., *SH2- and SH3-mediated Interactions between Focal Adhesion Kinase and Src.* 1998. **273**(1): p. 577-583.
35. Legate, K.R. and Fässler, R., *Mechanisms that regulate adaptor binding to β-integrin cytoplasmic tails.* 2009. **122**(2): p. 187-198.
36. Rohwedder, I., *Integrin mediated regulation of vascular maturation and atherogenesis*. 2013, LMU.
37. Martel, V., et al., *Conformation, localization, and integrin binding of talin depend on its interaction with phosphoinositides.* J Biol Chem, 2001. **276**(24): p. 21217-27.
38. Ling, K., et al., *Type I gamma phosphatidylinositol phosphate kinase targets and regulates focal adhesions.* Nature, 2002. **420**(6911): p. 89-93.
39. Conti, F.J., et al., *Progressive myopathy and defects in the maintenance of myotendinous junctions in mice that lack talin 1 in skeletal muscle.* Development, 2008. **135**(11): p. 2043-53.
40. Conti, F.J., et al., *Talin 1 and 2 are required for myoblast fusion, sarcomere assembly and the maintenance of myotendinous junctions.* Development, 2009. **136**(21): p. 3597-606.
41. Monkley, S.J., et al., *Disruption of the talin gene arrests mouse development at the gastrulation stage.* Dev Dyn, 2000. **219**(4): p. 560-74.
42. Papagrigoriou, E., et al., *Activation of a vinculin-binding site in the talin rod involves rearrangement of a five-helix bundle.* Embo j, 2004. **23**(15): p. 2942-51.
43. Turner, C.E., Glenney, J.R., Jr., and Burridge, K., *Paxillin: a new vinculin-binding protein present in focal adhesions.* J Cell Biol, 1990. **111**(3): p. 1059-68.
44. DeMali, K.A., Barlow, C.A., and Burridge, K., *Recruitment of the Arp2/3 complex to vinculin: coupling membrane protrusion to matrix adhesion.* J Cell Biol, 2002. **159**(5): p. 881-91.
45. Laukaitis, C.M., et al., *Differential dynamics of alpha 5 integrin, paxillin, and alpha-actinin during formation and disassembly of adhesions in migrating cells.* J Cell Biol, 2001. **153**(7): p. 1427-40.
46. Brakebusch, C. and Fässler, R., *The integrin–actin connection, an eternal love affair.* 2003. **22**(10): p. 2324-2333.
47. Hannigan, G.E., et al., *Regulation of cell adhesion and anchorage-dependent growth by a new beta 1-integrin-linked protein kinase.* Nature, 1996. **379**(6560): p. 91-6.
48. Nikolopoulos, S.N. and Turner, C.E., *Actopaxin, a new focal adhesion protein that binds paxillin LD motifs and actin and regulates cell adhesion.* J Cell Biol, 2000. **151**(7): p. 1435-48.
49. Nikolopoulos, S.N. and Turner, C.E., *Integrin-linked kinase (ILK) binding to paxillin LD1 motif regulates ILK localization to focal adhesions.* J Biol Chem, 2001. **276**(26): p. 23499-505.

50. Stiegler, A.L., et al., *Structural basis for paxillin binding and focal adhesion targeting of β-parvin.* J Biol Chem, 2012. **287**(39): p. 32566-77.
51. Moro, L., et al., *Integrins induce activation of EGF receptor: role in MAP kinase induction and adhesion-dependent cell survival.* Embo j, 1998. **17**(22): p. 6622-32.
52. DeMali, K.A., Balciunaite, E., and Kazlauskas, A., *Integrins enhance platelet-derived growth factor (PDGF)-dependent responses by altering the signal relay enzymes that are recruited to the PDGF beta receptor.* J Biol Chem, 1999. **274**(28): p. 19551-8.
53. Borges, E., Jan, Y., and Ruoslahti, E., *Platelet-derived growth factor receptor beta and vascular endothelial growth factor receptor 2 bind to the beta 3 integrin through its extracellular domain.* J Biol Chem, 2000. **275**(51): p. 39867-73.
54. Soldi, R., et al., *Role of alphavbeta3 integrin in the activation of vascular endothelial growth factor receptor-2.* Embo j, 1999. **18**(4): p. 882-92.
55. Tseng, H.-Y., *Identification and characterization of conformation-specific cytoplasmic integrin interactors*. 2015, Ludwig-Maximilians-Universität München.
56. Walker, J.L., Fournier, A.K., and Assoian, R.K., *Regulation of growth factor signaling and cell cycle progression by cell adhesion and adhesion-dependent changes in cellular tension.* 2005. **16**(4-5): p. 395-405.
57. Webb, D.J., et al., *FAK-Src signalling through paxillin, ERK and MLCK regulates adhesion disassembly.* Nat Cell Biol, 2004. **6**(2): p. 154-61.
58. Slack-Davis , J.K., et al., *PAK1 phosphorylation of MEK1 regulates fibronectin-stimulated MAPK activation.* Journal of Cell Biology, 2003. **162**(2): p. 281-291.
59. Cukierman, E., et al., *Taking cell-matrix adhesions to the third dimension.* Science, 2001. **294**(5547): p. 1708-12.
60. Kano, Y., et al., *Macromolecular Composition of Stress Fiber-Plasma Membrane Attachment Sites in Endothelial Cells In Situ.* 1996. **79**(5): p. 1000-1006.
61. Turner, C.E., et al., *Localization of paxillin, a focal adhesion protein, to smooth muscle dense plaques, and the myotendinous and neuromuscular junctions of skeletal muscle.* Experimental Cell Research, 1991. **192**(2): p. 651-655.
62. Choi, C.K., et al., *Actin and alpha-actinin orchestrate the assembly and maturation of nascent adhesions in a myosin II motor-independent manner.* Nat Cell Biol, 2008. **10**(9): p. 1039-50.
63. Giannone, G., et al., *Lamellipodial actin mechanically links myosin activity with adhesion-site formation.* Cell, 2007. **128**(3): p. 561-75.
64. Rottner, K., Hall, A., and Small, J.V., *Interplay between Rac and Rho in the control of substrate contact dynamics.* Curr Biol, 1999. **9**(12): p. 640-8.
65. Lazarides, E. and Burridge, K., *Alpha-actinin: immunofluorescent localization of a muscle structural protein in nonmuscle cells.* Cell, 1975. **6**(3): p. 289-98.
66. Zaidel-Bar, R., et al., *Early molecular events in the assembly of matrix adhesions at the leading edge of migrating cells.* J Cell Sci, 2003. **116**(Pt 22): p. 4605-13.
67. Pankov, R., et al., *Integrin dynamics and matrix assembly: tensin-dependent translocation of alpha(5)beta(1) integrins promotes early fibronectin fibrillogenesis.* J Cell Biol, 2000. **148**(5): p. 1075-90.
68. Ladoux, B. and Nicolas, A., *Physically based principles of cell adhesion mechanosensitivity in tissues.* Rep Prog Phys, 2012. **75**(11): p. 116601.
69. Linder, S. and Kopp, P., *Podosomes at a glance.* 2005. **118**(10): p. 2079-2082.
70. Lock, J.G.J., et al., *Reticular adhesions are a distinct class of cell-matrix adhesions that mediate attachment during mitosis.* Nature Cell Biology, 2018. **20**(11): p. 1290-1302.
71. Sit, B., Gutmann, D., and Iskratsch, T., *Costameres, dense plaques and podosomes: the cell matrix adhesions in cardiovascular mechanosensing.* J Muscle Res Cell Motil, 2019. **40**(2): p. 197-209.

72. Bloch, R.J., et al., *Costameres: repeating structures at the sarcolemma of skeletal muscle.* Clin Orthop Relat Res, 2002(403 Suppl): p. S203-10.
73. Jaka, O., et al., *Costamere proteins and their involvement in myopathic processes.* Expert reviews in molecular medicine, 2015. **17**: p. e12.
74. Ward, M. and Iskratsch, T., *Mix and (mis-)match – The mechanosensing machinery in the changing environment of the developing, healthy adult and diseased heart.* Biochimica et Biophysica Acta (BBA) - Molecular Cell Research, 2020. **1867**(3): p. 118436.
75. Woo, S. and Gomez, T., *Integrin-dependent Adhesion Contacts*, in *Encyclopedia of Neuroscience*, Binder, M.D., Hirokawa, N., and Windhorst, U., Editors. 2009, Springer Berlin Heidelberg: Berlin, Heidelberg. p. 1988-1992.
76. Huveneers, S. and Danen, E.H.J., *Adhesion signaling – crosstalk between integrins, Src and Rho.* 2009. **122**(8): p. 1059-1069.
77. Takai, Y., et al., *Rho as a regulator of the cytoskeleton.* Trends in Biochemical Sciences, 1995. **20**(6): p. 227-231.
78. DerMardirossian, C. and Bokoch, G.M., *GDIs: central regulatory molecules in Rho GTPase activation.* Trends Cell Biol, 2005. **15**(7): p. 356-63.
79. Ridley, A.J. and Hall, A., *The small GTP-binding protein rho regulates the assembly of focal adhesions and actin stress fibers in response to growth factors.* 1992. **70**(3): p. 389-399.
80. Ridley, A.J., et al., *The small GTP-binding protein rac regulates growth factor-induced membrane ruffling.* 1992. **70**(3): p. 401-410.
81. Nobes, C.D. and Hall, A., *Rho, rac, and cdc42 GTPases regulate the assembly of multimolecular focal complexes associated with actin stress fibers, lamellipodia, and filopodia.* 1995. **81**(1): p. 53-62.
82. Etienne-Manneville, S. and Hall, A., *Rho GTPases in cell biology.* Nature, 2002. **420**(6916): p. 629-635.
83. Jaffe, A.B. and Hall, A., *Rho GTPases: biochemistry and biology.* Annu Rev Cell Dev Biol, 2005. **21**: p. 247-69.
84. Chen, B., et al., *The WAVE regulatory complex links diverse receptors to the actin cytoskeleton.* Cell, 2014. **156**(1-2): p. 195-207.
85. Hahne, P., et al., *Scar/WAVE is localised at the tips of protruding lamellipodia in living cells.* FEBS Lett, 2001. **492**(3): p. 215-20.
86. Ismail, A.M., et al., *The WAVE regulatory complex is inhibited.* Nat Struct Mol Biol, 2009. **16**(5): p. 561-3.
87. Heasman, S.J. and Ridley, A.J., *Mammalian Rho GTPases: new insights into their functions from in vivo studies.* Nat Rev Mol Cell Biol, 2008. **9**(9): p. 690-701.
88. Peng, J., et al., *Disruption of the Diaphanous-related formin Drf1 gene encoding mDia1 reveals a role for Drf3 as an effector for Cdc42.* 2003. **13**(7): p. 534-545.
89. Ji, P., Jayapal, S.R., and Lodish, H.F., *Enucleation of cultured mouse fetal erythroblasts requires Rac GTPases and mDia2.* Nat Cell Biol, 2008. **10**(3): p. 314-21.
90. Zigmond, S.H., *Formin-induced nucleation of actin filaments.* 2004. **16**(1): p. 99-105.
91. Mitra, S.K. and Schlaepfer, D.D., *Integrin-regulated FAK-Src signaling in normal and cancer cells.* Curr Opin Cell Biol, 2006. **18**(5): p. 516-23.
92. Brugnera, E., et al., *Unconventional Rac-GEF activity is mediated through the Dock180-ELMO complex.* Nat Cell Biol, 2002. **4**(8): p. 574-82.
93. Chodniewicz, D. and Klemke, R.L., *Regulation of integrin-mediated cellular responses through assembly of a CAS/Crk scaffold.* Biochim Biophys Acta, 2004. **1692**(2-3): p. 63-76.
94. Arthur, W.T. and Burridge, K., *RhoA Inactivation by p190RhoGAP Regulates Cell Spreading and Migration by Promoting Membrane Protrusion and Polarity.* 2001. **12**(9): p. 2711-2720.

95. Arthur, W.T., Petch, L.A., and Burridge, K., *Integrin engagement suppresses RhoA activity via a c-Src-dependent mechanism.* 2000. **10**(12): p. 719-722.
96. Ren, X.-d., et al., *Focal adhesion kinase suppresses Rho activity to promote focal adhesion turnover.* 2000. **113**(20): p. 3673-3678.
97. Ohta, Y., Hartwig, J.H., and Stossel, T.P., *FilGAP, a Rho- and ROCK-regulated GAP for Rac binds filamin A to control actin remodelling.* Nat Cell Biol, 2006. **8**(8): p. 803-14.
98. Saitoh, T., et al., *Differential localization of non-muscle myosin II isoforms and phosphorylated regulatory light chains in human MRC-5 fibroblasts.* FEBS Lett, 2001. **509**(3): p. 365-9.
99. André, G., et al., *Smooth muscle specific Rac1 deficiency induces hypertension by preventing p116RIP3-dependent RhoA inhibition.* J Am Heart Assoc, 2014. **3**(3): p. e000852.
100. Ishizaki, T., et al., *The small GTP-binding protein Rho binds to and activates a 160 kDa Ser/Thr protein kinase homologous to myotonic dystrophy kinase.* Embo j, 1996. **15**(8): p. 1885-93.
101. Ishizaki, T., et al., *p160ROCK, a Rho-associated coiled-coil forming protein kinase, works downstream of Rho and induces focal adhesions.* FEBS Lett, 1997. **404**(2-3): p. 118-24.
102. Liu, J., Gao, H.Y., and Wang, X.F., *The role of the Rho/ROCK signaling pathway in inhibiting axonal regeneration in the central nervous system.* Neural Regen Res, 2015. **10**(11): p. 1892-6.
103. Noma, K., Oyama, N., and Liao, J., *Physiological role of ROCKs in the cardiovascular system.* 2006. **290 3**: p. C661-8.
104. Nakagawa, O., et al., *ROCK-I and ROCK-II, two isoforms of Rho-associated coiled-coil forming protein serine/threonine kinase in mice.* FEBS Lett, 1996. **392**(2): p. 189-93.
105. Schmandke, A., Schmandke, A., and Strittmatter, S.M., *ROCK and Rho: biochemistry and neuronal functions of Rho-associated protein kinases.* Neuroscientist, 2007. **13**(5): p. 454-69.
106. Tan, H.B., et al., *Rho/ROCK pathway and neural regeneration: a potential therapeutic target for central nervous system and optic nerve damage.* Int J Ophthalmol, 2011. **4**(6): p. 652-7.
107. Kimura, K., et al., *Regulation of Myosin Phosphatase by Rho and Rho-Associated Kinase (Rho-Kinase).* 1996. **273**(5272): p. 245-248.
108. Feng, J., et al., *Inhibitory phosphorylation site for Rho-associated kinase on smooth muscle myosin phosphatase.* J Biol Chem, 1999. **274**(52): p. 37385-90.
109. Wooldridge, A.A., et al., *Smooth muscle phosphatase is regulated in vivo by exclusion of phosphorylation of threonine 696 of MYPT1 by phosphorylation of Serine 695 in response to cyclic nucleotides.* J Biol Chem, 2004. **279**(33): p. 34496-504.
110. Ito, M., et al., *Myosin phosphatase: structure, regulation and function.* Mol Cell Biochem, 2004. **259**(1-2): p. 197-209.
111. Somlyo, A.P. and Somlyo, A.V., *Ca2+ sensitivity of smooth muscle and nonmuscle myosin II: modulated by G proteins, kinases, and myosin phosphatase.* Physiol Rev, 2003. **83**(4): p. 1325-58.
112. Maekawa, M., et al., *Signaling from Rho to the actin cytoskeleton through protein kinases ROCK and LIM-kinase.* Science, 1999. **285**(5429): p. 895-8.
113. Ohashi, K., et al., *Rho-associated kinase ROCK activates LIM-kinase 1 by phosphorylation at threonine 508 within the activation loop.* J Biol Chem, 2000. **275**(5): p. 3577-82.
114. Sumi, T., Matsumoto, K., and Nakamura, T., *Specific activation of LIM kinase 2 via phosphorylation of threonine 505 by ROCK, a Rho-dependent protein kinase.* J Biol Chem, 2001. **276**(1): p. 670-6.
115. Abe, K., et al., *Long-term treatment with a Rho-kinase inhibitor improves monocrotaline-induced fatal pulmonary hypertension in rats.* Circ Res, 2004. **94**(3): p. 385-93.
116. Higashi, M., et al., *Long-term inhibition of Rho-kinase suppresses angiotensin II-induced cardiovascular hypertrophy in rats in vivo: effect on endothelial NAD(P)H oxidase system.* Circ Res, 2003. **93**(8): p. 767-75.
117. Hyvelin, J.M., et al., *Inhibition of Rho-kinase attenuates hypoxia-induced angiogenesis in the pulmonary circulation.* Circ Res, 2005. **97**(2): p. 185-91.

118. Mallat, Z., et al., *Rho-associated protein kinase contributes to early atherosclerotic lesion formation in mice.* Circ Res, 2003. **93**(9): p. 884-8.
119. Miyata, K., et al., *Rho-kinase is involved in macrophage-mediated formation of coronary vascular lesions in pigs in vivo.* Arterioscler Thromb Vasc Biol, 2000. **20**(11): p. 2351-8.
120. Sato, M., et al., *Involvement of Rho-kinase-mediated phosphorylation of myosin light chain in enhancement of cerebral vasospasm.* Circ Res, 2000. **87**(3): p. 195-200.
121. Toshima, Y., et al., *A new model of cerebral microthrombosis in rats and the neuroprotective effect of a Rho-kinase inhibitor.* Stroke, 2000. **31**(9): p. 2245-50.
122. Uehata, M., et al., *Calcium sensitization of smooth muscle mediated by a Rho-associated protein kinase in hypertension.* Nature, 1997. **389**(6654): p. 990-4.
123. Fukumoto, Y., et al., *Acute vasodilator effects of a Rho-kinase inhibitor, fasudil, in patients with severe pulmonary hypertension.* Heart, 2005. **91**(3): p. 391-2.
124. Kishi, T., et al., *Rho-kinase inhibitor improves increased vascular resistance and impaired vasodilation of the forearm in patients with heart failure.* Circulation, 2005. **111**(21): p. 2741-7.
125. Masumoto, A., et al., *Possible involvement of Rho-kinase in the pathogenesis of hypertension in humans.* Hypertension, 2001. **38**(6): p. 1307-10.
126. Masumoto, A., et al., *Suppression of coronary artery spasm by the Rho-kinase inhibitor fasudil in patients with vasospastic angina.* Circulation, 2002. **105**(13): p. 1545-7.
127. Shibuya, M., et al., *Effects of fasudil in acute ischemic stroke: results of a prospective placebo-controlled double-blind trial.* J Neurol Sci, 2005. **238**(1-2): p. 31-9.
128. Garnock-Jones, K.P., *Ripasudil: first global approval.* 2014. **74**(18): p. 2211-2215.
129. Mulherkar, S. and Tolias, K.F., *RhoA-ROCK Signaling as a Therapeutic Target in Traumatic Brain Injury.* Cells, 2020. **9**(1).
130. Foth, B.J., Goedecke, M.C., and Soldati, D., *New insights into myosin evolution and classification.* 2006. **103**(10): p. 3681-3686.
131. Richards, T.A. and Cavalier-Smith, T., *Myosin domain evolution and the primary divergence of eukaryotes.* Nature, 2005. **436**(7054): p. 1113-8.
132. Conti, M.A. and Adelstein, R.S., *Nonmuscle myosin II moves in new directions.* 2008. **121**(1): p. 11-18.
133. Yuen, S.L., Ogut, O., and Brozovich, F.V., *Nonmuscle myosin is regulated during smooth muscle contraction.* Am J Physiol Heart Circ Physiol, 2009. **297**(1): p. H191-9.
134. Zhang, W. and Gunst, S.J., *Non-muscle (NM) myosin heavy chain phosphorylation regulates the formation of NM myosin filaments, adhesome assembly and smooth muscle contraction.* 2017. **595**(13): p. 4279-4300.
135. Morano, I., et al., *Smooth-muscle contraction without smooth-muscle myosin.* Nat Cell Biol, 2000. **2**(6): p. 371-5.
136. Vicente-Manzanares, M., et al., *Non-muscle myosin II takes centre stage in cell adhesion and migration.* Nature Reviews Molecular Cell Biology, 2009. **10**(11): p. 778-790.
137. Rodriguez, O.C. and Cheney, R.E., *A new direction for myosin.* Trends in Cell Biology, 2000. **10**(8): p. 307-311.
138. Dasbiswas, K., et al., *Ordering of myosin II filaments driven by mechanical forces: experiments and theory.* 2018. **373**(1747): p. 20170114.
139. Zhidkova, N.I., Belkin, A.M., and Mayne, R., *Novel isoform of beta 1 integrin expressed in skeletal and cardiac muscle.* Biochem Biophys Res Commun, 1995. **214**(1): p. 279-85.
140. van der Flier, A., et al., *A novel beta 1 integrin isoform produced by alternative splicing: unique expression in cardiac and skeletal muscle.* FEBS Lett, 1995. **369**(2-3): p. 340-4.
141. Brancaccio, M., et al., *Differential onset of expression of alpha 7 and beta 1D integrins during mouse heart and skeletal muscle development.* Cell Adhes Commun, 1998. **5**(3): p. 193-205.

142. van der Flier, A., et al., *Spatial and temporal expression of the beta1D integrin during mouse development.* Dev Dyn, 1997. **210**(4): p. 472-86.
143. Shai, S.-Y., et al., *Cardiac Myocyte-Specific Excision of the beta1 Integrin Gene Results in Myocardial Fibrosis and Cardiac Failure.* 2002. **90**(4): p. 458-464.
144. Belkin, A.M., et al., *Beta 1D integrin displaces the beta 1A isoform in striated muscles: localization at junctional structures and signaling potential in nonmuscle cells.* J Cell Biol, 1996. **132**(1-2): p. 211-26.
145. Israeli-Rosenberg, S., et al., *Integrins and integrin-associated proteins in the cardiac myocyte.* Circ Res, 2014. **114**(3): p. 572-586.
146. Flamme, I., Frolich, T., and Risau, W., *Molecular mechanisms of vasculogenesis and embryonic angiogenesis.* J Cell Physiol, 1997. **173**(2): p. 206-10.
147. Rupp, P.A. and Little, C.D., *Integrins in vascular development.* Circ Res, 2001. **89**(7): p. 566-72.
148. Malinin, N.L., Pluskota, E., and Byzova, T.V., *Integrin signaling in vascular function.* Curr Opin Hematol, 2012. **19**(3): p. 206-11.
149. Tabatabai, G. and Weller, M., *Role of Integrins in Angiogenesis*, in *Biochemical Basis and Therapeutic Implications of Angiogenesis*, Mehta, J.L. and Dhalla, N.S., Editors. 2013, Springer New York: New York, NY. p. 79-91.
150. Scheppke, L., et al., *Notch promotes vascular maturation by inducing integrin-mediated smooth muscle cell adhesion to the endothelial basement membrane.* Blood, 2012. **119**(9): p. 2149-58.
151. Mahabeleshwar, G.H., et al., *Mechanisms of integrin-vascular endothelial growth factor receptor cross-activation in angiogenesis.* Circ Res, 2007. **101**(6): p. 570-80.
152. Lakshmikanthan, S., et al., *Rap1 promotes VEGFR2 activation and angiogenesis by a mechanism involving integrin αvβ3.* Blood, 2011. **118**(7): p. 2015-2026.
153. Worthington, J.J., Klementowicz, J.E., and Travis, M.A., *TGFβ: a sleeping giant awoken by integrins.* Trends Biochem Sci, 2011. **36**(1): p. 47-54.
154. Drake, C.J. and Little, C.D., *The Morphogenesis of Primordial Vascular Networks*, in *Vascular Morphogenesis: In Vivo, In Vitro, In Mente*, Little, C.D., Mironov, V., and Sage, E.H., Editors. 1996, Birkhäuser Boston: Boston, MA. p. 3-19.
155. Rüegg, C. and Mariotti, A., *Vascular integrins: pleiotropic adhesion and signaling molecules in vascular homeostasis and angiogenesis.* Cellular and Molecular Life Sciences CMLS, 2003. **60**(6): p. 1135-1157.
156. Abraham, S., et al., *Integrin beta1 subunit controls mural cell adhesion, spreading, and blood vessel wall stability.* Circ Res, 2008. **102**(5): p. 562-70.
157. Kogata, N., et al., *Integrin-linked kinase controls vascular wall formation by negatively regulating Rho/ROCK-mediated vascular smooth muscle cell contraction.* Genes Dev, 2009. **23**(19): p. 2278-83.
158. Serini, G., Valdembri, D., and Bussolino, F., *Integrins and angiogenesis: A sticky business.* Experimental Cell Research, 2006. **312**(5): p. 651-658.
159. Small, J.V. and Gimona, M., *The cytoskeleton of the vertebrate smooth muscle cell.* Acta Physiol Scand, 1998. **164**(4): p. 341-8.
160. Shen, D., et al., *Aortic aneurysm generation in mice with targeted deletion of integrin-linked kinase in vascular smooth muscle cells.* Circ Res, 2011. **109**(6): p. 616-28.
161. Legate, K.R., et al., *ILK, PINCH and parvin: the tIPP of integrin signalling.* Nat Rev Mol Cell Biol, 2006. **7**(1): p. 20-31.
162. Tu, Y., et al., *A new focal adhesion protein that interacts with integrin-linked kinase and regulates cell adhesion and spreading.* J Cell Biol, 2001. **153**(3): p. 585-98.
163. Yamaji, S., et al., *A novel integrin-linked kinase-binding protein, affixin, is involved in the early stage of cell-substrate interaction.* J Cell Biol, 2001. **153**(6): p. 1251-64.

164. Korenbaum, E., Olski, T.M., and Noegel, A.A., *Genomic organization and expression profile of the parvin family of focal adhesion proteins in mice and humans.* Gene, 2001. **279**(1): p. 69-79.
165. Olski, T.M., Noegel, A.A., and Korenbaum, E., *Parvin, a 42 kDa focal adhesion protein, related to the alpha-actinin superfamily.* J Cell Sci, 2001. **114**(Pt 3): p. 525-38.
166. Qin, J. and Wu, C., *ILK: a pseudokinase in the center stage of cell-matrix adhesion and signaling.* Curr Opin Cell Biol, 2012. **24**(5): p. 607-13.
167. Gimona, M., et al., *Functional plasticity of CH domains.* FEBS Lett, 2002. **513**(1): p. 98-106.
168. Renault, L., Bugyi, B., and Carlier, M.F., *Spire and Cordon-bleu: multifunctional regulators of actin dynamics.* Trends Cell Biol, 2008. **18**(10): p. 494-504.
169. Yoshimi, R., et al., *The gamma-parvin-integrin-linked kinase complex is critically involved in leukocyte-substrate interaction.* J Immunol, 2006. **176**(6): p. 3611-24.
170. Chu, H., et al., *γ-Parvin Is Dispensable for Hematopoiesis, Leukocyte Trafficking, and T-Cell-Dependent Antibody Response.* 2006. **26**(5): p. 1817-1825.
171. Montanez, E., et al., *Alpha-parvin controls vascular mural cell recruitment to vessel wall by regulating RhoA/ROCK signalling.* Embo j, 2009. **28**(20): p. 3132-44.
172. Krüger, M., et al., *SILAC Mouse for Quantitative Proteomics Uncovers Kindlin-3 as an Essential Factor for Red Blood Cell Function.* Cell, 2008. **134**(2): p. 353-364.
173. Zhang, Y., et al., *Distinct roles of two structurally closely related focal adhesion proteins, alpha-parvins and beta-parvins, in regulation of cell morphology and survival.* J Biol Chem, 2004. **279**(40): p. 41695-705.
174. Sepulveda, J.L. and Wu, C., *The parvins.* Cell Mol Life Sci, 2006. **63**(1): p. 25-35.
175. Lorenz, S., et al., *Structural analysis of the interactions between paxillin LD motifs and alpha-parvin.* Structure, 2008. **16**(10): p. 1521-31.
176. Wang, X., et al., *The structure of alpha-parvin CH2-paxillin LD1 complex reveals a novel modular recognition for focal adhesion assembly.* J Biol Chem, 2008. **283**(30): p. 21113-9.
177. Matsuda, C., et al., *Affixin activates Rac1 via βPIX in C2C12 myoblast.* 2008. **582**(8): p. 1189-1196.
178. Pignatelli, J., et al., *Actopaxin (α-parvin) phosphorylation is required for matrix degradation and cancer cell invasion.* The Journal of biological chemistry, 2012. **287**(44): p. 37309-37320.
179. Rosenberger, G., et al., *Interaction of αPIX (ARHGEF6) with β-parvin (PARVB) suggests an involvement of αPIX in integrin-mediated signaling.* Human Molecular Genetics, 2003. **12**(2): p. 155-167.
180. Yamaji, S., et al., *Affixin interacts with α-actinin and mediates integrin signaling for reorganization of F-actin induced by initial cell–substrate interaction.* 2004. **165**(4): p. 539-551.
181. Nikolopoulos, S.N. and Turner, C.E., *Molecular dissection of actopaxin-integrin-linked kinase-Paxillin interactions and their role in subcellular localization.* J Biol Chem, 2002. **277**(2): p. 1568-75.
182. LaLonde, D.P., et al., *Actopaxin interacts with TESK1 to regulate cell spreading on fibronectin.* J Biol Chem, 2005. **280**(22): p. 21680-8.
183. Clarke, D.M., et al., *Phosphorylation of actopaxin regulates cell spreading and migration.* J Cell Biol, 2004. **166**(6): p. 901-12.
184. LaLonde, D.P., et al., *CdGAP associates with actopaxin to regulate integrin-dependent changes in cell morphology and motility.* Curr Biol, 2006. **16**(14): p. 1375-85.
185. Curtis, M., Nikolopoulos, S.N., and Turner, C.E., *Actopaxin is phosphorylated during mitosis and is a substrate for cyclin B1/cdc2 kinase.* Biochem J, 2002. **363**(Pt 2): p. 233-42.
186. Yang, Y., et al., *Formation and phosphorylation of the PINCH-1-integrin linked kinase-alpha-parvin complex are important for regulation of renal glomerular podocyte adhesion, architecture, and survival.* J Am Soc Nephrol, 2005. **16**(7): p. 1966-76.
187. Fukuda , T., et al., *CH-ILKBP regulates cell survival by facilitating the membrane translocation of protein kinase B/Akt.* Journal of Cell Biology, 2003. **160**(7): p. 1001-1008.

188. Wu, C., *The PINCH-ILK-parvin complexes: assembly, functions and regulation.* Biochim Biophys Acta, 2004. **1692**(2-3): p. 55-62.
189. Wu, C., *ILK interactions.* J Cell Sci, 2001. **114**(Pt 14): p. 2549-50.
190. Zhang, Y., et al., *Assembly of the PINCH-ILK-CH-ILKBP complex precedes and is essential for localization of each component to cell-matrix adhesion sites.* 2002. **115**(24): p. 4777-4786.
191. Wu, C., *PINCH, N(i)ck and the ILK: network wiring at cell-matrix adhesions.* Trends Cell Biol, 2005. **15**(9): p. 460-6.
192. Fukuda, T., et al., *PINCH-1 is an obligate partner of integrin-linked kinase (ILK) functioning in cell shape modulation, motility, and survival.* J Biol Chem, 2003. **278**(51): p. 51324-33.
193. Zhang, Y., et al., *Characterization of PINCH-2, a new focal adhesion protein that regulates the PINCH-1-ILK interaction, cell spreading, and migration.* Journal of Biological Chemistry, 2002. **277**(41): p. 38328-38338.
194. White, D.E., et al., *Targeted ablation of ILK from the murine heart results in dilated cardiomyopathy and spontaneous heart failure.* Genes Dev, 2006. **20**(17): p. 2355-60.
195. Zervas, C.G., Gregory, S.L., and Brown, N.H., *Drosophila integrin-linked kinase is required at sites of integrin adhesion to link the cytoskeleton to the plasma membrane.* 2001. **152**(5): p. 1007-1018.
196. Mackinnon, A.C., et al., *C. elegans PAT-4/ILK Functions as an Adaptor Protein within Integrin Adhesion Complexes.* Current Biology, 2002. **12**(10): p. 787-797.
197. Wickström, S.A., et al., *The ILK/PINCH/parvin complex: the kinase is dead, long live the pseudokinase!* 2010. **29**(2): p. 281-291.
198. Delcommenne, M., et al., *Phosphoinositide-3-OH kinase-dependent regulation of glycogen synthase kinase 3 and protein kinase B/AKT by the integrin-linked kinase.* 1998. **95**(19): p. 11211-11216.
199. Tu, Y., et al., *The LIM-only protein PINCH directly interacts with integrin-linked kinase and is recruited to integrin-rich sites in spreading cells.* Mol Cell Biol, 1999. **19**(3): p. 2425-34.
200. Braun, A., et al., *PINCH2 is a new five LIM domain protein, homologous to PINCHand localized to focal adhesions.* Exp Cell Res, 2003. **284**(2): p. 239-50.
201. Lin, X., et al., *C. elegans PAT-6/Actopaxin Plays a Critical Role in the Assembly of Integrin Adhesion Complexes In Vivo.* Current Biology, 2003. **13**(11): p. 922-932.
202. Norman, K.R., et al., *UNC-97/PINCH is involved in the assembly of integrin cell adhesion complexes in Caenorhabditis elegans body wall muscle.* Developmental Biology, 2007. **309**(1): p. 45-55.
203. Clark, K.A., McGrail, M., and Beckerle, M.C., *Analysis of PINCH function in Drosophila demonstrates its requirement in integrin-dependent cellular processes.* Development, 2003. **130**(12): p. 2611-21.
204. Li, S., et al., *PINCH1 regulates cell-matrix and cell-cell adhesions, cell polarity and cell survival during the peri-implantation stage.* J Cell Sci, 2005. **118**(Pt 13): p. 2913-21.
205. Sakai, T., et al., *Integrin-linked kinase (ILK) is required for polarizing the epiblast, cell adhesion, and controlling actin accumulation.* Genes Dev, 2003. **17**(7): p. 926-40.
206. Stanchi, F., et al., *Consequences of loss of PINCH2 expression in mice.* 2005. **118**(24): p. 5899-5910.
207. Lange, A., et al., *Integrin-linked kinase is an adaptor with essential functions during mouse development.* Nature, 2009. **461**(7266): p. 1002-1006.
208. Cheng, J., et al., *Mechanical stretch inhibits oxidized low density lipoprotein-induced apoptosis in vascular smooth muscle cells by up-regulating integrin alphavbeta3 and stablization of PINCH-1.* J Biol Chem, 2007. **282**(47): p. 34268-75.
209. Meder, B., et al., *PINCH proteins regulate cardiac contractility by modulating integrin-linked kinase-protein kinase B signaling.* Mol Cell Biol, 2011. **31**(16): p. 3424-35.
210. Bendig, G., et al., *Integrin-linked kinase, a novel component of the cardiac mechanical stretch sensor, controls contractility in the zebrafish heart.* Genes Dev, 2006. **20**(17): p. 2361-72.

211. Liang, X., et al., *Targeted ablation of PINCH1 and PINCH2 from murine myocardium results in dilated cardiomyopathy and early postnatal lethality.* Circulation, 2009. **120**(7): p. 568-76.
212. Lu, H., et al., *Integrin-Linked Kinase Expression Is Elevated in Human Cardiac Hypertrophy and Induces Hypertrophy in Transgenic Mice.* 2006. **114**(21): p. 2271-2279.
213. Liang, X., et al., *PINCH1 plays an essential role in early murine embryonic development but is dispensable in ventricular cardiomyocytes.* Mol Cell Biol, 2005. **25**(8): p. 3056-62.
214. Mulder, J., et al., *Inhibition of RhoA-mediated SRF activation by p116Rip.* FEBS Lett, 2005. **579**(27): p. 6121-7.
215. Gebbink, M.F., et al., *Identification of a novel, putative Rho-specific GDP/GTP exchange factor and a RhoA-binding protein: control of neuronal morphology.* J Cell Biol, 1997. **137**(7): p. 1603-13.
216. Surks, H.K., Richards, C.T., and Mendelsohn, M.E., *Myosin phosphatase-Rho interacting protein. A new member of the myosin phosphatase complex that directly binds RhoA.* J Biol Chem, 2003. **278**(51): p. 51484-93.
217. Koga, Y. and Ikebe, M., *p116Rip decreases myosin II phosphorylation by activating myosin light chain phosphatase and by inactivating RhoA.* J Biol Chem, 2005. **280**(6): p. 4983-91.
218. Lee, E. and Stafford, W.F., 3rd, *Interaction of Myosin Phosphatase Target Subunit (MYPT1) with Myosin Phosphatase-RhoA Interacting Protein (MRIP): A Role of Glutamic Acids in the Interaction.* PLoS One, 2015. **10**(10): p. e0139875.
219. Mulder, J., et al., *p116Rip is a novel filamentous actin-binding protein.* J Biol Chem, 2003. **278**(29): p. 27216-23.
220. Mulder, J., et al., *p116Rip targets myosin phosphatase to the actin cytoskeleton and is essential for RhoA/ROCK-regulated neuritogenesis.* Mol Biol Cell, 2004. **15**(12): p. 5516-27.
221. Riddick, N., Ohtani, K., and Surks, H.K., *Targeting by myosin phosphatase-RhoA interacting protein mediates RhoA/ROCK regulation of myosin phosphatase.* J Cell Biochem, 2008. **103**(4): p. 1158-70.
222. Surks, H.K., et al., *Regulation of myosin phosphatase by a specific interaction with cGMP- dependent protein kinase Iα.* Science, 1999. **286**(5444): p. 1583-1587.
223. Mahavadi, S., et al., *Inhibition of MLC20 phosphorylation downstream of Ca2+ and RhoA: A novel mechanism involving phosphorylation of myosin phosphatase interacting protein (M-RIP) by PKG and stimulation of MLC phosphatase activity.* Cell Biochem Biophys, 2014. **68**(1): p. 1-8.
224. Surks, H.K., Riddick, N., and Ohtani, K., *M-RIP targets myosin phosphatase to stress fibers to regulate myosin light chain phosphorylation in vascular smooth muscle cells.* J Biol Chem, 2005. **280**(52): p. 42543-51.
225. Homma, Y. and Emori, Y., *A dual functional signal mediator showing RhoGAP and phospholipase C-delta stimulating activities.* Embo j, 1995. **14**(2): p. 286-91.
226. Durkin, M.E., et al., *Gene structure, tissue expression, and linkage mapping of the mouse DLC-1 gene (Arhgap7).* Gene, 2002. **288**(1): p. 119-127.
227. Liao, Y.-C. and Lo, S.H., *Deleted in liver cancer-1 (DLC-1): A tumor suppressor not just for liver.* The International Journal of Biochemistry & Cell Biology, 2008. **40**(5): p. 843-847.
228. Yuan, B.Z., et al., *Cloning, characterization, and chromosomal localization of a gene frequently deleted in human liver cancer (DLC-1) homologous to rat RhoGAP.* Cancer Res, 1998. **58**(10): p. 2196-9.
229. Liao, Y.-C., et al., *The phosphotyrosine-independent interaction of DLC-1 and the SH2 domain of cten regulates focal adhesion localization and growth suppression activity of DLC-1.* Journal of Cell Biology, 2006. **176**(1): p. 43-49.
230. Zacharchenko, T., et al., *LD Motif Recognition by Talin: Structure of the Talin-DLC1 Complex.* Structure, 2016. **24**(7): p. 1130-41.
231. Scholz, R.-P., et al., *DLC1 interacts with 14-3-3 proteins to inhibit RhoGAP activity and block nucleocytoplasmic shuttling.* 2009. **122**(1): p. 92-102.

232. Tanaka, M., et al., *Colocalization of IQGAP1 with DLC-1 and PLC-δ1; Its potential role in coronary spasm.* 2019: p. 526152.
233. Sekimata, M., et al., *Morphological changes and detachment of adherent cells induced by p122, a GTPase-activating protein for Rho.* Journal of Biological Chemistry, 1999. **274**(25): p. 17757-17762.
234. Zhou, X., Thorgeirsson, S.S., and Popescu, N.C., *Restoration of DLC-1 gene expression induces apoptosis and inhibits both cell growth and tumorigenicity in human hepatocellular carcinoma cells.* Oncogene, 2004. **23**(6): p. 1308-1313.
235. Durkin, M.E., et al., *DLC-1, a Rho GTPase-activating protein with tumor suppressor function, is essential for embryonic development.* FEBS Letters, 2005. **579**(5): p. 1191-1196.
236. Sabbir, M.G., et al., *Identification and characterization of Dlc1 isoforms in the mouse and study of the biological function of a single gene trapped isoform.* BMC Biol, 2010. **8**: p. 17.
237. Durkin, M.E., et al., *DLC-1:a Rho GTPase-activating protein and tumour suppressor.* J Cell Mol Med, 2007. **11**(5): p. 1185-207.
238. Qian, X., et al., *Oncogenic inhibition by a deleted in liver cancer gene requires cooperation between tensin binding and Rho-specific GTPase-activating protein activities.* 2007. **104**(21): p. 9012-9017.
239. Yam, J.W.P., et al., *Interaction of Deleted in Liver Cancer 1 with Tensin2 in Caveolae and Implications in Tumor Suppression.* 2006. **66**(17): p. 8367-8372.
240. Lo, S.H., *Tensin.* Int J Biochem Cell Biol, 2004. **36**(1): p. 31-4.
241. Kim, T.Y., et al., *Effects of structure of Rho GTPase-activating protein DLC-1 on cell morphology and migration.* J Biol Chem, 2008. **283**(47): p. 32762-70.
242. Cao, X., et al., *Differential regulation of the activity of deleted in liver cancer 1 (DLC1) by tensins controls cell migration and transformation.* 2012. **109**(5): p. 1455-1460.
243. Tripathi, B.K., et al., *CDK5 is a major regulator of the tumor suppressor DLC1.* Journal of Cell Biology, 2014. **207**(5): p. 627-642.
244. Ravi, A., et al., *Epidermal growth factor activates the Rho GTPase-activating protein (GAP) Deleted in Liver Cancer 1 via focal adhesion kinase and protein phosphatase 2A.* J Biol Chem, 2015. **290**(7): p. 4149-62.
245. Tripathi, B.K., et al., *SRC and ERK cooperatively phosphorylate DLC1 and attenuate its Rho-GAP and tumor suppressor functions.* J Cell Biol, 2019. **218**(9): p. 3060-3076.
246. Shih, Y.P., et al., *Tensin1 positively regulates RhoA activity through its interaction with DLC1.* Biochim Biophys Acta, 2015. **1853**(12): p. 3258-65.
247. Campbell, N.A. and Reece, J.B., *Kreislaufsysteme verknüpfen alle Zellen des Körpers mit Austauschflächen*, in *Biologie*. 2009, Pearson Studium.
248. Woodcock, E.A. and Matkovich, S.J., *Cardiomyocytes structure, function and associated pathologies.* Int J Biochem Cell Biol, 2005. **37**(9): p. 1746-51.
249. Olson, E.N., *A decade of discoveries in cardiac biology.* Nat Med, 2004. **10**(5): p. 467-74.
250. Doll, S., et al., *Region and cell-type resolved quantitative proteomic map of the human heart.* Nat Commun, 2017. **8**(1): p. 1469.
251. Gray, H., *The heart*, in *Anatomy of the human Body*, Lewis, W.H., Editor. 1918, Philadelphia: Lea & Febiger, 1918: Bartleby.com, 2000.
252. Larsson, M., *Quantification and Visualization of Cardiovascular Function using Ultrasound*. 2009, KTH Technology and Health: Stockholm: KTH , 2009.
253. Institute, T.H. *Heart Anatomy*. [cited 2020; Available from: https://www.texasheart.org/heart-health/heart-information-center/topics/heart-anatomy/.
254. Adams, R.H. and Alitalo, K., *Molecular regulation of angiogenesis and lymphangiogenesis.* Nature Reviews Molecular Cell Biology, 2007. **8**(6): p. 464-478.
255. Aaronson, P.I., Ward, J.P.T., and Connolly, M.J., *The Cardiovascular System at a Glance*. 2020: Wiley.

256. Miller, L.M. and Gal, A., *Chapter 10 - Cardiovascular System and Lymphatic Vessels1*, in *Pathologic Basis of Veterinary Disease (Sixth Edition)*, Zachary, J.F., Editor. 2017, Mosby. p. 561-616.e1.
257. Müller, B., et al., *High-resolution tomographic imaging of microvessels*. Optical Engineering + Applications. Vol. 7078. 2008: SPIE.
258. Bailey, R., *The 3 layers of the heart wall*. 2019: ThoughtCo. website.
259. Miller, L.M. and Gal, A., *Cardiovascular System and Lymphatic Vessels*, in *Pathologic Basis of Veterinary Disease*, Zachary, J.F., Editor. 2017, Elsevier p. 561-616.e1.
260. Dzialowski, E.M. and Crossley, D.A., *Chapter 11 - The Cardiovascular System*, in *Sturkie's Avian Physiology (Sixth Edition)*, Scanes, C.G., Editor. 2015, Academic Press: San Diego. p. 193-283.
261. Rehman, I. and Rehman, A., *Anatomy, Thorax, Pericardium*. Updated 2018 Dec 9, StatPearls [Internet]. Treasure Island (FL): StatPearls Publishing; 2020.
262. Vekilov, D.P. and Grande-Allen, K.J., *Mechanical Properties of Diseased Veins.* Methodist DeBakey cardiovascular journal, 2018. **14**(3): p. 182-187.
263. Tucker, W.D., Arora, Y., and Mahajan, K., *Anatomy, Blood Vessels*. 2020: StatPearls [Internet].
264. OpenStax, *Structure and Function of Blood Vessels*, in *Anatomy and Physiology* OpenStax.
265. Wagner, D.D. and Frenette, P.S., *The vessel wall and its interactions.* Blood, 2008. **111**(11): p. 5271-5281.
266. Wagenseil, J.E. and Mecham, R.P., *Vascular extracellular matrix and arterial mechanics.* Physiol Rev, 2009. **89**(3): p. 957-89.
267. Mazurek, R., et al., *Vascular Cells in Blood Vessel Wall Development and Disease.* Adv Pharmacol, 2017. **78**: p. 323-350.
268. Betts, J.G., et al., *Anatomy & Physiology*. 2013: OpenStax.
269. Xin, M., Olson, E.N., and Bassel-Duby, R., *Mending broken hearts: cardiac development as a basis for adult heart regeneration and repair.* Nat Rev Mol Cell Biol, 2013. **14**(8): p. 529-41.
270. Howard, C.M. and Baudino, T.A., *Dynamic cell-cell and cell-ECM interactions in the heart.* J Mol Cell Cardiol, 2014. **70**: p. 19-26.
271. Baum, J. and Duffy, H.S., *Fibroblasts and myofibroblasts: what are we talking about?* J Cardiovasc Pharmacol, 2011. **57**(4): p. 376-9.
272. Tomasek, J.J., et al., *Myofibroblasts and mechano-regulation of connective tissue remodelling.* Nature Reviews Molecular Cell Biology, 2002. **3**(5): p. 349-363.
273. Reiss, K., et al., *Overexpression of insulin-like growth factor-1 in the heart is coupled with myocyte proliferation in transgenic mice.* Proc Natl Acad Sci U S A, 1996. **93**(16): p. 8630-5.
274. Zaruba, M.M. and Field, L.J., *The mouse as a model system to study cardiac regeneration.* Drug Discov Today Dis Models, 2008. **5**(3): p. 165-171.
275. Walsh, S.P., A.; Fleischmann, B. K.; Jovinge, S., *Cardiomyocyte cell cycle control and growth estimation in vivo—an analysis based on cardiomyocyte nuclei.* Cardiovascular Research, 2010. **86**(3): p. 365-373.
276. Dora, K.A., *Cell-cell communication in the vessel wall.* Vasc Med, 2001. **6**(1): p. 43-50.
277. Pouget, C., et al., *Somite-derived cells replace ventral aortic hemangioblasts and provide aortic smooth muscle cells of the trunk.* Development, 2006. **133**(6): p. 1013-22.
278. Risau, W. and Flamme, I., *Vasculogenesis.* Annu Rev Cell Dev Biol, 1995. **11**: p. 73-91.
279. Lilly, B., *We have contact: endothelial cell-smooth muscle cell interactions.* Physiology (Bethesda), 2014. **29**(4): p. 234-41.
280. Aplin, A.C., Fogel, E., and Nicosia, R.F., *MCP-1 promotes mural cell recruitment during angiogenesis in the aortic ring model.* 2010. **13**(3): p. 219-226.
281. Armulik, A., Abramsson, A., and Betsholtz, C., *Endothelial/pericyte interactions.* Circ Res, 2005. **97**(6): p. 512-23.

282. Hellström, M., et al., *Role of PDGF-B and PDGFR-beta in recruitment of vascular smooth muscle cells and pericytes during embryonic blood vessel formation in the mouse.* 1999. **126**(14): p. 3047-3055.
283. Hirschi, K.K., et al., *Gap junction communication mediates transforming growth factor-β activation and endothelial-induced mural cell differentiation.* 2003. **93**(5): p. 429-437.
284. Hirschi, K.K., et al., *Endothelial cells modulate the proliferation of mural cell precursors via platelet-derived growth factor-BB and heterotypic cell contact.* 1999. **84**(3): p. 298-305.
285. Kofler, N.M., et al., *Combined deficiency of Notch1 and Notch3 causes pericyte dysfunction, models CADASIL and results in arteriovenous malformations.* 2015. **5**(1): p. 1-13.
286. Lindahl, P., et al., *Pericyte loss and microaneurysm formation in PDGF-B-deficient mice.* 1997. **277**(5323): p. 242-245.
287. Lindblom, P., et al., *Endothelial PDGF-B retention is required for proper investment of pericytes in the microvessel wall.* 2003. **17**(15): p. 1835-1840.
288. Stratman, A.N., et al., *Endothelial-derived PDGF-BB and HB-EGF coordinately regulate pericyte recruitment during vasculogenic tube assembly and stabilization.* 2010. **116**(22): p. 4720-4730.
289. Wang, Q., et al., *Notch2 and Notch3 function together to regulate vascular smooth muscle development.* 2012. **7**(5): p. e37365.
290. Wang, Y., et al., *Notch3 establishes brain vascular integrity by regulating pericyte number.* 2014. **141**(2): p. 307-317.
291. Eklund, L. and Saharinen, P., *Angiopoietin signaling in the vasculature.* Exp Cell Res, 2013. **319**(9): p. 1271-80.
292. Carlson, T.R., et al., *Direct cell adhesion to the angiopoietins mediated by integrins.* J Biol Chem, 2001. **276**(28): p. 26516-25.
293. Cascone , I., et al., *Stable interaction between α5β1 integrin and Tie2 tyrosine kinase receptor regulates endothelial cell response to Ang-1.* Journal of Cell Biology, 2005. **170**(6): p. 993-1004.
294. Felcht, M., et al., *Angiopoietin-2 differentially regulates angiogenesis through TIE2 and integrin signaling.* The Journal of Clinical Investigation, 2012. **122**(6): p. 1991-2005.
295. Cines, D.B., et al., *Endothelial cells in physiology and in the pathophysiology of vascular disorders.* Blood, 1998. **91**(10): p. 3527-61.
296. Majesky, M.W., et al., *The adventitia: a progenitor cell niche for the vessel wall.* Cells Tissues Organs, 2012. **195**(1-2): p. 73-81.
297. Gutterman, D.D., *Adventitia-dependent influences on vascular function.* 1999. **277**(4): p. H1265-H1272.
298. Haurani, M.J. and Pagano, P.J., *Adventitial fibroblast reactive oxygen species as autacrine and paracrine mediators of remodeling: bellwether for vascular disease?* Cardiovasc Res, 2007. **75**(4): p. 679-89.
299. Shimizu, I. and Minamino, T., *Physiological and pathological cardiac hypertrophy.* Journal of Molecular and Cellular Cardiology, 2016. **97**: p. 245-262.
300. Hannigan, G.E., Coles, J.G., and Dedhar, S., *Integrin-Linked Kinase at the Heart of Cardiac Contractility, Repair, and Disease.* 2007. **100**(10): p. 1408-1414.
301. Guo, Y. and Pu, W.T., *Cardiomyocyte Maturation.* 2020. **126**(8): p. 1086-1106.
302. Männer, J., *The anatomy of cardiac looping: a step towards the understanding of the morphogenesis of several forms of congenital cardiac malformations.* Clin Anat, 2009. **22**(1): p. 21-35.
303. Scuderi, G.J. and Butcher, J., *Naturally Engineered Maturation of Cardiomyocytes.* Front Cell Dev Biol, 2017. **5**: p. 50.
304. Alkass, K., et al., *No Evidence for Cardiomyocyte Number Expansion in Preadolescent Mice.* Cell, 2015. **163**(4): p. 1026-1036.

305. Foglia, M.J. and Poss, K.D., *Building and re-building the heart by cardiomyocyte proliferation.* Development, 2016. **143**(5): p. 729-40.
306. Soonpaa, M.H., et al., *Cardiomyocyte DNA synthesis and binucleation during murine development.* Am J Physiol, 1996. **271**(5 Pt 2): p. H2183-9.
307. O'Meara, C.C., et al., *Transcriptional reversion of cardiac myocyte fate during mammalian cardiac regeneration.* Circ Res, 2015. **116**(5): p. 804-15.
308. Ahuja, P., Sdek, P., and MacLellan, W.R., *Cardiac myocyte cell cycle control in development, disease, and regeneration.* Physiol Rev, 2007. **87**(2): p. 521-44.
309. Zhang, Y., et al., *Dedifferentiation and proliferation of mammalian cardiomyocytes.* PLoS One, 2010. **5**(9): p. e12559.
310. Chacko, K.J., *Observations on the ultrastructure of developing myocardium of rat embryos.* J Morphol, 1976. **150**(3): p. 681-709.
311. Kim, H.D., et al., *Human fetal heart development after mid-term: morphometry and ultrastructural study.* J Mol Cell Cardiol, 1992. **24**(9): p. 949-65.
312. Siedner, S., et al., *Developmental changes in contractility and sarcomeric proteins from the early embryonic to the adult stage in the mouse heart.* J Physiol, 2003. **548**(Pt 2): p. 493-505.
313. Bhavsar, P.K., et al., *Developmental expression of troponin I isoforms in fetal human heart.* FEBS Letters, 1991. **292**(1): p. 5-8.
314. Bedada, F.B., et al., *Acquisition of a Quantitative, Stoichiometrically Conserved Ratiometric Marker of Maturation Status in Stem Cell-Derived Cardiac Myocytes.* Stem Cell Reports, 2014. **3**(4): p. 594-605.
315. O'Brien, T.X., Lee, K.J., and Chien, K.R., *Positional specification of ventricular myosin light chain 2 expression in the primitive murine heart tube.* 1993. **90**(11): p. 5157-5161.
316. Cooper, G., *Actin, Myosin, and Cell Movement.*, in *The Cell: A Molecular Approach*. 2000, Sunderland (MA): Sinauer Associates
317. Bhagavan, N.V. and Ha, C.-E., *Chapter 19 - Contractile Systems*, in *Essentials of Medical Biochemistry (Second Edition)*, Bhagavan, N.V. and Ha, C.-E., Editors. 2015, Academic Press: San Diego. p. 339-361.
318. Peter, A.K., et al., *The costamere bridges sarcomeres to the sarcolemma in striated muscle.* Prog Pediatr Cardiol, 2011. **31**(2): p. 83-88.
319. Samarel, A.M., *Costameres, focal adhesions, and cardiomyocyte mechanotransduction.* Am J Physiol Heart Circ Physiol, 2005. **289**(6): p. H2291-301.
320. Burbaum, L., et al., *Molecular-scale visualization of sarcomere contraction within native cardiomyocytes.* 2020: p. 2020.09.09.288977.
321. Ervasti, J.M., *Costameres: the Achilles' heel of Herculean muscle.* J Biol Chem, 2003. **278**(16): p. 13591-4.
322. Bers, D.M., *16 - Excitation–Contraction Coupling*, in *Cardiac Electrophysiology: From Cell to Bedside (Seventh Edition)*, Zipes, D.P., Jalife, J., and Stevenson, W.G., Editors. 2018, Elsevier. p. 151-159.
323. Stern, M.D. and Cheng, H., *Putting out the fire: what terminates calcium-induced calcium release in cardiac muscle?* Cell Calcium, 2004. **35**(6): p. 591-601.
324. Panerai, R.B., *A model of cardiac muscle mechanics and energetics.* Journal of Biomechanics, 1980. **13**(11): p. 929-940.
325. Huxley, H.E., *Fifty years of muscle and the sliding filament hypothesis.* Eur J Biochem, 2004. **271**(8): p. 1403-15.
326. Campbell, N.A. and Reece, J.B., *Muskelkontraktion erfordert die Interaktion von Muskelproteinen*, in *Biologie*. 2009, Pearson Studium. p. 1486-1487.
327. Coureux, P.D., Sweeney, H.L., and Houdusse, A., *Three myosin V structures delineate essential features of chemo-mechanical transduction.* Embo j, 2004. **23**(23): p. 4527-37.

328. Ecken, J.v.d., et al., *Cryo-EM structure of a human cytoplasmic actomyosin complex at near-atomic resolution.* Nature, 2016. **534**(7609): p. 724-728.
329. Llinas, P., et al., *How actin initiates the motor activity of Myosin.* Dev Cell, 2015. **33**(4): p. 401-12.
330. Sweeney, H.L. and Houdusse, A., *Structural and functional insights into the Myosin motor mechanism.* Annu Rev Biophys, 2010. **39**: p. 539-57.
331. Wilson, D.P., *Vascular Smooth Muscle Structure and Function*, in *Mechanisms of Vascular Disease: A Reference Book for Vascular Specialists [Internet]*, Fitridge R, T.M., Editor. 2011, Adelaide (AU): University of Adelaide Press.
332. Turner, C.J., et al., *α5 and αv integrins cooperate to regulate vascular smooth muscle and neural crest functions in vivo.* 2015. **142**(4): p. 797-808.
333. Moiseeva, E.P., *Adhesion receptors of vascular smooth muscle cells and their functions.* Cardiovascular Research, 2001. **52**(3): p. 372-386.
334. Owens, G.K., *Regulation of differentiation of vascular smooth muscle cells.* Physiol Rev, 1995. **75**(3): p. 487-517.
335. Holt, A.W. and Tulis, D.A., *Vascular Smooth Muscle as a Therapeutic Target in Disease Pathology, Muscle Cell and Tissue*, in *Muscle Cell and Tissue*, Sakuma, K., Editor. 2015, IntechOpen.
336. Doran, A.C., Meller, N., and McNamara, C.A., *Role of Smooth Muscle Cells in the Initiation and Early Progression of Atherosclerosis.* 2008. **28**(5): p. 812-819.
337. Hu, D., et al., *Vascular Smooth Muscle Cells Contribute to Atherosclerosis Immunity.* 2019. **10**(1101).
338. Bond, M. and Somlyo, A.V., *Dense bodies and actin polarity in vertebrate smooth muscle.* J Cell Biol, 1982. **95**(2 Pt 1): p. 403-13.
339. *Chapter 39 - Muscles*, in *Cell Biology (Third Edition)*, Pollard, T.D., et al., Editors. 2017, Elsevier. p. 671-691.
340. Ohashi, K., et al., *A 36-kDa protein of the dense bodies of smooth muscle cells.* J Biochem, 1994. **116**(6): p. 1354-9.
341. Xu, J.Q., et al., *Myosin filament structure in vertebrate smooth muscle.* Journal of Cell Biology, 1996. **134**(1): p. 53-66.
342. Small, J.V., *Studies on isolated smooth muscle cells: The contractile apparatus.* 1977. **24**(1): p. 327-349.
343. Owens, G.K., Kumar, M.S., and Wamhoff, B.R., *Molecular regulation of vascular smooth muscle cell differentiation in development and disease.* Physiol Rev, 2004. **84**(3): p. 767-801.
344. Rensen, S.S., Doevendans, P.A., and van Eys, G.J., *Regulation and characteristics of vascular smooth muscle cell phenotypic diversity.* Neth Heart J, 2007. **15**(3): p. 100-8.
345. Christen, T., et al., *Cultured porcine coronary artery smooth muscle cells. A new model with advanced differentiation.* Circ Res, 1999. **85**(1): p. 99-107.
346. Adachi, S., et al., *Skeletal and smooth muscle alpha-actin mRNA in endomyocardial biopsy samples of dilated cardiomyopathy patients.* Life Sci, 1998. **63**(20): p. 1779-91.
347. Woodcock-Mitchell, J., et al., *Alpha-smooth muscle actin is transiently expressed in embryonic rat cardiac and skeletal muscles.* Differentiation, 1988. **39**(3): p. 161-6.
348. Kern, S., et al., *Up-regulation of alpha-smooth muscle actin in cardiomyocytes from non-hypertrophic and non-failing transgenic mouse hearts expressing N-terminal truncated cardiac troponin I.* FEBS Open Bio, 2013. **4**: p. 11-7.
349. Milewicz, D.M., et al., *Genetic variants promoting smooth muscle cell proliferation can result in diffuse and diverse vascular diseases: Evidence for a hyperplastic vasculomyopathy.* Genetics in Medicine, 2010. **12**(4): p. 196-203.
350. Boucher, J., Gridley, T., and Liaw, L., *Molecular pathways of notch signaling in vascular smooth muscle cells.* Front Physiol, 2012. **3**: p. 81.

351. Sung, H.J., et al., *Oxidative stress produced with cell migration increases synthetic phenotype of vascular smooth muscle cells.* Ann Biomed Eng, 2005. **33**(11): p. 1546-54.
352. Brozovich, F.V., et al., *Mechanisms of Vascular Smooth Muscle Contraction and the Basis for Pharmacologic Treatment of Smooth Muscle Disorders.* Pharmacological reviews, 2016. **68**(2): p. 476-532.
353. McNeill, R.A. and Newsom-Davis, J.M. *Muscle*. 2019 [cited 2020; Available from: https://www.britannica.com/science/muscle.
354. Kuo, I.Y. and Ehrlich, B.E., *Signaling in muscle contraction.* Cold Spring Harb Perspect Biol, 2015. **7**(2): p. a006023.
355. Hirano, K., *Current topics in the regulatory mechanism underlying the Ca2+ sensitization of the contractile apparatus in vascular smooth muscle.* J Pharmacol Sci, 2007. **104**(2): p. 109-15.
356. Hirata, K., et al., *Involvement of rho p21 in the GTP-enhanced calcium ion sensitivity of smooth muscle contraction.* J Biol Chem, 1992. **267**(13): p. 8719-22.
357. Gong, M.C., et al., *Role of guanine nucleotide-binding proteins--ras-family or trimeric proteins or both--in Ca2+ sensitization of smooth muscle.* 1996. **93**(3): p. 1340-1345.
358. Gohla, A., Schultz, G., and Offermanns, S., *Role for G(12)/G(13) in agonist-induced vascular smooth muscle cell contraction.* Circ Res, 2000. **87**(3): p. 221-7.
359. Murthy, K.S., *Signaling for contraction and relaxation in smooth muscle of the gut.* Annu Rev Physiol, 2006. **68**: p. 345-74.
360. Kureishi, Y., et al., *Rho-associated kinase directly induces smooth muscle contraction through myosin light chain phosphorylation.* J Biol Chem, 1997. **272**(19): p. 12257-60.
361. Mukai, Y., et al., *Involvement of Rho-kinase in hypertensive vascular disease: a novel therapeutic target in hypertension.* Faseb j, 2001. **15**(6): p. 1062-4.
362. Rattan, S., Phillips, B.R., and Maxwell, P.J., *RhoA/Rho-kinase: pathophysiologic and therapeutic implications in gastrointestinal smooth muscle tone and relaxation.* Gastroenterology, 2010. **138**(1): p. 13-8.e1-3.
363. Kume, H., *RhoA/Rho-kinase as a therapeutic target in asthma.* Curr Med Chem, 2008. **15**(27): p. 2876-85.
364. Bei, Y., et al., *RhoA/Rho-kinase activation promotes lung fibrosis in an animal model of systemic sclerosis.* Exp Lung Res, 2016. **42**(1): p. 44-55.
365. Fountoulaki, K., Dagres, N., and Iliodromitis, E.K., *Cellular Communications in the Heart.* Card Fail Rev, 2015. **1**(2): p. 64-68.
366. Tirziu, D., Giordano, F.J., and Simons, M., *Cell Communications in the Heart.* 2010. **122**(9): p. 928-937.
367. Camelliti, P., Borg, T.K., and Kohl, P., *Structural and functional characterisation of cardiac fibroblasts.* 2005. **65**(1): p. 40-51.
368. Yamazaki, T., et al., *Endothelin-1 is involved in mechanical stress-induced cardiomyocyte hypertrophy.* 1996. **271**(6): p. 3221-3228.
369. Pontén, A., et al., *Transgenic overexpression of platelet-derived growth factor-C in the mouse heart induces cardiac fibrosis, hypertrophy, and dilated cardiomyopathy.* 2003. **163**(2): p. 673-682.
370. Ballard-Croft, C., et al., *Role of p38 mitogen-activated protein kinase in cardiac myocyte secretion of the inflammatory cytokine TNF-α.* 2001. **280**(5): p. H1970-H1981.
371. Bowers, S.L.K. and Baudino, T.A., *Cardiac myocyte–fibroblast interactions and the coronary vasculature.* 2012. **5**(6): p. 783-793.
372. Balligand, J.-L. and Cannon, P.J., *Nitric Oxide Synthases and Cardiac Muscle.* 1997. **17**(10): p. 1846-1858.
373. Barouch, L.A., et al., *Nitric oxide regulates the heart by spatial confinement of nitric oxide synthase isoforms.* Nature, 2002. **416**(6878): p. 337-339.

374. Gutstein, D.E., et al., *The organization of adherens junctions and desmosomes at the cardiac intercalated disc is independent of gap junctions.* 2003. **116**(5): p. 875-885.
375. Triggle, C.R., et al., *The endothelium: influencing vascular smooth muscle in many ways.* Can J Physiol Pharmacol, 2012. **90**(6): p. 713-38.
376. Straub, A.C., Zeigler, A.C., and Isakson, B.E., *The myoendothelial junction: connections that deliver the message.* Physiology (Bethesda), 2014. **29**(4): p. 242-9.
377. Evans, W.H. and Martin, P.E., *Gap junctions: structure and function (Review).* Mol Membr Biol, 2002. **19**(2): p. 121-36.
378. Saez, J.C., et al., *Plasma membrane channels formed by connexins: their regulation and functions.* Physiol Rev, 2003. **83**(4): p. 1359-400.
379. Artavanis-Tsakonas, S., Rand, M.D., and Lake, R.J., *Notch Signaling: Cell Fate Control and Signal Integration in Development.* 1999. **284**(5415): p. 770-776.
380. Gridley, T., *Notch signaling in the vasculature.* Curr Top Dev Biol, 2010. **92**: p. 277-309.
381. Meng, H., et al., *Von Willebrand factor inhibits mature smooth muscle gene expression through impairment of Notch signaling.* PLoS One, 2013. **8**(9): p. e75808.
382. Zhou, X.L. and Liu, J.C., *Role of Notch signaling in the mammalian heart.* Braz J Med Biol Res, 2014. **47**(1): p. 1-10.
383. Sauer, B. and Henderson, N., *Site-specific DNA recombination in mammalian cells by the Cre recombinase of bacteriophage P1.* Proc Natl Acad Sci U S A, 1988. **85**(14): p. 5166-70.
384. Altstätter, J.A.V., *Functional analysis of α-Parvin in vivo*. 2011.
385. Thievessen, I., *Funktionsanalyse von Fokalkontaktproteinen der Parvin-Familie durch Knockout in der Maus*. 2007.
386. Sohal, D.S., et al., *Temporally regulated and tissue-specific gene manipulations in the adult and embryonic heart using a tamoxifen-inducible Cre protein.* Circ Res, 2001. **89**(1): p. 20-5.
387. Littlewood, T.D., et al., *A modified oestrogen receptor ligand-binding domain as an improved switch for the regulation of heterologous proteins.* Nucleic Acids Res, 1995. **23**(10): p. 1686-90.
388. Wirth, A., et al., *G12-G13-LARG-mediated signaling in vascular smooth muscle is required for salt-induced hypertension.* Nat Med, 2008. **14**(1): p. 64-8.
389. Metzger, D., et al., *Targeted conditional somatic mutagenesis in the mouse: Temporally-controlled knock out of retinoid receptors in epidermal keratinocytes.* Nucelar Receptors, 2003. **364**: p. 379-+.
390. Gibson, D.G., et al., *Enzymatic assembly of DNA molecules up to several hundred kilobases.* Nature Methods, 2009. **6**(5): p. 343-345.
391. Gibson, D.G., *Chapter fifteen - Enzymatic Assembly of Overlapping DNA Fragments*, in *Methods in Enzymology*, Voigt, C., Editor. 2011, Academic Press. p. 349-361.
392. Ran, F.A., et al., *Genome engineering using the CRISPR-Cas9 system.* Nature Protocols, 2013. **8**(11): p. 2281-2308.
393. Labun, K., et al., *CHOPCHOP v3: expanding the CRISPR web toolbox beyond genome editing.* Nucleic Acids Research, 2019. **47**(W1): p. W171-W174.
394. Ackers-Johnson, M., et al., *A Simplified, Langendorff-Free Method for Concomitant Isolation of Viable Cardiac Myocytes and Nonmyocytes From the Adult Mouse Heart.* Circ Res, 2016. **119**(8): p. 909-20.
395. Afroze, T., et al., *Calcineurin-independent regulation of plasma membrane Ca2+ ATPase-4 in the vascular smooth muscle cell cycle.* Am J Physiol Cell Physiol, 2003. **285**(1): p. C88-95.
396. Meijering, E., Dzyubachyk, O., and Smal, I., *Methods for cell and particle tracking.* Methods Enzymol, 2012. **504**: p. 183-200.
397. Roux, K.J., et al., *A promiscuous biotin ligase fusion protein identifies proximal and interacting proteins in mammalian cells.* J Cell Biol, 2012. **196**(6): p. 801-10.

398. Kim, D.I., et al., *An improved smaller biotin ligase for BioID proximity labeling.* Mol Biol Cell, 2016. **27**(8): p. 1188-96.
399. Branon, T.C., et al., *Efficient proximity labeling in living cells and organisms with TurboID.* Nature Biotechnology, 2018. **36**(9): p. 880-887.
400. Rappsilber, J., Ishihama, Y., and Mann, M., *Stop and go extraction tips for matrix-assisted laser desorption/ionization, nanoelectrospray, and LC/MS sample pretreatment in proteomics.* Anal Chem, 2003. **75**(3): p. 663-70.
401. Tain, L.S., et al., *A proteomic atlas of insulin signalling reveals tissue-specific mechanisms of longevity assurance.* Mol Syst Biol, 2017. **13**(9): p. 939.
402. Schorr, S., et al., *Identification of signal peptide features for substrate specificity in human Sec62/Sec63-dependent ER protein import.* **n/a**(n/a).
403. Meier, F., et al., *Parallel Accumulation–Serial Fragmentation (PASEF): Multiplying Sequencing Speed and Sensitivity by Synchronized Scans in a Trapped Ion Mobility Device.* Journal of Proteome Research, 2015. **14**(12): p. 5378-5387.
404. Meier, F., et al., *Deep learning the collisional cross sections of the peptide universe from a million training samples.* 2020: p. 2020.05.19.102285.
405. Cox, J. and Mann, M., *MaxQuant enables high peptide identification rates, individualized p.p.b.-range mass accuracies and proteome-wide protein quantification.* Nat Biotechnol, 2008. **26**(12): p. 1367-72.
406. Cox, J., et al., *Andromeda: a peptide search engine integrated into the MaxQuant environment.* J Proteome Res, 2011. **10**(4): p. 1794-805.
407. Murgia, M., et al., *Single muscle fiber proteomics reveals unexpected mitochondrial specialization.* EMBO Rep, 2015. **16**(3): p. 387-95.
408. Cox, J., et al., *Accurate proteome-wide label-free quantification by delayed normalization and maximal peptide ratio extraction, termed MaxLFQ.* Mol Cell Proteomics, 2014. **13**(9): p. 2513-26.
409. Trowitzsch, S., et al., *New baculovirus expression tools for recombinant protein complex production.* Journal of Structural Biology, 2010. **172**(1): p. 45-54.
410. Bieniossek, C., Richmond, T.J., and Berger, I., *MultiBac: multigene baculovirus-based eukaryotic protein complex production.* 2008. **51**(1): p. 5.20. 1-5.20. 26.
411. Tyanova, S., et al., *The Perseus computational platform for comprehensive analysis of (prote)omics data.* Nat Methods, 2016. **13**(9): p. 731-40.
412. Hilenski, L.L., et al., *The role of beta 1 integrin in spreading and myofibrillogenesis in neonatal rat cardiomyocytes in vitro.* Cell Motil Cytoskeleton, 1992. **21**(2): p. 87-100.
413. Simpson, D.G., et al., *Contractile activity and cell-cell contact regulate myofibrillar organization in cultured cardiac myocytes.* J Cell Biol, 1993. **123**(2): p. 323-36.
414. Decker, M.L., et al., *Morphological analysis of contracting and quiescent adult rabbit cardiac myocytes in long-term culture.* Anat Rec, 1990. **227**(3): p. 285-99.
415. Qadota, H., et al., *High-resolution imaging of muscle attachment structures in Caenorhabditis elegans.* Cytoskeleton (Hoboken), 2017. **74**(11): p. 426-442.
416. Supharattanasitthi, W., et al., *CRISPR/Cas9-mediated one step bi-allelic change of genomic DNA in iPSCs and human RPE cells in vitro with dual antibiotic selection.* Scientific Reports, 2019. **9**(1): p. 174.
417. Vakulskas, C.A. and Behlke, M.A., *Evaluation and Reduction of CRISPR Off-Target Cleavage Events.* Nucleic Acid Ther, 2019. **29**(4): p. 167-174.
418. Kim, S., et al., *Highly efficient RNA-guided genome editing in human cells via delivery of purified Cas9 ribonucleoproteins.* Genome Res, 2014. **24**(6): p. 1012-9.
419. Staudt, D.W., et al., *High-resolution imaging of cardiomyocyte behavior reveals two distinct steps in ventricular trabeculation.* 2014. **141**(3): p. 585-593.

420. Jacot, J.G., Martin, J.C., and Hunt, D.L., *Mechanobiology of cardiomyocyte development.* Journal of Biomechanics, 2010. **43**(1): p. 93-98.
421. Jacot, J.G., McCulloch, A.D., and Omens, J.H., *Substrate stiffness affects the functional maturation of neonatal rat ventricular myocytes.* Biophys J, 2008. **95**(7): p. 3479-87.
422. McGrath, J.L., *Cell Spreading: The Power to Simplify.* Current Biology, 2007. **17**(10): p. R357-R358.
423. Ge, L., et al., *Topography-Mediated Fibroblast Cell Migration Is Influenced by Direction, Wavelength, and Amplitude.* ACS Applied Bio Materials, 2020. **3**(4): p. 2104-2116.
424. Fukata, M., Nakagawa, M., and Kaibuchi, K., *Roles of Rho-family GTPases in cell polarisation and directional migration.* Current Opinion in Cell Biology, 2003. **15**(5): p. 590-597.
425. Pereira, J.A., et al., *Integrin-linked kinase is required for radial sorting of axons and Schwann cell remyelination in the peripheral nervous system.* J Cell Biol, 2009. **185**(1): p. 147-61.
426. Nagaraj, N., et al., *Deep proteome and transcriptome mapping of a human cancer cell line.* Mol Syst Biol, 2011. **7**: p. 548.
427. Roux, K.J., et al., *BioID: A Screen for Protein-Protein Interactions.* Curr Protoc Protein Sci, 2018. **91**: p. 19.23.1-19.23.15.
428. Diviani, D., Soderling, J., and Scott, J.D., *AKAP-Lbc anchors protein kinase A and nucleates Galpha 12-selective Rho-mediated stress fiber formation.* J Biol Chem, 2001. **276**(47): p. 44247-57.
429. O'Connor, K.L., Chen, M., and Towers, L.N., *Integrin α6β4 cooperates with LPA signaling to stimulate Rac through AKAP-Lbc-mediated RhoA activation.* Am J Physiol Cell Physiol, 2012. **302**(3): p. C605-14.
430. Sanz-Moreno, V., et al., *Rac Activation and Inactivation Control Plasticity of Tumor Cell Movement.* Cell, 2008. **135**(3): p. 510-523.
431. Bludau, I. and Aebersold, R., *Proteomic and interactomic insights into the molecular basis of cell functional diversity.* Nature Reviews Molecular Cell Biology, 2020. **21**(6): p. 327-340.
432. Kostenko, S., Johannessen, M., and Moens, U., *PKA-induced F-actin rearrangement requires phosphorylation of Hsp27 by the MAPKAP kinase MK5.* Cell Signal, 2009. **21**(5): p. 712-8.
433. Liu, X., et al., *Prohibitin protects against oxidative stress-induced cell injury in cultured neonatal cardiomyocyte.* Cell stress & chaperones, 2009. **14**(3): p. 311-319.
434. Saleh, A., et al., *Cytoplasmic sequestration of the RhoA effector mDiaphanous1 by Prohibitin2 promotes muscle differentiation.* Scientific Reports, 2019. **9**(1): p. 8302.
435. Huet-Calderwood, C., et al., *Differences in binding to the ILK complex determines kindlin isoform adhesion localization and integrin activation.* J Cell Sci, 2014. **127**(Pt 19): p. 4308-21.
436. Ehrlicher, A.J., et al., *Mechanical strain in actin networks regulates FilGAP and integrin binding to filamin A.* Nature, 2011. **478**(7368): p. 260-3.
437. Heering, J., Erlmann, P., and Olayioye, M.A., *Simultaneous loss of the DLC1 and PTEN tumor suppressors enhances breast cancer cell migration.* Exp Cell Res, 2009. **315**(15): p. 2505-14.
438. Healy, K.D., et al., *DLC-1 suppresses non-small cell lung cancer growth and invasion by RhoGAP-dependent and independent mechanisms.* Mol Carcinog, 2008. **47**(5): p. 326-37.
439. Hannigan, G., Troussard, A.A., and Dedhar, S., *Integrin-linked kinase: a cancer therapeutic target unique among its ILK.* Nature Reviews Cancer, 2005. **5**(1): p. 51-63.
440. Cabodi, S., et al., *Integrin signalling adaptors: not only figurants in the cancer story.* Nature Reviews Cancer, 2010. **10**(12): p. 858-870.
441. Gardiner, H.M., *Response of the fetal heart to changes in load: from hyperplasia to heart failure.* Heart, 2005. **91**(7): p. 871-3.
442. Sopko, N., et al., *Significance of Thymosin β4 and Implication of PINCH-1-ILK-α-Parvin (PIP) Complex in Human Dilated Cardiomyopathy.* PLOS ONE, 2011. **6**(5): p. e20184.

443. Huang, Y. and Gunst, S.J., *Phenotype transitions induced by mechanical stimuli in airway smooth muscle are regulated by differential interactions of parvin isoforms with paxillin and Akt.* American journal of physiology. Lung cellular and molecular physiology, 2020. **318**(5): p. L1036-L1055.
444. Nakrieko, K.A., et al., *Modulation of integrin-linked kinase nucleo-cytoplasmic shuttling by ILKAP and CRM1.* Cell Cycle, 2008. **7**(14): p. 2157-66.
445. Wang, D., et al., *PINCH1 is transcriptional regulator in podocytes that interacts with WT1 and represses podocalyxin expression.* PLoS One, 2011. **6**(2): p. e17048.
446. Acconcia, F., et al., *Phosphorylation-dependent regulation of nuclear localization and functions of integrin-linked kinase.* 2007. **104**(16): p. 6782-6787.
447. Tsinias, G., et al., *High PINCH1 Expression in Human Laryngeal Carcinoma Associates with Poor Prognosis.* Analytical Cellular Pathology, 2018. **2018**: p. 1-12.
448. Fielding, A.B., et al., *Integrin-linked kinase localizes to the centrosome and regulates mitotic spindle organization.* 2008. **180**(4): p. 681-689.
449. Fielding, A.B., et al., *A critical role of integrin-linked kinase, ch-TOG and TACC3 in centrosome clustering in cancer cells.* 2011. **30**(5): p. 521-534.
450. He, Y., et al., *Kindlin-1 and -2 have overlapping functions in epithelial cells implications for phenotype modification.* Am J Pathol, 2011. **178**(3): p. 975-82.
451. Rognoni, E., Ruppert, R., and Fässler, R., *The kindlin family: functions, signaling properties and implications for human disease.* 2016. **129**(1): p. 17-27.
452. Campana, W.M., Myers, R.R., and Rearden, A., *Identification of PINCH in Schwann cells and DRG neurons: shuttling and signaling after nerve injury.* 2003. **41**(3): p. 213-223.
453. Chun, J., et al., *The subcellular localization control of integrin linked kinase 1 through its protein–protein interaction with caveolin-1.* Cellular Signalling, 2005. **17**(6): p. 751-760.
454. Hervy, M., Hoffman, L., and Beckerle, M.C., *From the membrane to the nucleus and back again: bifunctional focal adhesion proteins.* Current Opinion in Cell Biology, 2006. **18**(5): p. 524-532.
455. Kato, T., et al., *Atrial natriuretic peptide promotes cardiomyocyte survival by cGMP-dependent nuclear accumulation of zyxin and Akt.* 2005. **115**(10): p. 2716-2730.
456. Cattaruzza, M., Lattrich, C., and Hecker, M., *Focal adhesion protein zyxin is a mechanosensitive modulator of gene expression in vascular smooth muscle cells.* 2004. **43**(4): p. 726-730.
457. Woods, A.J., et al., *Interaction of paxillin with poly (A)-binding protein 1 and its role in focal adhesion turnover and cell migration.* 2005. **25**(9): p. 3763-3773.
458. Wu, R.F., et al., *Subcellular targeting of oxidants during endothelial cell migration.* 2005. **171**(5): p. 893-904.
459. Barstead, R.J. and Waterston, R.H., *The basal component of the nematode dense-body is vinculin.* 1989. **264**(17): p. 10177-10185.
460. Gettner, S.N., Kenyon, C., and Reichardt, L.F., *Characterization of beta pat-3 heterodimers, a family of essential integrin receptors in C. elegans.* 1995. **129**(4): p. 1127-1141.
461. Moulder, G., et al., *Talin requires beta-integrin, but not vinculin, for its assembly into focal adhesion-like structures in the nematode Caenorhabditis elegans.* 1996. **7**(8): p. 1181-1193.
462. Stanchi, F., et al., *Molecular dissection of the ILK-PINCH-parvin triad reveals a fundamental role for the ILK kinase domain in the late stages of focal-adhesion maturation.* J Cell Sci, 2009. **122**(Pt 11): p. 1800-11.
463. Mackenzie, N.C., et al., *MOVAS-1 cell line: a new in vitro model of vascular calcification.* Int J Mol Med, 2011. **27**(5): p. 663-8.
464. Chalmers, J.A., et al., *Vascular circadian rhythms in a mouse vascular smooth muscle cell line (Movas-1).* 2008. **295**(5): p. R1529-R1538.
465. Li, H., et al., *Applications of genome editing technology in the targeted therapy of human diseases: mechanisms, advances and prospects.* Signal Transduction and Targeted Therapy, 2020. **5**(1): p. 1.

466. Manghwar, H., et al., *CRISPR/Cas System: Recent Advances and Future Prospects for Genome Editing.* Trends in Plant Science, 2019. **24**(12): p. 1102-1125.
467. Carroll, K.J., et al., *A mouse model for adult cardiac-specific gene deletion with CRISPR/Cas9.* Proc Natl Acad Sci U S A, 2016. **113**(2): p. 338-43.
468. Guo, Y., et al., *Analysis of Cardiac Myocyte Maturation Using CASAAV, a Platform for Rapid Dissection of Cardiac Myocyte Gene Function In Vivo.* Circ Res, 2017. **120**(12): p. 1874-1888.
469. Xie, C., et al., *Genome editing with CRISPR/Cas9 in postnatal mice corrects PRKAG2 cardiac syndrome.* Cell Res, 2016. **26**(10): p. 1099-1111.
470. Inc., T.B. *Successful identification of monoallelic and biallelic mutants after CRISPR/Cas9 gene editing*. [cited 2020 24.07.]; Available from: https://www.takarabio.com/learning-centers/gene-function/gene-editing/crispr/cas9-knockouts/monoallelic-versus-biallelic-mutants.
471. Shyy, J.Y. and Chien, S., *Role of integrins in cellular responses to mechanical stress and adhesion.* Curr Opin Cell Biol, 1997. **9**(5): p. 707-13.
472. Maillet, M., van Berlo, J.H., and Molkentin, J.D., *Molecular basis of physiological heart growth: fundamental concepts and new players.* Nat Rev Mol Cell Biol, 2013. **14**(1): p. 38-48.
473. McMullen, J.R. and Jennings, G.L., *Differences between pathological and physiological cardiac hypertrophy: novel therapeutic strategies to treat heart failure.* Clin Exp Pharmacol Physiol, 2007. **34**(4): p. 255-62.
474. Hutchinson, K.R., Stewart, J.A., Jr., and Lucchesi, P.A., *Extracellular matrix remodeling during the progression of volume overload-induced heart failure.* Journal of molecular and cellular cardiology, 2010. **48**(3): p. 564-569.
475. Maulik, S.K. and Mishra, S., *Hypertrophy to failure: what goes wrong with the fibers of the heart?* Indian Heart J, 2015. **67**(1): p. 66-9.
476. Chen, H., et al., *Gene expression changes associated with fibronectin-induced cardiac myocyte hypertrophy.* Physiol Genomics, 2004. **18**(3): p. 273-83.
477. Ogawa, E., et al., *Outside-in signalling of fibronectin stimulates cardiomyocyte hypertrophy in cultured neonatal rat ventricular myocytes.* J Mol Cell Cardiol, 2000. **32**(5): p. 765-76.
478. Mishra, P.K., et al., *Guidelines for evaluating myocardial cell death.* 2019. **317**(5): p. H891-H922.
479. Chiong, M., et al., *Cardiomyocyte death: mechanisms and translational implications.* Cell Death & Disease, 2011. **2**(12): p. e244-e244.
480. Jacot, J.G., McCulloch, A.D., and Omens, J.H., *Substrate Stiffness Affects the Functional Maturation of Neonatal Rat Ventricular Myocytes.* Biophysical Journal, 2008. **95**(7): p. 3479-3487.
481. Hoffmann, J.-E., et al., *Symmetric exchange of multi-protein building blocks between stationary focal adhesions and the cytosol.* eLife, 2014. **3**: p. e02257.
482. Altstätter, J., et al., *α-parvin is required for epidermal morphogenesis, hair follicle development and basal keratinocyte polarity.* PLoS One, 2020. **15**(3): p. e0230380.
483. Vakaloglou, K.M., Chountala, M., and Zervas, C.G., *Functional analysis of parvin and different modes of IPP-complex assembly at integrin sites during Drosophila development.* 2012. **125**(13): p. 3221-3232.
484. Bachir, A.I., et al., *Integrin-Associated Complexes Form Hierarchically with Variable Stoichiometry in Nascent Adhesions.* Current Biology, 2014. **24**(16): p. 1845-1853.
485. Montanez, E., et al., *Kindlin-2 controls bidirectional signaling of integrins.* Genes Dev, 2008. **22**(10): p. 1325-30.
486. Zamir, E., et al., *Molecular diversity of cell-matrix adhesions.* 1999. **112**(11): p. 1655-1669.
487. Gumbiner, B.M., *Cell adhesion: the molecular basis of tissue architecture and morphogenesis.* 1996. **84**(3): p. 345-357.
488. Flevaris, P., et al., *A molecular switch that controls cell spreading and retraction.* 2007. **179**(3): p. 553-565.

489. Tojkander, S., Gateva, G., and Lappalainen, P., *Actin stress fibers – assembly, dynamics and biological roles.* 2012. **125**(8): p. 1855-1864.
490. Gagné, D., et al., *ILK supports RhoA/ROCK-mediated contractility of human intestinal epithelial crypt cells by inducing the fibrillogenesis of endogenous soluble fibronectin during the spreading process.* BMC Molecular and Cell Biology, 2020. **21**(1): p. 14.
491. Vouret-Craviari, V., et al., *ILK is required for the assembly of matrix-forming adhesions and capillary morphogenesis in endothelial cells.* J Cell Sci, 2004. **117**(Pt 19): p. 4559-69.
492. Oakes, P.W., et al., *Tension is required but not sufficient for focal adhesion maturation without a stress fiber template.* Journal of Cell Biology, 2012. **196**(3): p. 363-374.
493. Cai, Y., et al., *Cytoskeletal coherence requires myosin-IIA contractility.* J Cell Sci, 2010. **123**(Pt 3): p. 413-23.
494. Reinhart-King, C.A., Dembo, M., and Hammer, D.A., *The dynamics and mechanics of endothelial cell spreading.* Biophys J, 2005. **89**(1): p. 676-89.
495. Dang, I. and Gautreau, A., *Random Migration Assays of Mammalian Cells and Quantitative Analyses of Single Cell Trajectories.* Methods Mol Biol, 2018. **1749**: p. 1-9.
496. Burridge, K. and Wennerberg, K., *Rho and Rac take center stage.* Cell, 2004. **116**(2): p. 167-79.
497. Matsumura, F. and Hartshorne, D.J., *Myosin phosphatase target subunit: Many roles in cell function.* Biochem Biophys Res Commun, 2008. **369**(1): p. 149-56.
498. Riahi, R., et al., *Advances in Wound-Healing Assays for Probing Collective Cell Migration.* 2012. **17**(1): p. 59-65.
499. Lyon, C.A., et al., *Inhibition of N-cadherin retards smooth muscle cell migration and intimal thickening via induction of apoptosis.* J Vasc Surg, 2010. **52**(5): p. 1301-9.
500. Zhao, D., et al., *Over-expression of integrin-linked kinase correlates with aberrant expression of Snail, E-cadherin and N-cadherin in oral squamous cell carcinoma: implications in tumor progression and metastasis.* Clin Exp Metastasis, 2012. **29**(8): p. 957-69.
501. Gil, D., et al., *Integrin-linked kinase regulates cadherin switch in bladder cancer.* Tumour Biol, 2016. **37**(11): p. 15185-15191.
502. Fraccaroli, A., et al., *Endothelial Alpha-Parvin Controls Integrity of Developing Vasculature and Is Required for Maintenance of Cell-Cell Junctions.* 2015. **117**(1): p. 29-40.
503. Honda, S., et al., *Integrin-linked kinase associated with integrin activation.* Blood, 2009. **113**(21): p. 5304-13.
504. Honda, S., et al., *The integrin-linked kinase-PINCH-parvin complex supports integrin αIIbβ3 activation.* PLoS One, 2013. **8**(12): p. e85498.
505. Tucker, K.L., et al., *A dual role for integrin-linked kinase in platelets: regulating integrin function and alpha-granule secretion.* Blood, 2008. **112**(12): p. 4523-31.
506. Jones, C.I., et al., *Integrin-linked kinase regulates the rate of platelet activation and is essential for the formation of stable thrombi.* 2014. **12**(8): p. 1342-1352.
507. Friedrich, E.B., et al., *Integrin-Linked Kinase Regulates Endothelial Cell Survival and Vascular Development.* 2004. **24**(18): p. 8134-8144.
508. Gagné, D., et al., *Integrin-linked kinase regulates migration and proliferation of human intestinal cells under a fibronectin-dependent mechanism.* 2010. **222**(2): p. 387-400.
509. Zhang, Y., et al., *A critical role of the PINCH-integrin-linked kinase interaction in the regulation of cell shape change and migration.* J Biol Chem, 2002. **277**(1): p. 318-26.
510. Vallés, A.M., Beuvin, M., and Boyer, B., *Activation of Rac1 by paxillin-Crk-DOCK180 signaling complex is antagonized by Rap1 in migrating NBT-II cells.* J Biol Chem, 2004. **279**(43): p. 44490-6.
511. Nho, R.S., et al., *Role of integrin-linked kinase in regulating phosphorylation of Akt and fibroblast survival in type I collagen matrices through a beta1 integrin viability signaling pathway.* J Biol Chem, 2005. **280**(28): p. 26630-9.

512. Troussard, A.A., et al., *Conditional knock-out of integrin-linked kinase demonstrates an essential role in protein kinase B/Akt activation.* J Biol Chem, 2003. **278**(25): p. 22374-8.
513. Tan, C., et al., *Regulation of tumor angiogenesis by integrin-linked kinase (ILK).* Cancer Cell, 2004. **5**(1): p. 79-90.
514. Rhee, H.W., et al., *Proteomic mapping of mitochondria in living cells via spatially restricted enzymatic tagging.* Science, 2013. **339**(6125): p. 1328-1331.
515. Hung, V., et al., *Proteomic Mapping of the Human Mitochondrial Intermembrane Space in Live Cells via Ratiometric APEX Tagging.* Molecular Cell, 2014. **55**(2): p. 332-341.
516. Branon, T., Han, S., and Ting, A., *Beyond Immunoprecipitation: Exploring New Interaction Spaces with Proximity Biotinylation.* Biochemistry, 2017. **56**(26): p. 3297-3298.
517. Gupta, G.D., et al., *A Dynamic Protein Interaction Landscape of the Human Centrosome-Cilium Interface.* Cell, 2015. **163**(6): p. 1484-1499.
518. Baker, K.E. and Parker, R., *Nonsense-mediated mRNA decay: terminating erroneous gene expression.* Current Opinion in Cell Biology, 2004. **16**(3): p. 293-299.
519. Schweingruber, C., et al., *Identification of Interactions in the NMD Complex Using Proximity-Dependent Biotinylation (BioID).* PLoS One, 2016. **11**(3): p. e0150239.
520. Mili, S. and Steitz, J.A., *Evidence for reassociation of RNA-binding proteins after cell lysis: implications for the interpretation of immunoprecipitation analyses.* Rna, 2004. **10**(11): p. 1692-4.
521. Noritake, J., et al., *IQGAP1: a key regulator of adhesion and migration.* 2005. **118**(10): p. 2085-2092.
522. Wickström, S.A., et al., *Integrin-linked kinase controls microtubule dynamics required for plasma membrane targeting of caveolae.* Dev Cell, 2010. **19**(4): p. 574-88.
523. Chicurel, M.E., et al., *Integrin binding and mechanical tension induce movement of mRNA and ribosomes to focal adhesions.* Nature, 1998. **392**(6677): p. 730-3.
524. de Hoog, C.L., Foster, L.J., and Mann, M., *RNA and RNA binding proteins participate in early stages of cell spreading through spreading initiation centers.* Cell, 2004. **117**(5): p. 649-62.
525. Woods, A.J., et al., *Paxillin associates with poly(A)-binding protein 1 at the dense endoplasmic reticulum and the leading edge of migrating cells.* J Biol Chem, 2002. **277**(8): p. 6428-37.
526. Hüttelmaier, S., et al., *Raver1, a dual compartment protein, is a ligand for PTB/hnRNPI and microfilament attachment proteins.* J Cell Biol, 2001. **155**(5): p. 775-86.
527. Lim, S.T., *Nuclear FAK: a new mode of gene regulation from cellular adhesions.* Mol Cells, 2013. **36**(1): p. 1-6.
528. Sun, S., Wu, H.-J., and Guan, J.-L., *Nuclear FAK and its kinase activity regulate VEGFR2 transcription in angiogenesis of adult mice.* Scientific Reports, 2018. **8**(1): p. 2550.
529. Hartshorne, D.J., Ito, M., and Ikebe, M., *Myosin and Contractile Activity in Smooth Muscle*, in *Calcium Protein Signaling*, Hidaka, H., et al., Editors. 1989, Springer US: Boston, MA. p. 269-277.
530. Noda, M., et al., *Involvement of rho in GTP gamma S-induced enhancement of phosphorylation of 20 kDa myosin light chain in vascular smooth muscle cells: inhibition of phosphatase activity.* FEBS Lett, 1995. **367**(3): p. 246-50.
531. Matsui, T., et al., *Rho-associated kinase, a novel serine/threonine kinase, as a putative target for small GTP binding protein Rho.* Embo j, 1996. **15**(9): p. 2208-16.
532. Wu, X., Somlyo, A.V., and Somlyo, A.P., *Cyclic GMP-dependent stimulation reverses G-protein-coupled inhibition of smooth muscle myosin light chain phosphate.* Biochem Biophys Res Commun, 1996. **220**(3): p. 658-63.
533. Mizuno, Y., et al., *Myosin light chain kinase activation and calcium sensitization in smooth muscle in vivo.* Am J Physiol Cell Physiol, 2008. **295**(2): p. C358-64.
534. Holeiter, G., et al., *Deleted in liver cancer 1 controls cell migration through a Dia1-dependent signaling pathway.* Cancer Res, 2008. **68**(21): p. 8743-51.

535. Kim, T.Y., et al., *Role of DLC-1, a tumor suppressor protein with RhoGAP activity, in regulation of the cytoskeleton and cell motility.* Cancer Metastasis Rev, 2009. **28**(1-2): p. 77-83.
536. Kawai, K., et al., *Focal adhesion-localization of START-GAP1/DLC1 is essential for cell motility and morphology.* Genes Cells, 2009. **14**(2): p. 227-41.
537. Li, G., et al., *Full activity of the deleted in liver cancer 1 (DLC1) tumor suppressor depends on an LD-like motif that binds talin and focal adhesion kinase (FAK).* Proc Natl Acad Sci U S A, 2011. **108**(41): p. 17129-34.
538. Haining, A.W.M., et al., *Mechanotransduction in talin through the interaction of the R8 domain with DLC1.* PLoS Biol, 2018. **16**(7): p. e2005599.
539. Calderwood, D.A., et al., *The talin head domain binds to integrin β subunit cytoplasmic tails and regulates integrin activation.* 1999. **274**(40): p. 28071-28074.
540. McCleverty, C.J., Lin, D.C., and Liddington, R.C., *Structure of the PTB domain of tensin1 and a model for its recruitment to fibrillar adhesions.* Protein Sci, 2007. **16**(6): p. 1223-9.
541. Tripathi, B.K., et al., *Receptor tyrosine kinase activation of RhoA is mediated by AKT phosphorylation of DLC1.* J Cell Biol, 2017. **216**(12): p. 4255-4270.
542. Ko, F.C.F., et al., *PKA-induced dimerization of the RhoGAP DLC1 promotes its inhibition of tumorigenesis and metastasis.* Nature Communications, 2013. **4**(1): p. 1618.
543. Vossmeyer, D., et al., *Phospholipase Cγ binds α1β1 integrin and modulates α1β1 integrin-specific adhesion.* Journal of Biological Chemistry, 2002. **277**(7): p. 4636-4643.
544. Choi, J.H., et al., *Phospholipase C-gamma1 potentiates integrin-dependent cell spreading and migration through Pyk2/paxillin activation.* Cell Signal, 2007. **19**(8): p. 1784-96.
545. Kinjo, T., et al., *Enhanced p122RhoGAP/DLC-1 Expression Can Be a Cause of Coronary Spasm.* PLOS ONE, 2015. **10**(12): p. e0143884.
546. Lin, Q., et al., *IP(3) receptors regulate vascular smooth muscle contractility and hypertension.* JCI Insight, 2016. **1**(17): p. e89402.
547. Murakami, R., et al., *p122 Protein Enhances Intracellular Calcium Increase to Acetylcholine.* 2010. **30**(10): p. 1968-1975.
548. Wendling, O., et al., *Atp6ap2 ablation in adult mice impairs viability through multiple organ deficiencies.* Scientific Reports, 2017. **7**(1): p. 9618.
549. Li, L., et al., *Cardiomyocyte specific deletion of PP2A causes cardiac hypertrophy.* American journal of translational research, 2016. **8**: p. 1769-1779.
550. Lexow, J., et al., *Cardiac fibrosis in mice expressing an inducible myocardial-specific Cre driver.* Dis Model Mech, 2013. **6**(6): p. 1470-6.
551. Koitabashi, N., et al., *Avoidance of transient cardiomyopathy in cardiomyocyte-targeted tamoxifen-induced MerCreMer gene deletion models.* Circ Res, 2009. **105**(1): p. 12-5.
552. Bersell, K., et al., *Moderate and high amounts of tamoxifen in αMHC-MerCreMer mice induce a DNA damage response, leading to heart failure and death.* Dis Model Mech, 2013. **6**(6): p. 1459-69.
553. Hall, M.E., et al., *Systolic dysfunction in cardiac-specific ligand-inducible MerCreMer transgenic mice.* Am J Physiol Heart Circ Physiol, 2011. **301**(1): p. H253-60.
554. Manso, A.M., et al., *Loss of mouse cardiomyocyte talin-1 and talin-2 leads to β-1 integrin reduction, costameric instability, and dilated cardiomyopathy.* Proc Natl Acad Sci U S A, 2017. **114**(30): p. E6250-e6259.
555. Zemljic-Harpf, A.E., et al., *Cardiac-myocyte-specific excision of the vinculin gene disrupts cellular junctions, causing sudden death or dilated cardiomyopathy.* Mol Cell Biol, 2007. **27**(21): p. 7522-37.
556. Perkins, A.D., et al., *Integrin-mediated adhesion maintains sarcomeric integrity.* Developmental Biology, 2010. **338**(1): p. 15-27.

557. Fogh, B.S., Multhaupt, H.A., and Couchman, J.R., *Protein kinase C, focal adhesions and the regulation of cell migration.* J Histochem Cytochem, 2014. **62**(3): p. 172-84.
558. Weber, E.M., et al., *Pup mortality in laboratory mice – infanticide or not?* Acta Veterinaria Scandinavica, 2013. **55**(1): p. 83.
559. Mericskay, M., et al., *Inducible mouse model of chronic intestinal pseudo-obstruction by smooth muscle-specific inactivation of the SRF gene.* Gastroenterology, 2007. **133**(6): p. 1960-70.
560. Foo, S.S., et al., *Ephrin-B2 Controls Cell Motility and Adhesion during Blood-Vessel-Wall Assembly.* Cell, 2006. **124**(1): p. 161-173.

Acknowledgement

This thesis would not have been possible without the help of many people and I would like to express my sincere gratitude here.

I am thankful to Prof. Dr. Reinhard Fässler for giving me the opportunity to work on this exciting research topic.

Second, I would like to thank Prof. Dr. Dr. med. Oliver Söhnlein and Prof. Dr. Christian Wahl-Schott, for being part of my thesis committee, for offering advice, leaving room for valuable discussions and for their continuous support in times of doubt and difficulties. I am also grateful to Prof. Markus Sperandio for making things possible, for joining my thesis committee and for supporting me at the end of my thesis.

Most of all, I am especially thankful to Dr. Ralph Böttcher for giving me the possibility to work on this very interesting topic, the many helpful advices in meetings and discussions and for all his untiring support during the time of my PhD thesis. Thank you, Ralph, for all your encouragement, guidance and trust in me and my work. And thank you, for giving me the opportunity to grow as a scientist in my own speed and to support my personal growth.

Furthermore, I would like to thank my current lab members for the enjoyable working atmosphere and the important assistance in practical and theoretical questions. Special thanks to Hildegard Reiter (Mischa) for all her support in the daily lab life and all her encouraging words in difficult times; Alex Felber for his invaluable support with the animals (my life-saver); Dr. Peter Krenn for always answering my questions and offering help, and Jakob Reber for his perpetual and infectious scientific enthusiasm. Moreover, I would like to thank my former colleagues Dr. Tilman Ziegler, Dr. Valeria Samarelli, Dr. Wafa Bouaziz, Dr. Anita Wasik and Dr. Hui-yuan Tseng for all their support during our time in the lab and beyond.

In addition, I would like to thank Klaus Weber for constant technical support, Ines Lach-Kusevic for her administrative work and the animal caretakers, for their extremely valuable work and help with special wishes related to the animals. Furthermore, I would like to thank people from the Core facility, especially Dr. Martin Spitaler and Giovanni Cardone for their endless support in microscopic questions; Dr. Nagarjuna Nagaraj and Anja Wehner for giving me an understanding of the world of proteomics and interactomics; and Dr. Sabine Suppmann and Judith Scholz for their help in recombinant protein production.

Last but not least, I would like to thank my family for their continuous support and endless believe in me. I would like to thank Marian for loving me the way I am, for all his encouragements and for bearing all my bad days during the last year. And I would like to thank Markus for always believing in me and cheering me up in difficult times.

Affidavit

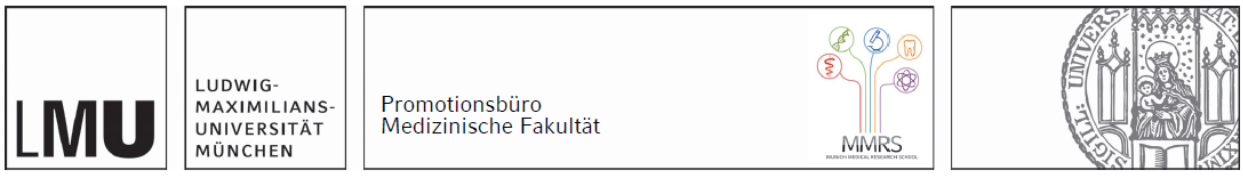

Scholze, Sarah

Surname, first name

Dietrichsteinstraße 68

Street

81249 Munich, Germany

Zip code, town, country

I hereby declare, that the submitted thesis entitled:

The role of parvins in the cardiovascular system

is my own work. I have only used the sources indicated and have not made unauthorized use of services of a third party. Where the work of others has been quoted or reproduced, the source is always given.

I further declare that the submitted thesis or parts thereof have not been presented as part of an examination degree to any other university.

Munich, 20.02.2021

place, date

Sarah Scholze

Signature doctoral candidate

Confirmation of congruency

LMU LUDWIG-MAXIMILIANS-UNIVERSITÄT MÜNCHEN

Promotionsbüro
Medizinische Fakultät

MMRS

Confirmation of congruency between printed and electronic version of the doctoral thesis

Scholze, Sarah

Surname, first name

Dietrichsteinstraße 68

Street

81249 Munich, Germany

Zip code, town, country

I hereby declare, that the submitted thesis entitled:

The role of parvins in the cardiovascular system

is congruent with the printed version both in content and format.

Munich, 20.02.2021

place, date

Sarah Scholze

Signature doctoral candidate

Appendix

In the following, papers I and II are reprinted.

Paper I

Tseng HY, Samarelli AV, Kammerer P, **Scholze S,** Ziegler T, Immler R, Zent R, Sperandio M, Sanders CR, Fässler R, Böttcher RT. LCP1 preferentially binds clasped αMβ2 integrin and attenuates leukocyte adhesion under flow. J Cell Sci. 2018 Nov 21;131(22):jcs218214

Paper II

Burbaum L, Schneider J, **Scholze S.**, Böttcher RT, Baumeister W, Schwille P, Plitzko JM, Jasnin M. Bridging length scales in sarcomere organization within native cardiomyocytes. bioRXiv. 2020 Sep 09.

© 2018. Published by The Company of Biologists Ltd | Journal of Cell Science (2018) 131, jcs218214. doi:10.1242/jcs.218214

RESEARCH ARTICLE

LCP1 preferentially binds clasped αMβ2 integrin and attenuates leukocyte adhesion under flow

Hui-yuan Tseng[1], Anna V. Samarelli[1], Patricia Kammerer[1], Sarah Scholze[1], Tilman Ziegler[1], Roland Immler[3], Roy Zent[4,5], Markus Sperandio[3], Charles R. Sanders[6], Reinhard Fässler[1,2] and Ralph T. Böttcher[1,2,*]

ABSTRACT

Integrins are α/β heterodimers that interconvert between inactive and active states. In the active state the α/β cytoplasmic domains recruit integrin-activating proteins and separate the transmembrane and cytoplasmic (TMcyto) domains (unclasped TMcyto). Conversely, in the inactive state the α/β TMcyto domains bind integrin-inactivating proteins, resulting in the association of the TMcyto domains (clasped TMcyto). Here, we report the isolation of integrin cytoplasmic tail interactors using either lipid bicelle-incorporated integrin TMcyto domains (α5, αM, αIIb, β1, β2 and β3 integrin TMcyto) or a clasped, lipid bicelle-incorporated αMβ2 TMcyto. Among the proteins found to preferentially bind clasped rather than the isolated αM and β2 subunits was L-plastin (LCP1, also known as plastin-2), which binds to and maintains the inactive state of αMβ2 integrin *in vivo* and thereby regulates leukocyte adhesion to integrin ligands under flow. Our findings offer a global view on cytoplasmic proteins interacting with different integrins and provide evidence for the existence of conformation-specific integrin interactors.

KEY WORDS: LCP1, Integrin inactivator, Leukocyte adhesion, Integrin interactome, Proteomics

INTRODUCTION

Integrins are α/β heterodimeric cell surface receptors that establish cell–cell and cell–extracellular matrix (ECM) interactions required for migration, proliferation, differentiation and survival. The α and β integrin subunits are composed of a large extracellular domain, a single transmembrane segment of ∼25 amino acids and a short cytoplasmic tail of 10–70 amino acids. Integrin binding to ligand leads to integrin clustering, the assembly of a protein network termed adhesome, and eventually the transduction of biochemical and biophysical signals (also called outside-in signaling).

A hallmark of integrins is their ability to adopt different affinities toward their ligand. The affinity switch from an unbound, low-affinity conformation to the bound, high-affinity conformation (called integrin activation or inside-out signaling) is believed to be mediated by the two adaptor protein families, talins and kindlins, which bind to specific sites in the β integrin cytoplasmic domain and to lipids of the nearby plasma membrane. The consequence of talin and kindlin binding is the dissociation of the transmembrane and cytoplasmic (TMcyto) domains of the α and β subunits, leading to the separation (unclasping) of the proximal legs of the α/β integrin ectodomain, followed by a conformational change in the extracellular domain that allows high-affinity ligand binding (Campbell and Humphries, 2011; Kim et al., 2011; Shattil et al., 2010). Although it is evident that the high-affinity conformation can be reversed, it is not entirely clear how this is achieved at the molecular level. Several proteins such as sharpin, filamin family members and ICAP, as well as phosphorylation of the β integrin tail, have been shown to displace talin and/or kindlin family proteins, leading to the association of integrin α/β TMcyto subunits through the interaction between GxxxG dimerization motifs in the outer half of the plasma membrane (called the outer plasma membrane clasp) and a salt bridge in the juxtamembrane region at the inner half of the plasma membrane (called the inner plasma membrane clasp) (Lau et al., 2009; Yang et al., 2009). Both the outer and the inner plasma membrane clasps constitute weak interactions, suggesting that proteins may exist that lock and/or maintain integrins in an inactive state. Such integrin inactivators could represent a regulatory mechanism that efficiently prevents unwanted integrin activation, which is particularly important for cells of hematopoietic origin (Schmidt et al., 2013). Furthermore, proteins interacting with inactive integrins would allow cells to distinguish between active and inactive integrins in other processes including integrin biosynthesis and intracellular integrin trafficking, which affect the levels of integrins at the cell surface and modulate signaling pathways (Bouvard et al., 2013; De Franceschi et al., 2015).

In the present paper, we developed a screening strategy to identify proteins that preferentially bind clasped α/β integrin tails. Among the proteins that favored binding of clasped αMβ2 integrin tails was L-plastin. Plastins are a family of three actin-bundling proteins with distinct expression patterns: T-plastin (also known as plastin-3) is broadly expressed, including in all cells with replicative potential (Lin et al., 1993), I-plastin (also known as plastin-1) is restricted to intestine and kidney cells, while L-plastin (LCP1, also known as plastin-2) expression occurs in leukocytes and in many malignant human cell lines of non-hematopoietic origin (Lin et al., 1988). Plastins consist of two amino-terminal EF-hands, implicated in Ca^{2+} binding, and two tandem actin-binding domains each composed of two calponin homology domains. Although plastins are primarily involved in regulation of the actin cytoskeleton, they possess additional properties and are involved in several cellular functions such as cell migration, neutrophil function, DNA repair and endocytosis (Delanote et al., 2005). LCP1 has been linked to integrins, yet the precise mechanism of how it regulates integrin function is unclear. LCP1 has been shown to interact with β integrin subunits (Le Goff et al., 2010), and to activate αMβ2 integrin in

[1]Department of Molecular Medicine, Max Planck Institute for Biochemistry, 82152 Martinsried, Germany. [2]DZHK (German Centre for Cardiovascular Research), partner site Munich Heart Alliance, 80802 Munich, Germany. [3]Walter Brendel Center for Experimental Medicine, Ludwig-Maximilians-University, 81377 Munich, Germany. [4]Division of Nephrology, Department of Medicine, Vanderbilt University, Nashville, 37232 Tennessee, USA. [5]Department of Medicine, Veterans Affairs Medical Center, Nashville, 37232 Tennessee, USA. [6]Department of Biochemistry, Center for Structural Biology, and Institute of Chemical Biology, Vanderbilt University School of Medicine, Nashville, 37232 Tennessee, USA.

*Author for correspondence (rboettch@biochem.mpg.de)

M.S., 0000-0002-7689-3613; R.T.B., 0000-0003-3050-7163

Received 27 March 2018; Accepted 7 September 2018

Journal of Cell Science (2018) 131, jcs218214. doi:10.1242/jcs.218214

polymorphonuclear neutrophils (PMNs) (Jones et al., 1998) and αVβ3 integrin in K562 cells (Wang et al., 2001). In contrast, however, LCP1$^{-/-}$ neutrophils exhibit no integrin activation defect but fail to mount an efficient integrin adhesion-dependent respiratory burst (Chen et al., 2003). Here, we show that LCP1 forms a ternary complex with αMβ2 integrin and negatively regulates integrin-mediated cell adhesion by maintaining αMβ2 integrin in an inactive conformation.

RESULTS

α and β integrin tail interactors isolated with bicelle-incorporated TMcyto domains

Due to the short cytoplasmic domains of integrin α and β subunits, direct integrin interactors such as talins and kindlins are in close proximity to the plasma membrane with which they interact to reinforce integrin tail binding and induce signaling (Anthis et al., 2009; Goult et al., 2010, 2009; Liu et al., 2011; Moore et al., 2012; Perera et al., 2011; Saltel et al., 2009). Previous studies employed yeast two-hybrid or pull-down experiments with either single α or β integrin cytoplasmic domains to identify specific binding partners (Legate and Fassler, 2009; Morse et al., 2014; Raab et al., 2010). However, these approaches do not detect binding partners whose interaction with the plasma membrane is crucial for integrin tail binding. To solve this issue we incorporated the recombinant integrin β1 TMcyto domain into bicelles as a membrane-mimetic environment. Bicelles form discoidal nanostructures that have been used to study the structure of different integrin TMcyto domains through the use of nuclear magnetic resonance (NMR) spectroscopy (Lau et al., 2008a,b, 2009; Lu et al., 2012; Surya et al., 2013). The bicelles used in this work were composed of the long-chain phospholipid 1,2-dimyristoyl-*sn*-glycero-3-phosphocholine (DMPC) and 6-cyclohexyl-1-hexylphosphocholine (Cyclofos-6) as the short-chain phospholipid that stabilizes the edge of the bilayer discs (Fig. S1A). As biological membranes contain negatively charged lipids (Leventis and Grinstein, 2010) we replaced 10% of DMPC with phosphatidylserine (POPS) and confirmed the phospholipid ratio in the bicelles through the use of liquid chromatography-mass spectrometry (LC-MS) (Fig. S1A–C). In line with previous studies (Lu et al., 2012; van Dam et al., 2004), changing the ratio of DMPC to Cyclofos-6, referred to as the q-value, gave rise to bicelles with hydrodynamic radii ranging from 3.16±0.08 nm (mean±s.e.m.; q=0.25) to 19.95±0.64 nm (q=4), as measured using dynamic light scattering (DLS) (Fig. S1D).

Next, we expressed His-tagged α5 and β1 integrin TMcyto domains in *E. coli*, purified them and determined their incorporation into bicelles by measuring their hydrodynamic radius via DLS. Although α5 and β1 integrin TMcyto domains were successfully incorporated into bicelles with a q-value of 0.25, their direct incorporation into bigger bicelles (q=2) failed (Fig. S1E). As *in silico* modeling suggests that the bicelle radius must be >8 nm to support membrane interactions of kindlin and talin proteins bound to β3 integrin, we tested the possibility of increasing the radius by mixing small and large bicelles. Indeed, incubation of q=0.25 bicelles with q=4 bicelles to produce a q=2* (asterisk indicates the generation of q=2 bicelles by incubating q=0.25 bicelles with q=4 bicelles) mixture resulted in a homogenous solution of bicelles with a hydrodynamic radius of 8.88±0.51 nm (Fig. S1D). Using this approach we incorporated α5 or β1 integrin TMcyto domains into q=0.25 bicelles and added an equal volume of q=4 bicelles, resulting in q=2* bicelles containing our protein of interest with a hydrodynamic radius of ∼10 nm (Fig. S2; Table S1).

To test whether negatively charged lipids in β1 integrin TMcyto-containing bicelles increase the association of proteins to β1 tails in pull-down experiments, we incubated His-tagged TMcyto domains of β1 and α5 integrins either incorporated into bicelles or left without bicelles with mouse fibroblast cell lysates and pulled down talin and kindlin-2, known to establish plasma membrane interactions for optimal integrin binding (Anthis et al., 2009; Goult et al., 2010, 2009; Liu et al., 2011; Moore et al., 2012; Perera et al., 2011). Due to the mild washing conditions, we observed a very weak binding of both proteins to α5 integrin TMcyto and empty beads. Importantly, however, β1 integrin TMcyto domain incorporated into bicelles bound significantly more talin (48%) and kindlin-2 (38%) compared to the β1 integrin TMcyto domain alone (Fig. 1A,B). These data show that the incorporation of integrin TMcyto domains into negatively charged bicelles can increase the affinity of proteins for the integrin cytoplasmic domains and thereby could promote the identification of novel integrin tail interactors in pull-down assays. To identify interacting partners of different integrin TMcyto domains, we recombinantly expressed α5, αM and αIIb as well as β1, β2 and β3 integrin TMcyto domains, incorporated them into q=0.25 bicelles, mixed those with q=4 bicelles and performed a pull-down with hypotonic cell lysates derived from mouse bone marrow-derived macrophages (BMDM). After pull-down, the interacting proteins were resolved using SDS-polyacrylamide gel electrophoresis (SDS-PAGE) and then identified through the use of liquid chromatography-tandem mass spectrometry (LC-MS/MS) (Fig. S3A).

Our analysis identified around 1500 proteins (Table S2). Label-free quantification revealed good reproducibility and consistency between replicates (Fig. S3B). Four, 43 and 156 proteins were significantly enriched in the α5, αM and αIIb cytoplasmic tail interactome, respectively, (Fig. 1C,D; Table S3), while 60, 55 and 107 proteins were enriched in β1, β2 and β3 pull-downs, respectively (Fig. 1C,D; Table S3). Interestingly, no common interactors were identified for all three integrin α cytoplasmic tails, while the β1, β2 and β3 subunits had 13 common interactors, including talin-1 and filamin-1 (also known as filamin-A) (Fig. 1D; Table S3). These results are in line with the presence of conserved motifs shared among the β1, β2 and β3 integrin cytoplasmic domains and highly divergent motifs in α integrin tails. These data demonstrate the feasibility of screening approaches based on bicelle-incorporated proteins and show qualitative differences between the interactomes of different integrin subunits.

Identification of conformation-specific αMβ2 integrin interactors

Various proteins bind to either α or β cytoplasmic tails to regulate the integrin activity state (Legate and Fassler, 2009). However, filamin-1 was very recently shown to simultaneously bind inactive, clasped αIIbβ3 integrins in order to maintain the inactive state (Liu et al., 2015). A shortcoming of earlier screening approaches is the use of single α or β integrin cytoplasmic domains, which do not recruit interactors that require both integrin tails for binding. To detect such integrin interactors we developed a strategy to mimic the heterodimeric integrin cytoplasmic tail conformation in its inactive, clasped state. Our method is based on the Jun–Fos dimerization domains (fused to the ectoplasmic N-termini of the TM domains) as 'velcro' to mediate heterodimer formation. Since a previous fluorescence resonance energy transfer (FRET) study revealed a spatial separation of the αM and β2 subunit cytoplasmic tails in the plasma membrane upon chemokine-induced integrin activation (Lefort et al., 2009), we decided to construct a Jun–Fos-dimerized αMβ2 TMcyto domain to clasp the αM and β2 TMcyto domains and used it as bait to search for interactors of integrins in the inactive

Journal of Cell Science (2018) 131, jcs218214. doi:10.1242/jcs.218214

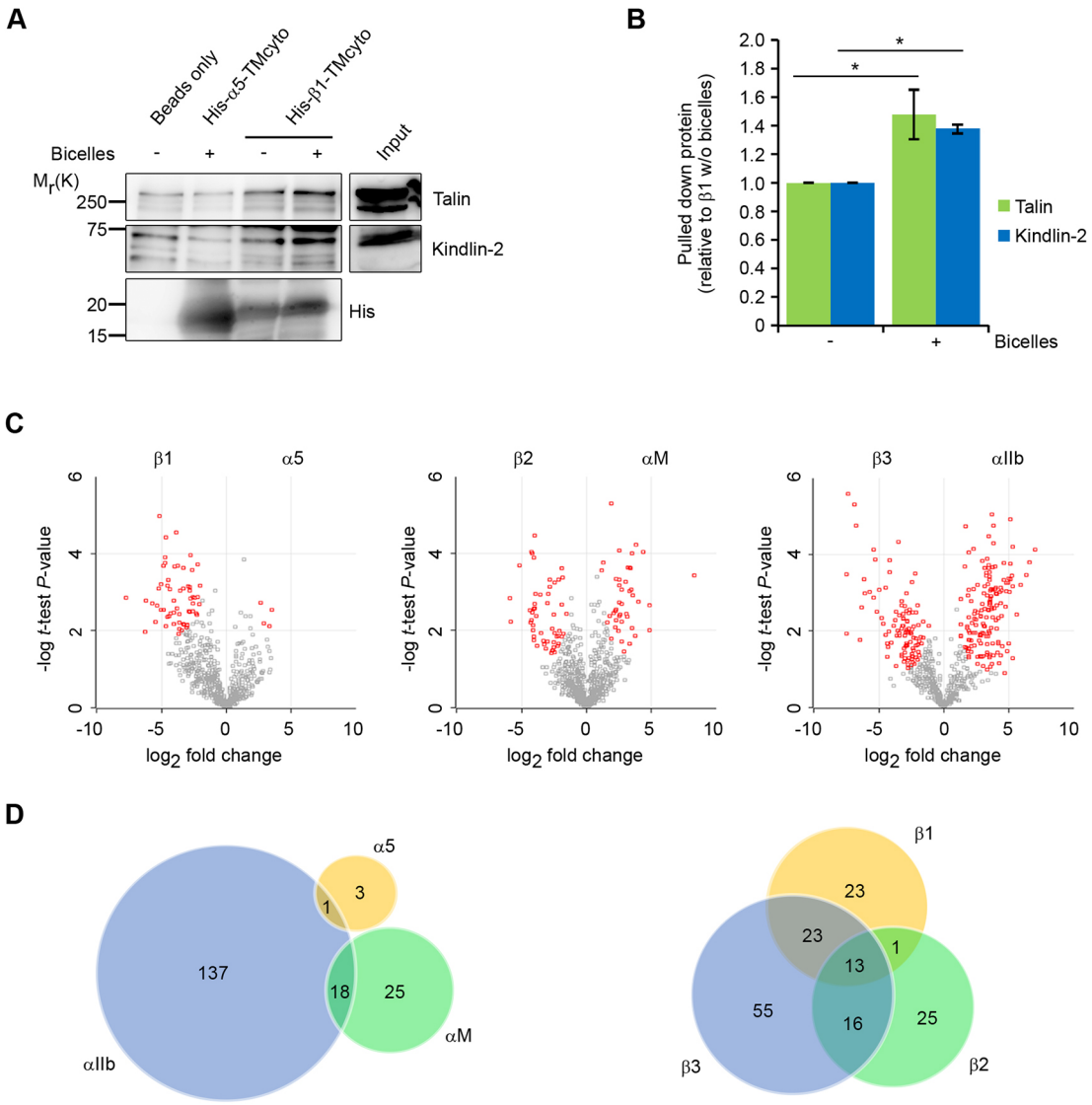

Fig. 1. Interactome analysis of individual, lipid-incorporated α and β integrin TMcyto domains. (A) Pull-down of talin and kindlin-2 using recombinant His-tagged α5–TMcyto or β1–TMcyto proteins with or without bicelle incorporation, from cell lysates. (B) Quantification of talin and kindlin-2 binding to His-tagged β1–TMcyto proteins with or without bicelle incorporation from western blots, using ImageJ (mean±s.e.m., n=3, *P<0.05). (C) Volcano plots of fold-change of protein intensities versus t-test P-value for binding to distinct α and β integrin subunits; statistically significant (P<0.05) interactors are labeled in red. (D) Overlap of proteins identified as interactors with the different α and β TMcyto domains illustrated as a Venn diagram.

state. To this end we expressed recombinant proteins consisting of an amino-terminal tag sequence (His or FLAG for purification and pull-down) followed by a cysteine–glycine (CG) linker, the Jun–Fos dimerization domains, a 4× glycine linker (GGGG) and the αM or β2 integrin TMcyto domains (Fig. 2A,B). The CG linker was inserted to ensure stability, a parallel orientation and a correct stagger of the coiled coil sequences within the dimer, while the GGGG linker was inserted to provide flexibility of the integrin tails. The proteins were expressed and purified from bacteria (Fig. 2B, lanes 2–4) and when incubated together, His–Fos–αM–TMcyto and FLAG–Jun–β2–TMcyto formed heterodimers in a 1:1 ratio (Fig. 2B, lane 1). DLS measurements revealed that the incorporation of αM or β2 TMcyto into bicelles increased their size from 8.88±0.51 nm (empty bicelles) to 10.05±0.26 nm or 10.25±0.31 nm, and after incorporation of the Jun–Fos-dimerized αMβ2 TMcyto to 11.17±0.49 nm (Fig. S2).

The Jun–Fos-dimerized αMβ2 TMcyto domains incorporated into bicelles were used to pull down proteins from BMDM lysates. The interactome was subjected to LC-MS/MS and the identified proteins were quantified using the label-free quantification algorithm of the MaxQuant software and compared with the interactome from individual αM and β2 TMcyto domains. We identified 1561 proteins, and application of the statistical t-test between β2 and αMβ2 interactors revealed 222 proteins that increased binding to associated αMβ2 integrins (Fig. 2C, Table S4), among them filamin-2 (also known as filamin-C), and moesin, which has been shown to displace talin-1 and inactivate integrins (Vitorino et al., 2015). Taken together, these results highlight the existence of cytoplasmic proteins that interact predominantly or exclusively with different αMβ2 integrin structural states (corresponding to clasped inactive state or non-clasped activated state heterodimers).

L-plastin (LCP1) maintains αMβ2 integrins in an inactive state

The hematopoietic-specific α-actinin family member L-plastin (LCP1) (Lebart et al., 2004) was among the proteins with the strongest increase in binding to the clasped αMβ2 TMcyto domain (Fig. 2C). LCP1 is an

Journal of Cell Science (2018) 131, jcs218214. doi:10.1242/jcs.218214

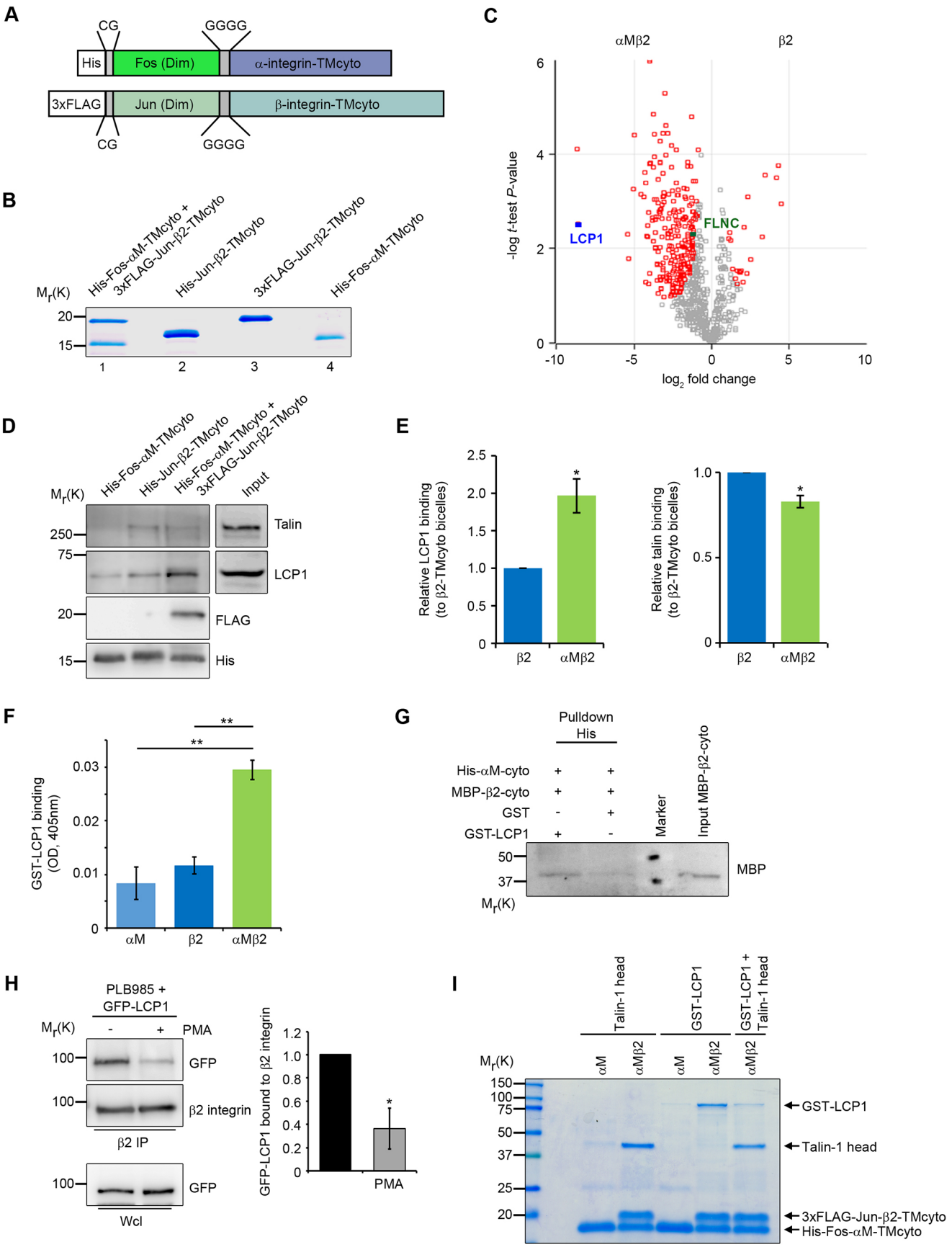

Fig. 2. See next page for legend.

Journal of Cell Science (2018) 131, jcs218214. doi:10.1242/jcs.218214

Fig. 2. Interactor screen with clasped α/β integrin TMcyto baits. (A) Schematic representation of the integrin TMcyto constructs. CG, cysteine-glycine motif to stabilize the dimer; Fos (Dim) and Jun (Dim), dimerization domain of Fos and Jun proteins; GGGG, glycine stretch to increase the flexibility of the integrin cytoplasmic tails. (B) Recombinant His–Fos–αM–TMcyto, His–Jun–β2–TMcyto, and 3×FLAG–Jun–β2–TMcyto were expressed and purified with Ni-NTA or FLAG–M2 beads as monomers (lane 2, 3, 4). Co-incubation of His–Fos–αM–TMcyto and 3×FLAG–Jun–β2–TMcyto followed by Ni-NTA reveals dimer formation (lane 1). (C) Volcano plot showing fold-change of protein intensities versus *t*-test *P*-value for cytosolic proteins interacting with αM–TMcyto versus αMβ2-TMcyo domains. Proteins with significantly increased binding to either αM or αMβ2 ($P<0.05$) are labeled in red. Filamin-2 (FLNC) and LCP1 are marked. (D) Western blot analysis of talin and LCP1 pulled down with individual αM–TMcyto and β2–TMcyto or clasped αMβ2–TMcyto domains embedded in bicelles. (E) Quantification of LCP1 and talin western blot band intensities shown in D (mean±s.e.m., $n=3$, $^{*}P<0.05$). (F) Quantification of GST or GST–LCP1 binding to immobilized His–Fos–αM–TMcyto, His–Jun–β2–TMcyto and the clasped His–Fos–αM–TMcyto/3×FLAG–Jun–β2–TMcyto dimer using solid-phase ligand-binding assays. Bound proteins were detected with anti-LCP1 antibodies. GST was used as control for nonspecific binding (mean±s.e.m., $n=3$, $^{**}P<0.01$). (G) Western blot showing the pull-down of MBP–β2–cyto with His–αM–cyto in the presence of GST–LCP1. (H) Western blot and densitometric analysis of β2 integrin co-immunoprecipitations for GFP and β2 integrin from lysates of PMA- or DMSO-treated PLB985 cells expressing GFP–LCP1. β2 integrin served as a loading control to quantify GFP–LCP1 binding (mean±s.e.m., $n=3$, $^{*}P<0.05$). (I) Binding of GST–LCP1 to His–Fos–αM–TMcyto or His–Fos–αM–TMcyto/3×FLAG–Jun–β2–TMcyto dimer was assessed in the absence or presence of recombinant talin-1 head. A representative SDS-PAGE of three independent experiments is shown.

actin-bundling protein that has been implicated in the formation and/or maintenance of integrin-associated adhesion structures (Jones et al., 1998; Morley, 2012; Wang et al., 2001). As LCP1 has been shown to interact with the cytoplasmic domain of β1 and β2 integrins (Le Goff et al., 2010), we first validated the interaction with bicelle-embedded, Jun–Fos-dimerized αMβ2 and individual β2 TMcyto domains in pull-down experiments. In line with our proteomics data, the Jun–Fos-dimerized αMβ2 TMcyto bait pulled down significantly more LCP1 than the β2 TMcyto bait. Conversely, talin was predominantly pulled down by the β2 TMcyto bait (Fig. 2D, E). Furthermore, purified recombinant glutathione S-transferase (GST)-tagged LCP1 also showed higher binding to clasped Jun–Fos-dimerized αMβ2 TMcyto compared to the individual αM and β2 TMcyto domains in ELISA assays (Fig. 2F). To further support the formation of a ternary complex between αM, β2 and LCP1 we performed pull-down experiments with recombinant GST, GST–LCP1, His–αM-cytoplasmic tail (His–αM–cyto), and maltose-binding protein–β2 cytoplasmic tail (MBP–β2–cyto) (Fig. S4A,B). These experiments revealed that His–αM–cyto was only able to pull down MBP–β2–cyto in the presence of GST–LCP1 but not in the presence of GST (Fig. 2G). GFP–LCP1 co-immunoprecipitated with β2 integrins from neutrophil-like PLB985 cell lysates and, importantly, this interaction was significantly reduced after agonist-induced integrin activation by phorbol 12-myristate 13-acetate (PMA) (Fig. 2H), indicating that LCP1 also preferentially interacts with inactive β2 integrins in cells. Finally, we tested whether LCP1 competes with talin for integrin binding similar to the integrin inactivator filamin-1 (Calderwood et al., 2001). To this end, we examined the binding of GST–LCP1 to dimeric αMβ2 integrin TMcyto in the absence or presence of excess amounts of purified talin-1 head domain and found that the talin-1 head reduced GST–LCP1 binding to Jun–Fos-dimerized αMβ2 TMcyto domains (Fig. 2I). Taken together, these findings indicate that LCP1 forms a ternary complex with cytosolic domains of αMβ2 integrin and competes with talin-1 for integrin tail binding.

LCP1 regulates β2 integrin-mediated functions and activity

The biochemical data suggests that LCP1 stabilizes the inactive conformation of αMβ2 integrins. In order to test this hypothesis we overexpressed GFP-tagged LCP1 in differentiated neutrophil-like PLB985 cells (Fig. S5A) and analyzed the levels of active αMβ2 integrin by fluorescence-activated cell sorting (FACS) using antibodies that recognize activation-induced epitopes. GFP–LCP1 but not GFP alone exerted a significant inhibitory effect on αMβ2 integrin activation (Fig. 3A) without altering the total cell-surface αMβ2 integrin levels (Fig. 3B). Interestingly, PMA- or tumor necrosis factor α (TNFα)-induced integrin activation failed to fully rescue the integrin activation defect in GFP–LCP1-overexpressing PLB985 cells (Fig. 3C).

Since LCP1 overexpression locks αMβ2 integrin in an inactive state, we expected that LCP1 depletion would render αMβ2 integrins more active. To deplete LCP1 we retrovirally expressed two different short hairpin RNAs (shRNA) in differentiated PLB985 and macrophage-like Raw264.7 cells (Fig. 3D; Fig. S5B), which reduced LCP1 levels by ∼85% and ∼70%, respectively. Surprisingly, LCP1 depletion did not change the levels of active αMβ2 in differentiated PLB985 cells (Fig. 3E) but instead increased the cell-surface levels of αMβ2 integrin in differentiated PLB985 (Fig. 3F) and Raw264.7 (Fig. S5C) cells without significantly altering αM and β2 integrin mRNA levels (Fig. S5D, E). Importantly, the increased αMβ2 integrin levels could be normalized after re-expression of shRNA-resistant wild-type LCP1 (Fig. 3G,H). LCP1 could potentially change cell-surface levels of β2 integrin without altering mRNA levels by affecting the total amount of β2 integrin protein in the cell or through altered surface presentation. We therefore analyzed β2 integrin protein levels and the stability of cell-surface β2 integrins in control and LCP1-depleted PLB985 and Raw264.7 cells. LCP1 levels had no effect on β2 integrin stability and protein levels in PLB985 cells (Fig. 3I,J) suggesting that changes in β2 integrin surface levels are due to altered protein trafficking. In contrast, LCP1 depletion in Raw264.7 cells reduced β2 integrin degradation and as consequence increased the total β2 integrin protein levels (Fig. 3K,L).

In line with a role of LCP1 as negative regulator of integrin activation, LCP1-depleted Raw264.7 cells showed increased adhesion to the integrin αMβ2 ligands fibrinogen and intercellular cell adhesion molecule-1 (ICAM-1) without prior agonist-induced integrin activation (Fig. 4A–D), even after sorting for equal αMβ2 integrin levels to control Raw264.7 cells (Fig. 4E,F). Interestingly, the increased adhesion of LCP1-depleted Raw264.7 cells was lost upon stimulation with PMA, which is a strong integrin activator (Fig. 4A,B), but not upon stimulation with TNFα (Fig. 4C,D). Similar results were obtained with LCP1-depleted differentiated PLB985 cells, which adhered more strongly to fibrinogen, and this effect was reversed on re-expression of LCP1 (Fig. 4G–I). Since phosphorylation of LCP1 on serine-5 and serine-7 regulates its actin bundling activity and localization (Morley, 2012), we next tested the effect of LCP1 phosphorylation on cell adhesion in PLB985 cells and its ability to interact with clasped αMβ2 integrin. To this end, we substituted serine-5 and serine-7 of LCP1, the major phosphorylation sites located in its regulatory headpiece domain (Lin et al., 1998; Shinomiya et al., 1995), with alanine (LCP1 SS/AA) or glutamic acid (LCP1 SS/EE). The serine-to-glutamic acid exchange strongly reduced the binding of GFP-tagged LCP1 (GFP–LCP1 EE) to Jun–Fos-dimerized αMβ2 TMcyto bait proteins compared to wild-type LCP1 and LCP1 SS/AA (Fig. 4H). As a result, expression of GFP–LCP1 EE in LCP1-depleted PLB985 cells failed to reduce cell adhesion to fibrinogen (Fig. 4I).

Journal of Cell Science (2018) 131, jcs218214. doi:10.1242/jcs.218214

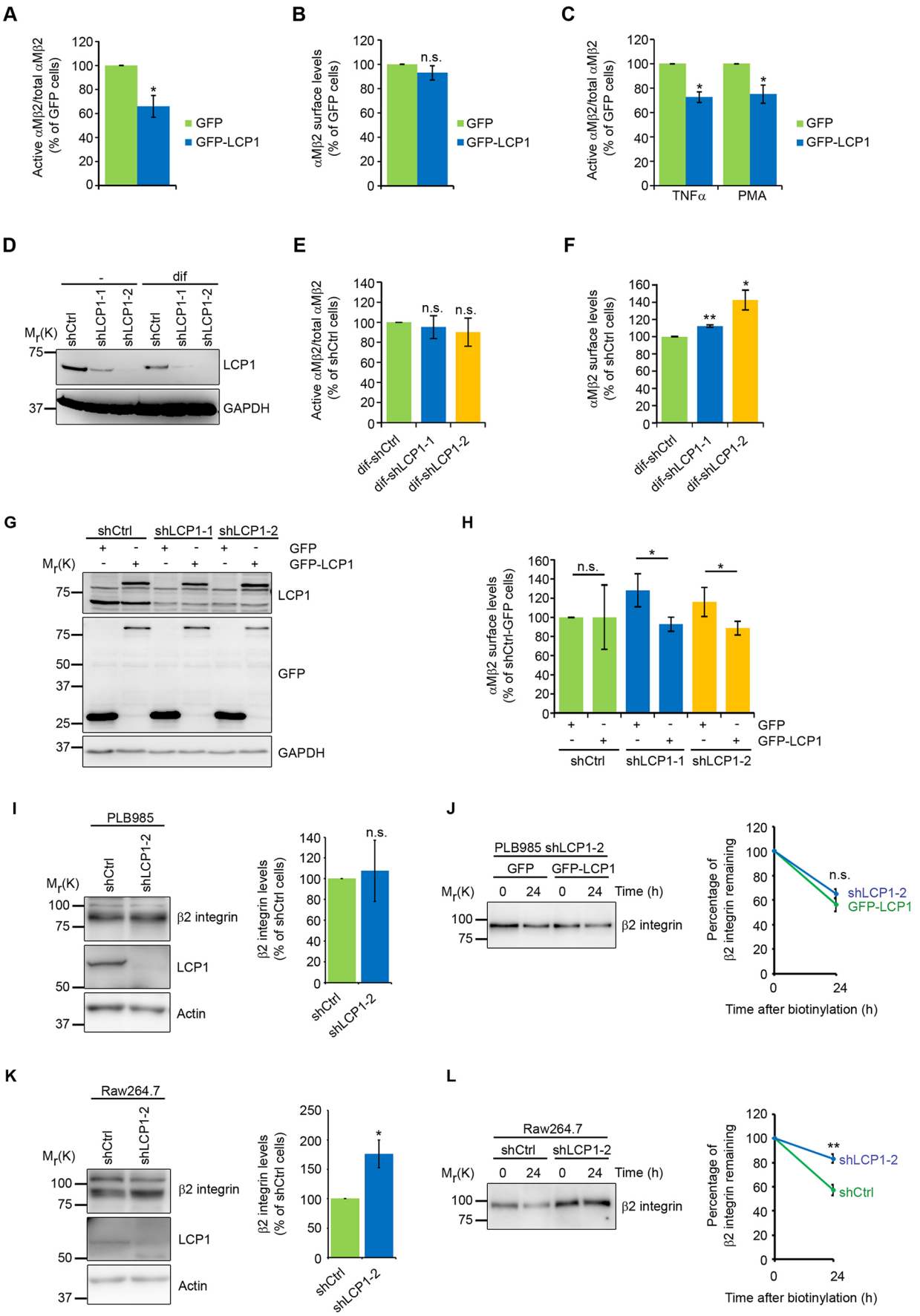

Fig. 3. See next page for legend.

Journal of Cell Science (2018) 131, jcs218214. doi:10.1242/jcs.218214

Fig. 3. LCP1 regulates αMβ2 integrin-mediated functions and activity. (A) Quantification of αMβ2 integrin activation in PLB985 cells overexpressing GFP–LCP1, determined by means of FACS using an antibody against an activation-induced epitope. Active αMβ2 integrin antibody binding levels were normalized to total cell-surface levels of αMβ2 integrin; values are normalized to GFP-expressing cells. (mean±s.e.m., n=5, *P<0.05). (B) αMβ2 integrin cell-surface expression in GFP–LCP1 overexpressing PLB985 cells relative to GFP-expressing PLB985 cells (values are normalized to GFP-expressing cells; mean±s.e.m.; n=5; n.s., not significant). (C) Quantification of active αMβ2 integrin cell-surface levels in GFP–LCP1-overexpressing PLB985 cells using FACS after TNFα- and PMA-induced integrin activation (active αMβ2 integrin levels were normalized to total cell-surface levels of αMβ2 integrin; values are normalized to GFP-expressing cells; mean±s.e.m., n=5, *P<0.05). (D) Western blot analysis of shRNA-mediated depletion of LCP1 in differentiated (dif) and undifferentiated PLB985 cells. Cells were infected with shCtrl or two different LCP1 shRNAs (shLCP1-1 and shLCP1-2). (E) Quantification of αMβ2 integrin activation in LCP1-depleted differentiated PLB985 cells using FACS (active αMβ2 integrin levels were normalized to total cell-surface levels of αMβ2 integrin; values are normalized to differentiated cells expressing shCtrl; mean±s.e.m.; n=3; n.s., not significant). (F) FACS analysis of αMβ2 cell-surface expression on LCP1-depleted differentiated PLB985 cells after LCP1 knockdown (values are normalized to shCtrl cells; mean±s.e.m., n=3, *P<0.05, **P<0.01). (G) Western blot of LCP1 and GFP in differentiated LCP1-depleted PLB985 cells after GFP–LCP1 re-expression. (H) Re-expression of shRNA-resistant GFP–LCP1 in LCP1-depleted PLB985 cells (shLCP1-1, shLCP1-2) restores αMβ2 integrin cell-surface levels. Expression of cell-surface αMβ2 integrin was determined using FACS (values are normalized to shCtrl–GFP; mean±s.e.m.; n=3; *P<0.05; **P<0.01, n.s., not significant). (I,K) Western blot and densitometric analysis of cell lysates from shCtrl and LCP1-depleted PLB985 (I) and Raw264.7 (K) cells for total β2 integrin protein levels. Actin served as a loading control to quantify β2 integrin levels (mean±s.e.m.; n=3; *P<0.05; n.s.; not significant). (J,L) Degradation of cell-surface β2 integrin was determined in PLB985 (J) and Raw264.7 (L) cells through biotinylation of cell-surface proteins and incubation for 0 h or 24 h, followed by streptavidin pull-down, western blot analysis and quantification (mean±s.e.m.; J, n=3; L, n=4; **P<0.01; n.s., not significant).

To test the influence of LCP1 on adhesion of PLB985 cells under flow conditions, we analyzed adhesion of LCP1-depleted and GFP–LCP1 overexpressing PLB985 cells using a microflow chamber. The experiments revealed that the number of adherent LCP1 knockdown cells per field of view (FOV) in fibrinogen-coated microflow chambers is significantly increased compared to shCtrl cells at baseline condition (Fig. 5A). By increasing shear stress levels in the flow chamber, control adherent cells detached faster compared to adherent LCP1-depleted PLB985 cells, indicating that the reduction in LCP1 levels induced resistance against shear forces (Fig. 5B). Conversely, GFP–LCP1-overexpressing cells adhered less compared to control cells at low shear (Fig. 5C) and detached faster after increasing the shear stress (Fig. 5D). Taken together, these results suggest that LCP1 negatively regulates adhesion strength and resistance to shear forces by maintaining αMβ2 integrin in an inactive conformation.

DISCUSSION

Integrins rely on the recruitment of proteins to their cytoplasmic tails to regulate their activity state, establish a connection to the actin cytoskeleton, initiate intracellular signaling and regulate their intracellular trafficking (Legate and Fassler, 2009; Margadant et al., 2011). Previous interaction studies identified cytoplasmic interactors of isolated α and β integrin subunits but most approaches are unable to detect interactors that require hetero-association of both integrin tails for binding. Therefore, we generated bait proteins for pull-down assays that consisted of clasped α/β integrin TMcyto domains. To ensure that integrin-interacting proteins requiring TMcyto–protein as well as plasma membrane–lipid interactions did not escape our detection, we embedded the clasped α/β TMcyto domains into bicelles. We used quantitative MS to compare the interactome of individual α and β integrin subunits (representing the unclasped, active conformation of an integrin transmembrane and cytoplasmic domain) with the clasped α/β integrin TMcyto domain (representing the inactive TMcyto-associated heterodimeric state) and found several integrin interactors that preferably bound to either single or clasped integrin TMcyto domains.

One important modification of our proteomic approach is the incorporation of integrin TMcyto domains into bicelles as a membrane-mimicking system to stabilize and support protein interactions with the integrin cytoplasmic tails. Integrins contain only short cytoplasmic domains and recruit their intracellular interactors in close proximity or even in direct contact with the plasma membrane. A number of intracellular integrin interactors, including talins and kindlins, contain membrane-binding sites that increase the association constant upon binding integrin tails and charged lipids (Anthis et al., 2009; Goult et al., 2010, 2009; Liu et al., 2011; Moore et al., 2012; Perera et al., 2011). Using integrin bait proteins incorporated into bicelles, we identified four, 43 and 156 proteins that were pulled down with α5, αM and αIIb cytoplasmic tails, respectively, and between 55 and 107 proteins with the different β integrin subunits. The number of potential interactors is slightly higher but still in the range of previously published proteomics interaction studies with α or β integrin peptides (Raab et al., 2010; Schiller et al., 2013). The increased number of interactors could be the result of less stringent, detergent-free washing conditions to preserve bicelle integrity or the presence of a membrane to facilitate and stabilize potential interactions. Indeed, the binding of talin and kindlin-2 to the β1 TMcyto domain increases after incorporation of the β1 TMcyto bait into bicelles. The charged membrane either presents an additional binding motif that adds to the overall affinity or favors optimal alignment of the two interactors for high-affinity binding, as has been shown for interaction of the talin FERM domain with the β3 cytoplasmic tail in the presence of negatively charged PtdIns(4,5)P2 (Moore et al., 2012). Despite the different pull-down approaches, we observed similar trends to those previously published regarding the number of interactors with the individual α or β cytoplasmic domains. For example, only a few proteins bind to α5 tails as compared to αIIb (Raab et al., 2010). Likewise, there are a higher number of β3 integrin interactors compared to β1 integrins (Schiller et al., 2013). Further modification of the bicelle composition, for example by adding specific phosphatidyl-inosites, would allow the analysis of protein recruitment to integrin cytosolic domains in specific membrane compartments.

An important property of integrins, usually not taken into account in proteomic-based screening approaches for interactors, is their ability to switch between conformational states. In their inactive state the TMcyto domains of the α and β integrin subunits are associated, while they become separated upon integrin activation. Cells distinguish between the two conformations during integrin activation on the cell surface to control ligand binding and the conformation-specific trafficking of integrins through the endosomal system (reviewed in De Franceschi et al., 2015). Evidence suggests that the inactive conformation of integrins may not be a default state but is dynamically regulated by the binding of intracellular proteins, referred to as integrin inactivators (Bouvard et al., 2013). Intracellular integrin inactivators trigger integrin inactivation and/or maintain integrins in an inactive state, thereby establishing a regulatory mechanism to efficiently prevent unwanted integrin activation. This mode of regulation is particularly important for αIIbβ3 integrin and β2-class integrins expressed on hematopoietic cells to prevent blood clotting or unwanted attachment of leukocytes to the vessel wall, with

Journal of Cell Science (2018) 131, jcs218214. doi:10.1242/jcs.218214

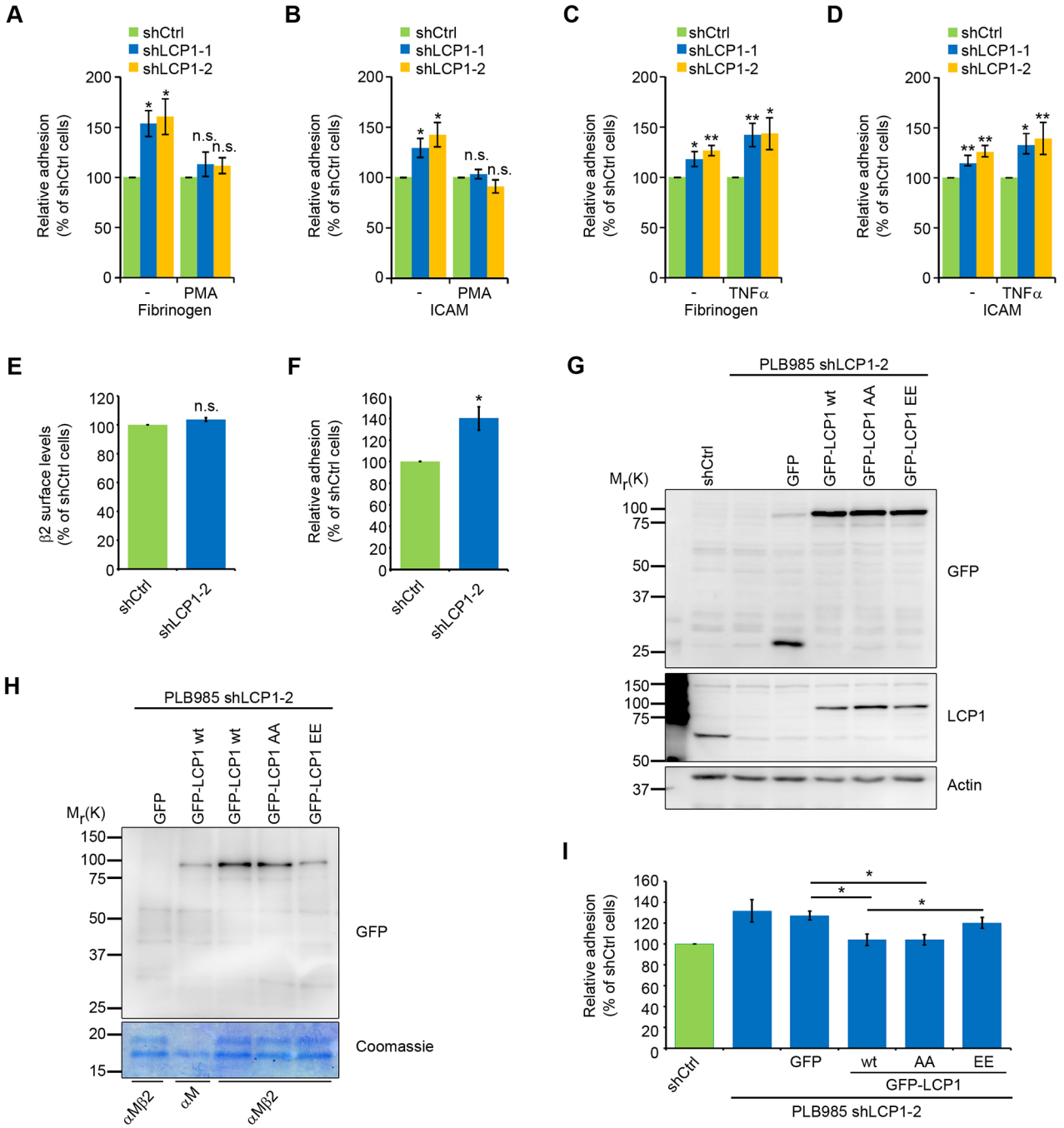

Fig. 4. LCP1 regulates αMβ2 integrin-mediated cell adhesion. (A–D) Quantification of cell adhesion of LCP1-depleted Raw264.7 cells on fibrinogen (10 µg/ml) (A,C) and ICAM-1 (4 µg/ml) (B,D) for 30 min with or without PMA (A,B) or TNFα (C,D) treatment; values are normalized to control cells (shCtrl) (mean±s.e.m.; *n*=3; **P*<0.05; ***P*<0.01; n.s., not significant). (E) FACS analysis of β2 integrin cell-surface expression on LCP1-depleted Raw264.7 cells sorted for equal β2 surface levels (values are normalized to shCtrl cells; mean±s.d., *n*=3, n.s. not significant). (F) Quantification of cell adhesion of control and LCP1-depleted Raw264.7 cells with equal αMβ2 integrin surface levels for 30 min on fibrinogen (10 µg/ml); values are normalized to control cells (shCtrl) (mean±s.e.m., *n*=4, **P*<0.05). (G) Western blot of LCP1 and GFP in differentiated LCP1-depleted PLB985 cells expressing GFP, or GFP-tagged wild-type or mutant LCP1 variants. (H) Western blot analysis to determine GFP–LCP1 binding to αMβ2–TMcyto domains with antibodies against GFP. Cell lysates of differentiated LCP1-depleted PLB985 cells expressing GFP, or GFP-tagged wild-type or mutant LCP1 variants, incubated with His–αM–TMcyto or clasped His–αM–TMcyto/3×FLAG–β2–TMcyto domains bound to Talon beads. Binding of recombinant integrin tails to the resin was verified using Coomassie Blue staining. A representative experiment of three independent experiments is shown. (I) Quantification of cell adhesion of differentiated control and LCP1-depleted PLB985 cells expressing GFP, or GFP-tagged wild-type or mutant LCP1 variants for 30 min on fibrinogen (100 µg/ml); values are normalized to control cells (shCtrl) (mean±s.d., *n*=5, **P*<0.05).

dramatic consequences for immune functions (Schmidt et al., 2013). With the exception of filamin-2 and moesin, however, we were unable to detect other prominent integrin tail-binding inactivators including sharpin, ICAP, etc. in our pull-down experiments.

To mimic the inactive heterodimeric integrin cytoplasmic tail conformation we developed a bait for pull-down experiments based on the Jun–Fos dimerization domains, which have been used to maintain heterodimeric association of recombinantly expressed α/β

Journal of Cell Science (2018) 131, jcs218214. doi:10.1242/jcs.218214

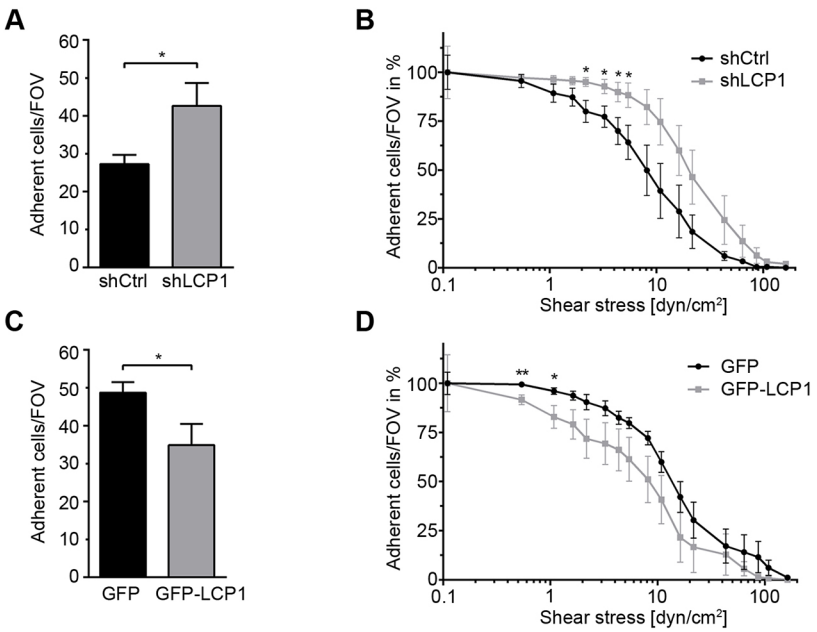

Fig. 5. LCP1 regulates αMβ2 integrin-mediated adhesion under shear flow. LCP1-overexpressing (GFP–LCP1) and LCP1-depleted (shLCP1) differentiated PLB985 cells and their controls (GFP and shCtrl, respectively) were allowed to attach to fibrinogen-coated flow chambers for 30 min, and then flow was initiated and flow rates increased every 30 s until all adherent cells detached. (A,C) Quantification of adherent (A) shLCP1 versus shCtrl cells/FOV and (C) GFP–LCP1 versus GFP cells/FOV at baseline conditions. (B,D) Percentage of adherent (B) shLCP1 versus shCtrl cells/FOV and (D) GFP–LCP1 versus GFP cells/FOV exposed to different shear stress levels (mean±s.e.m., n=7–8, $^{**}P$<0.01, $^{*}P$<0.05).

integrin ectodomains (Eble et al., 1998; Raynal et al., 2006). Unexpectedly, we observed a large number of proteins pulled down with the Jun–Fos-dimerized αMβ2 TMcyto tails compared to the single αM or β2 TMcyto domain. This could be due to the low stringency binding and washing conditions that pulled down low-affinity binding proteins and complexes as well as unspecific interactors with the Jun–Fos domains. Among the dimer-specific interactors, we identified filamin-2 and moesin, which have been shown to promote integrin inactivation (Das et al., 2011; Vitorino et al., 2015). Filamins have been established as negative regulators of integrin activation by competing with talin-1 for integrin β tails (Das et al., 2011; Ithychanda et al., 2009; Kiema et al., 2006). A recent NMR study showed that filamin-1 forms a ternary complex with the αIIb and β3 cytoplasmic tails to stabilize the integrin inner membrane clasp and thereby retains the integrin in a resting state (Liu et al., 2015). Moesin, a member of the ezrin, radixin and moesin (ERM) protein family, is phosphorylated by MAP4K4 and displaces talin-1 from integrin β tails, leading to integrin inactivation (Vitorino et al., 2015). Our proteomics data also suggest that moesin has binding sites for α and β tails and therefore binds associated αMβ2 integrins. However, further structural and biochemical analyses are necessary to support this hypothesis.

In addition to filamin-2 and moesin, we identified LCP1 as an interactor of clasped, inactive αMβ2 TMcyto tails. LCP1 is a member of the α-actinin family of actin crosslinking proteins, with a restricted expression pattern in hematopoietic cells and cancer tissue (reviewed in Delanote et al., 2005; Morley, 2012). Several members of the α-actinin family of proteins, particularly α-actinin-1, as well as filamin-1, link the actin cytoskeleton to the plasma membrane via interaction with integrins (Otey et al., 1990; Pavalko and LaRoche, 1993; Sharma et al., 1995). Previous studies have shown that LCP1 binds to the cytoplasmic domains of β1 and β2 integrins via its actin-binding domain (Le Goff et al., 2010). However, a structural characterization of how LCP1 engages the heterodimeric integrin cytoplasmic face has not been reported. Our pull-down and immunoprecipitation experiments suggest that LCP1 preferentially binds to clasped αMβ2 TMcyto tails and exhibits a lower affinity for the isolated αM and β2 cytoplasmic domains. A similar increased affinity has been observed for the ternary binding of filamin-1 to the cytoplasmic domains of αIIb and β3 integrin under clasped conditions (Liu et al., 2015).

To address the role of the LCP1–αMβ2 integrin complex, we analyzed the consequences of altering LCP1 protein levels on integrin activation in leukocytes. We found that LCP1 depletion leads to increased adhesion of macrophages and differentiated neutrophil-like PLB985 cells under resting conditions while LCP1 overexpression reduced the levels of active αMβ2 integrins on differentiated PLB985 cells. The increased adhesion of LCP1-depleted Raw264.7 cells to fibrinogen and ICAM-1 was lost upon treatment with PMA but not TNFα, confirming that PMA is the stronger integrin activator (Harokopakis and Hajishengallis, 2005). These findings suggest that the LCP1–αMβ2 complex stabilizes inactive integrins to prevent spontaneous and/or excess integrin activation in resting hematopoietic cells and the pathological consequences such as thrombosis or inflammation. Interestingly, neutrophils isolated from *LCP1* knockout mice have previously been reported to show diminished respiratory burst generation and increased adhesion under non-stimulatory conditions, while adhesion was normal after PMA, fMLP and TNFα stimulation (Chen et al., 2003). In addition, in previous studies LCP1 expression in CV-1 fibroblasts showed fewer and smaller focal contacts, often leading to the rounding-up of the cells (Arpin et al., 1994; Timmers et al., 2002). These observations would be in agreement with our findings that LCP1 stabilizes the inactive state of integrins. However, it has to be noted that LCP1 overexpression or knockdown could impact integrin function independent of its direct interaction with integrin cytosolic domains and that it might have additional functions affecting cell adhesion, including cytoskeletal alterations through its actin-bundling activity. We observed reduced binding of LCP1 SS/EE to clasped αMβ2 TMcyto domains. However, these mutations also increase the F-actin-binding activity of LCP1. With more structural information available, it will be possible to design LCP1 mutants that abolish integrin binding without affecting their interaction with actin to resolve the role of LCP1 in integrin activity regulation.

Finally, we found that depletion of LCP1 increased β2 integrin stability and cell-surface levels of αMβ2 integrin without changing β2 integrin mRNA levels in Raw264.7 cells, suggesting an

Journal of Cell Science (2018) 131, jcs218214. doi:10.1242/jcs.218214

additional role of LCP1 in reducing surface trafficking of inactive αMβ2 integrin. In contrast, depletion of LCP1 in differentiated PLB985 cells had only a small effect on cell-surface levels of αMβ2 integrin, and no discernable effect on integrin stability. Since cell-surface levels of β2 integrin were previously shown to remain unchanged in LCP1-depleted PMNs (Chen et al., 2003), it is possible that the effect of LCP1 on cell-surface levels of integrins is cell type-dependent. Several actin-regulatory proteins, including α-actinin-1 and LCP1, are involved in transmembrane protein trafficking (Burgueño et al., 2003; Foran et al., 2006; Schulz et al., 2004). Previous studies reported a role of Sac6P, the yeast LCP1 homolog, in the organization of the actin cytoskeleton and endocytosis of the maltose transporter (Adams et al., 1995; Penalver et al., 1997; Skau et al., 2011). Other studies have shown a role for LCP1 in E-cadherin endocytosis in colon cancer cells (Foran et al., 2006). Finally, there is evidence that LCP1 may also regulate the trafficking of transmembrane proteins by binding Rab5, a critical GTPase of the endocytic pathway (Hagiwara et al., 2011).

In conclusion, our study reveals that LCP1 regulates integrin-mediated cell adhesion by stabilizing the clasped conformation of αMβ2 integrin. Further investigations will be required to show how and to what extent α/β tail-binding integrin inactivators regulate dynamic adhesion and migration across a variety of cell types.

MATERIALS AND METHODS

Antibodies

The following antibodies, raised against the listed proteins, were used: Talin (8d4, Sigma; 1:1000), Kindlin-2 (MAB2617, Millipore; 1:1000), His (2365, Cell Signaling Technology; 1:1000), FLAG-M2-HRP (A8592, Sigma; 1:10,000), GAPDH (CB1001, Calbiochem; 1:2000), LCP1 (GTX 114524, Genetex; 1:1000), GFP (A11122, Invitrogen; 1:1000), β2 integrin (gift from Dr Melanie Laschinger, Technical University of Munich, Germany; 1:200), β2 integrin (sc-8420, Santa Cruz Biotechnology; 2-4 µg), activated αM integrin (301402, BioLegend; 1:100), αM integrin (301302, BioLegend; 1:100), MAC1-PE (12-0112, eBioscience; 1:200), MAC1-biotin (557395, PharMingen; 1:200), MBP-HRP (E8038, New England Biolabs; 1:1000).

The following secondary antibodies were used: goat anti-mouse Alexa Fluor 546 (A-11003, Life Technologies; 1:200), goat anti-mouse Alexa Fluor 488 (A-11029, Life Technologies; 1:200) donkey anti-mouse Alexa Fluor 647 (A-31571, Life Technologies; 1:200), goat anti-rat HRP (712035150, Dianova; 1:10,000), goat anti-mouse HRP (172-1011, Bio-Rad; 1:10,000) and goat anti-rabbit HRP (172-1019, Bio-Rad; 1:10,000), streptavidin-Cy5 (016160084, Dianova; 1:200).

Recombinant human ICAM-1/CD54 (ADP4-200) and mouse TNFα (410-MT) were obtained from R&D Systems.

Plasmids

For recombinant bacterial expression, integrin β1–TMcyto (residues from 719 to 799 of the full-length mouse β1 integrin subunit), integrin β2–TMcyto (residues from 698 to 771 of the full-length mouse β2 integrin subunit), β3–TMcyto (residues from 714 to 787 of the full-length mouse β3 integrin subunit), α5–TMcyto (residues from 993 to 1054 of the full-length mouse α5 integrin subunit), αIIb–TMcyto (residues from 986 to 1033 of the full-length mouse αIIb integrin subunit), αM–TMcyto (residues from 1106 to 1153 of the full-length mouse αM integrin subunit) were cloned in-frame with the Fos dimerization domain (residues from 161 to 200 of full-length mouse Fos protein) (αIIb–TMcyto, αM–TMcyto and α5–TMcyto) or Jun dimerization domain (residues from 277 to 318 of full-length mouse Jun protein) (β1–TMcyto, β2–TMcyto and β3–TMcyto) and subcloned into the pET15b vector (Clontech) to generate His–Fos–α5–TMcyto, His–Fos–αIIb–TMcyto, His–Fos–αM–TMcyto, His–Jun–β1–TMcyto, His–Jun–β2–TMcyto, and His–Jun–β3–TMcyto constructs. β2–cyto (residues from 726 to 771 of the full-length mouse β2 integrin subunit) was cloned into pCoofy35 and αM–cyto (residues from 1130 to 1153 of the full-length mouse αM integrin subunit) was cloned into pCoofy17 to generate MBP–β2–cyto and His–αM–cyto, respectively. The 6×His tag sequence was replaced with a 3×FLAG tag within pET16b vector to generate 3×FLAG–Jun–β2–TMcyto.

To stably knock down LCP1 in PLB985 cells, shRNA targeting the human LCP1 sequences were introduced into the pSUPER.retro vector (OligoEngine) to produce retroviral particles: 5′-AGTAGCCTCTC-CTGTATTT-3′ (shLCP1-1), 5′-AGAAGCTGCAGTGGTATTA-3′ (shLCP1-2). In Raw264.7 cells, shRNA target sequences directed against the mouse LCP1 sequence were introduced into the pSUPER.retro vector to produce retroviral particles: 5′-GATGGCATAGTTCTTTGTA-3′ (shLCP1-1), 5′-CAAGTAGCTTCTGCTATAA-3′ (shLCP1-2). The open reading frame of LCP1 was amplified through the use of PCR from the OCAA human library clone OCAAo5051D1183D (imaGenes) and cloned into pJET1.2 cloning vector (ThermoFisher). LCP1 SS/AA and SS/EE in which the serine 5 and serine 7 were substituted with alanine or glutamic acid were cloned using site-directed mutagenesis. The different LCP1 variants were cloned into pEGFP-N1 (Clontech), and RRL-CMV-GFP lentiviral vector (provided by Dr Alexander Pfeifer, University of Bonn, Germany). Wild-type LCP1 was subcloned into pGEX-6P-1 (GE Healthcare) to express GST-tagged LCP1.

Cell culture

Raw264.7 cells were cultured in Dulbecco's modified Eagle's medium (DMEM) (Gibco) and PLB985 cells in RPMI (Gibco), both supplemented with 10% (v/v) FBS at 37°C and 10% CO_2, and free of mycoplasma contamination. Differentiation of PLB985 cells into neutrophil-like cells was carried out as described (Pivot-Pajot et al., 2010). Briefly, differentiation was induced through incubation of PLB985 cells in RPMI medium supplemented with 5% (v/v) FBS and 1.25% (v/v) DMSO for five days. The medium was changed once on day three of the differentiation period.

Bone marrow was isolated from C57BL/6 mice and passed through a 70 µm cell strainer (BD Biosciences) to obtain single cell suspensions. 4×10^6 cells were seeded in 15 cm petri dishes (non-treated) and cultured at 37°C and 5% CO_2 in RPMI medium supplemented with 10% (v/v) FBS and 10% macrophage-colony stimulating factor (M-CSF) as described before (Schmidt et al., 2011). Non-adherent cells were removed after 24 h and adherent cells were cultured for an additional 6 days. The cells were lysed in hypotonic lysis buffer [10 mM Tris-HCl, pH 7.6; 5 mM KCl; 1.5 mM $MgCl_2$; 1 mM dithiothreitol (DTT), protease inhibitor cocktail (Roche) and phosphatase inhibitor cocktail 2 and 3 (Sigma)] and cleared by centrifugation.

Transient and stable transfection and transduction

Cells were transiently transfected using Lipofectamine 2000 (Life Technologies) according to the manufacturer's protocol. To generate stable cell lines, vesicular stomatitis virus G glycoprotein (VSV-G) pseudotyped retroviral and lentiviral vectors were produced through transient transfection of 293T (human embryonic kidney) cells. Viral particles were concentrated from cell culture supernatant as previously described (Pfeifer et al., 2000) and used for infection.

Flow cytometry

Flow cytometry was carried out with a FACSCantoTMII cytometer (BD Biosciences) equipped with FACS DiVa software (BD Biosciences) using standard procedures. Data analysis was carried out with the FlowJo program (version 9.4.10). Cells were incubated with primary antibodies diluted in FACS buffer [1% bovine serum albumin (BSA) in PBS (Sigma)] for 1 h on ice, washed twice with cold FACS buffer and finally incubated with the secondary antibody for 1 h on ice.

Adhesion assay

To measure cell adhesion, Raw264.7 and PLB985 cells were washed, resuspended in FBS-free growth medium and either left untreated or treated for 30 min with 100 ng/ml PMA or TNFα. Adhesion assays were performed in 96-well flat-bottom plates coated for 2 h at room temperature with 10 µg/ml fibrinogen (Sigma) or 4 µg/ml ICAM-1 (R&D systems). PLB985 cells were left to adhere on 96-well flat-bottom plates coated with 100 µg/ml fibrinogen (Sigma). Unspecific binding to the plates was blocked through incubating the wells with 1% BSA/PBS. The wells were washed once with PBS to remove excess BSA before seeding the cells (1×10^5 cells/well). After adhesion at 37°C, the wells were washed by means of immersion into a

plastic tray containing PBS. Adhered cells were fixed with methanol and stained with Crystal Violet overnight (20% methanol, 0.1% Crystal Violet in H_2O). After intense washings, cells were solubilized in 0.5% Triton X-100, and the number of cells was determined by measuring the absorbance at 595 nm using an ELISA reader.

Flow chamber assay

A detachment flow chamber assay was performed as described (Schymeinsky et al., 2009). Briefly, microflow chambers (2×0.2 mm; VitroCom) were coated with human fibrinogen (100 µg/ml in 0.1% BSA/PBS, Sigma) for 3 h at room temperature and blocked with 5% casein (Sigma-Aldrich) overnight at 4°C. Before the experiment, chambers were washed with 0.9% NaCl solution (Fresenius Kabi) and then 10^6 cells/ml (shLCP1, shCtrl, GFP or GFP–LCP1 PLB985 cells) suspended in perfusion medium (HBSS buffer containing 1 mM $CaCl_2$, 1 mM $MgCl_2$, 10 mM HEPES, 0.25% BSA, 0.1% glucose, pH 7.4) were introduced into the flow chamber. Flow was stopped for 30 min to allow cells to attach. Using a high-precision syringe pump (Harvard Apparatus), flow was started at very low shear stress (<0.5 dyn/cm^2) for 60 s to remove debris, and then flow rates were increased every 30 s up to a maximum of 160 dyn/cm^2. Experiments were performed with a Zeiss Axioskop2 (equipped with a 20× water objective, 0.5 NA and a Hitachi KP-M1AP camera) and recorded with VirtualDub (Version 1.9.11). The number of adherent cells/FOV was analyzed off-line for baseline conditions and indicated in percentage of baseline adhesion for every shear stress level in the generated movies.

Bicelle preparation

6-cyclohexyl-1-hexylphosphocholine (Cyclofos-6) was purchased from Anatrace. 1-palmitoyl-2-oleoyl-*sn*-glycero-3-phospho-L-serine (POPS) was purchased from Avanti Polar Lipids and 1,2-dimyristoyl-sn-glycero-3-phosphocholine (DMPC) was purchased from CordenPharma. Lipid stock solutions were prepared by weighing out 500 mg of DMPC in 5 ml of cyto buffer (139 mM K_2HPO_4, 8.8 mM NaH_2PO_4, 0.4 mM $MgCl_2$, 3.2 mM NaCl, pH 7.0), 200 mg of Cyclofos-6 in 4 ml of cyto buffer and 75 mg of POPS in 3.75 ml of cyto buffer. For 1 ml 3% bicelle solution, q=4 bicelles, 236 µl DMPC stock, 152 µl POPS stock, and 68 µl Cyclofos-6 stock plus 544 µl cyto buffer were mixed and repeatedly subjected to a temperature cycle: 45°C for 2 min, 5°C (or ice water) for 5 min. In between, the solution was carefully mixed to avoid foaming. The temperature cycle was repeated 10 times until the solution became clear. For 1 ml 3% q=0.25 bicelles, 72 µl DMPC stock, 56 µl POPS stock, and 400 µl Cyclofos-6 stock plus 472 µl of cyto buffer were mixed and incubated as described above. The stocks were snap frozen in liquid nitrogen and stored at −80°C.

LC-MS to determine lipid composition of bicelles

Bicelle samples (1%) were diluted 1:100 with 0.05% trifluoroacetic acid in H_2O for determination of their lipid compositions by liquid chromatography-mass spectrometry (LC-MS) using a micrOTOF (Bruker Daltonik) connected to an 1100 HPLC (Agilent). Analyses were performed on a YMC-Pack Butyl 30 mm column (YMC) with a water:acetonitrile (0.05% trifluoroacetic acid) gradient from 30–80% in 15 min at a mass range from 200–2000 m/z in positive mode. Extracted ion chromatograms at 350.2, 678.5 and 762.5 m/z were used to compare the relative ratio of the individual lipids.

Dynamic light scattering

Bicelle samples with different ratios of DMPC, POPS and Cyclofos-6 were freshly prepared, and measured with or without integrin TMcyto domain incorporation. The samples were measured using DLS (DynaPro NanoStar from Wyatt Technology). Each sample was measured at 4°C, the acquisition time was set to 5 s (×10) and each measurement was repeated three times. The effective hydrodynamic radius was calculated with DYNAMICS V7.1.7.16 (Wyatt Technology).

Expression and purification and incorporation of recombinant proteins into bicelles

His–αM–cyto, maltose binding protein (MBP)–β2–cyto, glutathione S-transferase (GST)–LCP1 were transformed into BL21(DE3) Arctic Express *E. coli*, and protein expression was induced with 1 mM IPTG at 18°C for 24 h before purification of the tagged proteins using Ni-NTA beads (Qiagen, 30210), Amylose resin (NEB, E8021), or GST•Bind Resin (Millipore, 70541) according to manufacturer's instruction. Plasmids encoding His–Fos–α5–TMcyto, His–Fos–αIIb–TMcyto, His–Fos–αM–TMcyto, 3×FLAG–Jun–β2–TMcyto, His–Jun–β1–TMcyto, His–Jun–β2–TMcyto and His–Jun–β3–TMcyto were transformed into BL21 (DE3) Arctic Express *E. coli*, and protein expression was induced with 1 mM isopropyl β-D-1-thiogalactopyranoside (IPTG) (30°C, 3 h for α integrin subunits TMcyto domains; 18°C, 24 h for β integrin subunits TMcyto domains). Afterwards, bacteria were pelleted using centrifugation, resuspended in TBS buffer (50 mM Tris-HCl, pH 7.4; 150 mM NaCl) containing 100 µg/ml lysozyme and 50 µg/ml DNase (ThermoFisher) and rotated at 4°C for 2 h. After the addition of Empigen (Sigma) (30% solution; 1 ml per 10 ml of lysate) the bacterial lysates were rotated at 4°C for 1 h and centrifuged 1500 ***g*** at 4°C for 1 h. To purify His- and FLAG-tagged proteins, supernatants were incubated with Ni-NTA agarose beads (Qiagen, 36113) and anti-FLAG M2 affinity gel (Sigma, A2220) for 2 h at 4°C followed by extensive washing of the beads three times with TBS buffer and twice with pre-equilibration buffer [20 mM imidazole; 50 mM Tris-HCl, pH 6.5; 150 mM NaCl in 1% bicelles, q=0.25, as described (Lu et al., 2012)]. The 6×His-tagged proteins were eluted with elution buffer (250 mM imidazole; 50 mM Tris-HCl, pH 7.4; 150 mM NaCl in 1% bicelles). The proteins were concentrated using Amicon Ultra Centrifugal filters (10 kDa molecular weight cutoff, Millipore) by a factor of 10 to obtain a final bicelle concentration of 10%.

Bicelle-incorporated integrin TMcyto pull-down assay

For pull-down experiments, 9× volume of cyto buffer (139 mM K_2HPO_4, 8.8 mM NaH_2PO_4, 0.4 mM $MgCl_2$, 3.2 mM NaCl, pH 7.0) was added to 10% TMcyto–bicelle solution to obtain a 1% bicelle solution. To increase the bicelle size after protein incorporation from q=0.25 bicelles into q=2 bicelles, 5.2× volume of 1% q=4 bicelles was added. Integrin TMcyto domains incorporated into q=2* bicelles were incubated with the soluble fraction of bone marrow-derived macrophage (BMDM) lysates generated with hypotonic buffer [10 mM Tris-HCl, 5 mM KCl, 1.5 mM $MgCl_2$, 1 mM DTT, protease inhibitor cocktail (Roche)] overnight at 4°C. Importantly, maximal 1.6× the volume of concentrated lysate was added to the TMcyto bicelle solution, which kept the bicelle concentration (above 0.35%) and the Cyclofos-6 concentration (above 2.7 mM) high enough to support bicelle formation. Afterwards, the bicelle–lysate mixture was incubated with Ni-NTA magnetic agarose beads (Qiagen) for 2 h at 4°C. After three washes with q=2* bicelle solution in cyto buffer, proteins were eluted from the beads by boiling with 80 µl 4× Laemmli sample buffer for 5 min, separated using SDS-PAGE and analyzed by means of LC-MS/MS or western blotting.

Mass spectrometry analysis of the pull-down samples

The samples were eluted from Ni-NTA magnetic agarose beads by boiling with Laemmli sample buffer and separated on NuPAGE Novex 4–12% Bis-Tris protein gels (ThermoFisher). The gel was fixed in 50% methanol, 10% acetic acid, 40% H_2O for 30 min at room temperature and stained with GelCode Blue Safe Protein Stain reagent (ThermoFisher). Each lane was cut into three bands and digested using the standard in-gel digestion protocol (Shevchenko et al., 2006). Briefly, the gel bands were cut into roughly 1 mm cubes and de-stained in ethanol solution before incubation with 20 mM DTT and 40 mM chloroacetamide to reduce and alkylate the proteins. The gel pieces were then rehydrated in trypsin solution (12.5 ng/µl in 50 mM ammonium bicarbonate) and incubated overnight at 37°C. After overnight digestion, the peptides were extracted in 30% acetonitrile and 3% trifluoroacetic acid solution followed by 100% acetonitrile solution. The extracted peptides were then desalted and concentrated using C_{18} StageTips (Rappsilber et al., 2003) prior to LC-MS/MS analysis. The peptides were separated on a 120 min gradient in a 15 cm reversed phase column [75 µm inner diameter columns (New Objective) packed in-house with 3 µm Reprosil C_{18} beads (Dr. Maisch HPLC) using EASY-nLC II (ThermoFisher)] and sprayed directly into a LTQ Orbitrap XL mass spectrometer via a nano-electrospray ion source (ThermoFisher).

Peptides were analyzed using a top five data-dependent acquisition method. Survey scans were acquired in the Orbitrap at a resolution of 60,000

(400 m/z) after accumulating a target of 1×10^6 ions within a maximum injection time of 1000 ms. From the survey scan, up to the top five most abundant precursors were selected and fragmented in the linear ion trap by means of collisional-induced dissociation with automatic gain control target value of 10,000 within a maximum injection time of 150 ms, and the fragmentation spectra were recorded in the ion trap. The peptide precursors selected for fragmentation were dynamically excluded for 90 s after a repeat count of one in order to minimize the repeat sequencing.

For each set of integrin heterodimer pull-downs, the raw files were processed using the MaxQuant computational platform (Cox and Mann, 2008) (version 1.5.1.8). The peak lists generated were searched against the Uniprot mouse proteome sequence database (59375 entries) using the Andromeda search engine (Cox et al., 2011). The peptide precursors were searched with an initial mass tolerance of 7 ppm and the fragment ions were searched with a tolerance of 0.5 Da. Carbamidomethylation of cysteine was used as a fixed modification and oxidation of methionine and amino terminal protein acetylation were set as variable modification for the database search. The minimum peptide length was set to six amino acids and the identifications were filtered at 1% for the peptide level and 5% for the protein level. The q-value (defined as local false discovery rate based on a target-decoy search with forward and reversed protein sequences) was used for assessing the confidence in the identification of individual proteins. The match between the runs feature was enabled and label-free protein quantitation was performed using the MaxLFQ algorithm (Cox et al., 2014).

All statistical analysis was performed using the Perseus bioinformatics platform (http://www.perseus-framework.org). Student's *t*-tests were used to compare two samples with permutation-based FDR (4%) for multiple hypothesis testing.

Solid-phase ligand-binding assays

To determine GST–LCP1 binding to the integrin TMcyto domains, 96-well MaxiSorp plates (Nunc) were coated overnight at 4°C with purified His–Fos–αM–TMcyto, His–Jun–β2–TMcyto and the dimer composed of His–Fos–αM–TMcyto/3×FLAG–Jun–β2–TMcyto at 1.25 mmol/ml in 50 mM sodium bicarbonate buffer, pH 9.6. Plates were blocked with SuperBlock (TBS) blocking buffer (ThermoFisher) for several hours at room temperature, washed twice with washing buffer (50 mM Tris-HCl, pH 7.5, containing 200 mM NaCl and 0.05% Tween) before adding GST or GST–LCP1 in M-PER buffer (ThermoFisher) and incubating overnight at 4°C. After extensive washing with washing buffer, bound proteins were detected with an anti-LCP1 antibody, followed by an anti-rabbit HRP-conjugated secondary antibody. HRP substrate (ATBS, Vector) was added to the wells, and absorbance was monitored at 405 nm. GST was used as control for non-specific binding.

Pull-down experiments using recombinant proteins

To analyze the ternary complex between the cytosolic domains of αM integrin, β2 integrin, and LCP1, His–αM–cyto was incubated with Ni-NTA beads for 3 h at 4°C followed by washing of the beads three times with TBS buffer (50 mM Tris-HCl, pH 7.4; 150 mM NaCl). Beads were incubated with GST, MBP–β2–cyto or GST–LCP1 and MBP–β2–cyto, and incubated for 2 h at 4°C. The beads were washed three times with TBS to remove unbound proteins. The proteins were eluted from the beads by boiling with 80 µl 4× Laemmli buffer for 5 min, separated by means of SDS-PAGE and analyzed through the use of western blotting with the anti-MBP antibody.

For the talin-1 head competition assays, recombinant His–Fos–αM–TMcyto and dimeric His–Fos–αM–TMcyto/3×FLAG–Jun–β2–TMcyto (5–10 µg) were incubated with 25 µl pre-cleared Talon Metal Affinity Resin (Clontech) in 0.5 ml TBS (50 mM Tris-HCl, pH 7.4; 150 mM NaCl) for 2 h at 4°C under rotation. The beads were washed three times with TBS and recombinant talin-1 head (80 µg), GST–LCP1 or a combination of both proteins were added to the beads in 0.5 ml binding buffer (50 mM Tris-HCl pH 7.5; 200 mM NaCl; 1 mM TCEP) supplemented with BSA 100 µg/ml. After incubation at 4°C overnight, the beads were washed extensively with binding buffer and the proteins were eluted twice with 50 µl elution buffer I (binding buffer plus 250 mM imidazol) using Spin Cups columns (ThermoFisher). Eluted samples were boiled with Laemmli loading buffer and analyzed by means of SDS-PAGE.

For the pull-down of GFP-tagged LCP1, PLB985 cells were lysed for 10 min on ice [lysis buffer: 150 mM NaCl; 1% Triton X-100; 50 mM Tris-HCl, pH 8.0; 2 mM EDTA; 0.05% Na-deoxycholate; Phosphatase Inhibitor Cocktail 2 and 3 (Sigma); cOmplete Mini Protease Inhibitor Cocktail Tablets (Roche)] and the lysate sonicated and cleared using centrifugation at 16,000 ***g*** for 10 min at 4°C. 1 mg of protein lysates were incubated with His–Fos–αM–TMcyto or dimeric His–Fos–αM–TMcyto/3×FLAG–Jun–β2–TMcyto (20 µg) bound to 50 µl pre-cleared Talon Metal Affinity Resin (Clontech) and incubated overnight at 4°C. Following repeated washes with lysis buffer, proteins were eluted from the beads using Laemmli buffer and analyzed by means of western blotting using antibodies against GFP. Binding of recombinant integrin tails to the resin was verified using Coomassie Blue staining.

Immunoprecipitation of β2 integrin

For the immunoprecipitation of endogenous β2 integrin, differentiated PLB985 cells expressing GFP–LCP1 were treated with DMSO or 100 ng/ml PMA for 30 min at 37°C before lysis in lysis buffer for 10 min on ice. After sonification and centrifugation at 16,000 ***g*** for 10 min at 4°C, 1 mg of protein lysates were incubated with 2–4 µg of the monoclonal mouse anti-β2 integrin antibody (Santa Cruz Biotechnology) for 2 h at 4°C under rotation. Washed Protein A/G PLUS-Agarose beads (Santa Cruz Biotechnology) (50 µl/sample) were added to the lysates and incubated overnight at 4°C under rotation. After three washes with lysis buffer and one with PBS, Laemmli loading buffer was added to the beads and boiled for 7 min at 95°C to elute bound proteins.

Stability of cell-surface integrins

The half-life of cell-surface proteins was determined as described previously by means of biotinylation (Böttcher et al., 2012). Briefly, cells were washed twice in cold PBS and surface-biotinylated with 0.2 mg/ml sulfo-NHS-LC-biotin (ThermoFisher) in PBS for 45 min at 4°C. Following washes with cold PBS the cells were incubated in regular growth medium for 0 h and 24 h at 37°C. Cells were lysed in IP buffer (50 mM Tris-HCl, pH 7.5; 150 mM NaCl; 1% Triton X-100; 0.1% sodium deoxycholate; 1 mM EDTA; protease inhibitors) and biotinylated proteins were pulled down with streptavidin-sepharose (GE Healthcare). After three washes with lysis buffer, samples were analyzed using SDS-PAGE and western blotting.

Quantitative real-time polymerase chain reaction

Total RNA was isolated from cultured cells using the RNeasy mini kit (Qiagen), of which 1000 ng was transcribed into cDNA using the iScript cDNA Synthesis kit (Bio-Rad). Quantitative real-time polymerase chain reaction (qRT-PCR) was performed with the LightCycler 480 (Roche) using SYBR green (Bio-Rad) and the following primers: β2 forward-1, 5′-CAGGAATGCACCAAGTACAAAGT-3′; β2 reverse-1, 5′-CCTGGTCC-AGTGAAGTTCAGC-3′; β2 forward-2, 5′-AACGGAAACAGCTATCT-CCAC-3′; β2 reverse-2, 5′-GAGTAGGAGAGATCCATGAG-3′; αM forward-1, 5′-ATGGACGCTGATGGCAATACC-3′; αM reverse-1, 5′-TCCCCATTCACGTCTCCCA-3′; αM forward-2, 5′-CCATGACCTTC-CAAGAGAATGC-3′; αM reverse-2, 5′-ACCGGCTTGTGCTGTAGTC-3′; GAPDH forward, 5′-TCCTGCACCACCAACTGCTTAGC-3′; GAPDH reverse, 5′-TGGATGCAGGGATGATGTTCTGG-3′. Each sample was measured in triplicate and values were normalized to GAPDH.

Statistical analysis

Statistical significance was determined using two-tailed unpaired Student's *t*-test. Results are expressed as the mean±standard error of the mean (s.e.m.), unless indicated otherwise. Bar graphs throughout the study were generated in Microsoft Office.

Acknowledgements

We thank Dr Karim Dib (Queen's University Belfast, UK) for providing PLB985 cells, Dr Nagarjuna Nagaraj (MPI Biochemistry, Martinsried, Germany) for help with the proteomic analysis, Dr Raphael Ruppert (MPI Biochemistry, Martinsried, Germany) for his support with the FACS analysis, Dr Jonas Aretz (MPI Biochemistry,

Martinsried, Germany) for the recombinant talin-1 head protein, Dr Sijo Mathew (Vanderbilt University, Nashville, USA) for help advice during bicelle preparation, Elisabeth Weyher for LC-MS analysis, and Hildegard Reiter for expert technical assistance. Some data in the paper forms part of the PhD thesis of Hui-yuan Tseng (2015, Ludwig-Maximilians-University, Munich, Germany).

Competing interests
The authors declare no competing or financial interests.

Author contributions
Conceptualization: R.F., R.T.B.; Methodology: H.T., P.K., R.Z., C.R.S., R.F., R.T.B.; Validation: H.T., R.F., R.T.B.; Investigation: H.T., A.V.S., S.S., T.Z., R.I., M.S., R.T.B.; Writing - original draft: H.T., R.F., R.T.B.; Writing - review & editing: A.V.S., R.I., R.Z., M.S., C.R.S., R.F., R.T.B.; Supervision: R.F., R.T.B.; Funding acquisition: R.F., R.T.B.

Funding
The work was supported by U.S. Department of Veterans Affairs Merit Review (grant 1I01BX002196 to R.Z.), National Institutes of Health (grants R01-DK075594 and R01-DK383069221 to R.Z.), the Deutsche Forschungsgemeinschaft (SFB914, project A05 to R.T.B. and R.F.; project B01 to M.S.), Deutsches Zentrum für Herz-Kreislaufforschung (grant 81Z1600313 to R.F.), the European Research Council (grant agreement 322652 to R.F.) and the Max-Planck-Gesellschaft. Deposited in PMC for release after 12 months.

Supplementary information
Supplementary information available online at
http://jcs.biologists.org/lookup/doi/10.1242/jcs.218214.supplemental

Reference
Adams, A. E., Shen, W., Lin, C. S., Leavitt, J. and Matsudaira, P. (1995). Isoform-specific complementation of the yeast sac6 null mutation by human fimbrin. *Mol. Cell. Biol.* **15**, 69-75.

Anthis, N. J., Wegener, K. L., Ye, F., Kim, C., Goult, B. T., Lowe, E. D., Vakonakis, I., Bate, N., Critchley, D. R., Ginsberg, M. H. et al. (2009). The structure of an integrin/talin complex reveals the basis of inside-out signal transduction. *EMBO J.* **28**, 3623-3632.

Arpin, M., Friederich, E., Algrain, M., Vernel, F. and Louvard, D. (1994). Functional differences between L- and T-plastin isoforms. *J. Cell Biol.* **127**, 1995-2008.

Böttcher, R. T., Stremmel, C., Meves, A., Meyer, H., Widmaier, M., Tseng, H.-Y. and Fässler, R. (2012). Sorting nexin 17 prevents lysosomal degradation of beta1 integrins by binding to the beta1-integrin tail. *Nat. Cell Biol.* **14**, 584-592.

Bouvard, D., Pouwels, J., De Franceschi, N. and Ivaska, J. (2013). Integrin inactivators: balancing cellular functions in vitro and in vivo. *Nat. Rev. Mol. Cell Biol.* **14**, 430-442.

Burgueño, J., Blake, D. J., Benson, M. A., Tinsley, C. L., Esapa, C. T., Canela, E. I., Penela, P., Mallol, J., Mayor, F., Jr, Lluis, C. et al. (2003). The adenosine A2A receptor interacts with the actin-binding protein alpha-actinin. *J. Biol. Chem.* **278**, 37545-37552.

Calderwood, D. A., Huttenlocher, A., Kiosses, W. B., Rose, D. M., Woodside, D. G., Schwartz, M. A. and Ginsberg, M. H. (2001). Increased filamin binding to beta-integrin cytoplasmic domains inhibits cell migration. *Nat. Cell Biol.* **3**, 1060-1068.

Campbell, I. D. and Humphries, M. J. (2011). Integrin structure, activation, and interactions. *Cold Spring Harb. Perspect Biol.* **3**, a004994.

Chen, H., Mocsai, A., Zhang, H., Ding, R.-X., Morisaki, J. H., White, M., Rothfork, J. M., Heiser, P., Colucci-Guyon, E., Lowell, C. A. et al. (2003). Role for plastin in host defense distinguishes integrin signaling from cell adhesion and spreading. *Immunity* **19**, 95-104.

Cox, J. and Mann, M. (2008). MaxQuant enables high peptide identification rates, individualized p.p.b.-range mass accuracies and proteome-wide protein quantification. *Nat. Biotechnol.* **26**, 1367-1372.

Cox, J., Neuhauser, N., Michalski, A., Scheltema, R. A., Olsen, J. V. and Mann, M. (2011). Andromeda: a peptide search engine integrated into the MaxQuant environment. *J. Proteome Res.* **10**, 1794-1805.

Cox, J., Hein, M. Y., Luber, C. A., Paron, I., Nagaraj, N. and Mann, M. (2014). Accurate proteome-wide label-free quantification by delayed normalization and maximal peptide ratio extraction, termed MaxLFQ. *Mol. Cell. Proteomics* **13**, 2513-2526.

Das, M., Ithychanda, S. S., Qin, J. and Plow, E. F. (2011). Migfilin and filamin as regulators of integrin activation in endothelial cells and neutrophils. *PLoS ONE* **6**, e26355.

De Franceschi, N., Hamidi, H., Alanko, J., Sahgal, P. and Ivaska, J. (2015). Integrin traffic - the update. *J. Cell Sci.* **128**, 839-852.

Delanote, V., Vandekerckhove, J. and Gettemans, J. (2005). Plastins: versatile modulators of actin organization in (patho)physiological cellular processes. *Acta Pharmacol. Sin.* **26**, 769-779.

Eble, J. A., Wucherpfennig, K. W., Gauthier, L., Dersch, P., Krukonis, E., Isberg, R. R. and Hemler, M. E. (1998). Recombinant soluble human alpha 3 beta 1 integrin: purification, processing, regulation, and specific binding to laminin-5 and invasin in a mutually exclusive manner. *Biochemistry* **37**, 10945-10955.

Foran, E., Mcwilliam, P., Kelleher, D., Croke, D. T. and Long, A. (2006). The leukocyte protein L-plastin induces proliferation, invasion and loss of E-cadherin expression in colon cancer cells. *Int. J. Cancer* **118**, 2098-2104.

Goult, B. T., Bouaouina, M., Harburger, D. S., Bate, N., Patel, B., Anthis, N. J., Campbell, I. D., Calderwood, D. A., Barsukov, I. L., Roberts, G. C. et al. (2009). The structure of the N-terminus of kindlin-1: a domain important for alphaiibbeta3 integrin activation. *J. Mol. Biol.* **394**, 944-956.

Goult, B. T., Bouaouina, M., Elliott, P. R., Bate, N., Patel, B., Gingras, A. R., Grossmann, J. G., Roberts, G. C. K., Calderwood, D. A., Critchley, D. R. et al. (2010). Structure of a double ubiquitin-like domain in the talin head: a role in integrin activation. *EMBO J.* **29**, 1069-1080.

Hagiwara, M., Shinomiya, H., Kashihara, M., Kobayashi, K.-I., Tadokoro, T. and Yamamoto, Y. (2011). Interaction of activated Rab5 with actin-bundling proteins, L- and T-plastin and its relevance to endocytic functions in mammalian cells. *Biochem. Biophys. Res. Commun.* **407**, 615-619.

Harokopakis, E. and Hajishengallis, G. (2005). Integrin activation by bacterial fimbriae through a pathway involving CD14, Toll-like receptor 2, and phosphatidylinositol-3-kinase. *Eur. J. Immunol.* **35**, 1201-1210.

Ithychanda, S. S., Das, M., Ma, Y.-Q., Ding, K., Wang, X., Gupta, S., Wu, C., Plow, E. F. and Qin, J. (2009). Migfilin, a molecular switch in regulation of integrin activation. *J. Biol. Chem.* **284**, 4713-4722.

Jones, S. L., Wang, J., Turck, C. W. and Brown, E. J. (1998). A role for the actin-bundling protein L-plastin in the regulation of leukocyte integrin function. *Proc. Natl. Acad. Sci. USA* **95**, 9331-9336.

Kiema, T., Lad, Y., Jiang, P., Oxley, C. L., Baldassarre, M., Wegener, K. L., Campbell, I. D., Ylanne, J. and Calderwood, D. A. (2006). The molecular basis of filamin binding to integrins and competition with talin. *Mol. Cell* **21**, 337-347.

Kim, C., Ye, F. and Ginsberg, M. H. (2011). Regulation of integrin activation. *Annu. Rev. Cell Dev. Biol.* **27**, 321-345.

Lau, T.-L., Dua, V. and Ulmer, T. S. (2008a). Structure of the integrin alphaIIb transmembrane segment. *J. Biol. Chem.* **283**, 16162-16168.

Lau, T.-L., Partridge, A. W., Ginsberg, M. H. and Ulmer, T. S. (2008b). Structure of the integrin beta3 transmembrane segment in phospholipid bicelles and detergent micelles. *Biochemistry* **47**, 4008-4016.

Lau, T.-L., Kim, C., Ginsberg, M. H. and Ulmer, T. S. (2009). The structure of the integrin alphaIIbbeta3 transmembrane complex explains integrin transmembrane signalling. *EMBO J.* **28**, 1351-1361.

Lebart, M.-C., Hubert, F., Boiteau, C., Ventéo, S., Roustan, C. and Benyamin, Y. (2004). Biochemical characterization of the L-plastin-actin interaction shows a resemblance with that of alpha-actinin and allows a distinction to be made between the two actin-binding domains of the molecule. *Biochemistry* **43**, 2428-2437.

Lefort, C. T., Hyun, Y.-M., Schultz, J. B., Law, F.-Y., Waugh, R. E., Knauf, P. A. and Kim, M. (2009). Outside-in signal transmission by conformational changes in integrin Mac-1. *J. Immunol.* **183**, 6460-6468.

Legate, K. R. and Fassler, R. (2009). Mechanisms that regulate adaptor binding to beta-integrin cytoplasmic tails. *J. Cell Sci.* **122**, 187-198.

Le Goff, E., Vallentin, A., Harmand, P. O., Aldrian-Herrada, G., Rebiere, B., Roy, C., Benyamin, Y. and Lebart, M. C. (2010). Characterization of L-plastin interaction with beta integrin and its regulation by micro-calpain. *Cytoskeleton (Hoboken)* **67**, 286-296.

Leventis, P. A. and Grinstein, S. (2010). The distribution and function of phosphatidylserine in cellular membranes. *Annu. Rev. Biophys.* **39**, 407-427.

Lin, C. S., Aebersold, R. H., Kent, S. B., Varma, M. and Leavitt, J. (1988). Molecular cloning and characterization of plastin, a human leukocyte protein expressed in transformed human fibroblasts. *Mol. Cell. Biol.* **8**, 4659-4668.

Lin, C. S., Park, T., Chen, Z. P. and Leavitt, J. (1993). Human plastin genes. Comparative gene structure, chromosome location, and differential expression in normal and neoplastic cells. *J. Biol. Chem.* **268**, 2781-2792.

Lin, C. S., Lau, A. and Lue, T. F. (1998). Analysis and mapping of plastin phosphorylation. *DNA Cell Biol.* **17**, 1041-1046.

Liu, J., Fukuda, K., Xu, Z., Ma, Y.-Q., Hirbawi, J., Mao, X., Wu, C., Plow, E. F. and Qin, J. (2011). Structural basis of phosphoinositide binding to kindlin-2 protein pleckstrin homology domain in regulating integrin activation. *J. Biol. Chem.* **286**, 43334-43342.

Liu, J., Das, M., Yang, J., Ithychanda, S. S., Yakubenko, V. P., Plow, E. F. and Qin, J. (2015). Structural mechanism of integrin inactivation by filamin. *Nat. Struct. Mol. Biol.* **22**, 383-389.

Lu, Z., Van Horn, W. D., Chen, J., Mathew, S., Zent, R. and Sanders, C. R. (2012). Bicelles at low concentrations. *Mol. Pharm.* **9**, 752-761.

Margadant, C., Monsuur, H. N., Norman, J. C. and Sonnenberg, A. (2011). Mechanisms of integrin activation and trafficking. *Curr. Opin. Cell Biol.* **23**, 607-614.

Moore, D. T., Nygren, P., Jo, H., Boesze-Battaglia, K., Bennett, J. S. and Degrado, W. F. (2012). Affinity of talin-1 for the beta3-integrin cytosolic domain is

modulated by its phospholipid bilayer environment. *Proc. Natl. Acad. Sci. USA* **109**, 793-798.
Morley, S. C. (2012). The actin-bundling protein L-plastin: a critical regulator of immune cell function. *Int. J. Cell Biol.* **2012**, 935173.
Morse, E. M., Brahme, N. N. and Calderwood, D. A. (2014). Integrin cytoplasmic tail interactions. *Biochemistry* **53**, 810-820.
Otey, C. A., Pavalko, F. M. and Burridge, K. (1990). An interaction between alpha-actinin and the beta 1 integrin subunit in vitro. *J. Cell Biol.* **111**, 721-729.
Pavalko, F. M. and Laroche, S. M. (1993). Activation of human neutrophils induces an interaction between the integrin beta 2-subunit (CD18) and the actin binding protein alpha-actinin. *J. Immunol.* **151**, 3795-3807.
Penalver, E., Ojeda, L., Moreno, E. and Lagunas, R. (1997). Role of the cytoskeleton in endocytosis of the yeast maltose transporter. *Yeast* **13**, 541-549.
Perera, H. D., Ma, Y.-Q., Yang, J., Hirbawi, J., Plow, E. F. and Qin, J. (2011). Membrane binding of the N-terminal ubiquitin-like domain of kindlin-2 is crucial for its regulation of integrin activation. *Structure* **19**, 1664-1671.
Pfeifer, A., Kessler, T., Silletti, S., Cheresh, D. A. and Verma, I. M. (2000). Suppression of angiogenesis by lentiviral delivery of PEX, a noncatalytic fragment of matrix metalloproteinase 2. *Proc. Natl. Acad. Sci. USA* **97**, 12227-12232.
Pivot-Pajot, C., Chouinard, F. C., El Azreq, M. A., Harbour, D. and Bourgoin, S. G. (2010). Characterisation of degranulation and phagocytic capacity of a human neutrophilic cellular model, PLB-985 cells. *Immunobiology* **215**, 38-52.
Raab, M., Daxecker, H., Edwards, R. J., Treumann, A., Murphy, D. and Moran, N. (2010). Protein interactions with the platelet integrin alpha(IIb) regulatory motif. *Proteomics* **10**, 2790-2800.
Rappsilber, J., Ishihama, Y. and Mann, M. (2003). Stop and go extraction tips for matrix-assisted laser desorption/ionization, nanoelectrospray, and LC/MS sample pretreatment in proteomics. *Anal. Chem.* **75**, 663-670.
Raynal, N., Hamaia, S. W., Siljander, P. R., Maddox, B., Peachey, A. R., Fernandez, R., Foley, L. J., Slatter, D. A., Jarvis, G. E. and Farndale, R. W. (2006). Use of synthetic peptides to locate novel integrin alpha2beta1-binding motifs in human collagen III. *J. Biol. Chem.* **281**, 3821-3831.
Saltel, F., Mortier, E., Hytönen, V. P., Jacquier, M.-C., Zimmermann, P., Vogel, V., Liu, W. and Wehrle-Haller, B. (2009). New PI(4,5)P2- and membrane proximal integrin-binding motifs in the talin head control beta3-integrin clustering. *J. Cell Biol.* **187**, 715-731.
Schiller, H. B., Hermann, M.-R., Polleux, J., Vignaud, T., Zanivan, S., Friedel, C. C., Sun, Z., Raducanu, A., Gottschalk, K.-E., Théry, M. et al. (2013). beta1- and alphav-class integrins cooperate to regulate myosin II during rigidity sensing of fibronectin-based microenvironments. *Nat. Cell Biol.* **15**, 625-636.
Schmidt, S., Nakchbandi, I., Ruppert, R., Kawelke, N., Hess, M. W., Pfaller, K., Jurdic, P., Fassler, R. and Moser, M. (2011). Kindlin-3-mediated signaling from multiple integrin classes is required for osteoclast-mediated bone resorption. *J. Cell Biol.* **192**, 883-897.
Schmidt, S., Moser, M. and Sperandio, M. (2013). The molecular basis of leukocyte recruitment and its deficiencies. *Mol. Immunol.* **55**, 49-58.
Schulz, T. W., Nakagawa, T., Licznerski, P., Pawlak, V., Kolleker, A., Rozov, A., Kim, J., Dittgen, T., Kohr, G., Sheng, M. et al. (2004). Actin/alpha-actinin-dependent transport of AMPA receptors in dendritic spines: role of the PDZ-LIM protein RIL. *J. Neurosci.* **24**, 8584-8594.
Schymeinsky, J., Gerstl, R., Mannigel, I., Niedung, K., Frommhold, D., Panthel, K., Heesemann, J., Sixt, M., Quast, T., Kolanus, W. et al. (2009). A fundamental role of mAbp1 in neutrophils: impact on beta(2) integrin-mediated phagocytosis and adhesion in vivo. *Blood* **114**, 4209-4220.
Sharma, C. P., Ezzell, R. M. and Arnaout, M. A. (1995). Direct interaction of filamin (ABP-280) with the beta 2-integrin subunit CD18. *J. Immunol.* **154**, 3461-3470.
Shattil, S. J., Kim, C. and Ginsberg, M. H. (2010). The final steps of integrin activation: the end game. *Nat. Rev. Mol. Cell Biol.* **11**, 288-300.
Shevchenko, A., Tomas, H., Havlis, J., Olsen, J. V. and Mann, M. (2006). In-gel digestion for mass spectrometric characterization of proteins and proteomes. *Nat. Protoc.* **1**, 2856-2860.
Shinomiya, H., Hagi, A., Fukuzumi, M., Mizobuchi, M., Hirata, H. and Utsumi, S. (1995). Complete primary structure and phosphorylation site of the 65-kDa macrophage protein phosphorylated by stimulation with bacterial lipopolysaccharide. *J. Immunol.* **154**, 3471-3478.
Skau, C. T., Courson, D. S., Bestul, A. J., Winkelman, J. D., Rock, R. S., Sirotkin, V. and Kovar, D. R. (2011). Actin filament bundling by fimbrin is important for endocytosis, cytokinesis, and polarization in fission yeast. *J. Biol. Chem.* **286**, 26964-26977.
Surya, W., Li, Y., Millet, O., Diercks, T. and Torres, J. (2013). Transmembrane and Juxtamembrane Structure of alphaL Integrin in Bicelles. *PLoS ONE* **8**, e74281.
Timmers, A. C., Niebel, A., Balague, C. and Dagkesamanskaya, A. (2002). Differential localisation of GFP fusions to cytoskeleton-binding proteins in animal, plant, and yeast cells. Green-fluorescent protein. *Protoplasma* **220**, 69-78.
Van Dam, L., Karlsson, G. and Edwards, K. (2004). Direct observation and characterization of DMPC/DHPC aggregates under conditions relevant for biological solution NMR. *Biochim. Biophys. Acta* **1664**, 241-256.
Vitorino, P., Yeung, S., Crow, A., Bakke, J., Smyczek, T., West, K., Mcnamara, E., Eastham-Anderson, J., Gould, S., Harris, S. F. et al. (2015). MAP4K4 regulates integrin-FERM binding to control endothelial cell motility. *Nature* **519**, 425-430.
Wang, J., Chen, H. and Brown, E. J. (2001). L-plastin peptide activation of alpha(v)beta(3)-mediated adhesion requires integrin conformational change and actin filament disassembly. *J. Biol. Chem.* **276**, 14474-14481.
Yang, J., Ma, Y.-Q., Page, R. C., Misra, S., Plow, E. F. and Qin, J. (2009). Structure of an integrin alphaIIb beta3 transmembrane-cytoplasmic heterocomplex provides insight into integrin activation. *Proc. Natl. Acad. Sci. USA* **106**, 17729-17734.

Supplementary information

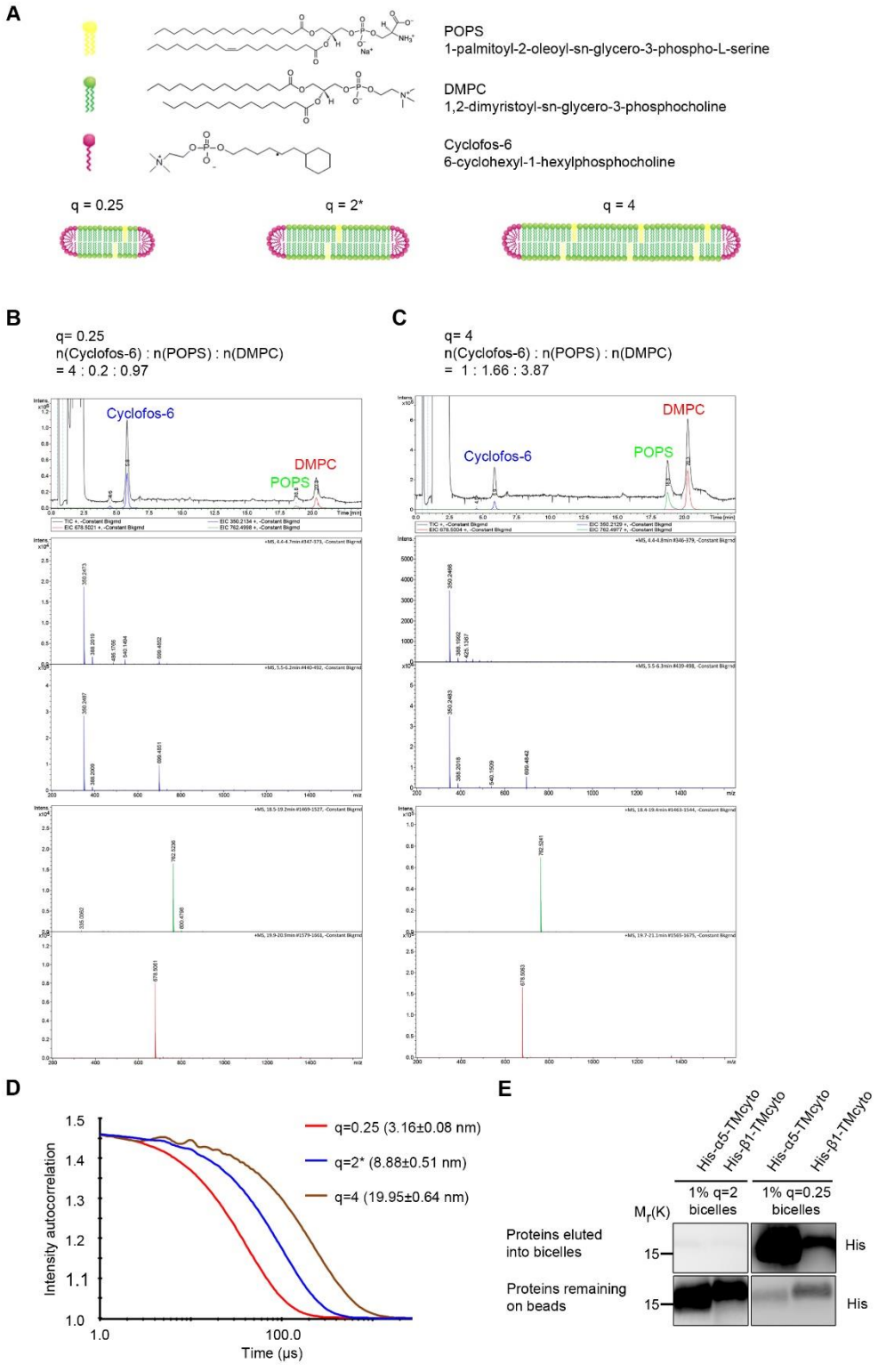

Figure S1. Lipid composition of bicelles. (A) Chemical structures of phospholipids used to generate the bicelles and cartoon illustration of architecture of and lipid distribution in bicelles. **(B, C)** The relative molar ratio of lipids and detergent in q=0.25 **(B)**, q=4 **(C)** bicelles was

determined by LC-MS. Cyclofos-6 (blue), POPS (green), DMPC (red). **(D)** Dynamic light scattering (DLS) curves of bicelles with different q-values to determine the hydrodynamic radii (nm) of the different bicelles (q=0.25: 3.16±0.08 nm; q=4: 19.95±0.64 nm; q=2*: 8.88±0.51nm, mean±s.e.m., n=3). **(E)** Western blot analysis for His-tagged α5 and β1 integrin TMcyto domains after incorporation into q=0.25 and q=2 bicelles. Proteins were successfully incorporated into q=0.25 bicelles but not into q=2 bicelles.

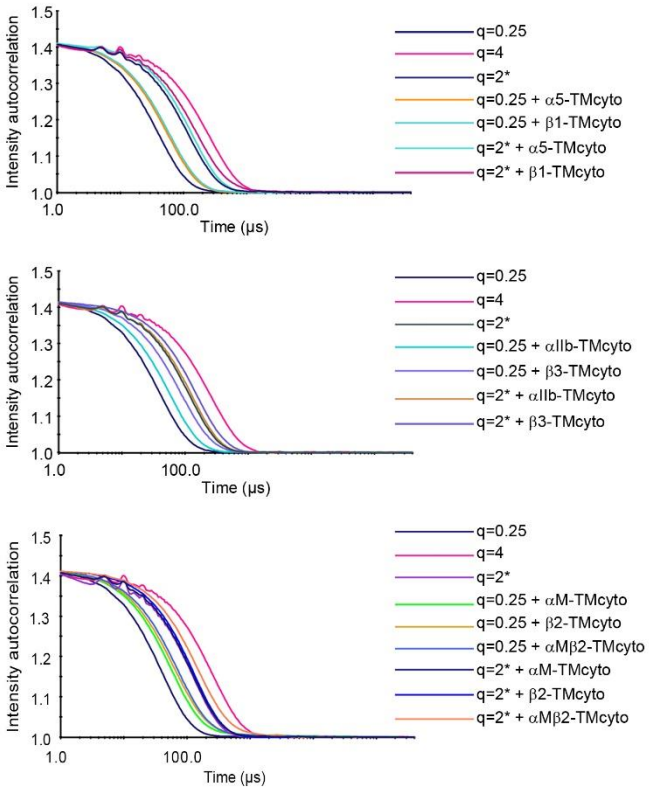

Figure S2. DLS measurement of bicelles before and after integrin TMcyto domain incorporation.

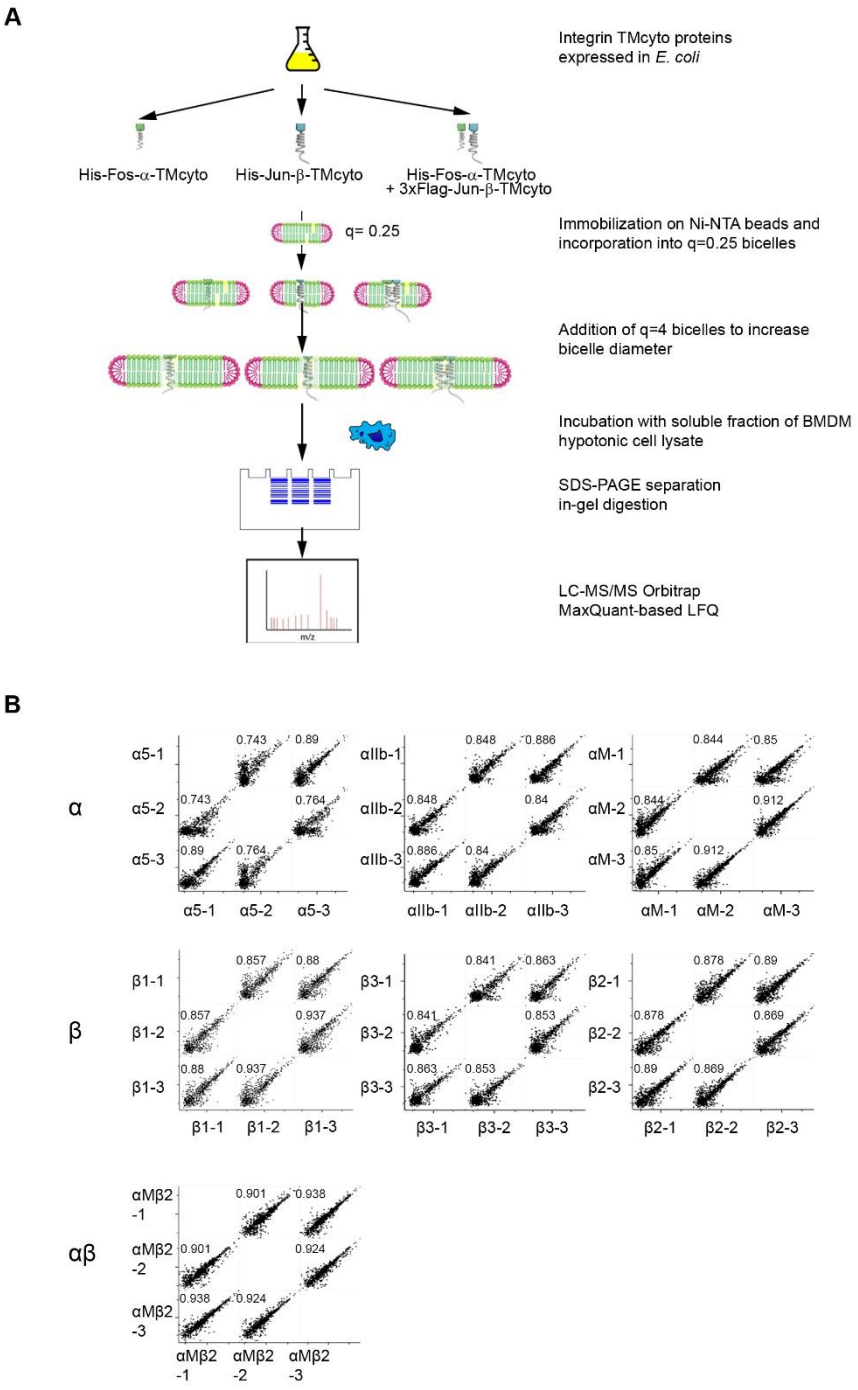

Figure S3. Workflow for incorporation of recombinant integrin TMcyto domains in bicelles, pull-downs and proteomic analysis. (A) Purified heterodimeric or monomeric integrin TMcyto domains were immobilized on Ni-NTA beads and incorporated into bicelle solutions (q=0.25). Bicelle size was increased by adding q=4 bicelles to obtain q=2* bicelles characterized by a hydrodynamic radius of ~10 nm, followed by the pull-down of proteins from hypotonic BMDM lysates. Interactors were identified by LC-MS/MS and analyzed by

MaxQuant LFQ intensity. **(B)** Multi-scatter plot of the protein LFQ intensities shows the reproducibility within the triplicate measurements of the different pull-downs. The indicated values correspond to Pearson correlation.

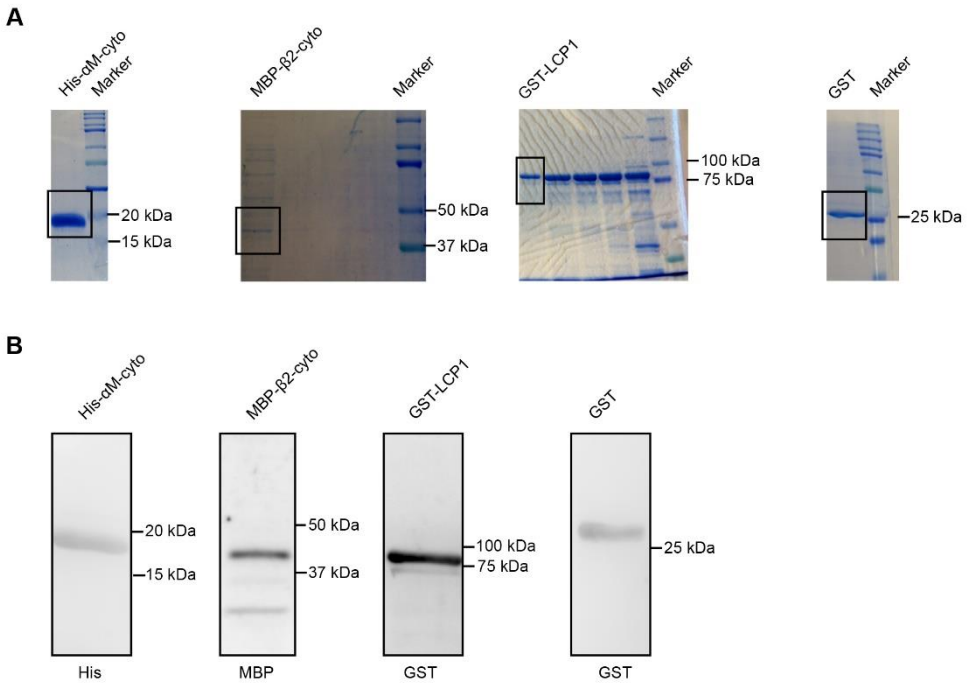

Figure S4. Expression of recombinant proteins used in pull-down experiments. (A, B) SDS-PAGE analysis of bacterially expressed and purified His-αM-cyto, MBP-β2-cyto, GST-LCP1, and GST stained either by Coomassie Blue **(A)** or by western blotting with antibodies against the indicated proteins **(B)**.

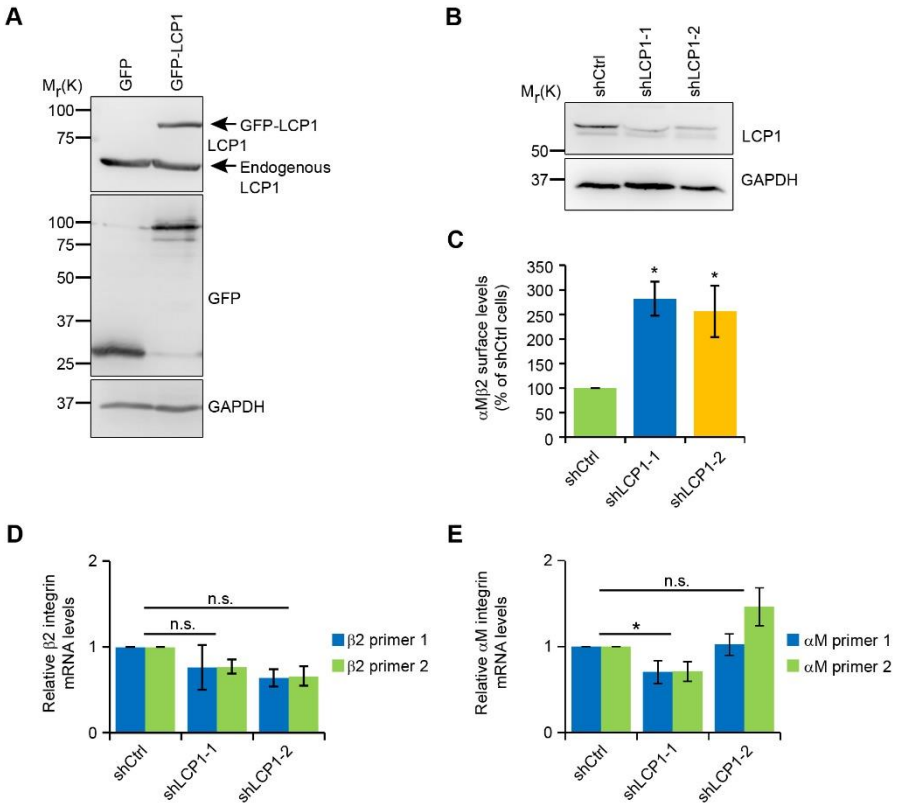

Figure S5. Regulation of αMβ2 integrin-surface levels by LCP1. (A) Western blot of GFP and GFP-LCP1 overexpressing PLB985 cells. **(B) Western blot analysis of** shRNA-mediated depletion of LCP1 in Raw264.7 cells. Cells were infected with shCtrl or two different LCP1 shRNA (shLCP1-1 and shLCP1-2). **(C)** FACS analysis of αMβ2 surface expression in LCP1-depleted Raw264.7 cells (values are normalized to shCtrl cells; mean±s.e.m., n=3, * $P < 0.05$). **(D, E)** Quantification of β2 **(D)** and αM integrin **(E)** mRNA levels in LCP1-depleted Raw264.7 cells determined by quantitative real-time PCR (values are normalized to shCtrl cells; mean±s.e.m., n=3, n.s. not significant, * $P < 0.05$).

Bicelles-integrin TMcyto	Hydrodynamic Radius (nm)
0.25-α5	4.54±0.22
0.25-β1	4.58±0.15
2*-α5	10.47±0.65
2*-β1	11.32±1.29
0.25-αIIb	12.65±1.67
0.25-β3	6.00±0.54
2*-αIIb	10.29±0.44
2*-β3	11.30±0.77
0.25-αM	4.41±0.20
0.25-β2	4.93±0.42
0.25-αMβ2	5.15±0.31
2*-αM	10.05±0.26
2*-β2	10.25±0.31
2*-αMβ2	11.17±0.49

Table S1: Hydrodynamic radii of bicelles after incorporation of indicated integrin α and β subunits determined by DLS.

Table S2: List of all proteins identified in pull-down experiments using bicelle-incorporated α or β TMcyto domains by mass-spectrometry (α5, β1, αIIb, β3, αM, and β2).

Click here to Download Table S2

Table S3: List of proteins with significant binding to lipid-incorporated α or β TMcyto domains. Overlap of proteins significantly binding to α or β TMcyto across the three different combinations (α5 vs β1; αIIb vs β3; αM vs β2).

Click here to Download Table S3

Table S4: List of proteins favoring binding to clasped αMβ2-TMcyto.

Click here to Download Table S4

Molecular-scale visualization of sarcomere contraction within native cardiomyocytes

Laura Burbaum[1,*], Jonathan Schneider[2,*], Sarah Scholze[3], Ralph T Böttcher[3], Wolfgang Baumeister[2], Petra Schwille[1], Jürgen M Plitzko[2], and Marion Jasnin[2,✉]

[1]Department of Cellular and Molecular Biophysics, Max Planck Institute of Biochemistry, Martinsried, Germany
[2]Department of Molecular Structural Biology, Max Planck Institute of Biochemistry, Martinsried, Germany
[3]Department of Molecular Medicine, Max Planck Institute of Biochemistry, Martinsried, Germany
[*]These authors contributed equally to this work

Sarcomeres, the basic contractile units of striated muscle, produce the forces driving muscular contraction through cross-bridge interactions between actin-containing thin filaments and myosin II-based thick filaments. Until now, direct visualization of the molecular architecture underlying sarcomere contractility has remained elusive. Here, we use *in situ* cryo-electron tomography to unveil sarcomere contraction in frozen-hydrated neonatal rat cardiomyocytes. We show that the hexagonal lattice of the thick filaments is already established at the neonatal stage, with an excess of thin filaments outside the trigonal positions. Structural assessment of actin polarity by subtomogram averaging reveals that thin filaments in the fully activated state form overlapping arrays of opposite polarity in the center of the sarcomere. Our approach provides direct evidence for thin filament sliding during muscle contraction and may serve as a basis for structural understanding of thin filament activation and actomyosin interactions inside unperturbed cellular environments.

cryo-electron tomography | molecular architecture | myofilament packing | quantitative analysis | subtomogram averaging | actin polarity | *in situ* structure | thin filament | tropomyosin | myosin state | heart muscle cells

Correspondence: ***jasnin@biochem.mpg.de***

Introduction

Muscle cells contain numerous myofibrils composed of adjoining micrometer-sized contractile units called sarcomeres (1). These large macromolecular assemblies feature thin filaments, made of polar actin filaments (F-actin) in complex with troponin (Tpn) and tropomyosin (Tpm), and bipolar thick filaments consisting of a myosin tail backbone decorated with myosin-II heads on either side of a head-free region (the so-called bare zone) (1). The sliding filament theory provided a framework for understanding the mechanism of muscle contraction based on the relative sliding between the myofilaments via cyclic interactions of myosin heads with F-actin (2-5). Five decades after these pioneering studies, much remains to be discovered at the structural level about how the molecular players of the actomyosin machinery cooperate within sarcomeres to produce contractile forces.

Muscle research has benefited greatly from the development of powerful X-ray sources and electron microscopes, allowing detailed views into muscle organization, time-resolved X-ray diffraction studies of contracting muscle, and three-dimensional (3D) reconstruction of actomyosin interactions (6-10). Thick filaments are known to be crosslinked in the central M-line and occupy the A-band (fig. S1A) (1, 11, 12). On either side of the M-line, interdigitating myofilaments organize into hexagonally packed arrays (1, 13, 14). Thin filaments extend throughout the I-bands toward the Z-disk, in which their barbed ends are anchored and crosslinked by α-actinin (fig. S1A) (1, 11, 12, 15, 16). At the molecular level, Ca^{2+}-binding to Tpn is thought to trigger a shift in the azimuthal position of Tpm on F-actin to uncover the myosin binding site which allows actomyosin interactions (17, 18). Yet, none of the approaches used so far has permitted molecular-scale imaging of sarcomere organization inside unperturbed cellular environments. Recent advances in cryo-electron tomography (cryo-ET) provide access to the 3D molecular architecture of the cellular interior (19, 20). Here, we use state-of-the-art cryo-ET methodologies to unravel sarcomere organization in frozen-hydrated neonatal cardiomyocytes across length scales, from the myofilament packing to the sliding and functional states of the thin filaments enabling contraction.

Results

Cardiomyocytes isolated from neonatal rat ventricles exhibit irregular, star-like morphology and spontaneous rhythmic contractions (movie S1). To explore the microscale organization of myofibrils mediating cell contractility, neonatal rat cardiac myocytes were immunolabelled for Tpn I (one of the three subunits of the Tpn complex), the heavy chain of cardiac myosin and α-actinin, as markers for the thin filament, the thick filament and the Z-disk, respectively. Myofibrils align into bundles along the principal axes of the neonatal cells (Fig. 1A and fig. S1, B and C). They feature regularly spaced Z-disks and A-bands, with a sarcomere length of 1.8 ± 0.2 µm (Fig. 1B and fig. S1D), similar to the value we found in adult mouse cells.

Unlike adult cardiomyocytes, the cell size is suitable for cryofixation by plunge-freezing (fig. S2, A and B). Neonatal cardiomyocytes were cultured on EM grids and plunge-frozen during spontaneous contraction (fig. S2B). 100- to 200-nm-thick vitrified cellular sections (so-called lamellas) were prepared using cryo-focused ion beam (cryo-FIB) milling (fig. S2C) (21). Transmission electron microscopy (TEM) images revealed cytoplasmic regions filled with long adjacent myofibrils surrounded by mitochondria and sarcoplasmic retic-

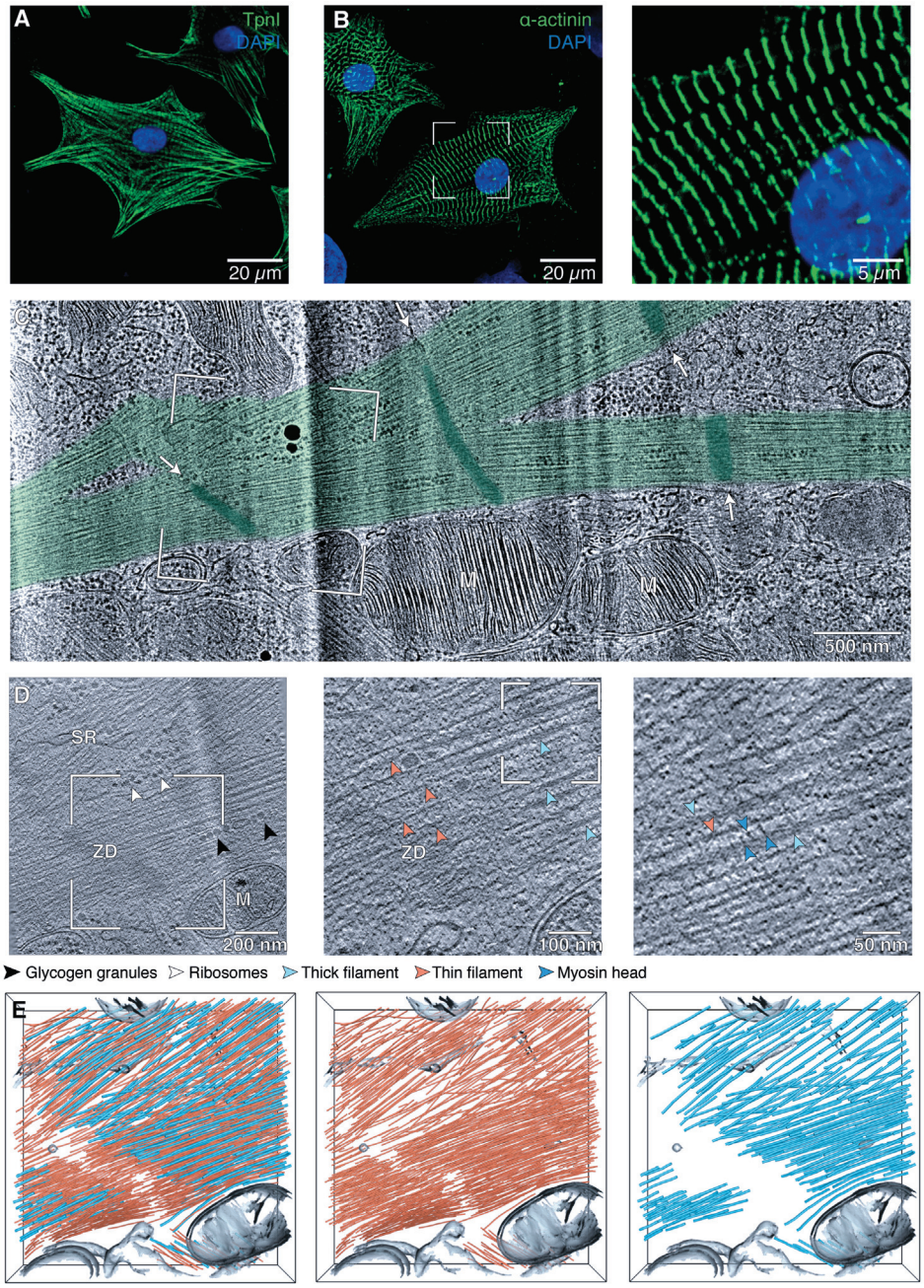

Fig. 1. Visualizing the myofibrillar interior *in situ*. (A-B) Myofibrils (A) in neonatal rat cardiomyocytes align with the main axes of the star-like shaped cells and feature regularly spaced Z-disks (B). (See fig. S1, B-D for more examples.) (C) TEM image of the enlarged framed area of a neonatal rat cardiomyocyte lamella shown in fig. S2D. Myofibrils (green) display periodic, electron-dense bands (dark green, white arrows) merging across adjoining parts. M, mitochondria. (D) Slice from a tomographic volume acquired at the framed area in (C), showing the myofibrillar architecture. SR, sarcoplasmic reticulum; ZD, Z-disk. Left inset: Z-disk periphery. Right inset: myosin heads extending toward thin filaments. (E) 3D rendering of the cellular volume shown in (D) revealing the nanoscale organization of thin (orange) and thick (cyan) filaments within unperturbed sarcomeres. (See also movie S2). Additional examples are provided in fig. S3.

ulum (Fig. 1C and fig. S2D). These myofibrils have a typical width of 470 ± 60 nm and display periodic, electron-dense bands that merge across adjoining parts (Fig. 1C and fig. S2D). The periodicity is comparable to the sarcomere length, suggesting that these bands may be either Z-disks or M-lines.

Myofibrils identified in the lamellas were imaged in 3D by cryo-ET. The reconstructed volumes permitted visualization of the thin and thick filaments, with diameters of 8.4 ± 0.9 nm and 17.4 ± 3.0 nm, respectively (Fig. 1D and fig. S3, A-C). Densities resembling the head domains of myosin II (10) bridge the space between interdigitating cardiac myofilaments (Fig. 1D, right). Macromolecular complexes of 34.4 ± 4.3 nm in diameter, most likely glycogen granules (22), are found outside and within the myofibrillar interior, whereas mitochondria, sarcoplasmic reticulum and ribosomes are found exclusively in the cytoplasmic space devoid of myofibrils (Fig. 1D and fig. S3, A-C).

The periodic, electron-dense bands observed in the TEM images are made of irregular, fuzzy structures that intersect with the thin filaments (Fig. 1D and fig. S3, A-C). Filament seg-

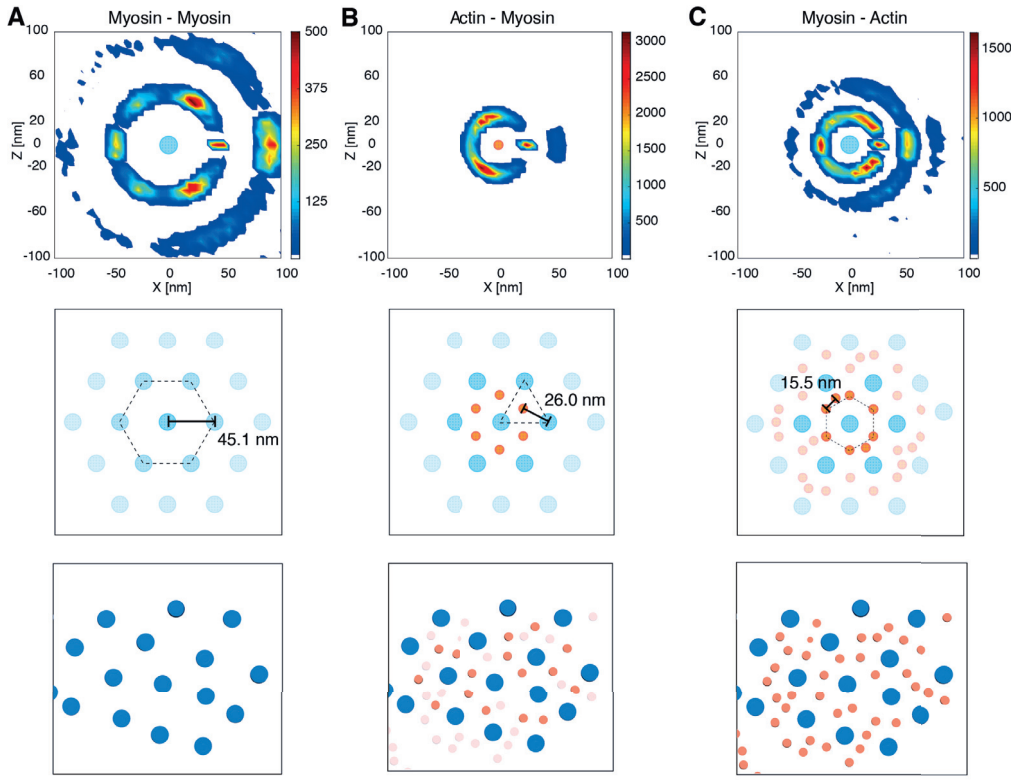

Fig. 2. Neonatal cardiac thick filaments are hexagonally packed with an excess of thin filaments outside the trigonal positions. (A-C) Quantitative analysis of the myofilament packing in neonatal rat cardiomyocytes (top, see methods in SM), schematic representation of the array (middle), and cross-section through the myofibril shown in fig. S3E (bottom). See fig. S5 for additional cross-section examples. Heat map of nearest neighbor positions around thick filaments ("Myosin", A and C, cyan-filled circle) or thin filaments ("Actin", B, orange-filled circle) in a plane perpendicular to the filament cross-sections and within the distance ranges determined in fig. S4. Thick filaments assemble into a hexagonal lattice with an interfilament distance of about 45 nm (A and fig S4A). Thin filaments are found at about 26 nm from three neighboring thick filaments (B and fig S4, B and C) and outside the trigonal positions of the lattice (C and fig S4D).

mentation provided a first glimpse at the native myofilament organization in 3D, revealing a gap between the thin filaments at the center of the band and the absence of thick filaments (Fig. 1E, fig. S3, D-F, and movie S2). Thus, the electron-dense structures correspond to Z-disks, with widths between 100 and 140 nm as has been reported for cardiac muscle (23, 24), and the regions depleted of thick filaments are I-bands, with lengths between 240 and 300 nm. Interestingly, we did not observe any myosin bare zone depleted of thin filaments (Fig. 1E, fig. S3, D-F, and movie S2).

We next quantitatively analyzed the 3D organization of the neonatal myofilaments using an approach described previously (25). Thick filaments organize in a hexagonal lattice with an interfilament distance of 45.1 ± 3.8 nm (Fig. 2A and fig. S4A). Thin filaments are found at the trigonal positions of the lattice, at a distance of 26.0 ± 2.4 nm from the thick filaments (Fig. 2B and fig. S4, B and C). However, the mean distance of 15.5 ± 1.4 nm between thin filaments indicates that they are also present outside the trigonal positions of the array (fig. S4D). This is in agreement with the ratio of thin-to-thick filaments of 3:1 found in these cells, as compared to the ratio of 2:1 reported in vertebrate muscle (26). Therefore, the packing of the thin filaments around the thick filaments we observed, both in real cross-sections and quantitatively, is less ordered than that found in skeletal muscle using X-ray diffraction (27-30) (Fig 2C and fig. S5). This indicates that cardiac sarcomere contraction is already possible with imperfect packing of the thin filaments, and suggests that thick filaments are an important determinant of myofilament organization.

Next, we exploited subtomogram averaging (31) to unveil the molecular organization of the thin filaments enabling sarcomere contraction. To this end, we first developed an approach to obtain the structure of the thin filaments by aligning and averaging multiple consecutive actin subunits along the filaments without imposing any helical symmetry (see methods in supplementary materials (SM)). Thin filaments located on one side of a Z-disk were used to generate a *de novo* structure of F-actin in complex with Tpm resolved at 20.7 Å (fig. S6, A-C). At this resolution, the positions of the actin subunits with respect to the two Tpm strands allow to discriminate between F-actin structures of opposite polarity (fig. S6D). Comparison with a pseudoatomic model of the F-actin-Tpm complex (10) permitted to allocate the barbed (+) and pointed (-) ends of the actin filament (Fig. 3A and fig. S6E).

We then sought to determine the polarity of the thin filaments within the native cardiac sarcomeres. Using a multireference alignment procedure based on the obtained *de novo* structure, we evaluated the polarity of each individual filament from a series of statistically independent estimates (see methods in SM; fig. S7, A and B). 69% of the thin filaments were assigned a polarity with confidence (fig. S7C) and visualized in

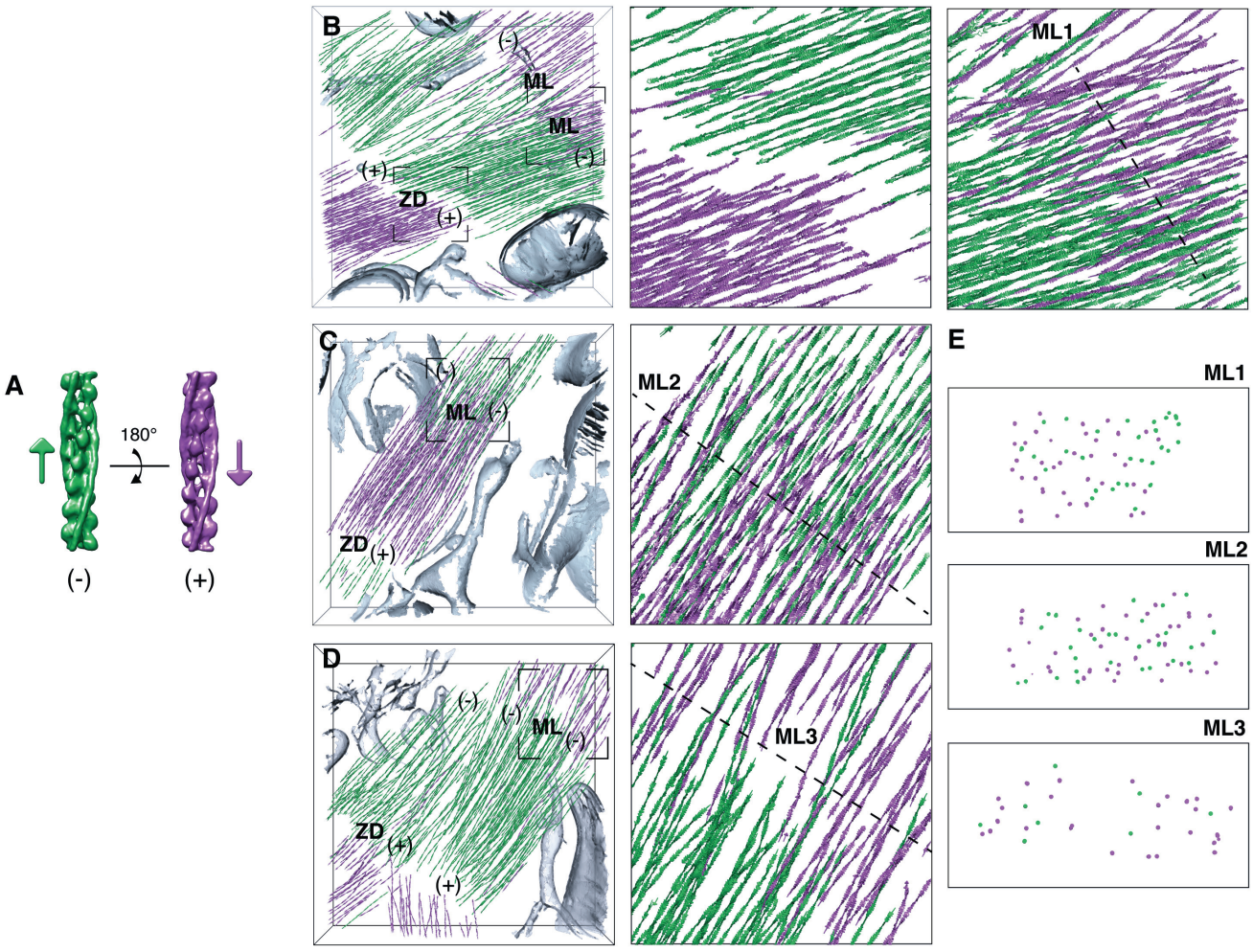

Fig. 3. Structural signature of sarcomere contraction. (A) *De novo* structure of the actin-Tpm filament in opposite orientations, represented by arrows pointing toward the barbed (+) end. (B-E) Polarity assignment for the cardiac thin filaments shown in Fig 1E and movie S2 (B and movie S3) and fig. S3, E and F (C and D, respectively, and movie S4). Filaments are represented by arrows colored according to the assigned polarity. The gaps between thin filaments facing each other with their barbed ends indicate the location of Z-disks (ZD). The overlap regions between thin filaments of opposite polarity at the pointed (-) ends correspond to M-lines (ML). Insets: Thin filament orientations at the framed Z-disk (B, middle) and M-lines (B-D, right) with their respective cross-sections (E). See fig. S8 for visualization of the unassigned filaments.

3D (Fig. 3). Filaments belonging to the same bundle shared the same polarity, while changes of polarity were observed between adjoining bundles (Fig. 3, B-D, left). In vicinity of the Z-disks, thin filaments face each other with their barbed ends, as has been previously reported (12, 15) (Fig. 3B, middle, and movie S3). Additionally, the analysis showed regions in which thin filaments of opposite polarity face each other with their pointed ends, revealing the location of M-lines (Fig. 3, B-D, left).

This allowed us to uncover the arrangement of the thin filaments in the center of the sarcomere, where arrays of opposite polarity are pulled toward each other during contraction. In two out of three M-lines, thin filaments of opposite polarity were found to overlap with each other, revealing their relative sliding (Fig. 3, B and C, and movie S4), as proposed by Gordon *et al*. (32). In the sarcomere shown in Fig. 3C, the overlap length is 281 nm, corresponding to 17% of the sarcomere length. This value is comparable to the values of 0.15 to 0.2 μm reported for the bare zone region (12), indicating that the sliding between these thin filaments occurs across the bare zone. The sarcomere length of 1.65 μm is smaller than the value of 1.8 ± 0.2 μm we measured in these cells, in agreement with sarcomere shortening. Cross-sections through the M-lines show that thin filaments of opposite polarities can contribute to the packing around the same thick filaments during their sliding (Fig. 3E, ML1 and ML2, and fig. S8, A and B). In the sarcomere shown in Fig. 3D, no clear overlap between thin filaments of opposite polarity was detectable at the M-line (Fig. 3, D and E, ML3, fig. S8C and movie S4), indicating that this sarcomere may be in a different contraction state.

We next used subtomogram averaging to determine the structures of the thin filaments associated to the observed M-line organizations. We first analyzed each tomogram individually in order to uncover potential differences in the Tpm position between sarcomeres. Tomograms acquired in cells where thin filaments of opposite polarity overlap in the M-line region provided a similar structure (Fig. 4E, left). In contrast, the data shown in Fig. 3D without clear overlap yielded a subtomogram average in which the Tpm density is shifted azimuthally on the surface of the actin filament (Fig. 4E), indicating that these filaments are in a different functional state.

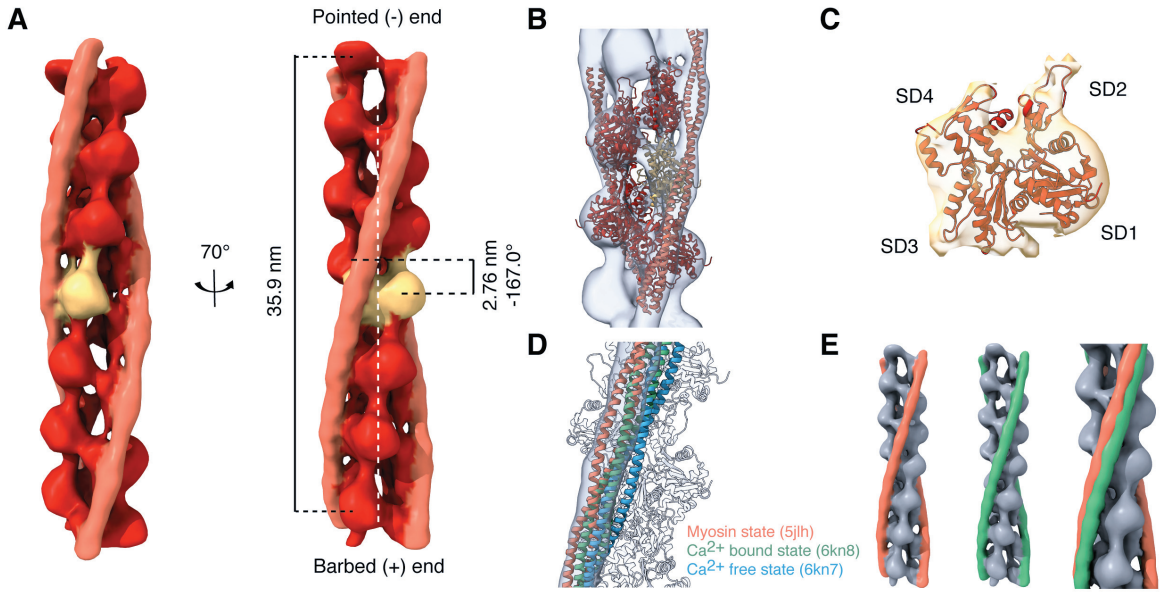

Fig. 4. *In situ* structure of the cardiac thin filament in two distinct functional states. (A) *In situ* subtomogram average of the sarcomeric actin filament (red and yellow) in complex with Tpm (orange) resolved at 13.2 Å (fig. S9A, orange curve, movie S5). (B-C) Fit of a pseudoatomic model of the F-actin-Tpm complex (10) into the subtomogram average (B) reveals F-actin polarity at the level of the actin monomers (C). (D) Docking of pseudoatomic models in different states (10, 18) into the map reveals that the thin filament is in the myosin state (see also fig. S9E). (E) The thin filaments shown in Fig. 3D provided a structure in which the Tpm density (green) is shifted azimuthally as compared to the Tpm density obtained from the thin filaments shown in Fig. 3C (orange).

To generate a higher-resolution average, the tomograms with comparable structures were combined. A refined subtomogram average of the cardiac thin filament was obtained at a resolution of 13.2 Å (Fig. 4A, fig. S9, A and B, and movie S5). The structure features thirteen fully resolved F-actin subunits surrounded by two Tpm strands which approximately follow the same helical twist (Fig. 4A and movie S5). The actin filament consists of a left-handed single helix with a pitch of 35.9 nm, a rise per actin subunit of 2.76 nm and an angular twist per molecule of -167.0° (Fig. 4A, right), in agreement with the literature (33). The central part of the structure exhibits a local resolution of 11.4 Å (fig. S9C), allowing docking of a pseudoatomic model of the F-actin-Tpm complex into the map (Fig. 4B and movie S5). F-actin polarity is evident at the level of the actin monomers (Fig. 4C and movie S5). Comparison with pseudoatomic models in different functional states (10, 18) shows that the thin filament is in the fully activated ("myosin") state that allows strong binding of the myosin heads (Fig. 4D and fig. S9, D, left, and E). This provides evidence at the molecular level that a majority of thin filaments in these sarcomeres are strongly bound to thick filaments, allowing their relative sliding and, thus, sarcomere contraction. Moreover, the Ca^{2+} bound state of the cardiac thin filament, which allows myosin head access but no strong binding (18), fitted best to the separate structure obtained from the data shown in Fig. 3D (fig. S9, D, right, and F), supporting that these sarcomeres are in a different state of the contraction cycle. This is in agreement with the distinct thin filament organization observed at the M-line, where arrays of opposite polarity are in close apposition to each other without clear overlapping part (Fig. 3D).

Conclusions

Our integrative approach permitted to directly visualize sarcomere organization in pristinely preserved cardiac muscle cells with molecular precision. Contracted sarcomeres, in which thin filaments are strongly bound to thick filaments, exhibit an overlap between thin filaments of opposite polarity in the M-line region, indicating that they slid past each other during contraction (fig. S10A). When the actomyosin binding is weaker, sarcomeres are found in an intermediate state, in which thin filaments of opposite polarity are in close apposition but do not overlap (fig. S10B). At the neonatal stage, contraction occurs despite an excess of thin filaments outside the trigonal positions of the thick-filament hexagonal lattice, including at the M-line where both actin polarities contribute to the overall packing (fig. S10A). Our work demonstrate that cryo-ET is able to reveal the polarity and functional states of the thin filaments *in situ*, and paves the way for structure determination of actomyosin interactions within cells.

ACKNOWLEDGEMENTS

The authors thank W. Wan, F. Beck, P.S. Erdmann and V. Lucic for technical and computational assistance; R. Poincloux for critical reading of the manuscript and helpful comments. This work was supported by the Max Planck Society and by the German Center for Cardiovascular Research (DZHK)-Munich Partner Site (to R.T.B.). This preprint was formatted using the HenriquesLab bioRxiv template.

AUTHOR CONTRIBUTIONS

L.B., J.S. and M.J. designed and interpreted experiments. S.S. prepared the cells and performed immunofluorescence imaging. L.B. performed cryo-FIB milling, cryo-ET, tomogram reconstruction, segmentation, and filament packing analysis with help from M.J. J.S. developed and applied the subtomogram averaging and polarity assessment approaches. R.T.B., W.B., P.S. and J.M.P. provided financial support and access to instrumentation. M.J. supervised the work and wrote the paper with contributions from all authors.

COMPETING INTERESTS

The authors declare no competing interest.

DATA AND MATERIALS AVAILABILITY

The *in situ* structures of the cardiac thin filament have been deposited in the EMDataBank under accession codes EMD-XXXX and EMD-YYYY.

References

1. J. M. Squire, Architecture and function in the muscle sarcomere. *Curr Opin Struct Biol* **7**, 247-257 (1997)

2. A. F. Huxley, R. Niedergerke, Structural changes in muscle during contraction; interference microscopy of living muscle fibres. *Nature* **173**, 971-973 (1954)

3. H. Huxley, J. Hanson, Changes in the cross-striations of muscle during contraction and stretch and their structural interpretation. *Nature* **173**, 973-976 (1954)

4. H. E. Huxley, The mechanism of muscular contraction. *Science* **164**, 1356-1365 (1969)

5. R. W. Lymn, E. W. Taylor, Mechanism of adenosine triphosphate hydrolysis by actomyosin. *Biochemistry* **10**, 4617-4624 (1971)

6. T. D. Lenart, J. M. Murray, C. Franzini-Armstrong, Y. E. Goldman, Structure and periodicities of cross-bridges in relaxation, in rigor, and during contractions initiated by photolysis of caged Ca^{2+}. *Biophys J* **71**, 2289-2306 (1996)

7. V. Lombardi *et al*., Elastic distortion of myosin heads and repriming of the working stroke in muscle. *Nature* **374**, 553-555 (1995)

8. K. A. Taylor *et al*., Tomographic 3D reconstruction of quick-frozen, Ca^{2+}-activated contracting insect flight muscle. *Cell* **99**, 421-431 (1999)

9. H. Iwamoto, N. Yagi, The molecular trigger for high-speed wing beats in a bee. *Science* **341**, 1243-1246 (2013)

10. J. von der Ecken, S. M. Heissler, S. Pathan-Chhatbar, D. J. Manstein, S. Raunser, Cryo-EM structure of a human cytoplasmic actomyosin complex at near-atomic resolution. *Nature* **534**, 724-728 (2016)

11. H. E. Huxley, J. Hanson, Structural basis of the cross-striations in muscle. *Nature* **172**, 530-532 (1953)

12. H. E. Huxley, Electron microscope studies on the structure of natural and synthetic protein filaments from striated muscle. *J Mol Biol* **7**, 281-308 (1963)

13. H. E. Huxley, X-ray analysis and the problem of muscle. *Proc R Soc Lond B Biol Sci* **141**, 59-62 (1953)

14. H. E. Huxley, Electron microscope studies of the organisation of the filaments in striated muscle. *Biochim Biophys Acta* **12**, 387-394 (1953)

15. H. Ishikawa, R. Bischoff, H. Holtzer, Formation of arrowhead complexes with heavy meromyosin in a variety of cell types. *J Cell Biol* **43**, 312-328 (1969)

16. K. Takahashi, A. Hattori, Alpha-actinin is a component of the Z-filament, a structural backbone of skeletal muscle Z-disks. *J Biochem* **105**, 529-536 (1989)

17. W. Lehman, R. Craig, P. Vibert, Ca^{2+}-induced tropomyosin movement in *Limulus* thin filaments revealed by three-dimensional reconstruction. *Nature* **368**, 65-67 (1994)

18. Y. Yamada, K. Namba, T. Fujii, Cardiac muscle thin filament structures reveal calcium regulatory mechanism. *Nat Commun* **11**, 153 (2020)

19. J. Mahamid *et al*., Visualizing the molecular sociology at the HeLa cell nuclear periphery. *Science* **351**, 969-972 (2016)

20. M. Beck, W. Baumeister, Cryo-electron tomography: can it reveal the molecular sociology of cells in atomic detail? *Trends Cell Biol* **26**, 825-837 (2016)

21. A. Rigort *et al*., Focused ion beam micromachining of eukaryotic cells for cryoelectron tomography. *Proc Natl Acad Sci U S A* **109**, 4449-4454 (2012)

22. B. Coulary, M. Aigle, J. Schaeffer, Evidence for glycogen structures associated with plasma membrane invaginations as visualized by freeze-substitution and the Thiery reaction in Saccharomyces cerevisiae. *J Electron Microsc* **50**, 133-137 (2001)

23. M. A. Goldstein, J. P. Schroeter, R. L. Sass, Optical diffraction of the Z lattice in canine cardiac muscle. *J Cell Biol* **75**, 818-836 (1977)

24. M. Yamaguchi, M. Izumimoto, R. M. Robson, M. H. Stromer, Fine structure of wide and narrow vertebrate muscle Z-lines. A proposed model and computer simulation of Z-line architecture. *J Mol Biol* **184**, 621-643 (1985)

25. M. Jasnin *et al*., Three-dimensional architecture of actin filaments in *Listeria monocytogenes* comet tails. *Proc Natl Acad Sci U S A* **110**, 20521-20526 (2013)

26. H. E. Huxley, The molecular basis of contraction in cross-striated muscles. In: *The Structure and Function of Muscle*. New York and London, Academic Press, 1960, vol.1, p. 183-227

27. G. F. Elliott, J. Lowy, C. R. Worthington, An X-ray and light-diffraction study of the filament lattice of striated muscle in the living state and in rigor. *J Mol Biol* **6**, 295-305 (1963)

28. G. F. Elliott, J. Lowy, B. M. Millman, X-ray diffraction from living striated muscle during contraction. *Nature* **206**, 1357-1358 (1965)

29. H. E. Huxley, W. Brown, The low-angle X-ray diagram of vertebrate striated muscle and its behaviour during contraction and rigor. *J Mol Biol* **30**, 383-434 (1967)

30. H. E. Huxley, Structural difference between resting and rigor muscle; Evidence from intensity changes in the low-angle equatorial X-ray diagram. *J Mol Biol* **37**, 507-514 (1968)

31. J. A. Briggs, Structural biology *in situ* - the potential of subtomogram averaging. *Curr Opin Struct Biol* **23**, 261-267 (2013)

32. A. M. Gordon, A. F. Huxley, F. J. Julian, The variation in isometric tension with sarcomere length in vertebrate muscle fibres. *J Physiol* **184**, 170-192 (1966).

33. T. Fujii, A. H. Iwane, T. Yanagida, K. Namba, Direct visualization of secondary structures of F-actin by electron cryomicroscopy. *Nature* **467**, 724-U117 (2010)

Materials and Methods

Isolation of neonatal rat ventricular cardiomyocytes. Three-days-old (P3) wild-type Wistar rats were killed by decapitation and the ribcage was opened. The heart was removed by pulling with forceps and transferred into a 35-mm Petri dish containing phosphate-buffered saline (PBS). The remaining blood was pumped out of the heart and the great vessels. Both atria and the connective tissue were removed. For each preparation, the ventricles of four hearts were mixed together, cut into small pieces and digested using the Neonatal Heart Dissociation kit (Miltenyi Biotec, Bergisch Gladbach, Germany). Briefly, the enzyme mix 1 was pre-heated for 5 min at 37°C and added to the enzyme mix 2. The harvested and chopped ventricular tissue was transferred to the tube containing the enzyme mix. The suspension was gently pipetted every 10 min for 1h. Following enzymatic digestion, the cells were passed through a 70-µm cell strainer and centrifuged at 300g for 15 min. The pellet was resuspended in 10 ml of cardiomyocyte medium. This medium consists of a 1:1 mixture of Dulbecco's modified Eagle medium (DMEM) and Ham's F12 medium (Life technologies, #31330-038) containing 5% horse serum, 5% fetal calf serum (FCS), 20 µM Cytarabine (Ara-C) (Sigma Aldrich, #C1768), 3 mM sodium pyruvate (Sigma #S8636), 2 mM L-glutamine (Thermo Fisher Scientific, #25030-081), 0.1 mM ascorbic acid (Sigma #A4034), 1:200 insulin-transferrin-selenium-sodium pyruvate (Invitrogen, #51300044), 0.2 % bovine serum albumin (BSA) (Sigma Aldrich, #A7409) and 100 U/ml penicillin-streptomycin (Thermo Fisher Scientific, #15140122). The resuspended pellet was pre-plated onto a non-coated cell culture dish for 90 min to reduce the number of cardiac fibroblasts. The supernatant was transferred to a 15 ml tube and centrifuged at 300g for 15 min. The pellet containing the neonatal rat ventricular cardiomyocytes from four hearts was resuspended in 4 ml of cardiomyocyte medium (that is, 1 heart eq./ml). Moreover, primary adult mouse ventricular cardiomyocytes were isolated following the protocol from Ackers-Johnson *et al*. (34).

Cardiomyocyte culture on EM grids and vitrification. Gold EM grids with Quantifoil R 2/1 holey carbon film (Quantifoil Micro Tools GmbH, Grossloebichau, Germany) were glow-discharged, sterilized by UV irradiation for 30 min and coated with fibronectin (10 µg/ ml, Merck, #341631). Six to eight EM grids were placed in 35-mm Petri dishes and 300 µl of cell suspension was added (that is, ∼1/3 heart eq. per dish). The cells were cultured at 37°C in 5% CO_2 for two days. To verify that the cells exhibit spontaneous rhythmic contractions prior to cryo-fixation, the grids were imaged at room temperature (RT) by bright field using a 20x (air, NA 0.8) Plan Achromat objective (Carl Zeiss, Jena, Germany) of a CorrSight microscope (Thermo Fisher Scientific). The grids were plunge-frozen using a Vitrobot Mark IV (Thermo Fisher Scientific) with 80% humidity and 10s blotting time in a 2:1 ethane/propane mixture cooled by liquid nitrogen.

Immunofluorescence microscopy. Cells used for immunofluorescence microscopy were cultured on a chambered coverslip with 8 wells (IBIDI #80826, Gräfelfing, Germany) coated with fibronectin (10 µg/ml at 37°C for 1h). After two days, the cells were rinsed in PBS, placed on ice and fixed in 4% paraformaldehyde (PFA) for 15 min. After PBS wash, the cells were permeabilized with 0.1% Triton X-100/PBS for 10 min and blocked with 3% BSA/PBS at 4°C for at least one 1h. Subsequently, the cells were incubated at 4°C with one of the following mouse monoclonal primary antibodies: anti-heavy chain cardiac myosin (Abcam, #ab50967), anti-α-actinin (Sigma-Aldrich, #A7811) or anti-cTnI (Thermo Fisher Scientific, #MA5-12960). The next day, the cells were washed with PBS (3 x 5 min) and incubated with an anti-mouse secondary antibody (Alexa Fluor™ 488 goat IgG (H+L), Thermo Fisher Scientific, #A11029) at RT for 1h in the dark. The cells were washed with PBS (2 x 5 min), stained with DAPI (1:6,000 in PBS) at RT for 15 min in the dark, washed again in PBS (2 x 5 min) and stored at 4°C. Confocal imaging was performed with a Zeiss LSM 780 confocal laser scanning microscope (Carl Zeiss, Oberkochen, Germany) equipped with a 40x (oil, NA 1.4) Plan-Apo objective (Carl Zeiss, Jena, Germany). The resulting images were analyzed with ImageJ software version 1.52p (https://imagej.net/Fiji).

Cryo-FIB milling. Plunge-frozen grids were clipped into Autogrids modified for cryo-FIB milling (35, 36). The Autogrids were mounted into a custom-built FIB shuttle cooled by liquid nitrogen and transferred using a cryo-transfer system (PP3000T, Quorum Technologies) to the cryo-stage of a dual-beam Quanta 3D FIB/SEM (Thermo Fisher Scientific) operated at liquid nitrogen temperature. During the loading step, the grids were sputter-coated with platinum in the Quorum prep-chamber (10 mA, 30s) to improve sample conductivity. To reduce curtaining artifacts, they were subsequently sputter-coated with organometallic platinum using the gas injection system (GIS, Thermo Fisher Scientific) in the microscope chamber operated for 8s at 26°C. Lamellas were prepared using a Gallium ion beam at 30 kV and stage tilts of 18-20°. 8-12 µm wide lamellas were milled in a step-wise manner using high currents of 0.5 nA for rough milling that were gradually reduced to 30 pA for fine milling and final cleaning steps. The milling process was monitored using the electron beam at 5 kV and 11.8 pA or 3 kV and 8.87 pA. For Volta phase plate (VPP) imaging, the lamellas were additionally sputter-coated with a platinum layer in the Quorum prep-chamber (10 mA, 3s).

Cryo-ET. The lamellas were loaded in a Titan Krios transmission electron microscope (Thermo Fisher Scientific) equipped with a 300-kV field-emission gun, VPPs (Thermo Fisher Scientific), a post-column energy filter (Gatan) and a 4k x 4k K2 Summit

direct electron detector (Gatan) operated using SerialEM (37). The VPPs were aligned and used as described previously (38). Low-magnification images were captured at 6,500x. High-magnification tilt series were recorded in counting mode at 42,000x (calibrated pixel size of 0.342 nm), typically from -50° to 70° with 2° steps, starting from a pre-tilt of 10° to correct for the lamella geometry, and a total dose of $\sim$ 100-120 $e^-/Å^2$. Three of the tilt series were collected unidirectionally with the VPPs at a target defocus of 0.5 µm. Ten of the tilt series were recorded without the VPP using a dose-symmetric tilt-scheme (39) and a target defocus range of -3.25 to -5 µm.

Tomogram reconstruction. Frames were aligned using MotionCorr2 (40) and dose-filtered by cumulative dose using the exposure-dependent attenuation function and critical exposure constants described in (41) and adapted for tilt series in (42, 43). Tilt series were aligned using patch tracking in IMOD (44) and tomograms were reconstructed with a binning factor of 4 (13.68 Å per pixel) using weighted back-projection. For visualization, tomograms were filtered using a deconvolution filter (https://github.com/dtegunov/tom_deconv). For subtomogram averaging, contrast transfer function (CTF) parameters for each tilt were estimated by CTFFIND4 (45). 3D-CTF corrected tomograms were generated using NovaCTF (46) and binned by a factor of 2 (6.84 Å per pixel).

Membrane and filament segmentation. The 4 x binned tomograms (pixel size of 13.68 Å) were used for segmentation. Membranes were generated automatically using TomoSegMemTV (47) and refined manually in Amira (Thermo Fisher Scientific). Thin and thick filaments were traced automatically in Amira using an automated segmentation algorithm based on a generic cylinder as a template (48). The cylindrical templates were generated with a length of 42 nm and diameters of 8 and 18 nm for the thin and thick filaments, respectively.

Nearest neighbor analysis and local packing analysis. The analysis developed in (25) was adapted to describe quantitatively the 3D organization of the cardiac myofilaments. A total of 4,770 thin filaments and 1,648 thick filaments extracted from 9 tomograms were used. Data analysis was performed in MATLAB (The MathWorks) using the coordinates of the filament centerlines exported from Amira as input. The coordinates of the filaments were resampled every 3 nm to give the same weight to every point along a filament.

Nearest neighbor analysis. The local direction at each point was evaluated as the local tangent of the filament at that point. For every point within a filament, the closest point of each neighboring filament was characterized by its distance, d, and relative orientation, ϑ, with respect to the reference point. The analysis was performed for filaments of the same type (that is, only thick filaments or only thin filaments) as well as for filaments of one type relative to the other (that is, neighboring thin filaments for the thick filaments, and reciprocally). The occurrences of (d, ϑ) were represented by a 2D histogram. The peak occurring at small ϑ (below 10°) indicates the presence of equidistant and nearly parallel filaments. The mean interfilament spacing was obtained from the distances with a number of occurrences higher than two third of the peak maximum (fig. S4).

Local packing analysis. A local reference frame (e1, e2, e3) was defined at every point along a filament as follows: e2 points in the local direction of the filament, e1 points in the direction of the nearest neighbor, and e3 is the cross-product of e1 and e2 (see (25)). (X, Y, Z) are the coordinates of a neighbor position in (e1, e2, e3). The local reference frames (e1, e2, e3) of all points along the filaments were aligned, and the occurrences of (X, Z) in the e1e3 plane within the distance range for parallel filaments were represented by a 2D histogram (Fig. 2, top).

Subtomogram averaging and polarity assessment.

Subtomogram sampling. Ten tomograms, acquired with a dose-symmetric tilt-scheme and a target defocus range of -3.25 to -5 µm, were used for subtomogram averaging and polarity assessment. The coordinates of the thin filaments extracted from Amira were resampled every 1.38 nm (corresponding to half of the axial rise per actin subunit in the actin filament) along the filament centerline using scripts described in (25). This was instrumental to correctly allocate every actin subunit during subtomogram alignment (42). Principal component analysis was used to generate a common direction for all the filaments in the network upon resampling (that is, filament coordinates were reordered so that the dot product between the direction of each filament and the first principal component was positive). The local tangent at each point along a filament served to calculate initial Euler angles (φ,ϑ,ψ) in the zxz-convention using scripts from (25) and TOM Toolbox (49). As a result, the filament centerline was aligned with the z-axis, allowing the φ angle to describe the in-plane rotation. Since this rotation cannot be determined directly from the tomogram, φ was randomized every 30°. Furthermore, subvolumes belonging to the same filament were assigned a unique identifier, which was used during the assessment of filament polarity exclusively.

De novo reference. Subtomogram averaging was performed using STOPGAP (https://github.com/williamnwan/STOPGAP). An initial reference was generated *de novo* from a single tomogram as follows. 84 thin filaments located on one side of a Z-disk and belonging to the same bundle (shown in orange in fig. S6A) were selected, based on the assumption that they had

the same polarity. 20,259 subtomograms were extracted from the resampled positions using a binning factor of 2 (6.84 Å per pixel) and a box size of 128^3 pixels^3 and a starting reference was generated by averaging all subvolumes. Due to the in-plane randomization, the initial structure resembles a featureless cylinder (fig. S6B). Several rounds of global alignment of the in-plane angle followed by local refinement of all Euler angles were conducted. Shift refinements were limited to 1.38 nm in each direction along the filament centerline. This averaging approach resulted in the emergence of the helical pattern of the thin filament (fig. S6B). Unbinned subvolumes were extracted using a box size of 128^3 pixels^3 and aligned iteratively, resulting in a refined structure of F-actin in complex with Tpm at a resolution of 20.7 Å (fig. S6, B and C). At this resolution, the positions of the actin subunits with respect to the two Tpm strands allowed to distinguish between F-actin structures of opposite polarities (fig. S6D). Comparison with a pseudoatomic model of the F-actin-Tpm complex (10) permitted to allocate the barbed (+) and pointed (-) end of the *de novo* F-actin structure (fig. S6E).

Polarity assessment. The 20.7 Å structure of F-actin in complex with Tpm was rotated by 180° around the x-axis to generate a second structure with opposite polarity (Fig. 3A and fig. S6D). Both structures were used to assess the polarity of the thin filaments in each tomogram using multireference alignment (fig. S7A). Each subvolume within a tomogram was extracted with a binning factor of 2 (6.84 Å per pixel) using a box size of 64^3 pixels^3 and aligned against both references independently. The scores of all the subtomograms belonging to the same filament were compared using unpaired Student's t-test (fig. S7B). On a total of 4,438 filaments (corresponding to 594,317 subvolumes) from 10 tomograms, 69% showed significant differences between the two directions ($p < 0.05$) and were assigned the respective polarity with confidence (fig. S7C). These filaments were kept for further processing. Polarity assignment was visualized with arrows pointing in the direction of the barbed ends of F-actin using the Place Object tool in UCSF Chimera (50, 51).

Subtomogram averaging of the thin filament. To generate a dataset with uniform polarity, the initial Euler angles from the subvolumes of opposite polarity were rotated by 180° around the x-axis. 409,896 subtomograms were extracted with a binning factor of 2 (6.84 Å per pixel) using a box size of 64^3 pixels^3. The 20.7 Å *de novo* structure of F-actin in complex with Tpm (fig. S6B) was low-pass filtered and used as initial reference. Global alignment of the in-plane angle was followed by several rounds of successive local refinement of the in-plane angle and all Euler angles. Simultaneously, shifts were refined within ± 1.38 nm along the filament centerline. Once all the positions were refined, distance thresholding was used to remove oversampled positions, keeping only one subtomogram per actin subunit. 160,617 unbinned subvolumes were extracted using a box size of 128^3 pixels^3. The dataset was split into two half sets that were refined independently.

To uncover potential changes in the azimuthal position of the Tpm strands between sarcomeres, each tomogram was then processed separately using the initial reference without Tpm density. The data shown in Fig. 3D yielded a subtomogram average in which the Tpm density was significantly shifted on F-actin. The other tomograms provided a comparable structure and the corresponding 133,587 particles were merged and further refined. The final maps were sharpened, weighted by the FSC and filtered to their respective resolution ($FSC_{0.143}$ = 17.3 and 13.2 Å, respectively, fig. S9A). Local resolution calculations were performed using RELION 3.0 (52) (fig. S9C). All maps were visualized using UCSF Chimera or UCSF Chimera X (53). Analysis of the distances and in-plane rotation between refined subvolumes belonging to the same filament permitted to determine the mean rise and angular twist of the F-actin structure.

Several pseudoatomic models containing F-actin in complex with Tpm in distinct functional states (10, 18) were docked into the maps using rigid body-fitting in UCSF Chimera. The fit was limited to the actin region to reveal the functional state matching the Tpm density best.

Supplementary references

34. M. Ackers-Johnson *et al*., A simplified, Langendorff-free method for concomitant isolation of viable cardiac myocytes and nonmyocytes from the adult mouse heart. *Circ Res* **119**, 909-920 (2016).

35. M. Marko, C. Hsieh, R. Schalek, J. Frank, C. Mannella, Focused-ion-beam thinning of frozen-hydrated biological specimens for cryo-electron microscopy. *Nat Methods* **4**, 215-217 (2007).

36. M. Schaffer *et al*., Cryo-focused ion beam sample preparation for imaging vitreous cells by cryo-electron tomography. *Bio-protocol* **5**, e1575 (2015).

37. M. Schorb, I. Haberbosch, W. J. H. Hagen, Y. Schwab, D. N. Mastronarde, Software tools for automated transmission electron microscopy. *Nat Methods* **16**, 471-477 (2019).

38. Y. Fukuda, U. Laugks, V. Lucic, W. Baumeister, R. Danev, Electron cryotomography of vitrified cells with a Volta phase plate. *J Struct Biol* **192**, 262-269 (2015).

39. W. J. Hagen, W. Wan, J. A. Briggs, Implementation of a cryo-electron tomography tilt-scheme optimized for high resolution subtomogram averaging. *J Struct Biol* **197**, 191-198 (2017).

40. S. Q. Zheng *et al*., MotionCor2: anisotropic correction of beam-induced motion for improved cryo-electron microscopy. *Nat Methods* **14**, 331-332 (2017).

41. T. Grant, N. Grigorieff, Measuring the optimal exposure for single particle cryo-EM using a 2.6 Å reconstruction of rotavirus VP6. *Elife* **4**, (2015).

42. F. K. Schur et al., An atomic model of HIV-1 capsid-SP1 reveals structures regulating assembly and maturation. *Science* **353**, 506-508 (2016).

43. W. Wan *et al*., Structure and assembly of the Ebola virus nucleocapsid. *Nature* **551**, 394-397 (2017).

44. J. R. Kremer, D. N. Mastronarde, J. R. McIntosh, Computer Visualization of Three-Dimensional Image Data Using IMOD. *J Struct Biol* **116**, 71-76 (1996).

45. A. Rohou, N. Grigorieff, CTFFIND4: Fast and accurate defocus estimation from electron micrographs. *J Struct Biol* **192**, 216-221 (2015).

46. B. Turonova, F. K. M. Schur, W. Wan, J. A. G. Briggs, Efficient 3D-CTF correction for cryo-electron tomography using NovaCTF improves subtomogram averaging resolution to 3.4 angstrom. *J Struct Biol* **199**, 187-195 (2017).

47. A. Martinez-Sanchez, I. Garcia, S. Asano, V. Lucic, J. J. Fernandez, Robust membrane detection based on tensor voting for electron tomography. *J Struct Biol* **186**, 49-61 (2014).

48. A. Rigort *et al*., Automated segmentation of electron tomograms for a quantitative description of actin filament networks. *J Struct Biol* **177**, 135-144 (2012).

49. S. Nickell *et al*., TOM software toolbox: acquisition and analysis for electron tomography. *J Struct Biol* **149**, 227-234 (2005).

50. E. F. Pettersen *et al*., UCSF Chimera–a visualization system for exploratory research and analysis. *J Comput Chem* **25**, 1605-1612 (2004).

51. K. Qu *et al*., Structure and architecture of immature and mature murine leukemia virus capsids. *Proc Natl Acad Sci U S A* **115**, E11751-E11760 (2018).

52. J. Zivanov *et al*., New tools for automated high-resolution cryo-EM structure determination in RELION-3. *Elife* **7**, e42166 (2018).

53. T. D. Goddard *et al*., UCSF ChimeraX: Meeting modern challenges in visualization and analysis. *Protein Sci* **27**, 14-25 (2018).

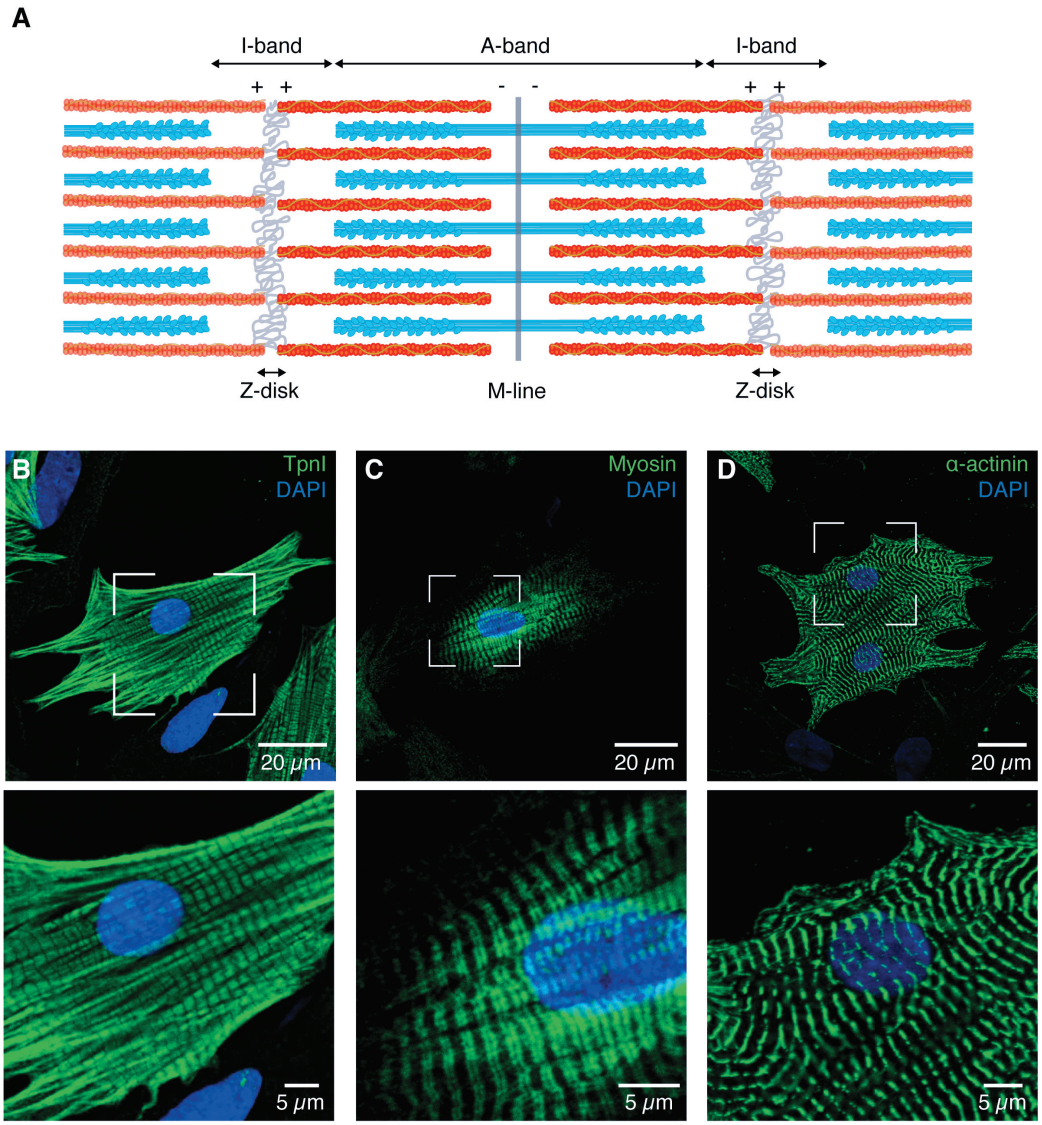

Fig. S1. Sarcomere organization at the microscale. (A) Schematic representation of adjoining micrometer-sized sarcomeres within a myofibril, showing the organization of the thick (cyan) and thin (red) filaments in this basic contractile unit of striated muscle. (B-D) Thin (B) and thick (C) filaments of neonatal rat cardiomyocytes assemble into myofibrils, which align with the main axes of the star-like shaped cells and display regularly spaced Z-disks (D). TpnI, troponin I.

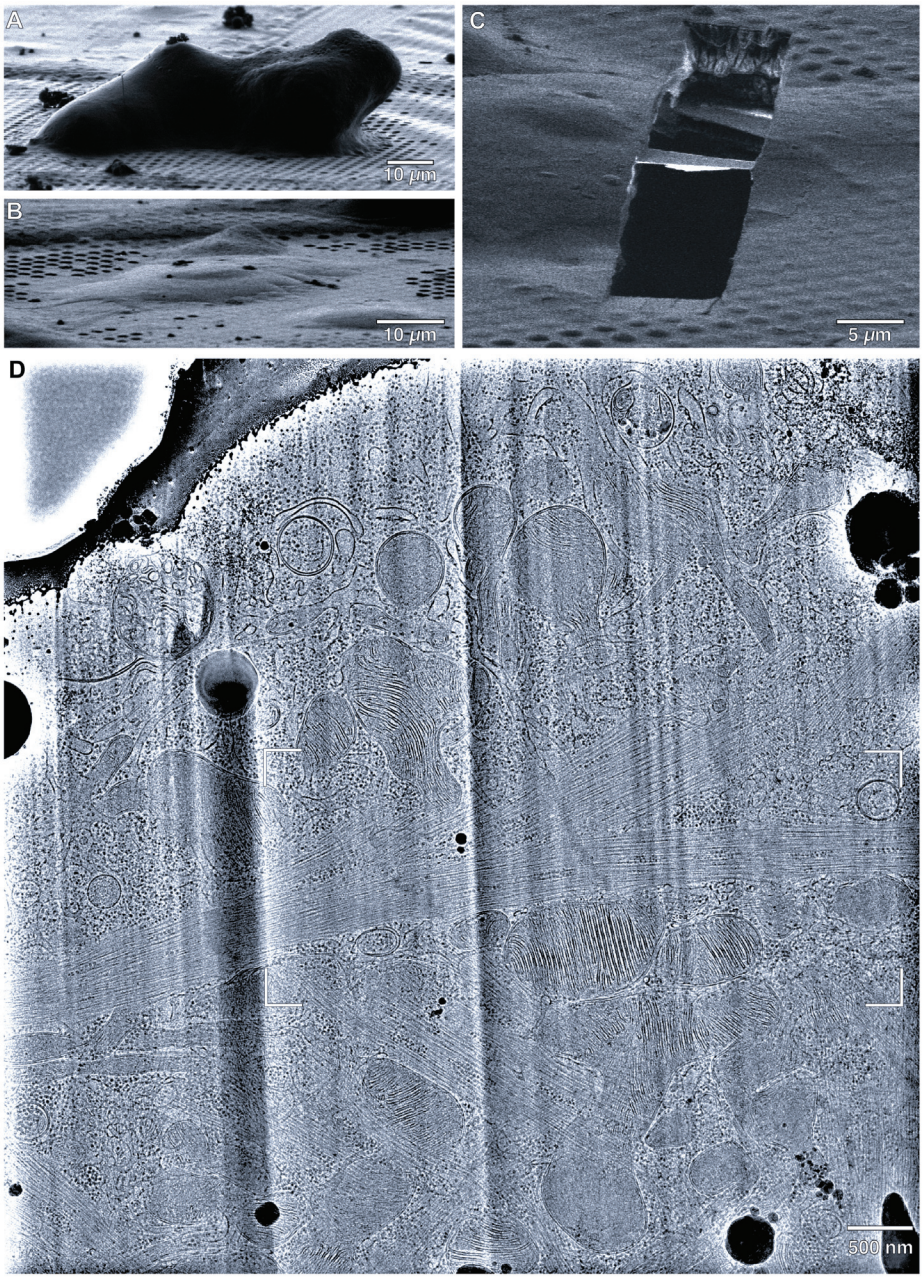

Fig. S2. Cryo-focused ion beam sample preparation of neonatal cardiomyocytes for cryo-ET imaging. (A) Scanning electron microscope (SEM) image of a frozen-hydrated adult mouse cardiomyocyte on an EM grid. Vitrification by plunge-freezing is not suitable for these cells because their thickness is larger than 10 µm. (B) Neonatal rat cardiomyocytes are thin, allowing optimal vitrification by plunge-freezing without the need for cryoprotectant. (C) 200-nm-thick lamella prepared in a plunge-frozen neonatal cardiomyocyte and imaged by FIB-induced secondary electrons. (D) Full TEM image of a neonatal cardiomyocyte lamella containing the cropped part shown in Fig. 1C.

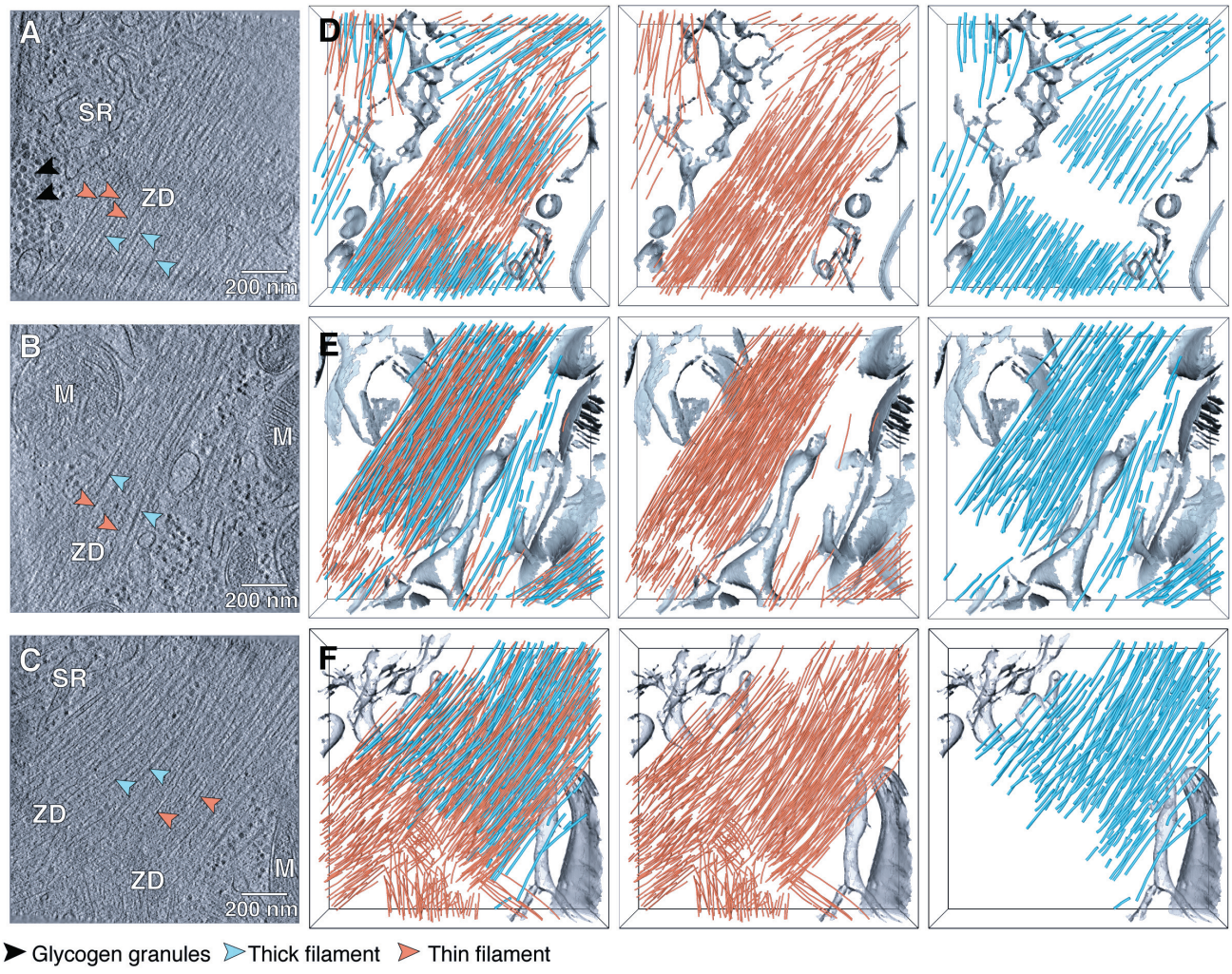

Fig. S3. Nanoscale sarcomere organization revealed by *in situ* cryo-ET. (A-C) Slices from tomographic volumes acquired in frozen-hydrated neonatal rat cardiomyocytes, revealing the myofibrillar environment. ZD, Z-disk; M, mitochondrium; SR: sarcoplasmic reticulum. (D-F) Corresponding 3D segmentation of the cellular volumes, showing the nanoscale organization of the thin (orange) and thick (cyan) filaments within unperturbed sarcomeres.

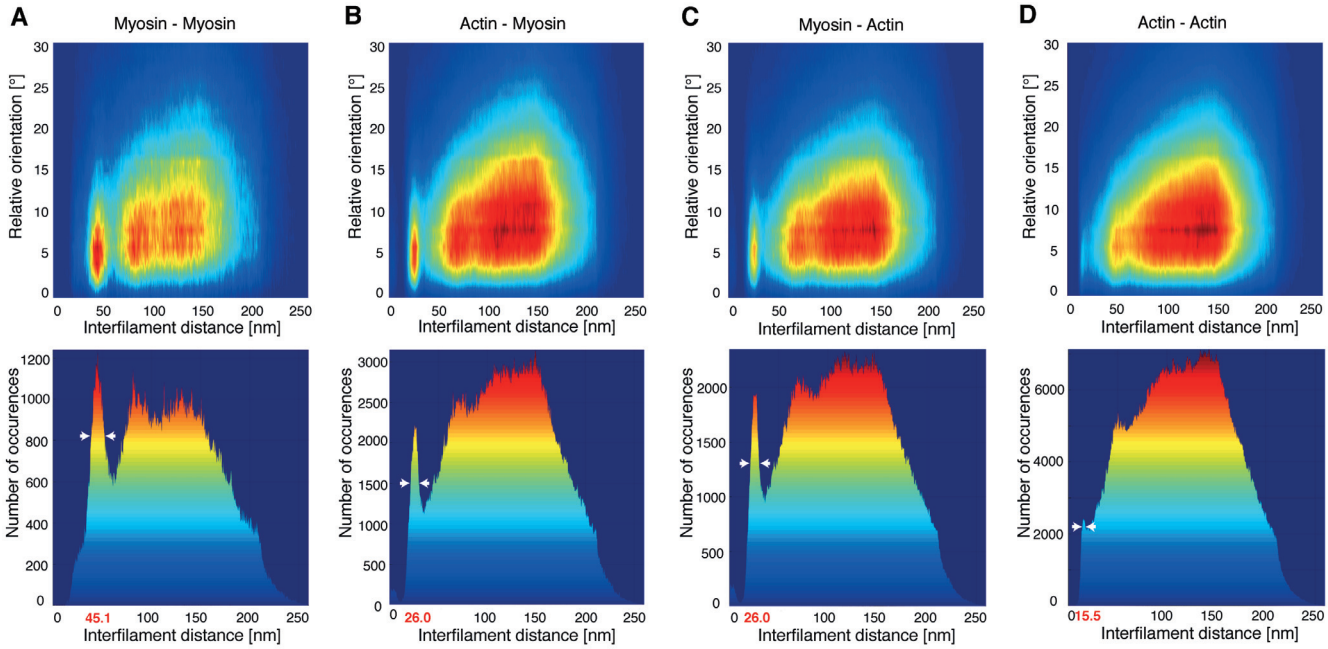

Fig. S4. Nearest-neighbor analysis of myofilaments in neonatal rat cardiomyocytes. (A-D) Top: 2D histogram of interfilament distances and relative orientations between thick filaments ("Myosin"; A), between thick and thin filaments ("Actin"; B and C), and between thin filaments (D). Bottom: corresponding histograms showing the number of occurrences of the interfilament distances. Thick filaments have an interfilament spacing of $\sim$ 45 nm (A) and are found at $\sim$ 26 nm from the thin filaments (B and C). Thin filaments have their nearest actin neighbors at $\sim$ 15.5 nm (D). White arrow heads indicate the distance range for parallel filaments.

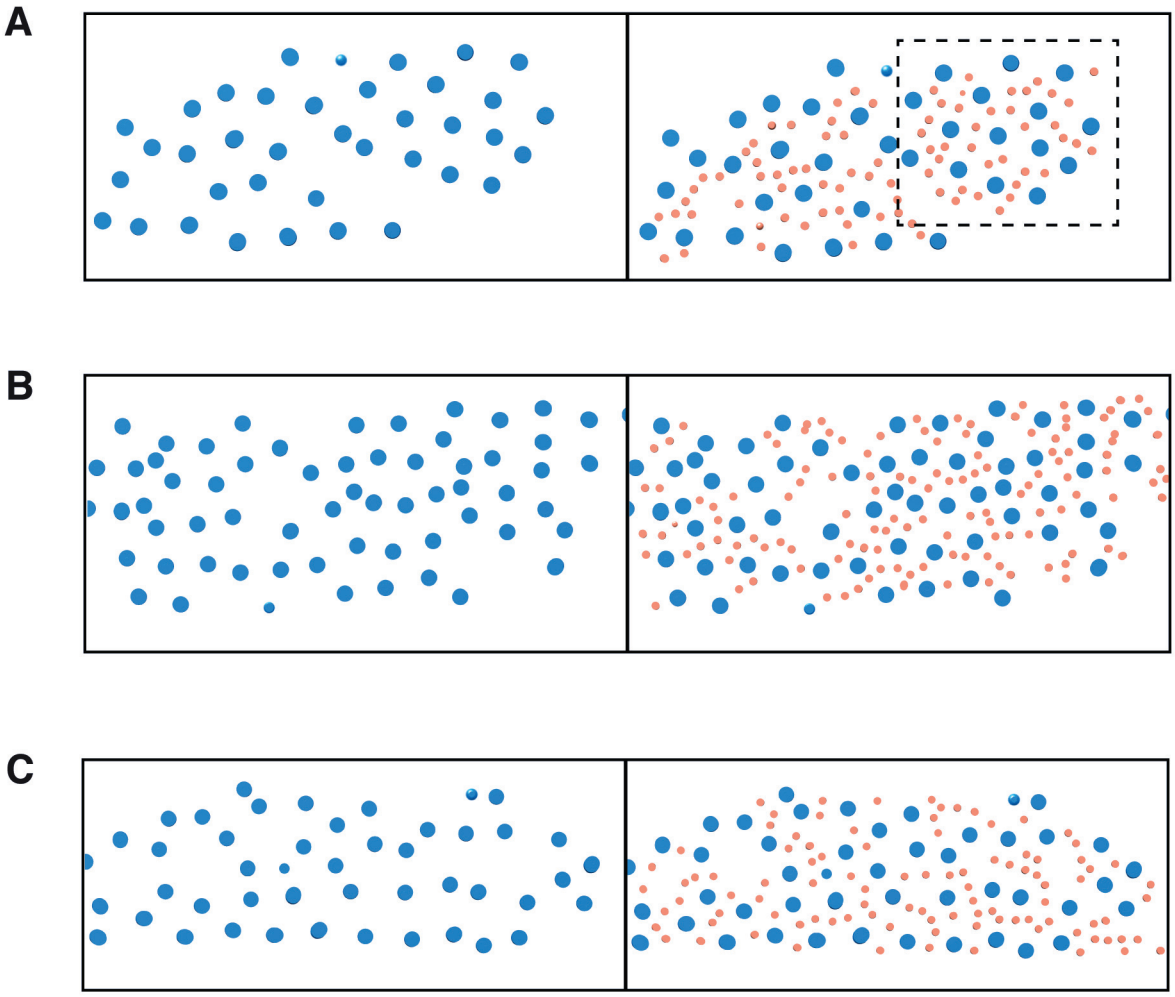

Fig. S5. Examples of cross-sections through myofibrils of neonatal rat cardiomyocytes. (A-C) Thick filaments (blue) are hexagonally packed and surrounded by thin filaments (orange, right) at the trigonal positions of the lattice and outside of them. The framed area in (A) is shown in Fig. 2C, bottom. The slices were obtained from the myofibrils shown in fig. S3E (A), Fig. 1E (B) and fig. S3F (C).

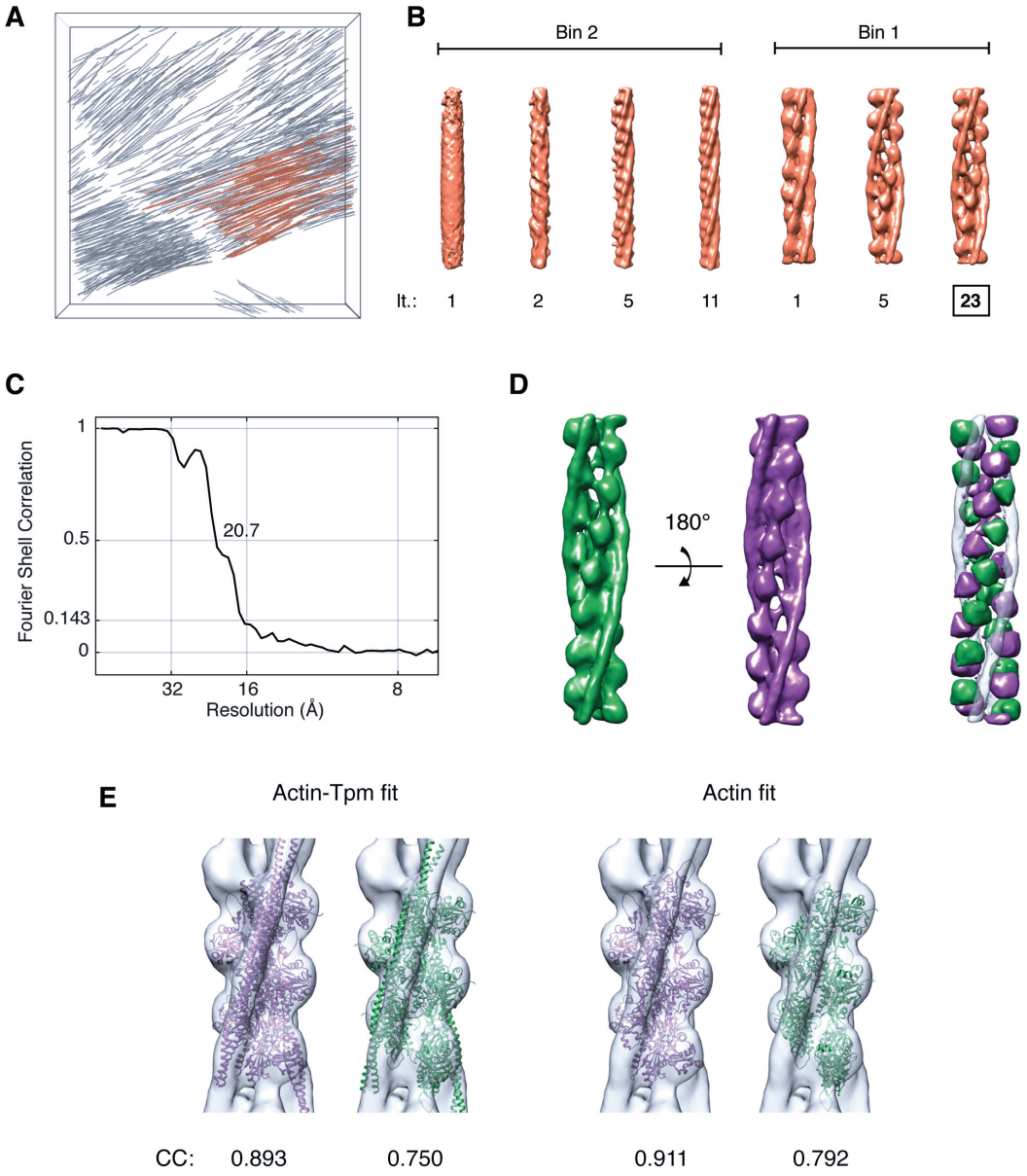

Fig. S6. *De novo* structure generation from cryo-ET data of cardiac thin filaments. (A) Thin filaments (orange) from the tomogram shown in Fig. 1D and movie S2 used for the generation of a *de novo* reference. (B) Iterative alignment using 2 x binned ("Bin2") and unbinned ("Bin1") data resulted in the emergence of the helical pattern of the thin filament and yielded a structure of F-actin in complex with Tpm resolved at 20.7 Å. It: Iteration number. (C) Corresponding Fourier shell correlation plot. Since the data was not processed using gold-standard refinement, a cutoff of 0.5 was used. (D) Difference map (right) generated by aligning the Tpm densities of the filament structures in opposite orientations (left; green and purple, respectively), revealing the actin positions associated to each polarity. (E) Both orientations (same color code as in (D)) of the pseudoatomic model of the F-actin-Tpm complex (pdb 5jlh) docked into the *in situ* map (grey) shown in purple in (D) (left), and corresponding fits using the actin densities only (right). The cross-correlation ("CC") results permitted to allocate the barbed (+) and pointed (-) end of the *de novo* F-actin structure (Fig. 3A).

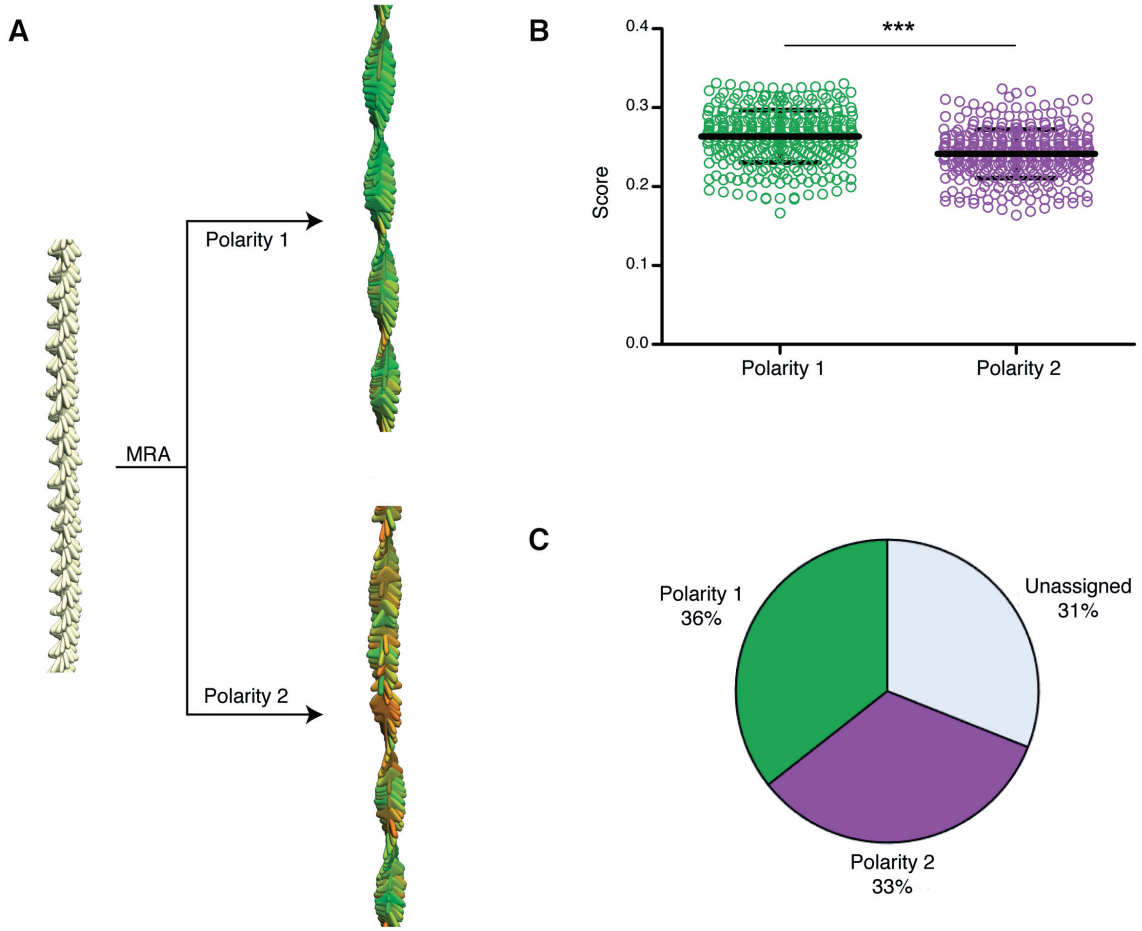

Fig. S7. Workflow for the polarity assessment of the thin filaments imaged by cryo-ET. (A) Multireference alignment ("MRA") procedure applied to one filament with oversampled positions aligned along the z-axis and in-plane randomization represented by yellow arrows (left). Each position is aligned independently against a reference of each polarity (in green and purple, respectively), resulting in refined orientations and scores (high scores, green; low scores, red) (right). Refinement against the green structure ("Polarity 1") leads to uniform helical pattern, whereas alignment against the purple structure ("Polarity 2") yields irregularities in the helical pattern. (B) Corresponding scores obtained for the single filament under each polarity, with the mean and standard deviation indicated. Unpaired Student's t-test revealed significant differences between both polarities (***: $p < 0.001$). (C) Pie chart representing the results of the polarity assignment for the entire dataset of 4,438 thin filaments with $p < 0.05$.

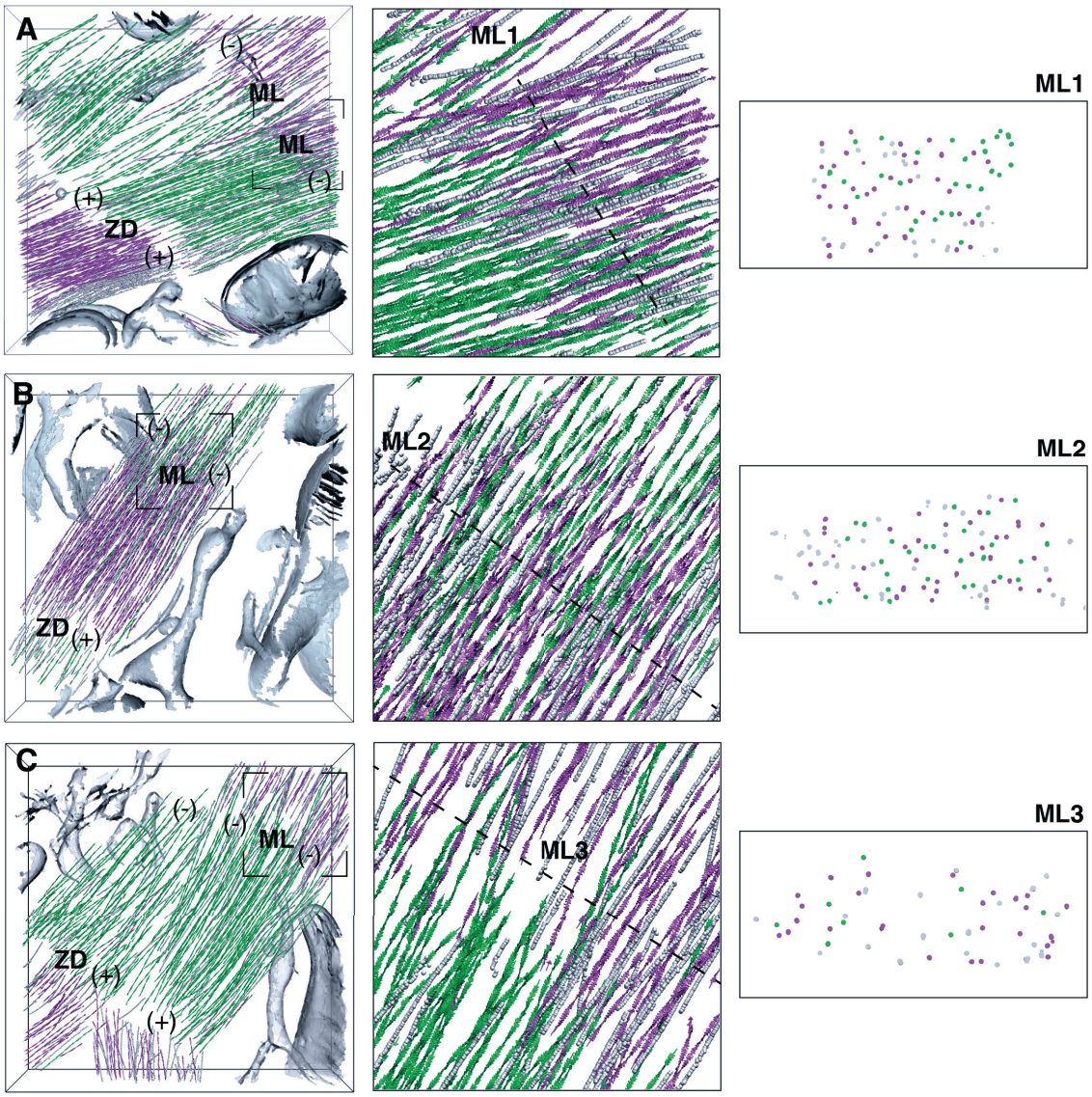

Fig. S8. Polarity assignment and packing of cardiac thin filaments at the center of the sarcomere. (A-C) Same examples as in Fig. 3 showing the unassigned filaments in grey, which correspond to 23% of the filaments in these datasets. Thin filaments with assigned polarity are represented by colored arrows pointing toward the barbed (+) end. ZD, Z-disk; ML, M-line. Insets: Thin filament orientations in the framed M-lines (middle) with their respective cross-sections (right).

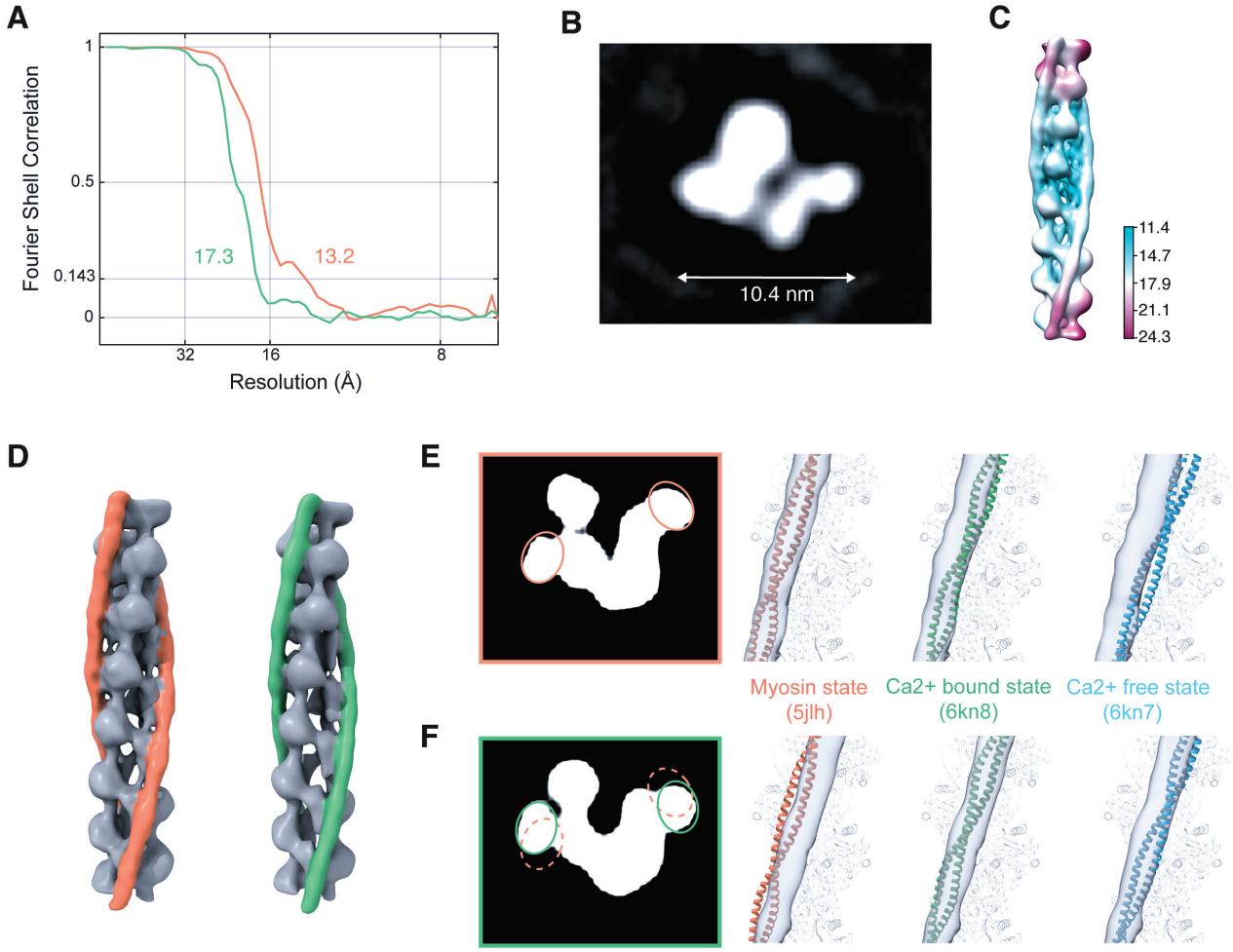

Fig. S9. Resolution and functional state of the native cardiac thin filament structures. (A) Gold-standard FSC plots of the subtomogram averages shown in Fig. 4A (orange curve) and E, middle (green curve). (B) x-y slice through the 13.2 Å map. (C) Local resolution estimation. Due to the averaging procedure, the resolution of the filament is the highest in the central subunits. (D-F) x-y slices through the 13.2 Å (E) and 17.3 Å (F) resolution structures shown in (D), in which the Tpm densities are highlighted in orange and green, respectively, and close up into the fits of the pseudoatomic models in different states into the maps.

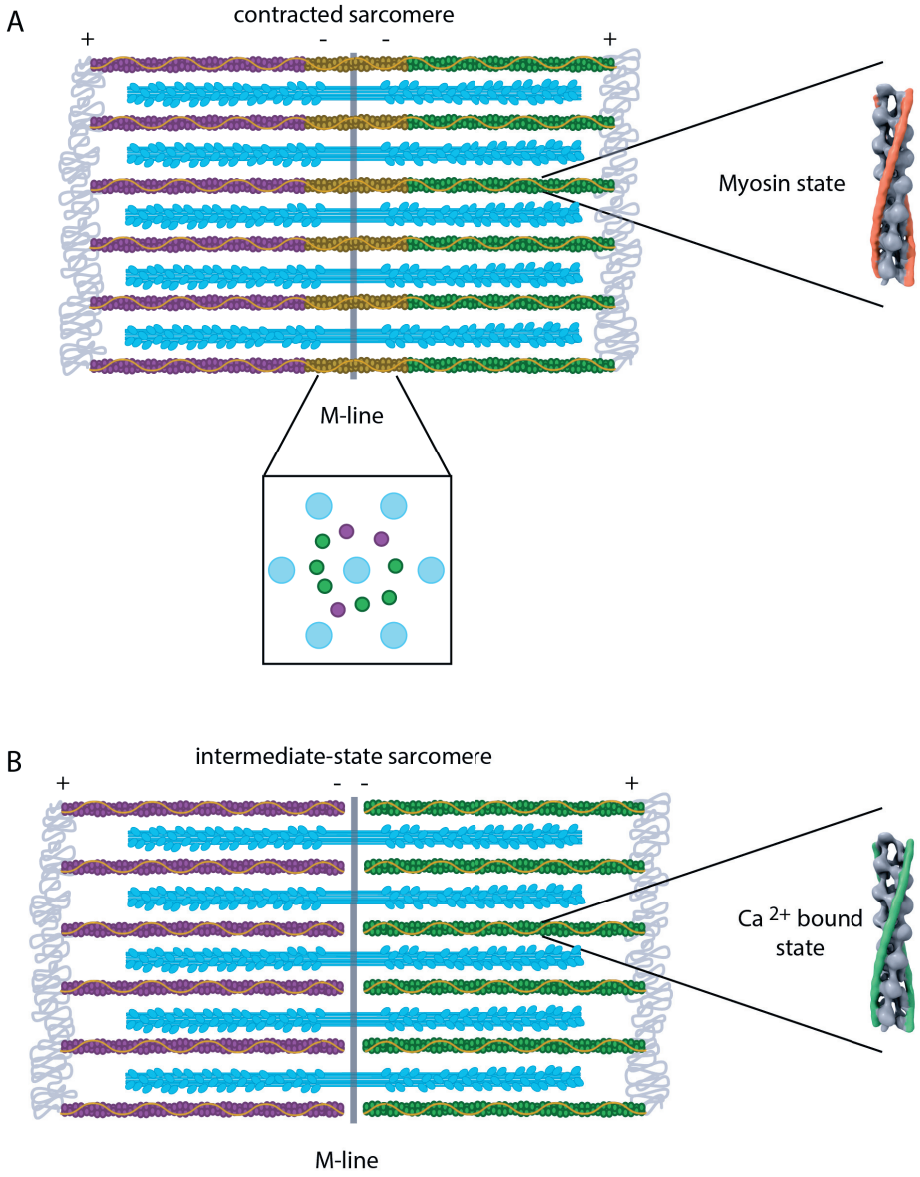

Fig. S10. Thin filament organization during sarcomere contraction. (A) Contracted sarcomeres, in which thin filaments are strongly bound to thick filaments, exhibit an overlap between thin filaments of opposite polarity in the bare zone region. (B) When the actomyosin interaction is weaker, sarcomeres are found in an intermediate state, in which thin filaments of opposite polarity are in close apposition but do not overlap.